UNIVERSITY HAMBURG

DOCTORAL THESIS

Spectroscopy on Copper Enzyme Model Complexes

AUTHOR:

SÖREN BUCHENAU

A thesis submitted in fulfillment of the requirements for the degree of PhD in Physics (Dr. rer. nat.)

at the

University Hamburg
Faculty of Mathematics, Informatics and Natural Sciences
Institute for Nanostructure and Solid-State Science

Hamburg
November 15, 2022

UNIVERSITY HAMBURG

Supervisor: (Gutachter)	Prof. MICHAEL RÜBHAUSEN Prof. SONJA HERRES-PAWLIS
Examination Board: (Prüfungskommission)	Prof. MICHAEL RÜBHAUSEN Prof. SONJA HERRES-PAWLIS Prof. NILS HUSE Prof. DOROTA KOZIEJ Prof. DANIELA PFANNKUCHE
Chairman of Examination Board: (Vorsitzende der Prüfungskommission)	Prof. DANIELA PFANNKUCHE
Date of Examination: (Datum der Disputation)	19.12.2022
Chairman of the Doctoral Committee Physics: (Vorsitzender Fach-Promotionsausschuss Physik)	Prof. WOLFGANG PARAK
Chairman of the Faculty Physics: (Leiter des Fachbereichs Physik)	Prof. GÜNTER SIGL
Dean of the MIN-Faculty: (Dekan der MIN-Fakultät)	Prof. NORBERT RITTER

Declaration of Authorship

Hiermit erkläre ich an Eides statt, dass ich die vorliegende Dissertationsschrift selbst verfasst und keine anderen als die angegebenen Quellen und Hilfsmittel benutzt habe.

I hereby declare upon oath that I have written the present dissertation independently and have not used further resources and aids than those stated in the dissertation.

November 15, 2022

Ort, den | City, date

Unterschrift | Signature

UNIVERSITY HAMBURG

Abstract

Department of Physics
Faculty of Mathematics, Informatics and Natural Sciences
Institute for Nanostructure and Solid-State Science

PhD in Physics

Spectroscopy on Copper Enzyme Model Complexes

by SÖREN BUCHENAU

In this work a variety of inelastic light scattering experiments are conducted to investigate the structure, the function and the structure-function relationship of a multitude of bio-inorganic model complexes. The spectroscopic range spans from from X-ray over deep UV to optical and mid-infrared wavelengths. The experimental setups are custom-designed to the samples and contain different cryo-setups and condensed matter or liquid sample environments. Different complexes were measured and the respective ligands themselves were tested in modified versions to shine light on what affects the properties of the entire complex. While Raman investigations showed characteristic vibrations, the X-ray absorption data was used to fully identify bond lengths and angles that are necessary to relate the structural formation of the complex to its function as a model complex in catalysis. The catalysis itself was monitored with operando Raman spectroscopy and the dynamics of a reaction with substrates was revealed. Investigating modified versions of a complex, suited as a model for entatic state chemistry, lead to a better understanding of the leading factors of the geometric and electronic structure that drive the electron self-exchange rate of entatic state model complexes. It was found that not only minimizing the structure difference $\Delta\tau_4$ is important to raise the electron self-exchange rate, but also optimizing the geometry to not favor either one of the binary options tetrahedral or square-planar. A difference frequency generation setup was successfully installed using many different nonlinear crystals to produce femtosecond mid-infrared laser light to be used as a tool to influence and manipulate the transient structure of the sample. It was successfully tested on experimentally less-challenging condensed matter systems such as a reflectivity probe on a trichalcogenide system and in its destined use in a mid-infrared pump and Raman probe setup on multilayer graphene systems. As such, the road is now paved for selective mid-infrared pump distortion of the low-energy vibrations in the ligand sphere in entatic state complexes and to investigate the influence that these transient modifications of the geometric structure will have on the function of the charge-transfer systems and the interplay of the ligand-metal relationship.

UNIVERSITÄT HAMBURG

Abstract

Fachbereich Physik
Fakultät für Mathematik, Informatik und Naturwissenschaften
Nanostruktur- und Festkörperphysik

Doktor in Physik

Spectroscopy on Copper Enzyme Model Complexes

von SÖREN BUCHENAU

In dieser Arbeit wurden unterschiedliche Experimente der inelastischen Lichtstreuung genutzt, um die Struktur, Funktion und die Struktur-Funktions-Beziehung unterschiedlicher bio-inorganischer Modelkomplexe zu untersuchen. Die Bandbreite von genutzten Wellenlängen reichte dabei von Röntgenstrahlen über UV und optische Wellenlängen hin bis zum mittleren Infrarot Bereich. Die Experimentellen Aufbauten beinhalteten unterschiedliche Cryo-Geräte und unterschiedliche Probenkammern für kondensierte oder flüssige Proben. Von den Komplexproben wurden modifizierte Versionen untersucht, um herauszufinden was genau die Eigenschaften des Komplexes beeinflusst. Während Raman Spektroskopie die charakteristischen Vibrationen der Komplexe messen kann, wurde Röntgenabsorptionsspektroskopie genutzt um die Bindungslängen und Atomabstände sowie Winkel exakt zu messen. Dies erlaubt Aussagen zur Struktur-Funktions-Beziehung des Komplexes in der Katalyse. Die enzymatische Katalyse selbst wurde mit Operando-Raman Spektroskopie live verfolgt und der Ablauf der Substrat-Umsetzung analysiert. Die Untersuchung von modifizierten Modelkomplexen für den entatischen Zustand hat zu neuer Erkenntnis geführt, welche Eigenschaften der geometrischen oder elektronischen Struktur einen größeren Einfluss auf die Elektronen-Selbstaustausch Rate haben. Es stellt sich heraus das nicht nur die Minimierung des Strukturunteschiedsparameters $\Delta\tau_4$ eine Rolle spielt, sondern auch das die Struktur keine der beiden binären Optionen von tetraedrisch oder quadratisch-planar bevorzugen sollte. Eine Difference-Frequency-Generation Einheit wurde erfolgreich installiert, in der mehrere nichtlineare Kristalle genutzt werden um femtosekunden-schnelle infrarote Laserpulse zu erzeugen, mit denen transiente Strukturveränderungen in der Probe erzeugt werden können. Erste Tests an experimenell weniger anspruchsvolleren Festkörperproben als Reflektivitätsprobe an Trichalcogenid-Systemen und als Infrarot-Pump mit einem Raman-Probe System an Graphen Proben waren erfolgreich. Es ist nun möglich die selektive Infrarotanregung der niederenergetischen Ligandenmoden zu nutzen, um den Einfluss den diese transienten Veränderungen der geometrischen und elektronischen Struktur auf die Funktion als Ladungs-Transfer System haben und die Wechselwirkung von Metallzentrum und Ligand zu untersuchen.

Acknowledgements

First, I want to thank Prof. Michael Rübhausen for the very productive and long-lasting professional support. After formally joining your research group in 2017 for my master thesis, it has now been more than five years that you directly, not only in form of lectures, supported my scientific career and I could have not imagined a better supervisor during this time.

I want to thank Dr. Benjamin Grimm-Lebsanft for all the support and cheering up during hard times over all those years. All discussions on political stuff, animal-cruelty free snacks at the beamline and highly optimized pizza manufacturing will never be forgotten!

I want to thank Sarah Scheitz for the very friendly and long-lasting relationship as colleagues and friends, starting from the trip to the USA at the end of 2018, while traveling was still possibility. I have always enjoyed the time with you and I would not mind sharing an office with you until retirement!

I want to thank Ferdinand Otto for unconditional support, especially by occasionally distracting me from all the worries and problems that have pushed me down during this project, which turns out to be a surprisingly common feature during a PhD project. If I could be only half as useful to your endeavors as you are to me, I would certainly be happy about that. We became friends as undergrads, which is now like . . . *many* years ago and I hope and am absolutely sure it will stay that way!

I want to thank Dr. Lewis Akinsinde, who made it over the PhD finish line bit earlier than me. You are the person I have worked together for longest time, since we worked together for Kornelius Nielsch and I have enjoyed the time with you over all these years!

I want to thank Dr. Tomke Glier for friendly and long-lasting work together, starting from doing homework in a team to conducting research side by side in the same research group over the years.

I want to thank Dr. Melissa Teubner not only for enlightening me on the various meanings of different pronunciation of german words and its meaning, but also for being the best lab partner one can imagine. I have always enjoyed the time together with you. Except of course when I again did not clean the glass cuvette to a real-chemists high standards.

I want to thank Stephanie Baer for relentless support on the bureaucracy front. I am still awaiting a dedicated talk explaining all the intricacies of the german bureaucratic university system, hiding away outside my sight in between my daily work and monthly paycheck.

I want to thank Christian Nweze for all the fun, productive and interesting discussions we had sharing the office over all this time.

Finally, I want to thank all many cooperation partners, students and other colleagues who have helped and supported me along the way - I would have not be able to do it without you!

Contents

List of Figures

List of Abbreviations

AGS	Silver Thiogallate
BEC	Bose-Einstein Condensation
DESY	Deutsches Elektronen-Synchrotron
DFG	Difference Frequency Generation
DFT	Density Functional Theory
EXAFS	Extended X-Ray Absorption Fine Structure
FTIR	Fourier-Transform Infrared
IMT	Insulator-to-Metal Transition
LMCT	Ligand to Metal Charge-Transfer
NIR	Near-Infrared
MMO	Methane Monooxygenase
MIR	Mid-Infrared
MIT	Metal-to-Insulator Transition
PHM	Peptidylglycine α-hydroxylating Monooxygenase
RMP	Raper-Mason Pathway
SHG	Second Harmonic Generation
SFE	Sum Frequency Generation
QPM	Quasi-Phase-Matching
WLC	White-Light Continuum
YAG	Yttrium Aluminium Garnet
XAS	X-Ray Absorption Spectroscopy
XANES	X-Ray Absorption Near Edge Structure
XRD	X-Ray Diffraction

Physical Constants

Speed of Light	$c_0 = 2.997\,924\,58 \times 10^{8}\,\mathrm{m\,s^{-1}}$
Elementary Charge	$e = 1.602\,176\,634 \times 10^{-19}\,\mathrm{C}$
Vacuum Permittivity	$\epsilon_0 = 8.854\,187\,812\,8 \times 10^{-12}\,\mathrm{Fm^{-2}}$
Planck Constant	$\hbar = 1.054\,571\,817 \times 10^{-34}\,\mathrm{J\,s}$
Boltzmann Constant	$k_\mathrm{B} = 1.380\,649 \times 10^{-23}\,\mathrm{J\,K^{-1}}$
Electron Mass	$m_\mathrm{e} = 9.109\,383\,701\,5 \times 10^{-31}\,\mathrm{kg}$
Magnetic Vacuum Permeability	$\mu_0 = 1.256\,637\,061\,4 \times 10^{-6}\,\mathrm{NA^{-2}}$

List of Symbols

A	Complex Amplitude	Vm^{-1}
e	Elementary Charge	C
E	Electric Field	Vm^{-1}
H	Hamiltonian	J
I	Intensity	Wm^{-2}
k	Wave Vector	m^{-1}
M	Dipole	Cm
n	Refractive Index	dimensionless
P	Polarization	$\mathrm{Cm}^{-}2$
q	Wave Vector	m^{-1}
Q	Normal Coordinate	m
r	Distance	m
t	Time	s
T	Temperature	K
α	Polarizability	$\mathrm{Cm}^2\mathrm{V}^{-1}$
γ	Damping	s^{-1}
Γ	Width	m^{-1}
Δ	Generic Difference	
λ	Wavelength	m
μ	Absorption	m^{-1}
ν	Ordinary Frequency	s^{-1}
τ	Time	s
τ_4	Geometric Configuration	Degree
θ	Angle	
$\theta^{\pm}$	Eigenfunction	
χ	EXAFS Signal	J
Ψ	Wave Function	
ω	Angular Frequency	s^{-1}
∇_t	Time Derivative	

1 Introduction

1.1 Inorganic Copper Complexes

Organic enzymes containing metal ions are highly prevalent in nature in both animals and plants,[1] and catalyze a variety of different chemical reactions. Although the metal atom makes up for almost nothing of the either the mass or the volume of the entire enzyme, it is of particular interest to the function the biomolecule. While several shells and anchors of organic ligands are helpful in shielding relevant parts against unwanted outside influences or play a role in stabilizing the molecule, the metal atoms are generally associated with the active sites, which lie at the heart of the process of catalyzing chemical reactions. The way in which this is realized, is that after a small molecule has bonded to the active site of an enzyme, its electronic structure, i.e. the electronic levels of the constituent atoms, are modulated by the enzyme. The energetic barrier for a structural change is lowered and the respective process is now more probable. From the fact that the change in electronic density is the functionality of an enzyme, it is directly intuitive, that the role of the metal atom is set to such a task: Metal atoms, such as Fe or Cu, are transition metals with many electrons and only part-filled outer shells. This stands in stark contrast to the organic atoms, that make up most of the volume of an enzyme and which do not contain the same richness of complicated electronic shells and potential modulations. Those organic atoms, especially the ones close to the metal atom, are more relevant in gauging the effectiveness and selectivity of the biomolecule towards some chemical process in different ways. Different ligands can slightly vary the electronic density in direct proximity to the metal, they can bridge several metal atoms in one cluster, allowing for cooperative effects. With their steric interaction, the ligands can bring the entire molecule in a geometrically pre-distorted state of higher energetization or simply take up electronic charges, that are excited from the metal atom after being pumped with photons etc. The complexity that arises from both, the electronically open-shell inorganic transition metal atoms together with the structurally more diverse organic ligands, opens up a many opportunities for scientific investigation.

Examples for such enzymes are tyrosinase or methane monooxygenase (MMO). **Tyrosinase** can be found in animals, plants, fungi and various prokaryotes.[2] It is an enzyme that controls the synthesis of melanin-type pigments[3] from tyrosine, acetate or catechol *via* the Raper-Mason pathway (RMP). Although first published in 1927,[4] the complicated process containing hydroxylation of monophenols and oxidation of diphenols with subsequent or simultaneous polymerization is not fully understood[5] and still under investigation. The possibility of converting mono- and diphenols to their respective quinones, which can additionally spontaneously react with amino groups, i.e. cross-linking proteins, leads to several applications of biological tyrosinase, e.g. for the production of dyes, biosensors, bioremediation of wastewater etc.[6]

Methane monooxygenases are enzymes that have the remarkable property to activate comparably inert C-H bonds in hydrocarbons.[7] In their most prominent form, they are either membrane-bound and copper-containing particulate MMO

(pMMO) [8] or cytosolic iron-containing soluble MMO (sMMO) [9]. They can be found in methanotropic bacteria, which use the MMO to oxidize methane to methanol. The ubiquitous methane is a waste-product from the generation of biomass by methanogens, which live in aerobic condition and produce 200-250 million metric tons annually. [7] The process of converting methane to methanol is of great scientific interest because methane is e.g. a comparably potent greenhouse gas. Additionally, methane makes up for approximately 70 to 90 % of natural gas, which is destined to become a transitional fuel for 21st century. [10]. The methane molecule is made of strong C-H bonds with a binding energy of 425 kJ/mol, it contains no functional groups or magnetic moments and its geometry is a non-distorted tetrahedron. Synthetic conversion of this very stable small molecule on an industrial scale is achieved by using excessive temperatures. These higher temperature regimes lead to several unwanted side products, which is generally reduced by additionally using catalysts to enhance the selectivity. [11]

We have so far illustrated, the powerful and multifaceted set of possibilities which are realized in biological inorganic metal enzymes and have also touched on processes that those enzymes can catalyze, which humans have yet found a way to master at ambient conditions. Those chemical processes are made possible, due to the highly sophisticated interactions of the organic ligands, their nature and geometry, and the transition metal atoms manifold of electronic states and various options to be covalently linked to the respective ligands. Understanding the rich phenomena that drive their catalytic activity is first and foremost of great interest of basic research. Additionally, a better understanding of the inner workings of such biomolecules opens up possibilities for enhancing and creating new industrial catalysts that either produce more of the desired product or reduce the output greenhouse gas emissions. The apparent complexity of biological enzymes containing hundreds or thousands of atoms, associated to individual amino acids, each linked in various chains in a specific order, folded following a strict pattern, renders the deliberate synthesis and targeted modification in a lab seemingly impossible. However, since we are mostly interested in only a tiny part of the enzymatic function, the active site of the inorganic complexes, it is possible to use synthetic inorganic copper model complexes. Organic ligands are synthesized, which can be activated on demand with e.g. oxygen to form a model complex. Having our sample of interest reduced to almost only the chemically active part, brings with it several experimental complications, but also advantages. Removing the substantial organic layers and reducing the steric protection of the active site to its bare minimum leads to a higher sensitivity to outside influences. Since the chemically active part is more exposed, special experimental steps have to be taken to ensure no unwanted contact with atmospheric oxygen or water. Additionally, the model complexes can require temperatures of -80 °C to remain stable for durations that allow for measurements. However, it is easier to slightly vary parameters of the final model complex, e.g., substituting a functional group to a certain ligand and investigating the consequences is easier in a small model complex than it would be otherwise. Additionally, reducing the sizable organic shell does not only yield the need for more sophisticated experimental techniques, but it also gives a more clear picture of the data, because it can be understood as a removal of background from the signal.

In the following parts, the two inorganic copper model complexes mimicking tyrosinase and MMO will be introduced together with the concept of what is called an *Entatic State*.

1.1.1 Tyrosinase Model Complex

A brief review of the history of tyrosinase model complexes and its their development is given in this chapter.

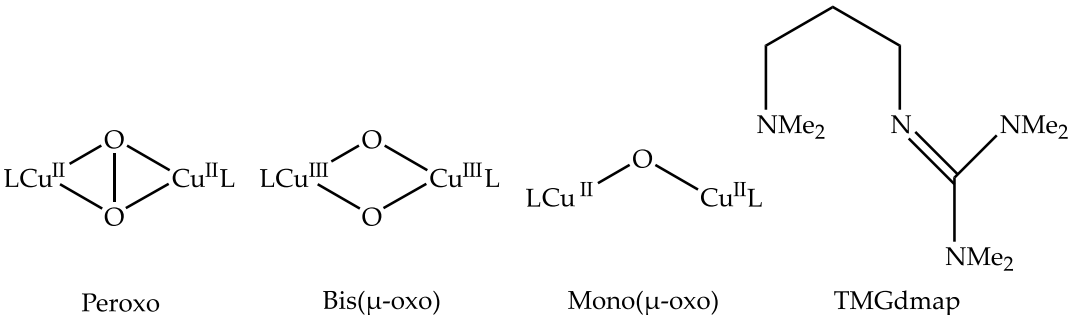

FIGURE 1.1: Various Cu_2O_2 and Cu_2O binding motifs are depicted together with the exemplary hybrid guanidine-amine ligand TMGdmap. The L stands symbolically for a remaining ligand.

Peroxo System
The first synthetic model complex incorporating copper, was reported by Karlin et. al in 1984.[12] They showed reversible copper-oxygen binding at -80 °C, which was the starting point of copper inorganic model systems. Tuczek et al. reported in 2000 on the first reversible model system at -80 °C and its hydroxylation of a phenolate to the corresponding catechol at -60 °C.[13] One year later, Itoh et al. conducted the first mechanistic study investigating the kinetics and found, similar to biological tyrosinase, indications of an electrophilic aromatic substitution.[14] Casella and Bubacco reported on the effects of the position of the functional group of the phenolic substrate for hydroxylation in 2002.[15] They investigated biological tyrosinase and observed inhibiting effects for the ortho position, a slow reaction for the meta position and a fast reaction for the para position. The bonding of the substrate to the complex, forming a copper-ligand-phenolate molecule, is subsequently followed by the oxygen activation, as shown by Tuczek et al. in 2010.[16] In 2012, major improvements towards the conversion to the catechol were reported by Stack et al., who achieved with two of their complexes a ratio of catechol to quinone from 50 % to 10 % and 70 % to 0 %.[17] Herres-Pawlis et al. were able to realize a conversion rate to catechol with 95 % and 90 % by using two different substrates in 2013.[18] They did not find any quinone side products. Two years later, the same group reported the hydroxylation rate of their model complex at -78 °C to be one fifth of the rate of natural tyrosinase at ambient temperatures.[19]

Bis(μ-oxo) System
Solomon and Stack et al.[20] reported in 2005 on a ligand, which after oxygenation forms a peroxo species at -120 °C. After adding the phenolate substrate, they observe the conversion to a bis(μ-oxo)[21] species before converting the phenolate to its respective catecholate and quinone with a 1:1 ratio. Additionally, Stack et al.[22] measured the formation of a transient superoxo species preceding the formation of the bis(μ-oxo) species by using a comparably slow ligand at -80 °C. In 2009, Herres-Pawlis et al.[23] published an article containing ligands which consist of amine or guanidine as functional groups and one propylene spacer each. They investigated

the hydroxylation of complexes with the organic ligands TMGdmap (hybrid ligand with guanidine and amine, see Fig. 1.1), btmgp (two guanidine groups) and TMPD (two amine groups), and found that the decreased outer-sphere oxidative strength and the higher phenolate accessibility to the reactive Cu_2O_2 core, are both related to a higher phenolate hydroxylation reactivity seen in the TMGdmap complex. The guanidine-only complex with btmgp led to no reactivity due to the lack of accessibility to the core. The amine-only complex with TMPD led to C-C coupled bisphenol products because of the one-electron outer-sphere oxidation strength, which converts the phenol *via* a proton coupled electron transfer to a phenoxyl radical, which then dimerizes. The hybrid variant TMGdmap appeared to attenuate the C-C radical coupling mechanism enough, while still allowing for a sufficient accessibility of the substrate to the chemically active Cu_2O_2 core. With that system, they achieved a catecholate to quinone ratio of 95 % to 5 %. Six years later, in 2015, the same group reported [24] on new hybrid guanidine-amine ligands. A conventional amine group is linked, *via* another propylene spacer, to a modified guanidine unit for three different ligands each. After oxygenation, all complexes also formed the bis(μ-oxo) binding motif but did not show superior hydroxylation capacities.

1.1.2 Methane Monooxygenase Model Complex

The challenging conversion of the inert methane to methanol was first reported in a zeolite bis(μ-oxo) model complex in 2005 by Schoonheydt et al. [25] at slightly elevated temperatures of 125 °C. More recent reviews on the zeolite inorganic model complex, summarizing the reaction mechanism and reactive intermediates, are published by Schoonheydt and Solomon et al. [26, 27] However, theoretical studies did show that replacing the zeolitic silicate ligand with protein ligands would retain the reactivity towards methane. [28] In general, even after many studies the reactive copper species, the active center [29–31] and the exact mechanism are still under debate. [30, 32, 33] Since that is the case, different CuO motifs have been proposed as MMO model complexes, which can be grouped in (i) mononuclear copper complexes, [29, 30, 34, 35] (ii) dinuclear copper intermediates [36–38] and (iii) trinuclear copper cluster. [39, 40]

1.1.3 Entatic State Model Complex

Enzymes in nature use copper in their active sites, because their large window of reduction potential [41] makes it possible for them to interact with many different electron transfer partners. The redox potential of the Cu^{II}/Cu^{I} redox couple is affected by the geometric constraints due to the direct ligands, the type of donor atoms and additionally by second-coordination-sphere effects. Cu^{I} as a system with a d^{10} shell configuration, generally forms a tetrahedral coordination with four adjacent atoms. In contrast, Cu^{II} has a d^{9} configuration and tends to form either six-coordinate distorted octahedrons or five-coordinate square-pyramidal or trigonal-bipyramidal geometries. There is no expectation that Cu^{II} should show a strong energetic preference for a certain geometry and the dynamic Jahn-Teller distortion in Cu^{II} gives it some plasticity. [42] Literature reports indeed show that from approximately 100 biological copper protein complexes investigated, Cu^{II} show a greater variety of geometries. [43] Note here, that the prevalence of only Cu^{II} geometries in square-planar configuration, changes to almost only Cu^{I} centers for the tetrahedral configuration. Although there is no need for association or dissociation of entire bonds for the configurational change of the geometry, relocation and twisting of bonds and bond angles is

still necessary.[42] The required reorganization energy can be lowered significantly e.g. by the constrained coordination of the ligands.[43] The concept of pre-energized states in metalloproteins and transition metal compounds was introduced in the 1950s.[44] The term *Entatic State* was described in 1968 by Vallee and Williams[45], who argued that an enzyme can be *poised for catalytic action in absence of substrate*. Since then, it was a controversial topic whether this pre-energetization stems from the simple geometric strain, induced onto the active site by the protein matrix or rather an electronic entatic state. Rorabacher et al. reported in 2007 on a copper complex, in which both oxidation states are very similar in structure. They report very high electron self-exchange rate and summarize their results as exemplary for a true geometric entatic state.[46] In modern terms, the entatic state is put into the form of an *energetization due to a misfit between ligands and metal ions*.[44, 47] In Fig. 1.2, an exemplary plot of the energetization vs. the geometric configuration for a copper atom with four nitrogen donors that form a square-planar configuration at $\tau_4 = 0$ is shown. When distorting the configuration over a peak energy at the seesaw-motif at

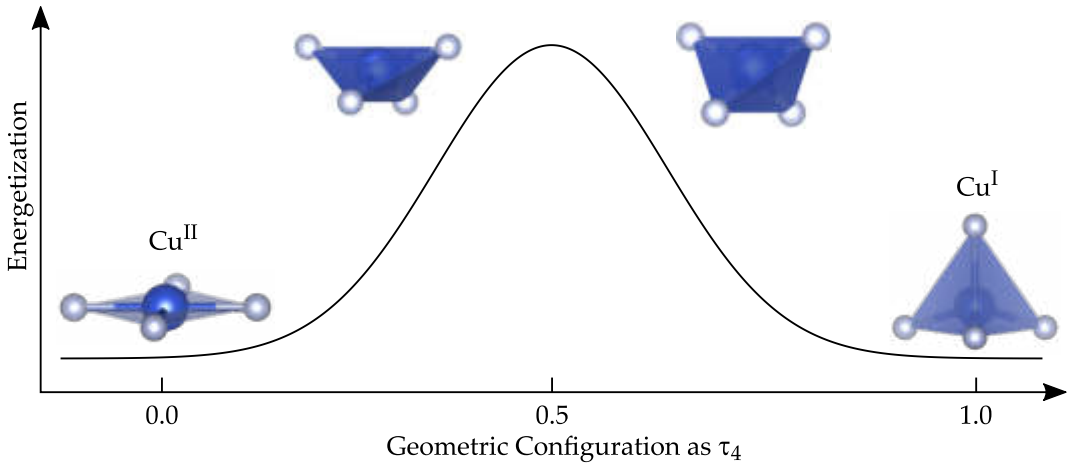

FIGURE 1.2: A schematic depiction of the entatic state principle. The copper centers (shown in blue) are coordinated to four donor nitrogen atoms (shown in grey). On either side, we see the archetypal square-planar or tetrahedral coordination. The ligands, omitted here for clarity, can constrain the geometry, such that the transformation from one state to the other requires less energy. In this simplified picture, the square-planar (D_{4h}) left side correlates to Cu^{II} and the tetrahedral (T_d) right side to Cu^{I}. The configuration at the peak is referred to as the seesaw (C_{2v}) geometry. The x-axis gives the four coordinate geometry index τ_4.

$\tau_4 = 0.5$, it falls back into an energetic minimum at the tetrahedral configuration at $\tau_4 = 1.0$. The quantification of the geometry configuration τ_4 is a clever and simple method by L. Yang et al.[48], in which we take the two largest $Cu-N_2$ angles α, β in the four-coordinate species and calculate $\tau_4 = 360° - (\alpha + \beta)/141°$ to have a scale from 0.0 to 1.0, for e.g. four-coordinate copper complexes. Note that in principle, Cu^{I} complexes can also be stabilized for values of $\tau_4 < 0.5$ and Cu^{II} complexes can also be stabilized for values of $\tau_4 > 0.5$.

1.2 Mid-Infrared-Pump and Raman-Probe Spectroscopy

Mid-infrared (MIR) light probes the low-energy excitation of a given sample. If an IR laser is not used in practical applications for its precision and power density, such as a laser cutting tool during surgery [49] or as a countermeasure in heat seeking missile defense, [50] the scientific purpose of MIR pump excitation can roughly be categorized into (i) probing localized organic vibrations and (ii) probing the effect of delocalized lattice vibrations over a molecule or solid-state crystal. Measuring the localized modes of different chemical functional groups, also called *group frequencies*, is commonly done to identify chemical species. The mid-infrared spectrum ranging from 2.5-12 µm is also referred to as the *fingerprint region*. Conducting spectroscopy experiments in the IR band to find signatures of certain molecular species is done e.g. in airborne trace gas analysis [51] or the detection of peroxide- and nitro-base explosives. [52] When MIR wavelengths are used to investigate material properties of crystals, they excite vibrations containing heavier nuclei that are strongly delocalized. While the regio-specificity is lost, one yields statistical information averaged over a wide range of the crystal structure.

The laser light at MIR wavelengths, used for these absorption and transmission experiments can additionally be given a different role in a pump-probe setup. Every molecule and crystal is a complicated construct of positive and negative charges, arranged in a certain way, oscillating around specific equilibrium position and every component *experiences* different short-range and long-range forces. This complicated set of interactions is transiently modified when lattice vibrations are excited by an MIR pump pulse and the modification and its implications can be probed by an optical probe pulse generating Raman scattered light.

1.2.1 Probing the Entatic State

Guanidine-stabilized model complexes have been synthesized and analyzed extensively by the group of Sonja Herres-Pawlis [47, 53, 54] and led to the result that [55] the structure of two guanidine-quinoline copper complexes is virtually similar, except for the oxidation state. A reversible electron transfer at 0.33 V connects both structures and the transient intermediate state of that electronic transition is accessible through vibrational modes, which are coupled to metal-to-ligand charge-transfer (MLCT) and ligand-to-metal charge-transfer (LMCT) states. In a subsequent work, [56] these charge-transfer processes were further studied by experiments including UV pump excitation which lead to a deeper understanding of the timescales of the intermediate electronic states. The drawback of pumping at optical or UV wavelengths is that the induced electronic transitions contain a high amount of energy and that allows for a myriad of different cascading excitation and relaxation mechanisms. To enhance the microscopic understanding of the interplay of the ligand modes, MIR wavelengths, which selectively drive individual ligand vibrations, can be employed in combination with a Raman probe setup. The negative drawback of complicated sequential interactions can be suppressed and the transient change in structure of the complex due to MIR pumping can be related to its function.

1.2.2 Low-Energy Excitations

When employing MIR wavelengths in condensed matter science, collective modes can be coherently investigated by probing low-energy resonances in the meV regime. [57] While optical light mostly interacts with valence electrons, MIR light gives

direct access to excitations such as lattice vibrations, rotations, spin precession and internal excitations of bound electron-hole pairs. [58] With this, it is possible to investigate many interesting phase transitions and phenomena, which occur in this order of magnitude of energy, such as photoinduced insulator-to-metal transitions [59] or optical melting of magnetic order. [60] This type of spectroscopy allows for fast and low-dissipation optical research and control of solid-state materials. When the pumped vibrational mode is excited in resonance, it is possible that the atomic deflection around the equilibrium position is so strong that anharmonic parts of the potential well can become relevant. [61] As will be shown the graphene system, the MIR pumping can increase the anharmonic coupling between two vibrations, leading to a lifting of a phononic degeneracy and by that induce order in the underlying crystal system.

2 Theory on Inelastic Scattering

In this work, we deal with different types of light, which will interact in different ways with varying types of samples. However, one consistent property throughout this thesis is the use of inelastic scattering, meaning the incident and scattered electromagnetic radiation will be of different energy. Knowing the energy of the incoming light from our light source, measuring the outgoing light and calculating the difference, allows us to draw information about the sample in question. With the advent of laser systems in the '60s[62] and dedicated synchrotron facilities in the '80s[63], a huge option of frequencies became available. The possibility of altering any sample by putting the sample in different environments, e.g. temperature, solvents etc., enriches the vast landscape of opportunities to increase the understanding even further. To start, we begin by introducing the Raman effect as one inelastic phenomenon of matter and light interaction.

2.1 Raman Theory

The inelastic scattering of photons was first predicted by Smekal et al.[64] in 1923. For the experimental observation, C. V. Raman was awarded the nobel prize in 1930. After several decades of the observation and understanding of elastic scattering of light by most notably J. Tyndall, J. C. Maxwell and J. W. S. Rayleigh, C. V. Raman reported in his landmark publication from 1928[65] on the first inelastic light scattering experiment. He concluded that at this point the world was *at the fringe of a fascinating new region of experimental research which promises to throw light on diverse problems relating to radiation and wave-theory, X-ray optics, atomic and molecular spectra, fluorescence and scattering, thermodynamics and chemistry. It all remains to be worked out*.

The inelastic light scattering is a process in which an incident photon with a certain amount of energy gets annihilated and a scattered photon with a different amount of energy is created. The scattering is mediated by the interaction of the photons with the electrons. With the mass of the electron m and the momentum $\boldsymbol{p}$ we yield the energy

$$H_0 = \frac{\boldsymbol{p}^2}{2m}. \tag{2.1}$$

We use the Coulomb gauge fixing condition $\nabla \boldsymbol{A} = 0$[66] for the vector field $\boldsymbol{A}$ to rewrite the canonical momentum with

$$\widetilde{\boldsymbol{p}}^2 \to \boldsymbol{p} - \frac{e}{c} \cdot \boldsymbol{A} \tag{2.2}$$

with the e as the elementary charge and c as the speed of light. We then find for the energy[67]

$$\frac{\widetilde{\boldsymbol{p}}^2}{2m} \to \underbrace{\frac{\boldsymbol{p}^2}{2m}}_{H_0} \underbrace{- \frac{e}{mc} \cdot [\boldsymbol{p}\boldsymbol{A} + \boldsymbol{A}\boldsymbol{p}]}_{H_{pA}} + \underbrace{\frac{1}{2m}\left(\frac{e}{c}\right)^2 \cdot \boldsymbol{A}^2}_{H_{A^2}}. \tag{2.3}$$

The energy of the interacting system is given as a superposition of the unperturbed Hamiltonian H_0 and the perturbed Hamiltonian H_{int}

$$H = H_0 + H_{\text{int}} \tag{2.4}$$
$$= H_0 + H_{pA} + H_{A^2}. \tag{2.5}$$

The H_{A^2} term in eq. 2.3 delivers the non-resonant contribution to the inelastic light scattering, while the H_{pA} term in eq. 2.3 is responsible for the resonant contribution. Resonant enhancement of the signal occurs when the excitation frequency of the incident light matches the energy difference between some initial and intermediate state of the system and can be calculated in second-order perturbation theory using H_{pA}.

The resonant H_{pA} term and the non-resonant H_{A^2} term in eq. 2.3 can be derived using the Feynman diagrams shown in Fig. 2.1 (a) and (b). In Fig. 2.1 (a) the incident light (wavy lines) couples *via* an interband transition to the phononic system *via* the electron-phonon vertex (circle) to excite a phonon (double line). The whole process is described as a four-photons Green function.[68, 69] Going from the top left to bottom right represents the Stokes process, in which one quantum of vibration is excited in the system while the photon gets scattered with a lower energy corresponding to the phonons energy. Going from the top right to the bottom left represents the anti-Stokes process in which one quantum of vibration is destroyed and transferred to the scattered photon. The non-resonant process shown in Fig. 2.1 (b) shows the two polarization bubbles of the free electrons, which screen the otherwise resonant H_{pA} interaction. This contribution, although relevant for Raman scattering in e.g. metals or superconductors, is negligible here and we focus on the diagram in Fig. 2.1 (a).

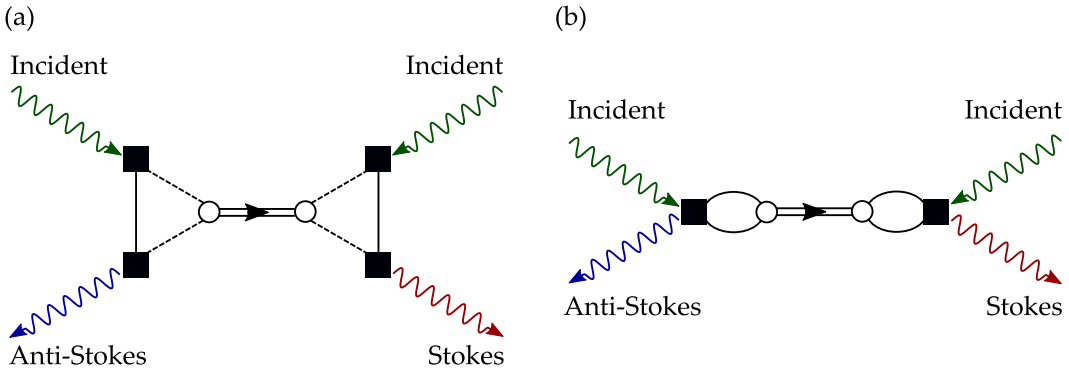

FIGURE 2.1: Feynman diagrams showing the (a) resonant contribution and (b) the non-resonant contribution to the Raman signal. The colors indicate energies, with blue lines representing a higher and red lines a lower energy compared to the green lines. The meaning of each pictorial component is given in Tab. 2.1.

In order to derive the expression for the scattering intensity we need to evaluate the imaginary part of the response function as

$$I(\omega) = -\text{Im}\left[\mathcal{R}(\omega)\right] \cdot \eta(\omega, T, \Omega) \tag{2.6}$$

with I as the collected intensity, $\mathcal{R}$ as the Raman response function and $\eta(\omega, T, \Omega)$ as a hybrid-correction factor that accounts for both, the thermal distribution of occupied vibrational levels *via* the Bose factor and for the effective scattering volume,

TABLE 2.1: Symbolic representations for the Feynman diagram.

	Meaning		Meaning
∿∿	Photon Propagator	——	Hole in Valence Band
═══	Phonon Propagator	-------	Electron in Conduction Band
○	Electron-Phonon	■	Photon-Electron
⟲	Polarization-Bubble		

which depends on the solid angle Ω subtended by the spectrometer. We write the photon-electron vertex for the resonant case as T_{pA} and the electron-phonon coupling vertex as g. The electronic interaction is given by the electric susceptibility χ as

$$\chi_{\text{el}} = \pi_{\text{im}} + \pi_{\text{re}} = -i\frac{\delta}{\delta^2 + (\omega - \omega_{\text{res}})^2} + \frac{\omega - \omega_{\text{res}}}{\delta^2 + (\omega - \omega_{\text{res}})^2} \tag{2.7}$$

$$\approx \frac{1}{\omega_{\text{res}}} \tag{2.8}$$

with δ as a width parameter and $\omega_{\text{res}} = \omega_r - \omega_i \pm \hbar\omega_0 \approx \omega_r - \omega_i$, since the phonon energy $\hbar\omega_0$ is orders of magnitude smaller than the resonance energy $\hbar\omega_{\text{res}}$, i.e. the incident laser energy. We use δ for the width to imply a typical sharp interband transition profile. Considering further that the resonance energy ω_{res} during the phonon-excitation process is large, we see that the electronic susceptibility couples to the phonon only by its real part, thus satisfying eq. 2.8. The phonon propagator (double line) is given as the Green function that solves the equation of motion of a phonon. We assume linear force constants, a damping factor γ and a resonance or natural frequency ω_0 and write the equation of motion of a damped harmonic oscillator as

$$\frac{\mathrm{d}^2}{\mathrm{dt}^2}x(t) + \gamma\frac{\mathrm{d}}{\mathrm{dt}}x(t) + \omega_0^2 x(t) = 0 \tag{2.9}$$

$$\underbrace{\left[\frac{\mathrm{d}^2}{\mathrm{dt}^2} + \gamma\frac{\mathrm{d}}{\mathrm{dt}} + \omega_0^2\right]}_{\widehat{L}} \cdot x(t) = 0. \tag{2.10}$$

Instead of solving the differential equation $\widehat{L} \cdot x = f$, with a generic function f, we can also solve the integral equation $x = Gf$, where G represents the Green function and can be understood symbolically as an *inverted* operator. It is defined by

$$\widehat{L}(t) \cdot G(t) = \delta(t) \tag{2.11}$$

in which the Dirac delta distribution is introduced as

$$\delta(t) = \begin{cases} +\infty & t = 0 \\ 0 & t \neq 0 \end{cases} \tag{2.12}$$

$$\int_{-\infty}^{\infty} \delta(t)\mathrm{d}t = 1 \tag{2.13}$$

$$\mathcal{F}[\delta(t)] = \delta(\omega) \stackrel{!}{=} 1. \tag{2.14}$$

We express the propagator G and the Dirac delta distribution δ by their inverse Fourier transforms and rewrite eq. 2.11 as

$$\underbrace{\left[\frac{\mathrm{d}^2}{\mathrm{d}t^2} + \gamma\frac{\mathrm{d}}{\mathrm{d}t} + \omega_0^2\right]}_{\widehat{L}(t)} \cdot \underbrace{\frac{1}{\sqrt{2\pi}}\int G(\omega)\mathrm{e}^{i\omega t}\mathrm{d}\omega}_{G(t)} = \underbrace{\frac{1}{\sqrt{2\pi}}\int \delta(\omega)\mathrm{e}^{i\omega t}\mathrm{d}\omega}_{\delta(t)}. \tag{2.15}$$

After applying the operator $\widehat{L}(t)$ to the exponential factor $\mathrm{e}^{i\omega t}$ and canceling out factors on each side, we find

$$\int G(\omega)\left[\omega_0^2 - \omega^2 + i\gamma\omega\right]\mathrm{d}\omega = \int 1\mathrm{d}\omega \tag{2.16}$$

which directly yields

$$G(\omega) = \frac{1}{\omega_0^2 - \omega^2 + i\gamma\omega} \tag{2.17}$$

$$= -i \cdot \frac{\gamma\omega}{(\omega_0^2 - \omega^2)^2 + (\gamma\omega^2)} + \frac{\omega_0^2 - \omega^2}{(\omega_0^2 - \omega^2)^2 + (\gamma\omega)^2}. \tag{2.18}$$

We collect all the factors of the response function and calculate

$$-\mathrm{Im}\left[\mathcal{R}(\omega)\right] = -\mathrm{Im}\left[(iT_{pA})^4 \cdot (ig)^2 \cdot \chi_{\mathrm{el}}^2 \cdot G(w)\right] \tag{2.19}$$

$$= -\mathrm{Im}\left[(iT_{pA})^4 \cdot (ig)^2 \cdot \frac{1}{\omega_{\mathrm{res}}^2} \cdot \frac{i\gamma\omega}{(\omega_0^2 - \omega^2)^2 + (\gamma\omega)^2}\right] \tag{2.20}$$

$$= +\mathrm{Im}\left[i \cdot T_{pA}^4 \cdot g^2 \cdot \frac{1}{\omega_{\mathrm{res}}^2} \cdot \frac{\gamma\omega}{(\omega_0^2 - \omega^2)^2 + (\gamma\omega)^2}\right]. \tag{2.21}$$

We plug the result into eq. 2.6 to find

$$I(\omega) = -\mathrm{Im}\left[\mathcal{R}(\omega)\right] \cdot \eta(\omega, T, \Omega) \tag{2.22}$$

$$= \underbrace{\eta(\omega, T, \Omega) \cdot \frac{T_{pA}^4\, g^2}{\omega_{\mathrm{res}}^2}}_{\text{intensity scaling}} \cdot \underbrace{\frac{\gamma\omega}{(\omega_0^2 - \omega^2)^2 + (\gamma\omega)^2}}_{\text{lorentzian shape}}. \tag{2.23}$$

Fitting Raman data is exemplary shown in Fig. 2.2 on graphene sheets investigated with a 515 nm incident laser wavelength. The zero energy is set to the center of the 515 nm laser so that the inelastic scattering signal can shown as the relative

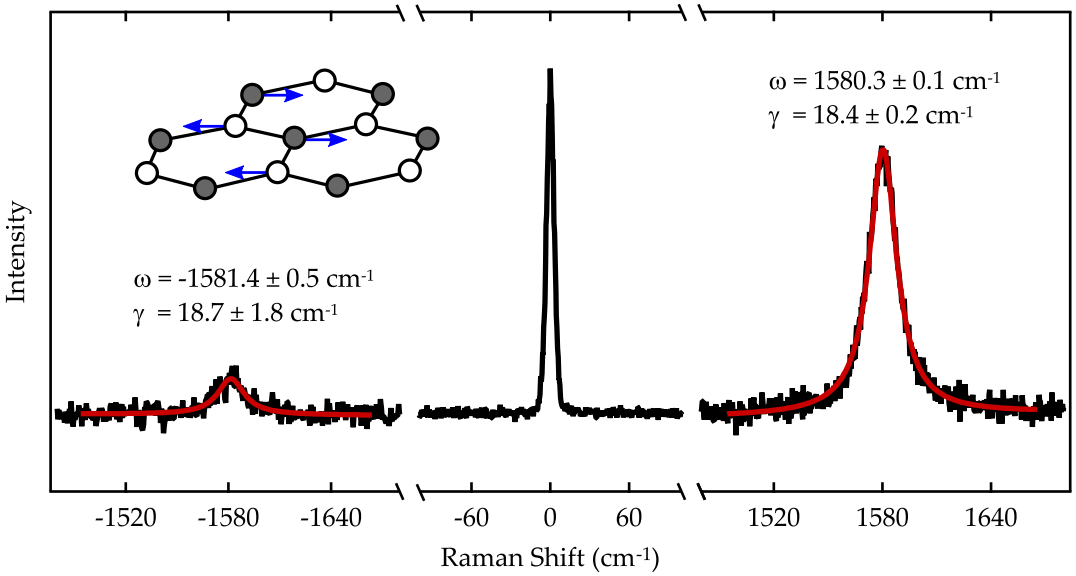

FIGURE 2.2: Exemplary Raman spectra of graphene taken at 515 nm. The data show the inelastic anti-Stokes and Stokes peak together with the elastic Rayleigh peak. Note that the Rayleigh peak is strongly attenuated during the measurement since it is generally several orders of magnitude more intense. The inset shows the corresponding motion of the carbon atoms during the vibration. The red lines are fits using eq. 2.23.

Raman shift. Stokes and anti-Stokes phonons are both fitted with eq. 2.23 and yield full widths at half maximum of approximately 18 cm^{-1}. That the anti-Stokes signal is much smaller is related to the Bose-Einstein distribution factor $n(\omega, T)$ that we captured in the scaling factor $\eta(\omega, T, \Omega)$ in eq. 2.6. It describes the occupation number of a phonon with energy ω at temperature T.

$$n = 1 + \frac{1}{e^{\hbar\omega\cdot\beta}} \tag{2.24}$$

with $\beta = (k_B T)^{-1}$. For a 1580 cm^{-1} phonon at room temperature, we find $n \approx 1$, which means that the average occupation of vibrational levels is in the groundstate. This makes the Stokes process of creating a vibrational quantum ($1 \rightarrow 2$) much more probable than the destruction of a vibrational quantum ($2 \rightarrow 1$) during the anti-Stokes process.

2.2 Nonlinear Optics

In this part, we will introduce the theoretical aspects of nonlinearity. Getting accustomed with several aspects of higher-order interaction in crystals is vital to be able to fully understand the inner workings of the difference frequency generation (DFG) unit, which will be introduced in section 3.1.4, and the theoretical framework for nonlinear phononics in graphene in section 5.3.

We assume a plane wave $E(z, t)$ traveling in z-direction induces a polarization $P(z, t)$, which can be split into a linear and a nonlinear term

$$P(z, t) = P_L(z, t) + P_{NL}(z, t). \tag{2.25}$$

Using Maxwell's equation in the scalar approximation, we can write the behavior of the electric field as

$$\frac{\partial^2}{\partial z^2}E(z,t) - \mu_0\frac{\partial^2}{\partial t^2}\left[\epsilon_0 E(z,t) + P_L(z,t)\right] = \mu_0\frac{\partial^2}{\partial t^2}P_{NL}(z,t) \tag{2.26}$$

with μ_0 as the magnetic permeability of the vacuum. We will constrain the nonlinear contribution to the quadratic term in the field as

$$P_{NL}(z,t) = \epsilon_0\chi^{(2)}E^2(z,t) \tag{2.27}$$

with the vacuum permittivity ϵ_0 and the second-order nonlinear tensor $\chi^{(2)}$. We are interested in the case of a birefringent medium, in which three plane waves are traveling. Following the convention of the literature,[70] they are named the signal wave $E_1(z,t)$, the idler wave $E_2(z,t)$ and the pump wave $E_3(z,t)$. For the three waves, energy and momentum conservation are

$$\hbar\omega_3 = \hbar\omega_2 + \hbar\omega_1 \tag{2.28}$$
$$\hbar k_3 = \hbar k_2 + \hbar k_1. \tag{2.29}$$

The corresponding field is a superposition of the waves as

$$E(z,t) = \frac{1}{2}\left(\underbrace{A_1(z)\mathrm{e}^{i(w_1t-k_1z)}}_{\text{Signal}} + \underbrace{A_2(z)\mathrm{e}^{i(w_2t-k_2z)}}_{\text{Idler}} + \underbrace{A_3(z)\mathrm{e}^{i(w_3t-k_3z)}}_{\text{Pump}}\right) + \text{c.c.} \tag{2.30}$$

Note that, the complex amplitude coefficients A_i are time-independent because of the assumed monochromaticity. Following eq. 2.27 and squaring the electric field to find the polarization, we get contributions at the frequencies

$$2\omega_1, \quad 2\omega_2, \quad 2\omega_3 \quad \text{Second Harmonic} \tag{2.31}$$
$$\omega_1+\omega_2, \quad \omega_1+\omega_3, \quad \omega_2+\omega_3 \quad \text{Sum Frequency} \tag{2.32}$$
$$\omega_3-\omega_1, \quad \omega_3-\omega_2, \quad \omega_2-\omega_1 \quad \text{Difference Frequency.} \tag{2.33}$$

The propagating waves are inducing these new frequencies in the crystal, which then start to propagate themselves with their respective phase velocities v_i. Since they have different phase velocities and are induced at different points in space, they all vanish due to deconstructive interference, unless the phase matching condition $\Delta k = k_3 - k_2 - k_1 = 0$ is satisfied. In a microscopic view, we would think of every single atom as a dipole, radiating spherical waves in space. Allowed frequencies by the phase matching condition are

$$\omega_1 + \omega_2 = \omega_3 \tag{2.34}$$
$$\omega_3 - \omega_2 = \omega_1 \tag{2.35}$$
$$\omega_3 - \omega_1 = \omega_2. \tag{2.36}$$

Concentrating only on those contributions and substituting the tensor $\chi^{(2)}$ with the effective nonlinear optical coefficient d_{eff}, we can summarize eq. 2.27 as

$$P_{NL}(z,t) = \epsilon_0 d_{\text{eff}} A_2^*(z) A_3(z) \cdot \mathrm{e}^{i[\omega_1 t - (k_3 - k_2)z]} \tag{2.37}$$

$$+\epsilon_0 d_{\text{eff}} A_1^*(z) A_3(z) \cdot \mathrm{e}^{i[\omega_2 t - (k_3 - k_1)z]} \tag{2.38}$$

$$+\epsilon_0 d_{\text{eff}} A_1(z) A_2(z) \cdot \mathrm{e}^{i[\omega_3 t - (k_1 + k_2)z]} + \text{c.c.} \tag{2.39}$$

We can now evaluate the forcing term on the righthand side in eq. 2.26

$$\mu_0 \frac{\partial^2 P_{NL}(z,t)}{\partial t^2} = -\epsilon_0 d_{\text{eff}} \Big(\omega_1^2 A_2^*(z) A_3(z) \cdot \mathrm{e}^{i[\omega_1 t - (k_3 - k_2)z]} \tag{2.40}$$

$$+\omega_2^2 A_1^*(z) A_3(z) \cdot \mathrm{e}^{i[\omega_2 t - (k_3 - k_1)z]} \tag{2.41}$$

$$+\omega_3^2 A_1(z) A_2(z) \cdot \mathrm{e}^{i[\omega_3 t - (k_1 + k_2)z]} \Big) \tag{2.42}$$

to see that polarization at a given frequency depends on the electric fields at the other two frequencies - i.e. the waves are nonlinearly coupled. For the calculation of eq. 2.26 for each frequency component, we use the slowly-varying envelope approximation to be able to drop second-order partial-derivatives. The approximation is thoroughly described in chapter 7 of Ref. [71] and it will suffice here to state, that since the envelope of the field $\hat{E}$ varies slowly in amplitude with the distance z, we can neglect the minor second-order contribution as

$$\left| \frac{\partial^2}{\partial z^2} \hat{A} \right| \ll \left| k \frac{\partial}{\partial z} \hat{A} \right|. \tag{2.43}$$

The coupled wave equations are now given as

$$\begin{cases} \frac{\partial A_1}{\partial z} = -i \frac{d_{\text{eff}} \omega_1}{c_0 n_1} A_2^* A_3 \cdot \mathrm{e}^{-i\Delta k z} \\ \frac{\partial A_2}{\partial z} = -i \frac{d_{\text{eff}} \omega_2}{c_0 n_2} A_1^* A_3 \cdot \mathrm{e}^{-i\Delta k z} \\ \frac{\partial A_3}{\partial z} = -i \frac{d_{\text{eff}} \omega_3}{c_0 n_3} A_1 A_2 \cdot \mathrm{e}^{-i\Delta k z} \end{cases} \tag{2.44}$$

with $n_i = \sqrt{\epsilon_{r,i}}$ as the refractive index and the aforementioned Δk as the wave-vector mismatch. We want to summarize two important features of eq. 2.44: (i) the change in amplitude of a field at a given frequency, depends on the product of the amplitudes of the other fields at their respective frequency (nonlinear coupling) and (ii) the exponential scaling factor is unity for no wave-vector mismatch and attenuates the field otherwise. In order to calculate the phase-mismatch factor,[72] we have to integrate the field over, e.g. the propagation length z inside the crystal of length L, which only effects the exponential factor

$$A(L) \sim \int_0^L \mathrm{e}^{i\Delta k z} \mathrm{d}z = \left(\frac{\mathrm{e}^{i\Delta k L} - 1}{i\Delta k} \right). \tag{2.45}$$

Squaring the expression for $A(L)$ to find the intensity with the Poynting vector, we get a sinc-like behavior of the attenuation with increasing phase-mismatch

$$I(L) = I^{\max} \cdot \left| \frac{\mathrm{e}^{i\Delta k L} - 1}{i\Delta k} \right|^2 = I^{\max} \cdot L^2 \mathrm{sinc}^2 \left(\frac{\Delta k L}{2} \right). \tag{2.46}$$

Fig. 2.3 gives an overview of the nonlinear processes with the photons shown as

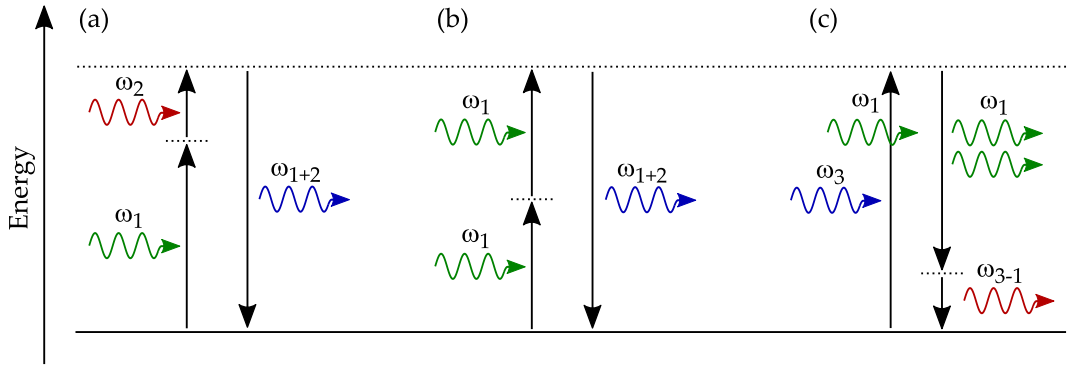

FIGURE 2.3: Different nonlinear processes are schematically shown with the energies of the idler (ω_1), the signal (ω_2) and the pump (ω_3). (a) shows the process of sum frequency excitation. (b) shows the process of second harmonic generation. (c) shows the difference frequency generation. The colors represent the difference in energy of the different laser pulses symbolically.

corpuscular objects. Fig. 2.3 (a) shows the sum frequency excitation (SFE) process, in which an idler and a signal photon are converted to pump photon. Fig. 2.3 (b) shows a specific case of SFE, where both incident photons have the same frequency and create a photon at twice the frequency, which is called second harmonic generation (SHG). Fig. 2.3 (c) shows the process of DFG, in which a pump and a signal photon create idler photons of lower frequency. If the intensity of the pump is significantly greater compared to the intensity of the signal, a positive feedback loop can be created in the following way: (i) the pump and signal beams create idler photons. (ii) Pump and idler photons can now generate more signal photons. The additional signal photons increase the generation of idler photons, which in turn generate more signal photons until the pump beam is depleted. This process referred to as optical parametric amplification (OPA).

In order to realize such a nonlinear process, we need to satisfy the phase matching condition $\Delta k = 0$, which can be written with $k = \omega n / c_0$ as

$$\omega_3 n_3 = \omega_1 n_1 + \omega_2 n_2 \tag{2.47}$$

$$\omega_3 n_3 = \omega_1 n_1 + (\omega_3 - \omega_1) n_2 \tag{2.48}$$

$$\omega_3 (n_3 - n_2) = \omega_1 (n_1 - n_2). \tag{2.49}$$

If we assume an isotropic crystal with a monotonous dispersion ($\partial n / \partial \omega$), e.g. $\omega_1 < \omega_2 < \omega_3$ and $n_1 < n_2 < n_3$ for positive dispersion, we directly see that eq. 2.49 has no solution, since the factors $n_3 - n_2$ and $n_1 - n_2$ have opposite signs. The same problem occurs when assuming a negative dispersion. Two ways[1] to resolve this problem are (i) using quasi-phase-matching (QPM) or (ii) using birefringence. For QPM, an artificial material with periodic modulation of the sign of the effective nonlinear coefficient d_{eff} is used. We will not focus on this strategy here and the interested reader is referred to the review by Hum and Fejer in Ref. [73]. To exploit birefringent crystals, which have different refractive indices along the ordinary (o) and extraordinary

[1]Since the refractive index n also depends on the temperature, temperature-dependent phase-matching is a possibility. Although not explicitly employed in this work, note that the Millennia diode laser (section 3.1.2) uses this principle for second harmonic phase-matching.

(e) direction, we use light beams with different polarizations. We therefore limit the model to uniaxial crystals with two refractive indices (o and e). The ordinary polarization experiences the index of refraction n_o, while the extraordinary polarization experiences an index of refraction between n_o and n_e as [74]

$$\frac{1}{n(\theta)^2} = \frac{\sin^2\theta}{n_e^2} + \frac{\cos^2\theta}{n_o^2} \tag{2.50}$$

with the angle θ between the optical axis and the crystal axis z. n is the principal value of the extraordinary index and $n(\theta)$ is equal to n_o for $\theta = 0°$ and equal to n_e for $\theta = 90°$. The wavelength-dependent refractive index n can be plotted with the

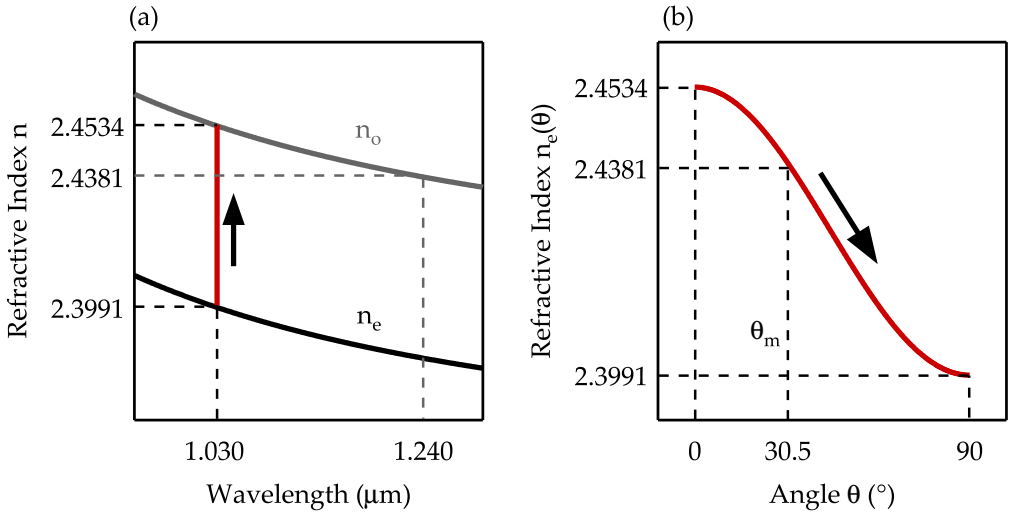

FIGURE 2.4: Exemplary depiction of the wavelength-dependent refractive index n. (a) shows the wavelength-dependent refractive index of the ordinary (o) and the extraordinary direction (e). The refractive index values of the 1030 nm and 1240 nm light are highlighted. (b) The experienced extraordinary refractive index $n_e(\theta)$ of the 1030 nm light can be tuned by changing the angle θ. At the critical angle θ_m, both light waves with different wavelengths experience the same index of refraction.

Sellmeier [75] equation

$$n^2 = A + \frac{B}{1 - C/\lambda^2} + \frac{D}{1 - E/\lambda^2} \tag{2.51}$$

with the phenomenological parameters A,B,C,D and E, which are found in Ref. [76]. Fig. 2.4 (a) shows the wavelength-dependent refractive index for the ordinary and extraordinary direction for the AGS crystal. Since it is a negative uniaxial crystal, n_e is smaller than n_o. Assuming, as an example, we choose 1030 nm light for the extraordinary direction and 1240 nm light for the ordinary direction, the angle has to be set to the critical angle $\theta = \theta_m$ to yield matching refractive indices $n_o = n_e(\theta)$. Using birefringent crystals to fulfill the phase matching condition from eq. 2.49 allows for constructive interference during the DFG process. With 1030 nm as 1.2 eV and 1240 nm as 1.0 eV, we yield 6200 nm for the mid-infrared laser light. An experimental characterization of an mid-IR pulse is shown exemplary in Fig. 3.4 in

chapter 3.1.4.

2.3 X-Ray Absorption Spectroscopy

In X-ray absorption (XAS) spectroscopy, core electrons are excited with high-energy X-rays and emitted from the atom. The X-ray beam is monochromatic for each individual data point, but the energy is continuously changed to yield the absorption as a function of energy $\mu(E)$. While the incident photon energy is lower than the energy it takes to kick the electron out of the potential well of the nucleus, no absorption takes place. If a symmetry allowed transition exists for the lowest unoccupied electronic bound state, a pre-edge feature can be observed. However, if the photon energy reaches the ionization energy, a sharp rise in the absorption $\mu(E)$ is observed, followed by an oscillatory pattern $\chi(E)$. Although it should be mentioned that there are different naming conventions, we will refer to the analysis of pre-edge and edge features as X-ray absorption near edge structure (XANES) and to the analysis of the oscillatory pattern as extended X-ray absorption fine structure (EXAFS).

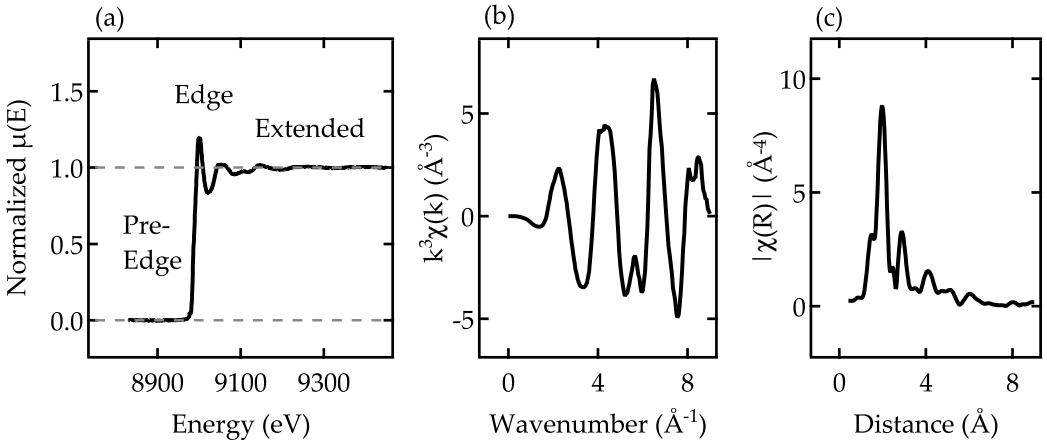

FIGURE 2.5: Exemplary XAS data are shown. (a) is the normalized energy-dependent absorption. The absorption edge for XANES and the oscillatory component in the extended region for EXAFS are both visible. (b) shows the weighted k-space data after removal of a smooth background of the absorption data. (c) Magnitude of the Fourier-transform of the k-space data.

XANES

When the energy of the X-ray beam is increased, the likelihood of interaction with matter changes.[77] This contribution gives a slowly varying background in the XAS data, which is not related to the specific sample in question. After removal of that type of background, a typical XAS spectrum looks like Fig. 2.5 (a). The additional normalization clamps the pre-edge tail on the zero line and the extended tail to the value one. The attenuation of the intensity in a XAS experiment is defined by the distance traveled inside the sample Δx and the energy-dependent absorption coefficient $\mu(E)$ as

$$\Delta I = \mathrm{e}^{\Delta x \cdot \mu(E)}. \tag{2.52}$$

The normalized absorption can be viewed as the absorption *per unit photon*. Having the intensity omitted, XANES is interested in the existence of a pre-edge feature and the precise position of the edge. There is some ambiguity as to whether the energy of the edge is located at $\mu = 0.5$ or at $\mathrm{d}^2\mu(E)/\mathrm{d}E^2 = 0$. These values should technically be equal for a well-behaved sigmoid function, but due to different normalizations, background-removal routines and potential pre-edge features, the values can differ slightly. Another point of ambiguity is that the energy-axis is calibrated with reference samples of the respective metal, but different papers might be using different reference data for their calibrations. If the electronic structure of the atom in question allows for a transition from a deep core level into a higher-lying free electronic state, a small pre-edge (relative to the absorption edge) can be observed.[78] Ligand-to-metal transitions can also be allowed.[79] The position of the absorption edge can be used to e.g. quantify the oxidation state of the atom, which allows one to draw conclusions about the chemical bonds and geometry of the metal-center.[77] If the metal atom is more oxidized, i.e. contains less electron density, the core electron is bound more tightly to the positive nucleus, which causes a blueshift of the absorption edge. An example for copper complexes is the characteristic 1s→3d signature, which can be observed for open-shell transition metal ions such as Cu^{II}. The electric dipole forbidden, but quadrupole allowed, transition gives a weak feature that also blueshifts in Cu^{III} complexes.[80] The transition can gain intensity by 4s mixing into the final state, since the 1s→4p transition is dipole allowed. Note that, XANES is a highly localized experimental technique, in that it focuses on the absorbing atom and its direct environment alone.

EXAFS

If we subtract the XANES signal as a sigmoid function, we yield the oscillatory part in the extended regime $\chi(E)$. It is conventional to set the energetic position of the edge as the starting value for $\chi(E)$. Since the energy is now above the absorption edge, meaning that we free the metal atom of one of its core level electrons, the underlying physics of the signal is defined solely by the remaining kinetic energy of the electron, which now occupies a vacuum state, separated from the Coulomb attraction of the nucleus. We can use

$$\Delta E = \frac{\hbar^2 k^2}{2m_e} \tag{2.53}$$

$$\Rightarrow k = \sqrt{\frac{2m_e(\Delta E)}{\hbar^2}}, \tag{2.54}$$

where ΔE is the excess energy above the edge and k is the wavevector of the electron, which is sometimes referred to as the *photoelectron*. If we use eq. 2.54 to transform the x-axis, we find $\chi(k)$ as shown in Fig. 2.5 (b). The function here is weighted with k^3 so that the function goes towards zero for $x = 0$ and that the oscillations for higher k-values can be seen clearly. This is a purely cosmetic effect for displaying the data. The photoelectron can now scatter at different atomic sites adjacent to the excited atom. Whether this causes constructive or deconstructive interference depends on the frequency of the photoelectron, which is the variable we continuously change while changing the X-ray energy. The final oscillatory signal shown in Fig. 2.5 (b) is further complicated by multiple scattering and other factors influencing the scattering process. The signal can be Fourier-transformed to show the information of the extended XAS data in real-space, as shown in Fig. 2.5 (c). The data can be fitted either

in real- or in k-space, to yield information such as the average bond distance, coordination number or coordinating species.[81] Note that, if the data is fitted in k-space, k-weighting the data prior to the Fourier-transform will obviously yield different signals. Stronger k-weighting dilutes the influence of region close to the absorption edge and emphasizes the region of higher k values.

Because the analysis of EXAFS data makes barely any prior assumptions on the sample, a complete investigations and derivation of each potential component of the EXAFS equation is far beyond the scope of this work. For this, the reader is referred to e.g. chapter 11 in Ref. [81] by Bruce Ravel or the more thorough review by J. J. Rehr and R. C. Albers in Ref. [82]. It will suffice here to motivate the equation by building it up piece by piece and add the respective contributions. When a photoelectron with the wavelength λ scatters from a different atom at a distance L and interferes with itself, we have the interference condition

$$2L = n\lambda \tag{2.55}$$

$$\frac{2L}{\lambda} = n \tag{2.56}$$

with n as an integer. Since trigonometric functions repeat every $2\pi n$, we further write the interference condition of the propagation of the photoelectron as

$$\chi = \sin 2\pi \cdot \frac{2L}{\lambda} \tag{2.57}$$

$$= \sin 2kL \tag{2.58}$$

with the wavenumber $k = 2\pi/\lambda$. When the photoelectron scatters at a different atomic site, we want to include the probability of elastic scattering $f(k)/k$ to be included. This factor is sometimes written as $f(k)$, $f(k)k^{-1}$ or even $f(k)k^{-2}$. When using the convention of the Union of Crystallography (IUCr 2011)[83] and picking $f(k)/k^{-1}$, the factor $f(k)$ has the dimension of length. Additionally, the elastic scattering can cause a phase shift $\delta(k)$, which now gives

$$\chi(k) = \frac{f(k)}{k} \sin 2kL + \delta(k). \tag{2.59}$$

Although we model the propagation of the photoelectron as a direct path, in principle the wavefunction is a spherical wave that induces spherical waves at other atomic sites and only constructive interference is what is observed in the end. The scattering probability should decrease as the spherical wavefunction smears out as $\sim L^{-2}$. If several atoms of the same or different type as the absorber atom are adjacent to it, we use N as the degeneracy and introduce the index i for summations over contributions of different types of atoms to find

$$\chi(k) = \sum_i N_i \frac{f_i(k)}{kL_i^2} \sin 2kL_i + \delta_i(k). \tag{2.60}$$

The following two contributions are sometimes categorized as intrinsic and extrinsic factors.[82] The first emission can be accompanied by a secondary emission caused by the sudden relaxation of the $N-1$ electron Fermi sea after excitation. This intrinsic effect is approximately accounted for by the amplitude reduction factor S_0, which is generally in the order of 0.7-1.0.[83] Extrinsic effects account for losses during propagation of the photoelectron, e.g. the excitation of plasmons, electron-hole

pairs or inelastic scattering. These interactions are accounted for by a phenomenological mean-free-path $\lambda(k)$ dependent factor $e^{-2R/\lambda(k)}$. For the last contribution, we have to consider that XAS is inherently a statistical measurement that gives the average over a range of properties. There can be *static disorder*, e.g. the absorber atoms can be placed in different environments due to crystal defects etc. Since covalent bonds vibrate in the order of 10^{13} Hz and typical core-hole lifetimes in XAS are 10^{-15} s, we observe an average over many parts of a vibration of each absorber, which is termed *thermal disorder*. The disorder-type contributions can be interpreted as a complex Debye-Waller factor which is expanded with a cumulant expansion in powers of k. If the contribution is small, one can stop at the first order term to yield $e^{-2k^2\sigma^2}$ with σ^2 as the mean square radial displacement.[82] The change in absorption due to many-body effects now gives

$$\chi(k) = S_0^2 \sum_i N_i \frac{f_i(k)}{kL_i^2} e^{-2L_i/\lambda(k)} e^{-2k^2\sigma_i^2} \sin 2kL_i + \delta_i(k). \tag{2.61}$$

This equation can be used to fit $\chi(k)$ data such as shown in Fig. 2.5 (b). After Fourier-transforming eq. 2.61, one can also choose to fit the real-space data, as shown in Fig. 2.5 (c). Since the EXAFS eq. 2.61 contains many different factors, it is only useful

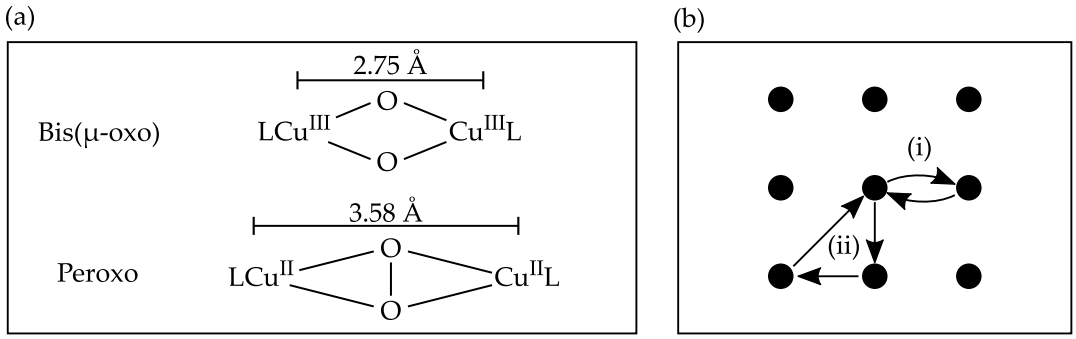

FIGURE 2.6: (a) shows two different Cu_2O_2 binding motifs with different Cu-Cu distances. (b) shows a cluster of atoms with an absorber atom in the center and two different exemplary scattering paths.

if some unknown and wanted properties can be complemented with known properties. If for example the type and amount of possible scattering atoms next to the absorber are not known, there is no way of distinguishing between S_0^2 and N_i during the fitting procedure and the EXAFS analysis will yield no information. Different Cu_2O_2 binding motifs were introduced in section 1.1.1 and a typical case for EXAFS is shown in Fig. 2.6 (a). Two copper-containing ligands are bridged by dioxygen, and the two competing copper-oxygen binding models are the bis(μ-oxo) and the peroxo motif. Theoretical calculations for an exemplary complex[84] give values which differ by approximately 1 Å for the two binding motifs. With a sub-Å resolution, EXAFS analysis can easily distinguish between both models. Note here, if only some ratio of the complexes exhibit one or the other motif or they exist in a dynamic equilibrium, one can also fit ratios of each archetypal structure. Fig. 2.6 (b) shows two exemplary scattering paths for (i) single scattering and (ii) double scattering with the central atom as the absorber atom. The many different possible scattering paths are modeled as the summation over the different contributions in the resulting signal in eq. 2.61.

3 Experimental Setup

3.1 Raman System

3.1.1 Laser

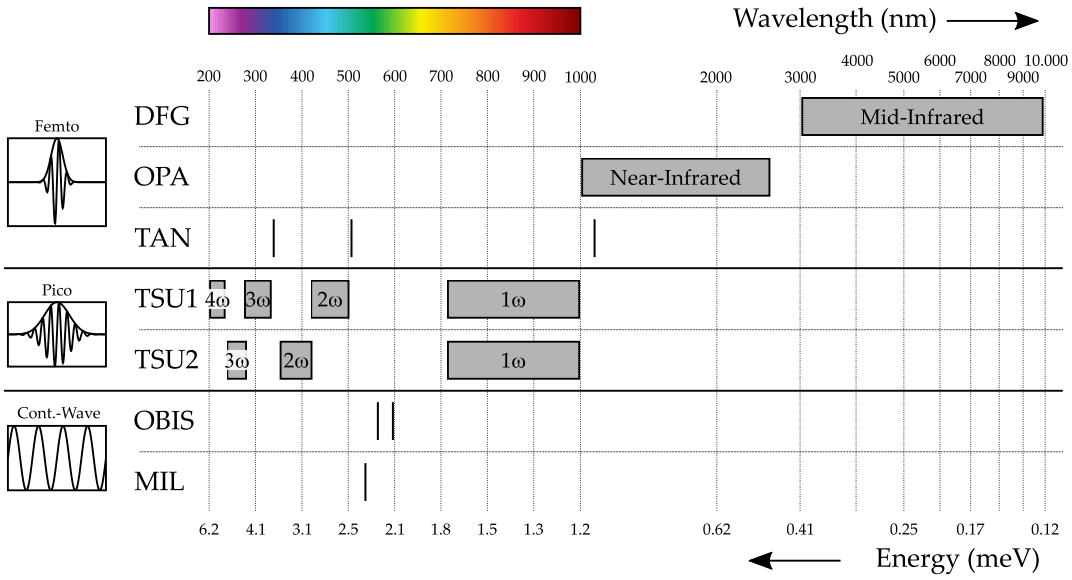

FIGURE 3.1: Available laser wavelengths for scattering experiments and temporal widths for pump-probe measurements. The pulse-widths can be in the range of hundreds of femtoseconds or single picoseconds or be continuous. The region of available wavelengths spans over 200 nm to 10 µm.

Lasers (acronym for *light amplification by stimulated emission of radiation*), in contrast to other light sources, radiate with a high degree of directionality and coherence. Among the many different types of laser, such as the conventional gas laser or the more recent quantum cascade lasers, this work uses solid-state lasers exclusively. The employed active gain media are e.g. titanium-sapphire, vanadate and a ytterbium-doped fiber. An active laser medium contains effectively two different energy levels. In principle, in an active medium, three different interaction processes can occur:[85] (i) the crystal absorbs a photon, (ii) a photon is spontaneously generated, (iii) the emission of a photon is stimulated by another photon. In the case of stimulated emission, the generated photon retains the aforementioned properties, e.g. the directionality or coherence. Inside the gain medium, the light gets absorbed if the the population of the lower energy level is higher than that of the higher energy level. A population inversion of the relative occupation numbers has to be created to continuously to ensure stimulated emission. At the startup of the laser, spontaneous emission takes place until after some finite time the population inversion is created and stimulated emission dominates.

The existing laser sources in the optical laboratory are shown in Fig. 3.1. The range of usable wavelengths is approximately 200 nm to 10 000 nm. The Tangerine (TAN) laser can be used to produce femtosecond pulses at 1030 nm, 515 nm, 343 nm or to pump the OPA or the DFG system. The continuous-wave Millennia laser produces 532 nm light and can be used to pump the Tsunami (TSU) systems to generate a variety of wavelengths with pulsewidth of picoseconds. The Obis laser can produce light at either 560 nm or 594 nm. The Tsunami and Tangerine laser systems are relevant for this work and both will be explained in the following paragraphs.

3.1.2 Tsunami System

The Tsunami laser system is distributed by *Spectra Physics Inc* (United States of America) and gets pumped by a 532 nm continuous-wave diode laser. The generated output light has a variable wavelength of 720 nm to 1000 nm at a repetition rate of 80 MHz. In subsequent higher harmonic units, the frequency can be doubled, tripled or quadrupled to reach wavelengths between 207 nm to 500 nm. The pulsewidth is in the order of picoseconds and can be measured with an autocorrelator.

Millennia Diode Laser
The Raman lab is equipped with two Tsunami HP units, which each gets pumped by a Millennia continuous-wave laser at 532 nm. The Millennia unit uses a fiber-coupled bar to supply the diode pump light for the optical resonator containing $Nb\,YVO_4$ (neodymium yttrium vanadate) crystal as a lasing medium. The most probable transition is at 1064 nm [86] and the emitted light is sent into the next cavity containing an LBO (lithium triborate) crystal for second harmonic generation. LBO has a smaller nonlinear coefficient than comparable materials, but it is less sensitive to misalignment of the phase-matching angle. Additionally, a compact low-power oven is implemented to correct the phase-matching angle with the temperature, without the need to align the crystal itself. The phase-matching angle for SHG of 1064 nm in LBO varies between 8 ° from 0 to 100 °C. [87] The continuous-wave light at 532 nm propagates into the Tsunami unit.

Tsunami Unit
The optical cavity of the Tsunami contains a Ti:sapphire crystal that absorbs in the blue to green region and emits infrared fluorescence at a large band of 600 nm to 1000 nm. Because of an overlap of the long-wavelength absorption and the short-wavelength emission, the shorter wavelengths cannot be used for the lasing process. Additional technical barriers (mirror coatings etc.) limit the usable wavelength range to 720 nm to 1000 nm. The mirror set for TSU1 is optimized for 840-1000 nm and the mirror set for the TSU2 is optimized for 720-850 nm. Typical input powers coming from the Millennia laser are 7-9 W. Inside the resonator, a birefringent filter made out of quartz plates is placed at the Brewster's angle and transforms the linearly polarized light to become elliptical. Only a narrow set of wavelengths undergoes a complete 180 °rotation and remains linearly polarized. The remaining wavelengths are attenuated and cannot reach the intensity required for the lasing threshold. By rotating the filter, the desired wavelength can be chosen. Since the monochromatic beam still contains different frequencies which experience pulse spreading due to the interaction with the optical components, a Gires-Tournois interferometer is used to apply negative group velocity dispersion to compensate the

pulsewidth broadening. This has to be adjusted for every wavelength. An acousto-optic modulator is used for mode-locking. A fraction of the output light is sent to the PulseCheck Autocorrelator (by *APE Angewandte Physik & Elektronik GmbH)*, which measures the temporal width of the pulse with a Michelson interferometer. Typical pulsewidths are approximately 2 ps.

Higher Harmonic Generation
Typical input powers for the higher harmonic generation units are 1-1.5 W. Two mirrors focus the fundamental 1ω wavelength into a first BBO crystal for second harmonic generation. The rotation angle of the crystal has to be adjusted for every wavelength to find the phase-matching condition. Residual 1ω can be combined with the 2ω at the next BBO crystal, to generate third harmonic light *via* sum frequency excitation. Since the propagation length of the 1ω and the 2ω are not perfectly equal, a delayline is used for the 2ω light to compensate for the time delay. The phase-matching condition has to be adjusted *via* rotation for every wavelength. The fourth harmonic generation is realized by simply repeating the second harmonic generation a second time. Typical output powers differ mostly with the chosen wavelength and are in the range of 60-120 mW for 2ω, 5-40 mW for 3ω and 1-4 mW for 4ω.

3.1.3 Tangerine System

The Tangerine laser system is distributed by *Amplitude Systemes* (France) and consists of a diode-pumped fiber amplifier system with ytterbium-doped photonic crystal fibers as the amplifying medium. It operates at a central frequency of 1030 nm. The Tangerine HP laser features an average power of 36 W, a pulsewidth of > 350 fs, an energy per pulse of > 200 µJ and a variable repetition rate from single shot to 40 MHz. It is generally operated at 170-500 kHz.

3.1.4 Difference Frequency Generation System

The MIR-pump and Raman-probe setup is shown in Fig. 3.2 (a). The Tangerine fiber laser is split directly into a SHG unit for the probe beam and a DFG unit for the pump beam. The DFG unit is shown explicitly in panel (b).

In the SHG unit, the 1030 nm fundamental frequency is converted to 515 nm in a BBO Type I crystal *via* second harmonic generation. The emitted light is sent onto a Bragg filter to cut away residual frequencies at the flanks and by that make the beam more monochromatic. Next, the light propagates over a delayline to be able to change the pump-probe time offset. The light has to travel the distance given by the delayline twice, so that the probe beam is delayed by ≈ 6.66 ps for every millimeter the delayline changes. The beam is cleaned up *via* a spatial filter before reaching the entrance optics. First, a pinhole aperture is positioned precisely in the focal point of the first plano-convex lens. Any unwanted imperfections of the laser profile intensity are blocked and the diverging beam is collimated again with another plano-convex lens to now form a more symmetric gaussian profile. The beam is widened before being focused on the sample and into the entrance optics of the UT-3 spectrometer. [67], which has a numerical aperture of 0.5. The spectrometer is equipped with two sets of holographic gratings, which can be used for either visible or ultraviolet frequencies to collect light in the range of 165 nm to 1000 nm.

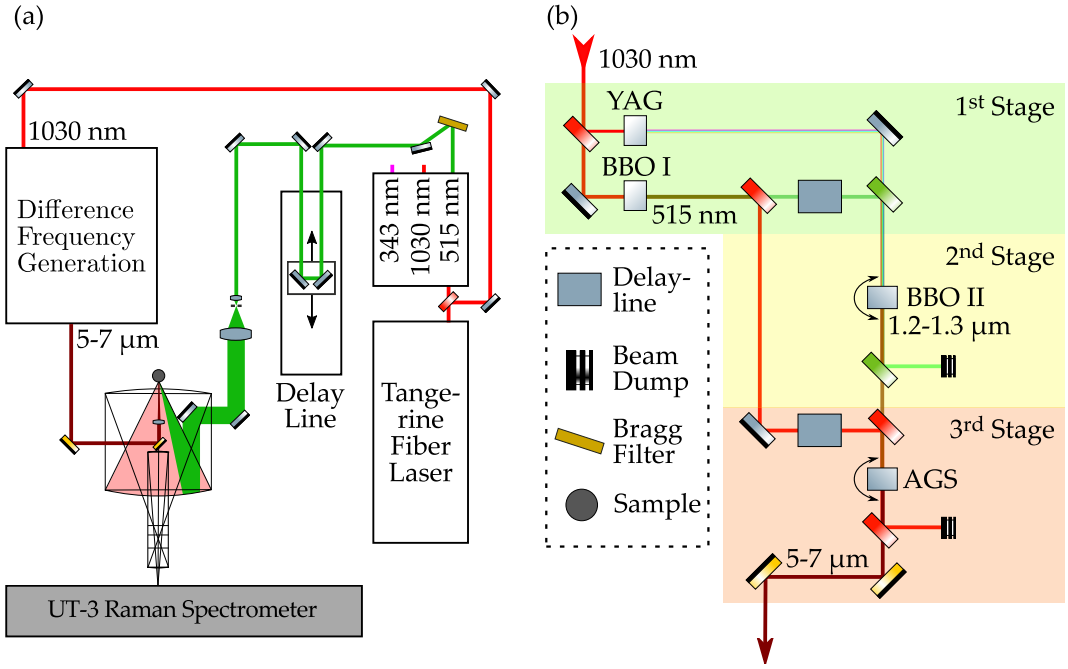

FIGURE 3.2: Schematic image of (a) the entire setup of the MIR-pump and Raman-probe setup and (b) the DFG unit.

The other part of the 1030 nm fundamental is sent into the DFG unit, which can be organized in three distinct stages, as shown in Fig. 3.2 (b). In the first stage, the fundamental is split into (i) a yttrium aluminum garnet (YAG) crystal for white-light continuum (WLC) generation, (ii) a beta barium borate (BBO) type-I crystal for second harmonic generation generation at 515 nm, and (iii) a remaining fundamental beam at 1030 nm. The remaining fundamental is sent directly to the third stage. The 515 nm light is sent over a delayline, so that in the second stage the white-light and the 515 nm can be overlapped in the next BBO type-II crystal not only spatially, but also temporally. Inside this BBO crystal, near-infrared (NIR) light is produced *via* optical parametric amplification and the remaining 515 nm is dumped. In the third stage, the 1030 nm fundamental and the NIR light are sent into a silver thiogallate (AGS) crystal for difference frequency generation. The MIR light is then sent directly onto the sample. The MIR wavelength is determined by a self-built Fourier-transform infrared (FTIR) device utilizing a pyroelectric sensor (distributed by *WiredSense*).

To obtain spatial overlap for the pump and the probe beam, a 100 µm pinhole was positioned in the focal point of the entrance objective of the spectrometer. The beam path of the MIR beam was optimized for maximum transmission through the pinhole. To ensure temporal overlap, the 515 nm beam was used to induce carriers in a silicon wafer [88] and the transmission of the MIR beam was measured as a function of the time delay, as shown in Fig 3.3. The inflection point of the transmission curve was used as the zero position.

In the following paragraphs, each nonlinear crystal and their nonlinear conversion processes will be explained.

Second Harmonic Generation with BBO Type I and Optical Parametric Amplification with BBO Type II

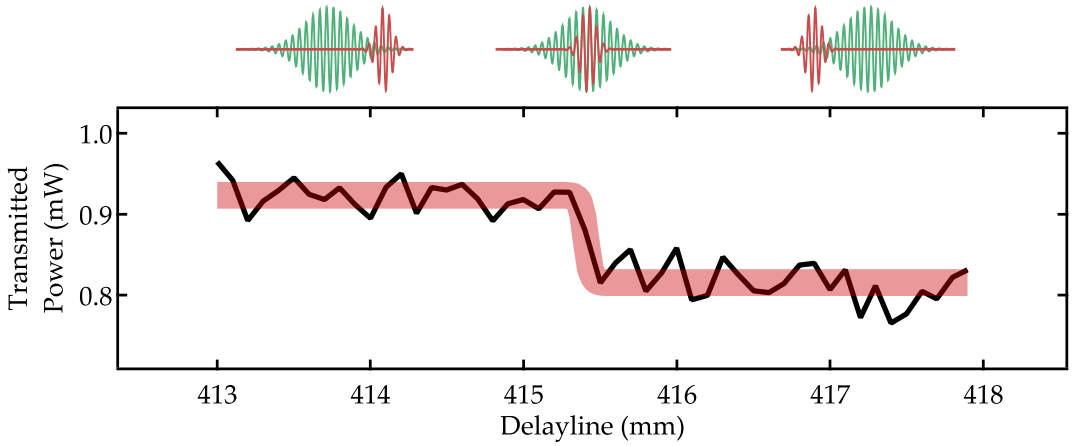

FIGURE 3.3: Exemplary transmitted power through a silicon substrate while changing the delay between the visible probe and the MIR pump laser. The delay is defined by the delayline in Fig. 3.2 (a). The schematics of pump and probe pulses at the top shows the relative time difference. When the delayline is set to increasing values, the probe pulse comes earlier and can induce a plasma in the silicon wafer, which decreases the transmission, as shown. The effect lasts for nanoseconds,[88] so it appears to be constant in the range of a few millimeters since 1 mm $\widehat{=}$ 6.66 ps for this setup.

The compound barium borate ($Ba(BO_2)_2$) was discovered in 1984.[89] It can crystallize in the alpha, beta or gamma phase. The alpha and beta phase are both interesting from a point of optics, but only the beta (=BBO) phase is nonlinear.[90] BBO is a negative uniaxial crystal, meaning that $n_e > n_o$ and that the refractive index is equal in two spatial dimensions. The underlying process of SHG is described in section 2.2 and shown in Fig. 2.3 (b). In both instances of SHG production, for the probe laser and inside the DFG unit, the BBO type I crystal upconverts two 1030 nm photons which are polarized in parallel into a 515 nm cross-polarized photon.

In the second stage, the BBO type II crystal uses cross-polarized 515 nm light and the white-light continuum to convert it to NIR light *via* optical parametric amplification. By rotation of around one axis, different wavelengths from the continuum are selected for conversion. The OPA process is mentioned in chapter 2.2 and follows the idea of difference frequency generation, but the intensity of the white-light is low compared the 515 nm beam. As a result, the selected wavelength component of the white-light is parametrically amplified together with the generated NIR beam.

White-Light Continuum with YAG

The creation of a WLC with a laser source was first observed in 1970.[91] This conversion of the monochromatic light to a broadband source is not governed by a single process, but rather a multitude of interacting nonlinear processes. The overall ensemble of interaction is related to different aspects within self-phase modulation, self-focusing, self-steepening, dispersion, diffraction, ionization and plasma generation.[92] To give a condensed walkthrough, the beam starts to self-focus due to the strong fields involved. The beam shrinking increases the intensity in turn, which creates a plasma by ionizing electrons, which then defocus the beam again. When those processes are in a dynamic equilibrium, is it referred to as a filament.

During the propagation, other effects such as self-steepening contribute to the broadening.[93] A thorough analysis of all the effects and their interactions goes beyond the scope of this work and the interested reader is referred to Ref. [94] for filamentation and to Ref. [95] for pulse self-compression. In order to create a WLC for the second stage, the 1030 nm fundamental is focused on a undoped YAG crystal which emits the fundamental and additionally a plateau on the blue and the red side of the fundamental with lower intensity. A technical analysis of the YAG crystal and comparable materials for femtosecond WLC generation can be found in Ref. [96].

Difference Frequency Generation with AGS

Historically, the first difference frequency generation system was reported in 1974 by A. S. Pine.[97] It was a continuous-wave system featuring the combination of an argon and a dye laser in a $LiNbO_3$ nonlinear crystal to produce wavelengths from 2.2-4.2 µm. In this work, silver thiogallate ($AgGaS_2$) was used as a nonlinear crystal. Like BBO, it is a negative uniaxial crystal.[98] It has a comparably low damage threshold and large absorption.[99] Inside the crystal, the fundamental 1030 nm light is mixed with the NIR light from the second stage, to produce MIR light *via* difference frequency generation. The underlying nonlinear mixing process is explained in chapter 2.2 and shown in Fig. 2.3 (c). After the MIR pulse is generated, it can be characterized by an FTIR device, as is exemplary shown in Fig. 3.4. The FTIR uses the principle of a Michelson interferometer by splitting up the beam with a beamsplitter onto two arms with mirrors, where one arm is moved at a known speed and the interference pattern is measured with a pyrodetector. The magnitude of the Fourier-transformed pulse with a center wavelength of 5000 nm (or 247.7 meV) and full width at half maximum of 5.6 meV is shown in Fig. 3.4 (a). The envelope of the absolute values of the interference measurement is shown in Fig. 3.4 (b) with a full width at half maximum of 715 fs. Note that in such an interferometric measurement, the pulse is measured itself with another probe pulse, so that the signal has to be deconvoluted to find the real pulsewidth. For gaussian pulses the autocorrelation factor is $\sqrt{2}$ yielding a pulsewidth of approximately 500 fs.

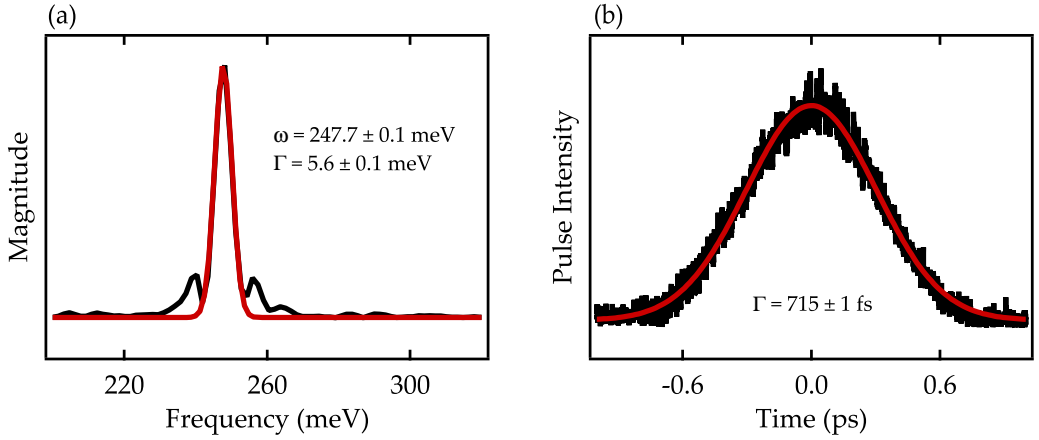

FIGURE 3.4: Exemplary characterization of a MIR pulse. (a) shows the shape in energy space and (b) the shape in temporal space. Red lines are gaussian fits.

3.2 X-Ray Absorption Spectroscopy Beamlines at PETRA III

The beamlines P64 [100] and P65 [101] are part of the extension hall at the PETRA III synchrotron at the *Deutsches Elektronen-Synchrotron* (DESY). The ongoing interest in high-brilliance X-ray light lead to several additional beamlines within the PETRA III extension project. Both beamlines, P64 and P65, are located in the northern *Paul P. Ewald* hall. P65 is the applied X-ray absorption beamline and P64 the advanced X-ray absorption beamline. The advanced P64 beamline features a photon flux of up to 10^{13} photons/s, whereas P65 delivers 10^{10}-10^{12} photons/s. The brilliance of the P64 and P65 beam is 10^{18} and $5 \cdot 10^{16}$ photons per second, milliampere and 0.1 % of bandwidth, respectively. The applied P65 beamline features an oven for above room temperature measurements and allows to work with toxic, flammable and oxidizing gases. Both beamlines have the option to use a helium-cryostat and allow for measurements at 4-44 keV energy with a resolution of $\Delta E/E = 1.4 \cdot 10^{-4}$. The focus size on the sample is approximately 150x50 µm and 1x0.5 mm for P64 and P65, respectively.

Undulators force oscillations onto the electron beam in the storage ring, which causes them to emit X-ray radiation. The native X-ray beam is cut smaller with liquid nitrogen- or water-cooled white-light slits at P64 and P65, respectively. Double-crystal monochromators [102] are used to make the beam monochromatic. Grazing incidence mirror with different coatings are used to reduce higher harmonics and to focus the beam. Another set of slits allows for further beam-shaping before reaching the first ionization chamber. Two ionization chambers, one before and one after the sample are used to determine the absorption. Foil references and fluorescence detectors can be used.

The software used for data analysis is *Athena* for the XAS and *Artemis* for EXAFS. The software packages are distributed under a free software license by Bruce Ravel and Matthew Newville and details can be found in Ref. [103].

4 Experiments on Bio-Inorganic Copper-Complexes

4.1 On the Metal Cooperativity in a Dinuclear Copper-Guanidine Complex for aliphatic C-H Bond Cleavage by Dioxygen

The author has contributed to the Raman measurements and the respective data analysis.

Cooperative effects between the two copper atoms are suggested to play a crucial role in some biological enzymatic processes. One example is the aliphatic hydroxylation from the enzyme peptidylglycine α-hydroxylating monooxygenase (PHM). It was proposed that each copper atom plays a different role during the catalytic conversion. Whereas one copper binds and activates dioxygen, the other stabilizes the intramolecular product with a ligand-metal charge-transfer. The research group of Prof. Hans-Jörg Himmel synthesized two novel bis-guanidine ligands **L1** and **L2**, which were used to investigate the cooperative effects in substrate conversion and to potentially find a model complex for PHM. When **L2** reacts with the respective copper salt, a mononuclear complex $[L_2Cu]BF_4$ is formed, which is shown in [4.1]-Scheme 4. When **L1** reacts with the copper salt, a dinuclear complex $[(L_1Cu)_2](BF_4)_2$ is formed ([4.1]-Scheme 3), in which one copper atom (Cu_A) is bound to four nitrogen atoms and is tucked away inside the complex and the other copper atom (Cu_B) is bound to two nitrogen donors and more exposed. The complex can be modified by different treatments to yield mononuclear or a trinuclear complexes, as shown in [4.1]-Scheme 5.

UV-Vis measurements after oxygenation of $[L_2Cu]BF_4$ and $[(L_1Cu)_2](BF_4)_2$, shown in [4.1]-Fig. 2, revealed strong changes of two bands that indicate oxygen binding to the complex. Notably, the $[L_2Cu]BF_4$ data indicated an end-on superoxo (Cu_1S^E) motif and a characteristic copper-oxygen charge-transfer. Copper-Oxygen binding motifs show vibrations at characteristic energies and Raman spectroscopy can be used to find them. The precursors were prepared in a glovebox (i.e. oxygen- and water-free environment) and filled in a glass cuvette, which is closed of with a lid that contains a septum. The precursors were cooled in a self-built cryostat [104] to the desired temperature of the complex (-40 °C to -80 °C) and oxygenated for 30 s to form the complex. The oxygenation is conducted *via* a cannula through the septum at approximately 0.02 bar overpressure. A color change can be observed and the solution is directly cooled to -100 °C, because the complexes are more stable at cooler temperatures. Raman experiments were conducted with the Tsunami laser system. The sample position has to adjusted carefully, since putting the focus spot too deep in the liquid attenuates the scattered light because of absorption in the sample and putting the focus spot to close the last glass surface can lead to deposits due to beam damage or glass signal in the Raman spectrum. For copper complex solutions with a concentration in tens of millimolar, distances of $\sim$ 30 µm to the glass interface are generally best fit. The flexible harmonic generation units with nonlinear BBO crystals were

used to produce second and third harmonic generation light from adjustable fundamental frequency to be able to use a broad range of frequencies. When performing experiments at different wavelengths, the spatial filter (see section 3.1.4) has to be adjusted for every wavelength, since the lens optics are not achromatic. 360 nm and 425 nm both displayed strong fluorescence and were not practical to use. Although both effects can occur at the same time, the Raman process is generally more unlikely to happen and it is not possible to collect the scattered light long enough because the fluorescence signal fills the CCD chip too fast.

The Raman signal of $[(L_1Cu)_2](BF_4)_2$ did not show any oxygen-related signal at fluorescence-free wavelengths, such as 283 nm. The bands visible in the UV-Vis are therefore attributed to rapidly formed decomposition products. However, the Raman signal of $[L_2Cu]BF_4$, measured at a wavelength of 330 nm with a power of 10 mW on a 20 µm spot, displayed a peak at 1136 cm^{-1}, which potentially stems from the O-O stretching vibration, indicating again the Cu_1S^E motif. For verification, an isotope-shift experiment is conducted. The frequency of Raman phonons scales with the masses of the constituent atoms as $\omega \sim 1/\sqrt{m}$. When exchanging the $^{16}O_2$ isotope for oxygenation with the $^{18}O_2$ isotope, a redshift is expected if the mode in question is indeed an oxygenation-related mode. The isotope-shift measurement are shown in [4.1]-Fig. 3 and a redshift of 65 cm^{-1} was observed, which is comparable to the shifts observed in the literature[105, 106] for Cu_1S^E complexes. More experiments and theoretical studies were conducted and it was found that the dinuclear $[(L_1Cu)_2]^{2+}$ complex might be a model complex for enzymatic PHM. The interaction between the two copper atoms during hydroxylation is found to be the driving force for the proton-coupled electron transfer within the C-H activation step, which similar in the biological enzyme.

On the Metal Cooperativity in a Dinuclear Copper-Guanidine Complex for aliphatic C-H Bond Cleavage by Dioxygen

ChemPubSoc Europe

DOI: 10.1002/chem.201901906

CHEMISTRY A European Journal Full Paper

Cooperative Effects

On the Metal Cooperativity in a Dinuclear Copper–Guanidine Complex for Aliphatic C–H Bond Cleavage by Dioxygen

Florian Schön,[a] Florian Biebl,[b] Lutz Greb,[a] Simone Leingang,[a] Benjamin Grimm-Lebsanft,[b] Melissa Teubner,[b] Sören Buchenau,[b] Elisabeth Kaifer,[a] Michael A. Rübhausen,[b] and Hans-Jörg Himmel*[a]

Abstract: Selective oxidation reactions of organic compounds with dioxygen using molecular copper complexes are of relevance to synthetic chemistry as well as enzymatic reactivity. In the enzyme peptidylglycine α-hydroxylating monooxygenase (PHM), the hydroxylating activity towards aliphatic substrates arises from the cooperative effect between two copper atoms, but the detailed mechanism has yet to be fully clarified. Herein, we report on a model complex showing hydroxylation of an aliphatic ligand initiated by dioxygen. According to DFT calculations, the proton-coupled electron-transfer (PCET) process leading to ligand hydroxylation in this complex benefits from cooperative effects between the two copper atoms. While one copper atom is responsible for dioxygen binding and activation, the other stabilizes the product of intramolecular PCET by copper–ligand charge transfer. The results of this work might pave the way for the directed utilization of cooperative effects in oxidation reactions.

Introduction

The distinguished ability of copper complexes to activate dioxygen has long been recognized.[1–8] Nature has developed a number of copper-containing oxidase enzymes with hugely varying binding modes of dioxygen to the copper in their active centers,[9–17] the most prominent of which are illustrated in Scheme 1 a. There are examples of well-characterized, mononuclear copper(II) end-on superoxo[18–23] (**Cu_1S^E**) or side-on (μ^2) superoxo[24–27] (**Cu_1S^S**) complexes, as well as copper(III) side-on (μ^2) peroxo[28] (**Cu_1P^S**) complexes. However, in the literature, there seems still to be a lack of copper complexes that mimic the structure or reactivity of enzymes such as tyramine β-monooxygenase (TβM), dopamine β-monooxygenase (DβM), or peptidylglycine α-hydroxylating monooxygenase (PHM). Several studies[29,30] have suggested a **Cu_1S^E** species as the key reactive intermediate in the aliphatic substrate hydroxylating activity of these enzymes, in which the active sites consist of two differently bound copper atoms (denoted as Cu_A and Cu_B), separated by about 11 Å.[31] Crystallographic characterization of

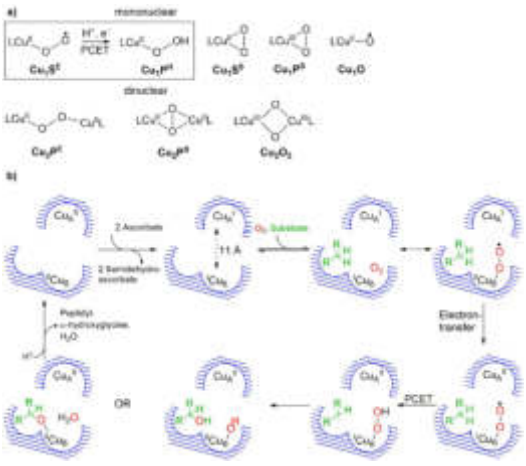

Scheme 1. a) Overview of some copper–dioxygen complexes and reaction products. b) Proposed mechanism for dioxygen activation with the enzyme PHM (adapted from Amzel et al., 1999, see ref. [30]).

the oxidized form of PHM revealed a mildly activated O_2 unit in an end-on superoxo complex with an O–O bond distance of 1.23 Å.[32] The dioxygen binds exclusively to the Cu_B atom. The role of the Cu_A atom is to provide electron density to the Cu_B site for the subsequent hydroxylation pathway. Scheme 1 b depicts one possible reaction pathway for the hydroxylation mechanism in PHM, as suggested by Amzel et al.,[30] but other pathways have been proposed, involving, for example, the oxyl radical **Cu_1O** formed from a **Cu_1S^E** species.[11,33,34] The mechanism of the electron-transfer pathway is not completely

[a] F. Schön, Dr. L. Greb, S. Leingang, Dr. E. Kaifer, Prof. H.-J. Himmel
Anorganisch-Chemisches Institut, Ruprecht-Karls-Universität Heidelberg
Im Neuenheimer Feld 270, 69120 Heidelberg (Germany)
E-mail: hans-jorg.himmel@aci.uni-heidelberg.de
Homepage: http://www.uni-heidelberg.de/fakultaeten/chemgeo/aci/himmel/

[b] F. Biebl, Dr. B. Grimm-Lebsanft, M. Teubner, S. Buchenau, Prof. M. A. Rübhausen
Institut für Nanostruktur- und Festkörperphysik
Universität Hamburg and Center for Free Electron Laser Science
Luruper Chaussee 149, 22761 Hamburg (Germany)

Supporting information and the ORCID identification number(s) for the author(s) of this article can be found under: https://doi.org/10.1002/chem.201901906.

clear, since the synthesis of model Cu_1S^E complexes is generally hampered by their high reactivity. In some cases, the products of proton-coupled electron-transfer (PCET) reactions, for example, with TEMPOH (Scheme 1 a, b, TEMPO = 2,2,6,6-tetramethylpiperidinyloxyl), have been isolated.[35]

Two types of hydroxylation are initiated by copper–dioxygen complexes: 1) aromatic hydroxylation[36] and aliphatic hydroxylation,[37] due to dinuclear oxo species that are not relevant to the above-mentioned enzymes, and 2) aliphatic hydroxylation attributable to mononuclear dioxygen complexes (Scheme 1 a), as described in the following. In 2009, Itoh et al. reported unique examples of direct aliphatic C–H bond cleavage reactions, leading to ligand hydroxylation as suggested for the above-mentioned enzymes, starting from Cu_1S^E complexes bearing an *N*-[2-(2-pyridyl)ethyl]-1,5-diazacyclooctane tridentate ligand (1^X, Scheme 2).[38,39] Aliphatic ligand hydroxylation

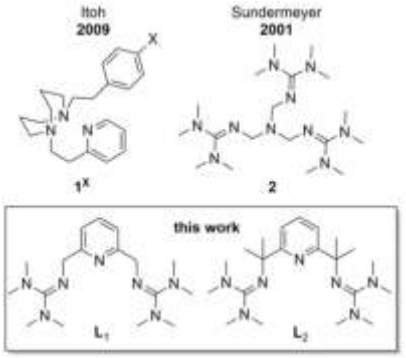

Scheme 2. Lewis structures of two ligands 1^X (X = OMe, Me, H, Cl, NO_2)[38,39] and **2**[48] used previously in aliphatic ligand hydroxylation reactions via Cu_1S^E complexes and the two bisguanidine ligands, 2,6-bis(tetramethylguanidinomethyl)pyridine (L_1) and 2,6-bis(1-tetramethylguanidino-1-methyl-ethyl)pyridine (L_2) used in this work.

has also been reported for a Cu_1S^E complex bearing the tris[2-(*N*-tetramethylguanidyl)ethyl]amine ligand (**2**, Scheme 2),[35,39] but only after reaction with a hydrogen atom donor (TEMPOH, phenols), or reaction of the Cu^I complex with PhIO. These findings were rationalized in terms of the formation of another species, a Cu_1P^H or Cu_1O complex, considered to be responsible for the hydroxylating activity.[35] There have been a few more examples of Cu^I complexes exhibiting aliphatic ligand oxidation when exposed to dioxygen, but in none of these cases could a Cu_1S^E complex be spectroscopically detected.[40–43]

Moreover, specific ligand design with sterically demanding groups is required to prevent the formation of higher nuclear complexes, either as peroxo complexes Cu_2P^E or Cu_2P^S [44,45] or a dioxo complex Cu_2O_2 [bis(μ-oxo)-dicopper(III)].[46] Several groups have studied the dioxygen binding of guanidine–copper complexes, and dinuclear oxo (Cu_2O_2) and peroxo (Cu_2P^S) complexes of bisguanidine ligands have been reported.[46,47] The ability of tris-guanidine–copper complexes (ligand **2**, Scheme 2) to form remarkably stable copper–superoxo complexes of the type Cu_1S^E is especially interesting,[18,21] since it allowed the first structural characterization of such a complex and a detailed evaluation of its reactivity.[19,35]

In recent years, our group has extensively explored the chemistry of copper complexes bearing guanidino-substituted aromatics as ligands.[49] We have also demonstrated their use as catalysts for oxidation reactions with dioxygen.[50] Herein, we report two new copper complexes with the bisguanidine ligands L_1 and L_2 (Scheme 2). They form mononuclear copper–dioxygen species that might be interesting in the context of enzymatic aliphatic C–H bond activation. The ligand design, with three N donor atoms for strong coordination and steric shielding of the coordinated metal center in the binding pocket, precludes the formation of dinuclear oxo-bridged complexes.

Results and Discussion

Synthesis of the copper(I) complexes

Reaction of L_1[51] with tetrakis(acetonitrile)copper(I) tetrafluoroborate, $[Cu(CH_3CN)_4]BF_4$, furnished the orange dinuclear complex $[(L_1Cu)_2](BF_4)_2$ in a high yield of 92% (Scheme 3). Its

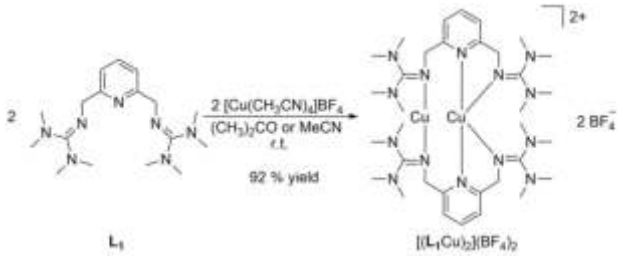

Scheme 3. Reaction leading to the dinuclear Cu^I complex $[(L_1Cu)_2](BF_4)_2$.

^1H NMR spectrum features a doublet and a triplet signal due to the pyridine ring, a singlet signal due to the methylene bridge, and two singlet signals due to the guanidino groups. These observations can be explained in terms of molecular dynamics, with the signals of the pyridine ligands being averaged due to the fast migration of these ligands from one copper atom to the other. All signals are downfield-shifted with respect to those of the free ligand. The UV/Vis spectrum shows a strong absorption at 210 nm ($\varepsilon = 27200\ M^{-1}cm^{-1}$) together with a shoulder at 272 nm ($\varepsilon = 8640\ M^{-1}cm^{-1}$) and a weak absorption at 357 nm ($\varepsilon = 883\ M^{-1}cm^{-1}$). Figure 1 a shows the structure of the $[(L_1Cu)_2]^{2+}$ complex, as derived from X-ray diffraction analysis of crystals grown from a solution in CH_3CN/Et_2O (see the Supporting Information for the similar structure of crystals grown from a solution in acetone/Et_2O). Interestingly, the two Cu^I atoms in this complex, separated by 2.871(1) Å, are very differently coordinated. One copper atom is bound by two guanidino nitrogen atoms and by the nitrogen atoms of the pyridine rings, leading to a relatively high coordination number of four. A space-filling model highlights the buried position of this copper atom in the core of the complex, leaving virtually no free space for dioxygen attack.

The second Cu^I atom exhibits a lower coordination number of two, as it is only bound by two guanidino nitrogen atoms.

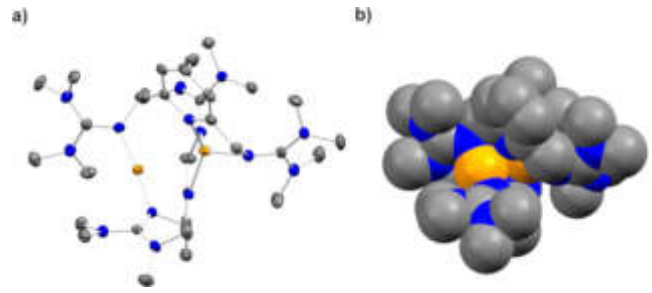

Figure 1. Structure of the dication $[(\mathbf{L_1}Cu)_2]^{2+}$ in crystals of $[(\mathbf{L_1}Cu)_2](BF_4)_2$ grown from CH_3CN/Et_2O solution (Cu atoms in orange, N atoms in blue, and C atoms in gray). Hydrogen atoms and counterions are omitted for clarity. The two copper atoms are separated by 2.871(1) Å (see the Supporting Information for structural details). a) Structure with thermal ellipsoids (drawn at the 50% probability level). b) Space-filling model.

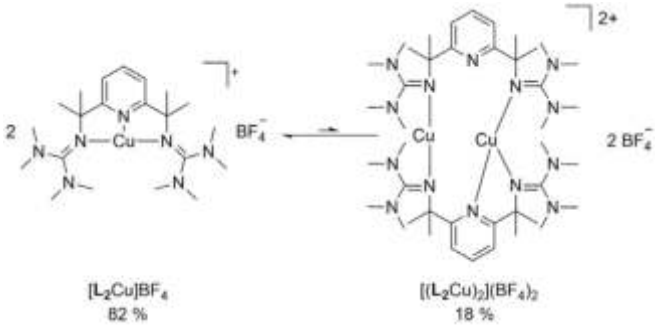

Scheme 4. Equilibrium between monomer and dimer for the complex $[(\mathbf{L_2}Cu)]BF_4$ in acetonitrile solution, favoring the monomer at room temperature.

Consequently, this copper atom is available for dioxygen attack (see the space-filling model in Figure 1 b).

Similar IR spectra were recorded for the complex in a KBr disk and dissolved in CH_3CN, indicating that the dimeric structure is preserved in solution (see the Supporting Information). ^{1}H DOSY NMR spectra were recorded for further assessment (see the Supporting Information for details). On the basis of these experiments, the diffusion constant of the free ligand $\mathbf{L_1}$ was estimated as $1.40\times10^{-9}\,m^2\,s^{-1}$ in CD_3CN solution. The diffusion constant of the copper complex obtained upon dissolving $[(\mathbf{L_1}Cu)_2](BF_4)_2$ in CD_3CN is significantly lower at $1.01\times10^{-9}\,m^2\,s^{-1}$, consistent with the presence of a dimeric complex unit in solution. Variable-temperature ^{1}H NMR spectroscopy was performed to study the effect of temperature on the dimerization process. Although the complex displays dynamic processes (rotation and inversion of the guanidino groups;[52] see the Supporting Information), a monomer–dimer equilibrium can be excluded. To support the experimental results, DFT calculations (TPSSh + D3/def2-TZVP) were carried out on the monomer $[\mathbf{L_1}Cu]^+$ and dimer $[(\mathbf{L_1}Cu)_2]^{2+}$. The solvent effect was estimated with the conductor-like screening model (COSMO, see the Supporting Information for details). The calculated structure of $[(\mathbf{L_1}Cu)_2]^{2+}$ was in very good agreement with the experimental structure. The root-mean-square deviation (RMSD) of the bond distances, as determined with the program aRMSD,[53] was only 0.35 Å (see the Supporting Information for details). According to these calculations, dimerization of $[\mathbf{L_1}Cu]^+$ is both exothermic and exergonic ($\Delta H = -182\,kJ\,mol^{-1}$ and $\Delta G = -107\,kJ\,mol^{-1}$ at 298 K, 1 bar), in full agreement with the experimental results. Hence, all results confirm that the $[(\mathbf{L_1}Cu)_2]^{2+}$ units found in the solid state are preserved in solution.

Next, we synthesized the new ligand $\mathbf{L_2}$ (see the Lewis structure in Scheme 2 and the experimentally derived solid-state structure in the Supporting Information), bearing methyl groups at the benzylic positions. By reaction with $[Cu(CH_3CN)_4]BF_4$, the complex $[\mathbf{L_2}Cu]BF_4$ was obtained in 88% isolated yield. Its structural characterization in the solid state was not possible, but all experimental results pointed to an equilibrium between a monomeric complex $[\mathbf{L_2}Cu]^+$ and its dimer $[(\mathbf{L_2}Cu)_2]^{2+}$ in acetonitrile solution (Scheme 4), with a strong preference for the monomeric complex at room temperature. From ^{1}H DOSY NMR spectra, a diffusion constant of $1.45\times10^{-9}\,m^2\,s^{-1}$ was estimated for the free ligand $\mathbf{L_2}$. For the copper complex, two species with significantly different diffusion constants were found. The dominant species exhibited a diffusion constant of $1.16\times10^{-9}\,m^2\,s^{-1}$, and the second species a smaller value of $1.04\times10^{-9}\,m^2\,s^{-1}$, close to that of $[(\mathbf{L_1}Cu)_2](BF_4)_2$. The obvious inference is that in CD_3CN solution a monomeric complex $[\mathbf{L_2}Cu]^+$ is formed, together with a small amount of dimeric complex $[(\mathbf{L_2}Cu)_2]^{2+}$. This conclusion was further supported by variable-temperature ^{1}H NMR measurements (see the Supporting Information). At high temperature (70 °C), only one species, $[\mathbf{L_2}Cu]^+$, was present. An additional weak set of signals appeared at room temperature, indicating the presence of a small amount of the dimer. A monomer:dimer ratio of 82:18 was estimated by signal integration. For both species, similar dynamic processes as for the $[(\mathbf{L_1}Cu)_2](BF_4)_2$ complex were detected. At −40 °C, the NMR spectrum of the dimeric species $[(\mathbf{L_2}Cu)_2](BF_4)_2$ showed an additional signal splitting (in contrast to that of $[(\mathbf{L_1}Cu)_2](BF_4)_2$), arising from the formation of diastereomeric centers due to the four additional methyl groups in $\mathbf{L_2}$ leading to hindered rotations and thus breaking symmetry (especially at low temperatures). Furthermore, nuclear Overhauser enhancement spectroscopy (NOESY) supported these findings through an exchange of signals from the guanidino groups as well as the aromatic rings in the major and minor products (see the Supporting Information). Finally, we calculated $[\mathbf{L_2}Cu]^+$ and its dimer, $[(\mathbf{L_2}Cu)_2]^{2+}$, in analogy to the complexes with ligand $\mathbf{L_1}$, and compared their energies. Surprisingly, the calculated global minimum-energy structure of $[(\mathbf{L_2}Cu)_2]^{2+}$ differed markedly from that of $[(\mathbf{L_1}Cu)_2]^{2+}$. One Cu^I atom in $[(\mathbf{L_2}Cu)_2]^{2+}$ exhibits a coordination number of three, being coordinated by two guanidino nitrogen atoms and one pyridine nitrogen atom. The second Cu^I atom is coordinated by two guanidino nitrogen atoms, as in $[(\mathbf{L_1}Cu)_2]^{2+}$. Furthermore, the Cu–Cu distance (3.699 Å) is very large (for a more detailed comparison, see the Supporting Information). Dimerization of $[\mathbf{L_2}Cu]^+$ was calculated to be mildly exothermic ($\Delta H = -42\,kJ\,mol^{-1}$) but endergonic ($\Delta G = +44\,kJ\,mol^{-1}$) at room temperature and 1 atm, consistent with the experimental results. The different structures of the two complexes also lead to different chemical reactivities.

For example, $[\mathbf{L_2}Cu]^+$ proved to be much more air-sensitive than $[(\mathbf{L_1}Cu)_2]^{2+}$.

Reactivity of the copper(I) complex solutions towards dioxygen

Next, the reactivities of the two complexes towards dioxygen were studied. In first experiments, solutions of $[\mathbf{L_2}Cu]BF_4$ and $[(\mathbf{L_1}Cu)_2](BF_4)_2$ in propionitrile were cooled to −80 °C and −40 °C, respectively, and changes in their UV/Vis spectra upon addition of pre-cooled propionitrile saturated with dioxygen were monitored. Figure 2 shows the changes in the UV/Vis spectra upon the addition of dioxygen.

For the monomeric copper complex $[\mathbf{L_2}Cu]BF_4$, a fast evolution (10 s) of intense bands at 359 nm ($\varepsilon = 1800\ L\,mol^{-1}\,cm^{-1}$) and 595 nm ($\varepsilon = 970\ L\,mol^{-1}\,cm^{-1}$) was observed, with first-order kinetics being followed for the reaction with dioxygen at −80 °C. The wavelengths of the absorption maxima and their extinction coefficients are close to those previously reported in the literature for an end-on superoxo complex, $\mathbf{Cu_1S^E}$.[2,23,35]

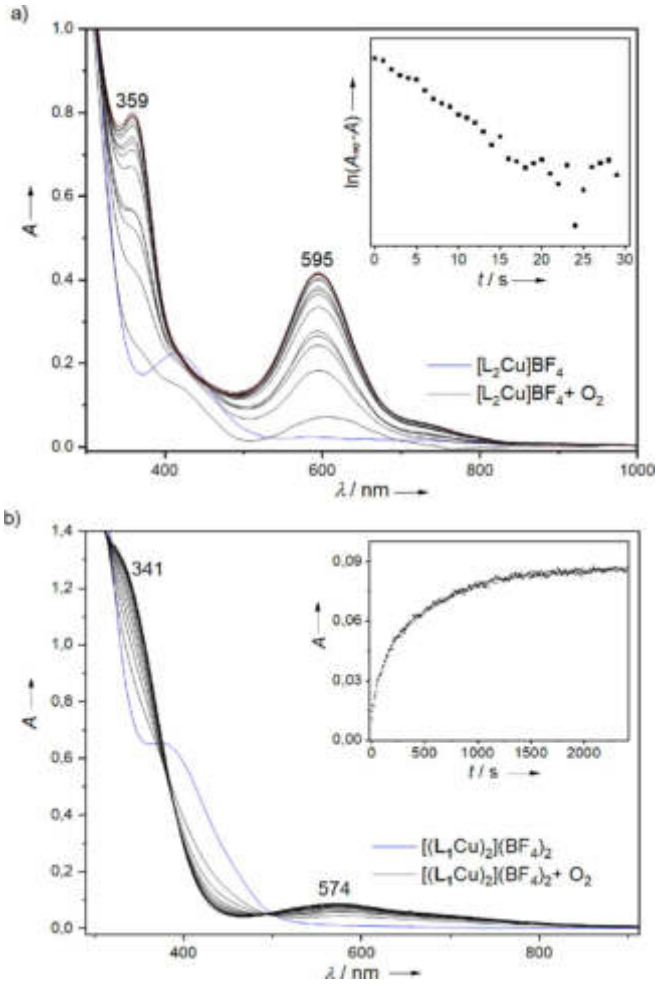

Figure 2. Spectral changes for the reaction of: a) $[\mathbf{L_2}Cu]BF_4$ (4.34×10^{-4} mol L^{-1}) for the first 30 s at −80 °C (inset: first-order plot of $\ln(A_\infty - A)$ vs. time, based on the absorbance change at 595 nm), and b) $[(\mathbf{L_1}Cu)_2](BF_4)_2$ (2.49×10^{-4} mol L^{-1}) for the first 2500 s at −40 °C (inset: absorbance change at 574 nm) in propionitrile with dioxygen.

Based on its high intensity, the absorption at 595 nm clearly qualifies as a characteristic copper–dioxygen charge-transfer transition. The formation of a side-on superoxo complex $\mathbf{Cu_1S^S}$,[2,25] or another dioxygen species, which typically display only weak d-d transitions in the region around 600 nm, can be excluded. The bands assigned to the $\mathbf{Cu_1S^E}$ complex then decreased with time ($t_{1/2} \approx 5$ min), showing the complex to be unstable, even at low temperature. Addition of TEMPOH induced a fast decrease in the bands at 595 and 359 nm (see the Supporting Information), as typically observed for end-on superoxo complexes.[2,23,35] The resonance Raman (rR) spectrum (excited with 329 nm light) of an oxygenated solution of $[\mathbf{L_2}Cu]BF_4$ at −93 °C included an O-isotope-sensitive signal at 1136 cm^{-1} ($\Delta^{18}O_2 = 65$ cm^{-1}, Figure 3). The peak position and

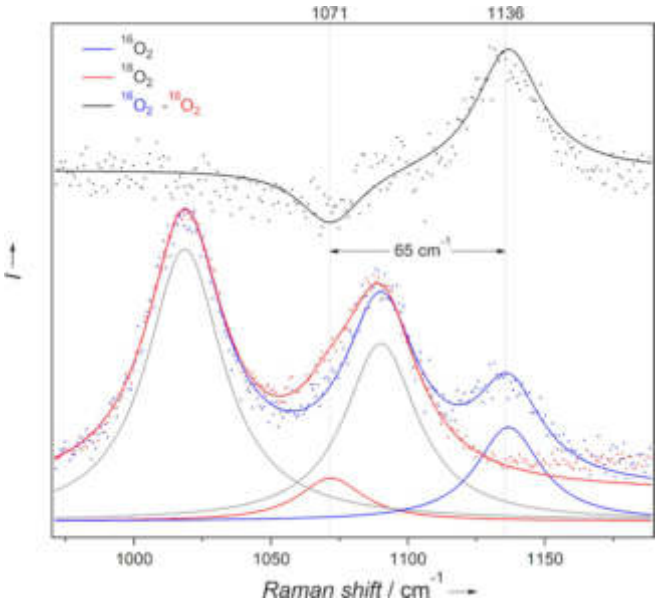

Figure 3. Resonance Raman spectra after the oxygenation of $[\mathbf{L_2}Cu]BF_4$ with $^{16}O_2$ or $^{18}O_2$ at −93 °C and difference spectrum ($^{16}O_2$–$^{18}O_2$), $\lambda_{ex} = 329$ nm, also showing the individual Lorentzians used for fitting the data.

associated isotope shift are similar to those reported for $\mathbf{Cu_1S^E}$ complexes[18,21,23,54] and can be assigned to the O–O stretching vibration, supporting the formulation of an $\mathbf{Cu_1S^E}$ complex here. Due to the monomer–dimer equilibrium, some of the dimeric complex $[(\mathbf{L_2}Cu)_2](BF_4)_2$ should be present at the low temperature of the experiment. However, due to the significantly higher reactivity of the monomeric complex towards dioxygen, it can be assumed that predominantly monomeric $[\mathbf{L_2}Cu]BF_4$ reacts with dioxygen in a steady-state manner, even at low temperature.

In the case of the dimeric complex $[(\mathbf{L_1}Cu)_2](BF_4)_2$, a much slower (>1500 s) evolution of two new bands [one at 341 nm ($\varepsilon = 4900\ L\,mol^{-1}\,cm^{-1}$) and another extremely broad one at 574 nm ($\varepsilon = 345\ L\,mol^{-1}\,cm^{-1}$)] was observed in the UV/Vis spectrum upon addition of dioxygen at −40 °C. No further changes were observed with time, showing the relevant species to be stable at −40 °C. Clearly, the band at 574 nm cannot be attributed to a charge-transfer transition due to its low ex-

tinction coefficient, but rather belongs to a Cu^{II} d–d transition. UV/Vis spectra were also recorded for dioxygen addition at a lower temperature (−80 °C), but gave essentially the same results. Low-temperature Raman measurements of an oxygenated solution of $[\mathbf{L_1}Cu]_2(BF_4)_2$ at −40 °C (λ_{ex} = 283 nm) showed no O-isotope-sensitive bands between 500 and 2000 cm^{-1}. On this basis, the bands are almost certainly not attributable to the initial copper–dioxygen complex, but to a rapidly formed decomposition product. The high positive charge and steric hindrance are factors that might be relevant for the differences in reactivity toward dioxygen between the dimeric complex $[(\mathbf{L_1}Cu)_2]^{2+}$ and the monomeric complex $[\mathbf{L_2}Cu]^{+}$.

Having studied the reactivity toward dioxygen at low temperature by UV/Vis spectroscopy, we repeated the reaction of $[(\mathbf{L_1}Cu)_2]^{2+}$ on a larger scale, varying the solvent and temperature (Scheme 5). After treating complex $[(\mathbf{L_1}Cu)_2](PF_6)_2$ with dioxygen in acetonitrile at room temperature, quenching the reaction mixture with water, extracting with dichloromethane, and redissolution in acetonitrile, complex [**3**] (Scheme 5 and Figure 4) was crystallized. Ligand $\mathbf{L_1}$ was not only hydroxylated, but further oxidized to a diketone. In addition, a chloride ion, abstracted from a dichloromethane solvent molecule, coordinated to the Cu^{II} atom. We repeated the reaction (Scheme 5) at −78 °C and passed Ar through the reaction mixture (ca. 5 min) at this low temperature to remove free (uncoordinated) dioxygen. After warming to room temperature and solvent removal in vacuo, dichloromethane was added.

The HR ESI mass spectrum of the reaction mixture displayed a peak corresponding to the mass of the doubly-hydroxylated complex [**4**] (see Scheme 5). This finding led us to the conclusion that oxidation to the ketone occurs in a secondary reaction after ligand hydroxylation. We then proceeded to study the reaction at low temperature, using acetone instead of acetonitrile as solvent. In this experiment, we injected dioxygen into a solution of the complex $[(\mathbf{L_1}Cu)_2](PF_6)_2$ in acetone at −78 °C for about 5 min, resulting in a greenish-blue mixture that was stored in a freezer (−80 °C, 7 d). After purging the solution with argon (ca. 5 min), warming to room temperature, and overlaying with Et_2O, blue crystals of the trinuclear copper complex [**5**] were obtained in 33% isolated yield (Scheme 5 and Figure 4). The three copper atoms are coordinated by three new monoanionic ligands that result from oxidative removal of one guanidino group and further reaction with an acetone solvent molecule. A central six-membered ring of alternating copper and oxygen atoms is formed, and coordination of the guanidino group and the pyridine nitrogen atoms complete a coordination number of four at each copper atom. In all three cases, an aliphatic ligand hydroxylation initially occurred.

Based on the accumulated experimental results, it is assumed that a labile $\mathbf{Cu_1S^E}$ complex is initially formed, leading to intramolecular ligand hydroxylation. The formation of higher nuclear complexes, that is, $\mathbf{Cu_2O_2}$ complexes (Scheme 1 a), which are also known for hydroxylating activity, can be excluded due to the steric hindrance of $[(\mathbf{L_1}Cu)_2]^{2+}$ (with a stable dimeric structure in MeCN solution), as illustrated in the space-filling model (Figure 1), and considering the results obtained with the complex $[\mathbf{L_2}Cu](BF_4)$. Furthermore, we tested the hydroxylating activity of $[(\mathbf{L_2}Cu)O_2]BF_4$ by addition of 10 equiv. of N2-benzyltetramethylguanidine (**6**) to the preformed $\mathbf{Cu_1S^E}$ complex at low temperatures and monitoring the UV/Vis spectra. Even after warming to room temperature, no hydroxylation products of **6** were found (GC-MS). Since methylation of the ligand is not expected to have a great impact on the reactivity at the copper atom, we exclude monomeric $[(\mathbf{L_1}Cu)O_2]BF_4$ as being responsible for the hydroxylation reaction in complexes [**3**], [**4**], and [**5**] (Scheme 5).

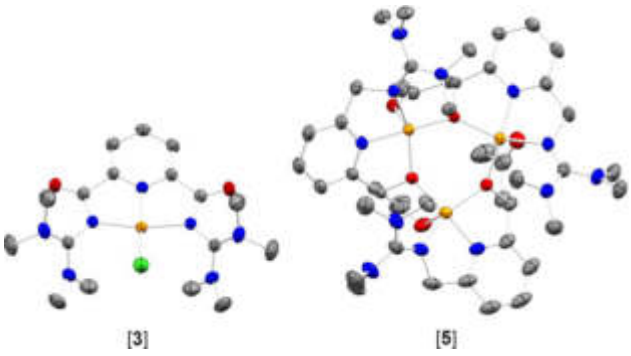

Figure 4. Structures of [**3**]PF_6 and [**5**]$(PF_6)_3$ (Cu atoms in orange, N atoms in blue, Cl atoms in green, O atoms in red, and C atoms in gray). Hydrogen atoms, co-crystallized solvent molecules, and counter-ions are omitted for clarity. Thermal ellipsoids are drawn at the 50% probability level (see the Supporting Information for details).

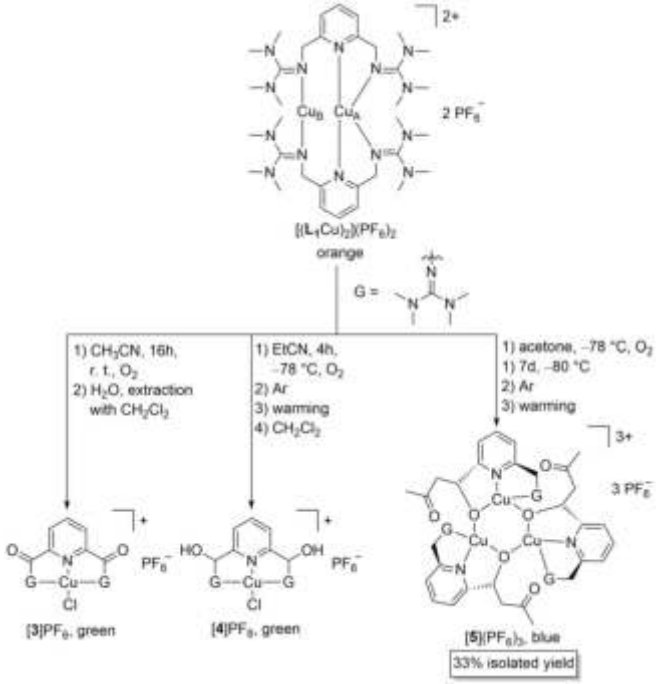

Scheme 5. Formation of the mononuclear Cu^{II} complexes [**3**]PF_6 and [**4**]PF_6, and the trinuclear Cu^{II} complex [**5**]$(PF_6)_3$, from reaction between $[(\mathbf{L_1}Cu)_2](PF_6)_2$ and dioxygen under different conditions (temperature, solvent).

Solid-state reaction of $[(L_1Cu)_2](BF_4)_2$ with dioxygen

Treatment of crushed crystals of $[(L_1Cu)_2](BF_4)_2$ with a mixture of $^{16}O_2$ and $^{18}O_2$ resulted in a color change from orange to green. After removal of the dioxygen with Ar, the reaction product was dissolved in dichloromethane. HR ESI-MS analysis (Figure 5a) showed peaks at *m/z* 441.1911 for

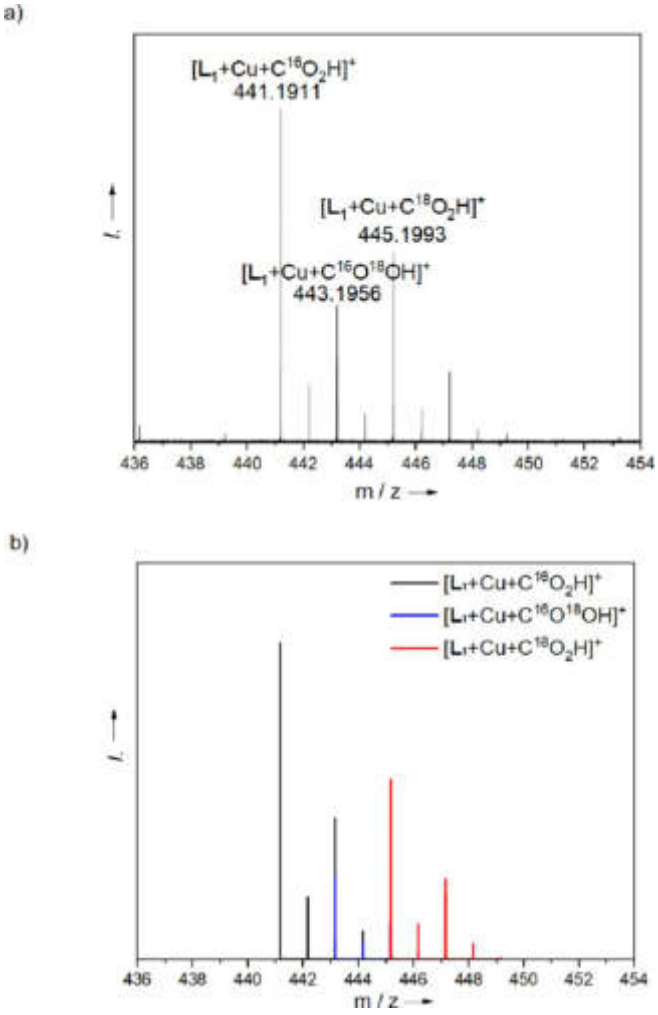

Figure 5. a) ESI mass spectra recorded in CH_2Cl_2 for $[(L_1Cu)_2](BF_4)_2$ after solid-state reaction with a mixture of $^{18}O_2$ and $^{16}O_2$. The Lewis structure of the suggested fragment is shown in the upper-right corner. b) Simulation of the fragments $[L_1+Cu+C^{16}O_2H]^+$, $[L_1+Cu+C^{16}O^{18}OH]^+$, and $[L_1+Cu+C^{18}O_2H]^+$.

$[L_1+Cu+C^{16}O_2H]^+$ and at *m/z* 443.1956 and 445.1993 due to $[L_1+Cu+C^{16}O^{18}OH]^+$ and $[L_1+Cu+C^{18}O_2H]^+$, respectively. CID experiments on the isolated ions (MS-MS) indicated the dissociation of $C^{16}O_2$, $C^{16}O^{18}O$, and $C^{18}O_2$, respectively, from these species, implying coordination of formate to the copper complex. Control experiments without the addition of dioxygen, as well as the incorporation of $^{18}O_2$ into the carbon dioxide, preclude the presence of impurities in the copper complex or the ESI mass spectrometer as sources of the observed mass signals. Therefore, it is assumed that one of the tetramethylguanidino groups is hydroxylated and further oxidized to formate by the copper complex. IR spectra, recorded for solid $[(L_1Cu)_2](BF_4)_2$ in KBr disks after reaction with $^{16}O_2$ or $^{18}O_2$, displayed some differences in the region around 1600 cm^{-1}, characteristic of ν(C=O) vibrations, indicating that hydroxylation took place in the solid state. Unfortunately, the presence of strong ν(C=N) vibrations of the remaining guanidino groups hampered unambiguous assignment of the IR absorption maxima in this region (see the Supporting Information).

DFT calculations

The structures of the two Cu_1S^E complexes were calculated to obtain more detailed information, considering both triplet and broken-symmetry states, using the TPSSh+D3 functional and the TZVP basis set. To evaluate the accuracy of our computations, we first carried out calculations on the unique example of a structurally characterized Cu_1S^E complex (for more details, see the Supporting Information), bearing the tris[2-(*N*-tetramethylguanidyl)ethyl]amine ligand (**2**, Scheme 2).[21] The calculated O–O bond length is 1.282 Å, in pleasing agreement with the experimentally determined value of 1.280(3) Å.[21,35]

In both cases, the triplet state is computed to be lower in energy (by 8.8 kJ mol^{-1} for $[L_2CuO_2]^+$ and by 22.2 kJ mol^{-1} for $[(L_1Cu)_2O_2]^{2+}$) than the broken-symmetry state. Figure 6 illustrates the optimized structures for the triplet ground states of the dinuclear $[(L_1Cu)_2O_2]^{2+}$ and mononuclear $[L_2CuO_2]^+$ Cu_1S^E complexes. The structural parameters for $[L_2CuO_2]^+$ include Cu–O distances of 1.936 and 2.734 Å and a Cu–O–O angle of 113.8°. The O–O bond length of 1.300 Å, as compared with a bond length of 1.21 Å in free dioxygen,[55] supports the formulation as a strongly activated superoxide. An example of a Cu_1S^E complex with a low degree of charge transfer is the enzyme PHM (O–O bond length of 1.23 Å),[32] whereas a strong degree of charge transfer in Cu_1S^E complexes results in O–O distances of around 1.29 Å.[23,56,57]

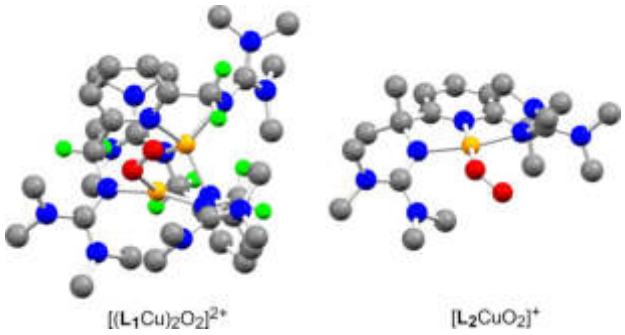

Figure 6. DFT-optimized structures of end-on triplet Cu^{II} superoxo complexes (Cu atoms in orange, O atoms in red, N atoms in blue, C atoms in gray, and H atoms from the methylene bridge $H(CH_2)$ in green). Other hydrogen atoms are omitted for clarity. The shortest Cu–O–O···$H(CH_2)$ distance is 3.188 Å.

The structural parameters calculated for the dinuclear complex $[(L_1Cu)_2O_2]^{2+}$ (2.254 and 3.050 Å for the Cu–O distances, 118.2° for the Cu–O–O angle, and 1.235 Å for the O–O bond length) indicate a much lower degree of charge transfer in the

copper–dioxygen complex, nearly identical to that reported for PHM.[32] As indicated by the space-filling model (Figure 1b), only the twofold-coordinated copper atom is accessible for O_2 coordination. The reduced ability of the copper atom in $[(\mathbf{L_1}Cu)_2O_2]^{2+}$ to donate electron density to the dioxygen unit might result from its low coordination number. A subsequent reaction to give higher nuclear complexes (see Scheme 1a) is prevented by the steric demand of the ligand. The calculations yielded no other energy minima for isomeric copper–dioxygen complexes. For example, starting with a structure with a side-on ($\mathbf{Cu_1S^S}$) bound dioxygen unit, the calculation converged to the structure of the end-on superoxo ($\mathbf{Cu_1S^E}$) complex.

Subsequently, the low-energy electronic excitations for $[\mathbf{L_2}CuO_2]^+$ were calculated with TD-DFT and compared with the excitations observed in the UV/Vis spectra (Figure 7a). For the monomeric complex $[\mathbf{L_2}CuO_2]^+$, the calculations predict a single strong electronic transition in the visible region at 596 nm, predominantly involving orbitals at the Cu^{II} atom and the superoxide unit. Hence, the calculations are in excellent agreement with the experimental spectrum, showing a strong band at 596 nm. To understand the hydroxylating reactivity of $[(\mathbf{L_1}Cu)_2]^{2+}$, we first examined the electronic structure of the initially formed $\mathbf{Cu_1S^E}$ complex based on DFT calculations. The spin density determined by a natural population analysis[58] mainly resides on the two oxygen atoms (0.87 and 0.85 e Å^{-3}, respectively) due to weak charge transfer in the copper–dioxygen complex, as indicated by the short O–O bond (1.235 Å). As already mentioned, the low coordination number of two for the Cu_B atom (Scheme 6) and the high total charge of 2+ of the complex could be responsible for this weak charge transfer in the copper–dioxygen complex. The spin density at the Cu_B atom is 0.20 e Å^{-3}. Interestingly, a small but significant spin density of 0.023 e Å^{-3} was found at the buried Cu_A atom. The existence of spin density at the fourfold coordinated Cu_A atom indicates its ability to transfer electron density to Cu_B (see below). The total spin density at the pyridine ring is very small at 0.0076 e Å^{-3}.

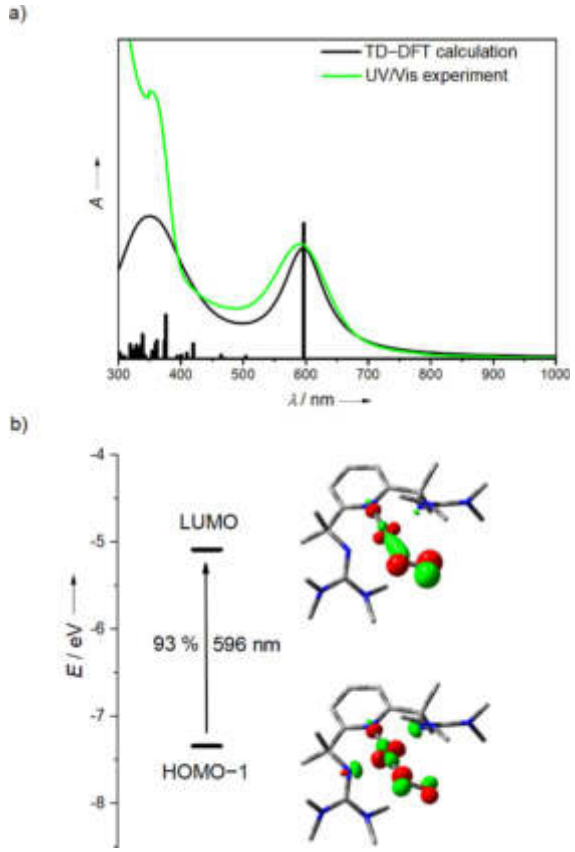

Figure 7. a) Comparison between the TD-DFT (TPSSh + D3/def2-TZVP) results for the 50 lowest-energy electronic excitations and the UV/Vis spectrum for $[\mathbf{L_2}CuO_2]^+$. b) Isodensity plots for the orbitals involved in the low-energy (charge-transfer) transition at 596 nm.

Having studied the electronic structure of the initially formed $\mathbf{Cu_1S^E}$ complex, quantum chemical calculations on the first steps of the hydroxylating mechanism were performed. According to the literature, three main intermediates ($\mathbf{Cu_1S^E}$, $\mathbf{Cu_1P^H}$, $\mathbf{Cu_1O}$) are considered for the hydroxylating activity of the enzyme PHM.[11,33,34] The formation of a $\mathbf{Cu_1P^H}$ complex (which could further react to afford a $\mathbf{Cu_1O}$ species) by proton transfer from a solvent molecule to the O_2 unit of the $\mathbf{Cu_1S^E}$ complex, as assumed from DFT calculations in the literature,[33] could be excluded. The high pK_a value of acetonitrile precludes this mechanism. In all three cases ([**3**]PF_6, [**4**]PF_6, and [**5**]$(PF_6)_3$), intramolecular proton-coupled electron transfer (PCET, Scheme 6a) to the dioxygen unit attached to Cu_B is assumed to be the first step of the reaction sequence, in analogy to the mechanism reported by Itoh et al.[39] One may identify two possible reaction sites for hydrogen atom abstraction at the methylene bridge, denoted **L** and **R** in Scheme 6a.

Hydrogen atom abstraction at the **L** reaction site can occur after rotation about the Cu–O bond, reducing the distance between the outer oxygen atom and the hydrogen atom to about 3.6 Å. A cooperative effect of the Cu_A center leads to a stabilization of the PCET product through delocalization of the spin density to Cu_A, as expressed by the two mesomeric structures $\mathbf{L_I}$ and $\mathbf{L_{II}}$ (Scheme 6a), and the guanidino groups. A natural population analysis indeed found spin density (Scheme 6b) not only at the activated methylene bridge (0.52 e Å^{-3}), but also at the pyridine ring as well as at the guanidino group. In addition, the spin density at the Cu_A atom increased from 0.023 e Å^{-3} ($[(\mathbf{L_1}Cu)_2(O_2)]^{2+}$) to 0.084 e Å^{-3}, in line with a partial oxidation of Cu_A as expressed by the Lewis structure $\mathbf{L_{II}}$. The relevance of structure $\mathbf{L_{II}}$ is further demonstrated by a significant shortening of the bonds highlighted in orange (see Scheme 6a; for detailed comparison, see the Supporting Information). The calculated Gibbs free energy change (at 298.15 K, 1 atm) for the intramolecular PCET process for $[(\mathbf{L_1}Cu)_2(O_2)]^{2+}$ of 46 kJ mol^{-1} is lower than that reported by Itoh et al.[39] for the analogous process in mononuclear copper complexes of ligand $\mathbf{1^X}$ (69 kJ mol^{-1} for X = H). This result demonstrates the importance of the cooperative effect of the Cu_A atom, which stabilizes the PCET product with respect to the $[(\mathbf{L_1}Cu)_2(O_2)]^{2+}$ starting complex through the resulting mesomeric stabilization of $\mathbf{L_I}$ and $\mathbf{L_{II}}$ (Scheme 6a). A transition state **TS1** was localized (see the Supporting Information). The relative free activation energy of 122 kJ mol^{-1} was estimated through a single-point

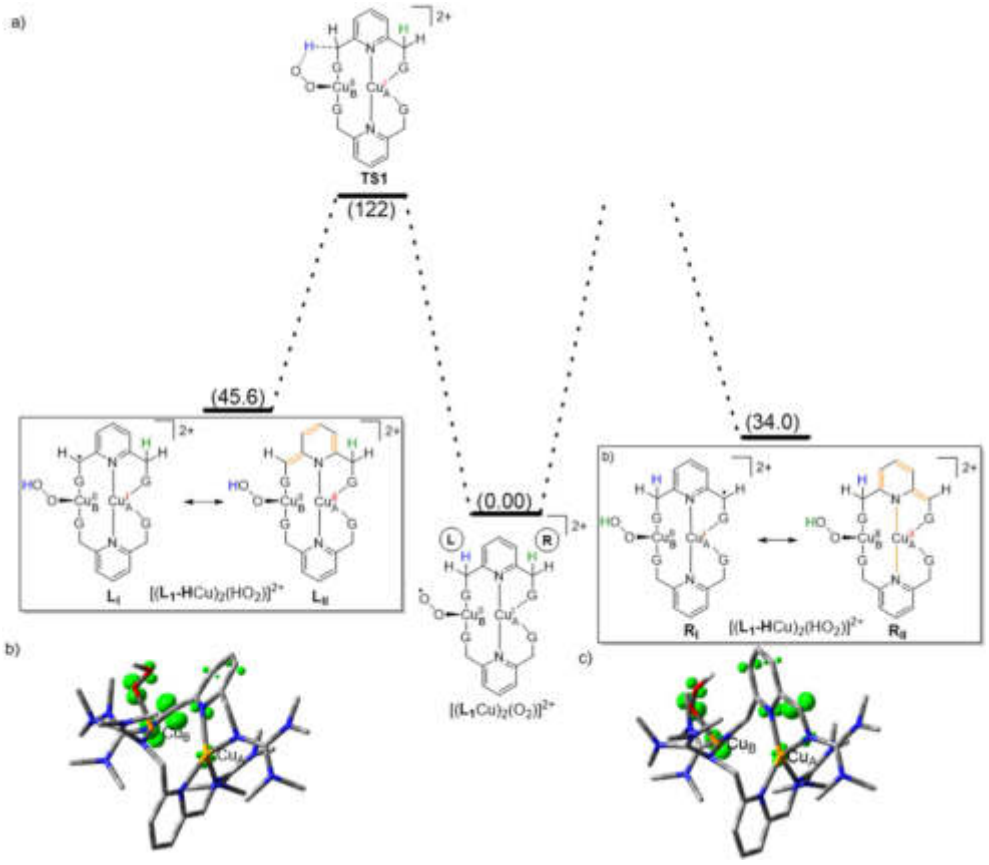

Scheme 6. a) Energy profile (in kJ mol^{-1}) of the proposed hydroxylation pathway (two possible reaction sites **L** and **R**). Bonds in $\mathbf{L_{II}}$ and $\mathbf{R_{II}}$ highlighted in orange are shortened in comparison with those in $[(\mathbf{L_1}Cu)_2(O_2)]^{2+}$. b, c) Calculated spin density for $[(\mathbf{L_1}Cu)_2(HO_2)]^{2+}$ (green circles, TPSSh + D3/def2-TZVP), hydrogen atoms (except OH) omitted for clarity (Cu atoms in orange, N atoms in blue, O atoms in red, and C atoms in gray).

calculation using COSMO ($\varepsilon_r = 37.50$). The hydrogen atom at reaction site **R** is closest to the superoxide oxygen at 3.188 Å, without the need of a further rotation. Moreover, the calculated free energy change (298.15 K, 1 atm) for the intramolecular PCET process is only 34 kJ mol^{-1}, which is 12 kJ mol^{-1} lower than that calculated for reaction site **L**. This can be explained by a better mesomeric stabilization of the PCET product in $\mathbf{R_I}$ and $\mathbf{R_{II}}$, leading to a high spin density at Cu_A of 0.13 e Å^{-3}. The spin density at Cu_B is 0.45 e Å^{-3}. Unfortunately, we were unable to find a transition state for this PCET process, and so it remains unclear as to whether reaction occurs at both **R** and **L** or preferentially at one of these sites. The relatively high activation energy of 122 kJ mol^{-1} is close to that estimated for the C–H bond cleavage in the enzyme PHM.[59] As emphasized previously, the environment plays an important role in calculating the activation barrier in this process, and the experimental value should be significantly lower. Therefore, we suggest an overestimation of the activation energy, especially due to the inaccuracy in calculating the solvent effect with COSMO.

Substrate oxidation experiments

To further illuminate the role of metal cooperativity in ligand hydroxylation, we tested the hydroxylation of external guanidine **6** with complex $[(\mathbf{L_1}Cu)_2](PF_6)_2$ and dioxygen (Scheme 7).

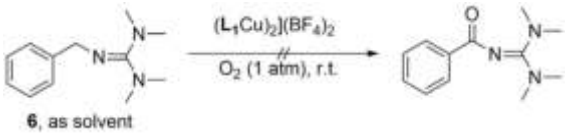

Scheme 7. Attempted hydroxylation of the external substrate **6** with $[(\mathbf{L_1}Cu)_2](PF_6)_2$. No reaction occurred, in line with the importance of metal cooperativity for the hydroxylation of $\mathbf{L_1}$ in the $[(\mathbf{L_1}Cu)_2]^{2+}$ complex.

No reaction was observed, even when the reaction was carried out in neat **6**, in accordance with the importance of metal cooperativity through the mesomeric stabilization of **I** and **II** (Scheme 6a).

Recently, the first example was reported of a nucleophilic copper superoxide inducing a catalytic aldol reaction, that is, with acetone, forming 4-hydroxy-4-methyl-2-pentanone at room temperature.[60] In this context, the isolation of diacetone alcohol (4-hydroxy-4-methyl-2-pentanone, Scheme 8) as a side

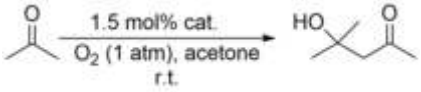

Scheme 8. Formation of 4-hydroxy-4-methyl-2-pentanone from acetone (cat. = $[(\mathbf{L_1}Cu)_2](PF_6)_2$ or $[\mathbf{L_2}CuO_2]PF_6$).

product in the course of the formation of [**5**] motivated us to test the two complexes $[(\mathbf{L_1}Cu)_2](PF_6)_2$ and $[\mathbf{L_2}CuO_2]PF_6$ in dioxygen activation in terms of the catalytic conversion of acetone.

Both complexes were applied at a catalytic level (1.5 mol%) and clearly showed catalytic conversions of acetone, with turnover numbers (TON) of 6.50 for $[(\mathbf{L_1}Cu)_2](PF_6)_2$ and 2.25 for the monomeric complex $[\mathbf{L_2}Cu]PF_6$.

Conclusions

We have reported the reactions of two new copper(I) complexes, bearing bisguanidine ligands, with dioxygen. With ligand $\mathbf{L_1}$, a dinuclear complex $[(\mathbf{L_1})Cu]_2^{2+}$ with two significantly different Cu^I atoms is formed, both in the solid state and in solution. Only one of the copper atoms is able to bind dioxygen, since the other is buried inside the ligand shell. In contrast, the slightly modified ligand $\mathbf{L_2}$ preferentially forms a mononuclear Cu^I complex $[(\mathbf{L_2})Cu]^+$. Both complexes are suggested to react with dioxygen to afford thermally labile end-on superoxo complexes ($\mathbf{Cu_1S^E}$) that differ in the degree of charge transfer. The dimeric complex $[(\mathbf{L_1}Cu)_2(O_2)]^{2+}$ exhibits a low degree of charge transfer, whereas for $[(\mathbf{L_2})Cu(O_2)]^+$ a strong degree of charge transfer is found.

Intramolecular hydrogen atom abstraction from the methylene bridge of $\mathbf{L_1}$ by the O_2 unit leads to ligand hydroxylation, initiating a reaction sequence that leads (depending on the reaction conditions) to either mononuclear or trinuclear copper complexes with oxidized ligand units. Considering the degree of charge transfer of the copper–dioxygen complexes and the resulting C–H activation, the complex $[(\mathbf{L_1})Cu]_2^{2+}$ might be a model for the enzyme peptidylglycine α-hydroxylating monooxygenase (PHM). Further analysis showed that the two copper atoms in $[(\mathbf{L_1}Cu)_2(O_2)]^{2+}$ communicate through charge transfer (as for PHM and its cofactor). This cooperative effect on the hydroxylating reaction between the two copper atoms was further studied by DFT computations, and was suggested to be the key driving force for the proton-coupled electron transfer in the C–H activation process.

Furthermore, both complexes mediate acetone dimerization to form 4-hydroxy-4-methyl-2-pentanone, similar to a recently reported nucleophilic $\mathbf{Cu_1S^E}$ complex.[60] Studies on the reactivity of the complex $[(\mathbf{L_2})Cu(O_2)]^+$, which is stable for minutes at low temperatures, as a potential nucleophile are currently underway in our laboratories.

Experimental Section

General

The copper complexes were stored under an inert argon atmosphere in a glovebox (MBraun Labmaster dp). All chemicals were purchased from Aldrich and used without further purification unless stated otherwise below. Solvents were dried with an MBraun solvent purification system, degassed by three freeze-pump-thaw cycles, and stored over molecular sieves prior to use. Propionitrile was purified and dried according to a literature procedure.[61] Dioxygen (Air Liquide, Alphagaz™, purity ≥99.998%) was dried by passage through a short column of supported P_4O_{10}. The syntheses of $\mathbf{L_1}$ and 2,6-bis(α-aminoisopropyl)pyridine followed literature procedures.[51,62] Elemental analyses were carried out at the Microanalytical Laboratory of the University of Heidelberg. NMR spectra were recorded on a Bruker Avance II 400 system (BBFO probe) or a Bruker Avance III 600 spectrometer (QNP Cryoprobe, inner coil tuned to ^{13}C, cold preamplifier). Prior to variable-temperature measurements, the temperature was calibrated by the method of Berger et al.[63] Solvent resonances were taken as references for all ^1H NMR or ^{13}C NMR spectra.[64] UV/Vis spectra were recorded with a Varian Cary 5000 spectrophotometer. For IR spectroscopy, samples of the compounds were prepared in KBr disks and examined on an FTIR spectrometer (Biorad, Model Merlin Excalibur FT 3000). ESI-MS and CID experiments of isolated ions (MS-MS) were conducted on a Bruker ApexQe hybrid 9.4 T FT-ICR mass spectrometer. Raman measurements were performed with a UT-3 Raman spectrometer,[65] using a frequency-doubled/tripled Ti:sapphire laser (Tsunami model 3960C-15HP, Spectra Physics Lasers Inc.) with a pulse width of 1.6–2.5 ps. The cryostat was a slightly modified version of a setup described previously[66] with a 1.4 mL screw-cap Suprasil® cuvette with septum (Hellma Analytics, Müllheim) for oxygenation, equipped with a Peltier element (QuickCool QC-127-1.4–6.0MS) and a cooling copper block enclosing three sides of the cuvette.

Synthesis and characterization

2,6-Bis(1-tetramethylguanidino-1-methyl-ethyl)pyridine ($\mathbf{L_2}$): Tetramethylurea (0.9 mL, 7.4 mmol) was dissolved in chloroform (6 mL). Oxalyl chloride (3.2 mL, 37 mmol) was added dropwise, and the solution was heated under reflux (80 °C) for 18 h. It was then left to cool to room temperature, the solvent was removed in vacuo, and the pale-yellow residue was washed with diethyl ether (3×10 mL). The colorless guanidinium chloride was dried under vacuum. 2,6-Bis(α-aminoisopropyl)pyridine (840 mg, 2.80 mmol) was dissolved in dichloromethane (20 mL), and dry triethylamine (1.7 mL, 12 mmol) was added. The chloroformamidinium chloride was redissolved in dichloromethane (15 mL) and the solution was slowly added to the diamine at −10 °C. The reaction mixture was stirred at −10 °C for 1 h, 10% HCl (10 mL) was added, the phases were separated, and the organic layer was washed with 10% HCl (2×10 mL). The combined aqueous layers were washed with dichloromethane (10 mL), and 50% KOH (20 mL) was added. The aqueous layer was then extracted with toluene (3×20 mL). The combined toluene phases were dried with K_2CO_3, and the solvent was removed in vacuo to leave a brown oil. Further purification was achieved by leaving a solution of the oil in acetonitrile in a freezer (−18 °C) for several days, whereupon crystallization occurred. The colorless crystals were dried in vacuo to afford a colorless powder (468 mg, 120 μmol, 43%). ^1H NMR (400 MHz, CD_3CN): $\delta = 7.47$ (m, 1H), 7.19 (d, $J = 7.8$ Hz, 2H), 2.63 (br s, 12H), 2.26 (br s, 12H), 1.50 ppm (s, 12H); ^{13}C NMR (100 MHz, CD_3CN): $\delta = 168.38$, 157.41, 135.81, 60.94, 32.14 ppm; elemental analysis calcd (%) for $C_{21}H_{39}N_7$ (389.59): C 64.74, H 10.09, N 25.17; found: C 64.38, H 9.90, N 25.25. Crystal data for $\mathbf{L_2}$: $C_{21}H_{39}N_7$, $M_r = 389.59\ g\,mol^{-1}$, 0.60 mm × 0.40 mm × 0.30 mm, monoclinic, space group *C*2/*c*, lattice constants $a = 24.238(5)$ Å, $b = 7.4070(15)$ Å, $c = 13.794(3)$ Å, $V = 2272.1(9)$ Å^3, $Z = 4$, $d_{calcd} = 1.139\ g\,cm^{-3}$, $Mo_{K\alpha}$ radiation (graphite-monochromated, $\lambda = 0.71073$ Å), $T = 120$ K, $\theta_{max} = 30.127°$, number of reflections measured: 3326, number of independent reflections: 2224, final *R* indices [$I > 2\sigma(I)$]: $R_1 = 0.0481$, $wR_2 = 0.1319$.

$[(\mathbf{L_1}Cu)_2](BF_4)_2$: A solution of tetrakis(acetonitrile)copper(I) tetrafluoroborate (94.0 mg, 299 μmol) and $\mathbf{L_1}$ (100 mg, 299 μmol) in acetone (1 mL) or acetonitrile (1 mL) was stirred for 1 h at room temperature. The solution was then overlayered with Et_2O (10 mL),

whereupon orange crystals separated overnight. The crystals were dried in vacuo to afford the product as an orange powder (110 mg, 138 μmol, 92%). ^{1}H NMR (600 MHz, CD_3CN): $\delta = 7.81$ (t, $J = 7.7$ Hz, 1H), 7.28 (d, $J = 7.7$ Hz, 2H), 4.50 (s, 4H), 2.79 (s, 12H), 2.52 ppm (s, 12H); ^{13}C NMR (150 MHz, CD_3CN): $\delta = 165.85$, 160.56, 139.42, 122.89, 57.83, 30.44, 39.37 ppm; elemental analysis calcd (%) for $C_{34}H_{62}N_{14}B_2Cu_2F_8$ (967.68): C 42.20, H 6.46, N 20.26; found: C 41.82, H 6.36, N 21.02; UV/Vis (CH_3CN, $c = 7.47\times10^{-5}$): λ_{max} (ε in $L\,mol^{-1}\,cm^{-1}$) = 210 (2.72×10^4), 272 (8.64×10^3), 357 nm (883). Crystal data for $[(\mathbf{L_1}Cu)_2(BF_4)_2]$: $C_{34}H_{62}N_{14}B_2Cu_2F_8$ from acetonitrile solution, $M_r = 967.68\ g\,mol^{-1}$, 0.40 mm × 0.25 mm × 0.15 mm, triclinic, space group $P\bar{1}$, lattice constants $a = 9.906(2)$ Å, $b = 11.162(2)$ Å, $c = 11.236(2)$ Å, $V = 1099.3(5)$ Å^3, $Z = 1$, $d_{calcd} = 1.462\ g\,cm^{-3}$, $Mo_{K\alpha}$ radiation (graphite-monochromated, $\lambda = 0.71073$ Å), $T = 120$ K, $\theta_{max} = 31.00°$, number of reflections measured: 13069, number of independent reflections: 10373, final R indices [$I > 2\sigma(I)$]: $R_1 = 0.0505$, $wR_2 = 0.1364$. Crystal data for $[(\mathbf{1}Cu)_2(BF_4)_2]$: $C_{34}H_{62}N_{14}B_2Cu_2F_8$ from acetone solution, $M_r = 967.68\ g\,mol^{-1}$, 0.80 mm × 0.60 mm × 0.50 mm, triclinic, space group $P\bar{1}$, lattice constants $a = 16.350(3)$ Å, $b = 20.870(4)$ Å, $c = 26.131(5)$ Å, $V = 8917(3)$ Å^3, $Z = 8$, $d_{calcd} = 1.442\ g\,cm^{-3}$, $Mo_{K\alpha}$ radiation (graphite-monochromated, $\lambda = 0.71073$ Å), $T = 120$ K, $\theta_{max} = 30.063°$, number of reflections measured: 13050, number of independent reflections: 8428, final R indices [$I > 2\sigma(I)$]: $R_1 = 0.0541$, $wR_2 = 0.1792$.

$[\mathbf{L_2}Cu]BF_4$: A solution of tetrakis(acetonitrile)copper(I) tetrafluoroborate (18.4 mg, 58.5 μmol) and $\mathbf{L_2}$ (23.4 mg, 58.5 μmol) in CH_3CN (2 mL) was stirred for 1 h at room temperature. The solvent was then removed in vacuo, the residue was washed with Et_2O (2× 2 mL), and the solid was dried in vacuo to afford the product as an orange powder (25.0 mg, 51.7 μmol, 88%). ^{1}H NMR (600 MHz, CD_3CN) for the monomer: $\delta = 7.72$ (m, 1H), 7.30 (m, 2H), 2.72 (s, 12H), 2.40 (s, 12H), 1.61 ppm (s, 12H); ^{13}C NMR (150 MHz, CD_3CN): $\delta = 167.27$, 160.75, 138.37, 117.19, 62.21, 40.32, 39.45, 29.67 ppm; elemental analysis calcd (%) for $C_{21}H_{39}N_7BCuF_4$ (539.94): C 46.71, H 7.28, N 18.16; found: C 46.73, H 7.31, N 19.09; UV/Vis (CH_3CN, $c = 6.00\times10^{-5}$): λ_{max} (ε in $L\,mol^{-1}\,cm^{-1}$) = 212 (3.76×10^4), 263 (1.44×10^4), 414 nm (686).

$[\mathbf{3}]PF_6$: A solution of tetrakis(acetonitrile)copper(I) hexafluorophosphate (112 mg, 299 μmol) and $\mathbf{L_1}$ (100 mg, 299 μmol) in acetonitrile (1.5 mL) was stirred for 1 h at room temperature. Dioxygen was then introduced by means of a syringe (1 bar overpressure) and the mixture was stirred for 16 h. Water (10 mL) was then added, and the mixture was extracted with dichloromethane (4×7 mL). The combined organic layers were dried over magnesium sulfate and the solvent was removed in vacuo. Green crystals of $[\mathbf{3}]PF_6$ were grown by slow evaporation of the volatiles from a saturated solution in acetonitrile. Crystal data for $[\mathbf{3}]PF_6$: $C_{17}H_{27}N_7CuO_2ClF_6P$, $M_r = 605.41\ g\,mol^{-1}$, 0.50 mm × 0.50 mm × 0.3 mm, orthorhombic, space group $Pnma$, lattice constants $a = 11.674(2)$ Å, $b = 14.092(2)$ Å, $c = 15.341(3)$ Å, $V = 2523.7(9)$ Å^3, $Z = 4$, $d_{calcd} = 1.593\ g\,cm^{-3}$, $Mo_{K\alpha}$ radiation (graphite-monochromated, $\lambda = 0.71073$ Å), $T = 120$ K, $\theta_{max} = 30.078°$, number of reflections measured: 3836, number of independent reflections: 2754, final R indices [$I > 2\sigma(I)$]: $R_1 = 0.0547$, $wR_2 = 0.1595$; HRMS (ESI+): m/z calcd for $C_{17}H_{27}N_7O_2CuCl$ [M^+]: 459.1211; found: 459.1213.

$[\mathbf{4}]PF_6$: A solution of tetrakis(acetonitrile)copper(I) hexafluorophosphate (56.0 mg, 150 μmol) and $\mathbf{L_1}$ (50.0 mg, 150 μmol) in propionitrile (2 mL) was stirred for 1 h at room temperature. The reaction mixture was then cooled to −78 °C, dioxygen was introduced by means of a syringe (0.2 bar overpressure), and the mixture was stirred for 4 h. After purging the resulting blue solution with argon (ca. 5 min) and allowing it to warm to room temperature (color change to green), the solvent was removed in vacuo and dichloromethane was added. HRMS (ESI$^+$): m/z calcd for $C_{17}H_{31}N_7O_2CuCl$ [M^+]: 463.1524; found: 463.1525.

$[\mathbf{5}](PF_6)_3$: A solution of tetrakis(acetonitrile)copper(I) hexafluorophosphate (112 mg, 299 μmol) and $\mathbf{L_1}$ (100 mg, 299 μmol) in acetone (3 mL) was stirred for 1 h at room temperature. Dioxygen was introduced by means of a syringe (−78 °C), and the mixture was filtered through a syringe filter. The solution was stored for 1 week in a freezer (−80 °C). Residual dioxygen was removed by bubbling Ar (ca. 5 min) through the reaction solution at −78 °C. Blue crystals were grown by diffusion of diethyl ether into the solution at −18 °C, which were collected by filtration and washed with cold acetone (2 mL) and diethyl ether (5 mL). The crystals were dried in vacuo to afford $[\mathbf{5}](PF_6)_3$ as a blue powder (50 mg, 33.3 μmol) in 33% isolated yield. Elemental analysis calcd (%) for $C_{45}H_{69}N_{12}Cu_3O_6(F_6P)_3(C_3H_6O)_{1.5}$ (1543.21): C 36.78, H 4.80, N 10.89; found: C 37.61, H 5.12, N 10.76; IR (KBr): $\nu = 3102$ (w), 2009 (w), 2947 (m), 2900 (m), 2812 (w), 1698 (s), 1611 (m), 1588 (s), 1477 (m), 1427 (m), 1400 (m), 1358 (m), 1339 (w), 1294 (w), 1255 (w), 1236 (w), 1166 (s), 1146 (w), 1115 (w), 1070 (m), 1054 (s), 1015 (w), 972 (w), 939 (w), 912 (m), 877 (m), 841 (s), 791 (m), 764 (m), 784 (w), 691 (m), 669 (w), 648 (m), 622 (m), 558 (s), 530 (w), 496 (m), 465 (w), 450 (w), 428 (w), 421 cm^{-1} (m); UV/Vis (CH_3CN, $c = 4.61\times10^{-5}$): λ_{max} (ε in $L\,mol^{-1}\,cm^{-1}$) = 218 (5.46×10^4), 267 (2.08×10^4), 334 (4.12×10^3), 336 nm (3.03×10^3). Crystal data for $[\mathbf{5}](PF_6)_3$: $C_{45}H_{69}N_{12}Cu_3O_6(F_6P)_3(C_3H_6O)_{1.5}$, $M_r = 1543.21\ g\,mol^{-1}$, 0.40 mm × 0.30 mm × 0.15 mm, monoclinic, space group $C2/c$, lattice constants $a = 23.840(5)$ Å, $b = 15.796(3)$ Å, $c = 37.282(8)$ Å, $V = 13543(5)$ Å^3, $Z = 8$, $d_{calcd} = 1.514\ g\,cm^{-3}$, $Mo_{K\alpha}$ radiation (graphite-monochromated, $\lambda = 0.71073$ Å), $T = 120$ K, $\theta_{max} = 29.182°$, number of reflections measured: 18224, number of independent reflections: 14550, final R indices [$I > 2\sigma(I)$]: $R_1 = 0.0567$, $wR_2 = 0.1718$.

Catalytic coupling of acetone to generate 4-hydroxy-4-methyl-2-pentanone: A solution of tetrakis(acetonitrile)copper(I) hexafluorophosphate (112 mg, 299 μmol) and the ligand ($\mathbf{L_1}$ or $\mathbf{L_2}$ (20 mmol), see Table 1) in acetone (1.5 mL) was stirred for 1 h at room temperature. Dioxygen was then introduced by means of a syringe (1 bar overpressure) and the mixture was stirred for 20 h. 4-Hydroxy-4-methyl-2-pentanone and acetone were separated by distillation from the residue. ^{1}H and ^{13}C NMR data were consistent with those reported previously.[67]

Table 1. Yield and weighting.

	$\mathbf{L_1}$ (100 mg, 299 μmol)	$\mathbf{L_2}$ (117 mg, 299 μmol)
Yield of diacetone alcohol	114 mg, 877 μmol, TON 6.50	77.9 mg, 671 μmol, TON 2.25

Note: A blank experiment with ligand alone did not lead to conversion of acetone.

Raman measurements

A laser beam was widened with a spatial filter and then focused on a cuvette inside a cryostat. The diameter of the focused spot was around 20 μm. Raman scattered light was captured with the entrance optics of a UT-3 triple-monochromator spectrometer.[65] A 30 mmol L^{-1} solution of the precursor in propionitrile was cooled in the cuvette cryostat to the desired temperature. Dioxygen was introduced via a cannula through the septum (0.02 bar overpressure for 30 s) until a distinct color change was observed. The solu-

tion was then rapidly frozen by cooling to −100 °C. The laser power used ahead of the entrance optics was 10.7 mW. Data were accumulated for 3×300 s and corrected for the spectral sensitivity of the instrument.

X-ray crystallographic study

Crystals suitable for single-crystal structure determination were taken directly from the mother liquor, taken up in perfluorinated polyether oil, and fixed on a cryo-loop. Full shells of intensity data were collected at low temperature with a Nonius Kappa CCD diffractometer ($Mo_{K\alpha}$ radiation, sealed X-ray tube, graphite monochromator). The data were processed with the standard Nonius software.[68] A multiscan absorption correction was applied to all intensity data using the SADABS program.[59] The structures were solved and refined using the SHELXTL software package (versions 2014/6 and 2018/3).[70,71] Graphical handling of the structural data during solution and refinement was performed with XPMA and OLEX2.[72] All non-hydrogen atoms were assigned anisotropic displacement parameters. Hydrogen atoms were generally introduced in calculated positions and refined with a riding model. Due to severe disorder, the electron density attributed to solvent of crystallization (acetone) was removed from the structure of [**5**]$(PF_6)_3$ by the BYPASS procedure,[73] as implemented in PLATON (squeeze/hybrid).[74] Partial structure factors from the solvent masks were included in the refinement as separate contributions to F_{calcd}. CCDC 1867620 (**L_2**), 1867616 ([**L_1**$Cu)_2$]$(BF_4)_2$) from acetonitrile solution, 1867618 ([**L_1**$Cu)_2$]$(BF_4)_2$) from acetone solution, 1867617 ([**5**]$(PF_6)_3$, and 1867619 ([**3**]PF_6) contain the supplementary crystallographic data for this paper. These data are provided free of charge by The Cambridge Crystallographic Data Centre.

Acknowledgements

The authors gratefully acknowledge continuous financial support by the Deutsche Forschungsgemeinschaft (DFG). The authors are grateful for the computational resources provided by the bwForCluster JUSTUS, funded by the Ministry of Science, Research and Arts and the Universities of the State of Baden–Württemberg, Germany, within the framework program bwHPC-C5. We thank Dr. J. Gross for support with ESI mass spectrometry.

Conflict of interest

The authors declare no conflict of interest.

Keywords: C–H activation · cooperative effects · copper · dioxygen complexes · oxidation

[1] *Copper–Oxygen Chemistry* (Eds.: K. D. Karlin, S. Itoh), Vol. 4, *Wiley Series on Reactive Intermediates in Chemistry and Biology*, **2011**, Wiley, Hoboken.
[2] L. M. Mirica, X. Ottenwaelder, T. D. P. Stack, *Chem. Rev.* **2004**, *104*, 1013–1045.
[3] S. Schindler, *Eur. J. Inorg. Chem.* **2000**, 2311–2326.
[4] A. Bhagi-Damodaran, M. A. Michael, Q. Zhu, J. Reed, B. A. Sandoval, E. N. Mirts, S. Chakraborty, P. Moënne-Loccoz, Y. Zhang, Y. Lu, *Nat. Chem.* **2017**, *9*, 257–263.
[5] S. Itoh, *Acc. Chem. Res.* **2015**, *48*, 2066–2074.
[6] C. J. Cramer, W. B. Tolman, *Acc. Chem. Res.* **2007**, *40*, 601–608.
[7] S. Fukuzumi, K. D. Karlin, *Coord. Chem. Rev.* **2013**, *257*, 187–195.
[8] E. A. Lewis, W. B. Tolman, *Chem. Rev.* **2004**, *104*, 1047–1076.
[9] E. I. Solomon, D. E. Heppner, E. M. Johnston, J. W. Ginsbach, J. Cirera, M. Qayyum, M. T. Kieber-Emmons, C. H. Kjaergaard, R. G. Hadt, L. Tian, *Chem. Rev.* **2014**, *114*, 3659–3853.
[10] J. B. Klinman, *Chem. Rev.* **1996**, *96*, 2541–2561.
[11] M. Rolff, F. Tuczek, *Angew. Chem. Int. Ed.* **2008**, *47*, 2344–2347; *Angew. Chem.* **2008**, *120*, 2378–2381.
[12] I. A. Koval, P. Gamez, C. Belle, K. Selmeczi, J. Reedijk, *Chem. Soc. Rev.* **2006**, *35*, 814–840.
[13] V. Mahadevan, R. J. M. K. Gebbink, T. D. P. Stack, *Curr. Opin. Chem. Biol.* **2000**, *4*, 228–234.
[14] M. Rolff, J. Schottenheim, G. Peters, F. Tuczek, *Angew. Chem. Int. Ed.* **2010**, *49*, 6438–6442; *Angew. Chem.* **2010**, *122*, 6583–6587.
[15] R. E. Cowley, J. Cirera, M. F. Qayyum, D. Rokhsana, B. Hedman, K. O. Hodgson, D. M. Dooley, E. I. Solomon, *J. Am. Chem. Soc.* **2016**, *138*, 13219–13229.
[16] E. Solem, F. Tuczek, H. Decker, *Angew. Chem. Int. Ed.* **2016**, *55*, 2884–2888; *Angew. Chem.* **2016**, *128*, 2934–2938.
[17] M. Rolff, J. Schottenheim, H. Decker, F. Tuczek, *Chem. Soc. Rev.* **2011**, *40*, 4077–4098.
[18] M. Schatz, V. Raab, S. P. Foxon, G. Brehm, S. Schneider, M. Reiher, M. C. Holthausen, J. Sundermeyer, S. Schindler, *Angew. Chem. Int. Ed.* **2004**, *43*, 4360–4363; *Angew. Chem.* **2004**, *116*, 4460–4464.
[19] D. Maiti, H. C. Fry, J. S. Woertink, M. A. Vance, E. I. Solomon, K. D. Karlin, *J. Am. Chem. Soc.* **2007**, *129*, 264–265.
[20] J. Y. Lee, R. L. Peterson, K. Ohkubo, J. Garcia-Bosch, R. A. Himes, J. Woertink, C. D. Moore, E. I. Solomon, S. Fukuzumi, K. D. Karlin, *J. Am. Chem. Soc.* **2014**, *136*, 9925–9937.
[21] C. Würtele, E. Gaoutchenova, K. Harms, M. C. Holthausen, J. Sundermeyer, S. Schindler, *Angew. Chem. Int. Ed.* **2006**, *45*, 3867–3869; *Angew. Chem.* **2006**, *118*, 3951–3954.
[22] M. P. Lanci, V. V. Smirnov, C. J. Cramer, E. V. Gauchenova, J. Sundermeyer, J. P. Roth, *J. Am. Chem. Soc.* **2007**, *129*, 14697–14709.
[23] P. J. Donoghue, A. K. Gupta, D. W. Boyce, C. J. Cramer, W. B. Tolman, *J. Am. Chem. Soc.* **2010**, *132*, 15869–15871.
[24] K. Fujisawa, M. Tanaka, Y. Moro-oka, N. Kitajima, *J. Am. Chem. Soc.* **1994**, *116*, 12079–12080.
[25] P. Chen, D. E. Root, C. Campochiano, K. Fujisawa, E. I. Solomon, *J. Am. Chem. Soc.* **2003**, *125*, 466–471.
[26] D. J. E. Spencer, N. W. Aboelella, A. M. Reynolds, P. L. Holland, W. B. Tolman, *J. Am. Chem. Soc.* **2002**, *124*, 2108–2109.
[27] N. W. Aboelella, E. A. Lewis, A. M. Reynolds, W. W. Brennessel, C. J. Cramer, W. B. Tolman, *J. Am. Chem. Soc.* **2002**, *124*, 10660–10661.
[28] A. M. Reynolds, B. F. Gherman, C. J. Cramer, W. B. Tolman, *Inorg. Chem.* **2005**, *44*, 6989–6997.
[29] For some examples, see: a) S. T. Prigge, R. E. Mains, B. A. Eipper, L. M. Amzel, *Cell. Mol. Life Sci.* **2000**, *57*, 1236–1259; b) W. A. Francisco, G. Wille, A. J. Smith, D. J. Merkler, J. P. Klinman, *J. Am. Chem. Soc.* **2004**, *126*, 13168–13169; c) P. Chen, E. I. Solomon, *J. Am. Chem. Soc.* **2004**, *126*, 4991–5000; d) J. P. Klinman, *J. Biol. Chem.* **2006**, *281*, 3013–3016.
[30] S. T. Prigge, A. S. Kolhekar, B. A. Eipper, R. E. Mains, L. M. Amzel, *Nat. Struct. Biol.* **1999**, *6*, 976–983.
[31] S. T. Prigge, A. S. Kolhekar, B. A. Eipper, R. E. Mains, L. M. Amzel, *Science* **1997**, *278*, 1300–1305.
[32] S. T. Prigge, B. A. Eipper, R. E. Mains, L. M. Amzel, *Science* **2004**, *304*, 864–867.
[33] B. N. Sánchez-Eguía, M. Flores-Alamo, M. Orio, I. Castillo, *Chem. Commun.* **2015**, *51*, 11134–11137.
[34] A. Crespo, M. A. Marti, A. E. Roitberg, L. M. Amzel, D. A. Estrin, *J. Am. Chem. Soc.* **2006**, *128*, 12817–12828.
[35] D. Maiti, D.-H. Lee, K. Gaoutchenova, C. Würtele, M. C. Holthausen, A. A. Sarjeant, J. Sundermeyer, S. Schindler, K. D. Karlin, *Angew. Chem. Int. Ed.* **2008**, *47*, 82–85; *Angew. Chem.* **2008**, *120*, 88–91.
[36] For some examples, see: a) B. Herzigkeit, B. M. Flöser, T. A. Engesser, C. Näther, F. Tuczek, *Eur. J. Inorg. Chem.* **2018**, 3058–3069; b) J. Becker, Y. Y. Zhyhadlo, E. D. Butova, A. A. Fokin, P. R. Schreiner, M. Förster, M. C. Holthausen, P. Specht, S. Schindler, *Chem. Eur. J.* **2018**, *24*, 15543; c) C. Würtele, O. Sander, V. Lutz, T. Waitz, F. Tuczek, S. Schindler, *J. Am. Chem. Soc.* **2009**, *131*, 7544–7545; d) S. Herres, A. J. Heuwing, U. Flörke, J. Schneider, G. Henkel, *Inorg. Chim. Acta* **2005**, *358*, 1089–1095; e) S.

Itoh, M. Taki, H. Nakao, P. L. Holland, W. B. Tolman, Jr., L. Que, S. Fukuzumi, *Angew. Chem. Int. Ed.* **2000**, *39*, 398 – 400; *Angew. Chem.* **2000**, *112*, 409 – 411; f) P. Comba, S. Knoppe, B. Martin, G. Rajaraman, C. Rolli, B. Shapiro, T. Sork, *Chem. Eur. J.* **2008**, *14*, 344 – 357; g) A. Arnold, R. Metzinger, C. Limberg, *Chem. Eur. J.* **2015**, *21*, 1198 – 1207; h) S. Palavicini, A. Granata, E. Monzani, L. Casella, *J. Am. Chem. Soc.* **2005**, *127*, 18031 – 18036.

[37] For some examples, see: a) O. Sander, A. Henss, C. Nähter, C. Würtele, M. C. Holthausen, S. Schindler, F. Tuczek, *Chem. Eur. J.* **2008**, *14*, 9714 – 9729; b) T. Matsumoto, H. Furutachi, S. Nagatomo, T. Tosha, S. Fujinami, T. Kitagawa, M. Suzuki, *J. Organomet. Chem.* **2007**, *692*, 111 – 121; c) A. Kunishita, J. Teraoka, J. D. Scanlon, T. Matsumoto, M. Suzuki, C. J. Cramer, S. Itoh, *J. Am. Chem. Soc.* **2007**, *129*, 7248 – 7249; d) K. D. Karlin, P. L. Dahlstrom, S. N. Cozzette, P. M. Scensny, J. Zubieta, *J. Chem. Soc. Chem. Commun.* **1981**, 881 – 882; e) T.-D. J. Stumpf, M. Steinbach, C. Würtele, J. Becker, S. Becker, R. Fröhlich, R. Göttlich, S. Schindler, *Eur. J. Inorg. Chem.* **2017**, 4246 – 4258; f) H. R. Lucas, L. Li, A. A. N. Sarjeant, M. A. Vance, E. I. Solomon, K. D. Karlin, *J. Am. Chem. Soc.* **2009**, *131*, 3230 – 3245.

[38] A. Kunishita, M. Kubo, H. Sugimoto, T. Ogura, K. Sato, T. Takui, S. Itoh, *J. Am. Chem. Soc.* **2009**, *131*, 2788 – 2789.

[39] A. Kunishita, M. Z. Ertem, Y. Okubo, T. Tano, H. Sugimoto, K. Ohkubo, N. Fujieda, S. Fukuzumi, C. J. Cramer, S. Itoh, *Inorg. Chem.* **2012**, *51*, 9465 – 9480.

[40] G. Izzet, J. Zeitouny, H. Akdas-Killig, Y. Frapart, S. Ménage, B. Doucziech, I. Jabin, Y. Le Mest, O. Reinaud, *J. Am. Chem. Soc.* **2008**, *130*, 9514 – 9523.

[41] G. Thiabaud, G. Guillemot, I. Schmitz-Afonso, B. Colasson, O. Reinaud, *Angew. Chem. Int. Ed.* **2009**, *48*, 7383 – 7386; *Angew. Chem.* **2009**, *121*, 7519 – 7522.

[42] T. Fujii, S. Yamaguchi, Y. Funahashi, T. Ozava, T. Tosha, T. Kitagawa, H. Masuda, *Chem. Commun.* **2006**, 4428 – 4430.

[43] T. Fujii, S. Yamaguchi, S. Hirota, H. Masuda, *Dalton Trans.* **2008**, 164 – 170.

[44] S. Itoh, H. Kumei, M. Taki, S. Nagatomo, T. Kitagawa, S. Fukuzumi, *J. Am. Chem. Soc.* **2001**, *123*, 6708 – 6709.

[45] T. Osako, K. Ohkubo, M. Taki, Y. Tachi, S. Fukuzumi, S. Itoh, *J. Am. Chem. Soc.* **2003**, *125*, 11027 – 11033.

[46] For some examples, see: a) S. Herres-Pawlis, U. Flörke, G. Henkel, *Eur. J. Inorg. Chem.* **2005**, 3815 – 3824; b) S. Herres-Pawlis, P. Verma, R. Haase, P. Kang, C. T. Lyons, E. C. Wasinger, U. Flörke, G. Henkel, T. D. P. Stack, *J. Am. Chem. Soc.* **2009**, *131*, 1154 – 1169; c) V. Mahadevan, Z. Hou, A. P. Cole, D. E. Root, T. K. Lal, E. I. Solomon, T. D. P. Stack, *J. Am. Chem. Soc.* **1997**, *119*, 11996 – 11997; d) J. A. Halfen, S. Mahapatra, E. C. Wilkinson, S. Kaderli, V. G. Young, Jr., L. Que, Jr., A. D. Zuberbühler, W. B. Tolman, *Science* **1996**, *271*, 1397 – 1400; e) A. Walli, S. Dechert, M. Bauer, S. Demeshko, F. Meyer, *Eur. J. Inorg. Chem.* **2014**, 4660 – 4676.

[47] D. Petrovic, L. M. R. Hill, P. G. Jones, W. B. Tolman, M. Tamm, *Dalton Trans.* **2008**, 887 – 894.

[48] V. Raab, J. Kipke, O. Burghaus, J. Sundermeyer, *Inorg. Chem.* **2001**, *40*, 6964 – 6971.

[49] For some recent examples, see: a) D. F. Schrempp, S. Leingang, M. Schnurr, E. Kaifer, H. Wadepohl, H.-J. Himmel, *Chem. Eur. J.* **2017**, *23*, 13607 – 13611; b) D. F. Schrempp, E. Schneider, E. Kaifer, H. Wadepohl, H.-J. Himmel, *Chem. Eur. J.* **2017**, *23*, 11636 – 11648; c) H. Herrmann, E. Kaifer, H.-J. Himmel, *Chem. Eur. J.* **2017**, *23*, 5520 – 5528; d) D. F. Schrempp, E. Kaifer, H. Wadepohl, H.-J. Himmel, *Chem. Eur. J.* **2016**, *22*, 16187 – 16199; e) S. Wiesner, A. Wagner, E. Kaifer, H.-J. Himmel, *Chem. Eur. J.* **2016**, *22*, 10438 – 10445; f) S. Wiesner, A. Wagner, O. Hübner, E. Kaifer, H.-J. Himmel, *Chem. Eur. J.* **2015**, *21*, 16494 – 16503; g) A. Ziesak, T. Wesp, O. Hübner, E. Kaifer, H. Wadepohl, H.-J. Himmel, *Dalton Trans.* **2015**, *44*, 19111 – 19125.

[50] F. Schön, E. Kaifer, H.-J. Himmel, *Chem. Eur. J.* **2019**, *21*, 8279 – 8288.

[51] P. Roquette, C. König, O. Hübner, N. Wagner, E. Kaifer, M. Enders, H.-J. Himmel, *Eur. J. Inorg. Chem.* **2010**, 4770 – 4782.

[52] a) V. Raab, J. Kipke, R. M. Gschwind, J. Sundermeyer, *Chem. Eur. J.* **2002**, *8*, 1682 – 1693; b) U. Wild, O. Hübner, A. Maronna, M. Enders, E. Kaifer, H. Wadepohl, H.-J. Himmel, *Eur. J. Inorg. Chem.* **2008**, 4440 – 4447; c) M. Reinmuth, U. Wild, E. Kaifer, M. Enders, H. Wadepohl, H.-J. Himmel, *Eur. J. Inorg. Chem.* **2009**, 4795 – 4808; d) M. Reinmuth, C. Neuhäuser, P. Walter, M. Enders, E. Kaifer, H.-J. Himmel, *Eur. J. Inorg. Chem.* **2011**, 83 – 90; e) P. Roquette, A. Maronna, M. Reinmuth, E. Kaifer, M. Enders, H.-J. Himmel, *Inorg. Chem.* **2011**, *50*, 1942 – 1955.

[53] A. Wagner, H.-J. Himmel, *J. Chem. Inf. Model.* **2017**, *57*, 428 – 438.

[54] M. Weitzer, S. Schindler, G. Brehm, S. Schneider, E. Hormann, B. Jung, S. Kaderli, A. D. Zuberbühler, *Inorg. Chem.* **2003**, *42*, 1800.

[55] *Anorganische Chemie* (Eds.: E. Riedel, C. Janiak), Vol. 7, **2007**, Walter de Gruyter, Berlin.

[56] C. E. Elwell, N. L. Gagnon, B. N. Neisen, D. Dhar, A. D. Spaeth, G. M. Yee, W. B. Tolman, *Chem. Rev.* **2017**, *117*, 2059 – 2107.

[57] A. de la Lande, H. Gérard, V. Moliner, G. Izzet, O. Reinaud, O. Parisel, *J. Biol. Inorg. Chem.* **2006**, *11*, 593 – 608.

[58] A. E. Reed, R. B. Weinstock, F. Weinhold, *J. Chem. Phys.* **1985**, *83*, 735 – 746.

[59] C. Meliá, S. Ferrerm, J. Řezáč, O. Parisel, O. Reinaud, V. Moliner, A. de la Lande, *Chem. Eur. J.* **2013**, *19*, 17328 – 17337.

[60] T. Abe, Y. Hori, Y. Shiota, T. Ohta, Y. Morimoto, H. Sugimoto, T. Ogura, K. Yoshizawa, S. Itoh, *Commun. Chem.* **2019**, *2*, 12.a) Further examples of nucleophilic superoxides include: W. D. Bailey, N. L. Gagnon, C. E. Elwell, A. C. Cramblitt, C. J. Bouchey, W. B. Tolman, *Inorg. Chem.* **2019**, *58*, 4706 – 4711; b) P. Pirovano, A. M. Magherusan, C. McGlynn, A. Ure, A. Lynes, A. R. McDonald, *Angew. Chem. Int. Ed.* **2014**, *53*, 5946 – 5950; *Angew. Chem.* **2014**, *126*, 6056 – 6060.

[61] A. Hoffmann, M. Wern, T. Hoppe, M. Witte, R. Haase, P. Liebhäuser, J. Glatthaar, S. Herres-Pawlis, S. Schindler, *Eur. J. Inorg. Chem.* **2016**, 4744 – 4751.

[62] L. Dahlenburg, H. Treffert, J. Dannhäuser, F. W. Heinemann, *Inorg. Chim. Acta* **2007**, *360*, 1474 – 1481.

[63] M. Findeisen, T. Brand, S. Berger, *Magn. Reson. Chem.* **2007**, *45*, 175 – 178.

[64] G. R. Fulmer, A. J. M. Miller, N. H. Sherden, H. E. Gottlieb, A. Nudelman, B. M. Stoltz, J. E. Bercaw, K. I. Goldberg, *Organometallics* **2010**, *29*, 2176 – 2179.

[65] B. Schulz, J. Bäckström, D. Budelmann, R. Maeser, M. Rübhausen, M. V. Klein, E. Schoeffel, A. Mihill, S. Yoon, *Rev. Sci. Instrum.* **2005**, *76*, 073107-1-073107-12.

[66] B. Grimm-Lebsanft, C. Brett, F. Strassl, D. Rukser, M. Biednov, F. Biebl, M. Naumova, A. Hoffmann, L. Akinsinde, D. Brückner, S. Herres-Pawlis, M. Rübhausen, *Inorg. Chim. Acta* **2018**, *481*, 176 – 180.

[67] A. E. Sheshenev, M. S. Baird, A. K. Croft, I. G. Bolesov, *Tetrahedron* **2009**, *65*, 10036 – 10046; M. Oelgemöller, P. Cygon, J. Lex, A. G. Griesbeck, *Heterocycles* **2003**, *59*, 669 – 684.

[68] DENZO-SMN, Nonius **1998**, http://www.nonius.nl.

[69] G. M. Sheldrick, SADABS, *Program for Empirical Absorption Correction*, University of Göttingen, Germany.

[70] a) G. M. Sheldrick, SHELXT, *Program for Crystal Structure Solution*, University of Göttingen, Germany, **2014 – 2018**; b) G. M. Sheldrick, *Acta Crystallogr. Sect. A* **2015**, *71*, 3 – 8.

[71] a) G. M. Sheldrick, SHELXL, *Program for Structure Refinement*, University of Göttingen, Germany, **2014 – 2018**; b) G. M. Sheldrick, *Acta Crystallogr. Sect. C* **2015**, *71*, 3 – 8.

[72] OLEX2: A complete structure solution, refinement, and analysis program, O. V. Dolomanov, L. J. Bourhis, R. J. Gildea, J. A. K. Howard, H. Puschmann, *J. Appl. Crystallogr.* **2009**, *42*, 339 – 341.

[73] a) P. van der Sluis, A. L. Spek, *Acta Crystallogr. Sect. A* **1990**, *46*, 194; b) A. L. Spek, *Acta Crystallogr. Sect. C* **2015**, *71*, 9.

[74] a) A. L. Spek, *PLATON*, Utrecht University, The Netherlands; b) A. L. Spek, *J. Appl. Crystallogr.* **2003**, *36*, 7.

Manuscript received: April 26, 2019

Accepted manuscript online: May 27, 2019

Version of record online: July 8, 2019

4.2 Exceptional Substrate Diversity in Oxygenation Reactions Catalyzed by a Bis(μ-oxo) Copper Complex

The author has contributed to the Raman and XAS measurements and the respective data analysis.

Although tyrosinase is well studied, all details of the the oxidation mechanism are still not fully understood. Some well-studied mimetic model complexes form Cu^{II}-peroxo and Cu^{III}-bis(μ-oxo) motifs, which exist in a dynamic equilibrium. Of those complexes, only a few systems show catalytic oxygenation reactivity. Examples are the systems from M. Réglier et al.[108], L. Casella et al.[109], F. Tuczek et al.[16], J. P. Lumb et al.[110] or S. Herres-Pawlis et al.[18] In [4.2] a novel hybrid guanidine ligand **L1** was used to form the bis(μ-oxo) dicopper(III) species shown in [4.2]-Scheme 1. The Fukui function f_k^- is introduced into Cu/O_2 chemistry, which allows a theoretical prediction of the hydroxylation position of different phenolic substrates, as shown in [4.2]-Tab. 2. The successful oxygenation of such substrates revealed a surprising amount of diversity, far beyond the scope of the biological enzyme. The different reactions and subsequent condensation reactions towards phenazines are shown in [4.2]-Tab. 1.

The UV-Vis measurement shown in [4.2]-Fig. 1 (a) shows a ligand-to-metal charge transfer (LMCT), indicating a bis(μ-oxo) dicopper(III) motif for the hybrid-guanidine ligand stabilized copper complex [O1](PF_6). For the Raman measurements, the precursor solutions (concentration of 20 mM) were cooled in a self-built cryostat[104] to -90 °C in a glass cuvette with a septum for oxygenation. The oxygenation was conducted *via* a cannula through the septum at approximately 0.02 bar overpressure for 2 min. The Tsunami laser system was adjusted to a fundamental frequency of 840 nm, to allow for second harmonic generation in a nonlinear BBO crystal to produce 420 nm light. The Raman spectra were taken at 37 mW with a 20 μm spot size, being approximately 30 μm inside the glass cuvette. The oxygenation was done once with the $^{16}O_2$ isotope and once with the $^{18}O_2$ isotope, following the concept laid out in section 4.1. The $^{16}O_2$ measurement did reveal a peak located at 620 cm^{-1}, which stems from the Cu_2O_2 core expansion breathing mode and another distinct peak at 530 cm^{-1}, which stems from Cu-N vibration. The $^{18}O_2$ isotope-shift measurement showed an expected redshift of the Cu_2O_2 peak of 29 cm^{-1}.

To verify the theoretical description of the complex as containing the bis(μ-oxo) motif, XAS measurements were performed at the P64 beamline at PETRA III (DESY, Hamburg, Germany),[100] shown in [4.2]-Fig. 1 (b) and (c). The sample preparation followed the routine outlined for the Raman measurements, except a special sample holder was used to be able to place the sample in the cryostat at the beamline. After 5 min of oxygenation at -90 °C inside the cuvette in the ethanol chiller[104], the complex formed. A pre-cooled syringe was used to transfer 75 μL to the sample holder which was directly frozen in a liquid nitrogen bath and subsequently placed in the cryostat at a temperature of -123 °C. XAS measurements were performed between 8780 to 9880 eV for one hour with 300 s per measurement. The analysis was carried out with the software Athena and Artemis.[103] All data were calibrated with the reference Cu-foil measurements. The X-ray absorption edge was found at 8987.0 eV which implies Cu^{III} with a bis(μ-oxo) motif.[80] Shoulders at 8987.3 and 8992.0 eV are 1s→4p and 1s→4p + shakedown transitions. The XANES measurement is shown in the supporting information in [4.2]-Fig. S2.

Exceptional Substrate Diversity in Oxygenation Reactions Catalyzed by a Bis(μ-oxo) Copper Complex

Chemistry–A European Journal | Communication
doi.org/10.1002/chem.202000664
Chemistry Europe
European Chemical Societies Publishing

Dioxygen Activation

Exceptional Substrate Diversity in Oxygenation Reactions Catalyzed by a Bis(μ-oxo) Copper Complex

Melanie Paul,[a] Melissa Teubner,[a, b] Benjamin Grimm-Lebsanft,[b] Christiane Golchert,[a] Yannick Meiners,[a] Laura Senft,[c] Kristina Keisers,[a] Patricia Liebhäuser,[a] Thomas Rösener,[a] Florian Biebl,[b] Sören Buchenau,[b] Maria Naumova,[d] Vadim Murzin,[d] Roxanne Krug,[e] Alexander Hoffmann,[a] Jörg Pietruszka,[e, f] Ivana Ivanović-Burmazović,[c] Michael Rübhausen,[b] and Sonja Herres-Pawlis*[a]

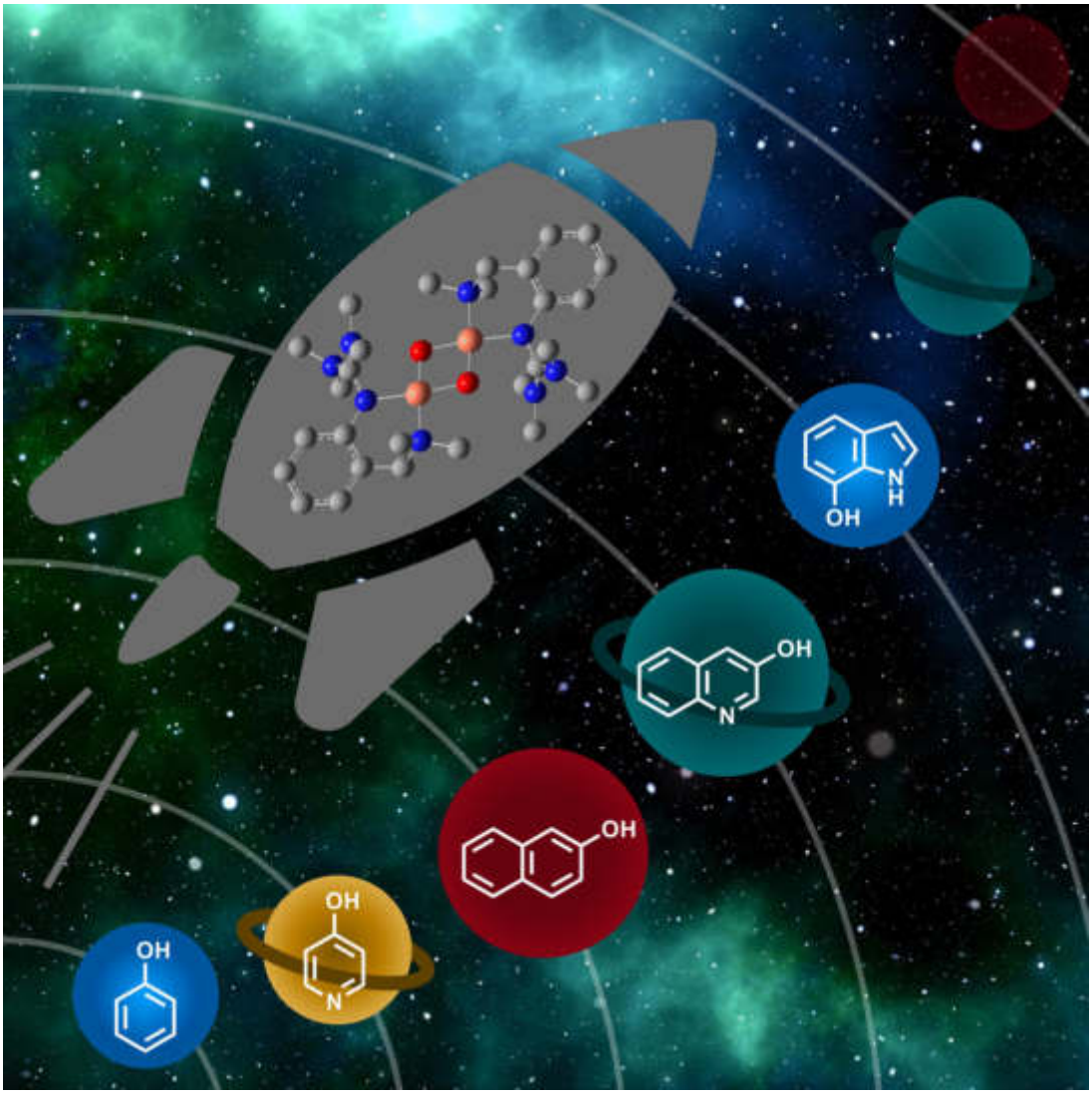

Abstract: The enzyme tyrosinase contains a reactive side-on peroxo dicopper(II) center as catalytically active species in C–H oxygenation reactions. The tyrosinase activity of the isomeric bis(μ-oxo) dicopper(III) form has been discussed controversially. The synthesis of bis(μ-oxo) dicopper(III) species $[Cu_2(\mu\text{-}O)_2(\mathbf{L1})_2](X)_2$ ($[\mathbf{O1}](X)_2$, $X = PF_6^-$, BF_4^-, OTf^-, ClO_4^-), stabilized by the new hybrid guanidine ligand 2-{2-((dimethylamino)methyl)phenyl}-1,1,3,3-tetramethylguanidine (**L1**), and its characterization by UV/Vis, Raman, and XAS spectroscopy, as well as cryo-UHR-ESI mass spectrometry, is described. We highlight selective oxygenation of a plethora of phenolic substrates mediated by $[\mathbf{O1}](PF_6)_2$, which results in mono- and bicyclic quinones and provides an attractive strategy for designing new phenazines. The selectivity is predicted by using the Fukui function, which is hereby introduced into tyrosinase model chemistry. Our bioinspired catalysis harnesses molecular dioxygen for organic transformations and achieves a substrate diversity reaching far beyond the scope of the enzyme.

The use of dioxygen as a readily available oxidizing agent is crucial for many biological and biomimetic oxidation processes, as well as industrial applications.[1] Natural copper enzymes, such as tyrosinase or particulate methane monooxygenase, successfully activate molecular dioxygen.[2] Tyrosinase, in particular, is essential in living organisms catalyzing phenol oxidation in melanin biosynthesis.[3] It converts phenols, for instance, L-tyrosine, via an electrophilic aromatic substitution through its catechol form to the final quinone form.[4] Although structure and reactivity of tyrosinases were studied extensively, many details of the oxidation mechanism are still under debate.[5] Recently, second shell residues at the active site (ca. 5.5–16 Å distance to Cu ions) were considered to direct the reactivity of the enzyme.[2b,6]

For understanding the mechanism of activation and transfer of O_2, synthetic model systems were developed mimicking enzymatic properties. Some well-studied Cu/O_2 species represent $\mu\text{-}\eta^2\text{:}\eta^2$-peroxo Cu^{II} [**P**] and bis(μ-oxo) Cu^{III} [**O**] complexes, which exist in a dynamic equilibrium due to a small isomerization barrier.[2b,7] In many functional tyrosinase systems, **[P]** cores are found,[8] but an increasing number of examples of functional [**O**] species has also been reported.[9] However, only few tyrosinase model systems feature catalytic oxygenation reactivity.[10] Réglier and co-workers presented the first system using the imine–pyridine ligand $BiPh(impy)_2$,[11] followed by Casella and co-workers by using the benzimidazole ligand L66,[12] which both stabilize binuclear Cu catalysts. Later, Tuczek and co-workers reported the mononucleating benzimidazole ligand L^{impy} promoting catalytic conversion of 2,4-di-*tert*-butyl phenol.[13] Over the years, Lumb and co-workers have focused on the chemo- and regioselectivity of tyrosinase-like reactions by using the amine DBED giving rise to several quinones, oxidative coupling, and cyclization products.[14] More complex phenolic substrates were oxygenated by Herres-Pawlis group by using bis(pyrazolyl)methane and guanidine ligands.[15]

Herein, we report the synthesis and characterization of hybrid guanidine-stabilized bis(μ-oxo) complex $[Cu_2(\mu\text{-}O)_2(\mathbf{L1})_2]^{2+}$ ($[\mathbf{O1}]^{2+}$, Scheme 1) along with its high catalytic activity in oxygenation and oxidation reactions of phenolic substrates and subsequent condensation reactions, offering a facile synthetic pathway to new phenazines.

Guanidines feature high basicity and strong N-donor abilities, enabling stabilization of metal ions with high oxidation states.[16] For instance, TMG_3tren is known to stabilize highly reactive Cu^{II} superoxo complexes.[17] By using $[\mathbf{O1}](PF_6)_2$, it is possible to promote selective C–H functionalization of complex phenolic substrates. To the best of our knowledge, no activity of tyrosinases towards complex phenolic substrates has been reported before. Compound $[\mathbf{O1}](PF_6)_2$ highlights a beneficial interplay of steric and electronic factors of the ligand regarding substrate accessibility of $[Cu_2O_2]$ core leading to a remarkable extension of the substrate scope. Using a variety of phenolic substances allows the synthesis of new quinones. In a consecu-

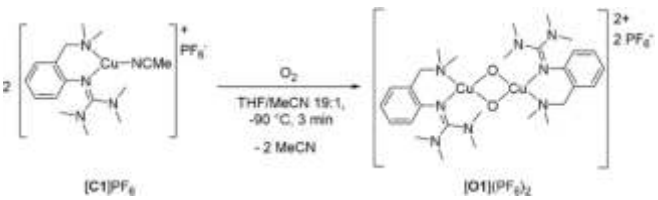

Scheme 1. Synthesis of bis(μ-oxo) species $[\mathbf{O1}](PF_6)_2$.

[a] *M. Paul, M. Teubner, C. Golchert, Y. Meiners, K. Keisers, Dr. P. Liebhäuser, Dr. T. Rösener, Dr. A. Hoffmann, Prof. Dr. S. Herres-Pawlis*
Department of Inorganic Chemistry
RWTH Aachen University, Landoltweg 1, 52074 Aachen (Germany)
E-mail: sonja.herres-pawlis@ac.rwth-aachen.de

[b] *M. Teubner, Dr. B. Grimm-Lebsanft, F. Biebl, S. Buchenau, Prof. Dr. M. Rübhausen*
Department of Physics, University of Hamburg
Luruper Chaussee 149, 22761 Hamburg (Germany)

[c] *L. Senft, Prof. Dr. I. Ivanović-Burmazović*
Department of Chemistry and Pharmacy
Friedrich-Alexander-University of Erlangen-Nürnberg
Egerlandstrasse 1, 91058 Erlangen (Germany)

[d] *Dr. M. Naumova, Dr. V. Murzin*
Deutsches Elektronen-Synchrotron DESY
Notkestrasse 85, 22607 Hamburg (Germany)

[e] *Dr. R. Krug, Prof. Dr. J. Pietruszka*
Institute of Bioorganic Chemistry
Heinrich Heine University Düsseldorf at Forschungszentrum Jülich
52425 Jülich (Germany)

[f] *Prof. Dr. J. Pietruszka*
Institute of Bio- and Geoscience (IBG-1: Biotechnology)
Forschungszentrum Jülich GmbH
52425 Jülich (Germany)

Supporting information and the ORCID identification number(s) for the author(s) of this article can be found under: https://doi.org/10.1002/chem.202000664.

tive reaction, quinones can condense with 1,2-phenylenediamine to phenazines, which feature antibacterial, antimalarial, and antitumor activities, and are used in dyes and pesticides.[18] We targeted to selectively obtain bent phenazines as special benefit of the [**O1**]$(PF_6)_2$-mediated hydroxylation, because the calculation of the Fukui function of the hydroxylation products indicated preferential formation of the corresponding quinone.

Inspired by a propylene-bridged hybrid guanidine ligand system that showed promising phenolase activity,[9k–l] we developed a related ligand system with a more rigid aromatic backbone. Compound 2-{2-((dimethylamino)methyl)phenyl}-1,1,3,3-tetramethylguanidine (**L1**) was synthesized in a three-step reaction and isolated in high yield (see the Supporting Information). Synthesis of the colorless, air- and moisture-sensitive Cu^{I} complex [**C1**]PF_6 was achieved by mixing equimolar amounts of **L1** and $[Cu(MeCN)_4]PF_6$ in acetonitrile at room temperature. Oxygenation of [**C1**]PF_6 in THF at −90 °C led to the formation of the khaki colored species [**O1**]$(PF_6)_2$ (Scheme 1).[19] Compound [**O1**]$(PF_6)_2$ showed ligand-to-metal-charge transfer (LMCT) features at 280 nm ($\varepsilon = 40000\ M^{-1}cm^{-1}$) and 392 nm ($21\,000\ M^{-1}cm^{-1}$) in the UV/Vis spectrum[20] (Figure 1 a), which are characteristic for bis(μ-oxo) dicopper(III) species.[8,21] Similar UV/Vis features were obtained by using different weakly coordinating anions (BF_4^-, ClO_4^-, OTf^-; Figure S17 and Table S3 in the Supporting Information). Incorporated O_2 of [**O1**]$(PF_6)_2$ was resistant to cycles of evacuation and purging with N_2. Laser excitation at 420 nm led to a resonance Raman spectrum with a characteristic vibration at 620 cm^{-1}, which was attributed to the symmetrical Cu_2O_2 core expansion (breathing mode), thus evidencing the formation of a bis(μ-oxo) species (Figure 1 b). $^{16}O_2/^{18}O_2$ isotope exchange measurements in THF exhibited a shift to 591 cm^{-1}, which is in good agreement with theoretical calculations (Table S13 in the Supporting Information). The signal at 530 cm^{-1} is caused by the N(amine)–Cu vibration.

Theoretical studies on [**O1**]$(PF_6)_2$ were performed to investigate geometry and Raman features (Figure 2). The calculations showed that the **O** species is favored by 10 kcal mol^{-1} over the **P** species (Table S11 in the Supporting Information). Key bond lengths around the Cu atoms were determined by Cu K-edge EXAFS (Figure 1 c–d, and section 1.3 in the Supporting Information) and agree well with the theoretical model. Moreover, the edge position is in accordance with the assignment as Cu^{III}. For quantification of the formation of [**O1**]$(PF_6)_2$, spectrophotometric back titration of [**O1**]$(PF_6)_2$ was performed by using ferrocene monocarboxylic acid (FcCOOH).[9k,l] Following the decay of the LMCT band at 392 nm, titration of [**O1**]$(PF_6)_2$ with FcCOOH revealed >90% formation of [**O1**]$(PF_6)_2$ (Figures S18 and 19 in the Supporting Information). To elucidate the Cu–O_2 stoichiometry of [**O1**]$(PF_6)_2$, cryo-UHR-ESI mass spectrometry was performed (Figure S20). The isotopic pattern and corresponding *m/z* values are in accordance with the calculated spectrum of the monocationic species [**O1**]$(PF_6)^+$ with a 2:1 Cu-O_2 ratio.

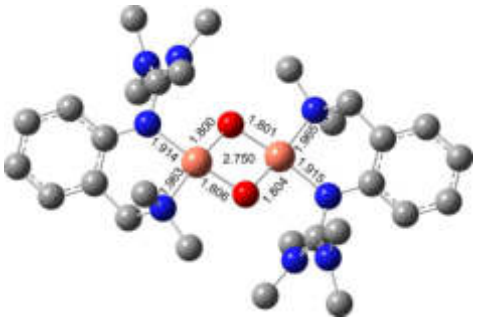

Figure 2. DFT model of $[\mathbf{O1}]^{2+}$ (TPSSh/def2-TZVP, THF-PCM), selected bond lengths [Å] and Cu···Cu vector [Å].

Thermal decomposition kinetics of [**O1**]$(PF_6)_2$ revealed a first-order decay at low temperatures (Figures S21 and 22 in the Supporting Information). Half-life times of [**O1**]$(PF_6)_2$ in THF of 1 h at −80 °C and five minutes at −74 °C were determined. Thermal decomposition products of [**O1**]$(PF_6)_2$ were identified by crystallization as a dicationic μ-alkoxo-μ-hydroxo copper(II) complex [**H1**]$(PF_6)_2$ with a Cu···Cu distance of 2.953(1) Å (Figure 3). Each copper atom is coordinated in a distorted square-planar fashion. The average Cu–O bond length (1.92 Å) is shorter compared to that in the mixed phenolato hydroxo-bridged dicopper(II) species (1.96 Å) reported by Karlin and coworkers.[22] Concomitant formation of yellow blocks was observed, which contain the protonated ligand [(**L1**)H_2]$(PF_6)_2$.

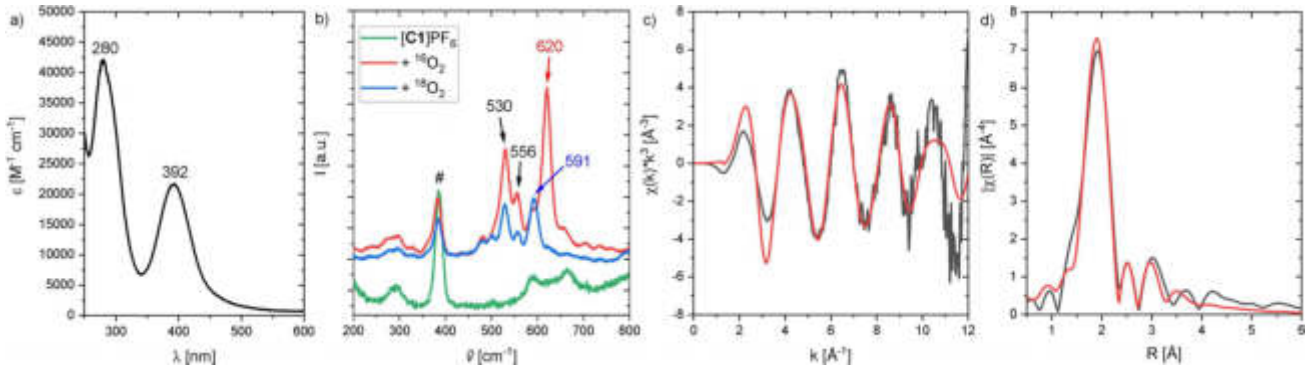

Figure 1. a) UV/Vis spectrum of [**O1**]$(PF_6)_2$ (0.5 mM) in THF at −90 °C; b) resonance Raman spectra of [**O1**]$(PF_6)_2$ in THF with excitation at 420 nm (blue: $^{18}O_2$, red: $^{16}O_2$, green: [**C1**]PF_6, #: solvent); c) k^3-weighted Cu K-edge EXAFS of [**O1**]$(PF_6)_2$ (black: experimental, red: calculated fit); and d) phase-corrected Cu-K-edge Fourier transform of EXAFS of [**O1**]$(PF_6)_2$ (black: experimental, red: calculated fit).

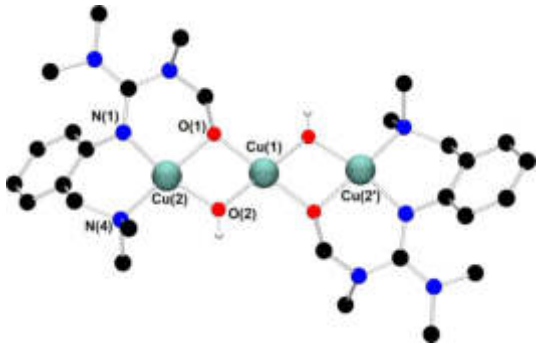

Figure 3. Molecular structure of $[\mathbf{H1}]^{2+}$ in crystals of $[\mathbf{H1}](PF_6)_2$. H atoms, except for the H atom of μ-OH groups, counterions, and solvent molecules are omitted for clarity. Selected interatomic distances [Å] and angles [°]: Cu(1)–O(1) 1.912(2), Cu(1)–O(2) 1.893(2), Cu(2)–O(1) 1.923(2), Cu(2)–O(2) 1.932(2), Cu(1)···Cu(2) 2.953(1), Cu(2)–N(1) 1.986(2), Cu(2)–N(4) 2.019(3); N(1)-Cu(2)-N(4) 94.9(1), O(1)-Cu(2)-O(2) 76.8(1), Cu(2)-O(1)-Cu(1) 100.7(1), Cu(2)-Cu(1)-Cu(2′) 180.0.

Bis(μ-hydroxo) species are commonly observed as decay products[9,18a] and often resulted from intramolecular hydroxylation of C–H bonds in α- or β-position of N-donor groups.[23] Interestingly, $[\mathbf{H1}]^{2+}$ is the first example of a trinuclear μ-alkoxo-μ-hydroxo copper(II) complex cation. Only few examples of alkoxo-hydroxo copper(II) species have been reported to date.[7b,23] Mechanistic studies on intramolecular hydroxylation of the supporting ligand upon warming of the bis(μ-oxo) species were proposed by Itoh, Tolman and co-workers stating a mixed alkoxo-hydroxo copper(II) complex as intermediate species to form thermodynamically stable bis(μ-hydroxo) and bis(μ-alkoxo) complexes.[23a,24] In case of $[\mathbf{H1}]^{2+}$, the chemoselective attack of the equatorially located methyl groups of the guanidine moiety over the axially disposed aminomethyl groups is favored due to geometric constraints, similar to observations made by Tolman and co-workers.[23c,25]

Aiming to expand the commonly used substrate scope of simple phenols, catalytic hydroxylation activity of $[\mathbf{O1}](PF_6)_2$ was evaluated towards a variety of challenging phenolic substrates, including phenols, pyridinols, naphthols, quinolinols, and indolols (Table 1 and section 2.6 in the Supporting Information), quinones and phenazines of which are biologically relevant and difficult to synthesize. We report the hydroxylation of a multitude of these substrates by $[\mathbf{O1}](PF_6)_2$ along with transformation of the quinone into a phenazine. Remarkably that until now, catalytic conversion of phenols was mostly reported for side-on peroxo copper complexes as catalytically active species.[11–13,15] Oxygenation reactions were performed following a protocol established by Bulkowski and modified by Tuczek and co-workers by using 25 equivalents of substrate and 50 equivalents of NEt_3 (Table 1, Reaction (a)).[13a,26] Reaction (a) was monitored by UV/Vis spectroscopy at −90 °C for one hour as optical spectra remained constant after that time. Reactive quinones were subsequently converted in a one-pot reaction into their corresponding phenazines at room temperature by using 1,2-phenylenediamine (Table 1, Reaction (b)).

When simple phenols were used, $[\mathbf{O1}](PF_6)_2$ showed, besides the expected hydroxylation activity, also C–O coupling chemistry (Table S8 in the Supporting Information, entries 1–4). UV/Vis spectra showed a low intensity absorption band at 510 and 530 nm (Figures S39 and 40 in the Supporting Information).

Table 1. Catalytic oxygenation of phenolic substrates[a] and subsequent condensation of the quinone by using 1,2-phenylenediamine.[b]

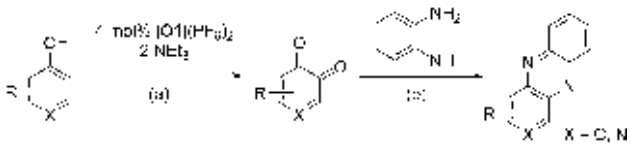

Entry	Substrate	Conv. [%]	Product (quinone/phenazine)		Yield[c] [%]	TON[d]
1	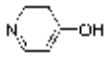	>99		(**Q1**)	[e]	[f]
2	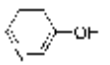	>99		(**Q1**)	[e]	[f]
3	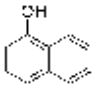	80	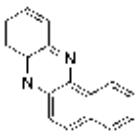	(**P1**)	22	11
4	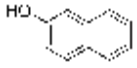	89		(**P1**)	31	16
5	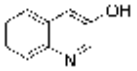	95	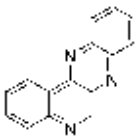	(**P2**)	32	16
6	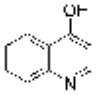	87		(**P2**)	21	11
7	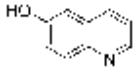	>99	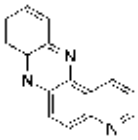	(**P3**)	30	15
8	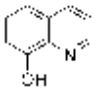	28	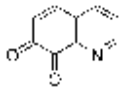	(**Q2**)	–	14[g]
9	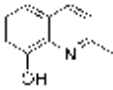	24	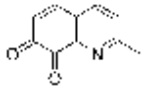	(**Q3**)	–	12[g]
10	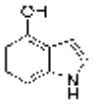	81	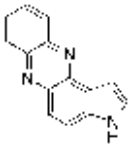	(**P4**)	19	10
11	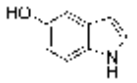	88		(**P4**)	26	13
12	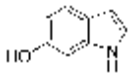	92	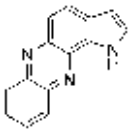	(**P5**)	27	14
13	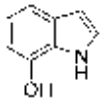	84		(**P5**)	31	16

[a] Conditions: THF, −90 °C, 1 h. [b] Conditions: THF, −90 °C, then rt, overnight. [c] Isolated yield after column chromatography. [d] Based on isolated yield in correlation with conc. of $[\mathbf{O1}](PF_6)_2$. [e] Quinone too reactive to be isolated. [f] No extinction coefficient of the quinone reported. [g] Determined after reaction (a) by UV/Vis spectra and based on conc. of $[\mathbf{O1}](PF_6)_2$.

EPR measurements revealed the hyperfine splitting pattern typical for a radical-free, metal-centered Cu^{II} species, ruling out the formation of a semiquinone species (Figure S41).[27]

An interesting substrate for the catalytic oxygenation is 8-quinolinol.[15,28] Although 7,8-quinolinedione (**Q2**) was formed with 14 turnovers (entry 8), methyl substitution in 2-position resulted in a TON of 12 (**Q3**, entry 9). However, formation of the respective phenazine was observed in neither case (Figures S50 and 51 in the Supporting Information), presumably due to the smaller Fukui function $f+$ at the corresponding C atoms of **Q2** and **Q3** (Table S15). Conversion of other quinolinols was not reported before in Cu/O_2 chemistry. Compounds 3- and 4-quinolinol were transformed into their quinone (absorption band at 370 nm, Figures S47 and 48 in the Supporting Information) and isolated as quinolino[3,4-b]quinoxaline (**P2**; entries 5–6). 6-Quinolinol was oxidized into 5,6-quinolinedione (entry 7), which showed absorption bands at 325, 340, and 370 nm (Figure S49). Pyrido[3,2-a]phenazine (**P3**) was isolated in 15 turnovers after column chromatography and sublimation, and crystallized from DMSO (see the Supporting Information).

In contrast to reactions with phenols and 8-quinolinol, no conversion of pyridinols has been reported to date. When 3- and 4-pyridinol (entries 1–2) were used, an intense absorption band at 375 nm, similar to that in 3- and 4-quinolinol, was observed in both cases within less than one minute (Figures S42 and 43 in the Supporting Information), indicating formation of 3,4-pyridoquinone (**Q1**). A fast drop in intensity illustrates high reactivity of the quinone even at low temperatures, leading to C–O coupled dimers (see the Supporting Information).[29] Theoretical studies revealed lesser stability of 3,4-pyridoquinone compared to its most stable 2,5-isomer.[30] However, no other study exists that reports on pyridoquinones.

Naphthoquinones are accessible from 1- and 2-naphthol in the presence of an oxidizing agent.[31] Both naphthols were converted via [**O1**]$(PF_6)_2$ into the corresponding quinone, which resulted in the formation of benzo[a]phenazine[31c] (**P1**) upon treatment with 1,2-phenylenediamine (entries 3–4, Figures S44 and 45 in the Supporting Information). Compound **P1** was purified by column chromatography and isolated with a TON of 11–16. Consistent with observations made by Krohn and co-workers, no formation of the linear phenazine was observed.[31c] The control experiment by using 1-methyl 2-naphthol (Table S8, entry 7) showed no product formation as was expected (Figure S46), because the 1-position is occupied by the methyl substituent inhibiting the oxygenation process.

Although related bicyclic indolols possess an easily accessible pyrrole ring, C–H functionalization of the phenyl ring remains challenging.[32] When [**O1**]$(PF_6)_2$ was used, 4- and 5-indolol were converted into 4,5-indoledione, which was captured as pyrrolo[3,2-a]phenazine (**P4**) in 10–13 turnovers (entries 10–11, Figures S52 and 53). Similarly, 6- and 7-indolol (Figures S54 and 55) were transformed into pyrrolo[2,3-a]phenazine (**P5**, TON = 14–16) and crystallized from hexane (entries 12–13). The control experiment revealed no oxygenation activity on 6-indolol in the absence of supporting ligand **L1** (Figure S36), thus evidencing the necessity of the stabilizing ligand system.

The accompanying DFT calculations based on the negative Fukui function were used to determine the location of the electrophilic attack, which are in good agreement with the observed products (for substrates with two product possibilities, see Tables 1 and 2 and section 3.2 in the Supporting Information). The Fukui function describes the electron density in a frontier orbital, in this case f_k^- denotes the initial part for an electrophilic reaction. A large value for f_k^- indicates the preferred site for an electrophilic attack—in this case, the tyrosinase-like hydroxylation. In all cased studied herein, the Fukui function points to the experimentally observed hydroxylation site finally yielding the bent phenazines.

Table 2. Summary of calculated Fukui function [f_k^-] of phenolic substrates with two possible products.

Entry	Substrate	f_k^-	C atom position
1	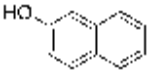	21.14 0.74	1 3
2	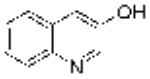	1.38 15.17	2 4
3	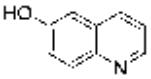	23.93 0.91	5 7
4	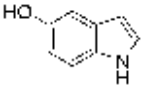	19.93 1.05	4 6
5	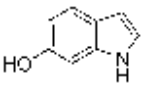	2.03 11.99	5 7

It has to be highlighted that the phenazines **P3**, **P4**, and **P5** are new and fully characterized.[33] Thus, the combination of tyrosinase-like hydroxylation reactivity with the condensation of quinones with diamines allows synthetic access to a multitude of new phenazines.

Although tyrosinase (from *Aspergillus oryzae*) oxidizes phenol quantitatively,[34] the enzyme exhibited no reactivity towards naphthols, quinolinols, and indolols (Table S10 in the Supporting Information). Thus, the bis(μ-oxo) species [**O1**]$(PF_6)_2$ demonstrates an exceptional broad substrate scope to which the enzyme itself gave no access.

In summary, we established the synthesis of the aromatic hybrid guanidine-stabilized bis(μ-oxo) species $[\mathbf{O1}]^{2+}$, which was clearly evidenced by its spectroscopic properties. Compound [**O1**]$(PF_6)_2$ revealed a moderate stability at low temperatures with a distinguished activity towards a large variety of phenolic substrates. DFT calculations enabled a prognosis of the hydroxylation position by Fukui function, which fully agreed with experimental results. The Fukui function was introduced as new predictive tool for Cu/O_2 chemistry. Moreover, our present findings clearly show efficient C–H activation of mono- and bicyclic phenolic substrates, stating an atom-eco-

nomic strategy to design new phenazines. A bioinspired model system, such as [**O1**](PF$_6$)$_2$, indicates tyrosinase-like activity of **O** cores and exceeds evidently the enzymatically limited substrate scope. This study opens the door to future developments on tyrosinase model systems with high relevance to atom-economic oxygen-transfer reactions with synthetic importance.

Acknowledgements

We acknowledge financial support provided by the German Research Foundation (DFG), in framework of Priority Program "Reactive Bubbly Flows" SPP 1740 (HE 5480/10-2, http://www.dfg-spp1740.de/), International Research Training Group SeleCa and further projects (RU 773/8-1). We also acknowledge computing time and support provided by OCuLUS Cluster at PC^2 Paderborn and support at beamline P64 by Marcel Görlitz and Dr. Wolfgang Caliebe.

Conflict of interest

The authors declare no conflict of interest.

Keywords: copper catalysis · dioxygen activation · guanidines · phenazines · tyrosinase

[1] a) A. N. Campbell, S. S. Stahl, *Acc. Chem. Res.* **2012**, *45*, 851 – 863; b) S. D. McCann, S. S. Stahl, *Acc. Chem. Res.* **2015**, *48*, 1756 – 1766.

[2] a) E. I. Solomon, D. E. Heppner, E. M. Johnston, J. W. Ginsbach, J. Cirera, M. Qayyum, M. T. Kieber-Emmons, C. H. Kjaergaard, R. G. Hadt, L. Tian, *Chem. Rev.* **2014**, *114*, 3659 – 3853; b) C. E. Elwell, N. L. Gagnon, B. D. Neisen, D. Dhar, A. D. Spaeth, G. M. Yee, W. B. Tolman, *Chem. Rev.* **2017**, *117*, 2059 – 2107.

[3] a) Y. Matoba, T. Kumagai, A. Yamamoto, H. Yoshitsu, M. Sugiyama, *J. Biol. Chem.* **2006**, *281*, 8981 – 8990; b) A. Bijelic, M. Pretzler, C. Molitor, F. Zekiri, A. Rompel, *Angew. Chem. Int. Ed.* **2015**, *54*, 14677 – 14680; *Angew. Chem.* **2015**, *127*, 14889 – 14893.

[4] a) V. Kahn, N. Ben-Shalom, *Pigment Cell Res.* **1998**, *11*, 24 – 33; b) M. del Mar Garcia-Molina, J. L. Muñoz-Muñoz, F. Garcia-Molina, P. A. García-Ruiz, F. Garcia-Canovas, *J. Agric. Food Chem.* **2012**, *60*, 6447 – 6453.

[5] a) T. A. G. Large, V. Mahadevan, W. Keown, T. D. P. Stack, *Inorg. Chim. Acta* **2019**, *486*, 782 – 792; b) L. Chiang, E. C. Wasinger, Y. Shimazaki, V. Young, T. Storr, T. D. P. Stack, *Inorg. Chim. Acta* **2018**, *481*, 151 – 158; c) D. A. Quist, D. E. Diaz, J. J. Liu, K. D. Karlin, *J. Biol. Inorg. Chem.* **2017**, *22*, 253 – 288.

[6] a) M. Kanteev, M. Goldfeder, A. Fishman, *Protein Sci.* **2015**, *24*, 1360 – 1369; b) B. Deri, M. Kanteev, M. Goldfeder, D. Lecina, V. Guallar, N. Adir, A. Fishman, *Sci. Rep.* **2016**, *6*, 34993; c) A. Singha, A. Rana, A. Dey, *Inorg. Chim. Acta* **2019**, *487*, 63 – 69.

[7] a) C. J. Cramer, B. A. Smith, W. B. Tolman, *J. Am. Chem. Soc.* **1996**, *118*, 11283 – 11287; b) V. Mahadevan, Z. Hou, A. P. Cole, D. E. Root, T. K. Lal, E. I. Solomon, T. D. P. Stack, *J. Am. Chem. Soc.* **1997**, *119*, 11996 – 11997.

[8] P. Liebhäuser, A. Hoffmann, S. Herres-Pawlis in *Reference Module in Chemistry, Molecular Sciences and Chemical Engineering*, https://doi.org/10.1016/B978-0-12-409547-2.11554-9.

[9] a) D. A. Handley, P. B. Hitchcock, T. H. Lee, G. J. Leigh, *Inorg. Chim. Acta* **2001**, *316*, 59 – 64; b) J. Mukherjee, R. Mukherjee, *Dalton Trans.* **2006**, *6*, 1611; c) L. M. Mirica, T. D. P. Stack, *Inorg. Chem.* **2005**, *44*, 2131 – 2133; d) A. Kunishita, M. Kubo, H. Ishimaru, T. Ogura, H. Sugimoto, S. Itoh, *Inorg. Chem.* **2008**, *47*, 12032 – 12039; e) S. Hong, L. M. R. Hill, A. K. Gupta, B. D. Naab, J. B. Gilroy, R. G. Hicks, C. J. Cramer, W. B. Tolman, *Inorg. Chem.* **2009**, *48*, 4514 – 4523; f) M. Taki, S. Teramae, S. Nagatomo, Y. Tachi, T. Kitagawa, S. Itoh, S. Fukuzumi, *J. Am. Chem. Soc.* **2002**, *124*, 6367 – 6377; g) A. P. Cole, V. Mahadevan, L. M. Mirica, X. Ottenwaelder, T. D. P. Stack, *Inorg. Chem.* **2005**, *44*, 7345 – 7364; h) C. Citek, C. T. Lyons, E. C. Wasinger, T. D. P. Stack, *Nat. Chem.* **2012**, *4*, 317 – 322; i) L. Chiang, W. Keown, C. Citek, E. C. Wasinger, T. D. P. Stack, *Angew. Chem. Int. Ed.* **2016**, *55*, 10453 – 10457; *Angew. Chem.* **2016**, *128*, 10609 – 10613; j) C. C. L. McCrory, A. Devadoss, X. Ottenwaelder, R. D. Lowe, T. D. P. Stack, C. E. D. Chidsey, *J. Am. Chem. Soc.* **2011**, *133*, 3696 – 3699; k) S. Herres-Pawlis, P. Verma, R. Haase, P. Kang, C. T. Lyons, E. C. Wasinger, U. Flörke, G. Henkel, T. D. P. Stack, *J. Am. Chem. Soc.* **2009**, *131*, 1154 – 1169; l) S. Herres-Pawlis, R. Haase, P. Verma, A. Hoffmann, P. Kang, T. D. P. Stack, *Eur. J. Inorg. Chem.* **2015**, 5426 – 5436.

[10] J. N. Hamann, B. Herzigkeit, R. Jurgeleit, F. Tuczek, *Coord. Chem. Rev.* **2017**, *334*, 54 – 66.

[11] M. Réglier, C. Jorand, B. Waegell, *J. Chem. Soc. Chem. Commun.* **1990**, 1752 – 1755.

[12] L. Casella, M. Gullotti, R. Radaelli, P. Di Gennaro, *J. Chem. Soc. Chem. Commun.* **1991**, 1611.

[13] a) M. Rolff, J. Schottenheim, G. Peters, F. Tuczek, *Angew. Chem. Int. Ed.* **2010**, *49*, 6438 – 6442; *Angew. Chem.* **2010**, *122*, 6583 – 6587; b) B. Herzigkeit, B. M. Flöser, N. E. Meißner, T. A. Engesser, F. Tuczek, *ChemCatChem* **2018**, *10*, 5402 – 5405; c) J. N. Hamann, F. Tuczek, *Chem. Commun.* **2014**, *50*, 2298 – 2300; d) B. Herzigkeit, B. M. Flöser, T. A. Engesser, C. Näther, F. Tuczek, *Eur. J. Inorg. Chem.* **2018**, 3058 – 3069; e) B. Herzigkeit, R. Jurgeleit, B. M. Flöser, N. E. Meißner, T. A. Engesser, C. Näther, F. Tuczek, *Eur. J. Inorg. Chem.* **2019**, 2258 – 2266; f) J. Schottenheim, C. Gernert, B. Herzigkeit, J. Krahmer, F. Tuczek, *Eur. J. Inorg. Chem.* **2015**, 3501 – 3511.

[14] a) K. V. N. Esguerra, Y. Fall, J. P. Lumb, *Angew. Chem. Int. Ed.* **2014**, *53*, 5877 – 5881; *Angew. Chem.* **2014**, *126*, 5987 – 5991; b) M. S. Askari, L. A. Rodríguez-Solano, A. Proppe, B. McAllister, J.-P. Lumb, X. Ottenwaelder, *Dalton Trans.* **2015**, *44*, 12094 – 12097; c) Z. Huang, O. Kwon, H. Huang, A. Fadli, X. Marat, M. Moreau, J.-P. Lumb, *Angew. Chem. Int. Ed.* **2018**, *57*, 11963 – 11967; *Angew. Chem.* **2018**, *130*, 12139 – 12143.

[15] a) A. Hoffmann, C. Citek, S. Binder, A. Goos, M. Rübhausen, O. Troeppner, I. Ivanović-Burmazović, E. C. Wasinger, T. D. P. Stack, S. Herres-Pawlis, *Angew. Chem. Int. Ed.* **2013**, *52*, 5398 – 5401; *Angew. Chem.* **2013**, *125*, 5508 – 5512; b) F. Strassl, A. Hoffmann, B. Grimm-Lebsanft, D. Rukser, F. Biebl, M. Tran, F. Metz, M. Rübhausen, S. Herres-Pawlis, *Inorganics* **2018**, *6*, 114.

[16] a) J. Stanek, T. Rösener, A. Metz, J. Mannsperger, A. Hoffmann, S. Herres-Pawlis, *Top. Heterocycl. Chem.* **2015**, *51*, 95 – 164; b) S. Herres-Pawlis, S. Binder, A. Eich, R. Haase, B. Schulz, G. Wellenreuther, G. Henkel, M. Rübhausen, W. Meyer-Klaucke, *Chem. Eur. J.* **2009**, *15*, 8678 – 8682; c) A. Hoffmann, M. Wern, T. Hoppe, M. Witte, R. Haase, P. Liebhäuser, J. Glatthaar, S. Herres-Pawlis, S. Schindler, *Eur. J. Inorg. Chem.* **2016**, 4744 – 4751; d) D. Schurr, F. Strassl, P. Liebhäuser, G. Rinke, R. Dittmeyer, S. Herres-Pawlis, *React. Chem. Eng.* **2016**, *1*, 485 – 493.

[17] a) M. Schatz, V. Raab, S. P. Foxon, G. Brehm, S. Schneider, M. Reiher, M. C. Holthausen, J. Sundermeyer, S. Schindler, *Angew. Chem. Int. Ed.* **2004**, *43*, 4360 – 4363; *Angew. Chem.* **2004**, *116*, 4460 – 4464; b) D. Maiti, D.-H. Lee, K. Gaoutchenova, C. Würtele, M. C. Holthausen, A. A. Narducci Sarjeant, J. Sundermeyer, S. Schindler, K. D. Karlin, *Angew. Chem. Int. Ed.* **2008**, *47*, 82 – 85; *Angew. Chem.* **2008**, *120*, 88 – 91.

[18] a) B. Cross, C. L. Dunn, D. H. Payne, J. D. Tipton, *J. Sci. Food Agric.* **1969**, *20*, 340 – 344; b) N. Guttenberger, W. Blankenfeldt, R. Breinbauer, *Bioorg. Med. Chem.* **2017**, *25*, 6149 – 6166; c) V. F. de Andrade-Neto, M. O. F. Goulart, J. F. da Silva Filho, M. J. da Silva, M. do C. F. R. Pinto, A. V. Pinto, M. G. Zalis, L. H. Carvalho, A. U. Krettli, *Bioorg. Med. Chem. Lett.* **2004**, *14*, 1145 – 1149; d) A. K. Jana, *J. Photochem. Photobiol. A* **2000**, *132*, 1 – 17; e) A. V. Gulevskaya, *Eur. J. Org. Chem.* **2016**, 4207 – 4214; f) F. B. Mortzfeld, J. Pietruszka, I. R. Baxendale, *Eur. J. Org. Chem.* **2019**, 5424 – 5433; g) J. N. Hamann, M. Rolff, F. Tuczek, *Dalton Trans.* **2015**, *44*, 3251 – 3258; h) A. Chaudhary, J. M. Khurana, *Res. Chem. Intermed.* **2018**, *44*, 1045 – 1083; i) Y. Xiao, W. Hu, S. Sun, J.-T. Yu, J. Cheng, *Synlett* **2019**, *30*, 2113 – 2122; j) S. Banerjee, *Arkivoc* **2016**, 82 – 110; k) M. Bilal, S. Guo, H. M. N. Iqbal, H. Hu, W. Wang, X. Zhang, *World J. Microbiol. Biotechnol.* **2017**, *33*, 191; l) A. Cimmino, A. Evidente, V. Mathieu, A. Andolfi, F. Lefranc, A. Kornienko, R. Kiss, *Nat. Prod. Rep.* **2012**, *29*, 487 – 501.

[19] Formation of [**O1**](PF$_6$)$_2$ at −80 °C led to smaller extinction at 392 nm (20000 $M^{-1}cm^{-1}$, −5%) in the UV/Vis spectrum compared to the forma-

tion at −90 °C. Formation of [**O1**](PF$_6$)$_2$ at −74 °C led to a significant loss in quantity (16000 м$^{-1}$cm^{-1}, −24%) (see Supporting Information).
[20] High extinction of [**O1**](PF$_6$)$_2$ at 280 nm is caused by overlapping in-plane π_{o^*} to d_{xy} CT transition and π to π^* transition of the aromatic ligand backbone.
[21] L. M. Mirica, X. Ottenwaelder, T. D. P. Stack, *Chem. Rev.* **2004**, *104*, 1013–1045.
[22] K. D. Karlin, J. C. Hayes, Y. Gultneh, R. W. Cruse, J. W. McKown, J. P. Hutchinson, J. Zubieta, *J. Am. Chem. Soc.* **1984**, *106*, 2121–2128.
[23] a) S. Itoh, M. Taki, H. Nakao, P. L. Holland, W. B. Tolman, L. Que, Jr., S. Fukuzumi, *Angew. Chem. Int. Ed.* **2000**, *39*, 398–400; *Angew. Chem.* **2000**, *112*, 409–411; b) H. Arii, Y. Saito, S. Nagatomo, T. Kitagawa, Y. Funahashi, K. Jitsukawa, H. Masuda, *Chem. Lett.* **2003**, *32*, 156–157; c) S. Mahapatra, J. A. Halfen, W. B. Tolman, *J. Am. Chem. Soc.* **1996**, *118*, 11575–11586; d) M. Enomoto, T. Aida, *J. Am. Chem. Soc.* **1999**, *121*, 874–875.
[24] a) E. A. Lewis, W. B. Tolman, *Chem. Rev.* **2004**, *104*, 1047–1076; b) J. A. Halfen, V. G. Young, W. B. Tolman, *Inorg. Chem.* **1998**, *37*, 2102–2103; c) S. Itoh, H. Nakao, L. M. Berreau, T. Kondo, M. Komatsu, S. Fukuzumi, *J. Am. Chem. Soc.* **1998**, *120*, 2890–2899.
[25] S. Mahapatra, S. Kaderli, A. Llobet, Y.-M. Neuhold, T. Palanché, J. A. Halfen, V. G. Young, T. A. Kaden, L. Que, A. D. Zuberbühler, W. B. Tolman, *Inorg. Chem.* **1997**, *36*, 6343–6356.
[26] J. E. Bulkowski, *Binucleating Ligand–Metal Complexes as Oxidation Catalysts*, US Patent 4,545,937, **1985**.
[27] P. Verma, J. Weir, L. Mirica, T. D. P. Stack, *Inorg. Chem.* **2011**, *50*, 9816–9825.
[28] a) P. Liebhäuser, K. Keisers, A. Hoffmann, T. Schnappinger, I. Sommer, A. Thoma, C. Wilfer, R. Schoch, K. Stührenberg, M. Bauer, M. Dürr, I. Ivanović-Burmazović, S. Herres-Pawlis, *Chem. Eur. J.* **2017**, *23*, 12171–12183; b) C. Wilfer, P. Liebhäuser, A. Hoffmann, H. Erdmann, O. Grossmann, L. Runtsch, E. Paffenholz, R. Schepper, R. Dick, M. Bauer, M. Dürr, I. Ivanovic-Burmazovic, S. Herres-Pawlis, *Chem. Eur. J.* **2015**, *21*, 17639–17649.
[29] Turnovers could not be determined, because no extinction coefficient of the quinone is reported elsewhere in the literature.
[30] I. Yavari, Z. Nader, *Dye. Pigment.* **2007**, *75*, 474–478.
[31] a) A. K. Mishra, J. N. Moorthy, *J. Org. Chem.* **2016**, *81*, 6472–6480; b) A. Wu, Y. Duan, D. Xu, T. M. Penning, R. G. Harvey, *Tetrahedron* **2010**, *66*, 2111–2118; c) H. Hussain, S. Specht, S. R. Sarite, M. Saeftel, A. Hoerauf, B. Schulz, K. Krohn, *J. Med. Chem.* **2011**, *54*, 4913–4917.
[32] J. A. Leitch, Y. Bhonoah, C. G. Frost, *ACS Catal.* **2017**, *7*, 5618–5627.
[33] Furthermore, we report NMR, IR, and MS analytical data for **P2**. Another synthetic route and elemental analysis data have been published previously: L. R. Morgan, R. J. Schunior, J. H. Boyer, *J. Org. Chem.* **1963**, *28*, 260–261.
[34] a) R. Krug, D. Schröder, J. Gebauer, S. Suljić, Y. Morimoto, N. Fujieda, S. Itoh, J. Pietruszka, *Eur. J. Org. Chem.* **2018**, 1789–1796; b) L. Penttinen, C. Rutanen, J. Jänis, J. Rouvinen, N. Hakulinen, *ChemBioChem* **2018**, *19*, 2348–2352.

Manuscript received: February 6, 2020
Revised manuscript received: February 26, 2020
Accepted manuscript online: February 27, 2020
Version of record online: May 19, 2020

4.3 Catalytic Oxygenation of Hydrocarbons by Mono-μ-oxo Dicopper(II) Species Resulting from O-O Cleavage of Tetranuclear Cu^{I}/Cu^{II} Peroxo Complexes

The author has contributed to the Raman and XAS measurements and the respective data analysis.

The conversion of inert C-H bonds is possible in the industry under harsh conditions or under ambient conditions for methanotropic bacteria using either copper (pMMO) or iron (sMMO) containing enzymes. In [4.3] the N-donor ligands **bdpdz**[112] and **bdptz**[113] were combined with the copper salts $[Cu(CH_3CN)_4]X$ (X= PF_6, OTf) to form the precursors **1a**-X (with **bdpdz**) and **1b**-X (with **bdptz**). Both precursors were successfully oxygenated at -90 °C with (i) O_2, (ii) PhIO and (iii) N_2O to form the corresponding complexes **2a**-X and **2b**-X, as shown in [4.3]-Scheme 1.This implies that the complexes bind dioxygen to form a tetranuclear μ_4-peroxo species **3a** or **3b**, prior to the cleavage of the oxygen bond to form two dinuclear peroxo complexes **2a** or **2b**, as shown in [4.3]-Scheme 2. Although Ref. [114] reported with some ambiguity on a chlorine-bridged tetranuclear motif, it is generally rare to find clear and concise data on tetranuclear model complexes such as the one identified in [4.3] with Raman, XAS and other tools. The paper [4.3] further contains oxygenation reactions with aliphatic substrates, reactivity studies and proposes a reaction mechanism for the C-H to C-OH conversion.

Raman experiments were conducted with the Tsunami laser system, using the nonlinear BBO crystals to work at the frequency-doubled wavelength of 397 nm. The precursor solution (**1a** and **1b**) was filled in a glass cuvette with a concentration of 12.5 mM and a lid containing a septum in the glovebox, to ensure no unwanted exposure to water or oxygen. The cuvette was cooled to -90 °C in a self-built cryostat.[104] The focus spot was adjusted with a micrometer screw to be 30 μm inside the cuvette. The Raman measurements were taken at 10-15 mW. The precursor was oxygenated *via* a cannula through the septum at 0.02 bar overpressure for a time of (i) 15 min for dioxygen and (ii) 30 min for nitrous oxide. A platinum-based resistance temperature detector is used to measure the temperature inside the cuvette and feed the information to the cryostat, which uses ethanol as a cooling agent for the sample-surrounding copper block and a peltier cooling-element for precise and adjustable temperature control.

Raman spectra on oxygenated solutions are shown in [4.3]-Fig. 1 (b) and (c) for **1a** and **1b** at -35 °C, respectively. The observed vibrations indicate a Cu_2O complex, as is the case for e.g. the peak at 623 cm^{-1} for the **1b** complex which stems from a antisymmetric Cu-O vibration.[115, 116] This idea is further underlined by the Raman data on samples oxygenated with nitrous oxide, which show the same vibration at 623 cm^{-1} that comes from a mono-μ-oxo motif at -35 °C and is shown in [4.3]-Fig. 1 (c). The identification of these modes as oxygen-related is proven by isotope-shift measurements with the $^{18}O_2$ isotope. Conducting the isotope-shift measurements for **1a** and **1b** at a cooler temperature of -90 °C, reveals for both complexes oxygen-related vibrations that can only be attributed to the tetranuclear mixed-valent Cu_4O_2 core. For example, the O-O stretching mode was found for both complexes at 854 cm^{-1}, as reported in the literature.[117, 118] The data are shown in [4.3]-Fig. 2 (a). The mixed-valent tetranuclear motif is now established and heating the solution up to -50 °C and -35 °C causes the respective modes to vanish and the antisymmetric Cu-O mode from the Cu_2O core to emerge, as shown in [4.3]-Fig. 2 (b). Cooling

down again did not recover the tetranuclear spectrum, showing that the O-O bond cleavage is irreversible.

The chemical sequence shown in [4.3]-Scheme 2 is now established. The dinuclear precursors **1a** and **1b** form the mixed-valent tetranuclear complexes **3a** and **3b** at -90 °C and while heating, the O-O bond is cleaved and the dinuclear mono-μ-oxo complexes **2a** and **2b** are formed. Next, XAS measurements were performed to further corroborate the established concept and to yield detailed information on the bond lengths and interatomic distances at the Cu cores. XAS measurements were performed at the P65 beamline[101] at PETRA III (DESY, Hamburg, Germany). The samples were measured in the energy range of 8829 eV to 9979 eV. The samples were prepared under oxygen- and water-free atmosphere and transferred to a self-built PEEK cuvette with a lid containing a septum for oxygenation. The windows were sealed by pressing Kapton foil (polyimide foil by *DuPont*) on a teflon O-ring by screwing in PEEK screws. For oxygenation, the cuvette was placed in liquid nitrogen to freeze and was subsequently removed. The solution was allowed to warm up to the freezing point, so that a cannula with oxygen could be inserted for 5 min of oxygenation. The cuvette was immediately placed in the liquid nitrogen bath to prevent excess heating. This procedure was repeated three times in total, before the cuvette was placed in liquid nitrogen again and put in the cryostat at -173 °C. For the -35 °C measurements, the cryostat was heated to -35 °C and kept at that temperature for one hour before being set to -173 °C again. All XAS data were analyzed with the software Athena and Artemis[103]. The XANES data are shown in [4.3]-Fig. 3 (a) and (b), the EXAFS data are shown in (c) and (d). Since the precursor contains only-Cu^{I}, the tetranuclear peroxo complex contains Cu^{I}/Cu^{II} and the dinuclear mono-μ-oxo complex contains only-Cu^{II}, the expectation and observation in the edge shows a blueshift with increasing oxidation number. Additionally, as shown in [4.3]-Fig. 3 (b) a pre-edge feature appears and becomes stronger at 8977.5 eV for the tetranuclear peroxo and subsequently the dinuclear mono-μ-oxo complex. [4.3]-Fig. 3 (c) and (d) show the EXAFS data as $\chi(k)$ and as the magnitude of $\chi(R)$, respectively. Most notably, the analysis did show a Cu-Cu atomic distance of 3.55 Å for the tetranuclear complex and 3.19 Å for the dinuclear complex, showing a distinct difference in molecular structure due to oxygen bond cleavage.

Catalytic Oxygenation of Hydrocarbons by Mono-μ-oxo Dicopper(II) Species Resulting from O-O Cleavage of Tetranuclear Cu^{I}/Cu^{II} Peroxo Complexes

GDCh Research Articles Angewandte International Edition Chemie

Check for updates

Copper Monooxygenases

How to cite: *Angew. Chem. Int. Ed.* **2021**, *60*, 14154–14162
International Edition: doi.org/10.1002/anie.202101035
German Edition: doi.org/10.1002/ange.202101035

Catalytic Oxygenation of Hydrocarbons by Mono-μ-oxo Dicopper(II) Species Resulting from O−O Cleavage of Tetranuclear Cu^{I}/Cu^{II} Peroxo Complexes

Ramona Jurgeleit, Benjamin Grimm-Lebsanft, Benedikt Maria Flöser, Melissa Teubner, Sören Buchenau, Laura Senft, Jonas Hoffmann, Maria Naumova, Christian Näther, Ivana Ivanović-Burmazović, Michael Rübhausen, and Felix Tuczek**

Dedicated to Professor Wolfgang Kaim on the occasion of his 70th birthday

Abstract: *One of the challenges of catalysis is the transformation of inert C−H bonds to useful products. Copper-containing monooxygenases play an important role in this regard. Here we show that low-temperature oxygenation of dinuclear copper(I) complexes leads to unusual tetranuclear, mixed-valent μ_4-peroxo $[Cu^{I}/Cu^{II}]_2$ complexes. These* $\boldsymbol{Cu_4O_2}$ *intermediates promote irreversible and thermally activated O−O bond homolysis, generating* $\boldsymbol{Cu_2O}$ *complexes that catalyze strongly exergonic H-atom abstraction from hydrocarbons, coupled to O-transfer. The* $\boldsymbol{Cu_2O}$ *species can also be produced with N_2O, demonstrating their capability for small-molecule activation. The binding and cleavage of O_2 leading to the primary* $\boldsymbol{Cu_4O_2}$ *intermediate and the* $\boldsymbol{Cu_2O}$ *complexes, respectively, is elucidated with a range of solution spectroscopic methods and mass spectrometry. The unique reactivities of these species establish an unprecedented, 100 % atom-economic scenario for the catalytic, copper-mediated monooxygenation of organic substrates, employing both O-atoms of O_2.*

Introduction

The transformation of inert C−H bonds to useful products is one of the great challenges of chemistry.[1] Successful strategies to address this problem will preferentially involve catalysts based on earth-abundant metals, operating under mild conditions and in an atom- as well as energy efficient fashion.[2] One of the most interesting candidates in this regard is copper, also due to its role in copper-dependent monooxygenases.[3a,b,4] For example, methane monooxygenases (MMOs) enable methanotrophic bacteria to catalyze the conversion of methane to methanol under ambient conditions. Mimicking this reactivity with synthetic model systems thus is of high scientific and technological interest.[2–7] Whereas nature's predominant form of MMO, particulate methane monooxygenase (pMMO), contains copper, a dinuclear iron active site performs this reaction in soluble methane monooxygenase (sMMO). The identity of the active site in pMMO is, however, subject to controversy. The methane-to-methanol conversion mediated by this enzyme has been proposed to occur (i) on a mononuclear copper

[*] R. Jurgeleit, Dr. B. M. Flöser, Prof. Dr. C. Näther, Prof. Dr. F. Tuczek
Institute of Inorganic Chemistry
Christian-Albrechts-University of Kiel
Max-Eyth-Strasse 2, 24118 Kiel (Germany)
E-mail: ftuczek@ac.uni-kiel.de

Dr. B. Grimm-Lebsanft, M. Teubner, S. Buchenau, Prof. Dr. M. Rübhausen
Institut für Nanostruktur- und Festkörperphysik
Center for Free Electron Laser Science (CFEL)
Universität Hamburg
Luruper Chaussee 149, 22761 Hamburg (Germany)
E-mail: mruebhau@physnet.uni-hamburg.de

Dr. B. M. Flöser
Max Planck Institute for Chemical Energy Conversion
Stiftstrasse 34–36, 45470 Mühlheim an der Ruhr (Germany)

M. Teubner
Department of Inorganic Chemistry, RWTH Aachen University
Landoltweg 1, 52074 Aachen (Germany)

L. Senft, Prof. Dr. I. Ivanović-Burmazović
Department of Chemistry and Pharmacy
Friedrich-Alexander-University of Erlangen-Nürnberg
Egerlandstrasse 1, 91058 Erlangen (Germany)

J. Hoffmann
Institute for Analytical and Organic Chemistry
University of Bremen
Leobener Strasse 7, 28359 Bremen (Germany)

J. Hoffmann
MAPEX, Center for Materials and Processes
University of Bremen
Bibliothekstrasse 1, 28359 Bremen (Germany)

Dr. M. Naumova
DESY, Deutsches Elektronen-Synchrotron (DESY)
Notkestrasse 85, 22607 Hamburg (Germany)

Prof. Dr. I. Ivanović-Burmazović
Department Chemie, Ludwig-Maximilians-Universität München
Butenandtstrasse 5–13, Haus D, 81377 München (Germany)

Supporting information and the ORCID identification number(s) for the author(s) of this article can be found under: https://doi.org/10.1002/anie.202101035.

site,[4b,c,8,9] (ii) through a dinuclear copper–oxygen species[10–12] or (iii) within a tricopper cluster.[1,6,13,14]

In both forms of MMO, just like in other copper- and iron-containing monooxygenases,[1,3a,b] the oxygen atom of O_2 that is not transferred to the organic substrate is converted to water. This is the reason for the fact that these enzymes require two reducing equivalents per transferred O-atom, usually from NAD(P)H.[3c,15,16] Whereas the formation of water adds thermodynamic driving force to the oxygenation reaction,[3c,15,16] the synthesis of these reductants consumes energy,[3c,16] and doubtlessly a significant advantage would be achieved if both O-atoms of O_2 could be used for oxygen transfer. Although such a mechanism does not seem to exist in nature, we herein provide evidence for exactly this scenario in synthetic model chemistry. Specifically, we show that low-temperature oxygenation of dinuclear Cu^I complexes supported by the ligands **bdpdz**[17] and **bdptz**[18] leads to tetranuclear, mixed-valent μ_4-peroxo $[Cu^I/Cu^{II}]_2$ complexes. Upon warming to 238 K, these undergo homolytic O–O bond cleavage, generating two mono-μ-oxo dicopper(II) complexes which in turn catalyze O transfer to organic substrates. Notably, a related dicopper mono-μ-oxo species has been found to perform the challenging methane-to-methanol conversion in oxygen-activated, copper-containing Cu-ZSM-5, serving as an inorganic model system of pMMO.[11] Therefore, the **Cu_2O** motif has also been discussed as a possible intermediate in the enzyme and currently is considered as one of the important copper–oxygen species besides the common **Cu_2O_x** cores.[19–24] These developments have spurred an intense search for new dicopper complexes exhibiting a μ-oxo unit. In the meantime, a limited number of such systems has been synthesized and characterized. An excellent review describing these reports has been published by Limberg et al.[19]

Results and Discussion

The multidentate N-donor ligands **bdpdz**[17] and **bdptz**[18] exhibiting a central pyridazine and a phthalazine moiety, respectively, were synthesized by slight modifications of the published procedures; the latter ligand was characterized by X-ray structure determination (Supporting Information Sections S2 and S3.1). Addition of two equivalents of $[Cu(CH_3CN)_4]PF_6$ or $[Cu(CH_3CN)_4]OTf$ to these ligands in acetonitrile provided the complexes $[Cu^I_2(\mathbf{bdpdz})(CH_3CN)_2]X_2$ (**1a**-X) and $[Cu^I_2(\mathbf{bdptz})(CH_3CN)_2]X_2$ (**1b**-X; X = PF_6 or OTf) in almost quantitative yields.[25] Attempts to obtain single crystals of **1b**-OTf yielded red crystals which were investigated by single-crystal X-ray diffraction analysis. The molecular structure obtained, however, revealed a trinuclear mixed-valent $Cu^ICu^{II}Cu^I$-complex, demonstrating the ability of these ligands to accommodate both copper(I) and copper(II) centers (see below and Section S3.2).[25]

Low-temperature oxygenation of **1a**-OTf, **1a**-PF_6, **1b**-OTf and **1b**-PF_6 was performed in acetone by employing O_2 as well as two oxygen-atom transfer (OAT) reagents and monitored by UV/Vis and resonance Raman spectroscopy. The obtained results were corroborated by ESI mass spectrometry and X-ray absorption spectroscopy, complemented by DFT calculations. Combined evidence from these data leads to characterization of a mono-μ-oxo dicopper(II) species (Scheme 1) along with the identification of an unusual tetranuclear mixed-valent μ_4-peroxo $[Cu^I/Cu^{II}]_2$ intermediate in both types of complexes (see below).

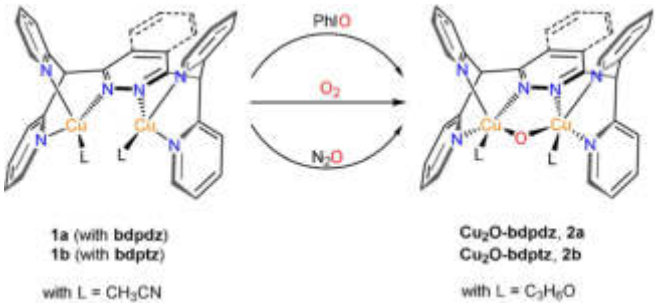

Scheme 1. Access to the **Cu_2O** complexes: The counterions X are hexafluorophosphate (PF_6^-) or triflate (OTf^-) and are omitted for clarity.

Upon reaction of **1a** and **1b** with dioxygen at 183 K the color of the solution changes from yellow to pale green, going along with a change of the initial spectrum of the precursor (Figure 1a, black) to a product spectrum containing two absorption features—a broad shoulder at 390 nm (ε = 2770 $M^{-1}cm^{-1}$) and a band at 621 nm (ε = 222 $M^{-1}cm^{-1}$) (Figure 1a, blue; Table 1). The formation of a pale green solution was already described for **1b**-OTf by Lippard and co-workers in different solvents at 195 K.[25] Gradual warming of the solution to 248 K causes a deepening of the color to intense green. In the corresponding spectrum (Figure 1a, red) the near-UV band splits into two shoulders at 370 nm (ε = 2642 $M^{-1}cm^{-1}$) and 421 nm (ε = 1350 $M^{-1}cm^{-1}$) whereas the 621 nm band shifts to 630 nm (ε = 213 $M^{-1}cm^{-1}$). The intense green color, which for the first time has been associated with a μ-oxo dicopper(II) moiety by Karlin et al. in 1984, is a strong indication for the formation of a **Cu_2O** core.[19,26] In order to test this hypothesis we employed the common OAT reagent iodosobenzene[12,19,27] to generate the **Cu_2O** species (Scheme 1). In fact, upon reaction of **1a**/**1b** with PhIO in acetone at 238 K the color changes from yellow to intense green and a spectrum emerges (Figure 1a inset, violet) that is very similar to that obtained with O_2. We also investigated whether the same species can be obtained using nitrous oxide as OAT reagent.[28–30] To this end, **1b**-PF_6 was reacted at 193 K with N_2O and the temperature was slowly increased to 233 K (Figure S18). A color change from yellow to intense green occurred which was accompanied by N_2 evolution (Supplementary Video 1). The final spectrum (Figure 1a, inset, green) was again found to be almost identical to that obtained for the reaction with PhIO and O_2, respectively, exhibiting two shoulders at 369 nm (ε = 2593 $M^{-1}cm^{-1}$) and 416 nm (ε = 1378 $M^{-1}cm^{-1}$) and a distinct absorption band at 631 nm (ε = 220 $M^{-1}cm^{-1}$). Notably, absorption features around 600 nm have been observed for other **Cu_2O** complexes as well (Table S6), supporting our assignment.[12,19,27,31,32]

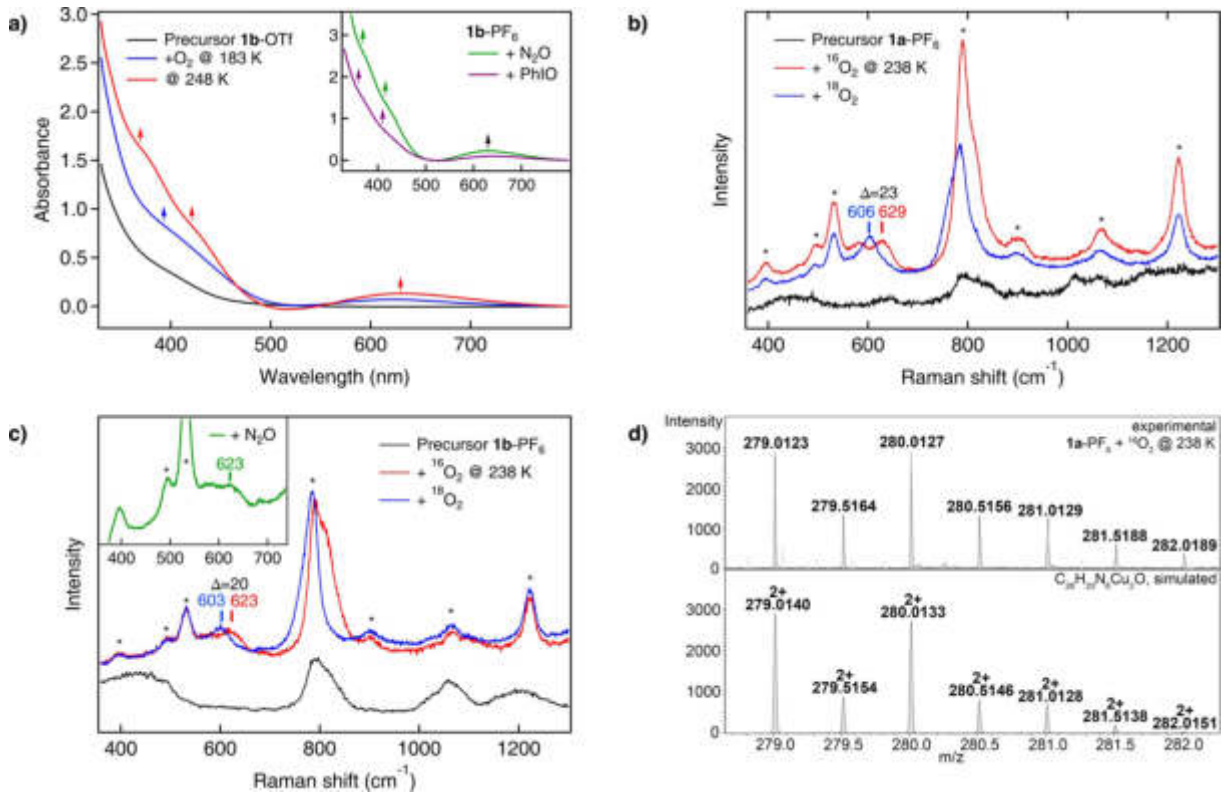

Figure 1. Generating the mono-μ-oxo species. a) Reaction with dioxygen: Absorption spectra of an acetone solution of **1b**-OTf before (black) and upon reaction with O_2 (blue, red). The UV/Vis spectra of the green solution obtained after reaction of **1b**-PF_6 dissolved in acetone with nitrous oxide (green) at 233 K or with an excess of PhIO (violet) at 238 K are shown in the inset. b) Resonance Raman spectra of **1a**-PF_6 before (black) and upon reaction with $^{16}O_2$ (red) and $^{18}O_2$ (blue) at 238 K. c) Resonance-enhanced vibrational spectra of **1b**-PF_6 before (black) and after the reaction with $^{16}O_2$ (red), $^{18}O_2$ (blue) and upon reaction with nitrous oxide (green) at 238 K. d) Characteristic cutout of the UHR-ESI mass spectrum obtained upon reaction of **1a**-PF_6 with $^{16}O_2$ at 238 K, confirming the formation of the mono-μ-oxo complex. The corresponding species is also detected in the experiment with $^{18}O_2$ (see Figure S35). General remarks: UV/Vis: $l = 1$ cm. Raman: The asterisks mark solvent signals of acetone. The laser excitation wavelength was 393 nm.

Table 1: Spectroscopic data elucidating the binding and cleavage of O_2. Overview of the experimentally and theoretically obtained data for the **bdpdz** (**1a**) and **bdptz** (**1b**) systems after oxygenation, leading to the corresponding Cu_2O (**2a/b**) or Cu_4O_2 (**3a/b**) complexes.

	Cu_2O					Cu_4O_2[b]			
Absorption feature	*TDDFT*[a]	***2a***-PF_6	***2a***-*OTf*	***2b***-PF_6	***2b***-*OTf*	***3a***-PF_6	***3a***-*OTf*	***3b***-PF_6	***3b***-*OTf*
λ [nm]	390/380	370 (2739)	371 (2391)	368 (2488)	370 (2642)	397 (1956)	398 (2754)	393 (2150)	390 (2770)
(ε [$M^{-1}cm^{-1}$])	431/434	421 (1282)	422 (1119)	417 (1343)	421 (1350)	N.A.	N.A.	N.A.	N.A.
	554 + 701/572	630 (264)	630 (219)	633 (207)	630 (213)	619 (200)	613 (160)	619 (168)	621 (222)
Vibrational mode	*DFT*[c]	***2a***-PF_6	***2a***-*OTf*	***2b***-PF_6	***2b***-*OTf*	*DFT*[d]	***3a***-PF_6	***3b***-PF_6	***3b***-*OTf*
($\Delta^{18}O_2$) [cm^{-1}]									
ν_{Cu-O}[e]	563 (35)/ 587 (29)	629 (23)	619 (11)	623 (20)	619 (8)	523 (28)/ 534 (27)	607 (14)	607 (16)	604 (8)
ν_{O-O}	N.A.	N.A.	N.A.	N.A.	N.A.	854 (50)/ 849 (49)	854 (62)	854 (52)	855 (57)

General remarks: Solvent: acetone; oxygenations were carried out at least duplicate; values presented here are averaged; $c = 0.6$–1.0 mM. [a] Values are given as follows: **2a (bdpdz)/2b (bdptz)**. Based on the assumption that acetone is the coordinating solvent; values with acetonitrile instead of acetone can be found in Table S9. DFT: B3LYP/def2-TZVP(-f). [b] The given molar absorption coefficients at these maxima are based on the assumption that the species is tetranuclear. [c] Based on the assumption that acetone is the coordinating solvent; values without acetone or with acetonitrile can be found in Table S9. DFT: PBE-D3(BJ)/def2-SVP. Detailed assignments as well as schematic representations of the vibrational modes can be found in Section S6.1. [d] Calculations were performed without any coligands like acetone or acetonitrile. **1a**: $d_{O-O} = 1.412$ Å and **1b**: $d_{O-O} = 1.414$ Å. DFT: PBE-D3(BJ)/def2-SVP. Detailed assignments as well as schematic representations of the vibrational modes can be found in Section S6.1. [e] $\nu_{Cu-O} = \nu^{as}{}_{Cu-O}$; $\nu^{s}{}_{Cu-O}$ not observed.

In order to provide further spectroscopic evidence for the formation of Cu_2O cores, resonance Raman (rR) spectroscopy was employed. Upon reaction of **1a**-PF_6 with dioxygen at 238 K, an isotope-sensitive peak emerges at 629 cm^{-1} ($\Delta =$

23 cm^{-1}; Figure 1b). DFT calculations performed for the **Cu_2O** complex of **1a** predict a symmetric and an antisymmetric Cu–O vibration at 437 cm^{-1} ($\Delta = 19$ cm^{-1}) and 563 cm^{-1} ($\Delta = 35$ cm^{-1}), respectively (Table 1 and Section S6.1 for a full vibrational analysis). Based on its frequency, the observed mode is assigned to the antisymmetric vibration whereas the symmetric vibration is not observed. This can be explained by assuming that the oxo→Cu^{II} CT transition is localized.[33] The excited state thus exhibits a distortion along ν^{as}_{Cu-O}, and only this mode gets resonantly enhanced.[33]

Similar observations were made for **1b**-PF_6 upon reaction with dioxygen at 238 K. In this case, ν^{as}_{Cu-O} appears at 623 cm^{-1} ($\Delta = 20$ cm^{-1}; Figure 1c).[33] The observed vibrational frequencies and isotope shifts are in good agreement with the literature (Table 1 and Table S8).[11,12,19,20,27,34–36]

To further confirm the identity of the **Cu_2O** complex and support the respective UV/Vis data (see above), rR investigations were also performed with nitrous oxide (Figure 1c). Addition of N_2O into a solution of **1b**-PF_6 at 193 K leads to the emergence of two new peaks in the rR spectrum both of which can be attributed to free N_2O (Figure S19).[37] Upon increasing the temperature the N_2O features decrease in intensity and N_2 is liberated (see above). At 238 K a new peak emerges at 623 cm^{-1} (Figure 1c, inset), in analogy to the reaction with dioxygen (Figure 1c, red). To the best of our knowledge, no other low-molecular weight dicopper(I) complex has so far been found to form a mono-μ-oxo core with N_2O at such low temperatures, underscoring the extraordinary capability of our systems for small-molecule activation.[19,22,28,29,30,38,39]

The spectroscopic data are corroborated by UHR-ESI MS. Reaction of **1a**-PF_6 with dioxygen (or PhIO; Section S4.1) at 238 K provides the mass spectrum shown in Figure 1d, which is in excellent agreement with the calculated spectrum and isotopic distribution pattern of the doubly positively charged **Cu_2O** species $[\mathbf{2a}\text{-}PF_6]^{2+}$ (m/z: calc. 279.0140, obs. 279.0123). Upon reaction with $^{18}O_2$ the peak shifts by one mass unit to m/z 280.0137, as expected (Figure S35).

The fact that **1a** and **1b** are able to form **Cu_2O** species not only by using OAT reagents but also by reaction with O_2 suggests that they are able to bind dioxygen and subsequently cleave the O–O bond of the resulting peroxo complex (cf. Scheme 2). Correspondingly, we assume that the UV/Vis spectrum observed upon oxygenation of **1b** at 183 K (Figure 1a, blue) does not originate from a **Cu_2O** complex, but rather from the initially formed dioxygen adduct.

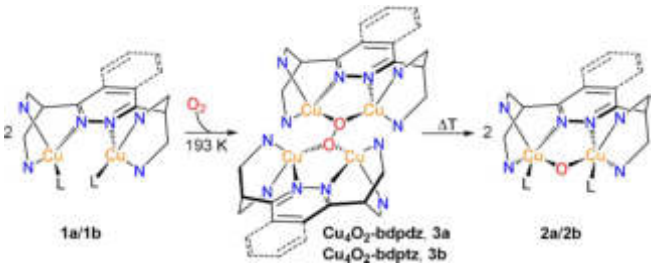

Scheme 2. Formation of the **Cu_2O** core via homolytic O–O bond cleavage of the tetranuclear, mixed-valent μ_4-peroxo species (**Cu_4O_2**). The pyridine rings have been omitted for clarity and simplified by the N-donor atoms.

In order to obtain more information about this intermediate and its O–O cleavage leading to the **Cu_2O** species, variable-temperature rR experiments were performed. Reaction of **1b**-PF_6 with dioxygen at 193 K leads to a rR spectrum which exhibits two isotope-sensitive peaks at 854 and 607 cm^{-1} ($\Delta = 52$ and 16 cm^{-1}, respectively; Figure 2a, red and blue). Importantly, the observed Raman spectrum is not compatible with a 1:1 adduct of **1b** and dioxygen (cf. Section S6.7 and Scheme S5), but can only be interpreted on the basis of a tetranuclear mixed-valent μ_4-peroxo $[Cu^I/Cu^{II}]_2$ complex with a **Cu_4O_2** core (Scheme 2, center). A DFT-based vibrational analysis of this species is presented in Section S6.1. Correspondingly, the peak at 854 cm^{-1} is attributed to the O–O stretch and the peak at 607 cm^{-1} to a Cu–O mode (Table 1). Similar results are obtained upon reaction of **1a**-PF_6 with dioxygen at 193 K with ν_{O-O} being observed at 854 cm^{-1} ($\Delta =$ 62 cm^{-1}) and ν_{Cu-O} at 607 cm^{-1} ($\Delta = 14$ cm^{-1}; Figure S29). Note that O–O stretches around 850 cm^{-1} have also been observed in other **Cu_4O_2** clusters (cf. Table S8).[34–36,40]

Upon increasing the temperature from 193 K (Figure 2b, blue) to 223 K (Figure 2b, green) the peroxo-core associated features (including the O–O stretch) clearly vanish, and further warming to 238 K leads to a spectrum (Figure 2b, red) that is identical to the red trace of Figure 1c; i.e., corresponds to the mono-μ-oxo species (Figure S30). This confirms that the tetranuclear peroxo complex promotes thermally activated, homolytic O–O bond cleavage, leading to two **Cu_2O** species. Supposedly, this process does not occur in a single step as shown in Figure 2a, but involves a more complex reaction sequence.[36] In any case, if the solution containing the **Cu_2O** species of **1b**-OTf is cooled again from 238 K down to 203 K (Figure 2c), the features of the **Cu_4O_2** core do not reappear, but the mono-μ-oxo feature at 619 cm^{-1} is retained. These observations are supported by UV/Vis spectroscopy (Figures S20 and S21). The transformation process shown in Scheme 2 thus is irreversible.

To support the low-temperature spectroscopic data, cryo-UHR-ESI MS was employed again. Upon reaction of an acetone solution of **1a**-OTf with O_2 at 183 K the mass spectrum presented in Figure 2d is obtained, which shows a peak with an isotopic pattern and m/z value corresponding to the **Cu_4O_2** trication $[\mathbf{3a}\text{-OTf}]^{3+}$ (Scheme 2). Note that this species contains two Cu^I, two Cu^{II} and one peroxide, as anticipated. Along with two **bdpdz** ligands and one triflate this leads to the observed m/z value of 421.6674 (m/z calc. 421.6695) and total charge of 3+. Upon reaction with $^{18}O_2$ the characteristic peak shifts by 4/3 mass units to m/z 423.0011 (m/z calc. 423.0057; Figure S36). Importantly, no mono-μ-oxo species can be detected at 183 K for **1a**-OTf, in agreement with the thermally activated character of the **Cu_4O_2**→**Cu_2O** conversion (see above).

Detailed information on the oxidation state and the nearest-neighbor environment of the copper centers in the **Cu_2O** and **Cu_4O_2** complexes is provided by extended X-ray absorption fine structure (EXAFS) and X-ray absorption near-edge structure (XANES). Upon oxygenation of the Cu^I

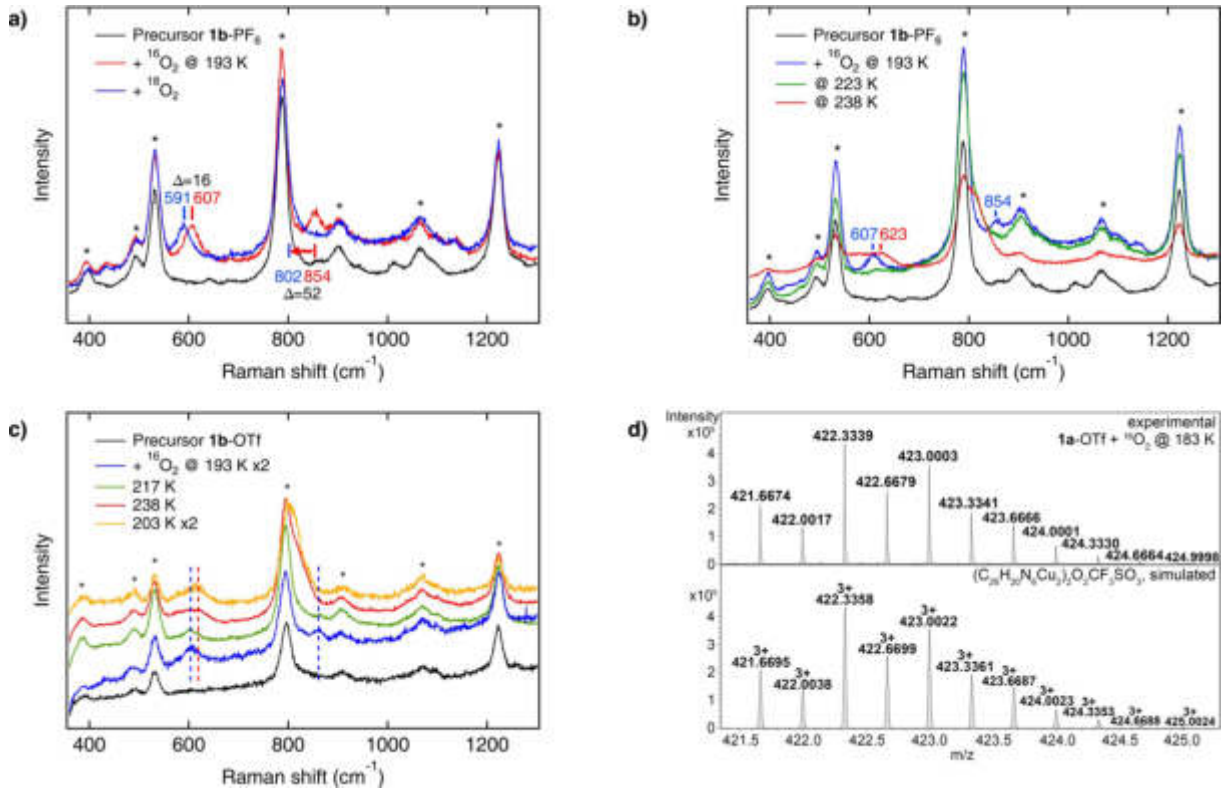

Figure 2. Mechanistic investigations: Breaking the O—O bond. a) Resonance Raman spectra of **1b**-PF_6 before (black) and after the reaction with $^{16}O_2$ (red) and $^{18}O_2$ (blue) at 193 K. b) Resonance Raman spectra of **1b**-PF_6 before (black) and upon reaction with dioxygen at three different temperatures (blue: 193 K; green: 223 K; red: 238 K). c) O—O bond homolysis of the Cu_4O_2 intermediate is irreversible; i.e., once the Cu_2O complex of **1b**-OTf is formed (red), the spectrum of the mono-μ-oxo species is retained after re-cooling (orange). The spectra at 193 K and 203 K are rescaled by factor 2. d) Characteristic cutout of the UHR-ESI mass spectrum obtained upon reaction of **1a**-OTf with $^{16}O_2$ at 183 K, confirming the mixed-valent μ_4-peroxo complex. The corresponding species is also detected in the experiment with $^{18}O_2$ (see Figure S36). General remarks: Raman: The asterisks mark solvent signals of acetone. The laser excitation wavelength was 393 nm.

precursor (**1b**-PF_6) to the Cu_4O_2 complex (**3b**-PF6) and further conversion to the Cu_2O species (**2b**-PF_6), the edge position (measured at 50% of the edge jump) in the Cu K-edge XANES spectra shifts to higher energy by 0.7 and by additional 0.2 eV, respectively, reflecting a stepwise transition from Cu^I to Cu^{II}. Moreover, the spectrum of **1b**-PF_6 (Figure 3a,b, black) shows a distinct feature at 8982.2 eV, the intensity of which is reduced by about 40% upon oxygenation at 193 K, leading to **3b**-PF_6 (Figure 3a,b, blue). At 238 K, a further intensity decrease by about 10% is observed which reflects the conversion of **3b**-PF_6 to **2b**-PF_6 (Figure 3a,b, red). This feature is assigned to the electric-dipole allowed transition from Cu 1s to the lowest-energy Cu 4p orbitals.[41] Through antibonding interactions deriving from the bridging peroxo and oxo ligands, respectively, these orbitals are partially shifted to higher energy, explaining the intensity decrease of the peak at 8982.2 eV and intensity increase of peaks at higher energy (Figure 3a). Concomitantly, a pre-edge feature appears at 8977.5 eV for the Cu_4O_2 intermediate that gets more intense upon conversion to the Cu_2O species, reflecting the emergence and further increase of Cu^{II} character (Figure 3b).[42,43] Similar observations are made for **1a**-PF_6 before and after reaction with dioxygen at 183 K and 238 K (Section S8.1).

Further structural insights are provided by EXAFS analysis. For the Cu_4O_2 and Cu_2O complexes of **1b**-PF_6 the phase-corrected Cu K-edge Fourier transform of EXAFS can be found in Figure 3c and 3d, respectively; the insets show the k^3-weighted Cu K-edge EXAFS. Similar results are obtained for **1a**-PF_6 (Section S8.1). Good agreement between the data and the fits is obtained by use of theoretical models with two acetone coligands for the Cu_2O and no solvent ligands for the Cu_4O_2 species. The most important bond lengths and interatomic distances around the Cu centers derived from Cu K-edge EXAFS are shown in Figure 4. Apart from O—O cleavage, the most significant structural change relates to the Cu–Cu distance which decreases by 0.36 Å upon going from the Cu_4O_2 to the Cu_2O complex.

The ability of the mono-μ-oxo complexes **2a** and **2b** to catalyze the monooxygenation of hydrocarbons was evaluated with a range of aliphatic substrates exhibiting bond dissociation energies (BDEs) from 75 to 82 kcal mol^{-1}; i.e., 9*H*-xanthene (XEN),[44,45] 9,10-dihydro-anthracene (DHA),[45–47] fluorene,[44,45,48] triphenylmethane[45,49] and diphenylmethane (DPM)[44] (Table 2 and Section S10). A three-step protocol was applied in these experiments, and quantification was done by use of GC–MS (cf. Sections S2.8 and S10). Addition of 20 equiv of xanthene (BDE = 75 kcal mol^{-1}) to the Cu_2O derivatives of **1a** and **1b** resulted in the conversion

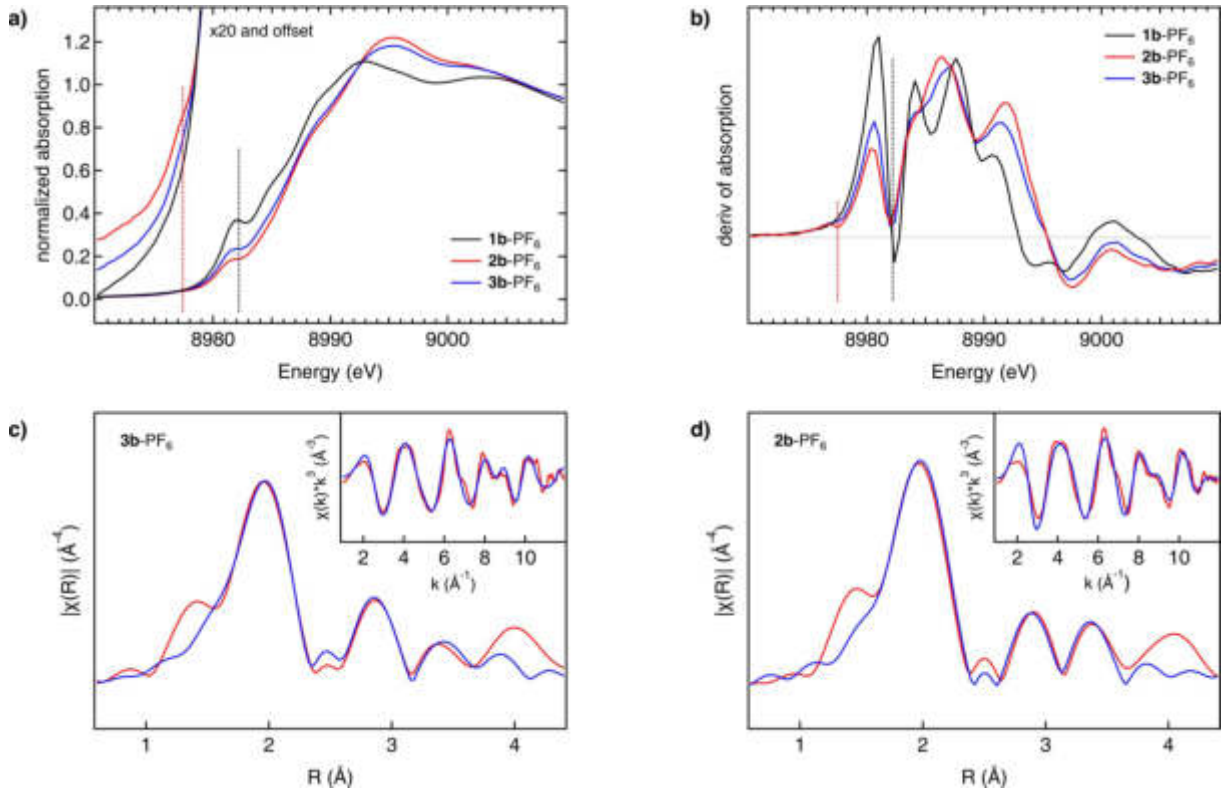

Figure 3. Gaining electronic and structural insights into the reaction of the Cu^{I} precursors with O_2. a) Cu K-edge XANES spectra of the precursor **1b**-PF_6 before (black line, Cu^{I}) and after the reaction with dioxygen at 183 K (blue line, $\mathbf{Cu_4O_2}$) and 238 K (red line, $\mathbf{Cu_2O}$) with enlarged pre-edge region. b) Derivatives of the spectra given in (a), showing the XANES region in more detail (see text). c) Phase-corrected Cu K-edge Fourier transform of EXAFS of **3b**-PF_6 at 183 K (red). Inset: k^3-weighted Cu K-edge EXAFS of **3b**-PF_6 (red). The best fit for both spectra is shown in blue. d) Phase-corrected Cu K-edge Fourier transform of EXAFS of **2b**-PF_6 at 238 K (red). Inset: k^3-weighted Cu K-edge EXAFS of **2b**-PF_6 (red). The best fit (blue) is obtained by using the theoretical model with two acetone ligands coordinating with their carbonyl O-atoms (O)s.

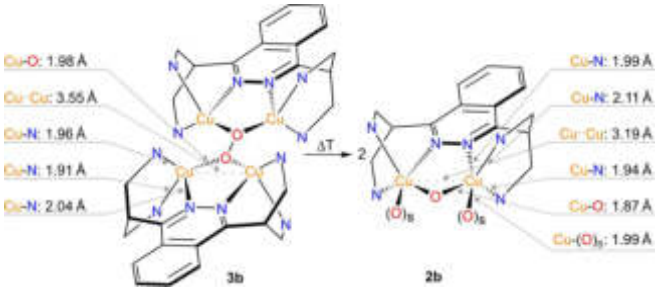

Figure 4. Key geometric parameters (selected bond lengths and Cu···Cu distances) of the oxygenated complexes (**2b** and **3b**) of **1b**-PF_6 based on EXAFS data. The pyridine rings have been omitted for clarity and simplified by the N-donor atoms.

Table 2: Catalytic activity for the oxygenation of hydrocarbons. Overview of the obtained data for the catalytic activity of the model systems **2a** and **2b** towards various substrates.

BDE [kcal mol^{-1}]	Substrate→Product	TON[a] **2a**-PF_6/**2a**-OTf	TON[a] **2b**-PF_6/**2b**-OTf
75	XEN→XON	1/3	1/2
78	DHA→A	3/2	2/1
78	DHA→AQ[b]	3/2	4/5
82	DPM→Ph_2CO	2/2	2/2

General remarks: Conditions: 1 equiv of **2a** or **2b** and 20, 10 or 50 equiv of XEN, DHA or DPM, respectively, were applied (cf. Section S2.8). Blind reactions were also performed using $[Cu(CH_3CN)_4]PF_6$ or $[Cu(CH_3CN)_4]OTf$ and O_2 instead of **2a** or **2b**. All control experiments lead to poorer results compared to the activity with **2a** or **2b** (see Table S17). For abbreviations see text. [a] TON = Turnover Number; is defined as the equiv of product made per equiv of catalyst (= $\mathbf{Cu_2O}$ complex). [b] 10 equiv of DHA were used; representing 20-fold excess of substrate. The given TON refers to the initially formed disecondary alcohol and does not include the subsequent oxidation.

to 9*H*-xanthen-9-one (XON). Yields between 7 and 13%, corresponding to a TON of 1–3, were obtained (Table 2). Subsequently, the activities of **2a** and **2b** towards the conversion of DHA (BDE = 78 kcal mol^{-1}) to 9,10-anthraquinone (AQ) were tested. Employing 10 equiv of DHA led to TONs between 2 and 5 (11–24%), the highest TON being achieved with **2b**-OTf (Table 2 and Scheme 3).

To confirm that the AQ oxygen atoms derive from dioxygen, these experiments were repeated with $^{18}O_2$ instead of $^{16}O_2$, leading to a shift of the AQ peak in the HR-EI MS by 4 mass units (Section S10.3). As a side reaction the formation of anthracene (A; 6–14% corresponding to a TON of 1–3) via double H-atom transfer (HAT) was observed (Scheme 3, left). This dehydrogenation as well as two-electron oxidation of the initially formed disecondary alcohols generate water (Scheme 3), which possibly deactivates the catalyst.[12,19]

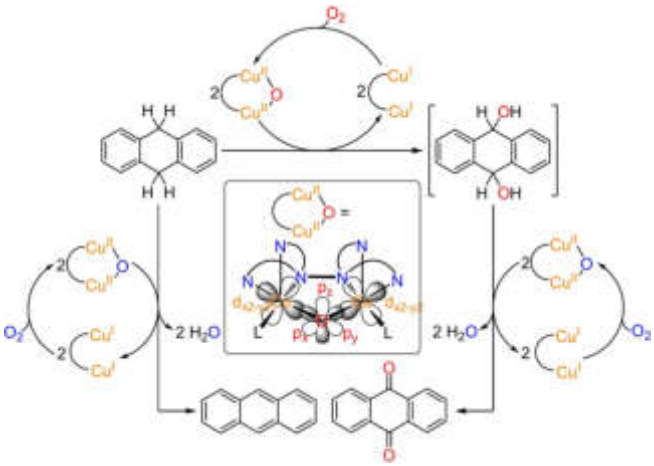

Scheme 3. Reactivity studies and proposed mechanism for the oxygenation of DHA. Reaction of DHA in the presence of the **Cu_2O** catalyst leads to anthraquinone (AQ) via a disecondary alcohol (9,10-dihydroxy-9,10-dihydroanthracene) which is formed as primary oxygenation product. The subsequent oxidation may also be catalyzed by the **Cu_2O** species (right). As a byproduct, anthracene is formed by twofold H-atom abstraction proceeding without O-transfer (left). In all reactions the formed Cu^I–Cu^I species are re-oxidized to the **Cu_2O** complex with O_2, following the pathway of Scheme 2. In contrast to the actual monooxygenation reaction (top), both the twofold two-electron oxidation of the disecondary alcohol and the double HAT generate water which may deactivate the catalyst. Inset: Simplified structure of the **Cu_2O** complex showing the orbitals involved in the substrate oxygenation, i.e., the $d_{x^2-y^2}$ orbitals of the copper centers and the p_x, p_y and p_z orbitals of the oxo ligand. L = coordinating solvent molecule (C_3H_6O).

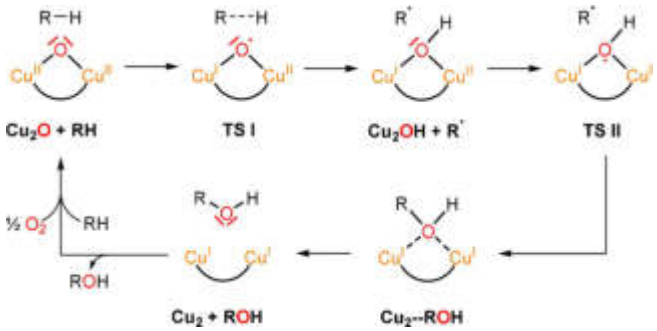

Scheme 4. Proposed reaction mechanism for the hydrocarbon-to-alcohol conversion. Starting from the **Cu_2O** complex and the hydrocarbon (RH), a transition state (TS I) is proposed leading to the **Cu_2OH** complex. In the next step, the R radical binds to the mixed-valent **Cu_2OH** species, leading to TS II and finally the alcohol (ROH) is released. The reaction can proceed again, when the dicopper(I) complex **Cu_2** is reacted with dioxygen.

To clearly demonstrate that the **Cu_2O** species is the actual source of the oxygen atom incorporated into the substrate, we performed reactivity studies towards DHA under anaerobic conditions. Before adding DHA, the solution was purged with N_2 to remove dioxygen, and the further reaction was performed anaerobically. Importantly, GC–MS analysis showed a conversion to AQ similar to that obtained in an analogous experiment where O_2 was present during reaction with the substrate (Table S20). Moreover, the formation of AQ could also be detected if N_2O was employed instead of O_2 to generate the **Cu_2O** intermediate (Section S10.4).

Oxygenation of 50 equiv of diphenylmethane (BDE = 82 kcal mol^{-1}) led to benzophenone (Ph_2CO) with a TON of 2 for all catalysts (Table 2). In order to theoretically explore whether our **Cu_2O** complexes may also be able to break the C–H bond of substrates with higher BDEs than diphenylmethane the O–H bond dissociation free energy (BDFE) of the μ-hydroxo Cu^I/Cu^{II} complex resulting from HAT to the **Cu_2O** complex was determined by DFT (Section S9.4). Notably, this calculation gave a value of 111 kcal mol^{-1}, even exceeding the CH-BDFE of methane (96 kcal mol^{-1}).[50]

The origin of this strong HAT activity lies in the geometric and electronic structure of this species. In particular, the doubly filled, in-plane p_x and p_y orbitals of the bridging oxo group each overlap with a singly occupied Cu-$d_{x^2-y^2}$ orbital, representing the SOMO of each copper-containing subunit (Scheme 3, inset). Upon approach of a C–H group from the substrate to the oxo group, one electron shifts from O-p_x to the right copper (or O-p_y to the left copper; cf. Scheme 4). This leaves a single electron in the respective p orbital which abstracts an H-atom from the substrate, forming an O–H bond and an alkyl radical.[19,51]

In the second step one electron shifts from the other doubly occupied, in-plane oxygen p orbital to the remaining Cu^{II} center and a C–O bond is formed with the alkyl radical generated in the initial HAT process. As a result, one O-atom is inserted into the C–H bond of the substrate, and the oxygenated product (i.e., the alcohol) is weakly bound to two closed-shell Cu^I centers, allowing its facile release. A new catalytic cycle starts with the bonding of O_2 to the dicopper(I) complex, regenerating the active **Cu_2O** species (Scheme 4).

Conclusion

Copper-dependent monooxygenases like pMMO transform inert C–H bonds under ambient conditions, using dioxygen and NAD(P)H. Thereby one oxygen atom of O_2 is incorporated into the substrate and the other oxygen atom is converted to water. In this study we describe small-molecule dicopper(I) complexes which also oxygenate hydrocarbons to the corresponding alcohols and ketones in the presence of dioxygen. In contrast to the enzyme, however, both oxygen atoms of O_2 are transferred to the organic substrates and no reductant is needed. Using a range of solution spectroscopies, we monitor the initial binding of O_2 in a tetranuclear copper intermediate as well as its homolytic cleavage, leading to two mono-μ-oxo dicopper(II) complexes which in turn catalytically oxygenate a variety of hydrocarbons. Although the BD(F)Es of these are well below that of methane, the calculated BDFE of our **Cu_2O** species exceeds the C–H BDFE of the latter substrate. This derives from their unique electronic and geometric structure, allowing facile electron transfer from doubly occupied O-2p orbitals into singly occupied Cu-$d_{x^2-y^2}$ orbitals upon approach of the substrate. In combination, the formation of highly reactive **Cu_2O** species from dioxygen and their catalytic oxygen-transfer activity to hydrocarbons establish an unprecedented, 100% atom-eco-

nomic scenario for the monooxygenation of organic substrates from gaseous O_2.

Acknowledgements

The authors thank CAU Kiel for support of this research. Moreover, parts of this research were carried out at beamline P64 and P65 at the PETRA III storage ring at DESY, a member of the Helmholtz Association. We thank Wolfgang Caliebe and Edmund Welter for their support at beamline P64 and P65, respectively. B.G.-L. gratefully acknowledges the Bundesministerium für Bildung und Forschung (BMBF) project 05K19GU5 for funding. S.B. gratefully acknowledges the Deutsche Forschungsgemeinschaft (DFG) for financial support under project RU 773/8-1. Open access funding enabled and organized by Projekt DEAL.

Conflict of interest

The authors declare no conflict of interest.

Keywords: catalysis · copper · metalloenzymes · oxygenation · Raman spectroscopy

[1] V. C.-C. Wang, S. Maji, P. P.-Y. Chen, H. K. Lee, S. S.-F. Yu, S. I. Chan, *Chem. Rev.* **2017**, *117*, 8574 – 8621.
[2] a) M. Y. He, Y. H. Sun, B. X. Han, *Angew. Chem. Int. Ed.* **2013**, *52*, 9620 – 9633; *Angew. Chem.* **2013**, *125*, 9798 – 9812; b) Z. Zakaria, S. K. Kamarudin, *Renewable Sustainable Energy Rev.* **2016**, *65*, 250 – 261.
[3] a) M. Rolff, J. Schottenheim, H. Decker, F. Tuczek, *Chem. Soc. Rev.* **2011**, *40*, 4077 – 4098; b) J. N. Hamann, B. Herzigkeit, R. Jurgeleit, F. Tuczek, *Coord. Chem. Rev.* **2017**, *334*, 54 – 66; c) T. Baba, A. Miyaji in *Application of Biocatalysts for the Production of Methanol from Methane. In: Catalysis and the Mechanism of Methane Conversion to Chemicals*, Springer, Singapore, **2020**, pp. 73 – 101..
[4] a) M. O. Ross, A. C. Rosenzweig, *J. Biol. Inorg. Chem.* **2017**, *22*, 307 – 319; b) M. O. Ross, F. MacMillan, J. Wang, A. Nisthal, T. J. Lawton, B. D. Olafson, S. L. Mayo, A. C. Rosenzweig, B. M. Hoffman, *Science* **2019**, *364*, 566 – 570; c) C. W. Koo, A. C. Rosenzweig, *Chem. Soc. Rev.* **2021**, *50*, 3424 – 3436; d) R. B. Jackson, E. I. Solomon, J. G. Canadell, M. Cargnello, C. B. Field, *Nat. Sustainability* **2019**, *2*, 436 – 438.
[5] a) R. Sharma, H. Poelman, G. B. Marin, V. V. Galvita, *Catalysts* **2020**, *10*, 194; b) J. Y. Lee, K. D. Karlin, *Curr. Opin. Chem. Biol.* **2015**, *25*, 184 – 193.
[6] Y.-H. Chen, C.-Q. Wu, P.-H. Sung, S. I. Chan, P. P.-Y. Chen, *ChemCatChem* **2020**, *12*, 3088 – 3096.
[7] Y. Liang, J. Wei, X. Qiu, N. Jiao, *Chem. Rev.* **2018**, *118*, 4912 – 4945.
[8] L. Cao, O. Caldararu, A. C. Rosenzweig, U. Ryde, *Angew. Chem. Int. Ed.* **2018**, *57*, 162 – 166; *Angew. Chem.* **2018**, *130*, 168 – 172.
[9] S. Y. Ro, L. F. Schachner, C. W. Koo, R. Purohit, J. P. Remis, G. E. Kenney, B. W. Liauw, P. M. Thomas, S. M. Patrie, N. L. Kelleher, A. C. Rosenzweig, *Nat. Commun.* **2019**, *10*, 2675.
[10] M. Miyanishi, T. Abe, Y. Hori, Y. Shiota, K. Yoshizawa, *Inorg. Chem.* **2019**, *58*, 12280 – 12288.
[11] J. S. Woertink, P. J. Smeets, M. H. Groothaert, M. A. Vance, B. F. Sels, R. A. Schoonheydt, E. I. Solomon, *Proc. Natl. Acad. Sci. USA* **2009**, *106*, 18908 – 18913.
[12] P. Haack, A. Kärgel, C. Greco, J. Dokic, B. Braun, F. F. Pfaff, S. Mebs, K. Ray, C. Limberg, *J. Am. Chem. Soc.* **2013**, *135*, 16148 – 16160.
[13] S. I. Chan, Y. J. Lu, P. Nagababu, S. Maji, M. C. Hung, M. M. Lee, I. J. Hsu, P. D. Minh, J. C. H. Lai, K. Y. Ng, S. Ramalingam, S. S. F. Yu, M. K. Chan, *Angew. Chem. Int. Ed.* **2013**, *52*, 3731 – 3735; *Angew. Chem.* **2013**, *125*, 3819 – 3823.
[14] P. P.-Y. Chen, R. B.-G. Yang, J. C.-M. Lee, S. I. Chan, *Proc. Natl. Acad. Sci. USA* **2007**, *104*, 14570 – 14575.
[15] V. Ullrich, *Angew. Chem. Int. Ed. Engl.* **1972**, *11*, 701 – 712; *Angew. Chem.* **1972**, *84*, 689 – 701.
[16] D. Holtmann, F. Hollmann, *ChemBioChem* **2016**, *17*, 1391 – 1398.
[17] J. Manzur, A. M. García, R. Letelier, E. Spodine, O. Peña, D. Grandjean, M. M. Olmstead, B. C. Noll, *J. Chem. Soc. Dalton Trans.* **1993**, 905 – 911.
[18] A. M. Barrios, S. J. Lippard, *J. Am. Chem. Soc.* **1999**, *121*, 11751 – 11757.
[19] P. Haack, C. Limberg, *Angew. Chem. Int. Ed.* **2014**, *53*, 4282 – 4293; *Angew. Chem.* **2014**, *126*, 4368 – 4380.
[20] M. Réglier, C. Jorand, B. Waegell, *J. Chem. Soc. Chem. Commun.* **1990**, 1752 – 1755.
[21] B. E. R. Snyder, M. L. Bols, R. A. Schoonheydt, B. F. Sels, E. I. Solomon, *Chem. Rev.* **2018**, *118*, 2718 – 2768.
[22] S. Yelin, C. Limberg, *Catal. Lett.* **2020**, *150*, 1 – 11.
[23] G. Ali, P. E. VanNatta, D. A. Ramirez, K. M. Light, M. T. Kieber-Emmons, *J. Am. Chem. Soc.* **2017**, *139*, 18448 – 18451.
[24] a) L. M. Mirica, X. Ottenwaelder, T. D. P. Stack, *Chem. Rev.* **2004**, *104*, 1013 – 1046; b) E. I. Solomon, J. W. Ginsbach, D. E. Heppner, M. T. Kieber-Emmons, C. H. Kjaergaard, P. J. Smeets, L. Tian, J. S. Woertink, *Faraday Discuss.* **2011**, *148*, 11 – 39; c) W. Keown, J. B. Gary, T. D. P. Stack, *J. Biol. Inorg. Chem.* **2017**, *22*, 289 – 305; d) C. E. Elwell, N. L. Gagnon, B. D. Neisen, D. Dhar, A. D. Spaeth, G. M. Yee, W. B. Tolman, *Chem. Rev.* **2017**, *117*, 2059 – 2107.
[25] J. Kuzelka, S. Mukhopadhyay, B. Spingler, S. J. Lippard, *Inorg. Chem.* **2004**, *43*, 1751 – 1761.
[26] K. D. Karlin, Y. Gultneh, J. C. Hayes, J. Zubieta, *Inorg. Chem.* **1984**, *23*, 519 – 521.
[27] P. Haack, C. Limberg, K. Ray, B. Braun, U. Kuhlmann, P. Hildebrandt, C. Herwig, *Inorg. Chem.* **2011**, *50*, 2133 – 2142.
[28] W. B. Tolman, *Angew. Chem. Int. Ed.* **2010**, *49*, 1018 – 1024; *Angew. Chem.* **2010**, *122*, 1034 – 1041.
[29] M.-L. Tsai, R. G. Hadt, P. Vanelderen, B. F. Sels, R. A. Schoonheydt, E. I. Solomon, *J. Am. Chem. Soc.* **2014**, *136*, 3522 – 3529.
[30] S. R. Pauletaa, M. S. P. Carepob, I. Moura, *Coord. Chem. Rev.* **2019**, *387*, 436 – 449.
[31] H. O. Obias, Y. Lin, N. N. Murthy, E. Pidcock, E. I. Solomon, M. Ralle, N. J. Blackburn, Y.-M. Neuhold, A. D. Zuberbühler, K. D. Karlin, *J. Am. Chem. Soc.* **1998**, *120*, 12960 – 12961.
[32] N. Kitajima, T. Koda, Y. Moro-oka, *Chem. Lett.* **1988**, *17*, 347 – 350.
[33] J. Ling, L. P. Nestor, R. S. Czernuszewicz, T. G. Spiro, R. Fraczkiewicz, K. D. Sharma, T. M. Loehr, J. Sanders-Loehr, *J. Am. Chem. Soc.* **1994**, *116*, 7682 – 7691.
[34] M. R. Churchill, G. Davies, M. A. El-Sayed, J. A. Fournier, J. P. Hutchinson, J. A. Zubieta, *Inorg. Chem.* **1984**, *23*, 783 – 787.
[35] M. A. El-Sayed, A. El-Toukhy, G. Davies, *Inorg. Chem.* **1985**, *24*, 3387 – 3390.
[36] G. Davies, M. A. El-Sayed, M. Henary, *Inorg. Chem.* **1987**, *26*, 3266 – 3272.
[37] W. C. Trogler, *Coord. Chem. Rev.* **1999**, *187*, 303 – 327.
[38] D. Xiao, E. Bloch, J. A. Mason, W. L. Queen, M. R. Hudson, N. Planas, J. Borycz, A. L. Dzubak, P. Verma, K. Lee, F. Bonino, V. Crocellà, J. Yano, S. Bordiga, D. G. Truhlar, L. Gagliardi, C. M. Brown, J. R. Long, *Nat. Chem.* **2014**, *6*, 590 – 595.

[39] P. Vanelderen, J. Vancauwenbergh, B. F. Sels, R. A. Schoonheydt, *Coord. Chem. Rev.* **2013**, *257*, 483 – 494.
[40] a) J. Reim, B. Krebs, *Angew. Chem. Int. Ed. Engl.* **1994**, *33*, 1969 – 1971; *Angew. Chem.* **1994**, *106*, 2040 – 2041; b) J. Reim, R. Werner, W. Haase, B. Krebs, *Chem. Eur. J.* **1998**, *4*, 289 – 298; c) F. Meyer, H. Pritzkow, *Angew. Chem. Int. Ed.* **2000**, *39*, 2112 – 2115; *Angew. Chem.* **2000**, *112*, 2199 – 2202.
[41] L.-S. Kau, D. J. Spira-Solomon, J. E. Penner-Hahn, K. O. Hodgson, E. I. Solomon, *J. Am. Chem. Soc.* **1987**, *109*, 6433 – 6442.
[42] J. L. DuBois, P. Mukherjee, T. D. P. Stack, B. Hedman, E. I. Solomon, K. O. Hodgson, *J. Am. Chem. Soc.* **2000**, *122*, 5775 – 5787.
[43] N. C. Tomson, K. D. Williams, X. Dai, S. Sproules, S. DeBeer, T. H. Warren, K. Wieghardt, *Chem. Sci.* **2015**, *6*, 2474 – 2487.
[44] X. Zhang, F. G. Bordwell, *J. Org. Chem.* **1992**, *57*, 4163 – 4168.
[45] M. A. Ehudin, D. A. Quist, K. D. Karlin, *J. Am. Chem. Soc.* **2019**, *141*, 12558 – 12569.
[46] E. I. Solomon, D. E. Heppner, E. M. Johnston, J. W. Ginsbach, J. Cirera, M. Qayyum, M. T. Kieber-Emmons, C. H. Kjaergaard, R. G. Hadt, L. Tian, *Chem. Rev.* **2014**, *114*, 3659 – 3853.
[47] F. G. Bordwell, J. Cheng, G. Z. Ji, A. V. Satish, X. Zhang, *J. Am. Chem. Soc.* **1991**, *113*, 9790 – 9795.
[48] F. G. Bordwell, J.-P. Cheng, J. A. Harrelson, *J. Am. Chem. Soc.* **1988**, *110*, 1229 – 1231.
[49] M. Mitra, H. Nimir, S. Demeshko, S. S. Bhat, S. O. Malinkin, M. Haukka, J. Lloret-Fillol, G. C. Lisensky, F. Meyer, A. A. Shteinman, W. R. Browne, D. A. Hrovat, M. G. Richmond, M. Costas, E. Nordlander, *Inorg. Chem.* **2015**, *54*, 7152 – 7164.
[50] A. Najafian, T. R. Cundari, *Organometallics* **2018**, *37*, 3111 – 3121.
[51] J. Xu, B. Liu, *J. Phys. Chem. C* **2019**, *123*, 10356 – 10366.

Manuscript received: January 22, 2021
Revised manuscript received: April 13, 2021
Accepted manuscript online: April 15, 2021
Version of record online: May 7, 2021

4.4 Influence of the Amine Donor on Hybrid Guanidine-stabilized Bis(μ-oxido) Dicopper(III) Complexes and their Tyrosinase-like Oxygenation Activity Towards Polycyclic Aromatic Alcohols

The author has contributed to the Raman measurements and the respective data analysis.

In [4.4] a series of modified hybrid guanidine ligands were used to investigate the effects of a continuously increasing steric demand and decreasing donor strength of the Cu_2O_2 core have on the properties of the complex. Properties of interest are (i) the core geometry, leading to different electronic properties and (ii) the activity and specificity towards catalytic oxygenation towards challenging substrates. In chapter 4.2 on the paper [4.2], we saw a broad range of substrates being oxygenated by a complex with hybrid guanidine ligands. The ligand used in this research article consisted of one guanidine unit bridged by an aromatic backbone to an amine unit. Previously in [4.2], this complex was studied with both functional groups being methylated. In [4.4], this ligand **L1** forms the mononuclear Cu^{I} complex **C1**, which can be oxygenated to form the bis(μ-oxido) dinuclear Cu^{III} complex **O1**. Additionally, the ligand was modified so that the two methyl groups bonded to the nitrogen of the amine unit are exchanged for diethyl (**L2, C2, O2**) or a propyl (**L3, C3, O3**) groups. With different theoretical and experimental techniques, Raman spectroscopy being one of them, it was found that with higher steric demand and donor strength of the amine unit of the ligands (from **L1** to **L3**) the Cu_2O_2 core is elongated, the Cu_2O_2 vibration experiences a redshift and the complex formation is slower and the resulting complex less stable.

The Raman spectra for **O1**, **O2** and **O3** are shown in [4.4]-Fig. 4. The **O1** spectra is reprinted from [4.2] and the corresponding description can be found in section 4.2. The preparation of **O2** and **O3** is identical, apart from less significant details. The concentration of the precursor solution was 10 instead of 20 mM and the spectra were recorded at 532 nm with the continuous wave Millennia laser at 42 mW. Employing the Tsunami laser system at 405 nm to measure at a more comparable wavelength to the 420 nm used in [4.2], yielded the same frequencies for the breathing mode that are shown in the publication, but both spectra showed strong fluorescence together with the Raman peaks.

Influence of the Amine Donor on Hybrid Guanidine-stabilized Bis(μ-oxido) Dicopper(III) Complexes and their Tyrosinase-like Oxygenation Activity Towards Polycyclic Aromatic Alcohols

Journal of Inorganic Biochemistry 224 (2021) 111541

Contents lists available at ScienceDirect

Journal of Inorganic Biochemistry

journal homepage: www.elsevier.com/locate/jinorgbio

Influence of the amine donor on hybrid guanidine-stabilized Bis(μ-oxido) dicopper(III) complexes and their tyrosinase-like oxygenation activity towards polycyclic aromatic alcohols

Melanie Paul [a], Melissa Teubner [a,b], Benjamin Grimm-Lebsanft [b], Sören Buchenau [b], Alexander Hoffmann [a,*], Michael Rübhausen [b], Sonja Herres-Pawlis [a,*]

[a] Institute of Inorganic Chemistry, RWTH Aachen University, Landoltweg 1a, 52074 Aachen, Germany
[b] Department of Physics, Universität Hamburg, Luruper Chaussee 149, 22761 Hamburg, Germany

ARTICLE INFO

Keywords:
Copper catalysis
Dioxygen activation
Guanidine
DFT study
Tyrosinase model complexes

ABSTRACT

The tyrosinase-like activity of hybrid guanidine-stabilized bis(μ-oxido) dicopper(III) complexes $[Cu_2(\mu\text{-}O)_2(L)_2](X)_2$ (L = 2-{2-((Diethylamino)methyl)phenyl}-1,1,3,3-tetramethylguanidine (TMGbenzNEt$_2$, **L2**) and 2-{2-((Di-*iso*propylamino)methyl)phenyl}-1,1,3,3-tetramethylguanidine (TMGbenzN*i*Pr$_2$, **L3**); X = PF_6^-, BF_4^-, $CF_3SO_3^-$) is described. New aromatic hybrid guanidine amine ligands were developed with varying amine donor function. Their copper(I) complexes were analyzed towards their ability to activate dioxygen in the presence of different weakly coordinating anions. The resulting bis(μ-oxido) species were characterized at low temperatures by UV/Vis and resonance Raman spectroscopy, cryo-ESI mass spectrometry and density functional theory calculations. Small structural changes in the ligand sphere were found to influence the characteristic ligand-to-metal charge transfer (LMCT) features of the bis(μ-oxido) species, correlating a redshift in the UV/Vis spectrum with weaker N-donor function of the ligand. DFT calculations elucidated the influence of the steric and electronic properties of the bis(μ-oxido) species leading to a higher twist of the Cu_2O_2 plane against the CuN_2 plane and a stretching of the Cu_2O_2 core. Despite their moderate stability at −100 °C, the bis(μ-oxido) complexes exhibited a remarkable activity in catalytic oxygenation reactions of polycyclic aromatic alcohols. Further the selectivity of the catalyst in the hydroxylation reactions of challenging phenolic substrates is not changed despite an increasing shield of the reactive bis(μ-oxido) core. The generated quinones were found to form exclusively bent phenazines, providing a promising strategy to access tailored phenazine derivatives.

1. Introduction

The activation of molecular oxygen for the application as oxidation catalyst states one major purpose in chemical research [1–3]. In nature, copper enzymes set an example by their ability to activate dioxygen and to catalyze organic transformation reactions [4,5]. Tyrosinase represents a copper-containing enzyme, which is responsible for the hydroxylation of monophenols and the oxidation of *ortho*-catechols to generate *ortho*-quinones [6,7]. The enzyme is present in numerous organisms, controlling the production of the pigment melanin from L-tyrosine [8,9]. The molecular mechanisms of the activation and transfer of dioxygen still remain challenging, although many efforts were made to understand the structure-activity relationship of the active sites of the enzyme [5,10–17]. Some extensively studied copper-dioxygen model complexes are the μ-η^2:η^2-peroxido dicopper(II) [**P**] and the bis(μ-oxido) dicopper(III) [**O**] species, which are able to interconvert into each other due to their small isomerization barrier [5,18,19]. In [**O**] species, the Cu_2O_2 rhomb is significantly influenced by electronic and steric properties of the supporting N-donor ligand system. Systematic studies on the spectroscopic properties of the [**O**] species by small modifications of the N-donor moieties are available, which involve amine, histidine, imidazole and guanidine ligands developed by the groups of Tolman [20], Stack [21–27], Solomon [21,23], and Herres-Pawlis [28–31] (Fig. 1).

Geometric elongation and compression of the Cu_2O_2 rhomb was identified by X-ray diffraction and EXAFS analysis as well as density functional theory (DFT) calculations in those studies. The perturbations of the Cu_2O_2 geometry were primarily attributed to the steric bulk of the ligand system: the higher the steric demand of the ligand sphere, the

* Corresponding authors.
E-mail addresses: alexander.hoffmann@ac.rwth-aachen.de (A. Hoffmann), sonja.herres-pawlis@ac.rwth-aachen.de (S. Herres-Pawlis).

https://doi.org/10.1016/j.jinorgbio.2021.111541
Received 9 May 2021; Received in revised form 30 June 2021; Accepted 11 July 2021
Available online 21 July 2021
0162-0134/

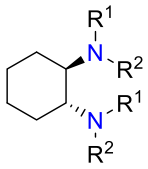

TMCHD (R^1 = R^2 = Me) [19,21,22]
MECHD (R^1 = Me, R^2 = Et) [19,21,22]
TECHD (R^1 = R^2 = Et) [19,21,22]

TMED (R^1 = R^2 = Me) [23]
Me_2Et_2ED (R^1 = Me, R^2 = Et) [22]
TEED (R^1 = R^2 = Et) [21,22]

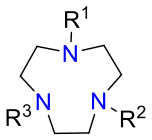

Me_3TACN (R^1 = R^2 = R^3 = Me) [19]
Bz_3TACN (R^1 = R^2 = R^3 = Bz) [20]
***i*Pr_2BzTACN** (R^1 = R^2 = *i*Pr, R^3 = Bz) [20]
***i*Pr_3TACN** (R^1 = R^2 = R^3 = *i*Pr) [20]

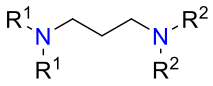

PD (R^1 = R^2 = H) [24]
DMPD (R^1 = H, R^2 = Me) [24]
TMPD (R^1 = R^2 = Me) [24]

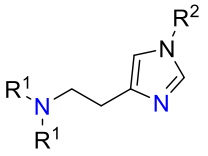

Me_3His (R^1 = Me, R^2 = Me) [25]
***n*BuHis** (R^1 = H, R^2 = *n*Bu) [25]

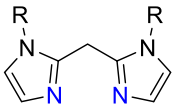

***n*BuBIM** (R = *n*Bu) [27]

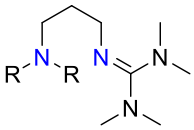

TMGdmap (R = Me) [28,29]
TMGdeap (R = Et) [29]

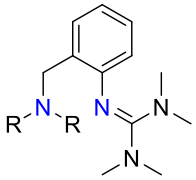

TMGbenza (R = Me) [31]
$TMGbenzNEt_2$ (R = Et) *(this work,* **L2***)*
TMGbenzN*i*Pr_2 (R = *i*Pr) *(this work,* **L3***)*

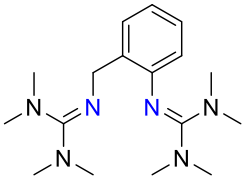

TMG_2tol [30]

Fig. 1. Selected N-donor ligand systems for the stabilization of bis(μ-oxido) dicopper(III) complexes (CHD = cyclohexyl diamine, ED = ethylenediamine, TACN = trisazacyclononane, PD = propylenediamine, TM = tetramethyl, ME = methyl ethyl, TE = tetraethyl, DM = dimethyl, His = histamine, BIM = bis(imidazolyl) methane, TMG = tetramethyl guanidine, dmap = dimethylamino propylene, deap = diethylamino propylene, tol = toluene).

more elongated the Cu_2O_2 rhomb, and vice versa [22]. Also, the twist angle of the CuN_2 plane relative to the Cu_2O_2 plane was found to play an important role in the stabilization of the highly reactive [**O**] species and their ligand-to-metal charge transfer (LMCT) energies [29,32]. Besides the common direct synthesis of [**O**] species, Stack and co-workers demonstrated that [**O**] species can be synthesized indirectly by ligand exchange reactions driven by the more donating and thermodynamically supporting ligand system, which also influence the LMCT transition energies of the [**O**] species [26,27].

Most of the amine-stabilized [**O**] species are limited to the stoichiometric hydroxylation of exogenous substrates. Reported synthetic model systems mimicking the functionality of the active site of tyrosinase mostly involve the [**P**] core [5,15,16,33], but a few [**O**] species were also reported over the last years [31,34,35]. Catalytic oxygenation features were first presented by Réglier and co-workers in 1990 by using an imine-pyridine ligand system to support the copper-catalyzed oxygenation of 2,4-di-*tert*-butyl phenol to 3,5-di-*tert*-butyl quinone [36]. Another binuclear catalyst was shown by Casella and co-workers employing benzimidazole ligand **L66** [37]. Further systems were developed in recent years by the groups of Lumb and Stack [38–40], Tuczek [41–46] and Herres-Pawlis [31,34,35,47–50], demonstrating the diversity of stabilizing N-donor ligand systems in copper-catalyzed hydroxylation reactions of (poly)cyclic aromatic alcohols. Besides pyridinyl, pyrazolyl, imine and amine donor units, guanidines are known for their high basicity, enabling the stabilization of high oxidation states of copper complexes such as bis(μ-oxido) and superoxido motifs [28,30–32,34,51–58].

Recently, we reported the stabilization of an [**O**] species by the hybrid guanidine amine ligand TMGbenza (**L1**) in the presence of weakly-coordinating anions at low temperatures [31]. The bis(μ-oxido) complex depicted high tyrosinase-like reactivity towards diverse phenolic substrates. The high selectivity of the catalyst in the oxygenation reactions was achieved by a beneficial interplay of the strong, sterically demanding guanidine function and the spatially smaller, weaker amine donor. The formed quinones were directly transformed into more stable phenazine derivatives, which are of major interest due to their antibacterial, antitumor and antimalarial features [59–66]. A recent study on a **L1**-stabilized [**O**] species in the presence of coordinating halide anions revealed the existence of a supporting iodide-bridge between the formally copper(III) centers and the formation of iodidocuprate anions, yielding a room temperature stable [**O**] complex with catalytic activity [34].

Aiming to inhibit the formation of unreactive bischelate copper(I) species, we herein report the synthesis and characterization of two novel hybrid guanidine amine ligands with modified amine donor moiety to increase the steric demand of the ligand system (Fig. 1). The monochelate copper(I) complexes stabilized by **L2** and **L3** are tested towards their ability to activate molecular oxygen to form reactive [**O**] complexes. The formally copper(III) species is evaluated as catalyst in oxygenation reactions of polycyclic aromatic alcohols, including naphthols and quinolinols. Generated quinones are transformed in a one-pot reaction into phenazines by using 1,2-phenylenediamine. The structure-reactivity is compared to related hybrid guanidine systems published previously and the influence of different amine donor abilities of the

ligand system on the bis(μ-oxido) complex and its catalytic activity are evaluated.

2. Materials and methods

2.1. General remarks

All synthetic procedures were performed under an inert atmosphere of nitrogen with the use of standard Schlenk or glovebox techniques. All chemicals were purchased commercially (Table S1 in the Supporting Information) and used without further purification unless otherwise noted. Solvents were purified under nitrogen atmosphere via distillation from CaH_2 or sodium/benzophenone ketyl radical. Copper salts [67], Vilsmeier salt chloro-*N,N,N′,N′*-tetramethylformamidinium chloride [68–70] and hybrid guanidine ligand TMGbenza (**L1**) [31] were synthesized according to literature procedures. Triethylamine was purified by distillation from CaH_2. Molecular sieves (3 Å, AppliChem) were flame-dried prior to use. Thin layer chromatography sheets were purchased from Macherey-Nagel (SiO_2, layer thickness 0.20 mm, fluorescent indicator). Column chromatography was performed on Geduran Si 60 (40–63 μm, Merck).

2.2. Instruments

^{1}H and ^{13}C{^{1}H} NMR spectra were recorded on a Bruker Avance II 400 and Bruker Avance III HD 400 spectrometer at 25 °C in NMR tubes, respectively. Resonances were referenced to the residual solvent signal, relative to TMS. Chemical shifts were assigned with the use of two-dimensional NMR experiments (COSY, HSQC, HMBC). All NMR data were deposited as original data in the Chemotion Repository and are published under an Open Access model. The link to the original data is given in the analytical description. NMR spectra of the compounds are also shown in the supporting information (Fig. S1 – S14, Fig. S16 – S21 and Fig. 23 —S26).

ESI mass spectra were recorded on a Thermo Fisher Scientific LTQ Orbitrap XL spectrometer at a source voltage of 4.49 kV and a capillary temperature of 299.54 °C.

Cryospray-ionization mass spectrometry (CSI-MS) measurements were performed on an UHR-TOF Bruker Daltonik maXis II, an ESI-quadrupole time-of-flight (qToF) mass spectrometer capable of a resolution of at least 80.000 FWHM, which was coupled to a Bruker Daltonik Cryospray unit. Detection was either in positive or in the negative ion mode; the source voltage was 3.5 kV. The drying gas (N_2), to achieve solvent removal, and the spray gas were both held at −80 °C. The mass spectrometer was calibrated subsequently to every experiment via direct infusion of a L-proline sodium salt solution, which provided a *m/z* range of singly charged peaks up to 3000 Da in both ion modes.

FT-IR spectra were recorded on a Shimadzu IR Tracer 100 equipped with a CsI beam splitter in combination with an ATR unit (Quest model from Specac utilizing a robust monolithic crystalline diamond) in a resolution of 2 cm^{-1} and on a ThermoFisher Avatar™ 360 spectrometer with the use of KBr pellets or NaCl plates in a resolution of 2 cm^{-1}.

UV/Vis spectroscopic measurements were carried out on a Cary 60 spectrophotometer of Agilent Technologies connected via a Cary 50 fiber optic coupler and combined with a fiber-optic quartz glass immersion probe (Hellma, 1 mm) and a tailored Schlenk cell.

Resonance Raman measurements were performed with the UT-3 Raman spectrometer [71], combined with a 532 nm diode cw laser (Millennia, Spectra Physics Lasers Inc.). The cryostat was a slightly modified version of a setup described previously [72] with a 3.5 mL screw cap Suprasil cuvette with septum (117104F-10-40, Hellma) for oxygenation, equipped with a Peltier element (QC-127-1.4-6.0MS, QuickCool) and a cooling copper block which encloses three sides of the cuvette. The laser beam was widened with a spatial filter and then focused on the cuvette inside the cryostat. The focus spot size was around 20 μm in diameter. With a micrometer screw, a focal depth of around 50 μm inside the cuvette was adjusted. Raman scattered light was captured with the entrance optics of the UT-3 triple monochromator spectrometer [71]. The complexes [**C2**]PF_6 - [**C3**]PF_6 with a concentration of 10 mmol L^{-1} in tetrahydrofuran/acetonitrile (80:20) were cooled in the cuvette cryostat to below −90 °C. Dioxygen was added via a cannula through the septum (0.02 bar overpressure for 10 min for [**C2**]PF_6 and 15 min for [**C3**]PF_6) until a distinct color change was observed. The used laser power in front of the entrance optics was 42 mW. Data was accumulated for up to 120 s.

2.3. Computational details

Density functional theory (DFT) calculations were performed by using Gaussian 16, Revision B.01 [73] using the TPSSh functional [74–76] and the Ahlrichs type basis set def2-TZVP [77–80]. The D3 dispersion with Becke-Johnson damping GD3BJ was applied for empirical dispersion correction, which is implemented in Gaussian16, Revision B.01 [81–84]. No solvent model was used in the DFT calculations because no stable minimum was observed for the new oxido species. In the complexes the space between ligands and central ion / Cu_2O_2 core is inaccessible for solvent molecules which leads to a number of numerical problems during the calculations. These numerical problems prevent a stable minimum, especially for the oxido species **[O3]**$^{2+}$.

NBO calculations were accomplished using the program suite NBO 7.0 delivering the NBO charges and the charge-transfer energies by second order perturbation theory [85–87].

2.4. Synthetic procedures

Ligand step 1: N,N-alkyl-(2-nitrophenyl)methanamine synthesized according to a modified literature procedure [31,88]

Dialkyl amine (255.5 mmol, 5.1 eq) was added dropwise to a stirred solution of 2-nitrobenzyl bromide (10.8 g, 50.0 mmol, 1.0 eq) in ethanol (120 mL). The mixture was refluxed for 6 h. The yellow solution was acidified to pH 1 by using concentrated hydrochloric acid. The solvent was removed under reduced pressure. The pH level of the resulting mixture was adjusted to 14 by using aqueous NaOH solution. The solution was extracted with diethyl ether (4 × 100 mL). The combined organic layers were washed with saturated aqueous NaCl solution, dried over Na_2SO_4 and evaporated to dryness.

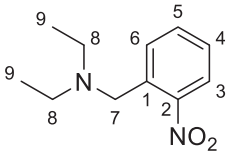

***N,N*-Diethyl-(2-nitrophenyl)methanamine** (**3**) [89]: The product was isolated as an orange oil (10.2 g, 48.9 mmol, 98%). **^{1}H NMR** (400 MHz, Chloroform-*d*, 25 °C): δ [ppm] = 7.80 (dd, J = 8.0, 1.2 Hz, 1H, H3), 7.75–7.71 (m, 1H, H6), 7.55–7.50 (m, 1H, H5), 7.38–7.33 (m, 1H, H4), 3.84 (s, 2H, H7), 2.49 (q, J = 7.1 Hz, 4H, H8), 0.99 (t, J = 7.1 Hz, 6H, H9). **^{13}C{^{1}H} NMR** (101 MHz, Chloroform-*d*, 25 °C): δ [ppm] = 149.8 (C2), 136.3 (C1), 132.5 (C5), 131.0 (C6), 127.5 (C4), 124.3 (C3), 54.9 (C7), 47.3 (C8), 11.9 (C9). **HRMS-ESI+** (MeCN): *m/z* calc. For $[(C_{11}H_{16}N_2O_2)+H]^+$: 209.12845, found: 209.12850. **IR** (ATR): $\tilde{\nu}$ [cm^{-1}] = 2969 (w, C–H_{arom}), 2935 (vw, C–H_{arom}), 2874 (vw, C–H_{aliph}), 2803 (vw, C–H_{aliph}), 1610 (vw), 1522 (s, N—O), 1446 (w),

1385 (w), 1359 (m), 1345 (m, N—O), 1297 (w), 1240 (vw), 1203 (m), 1167 (m), 1119 (w), 1060 (m), 1043 (w), 994 (vw), 969 (vw), 857 (m) 816 (w), 780 (m), 726 (vs), 704 (vw), 678 (w), 666 (w). Additional information on the NMR spectra of the target compound including original data files is available via Chemotion Repository: doi:10.14272/ZZLYWHZNBDCOFU-UHFFFAOYSA-N.1

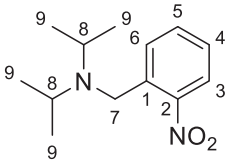

***N,N*-Di-*iso*propyl-(2-nitrophenyl)methanamine (4)**: The product was isolated as a yellow oil (11.3 g, 47.9 mmol, 96%). **^{1}H NMR** (400 MHz, Chloroform-*d*, 25 °C): δ [ppm] = 7.99–7.96 (m, 1H, H3), 7.83 (dd, J = 8.1, 1.3 Hz, 1H, H6), 7.57–7.52 (m, 1H, H4), 7.35–7.29 (m, 1H, H5), 3.94 (s, 2H, H7), 3.00 (hept, J = 6.6 Hz, 2H, H8), 1.00 (d, J = 6.6 Hz, 12H, H9). **^{13}C{^{1}H} NMR** (101 MHz, Chloroform-*d*, 25 °C): δ [ppm] = 149.2 (C2), 139.1 (C1), 132.7 (C4), 130.9 (C6), 127.0 (C5), 124.2 (C3), 48.9 (C8), 46.5 (C7), 20.8 (C9). **HRMS-EI**: *m/z* calc. For [$C_{13}H_{20}N_2O_2$]: 236.1519, found: 236.1513. **IR** (ATR): $\tilde{\nu}$ [cm^{-1}] = 2967 (m, C–H_{arom}), 2932 (w, C–H_{arom}), 1607 (vw), 1577 (vw), 1522 (vs, N—O),1463 (m), 1383 (m), 1366 (m), 1341 (m, N—O), 1296 (w), 1206 (m), 1177 (m), 1159 (m), 1139 (m), 1119 (m), 1053 (w), 1041 (w), 1030 (w), 961 (w), 938 (w), 887 (w), 856 (m), 789 (m), 751 (w), 726 (s), 678 (m), 666 (vw), 610 (vw), 564 (vw), 525 (vw). Additional information on the NMR spectra of the target compound including original data files is available via Chemotion Repository: doi:10.14272/WHORYBNTUMXXTK-UHFFFAOYSA-N.1

Ligand step 2: 2-{(Dialkylamino)methyl}aniline synthesized according to a modified literature procedure [31,88]

A solution of *N,N*-dialkyl-(2-nitrophenyl)methanamine (47.9 mmol, 1.0 eq) in dried methanol (150 mL) was added to a suspension of $FeCl_3$ (389 mg, 2.4 mmol, 0.05 eq), charcoal (3.0 g) and hydrazine monohydrate (9.7 mL, 311.4 mmol, 6.2 eq) in two aliquots. The first portion was added dropwise initially. After stirring for 30 min at 65 °C, the remaining portion was added dropwise to the black suspension. The mixture was stirred at 65 °C for additional 5 h and then at room temperature overnight. The suspension was filtered and the filtrate was evaporated to dryness. The residue was dissolved in dichloromethane, dried over Na_2SO_4 and dried under reduced pressure.

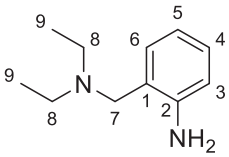

2-{(Diethylamino)methyl}aniline (6) [89]**:** The title compound was isolated as a yellow solid (7.51 g, 42.1 mmol, 86%). **^{1}H NMR** (400 MHz, Chloroform-*d*, 25 °C): δ [ppm] = 7.11–7.05 (m, 1H, H3), 6.99 (ddt, J = 7.4, 1.0, 0.4 Hz, 1H, H5), 6.68–6.60 (m, 2H, H4 + H6), 4.85 (s, 2H, NH_2), 3.59 (s, 2H, H7), 2.50 (q, J = 7.1 Hz, 4H, H8), 1.03 (t, J = 7.1 Hz, 6H, H9). **^{13}C{^{1}H} NMR** (101 MHz, Chloroform-*d*, 25 °C): δ [ppm] = 147.3 (C2), 130.4 (C5), 128.2 (C3), 123.5 (C1), 117.5 (C6), 115.5 (C4), 57.6 (C7), 46.4 (C8), 11.6 (C9). **HRMS-ESI+** (MeCN): *m/z* calc. For [($C_{11}H_{18}N_2$) + H]$^+$: 179.15427, found: 179.15469. **IR** (ATR): $\tilde{\nu}$ [cm^{-1}] = 3438 (vw, N—H), 3284 (vw, N—H), 2968 (m, C–H_{arom}), 2932 (w, C–H_{arom}), 2874 (w, C–H_{aliph}), 1615 (m, C=C), 1495 (m), 1459 (m), 1384 (m), 1371 (m), 1363 (w), 1314 (w), 1286 (m), 1240 (vw), 1195 (m), 1166 (m), 1118 (w), 1087 (w), 1054 (m), 1037 (m), 980 (w), 966 (w), 928 (w), 912 (w), 778 (w), 746 (vs), 719 (m), 624 (m), 561 (vw), 540 (m). Additional information on the NMR spectra of the target compound including original data files is available via Chemotion Repository: doi:10.14272/XUNNOCZTJBRTEX-UHFFFAOYSA-N.1

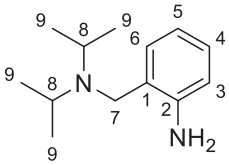

2-{(Di-*iso*propylamino)methyl}aniline (7): The title compound was isolated as a yellow solid (8.11 g, 39.3 mmol, 82%).**^{1}H NMR** (400 MHz, Chloroform-*d*, 25 °C): δ [ppm] = 7.09 (td, J = 7.7, 1.5 Hz, 1H, H3), 7.04 (d, J = 7.4 Hz, 1H, H5), 6.68 (td, J = 7.4, 1.2 Hz, 1H, H6), 6.61 (dd, J = 7.8, 0.9 Hz, 1H, H4), 4.90 (s, 2H, NH_2), 3.76 (s, 2H, H7), 3.09 (hept, J = 6.7 Hz, 2H, H8), 1.09 (d, J = 6.7 Hz, 12H, H9). **^{13}C{^{1}H} NMR** (101 MHz, Chloroform-*d*, 25 °C): δ [ppm] = 147.5 (C2), 130.5 (C5), 127.9 (C3), 123.9 (C1), 117.5 (C6), 115.4 (C4), 48.9 (C7), 47.0 (C8), 20.2 (C9). **HRMS-ESI+** (MeOH): *m/z* calc. For [($C_{13}H_{22}N_2$) + H]$^+$: 207.18557, found: 207.18501. **IR** (ATR): $\tilde{\nu}$ [cm^{-1}] = 2965 (m, C–H_{arom}), 2927 (vw, C–H_{arom}), 2871 (vw, C–H_{aliph}), 1613 (m, C=C), 1493 (m), 1458 (m), 1383 (w),1363 (m), 1311 (w), 1282 (w), 1244 (vw), 1199 (w), 1175 (m), 1120 (w), 1087 (w), 1014 (w), 952 (w), 927 (w), 872 (vw), 745 (vs), 700 (vw), 628 (w), 544 (w), 526 (w). Additional information on the NMR spectra of the target compound including original data files is available via Chemotion Repository: doi:10.14272/BHTORDOUUFFJPO-UHFFFAOYSA-N.1

Ligand Step 3: 2-{2-((Dialkylamino)methyl)phenyl}-1,1,3,3-tetramethylguanidine synthesized after the general scheme [31].

To a stirring solution of 2-{(dialkylamino)methyl}aniline (39.3 mmol, 1.0 eq) in dried acetonitrile (40 mL), triethyl amine (5.4 mL, 39.3 mmol, 1.0 eq) was added at room temperature. A solution of chloro-*N,N,N′,N′*-tetramethylformamidinium chloride (6.71 g, 39.3 mmol, 1.0 eq) in dried acetonitrile (40 mL) was added dropwise to the reaction mixture. The reaction solution was refluxed for 8 h. After cooling the reaction mixture down to room temperature, aqueous NaOH solution (1.57 g, 39.3 mmol, 1.0 eq, in 15 mL) was added. All volatiles were removed under reduced pressure. Aqueous KOH solution (50 wt%, 50 g in 50 mL) was added and the mixture was extracted with acetonitrile (4 × 80 mL). The combined organic layers were dried over Na_2SO_4 and charcoal, filtered and evaporated to dryness.

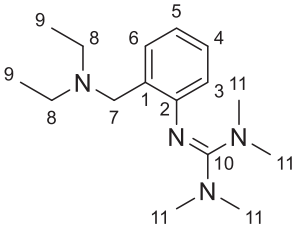

2-{2-((Diethylamino)methyl)phenyl}-1,1,3,3-tetramethylguanidine (TMGbenzNEt$_2$, L2): The crude product was purified by vacuum distillation (140 °C, 3 × 10^{-2} mbar) to give a light-yellow oil (10.9 g, 39.6 mmol, 94%). **^{1}H NMR** (400 MHz, Acetonitrile-d_3, 25 °C): δ [ppm] = 7.29 (ddt, J = 7.5, 1.0, 0.4 Hz, 1H, H3), 7.05–6.99 (m, 1H, H5), 6.78 (td, J = 7.4, 1.3 Hz, 1H, H4), 6.39 (dd, J = 7.8, 1.2 Hz, 1H, H6), 3.42 (s, 2H, H7), 2.62 (s, 12H, H11), 2.46 (q, J = 7.1 Hz, 4H, H8), 0.99 (t, J = 7.1 Hz, 6H, H9). **^{13}C{^{1}H} NMR** (101 MHz, Acetonitrile-d_3, 25 °C): δ [ppm] = 159.3 (C10), 151.7 (C2), 131.8 (C1), 129.9 (C3), 127.4 (C5), 121.9 (C6), 120.3 (C4), 54.5 (C7), 47.9 (C8), 39.8 (C11), 12.5 (C9). **HRMS-EI:** *m/z* calc. For [$C_{16}H_{28}N_4$]: 276.2311, found: 276.2308. **IR** (ATR): $\tilde{\nu}$ [cm^{-1}] = 2967 (w, C–H_{arom}), 2929 (w, C–H_{arom}), 2870 (w, C–H_{aliph}), 2791 (w, C–H_{aliph}), 1608 (s), 1586 (vs, C=N), 1566 (vs), 1499 (m), 1479 (m), 1447 (m), 1425 (m), 1370 (vs), 1234 (w), 1207 (w), 1166 (w), 1135 (s), 1098 (w), 1057 (w), 1040 (w), 1017 (s), 924 (w), 858 (w), 776 (m), 742 (m), 729 (m), 701 (w), 627 (w), 540 (w). Additional information on the NMR spectra of the target compound including original

data files is available via Chemotion Repository: doi:10.14272/LNVNFNCAAMQZFE-UHFFFAOYSA-N.1

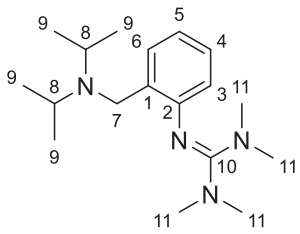

2-{2-((Di-*iso*propylamino)methyl)phenyl}-1,1,3,3-tetramethylguanidine (TMGbenzN*i*Pr$_2$, L3): The crude product was purified by vacuum distillation (170 °C, 5×10^{-2} mbar) to give a yellow oil (10.4 g, 34.1 mmol, 87%). **^{1}H NMR** (400 MHz, Acetonitrile-d_3, 25 °C): δ [ppm] = 7.41 (ddt, J = 7.6, 1.3, 0.4 Hz, 1H, H3), 7.02–6.96 (m, 1H, H5), 6.80–6.75 (m, 1H, H4), 6.37 (dd, J = 7.8, 1.3 Hz, 1H, H6), 3.51 (s, 2H, H7), 3.02 (hept, J = 6.6 Hz, 2H, H8), 2.63 (s, 12H, H11), 1.00 (d, J = 6.6 Hz, 12H, H9). **^{13}C{^{1}H} NMR** (101 MHz, Acetonitrile-d_3, 25 °C): δ [ppm] = 159.4 (C10), 151.3 (C2), 133.8 (C1), 129.6 (C3), 127.0 (C5), 121.7 (C6), 120.3 (C4), 48.7 (C8), 45.4 (C7), 39.8 (C11), 21.0 (C9). **HRMS-EI**: *m/z* calc. For [$C_{18}H_{32}N_4$]: 304.2621, found: 304.2613. **IR** (ATR): $\tilde{\nu}$ [cm^{-1}] = 2961 (m, C–H$_{arom}$), 2929 (m, C–H$_{arom}$), 2875 (w, C–H$_{aliph}$), 2802 (vw, C–H$_{aliph}$), 1607 (m), 1586 (vs, C═N), 1566 (s), 1499 (m), 1479 (m), 1448 (m), 1425 (m), 1372 (vs), 1274 (w), 1251 (w), 1233 (w), 1206 (m), 1174 (m), 1135 (vs), 1106 (m), 1058 (w), 1016 (s), 929 (w), 856 (m), 780 (m), 755 (m), 742 (m),720 (m), 627 (w), 617 (w), 569 (w), 541 (m). Additional information on the NMR spectra of the target compound including original data files is available via Chemotion Repository: doi:10.14272/QUXYBCGZDQRMFG-UHFFFAOYSA-N.1

Synthesis of [Cu(L)(MeCN)]X ([C]X, X$^-$ = PF_6^-, BF_4^-, $CF_3SO_3^-$ (OTf^- or triflate)).

A solution of ligand **L** (**L2**: 27.6 mg, **L3**: 30.4 mg, 0.10 mmol, 1.0 eq) in dried acetonitrile (2.0 mL) was added dropwise to a stirring solution of [Cu(MeCN)$_4$]X (X$^-$ = PF_6^-: 37.3 mg, BF_4^-: 31.5 mg, OTf^-: 37.7 mg, 0.10 mmol, 1.0 eq) in dried acetonitrile (3.0 mL) during a period of 10 min. The solution was stirred for 2 h and evaporated to dryness (Caution! The complex is very sensitive to oxygen which is indicated by partial coloration of the precipitate or oil to light-green). The residue was washed with dried pentane (3 × 1.0 mL) and dried in vacuo.

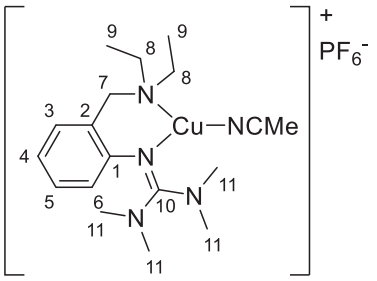

[Cu(L2)(MeCN)]PF_6 ([C2]PF_6): The title compound was isolated as a light-yellow solid (47 mg, 0.089 mmol, 89%). **^{1}H NMR** (400 MHz, Acetonitrile-d_3, 25 °C): δ [ppm] = 7.23–7.17 (m, 2H, H4 + H6), 6.91 (td, J = 7.4, 1.3 Hz, 1H, H5), 6.44 (dt, J = 7.7, 0.9 Hz, 1H, H3), 3.59 (s, 2H, H7), 2.95–2.47 (m, 16H, H8 + H11), 1.12 (t, J = 7.1 Hz, 6H, H9). **^{13}C{^{1}H} NMR** (101 MHz, Acetonitrile-d_3, 25 °C): δ [ppm] = 165.0 (C10), 151.6 (C1), 133.2 (C4), 130.2 (C6), 128.5 (C2), 123.1 (C3), 122.3 (C5), 59.2 (C7), 48.2 (C8), 40.1 (C11), 10.0 (C9). **^{19}F{^{1}H} NMR** (377 MHz, Acetonitrile-d_3, 25 °C): δ [ppm] = −72.86 (d, J = 706.5 Hz, PF_6). **^{31}P{^{1}H} NMR** (162 MHz, Acetonitrile-d_3, 25 °C): δ [ppm] = −144.59 (hept, J = 706.4 Hz, PF_6). **HRMS-ESI+** (MeCN): *m/z* calc. For [($C_{16}H_{28}N_4$)Cu]$^+$: 339.16045, found: 339.16115, calc. For [($C_{16}H_{28}N_4$)Cu(CH_3CN)]$^+$: 380.18699, found: 380.18816. **IR** (KBr): $\tilde{\nu}$ [cm^{-1}] = 3067 (w, C–H$_{arom}$), 3023 (m, C–H$_{arom}$), 3002 (m, C–H$_{arom}$), 2960 (m, C–H$_{arom}$), 2935 (m, C–H$_{arom}$), 2871 (m, C–H$_{aliph}$), 2844 (m, C–H$_{aliph}$), 2801 (w, C–H$_{aliph}$), 1598 (m), 1555 (vs, C═N), 1527 (vs), 1486 (s), 1477 (s), 1447 (s), 1424 (s), 1408 (vs), 1332 (s), 1266 (m), 1238 (m), 1163 (m), 1061 (m), 1037 (s), 838 (vs, PF_6), 750 (s, PF_6), 727 (m), 701 (m), 556 (vs, PF_6), 517 (w), 462 (w, PF_6). Additional information on the NMR spectra of the target compound including original data files is available via Chemotion Repository: doi:10.14272/FFIOOAUERPRGCO-UHFFFAOYSA-N.1

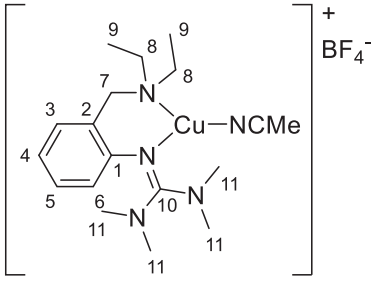

[Cu(L2)(MeCN)]BF_4 ([C2]BF_4): The title compound was isolated as a light-yellow solid (37 mg, 0.079 mmol, 79%). **^{1}H NMR** (400 MHz, Acetonitrile-d_3, 25 °C): δ [ppm] = 7.23–7.17 (m, 2H, H4 + H6), 6.90 (td, J = 7.4, 1.3 Hz, 1H, H5), 6.44 (dt, J = 7.7, 0.9 Hz, 1H, H3), 3.59 (s, 2H, H7), 2.96–2.47 (m, 16H, H8 + H11), 1.12 (t, J = 7.1 Hz, 6H, H9). **^{13}C{^{1}H} NMR** (101 MHz, Acetonitrile-d_3, 25 °C): δ [ppm] = 165.0 (C10), 151.6 (C1), 133.2 (C4), 130.2 (C6), 128.5 (C2), 123.1 (C3), 122.3 (C5), 59.2 (C7), 48.3 (C8), 40.1 (C11), 10.0 (C9). **^{19}F{^{1}H} NMR** (377 MHz, Acetonitrile-d_3, 25 °C): δ [ppm] = −151.78 (s, BF_4). **HRMS-ESI+** (MeCN): *m/z* calc. For [($C_{16}H_{28}N_4$)Cu]$^+$: 339.16045, found: 339.16074, calc. For [($C_{16}H_{28}N_4$)Cu(CH_3CN)]$^+$: 380.18699, found: 380.18610. **IR** (KBr): $\tilde{\nu}$ [cm^{-1}] = 3062 (w, C–H$_{arom}$), 2998 (m, C–H$_{arom}$), 2951 (m, C–H$_{arom}$), 2883 (m, C–H$_{aliph}$), 2827 (m, C–H$_{aliph}$), 1554 (vs, C═N), 1532 (vs), 1483 (s), 1452 (m), 1429 (s), 1408 (s), 1400 (s), 1332 (m), 1267 (m), 1238 (m), 1197 (m), 1164 (m), 1097 (vs, BF_4), 1054 (vs, BF_4), 1034 (vs, BF_4), 913 (m), 864 (m), 824 (w), 782 (m), 753 (m, BF_4), 730 (m), 705 (m), 621 (w), 520 (m, BF_4), 467 (m), 450 (w). Additional information on the NMR spectra of the target compound including original data files is available via Chemotion Repository: doi:10.14272/PTEOGYLGFQZBHG-UHFFFAOYSA-N.1

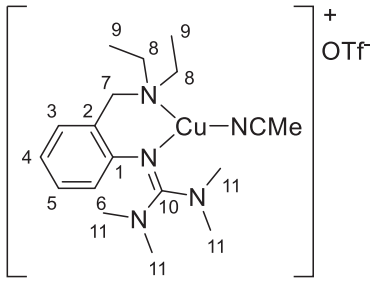

[Cu(L2)(MeCN)]OTf ([C2]OTf): The title compound was isolated as a light-yellow solid (38 mg, 0.071 mmol, 71%). **^{1}H NMR** (400 MHz, Acetonitrile-d_3, 25 °C): δ [ppm] = 7.23–7.17 (m, 2H, H4 + H6), 6.90 (td, J = 7.4, 1.3 Hz, 1H, H5), 6.44 (dd, J = 7.8, 0.8 Hz, 1H, H3), 3.58 (s, 2H, H7), 2.96–2.43 (m, 16H, H8 + H11), 1.12 (t, J = 7.2 Hz, 6H, H9). **^{13}C{^{1}H} NMR** (101 MHz, Acetonitrile-d_3, 25 °C): δ [ppm] = 165.0 (C10), 151.6 (C1), 133.2 (C4), 130.2 (C6), 128.5 (C2), 123.8 (OTf), 123.1 (C3), 122.3 (C5), 59.2 (C7), 48.2 (C8), 40.1 (C11), 10.0 (C9). **^{19}F{^{1}H} NMR** (377 MHz, Acetonitrile-d_3, 25 °C): δ [ppm] = −79.23 (s, OTf). **HRMS-ESI+** (MeCN): *m/z* calc. For [($C_{16}H_{28}N_4$)Cu]$^+$: 339.16045, found: 339.16207, calc. For [($C_{16}H_{28}N_4$)Cu(CH_3CN)]$^+$: 380.18699, found: 380.18902. **IR** (KBr): $\tilde{\nu}$ [cm^{-1}] = 3058 (w, C–H$_{arom}$), 2969 (m, C–H$_{arom}$), 2936 (m, C–H$_{arom}$), 2873 (m, C–H$_{arom}$), 2803 (w, C–H$_{aliph}$), 1546 (s, C═N), 1528 (s), 1487 (m), 1471 (m), 1423 (m), 1397 (s), 1330 (m),

1267 (vs, OTf), 1223 (m, OTf), 1153 (s, OTf), 1047 (m), 1031 (vs, OTf), 929 (w), 864 (m), 791 (m), 753 (m, OTf), 730 (w), 655 (m), 638 (vs, OTf), 572 (m), 517 (m), 473 (w). Additional information on the NMR spectra of the target compound including original data files is available via Chemotion Repository: doi:10.14272/PVOWJBLMSRTONC-UHFFFAOYSA-M.1

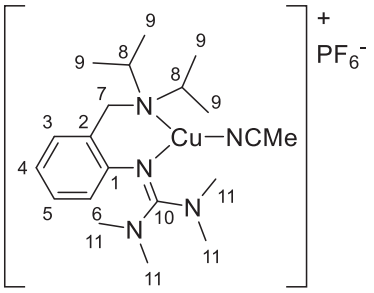

[Cu(L3)(MeCN)] PF_6 ([C3] PF_6): The title compound was isolated as a light-yellow solid (30 mg, 0.054 mmol, 54%). **^{1}H NMR** (400 MHz, Acetonitrile-d_3, 25 °C): δ [ppm] = 7.28–7.23 (m, 1H, H6), 7.23–7.17 (m, 1H, H4), 6.98–6.90 (m, 1H, H5), 6.53–6.38 (m, 1H, H3), 3.77 (s, 2H, H7), 3.22 (hept, J = 6.5 Hz, 2H, H8), 2.74 (s, 12H, H11), 1.20 (d, J = 6.6 Hz, 12H, H9). **^{13}C{^{1}H} NMR** (101 MHz, Acetonitrile-d_3, 25 °C): δ [ppm] = 165.7 (C10), 150.7 (C1), 132.7 (C6), 130.1 (C2), 129.9 (C4), 123.0 (C3 + C5), 54.1 (C8), 52.1 (C7), 40.3 (C11), 20.9 (C9). **^{19}F{^{1}H} NMR** (377 MHz, Acetonitrile-d_3, 25 °C): δ [ppm] = −72.87 (d, J = 706.6 Hz, PF_6). **^{31}P{^{1}H} NMR** (162 MHz, Acetonitrile-d_3, 25 °C): δ [ppm] = −144.59 (hept, J = 706.5 Hz, PF_6). **HRMS-ESI+** (MeCN): *m/z* calc. For $[(C_{18}H_{32}N_4)Cu]^+$: 367.19175, found: 367.19254, calc. For $[(C_{18}H_{32}N_4)Cu(CH_3CN)]^+$: 408.21830, found: 408.21786. **IR** (KBr): $\tilde{\nu}$ [cm^{-1}] = 3058 (m, C–H_{arom}), 2966 (m, C–H_{arom}), 2938 (m, C–H_{arom}), 2893 (m, C–H_{aliph}), 2873 (m, C–H_{aliph}), 2800 (m, C–H_{aliph}), 1598 (m), 1551 (s, C═N), 1527 (s), 1488 (m), 1473 (m), 1450 (m), 1424 (m), 1397 (s), 1331 (m), 1269 (m), 1236 (m), 1170 (m), 1159 (m), 1113 (m), 1065 (m), 1034 (m), 988 (w), 839 (vs, PF_6), 751 (m, PF_6), 724 (m), 703 (m), 557 (s, PF_6), 458 (w, PF_6). Additional information on the NMR spectra of the target compound including original data files is available via Chemotion Repository: doi:10.14272/LKAMFMLEEUDGOQ-UHFFFAOYSA-N.1

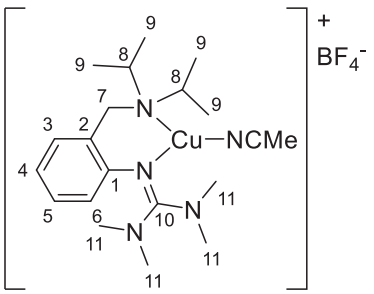

[Cu(L3)(MeCN)] BF_4 ([C3] BF_4): The title compound was isolated as a light-yellow solid (34 mg, 0.068 mmol, 68%). **^{1}H NMR** (400 MHz, Acetonitrile-d_3, 25 °C): δ [ppm] = 7.28–7.23 (m, 1H, H6), 7.19 (td, J = 7.7, 1.5 Hz, 1H, H4), 6.92 (td, J = 7.4, 1.3 Hz, 1H, H5), 6.44 (d, J = 7.8 Hz, 1H, H3), 3.76 (s, 2H, H7), 3.22 (hept, J = 6.6 Hz, 2H, H8), 2.72 (s, 12H, H11), 1.20 (d, J = 6.6 Hz, 12H, H9). **^{13}C{^{1}H} NMR** (101 MHz, Acetonitrile-d_3, 25 °C): δ [ppm] = 165.7 (C10), 150.6 (C1), 132.7 (C6), 130.2 (C2), 129.9 (C4), 123.1 (C3), 122.8 (C5), 54.2 (C8), 52.2 (C7), 40.3 (C11), 21.0 (C9). **^{19}F{^{1}H} NMR** (377 MHz, Acetonitrile-d_3, 25 °C): δ [ppm] = −151.76 (s, BF_4). **HRMS-ESI+** (MeCN): *m/z* calc. For $[(C_{18}H_{32}N_4)Cu]^+$: 367.19175, found: 367.19348, calc. For $[(C_{18}H_{32}N_4)Cu(CH_3CN)]^+$: 408.21830, found: 408.21763. **IR** (KBr): $\tilde{\nu}$ [cm^{-1}] = 3062 (w, C–H_{arom}), 2966 (m, C–H_{arom}), 2931 (m, C–H_{arom}), 2891 (m, C–H_{aliph}), 2873 (m, C–H_{aliph}), 2803 (w, C–H_{aliph}), 1550 (vs, C═N), 1534 (vs), 1477 (m), 1449 (m), 1426 (m), 1395 (m), 1327 (m), 1270 (w), 1235 (w), 1208 (m), 1158 (m), 1140 (m), 1050 (vs, BF_4), 866 (w), 827 (w), 760 (m), 749 (m, BF_4), 708 (w), 520 (w, BF_4), 451 (w). Additional information on the NMR spectra of the target compound including original data files is available via Chemotion Repository: doi:10.14272/XCTDJIMIPLJWIC-UHFFFAOYSA-N.1

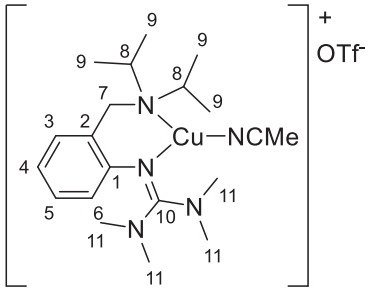

[Cu(L3)(MeCN)] OTf ([C3] OTf): The title compound was isolated as a light-yellow solid (35 mg, 0.062 mmol, 62%). **^{1}H NMR** (400 MHz, Acetonitrile-d_3, 25 °C): δ [ppm] = 7.27–7.23 (m, 1H, H6), 7.19 (td, J = 7.7, 1.6 Hz, 1H, H4), 6.92 (td, J = 7.4, 1.3 Hz, 1H, H5), 6.43 (d, J = 7.8 Hz, 1H, H3), 3.76 (s, 2H, H7), 3.22 (hept, J = 6.5 Hz, 2H, H8), 2.72 (s, 12H, H11), 1.20 (d, J = 6.6 Hz, 12H, H9). **^{13}C{^{1}H} NMR** (101 MHz, Acetonitrile-d_3, 25 °C): δ [ppm] = 165.7 (C10), 150.6 (C1), 132.8 (C6), 130.2 (C2), 129.9 (C4), 123.8 (OTf), 123.1 (C3), 122.8 (C5), 54.2 (C8), 52.3 (C7), 40.3 (C11), 21.0 (C9). **^{19}F{^{1}H} NMR** (377 MHz, Acetonitrile-d_3, 25 °C): δ [ppm] = −79.24 (s, OTf). **HRMS-ESI+** (MeCN): m/z calc. For $[(C_{18}H_{32}N_4)Cu]^+$: 367.19175, found: 367.19436, calc. For $[(C_{18}H_{32}N_4)Cu(CH_3CN)]^+$: 408.21830, found: 408.21804. **IR** (KBr): $\tilde{\nu}$ [cm^{-1}] = 3059 (w, C–H_{arom}), 2966 (m, C–H_{arom}), 2934 (m, C–H_{arom}), 2892 (m, C–H_{aliph}), 2876 (m, C–H_{aliph}), 2799 (w, C–H_{aliph}), 1543 (vs, C═N), 1530 (vs), 1472 (s), 1424 (s), 1396 (s), 1330 (m), 1267 (vs, OTf), 1223 (m, OTf), 1156 (vs, OTf), 1064 (m), 1048 (s, OTf), 1031 (vs, OTf), 930 (w), 866 (w), 842 (w), 826 (w), 790 (w), 753 (m, OTf), 656 (m), 638 (vs, OTf), 572 (m), 547 (w), 517 (m). Additional information on the NMR spectra of the target compound including original data files is available via Chemotion Repository: doi:10.14272/HNRHNIXGNDHWER-UHFFFAOYSA-M.1

Synthesis of bis(μ-oxido) species [O] X_2:

Dried and degassed tetrahydrofuran (9.5 mL) was saturated with molecular oxygen at −100 °C. The colorless precursor complex [**C**]X ($X^- = PF_6^-$, BF_4^-, $CF_3SO_3^-$ (triflate, OTf^-), 0.010 mmol, 2.0 eq) in acetonitrile (0.5 mL) was prepared under inert conditions and added rapidly via a Hamilton syringe. The reaction solution stained immediately. The formation of [**O**]X_2 ($X^- = PF_6^-$, BF_4^-, $CF_3SO_3^-$, 0.005 mmol, 1.0 eq) was followed by UV/Vis spectroscopy.

2.5. Catalytic oxygenation reactions of phenolic substrates

Flame-dried molecular sieves (400 mg, 3 Å) were placed in a flask. Dried and degassed tetrahydrofuran (18 mL) was added and saturated with molecular oxygen at −100 °C. The precursor complex [**C**]PF_6 (0.10 mmol, 2 eq) in acetonitrile (2 mL) was prepared under inert conditions, added rapidly via a Hamilton syringe and the bis(μ-oxido) complex [**O**]$(PF_6)_2$ (0.005 mmol, 1 eq) was formed. The substrate solution was prepared by dissolving the substrate (1.25 mmol, 25 eq) in dried solvent (2-naphthol: 2 mL tetrahydrofuran, 6-quinolinol: 8 mL methanol) and subsequent adding of triethylamine (0.35 mL, 2.50 mmol, 50 eq). The solution was injected in one portion into the reaction mixture and stirred at −100 °C for the respective time (2-naphthol: 2 h, 6-quinolinol: 3 h, see also Table 8). 1,2-Phenylenediamine solution (270.3 mg, 2.50 mmol, 50 eq) was prepared by dissolving it in dried tetrahydrofuran (2 mL) and then added to the reaction mixture. After stirring overnight at room temperature, the reaction was quenched by using hydrochloric acid (0.5 M, 50 mL) and EDTA (one spatula). The

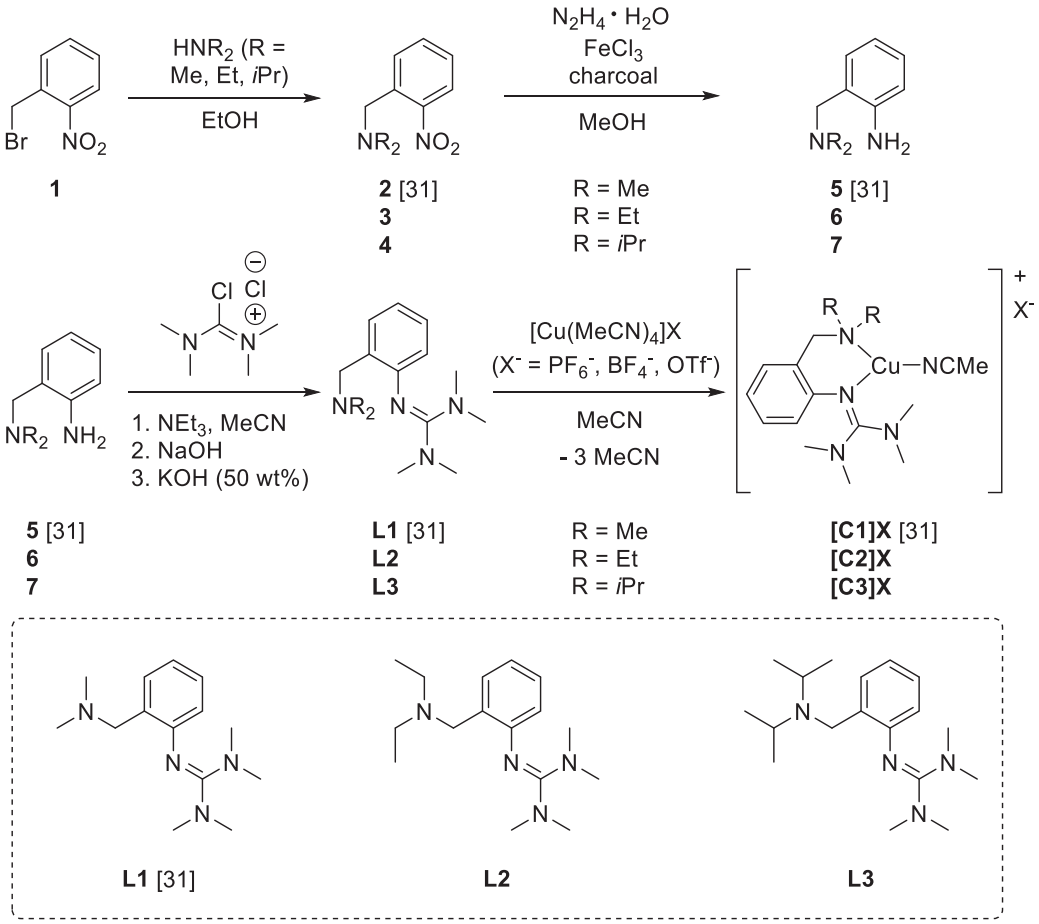

Scheme 1. Synthesis of hybrid guanidine ligands **L1-L3** and their corresponding Cu(I) complexes.

organic solvents were removed under reduced pressure. The aqueous phase was extracted with dichloromethane (4 × 100 mL). The combined organic layers were dried over Na_2SO_4 and evaporated to dryness. The crude product was purified via column chromatography and analyzed by NMR spectroscopy.

3. Results and discussion

3.1. Synthesis of ligands and Cu(I) complexes

In analogy to our previously reported hybrid guanidine ligand system TMGbenza (**L1**) [31], two related ligands were developed by modification of the amine donor unit to evaluate the influence on the steric effects and the donor strength of the ligand system on dioxygen activation and transfer processes (Scheme 1). Ligand **L1** [31] contains a permethylated amine moiety, which is substituted by a diethyl or di-*iso*propyl group to give the new hybrid guanidine ligands TMGbenzNEt$_2$ (**L2**, IUPAC name: 2-{2-((diethylamino)methyl)phenyl}-1,1,3,3-tetramethylguanidine) and TMGbenzN*i*Pr$_2$ (**L3**, IUPAC name: 2-{2-((di-*iso*propylamino)methyl)phenyl}-1,1,3,3-tetramethylguanidine).

Starting from 2-nitrobenzyl bromide, ligands **L2** and **L3** were synthesized in a three-step reaction based on a protocol reported previously [31] and isolated in high yields. The ^{1}H NMR and ^{13}C{^{1}H} NMR spectra show that the modification of the amine donor primarily influences the methylene group of the ligand (Table 1).

Table 1
Selected chemical shifts [ppm] of the hybrid guanidine ligands **L1**, **L2** and **L3**.

		L1	L2	L3
^{1}H NMR	$\underline{CH}_2$	3.30	3.42	3.51
^{13}C{^{1}H} NMR	$\underline{CH}_2$	60.6	54.5	45.4
	$CH_2\underline{C}$(Ph)	130.8	131.8	133.8

The resonances of the carbon atom of the methylene group in the ^{13}C{^{1}H} NMR spectra shifted to lower chemical shifts and those of neighbored carbon and hydrogen atoms shifted to higher chemical shifts accordingly. This shift results from the positive inductive effect of the alkyl substituents, which is most pronounced in **L1** and diminished with increasing alkyl chain length. This effect causes more electron density in the NMe_2 moiety in **L1** compared to the NEt_2 moiety in **L2** and the N*i*Pr$_2$ moiety in **L3**, reflecting the electron donating abilities of the ligand system.

Employing equimolar amounts of the ligand **L2**-**L3** and the copper salt [Cu(MeCN)$_4$]X ($X^- = PF_6^-$, BF_4^-, OTf^-) in acetonitrile at room temperature led to the formation of the monochelate copper(I) complexes [**C2**]X and [**C3**]X ($X^- = PF_6^-$, BF_4^-, OTf^-; Scheme 1). Ligands and complexes were stored in a glovebox under nitrogen atmosphere due to their moisture- and/or air-sensitivity. ESI-MS measurements reveal the formation of the desired monochelate copper(I) species. A bischelate species was observed in neither case, which is redirected to the enlarged steric demand of **L2** and **L3**. The ^{1}H NMR and ^{13}C{^{1}H} NMR spectra of the complexes [**C2**]X and [**C3**]X with different weakly coordinating anions are each mainly similar, revealing no visible electronic impact of the weakly coordinating anions on the complex cation. This agrees well with the NMR spectra of complexes [**C1**]X [31]. The modification of the amine moiety from NMe_2 to N*i*Pr$_2$, however, led to a shifted resonance of the carbon atom of the guanidine moiety within the complexes [**C1**]X to [**C3**]X to higher chemical shifts independent of the present anion, revealing the electronic influence of the diminished amine donor abilities on the guanidine moiety (see Table 2).

Table 2
Chemical shifts of C_{gua} of **L1-L3**-stabilized Cu(I) complexes [**C1**]X-[**C3**]X ($X^- = PF_6^-$, BF_4^-, OTf^-) in the $^{13}C\{^1H\}$ NMR spectra [ppm].

	[C1–3] PF_6	[C1–3] BF_4	[C1–3] OTf
L1	164.7	164.7	164.6
L2	165.0	165.0	165.0
L3	165.7	165.7	165.7

Table 3
Wavenumbers of the C═N stretching mode of the Cu(I) complexes [**C1**]X-[**C3**]X ($X^- = PF_6^-$, BF_4^-, OTf^-) in the IR spectra [cm^{-1}]. Due to the low resolution and broad characteristic guanidine vibrations, no shift can be detected for the copper complexes with hexafluoridophosphate as anion.

	[C1–3] PF_6	[C1–3] BF_4	[C1–3] OTf
L1	1555	1557	1549
L2	1555	1554	1546
L3	1551	1550	1543

Also, the obtained wavenumbers of the C═N vibration of the guanidine moiety in complexes [**C1**]X to [**C3**]X shifted to slightly lower values from **L1**- to **L3**-stabilized copper(I) complexes (Table 3). A similar trend was observed in several pairs of hybrid guanidine amine-stabilized zinc(II) chloride complexes upon modification of the amine moiety from NMe_2 to NEt_2 [90].

These observations clearly show that the guanidine moiety responds to the decreased electron donating properties of the amine moiety from **L1** to **L3** in the copper(I) species.

3.2. Dioxygen activation

Cu(I) complexes [**C2**]X and [**C3**]X ($X^- = PF_6^-$, BF_4^-, OTf^-; Fig. S15 and S22 depict the UV/Vis spectrum of [**C2**]PF_6 and [**C3**]PF_6) were oxygenated at low temperatures in a mixture of tetrahydrofuran/acetonitrile (19:1) by bubbling molecular oxygen through a precooled tetrahydrofuran solution and injecting complexes [**C2**]X and [**C3**]X in acetonitrile (Scheme 2). Dioxygen activation was indicated by an immediate color change. The obtained UV/Vis spectroscopic characteristic transitions of bis(μ-oxido) complexes [**O1**]X_2 - [**O3**]X_2 ($X^- = PF_6^-$, BF_4^-, OTf^-) are summarized in Table 4. The formation of [**O2**]$(PF_6)_2$ and [**O3**]$(PF_6)_2$ were analyzed by UV/Vis spectroscopy (Fig. 2). The green bis(μ-oxido) species [**O2**]$(PF_6)_2$ (Fig. 2, left) displayed two distinct absorption bands at 280 nm (40,000 M^{-1} cm^{-1}) and 400 nm (20,000 M^{-1} cm^{-1}). The transition at higher wavelength slightly shifted in comparison to our previously reported system [**O1**]$(PF_6)_2$ (UV/Vis features at 280 nm (40,000 M^{-1} cm^{-1}) and 392 nm (21,000 M^{-1} cm^{-1})) [31]. Similar UV/Vis spectroscopic features were obtained by using bis(μ-oxido) complexes [**O2**]$(BF_4)_2$ and [**O2**]$(OTf)_2$ (Figs. S27 and S28), underlining the independence of the absorption bands from the present weakly-coordinating anions. All complexes [**O2**]$(X)_2$ ($X^- = PF_6^-$, BF_4^-, OTf^-) were formed within 15–40 min at −100 °C and revealed a stability of at least 90 min. Higher temperatures caused a fast decay of the bis(μ-oxido) species, followed by discoloration of the reaction solution to yellow.

The orange bis(μ-oxido) species [**O3**]$(PF_6)_2$ (Fig. 2, right) showed besides the two absorption bands at 280 nm (38,000 M^{-1} cm^{-1}) and 423 nm (16,000 M^{-1} cm^{-1}) an additional smaller UV/Vis feature at 330 nm (9000 M^{-1} cm^{-1}). The transition at higher wavelength shifted in comparison to [**O2**]$(PF_6)_2$ to higher wavelengths. Accordingly, the species [**O3**]$(BF_4)_2$ and [**O3**]$(OTf)_2$ exhibited similar UV/Vis spectra (Figs. S29 and S30). All **L3**-stabilized bis(μ-oxido) species were generated within 25–40 min at −100 °C and revealed a stability of at least 60 min.

To get further insights in the electronic situation of the oxido species we performed density functional theory calculations (DFT). In accordance with previous benchmark studies [50,55,91–94], we used the hybrid functional TPSSh [74–76] with the Ahlrichs type basis set def2-TZVP [77–80] and empirical dispersion correction with Becke-Johnson damping GD3BJ [81–84]. In all three oxido species the Cu–N_{gua} bond lengths are shorter than the Cu–N_{amine} bond lengths, suggesting that the guanidine units possesses the better donor ability (see Table 5). With larger steric encumbrance of the amine donor, the Cu–N bond lengths and the Cu···Cu distance increase. Moreover, the Cu—O bond length elongates slightly whereas the O···O distance decreases. The higher steric hindrance of the amine donor leads to a stretching of the Cu_2O_2 moiety. Furthermore, the dihedral angle between the Cu_2O_2 plane and the CuN_2 plane increases indicating a higher twist of the Cu_2O_2 core and the ligands.

Natural population analysis (NBO) helps to evaluate the donor ability of the ligands [50,85–87]. The guanidine N-donor atom in the ligands is more negatively charged than the amine N-donor atom. Moreover, the guanidine N-donor atom as well as the amine N-donor atom display a slightly more negative value with higher steric demand of the amine donor (Table 6). A more negative value means a more basic character of the N-donor atom. The charge transfer energies (obtained by second order perturbation theory) for the donation of the N-donor atoms reveal that the guanidine N-donor atom possesses a larger donor strength in comparison to the amine N-donor atom. The donor strength

Table 4
Experimental UV/Vis spectroscopic features of the bis(μ-oxido) species [**O1**]X_2 - [**O3**]X_2 ($X^- = PF_6^-$, BF_4^-, OTf^-, see also Fig. S27 – S31 in the Supporting Information).

[O] X_2	λ [nm] (ε [M^{-1} cm^{-1}])	λ [nm] (ε [M^{-1} cm^{-1}])
[**O1**]$(PF_6)_2$ [31]	392 (21000)	280 (40000)
[**O1**]$(BF_4)_2$ [31]	392 (21000)	280 (40000)
[**O1**]$(OTf)_2$ [31]	396 (21000)	284 (39000)
[**O2**]$(PF_6)_2$	400 (20000)	280 (40000)
[**O2**]$(BF_4)_2$	399 (19000)	279 (36000)
[**O2**]$(OTf)_2$	397 (19000)	280 (35000)
[**O3**]$(PF_6)_2$	423 (16000)	280 (38000)
[**O3**]$(BF_4)_2$	422 (14000)	277 (33000)
[**O3**]$(OTf)_2$	421 (17000)	280 (38000)

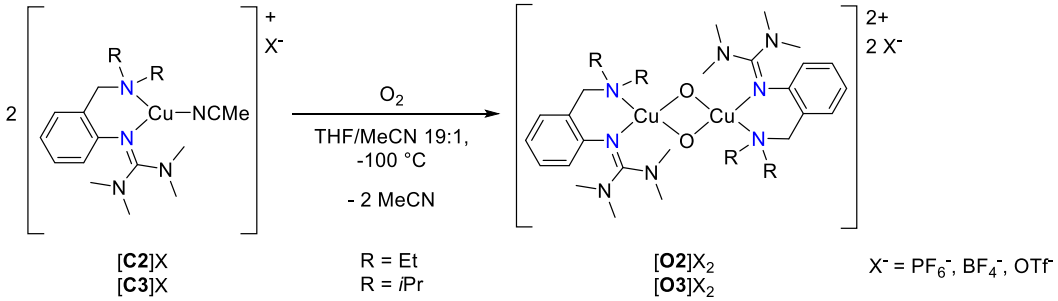

Scheme 2. Oxygenation of Cu(I) species [**C2**]X and [**C3**]X ($X^- = PF_6^-$, BF_4^-, OTf^-).

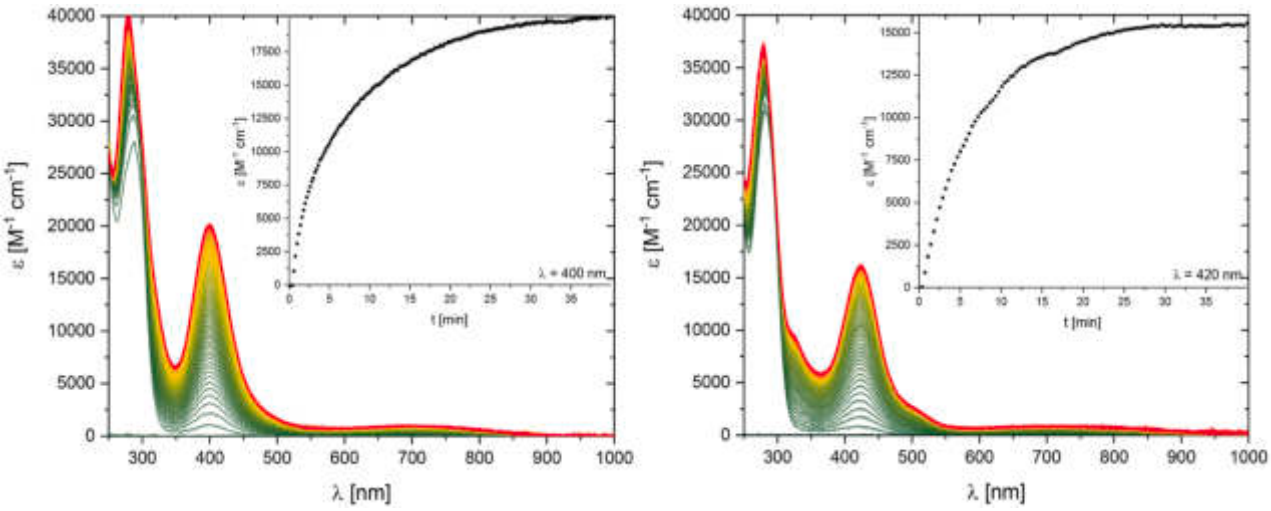

Fig. 2. UV/Vis spectra of the formation of [**O2**](PF$_6$)$_2$ (left) and [**O3**](PF$_6$)$_2$ (right, 0.5 mM) in tetrahydrofuran at −100 °C (Insets: time-resolved formation of [**O2**](PF$_6$)$_2$ at 400 nm and [**O3**](PF$_6$)$_2$ at 420 nm).

Table 5
Key geometric parameters of the oxido species [**O1**]$^{2+}$ – [**O3**]$^{2+}$ (Gaussian16, TPSSh/def2-TZVP, GD3BJ).

	[**O1**]$^{2+}$	[**O2**]$^{2+}$	[**O3**]$^{2+}$
Bond lengths [Å]			
Cu – N$_{gua}$	1.917, 1.917	1.921, 1.928	1.928, 1.934
Cu – N$_{amine}$	1.967, 1.967	1.985, 1.991	1.996, 2.006
Cu – O	1.802, 1.807	1.805, 1.807	1.807, 1.810
	1.802, 1.807	1.803, 1.809	1.809, 1.811
O···O	2.326	2.309	2.296
Cu···Cu	2.759	2.777	2.793
Dihedral angle [°]			
∢(Cu$_2$O$_2$, CuN$_2$)	5.0	8.4	17.3

of the amine N-donor atoms diminishes from [**O1**]$^{2+}$ to [**O3**]$^{2+}$ indicated by the smaller values of the charge transfer energies and the elongation of the Cu–N$_{amine}$ bond lengths.

The difference in the steric and electronic properties of [**O1**]$^{2+}$ to [**O3**]$^{2+}$ results in an elongation of the Cu–N$_{gua}$ bond and the Cu–N$_{amine}$ bond accompanied by a higher twist of the Cu$_2$O$_2$ plane and the CuN$_2$ plane, and a stretching of the Cu$_2$O$_2$ core. All these effects diminish the orbital overlap of the N-donor with the copper ions.

The experimental UV/Vis spectra depict the characteristic UV/Vis bands: one at 280 nm and another one at 392 nm in [**O1**](PF$_6$)$_2$ being redshifted to 400 nm in [**O2**](PF$_6$)$_2$ up to 423 nm in [**O3**](PF$_6$)$_2$. This redshift is well reproduced with time-dependent DFT calculations of the oxido species ([**O1**]$^{2+}$: 375 nm; [**O2**]$^{2+}$: 382 nm; [**O3**]$^{2+}$: 398 nm; see Figs. S42 – S44). A natural transition orbital (NTO) [95] analysis assigns the characteristic band at 280 nm to an in plane transition of the bonding interaction of a copper d orbital with the π_σ* orbital of the oxido ion (highest occupied natural transition orbital, HONTO; Fig. 3 and Fig. S45) to the antibonding interaction of the Cu d orbitals with the σ* orbital of the oxido ion (lowest unoccupied natural transition orbital, LUNTO; Fig. 3 and Fig. S46). The transition at higher wavelength is an in plane transition of the bonding interaction of a Cu d orbital with the σ* of the oxido ion and antibonding to the N-donors (HONTO, Fig. 3 and Fig. S47) to the antibonding interaction of a copper d orbital with the π_σ* orbital of the oxido ion and antibonding with the N-donor (LUNTO, Fig. 3 and Fig. S48). These two characteristic bands are known for oxido species with N-donor ligands [13]. Besides the two characteristic transitions, in [**O3**]$^{2+}$ a shoulder at 330 nm (Fig. 2) is observed. This transition is traced back to the transition from a linear combination of the π_σ* orbital with the π_v* orbital and contribution of the ligand to the antibonding interaction of the copper d orbital with the σ* orbital of the oxido ions and antibonding to the N-donors. The orbitals look already distorted due to the steric influence of the amine donor.

Table 6
NBO charges and charge transfer (CT) energies for selected atoms of [**O1**]$^{2+}$ – [**O3**]$^{2+}$ (NBO7.0; TPSSh/def2-TZVP, GD3BJ).

	[**O1**]$^{2+}$	[**O2**]$^{2+}$	[**O3**]$^{2+}$
NBO charges [e units]			
Cu	1.35	1.36	1.37
N$_{gua}$	−0.70, −0.70	−0.71, −0.72	−0.72, −0.72
N$_{amine}$	−0.40, −0.40	−0.40, −0.40	−0.42, −0.42
O	−0.96, −0.96	−0.96, −0.96	−0.97, −0.98
CT energies [kcal mol^{-1}]			
N$_{gua}$ ➔ Cu	31.9, 31.9	22.0, 27.8	27.1, 29.3
N$_{amine}$ ➔ Cu	20.1, 20.1	17.5, 18.3	14.5, 15.3

The observed redshift is based on several effects: the increasing steric demand (methyl group to isopropyl group) and the lower donor ability of the amine N-donor ($NMe_2 > NEt_2 > NiPr_2$) lead to a higher twist between the Cu$_2$O$_2$ core and the CuN$_2$ plane (also shown in the NTOs of the bis(μ-oxido) species) and a stretching of the Cu$_2$O$_2$ rhomb. Both effects result in a poorer orbital overlap and a redshift. As third effect (but also in conjunction with the first two), the energies of the canonical orbitals

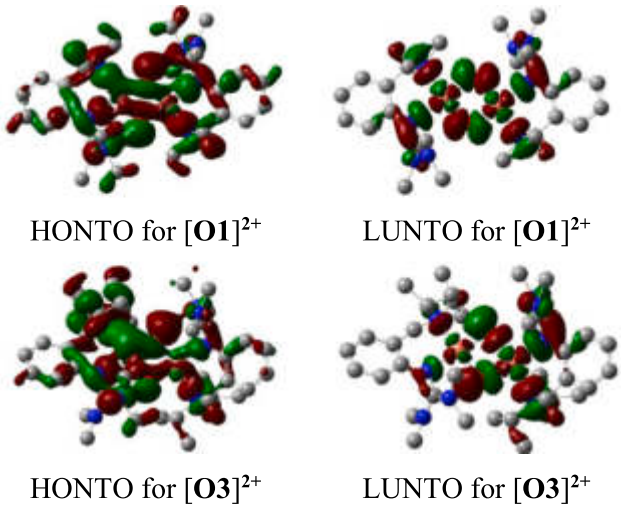

Fig. 3. NTO representations of LUNTOs and HONTOs for [**O1**]$^{2+}$ and [**O3**]$^{2+}$ of the characteristic transition at higher wavelength.

Table 7
Selected structural and spectroscopic parameters of bis(μ-oxido) species stabilized by bidentate and tridentate ligands.

Oxido[a] species	ligand system	UV/Vis, λ [nm] (ε [mM^{-1} cm^{-1}])	rRaman $\tilde{\nu}$ [cm^{-1}]	Cu···Cu [Å]	Cu–O[b] [Å]	Cu–N[b] [Å]
$[O1]^{2+}$	TMGbenza [31]	392 (21), 280 (40)	620	2.66[c]	1.89[c]	2.01, 2.06[c]
				2.76[d]	1.80[d]	1.92, 1.97[d]
$[O2]^{2+}$	$TMGbenzNEt_2$	399 (21), 280 (40)	615	2.78[d]	1.81[d]	1.92, 1.99[d]
$[O3]^{2+}$	$TMGbenzNiPr_2$	423 (18), 280 (38)	607	2.79[d]	1.81[d]	1.93, 2.00[d]
RC1	TMGdmap [28,29]	385 (18), 297 (20)	617 [96]	2.78[c]	1.82[c]	1.96, 1.96[c]
				2.76[d]	1.79[d]	1.91, 2.00[d]
RC2	TMGdeap [29]	392 (18), 297 (15)	–	–	–	–
RC3	TMG_2tol [30]	395 (12), 290 (38)	600	2.75[d]	1.81[d]	1.92[d]
RC4	TMCHD [19,21,22]	399 (25), 301 (20)	605	–	–	–
RC5	MECHD [19,21,22]	408 (28), 313 (21)	610	2.74[e]	1.80[e]	–
				2.73[c]	1.81[c]	
RC6	TECHD [19,21,22]	413 (23), 319 (17)	616	–	–	–
RC7	TMED [23]	392 (18)	607	2.74[c]	1.80[c]	1.96[c]
				2.77[d]	1.81[d]	1.97[d]
RC8	Me_2Et_2ED [22]	397 (21), 297 (18)	–	–	–	–
RC9	TEED [21,22]	407 (24), 307 (17)	603	2.74[c]	1.80[c]	
RC10	PD [24]	375 (23), 278 (21)	–	2.77[c]	1.86[c]	2.00[c]
				2.71[d]	1.80[d]	1.94[d]
RC11	DMPD [24]	390 (28), 290 (20)	–	2.81[c]	1.82[c]	1.96[c]
				2.78[d]	1.81[d]	1.99, 1.91[d]
RC12	TMPD [24]	403 (29), 302 (19)	608	2.85[c]	1.84[c]	2.02[c]
				2.83[d]	1.81[d]	2.00[d]
RC13	Me_3His [25]	380 (30), 280 (25)	–	2.80[c]	1.82[c]	1.97[c]
				2.77[d]	1.81[d]	1.98, 1.91[d]
RC14	*n*BuHis [25]	363 (28), 262 (30)	–	2.78[c]	1.82[c]	1.96[c]
				2.73[d]	1.81[d]	1.95, 1.91[d]
RC15	*n*BuBIM [27]	349 (24), 251 (35)	–	2.78[c]	1.84[c]	1.94[c]
				2.69[d]	1.76[d]	1.89[d]
RC16	Me_3TACN [19]	412 (18), 307 (16)	604	2.77[c]	–	–
RC17	Bz_3TACN [20]	430 (14), 318 (12)	603	2.79[e]	1.81[e]	–
RC18	$iPr_2BzTACN$ [20]	436 (16), 322 (12)	594	–	–	–
RC19	iPr_3TACN [20]	448 (13), 324 (11)	589	–	–	–

a) RC = reference bis(μ-oxido) complex in the presence of a weakly coordinating anion, b) Cu—O values are averaged; Cu—N values are averaged in some cases, c) derived from EXAFS data, d) determined by DFT calculations, e) derived from X-ray data.

differ depending of the ligand. The energetic difference between the LUMO+1 (LUMO: lowest unoccupied molecular orbital) and the LUMO diminishes from $[O1]^{2+}$ to $[O3]^{2+}$ (see Table S2 and S3). Thus, the LUMO+1 is more stabilized in energy with weaker amine donor with higher twist. On the other hand, the HOMO-8 (HOMO: highest occupied molecular orbital; key orbital for the 400 nm transition) is higher in energy relative to the HOMO with weaker amine donor (see Table S2 and S3). This has the consequence that the energy for the transition becomes smaller from $[O1]^{2+}$ to $[O3]^{2+}$ resulting in a redshift of the characteristic Cu_2O_2 core transition at higher wavelength.

A shift of the characteristic bands in dependence of the N-donor ligand system was reported previously (Table 7, for a scheme of the ligands see Fig. 1). A similar system to TMGbenza is represented by TMGdmap [28]. In TMGdmap, the spacer is a propylene bridge and the ligand possesses also the NMe_2 and TMG donor functions. Here we find the characteristic bands of oxido species **RC1** in the same region [28,29,55], but a smaller twist with 1.8° between the Cu_2O_2 core and the CuN_2 plane compared to $[O1]^{2+}$ (5.0°) and a slightly longer Cu···Cu vector (2.747; $[O1]^{2+}$: 2.759 Å) and O···O distances (2.336 Å, $[O1]^{2+}$: 2.326 Å). The bisguanidine ligand TMG_2tol exhibits the same backbone but only one type of donor at both positions [30]. The oxido species **RC3** with the ligand TMG_2tol shows a small shift of the characteristic UV/vis band at higher wavelength. This shift is a result of the higher twist with 6.9°(av) between the Cu_2O_2 core and the CuN_2 plane, whereas the Cu···Cu vector and the O···O distances remains constant to the oxido species **RC1**. The TMG moieties with the high sterically demand lead to two different twist angles of 2.4° and 11.4°. Herres-Pawlis, Stack and co-workers also observed a redshift from 385 nm to 392 nm upon modification of the amine unit in TMGdmap from NMe_2 to NEt_2 (see **RC2**), which was redirected to steric effects of the ligand system [29].

Stack, Solomon and co-workers examined very carefully a huge number of Cu_2O_2 species and reported also UV/Vis and Raman spectra [19,21,22]. The ligands are based on peralkylated bidentate *trans*-(1*R*, 2*R*)-cyclohexanediamine and 1,2-ethanediamine skeletons or tridentate polyazacyclononane ligands. The ligands varied from tetramethyl to dimethyl-diethyl to tetraethyl derivatives. They studied the influence of the steric demand of the substituent on the spectroscopic features and the geometry of the Cu_2O_2 rhomb. For the cyclohexanediamine derivatives, they reported a redshift with higher steric demand of the ligand (**RC4-RC6**). This is a result of the steric pressure of the ligand system of the oxido species resulting in an elongation of the Cu_2O_2 rhomb. The authors do not rule out an influence of the twist of the CuN_2 plane and the Cu_2O_2 rhomb. This trend was also reported for the polyazacyclononane-based species **RC16-RC19** and the 1,2-ethylenediamine systems **RC7-RC9**. The study based on **RC7-RC9** is supported by a report in 2015: This trend was also observed upon the variation of the N-donor moieties from the primary amine propane-1,3-diamine (PD) to a hybrid version (NH_2, NMe_2) to permethylated amine tetramethyl propylenediamine (TMPD) (see **RC10-RC12**): a redshift of the optical bands is observed together with an elongated Cu···Cu vector due to steric considerations and diminished donor ability of the ligands with PD being the smallest and strongest ligand [26]. Stack reported in 2019 a systematic study on oxido complexes with the ligands TMPD (**RC12**), N_α, N_α,N_τ-trimethyl-histamine (Me_3His, **RC13**), N_τ-n-butylhistamine (*n*BuHis, **RC14**) and bis(1-*n*-butylimidazol-2-yl)methane (*n*BuBIM, **RC15**). In this series, the donor character varied (TMPD < Me_3His < nBuHis < nBuBIM) correlating to a systematic blueshift of the optical transitions due to the stronger donation and better orbital overlap of the donors [27]. Furthermore, the Cu···Cu vector and the Cu–N bond lengths diminished with better donor ability of the ligand. All these findings clearly show that the stronger the N-donor moieties are, the more blue-shifted is the absorption band of the [**O**] species and vice versa.

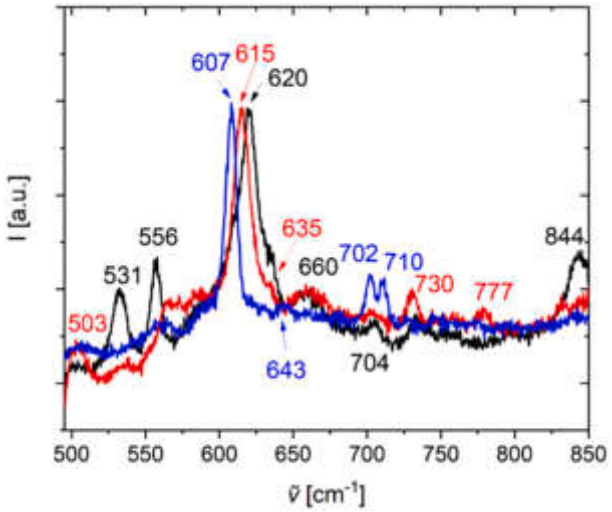

Fig. 4. Resonance Raman spectra of [**O1**]$(PF_6)_2$ (black), [**O2**]$(PF_6)_2$ (red) and [**O3**]$(PF_6)_2$ (blue) in a mixture of tetrahydrofuran/acetonitrile (80:20) at −90 °C ([**O2**]$(PF_6)_2$ and [**O3**]$(PF_6)_2$ excitation at 532 nm; [**O1**]$(PF_6)_2$ excitation at 420 nm [31]). (For interpretation of the references to color in this figure legend, the reader is referred to the web version of this article.)

Resonance Raman spectroscopic measurements provides further insights into the donor ability and the electronic situation of the Cu_2O_2 rhomb. For this purpose, resonance Raman spectra of the bis(μ-oxido) species [**O2**]$(PF_6)_2$ and [**O3**]$(PF_6)_2$ were recorded in a tetrahydrofuran/acetonitrile mixture (80:20) at −90 °C with an excitation wavelength of 532 nm (see section 2.8.2 in the Supporting Information and Figs. S49 – S51). Fig. 4 depicts the resonance Raman spectra of [**O2**]$(PF_6)_2$ and [**O3**]$(PF_6)_2$ in comparison to [**O1**]$(PF_6)_2$ (excitation at 420 nm) [31].

The resonance Raman spectra depict vibrations at 615 cm^{-1} for [**O2**]$(PF_6)_2$ and 607 cm^{-1} for [**O3**]$(PF_6)_2$, which result from the characteristic breathing Raman modes of the bis(μ-oxido) species (Fig. 4, Figs. S49 und S50). The characteristic vibration at 620 cm^{-1} of [**O1**]$(PF_6)_2$ was already reported previously (Fig. S51) [31]. A comparison of the Raman spectra reveals a slight frequency shift to smaller wavenumbers from [**O1**]$(PF_6)_2$ to [**O3**]$(PF_6)_2$ also reproduced in the calculated Raman spectra (Table S4). This shift may be due to the deformation of the Cu_2O_2 rhomb. Besides the characteristic Cu_2O_2 rhomb Raman modes, further vibrations of the aromatic backbone and the Cu–N_{amine} and Cu–N_{gua} stretching mode are observed (Fig. 4, Fig. S49 – S51, Table S4). Thus, we can evaluate the variation of the amine donor strength by the Raman mode. The Raman mode of the Cu–N_{amine} bond stretching shifts to smaller wavenumbers from [**O1**]$(PF_6)_2$ to [**O3**]$(PF_6)_2$ (Fig. 4, Table S4) in line with the weakening of the donor. A comparison of the computed Raman spectra with the experimental ones shows that Raman modes for the Cu–N_{gua} bond appear only as a combination of the Cu–N_{gua} vibration mixed with those of the aromatic system and/or Cu–N_{amine} bond.

The effect of the systematic variation of the N-donor moieties on the characteristic UV/Vis and resonance Raman features of bis(μ-oxido) dicopper(III) complexes was investigated in only few studies [19,21,22]. The ligands were explained in the UV/Vis spectra section above and discussed. Stack and Solomon found for cyclohexanamine systems **RC4-RC6** a slight frequency shift in the resonance Raman spectra (from 605 cm^{-1} to 610 cm^{-1} to 616 cm^{-1}), when both amine moieties are varied from permethylated to a hybrid version (NMe_2, NEt_2) to perethylated [19,21,22]. They attributed these small shifts in frequencies to be indicative for only the Cu_2O_2 rhomb, as they observed larger shifts hinging on small perturbations [21]. Solomon and Stack also observed a frequency shift in the Raman spectrum of the Cu—N stretching mode to smaller wavenumbers for ligands with higher steric demand [65]. Using TACN systems (**RC16-RC19**), they observed the reversed trend (Me_3TACN (OTf⁻: 604 cm^{-1}), Bz_3TACN (OTf⁻: 603, 595 cm^{-1}); Bz_3TACN

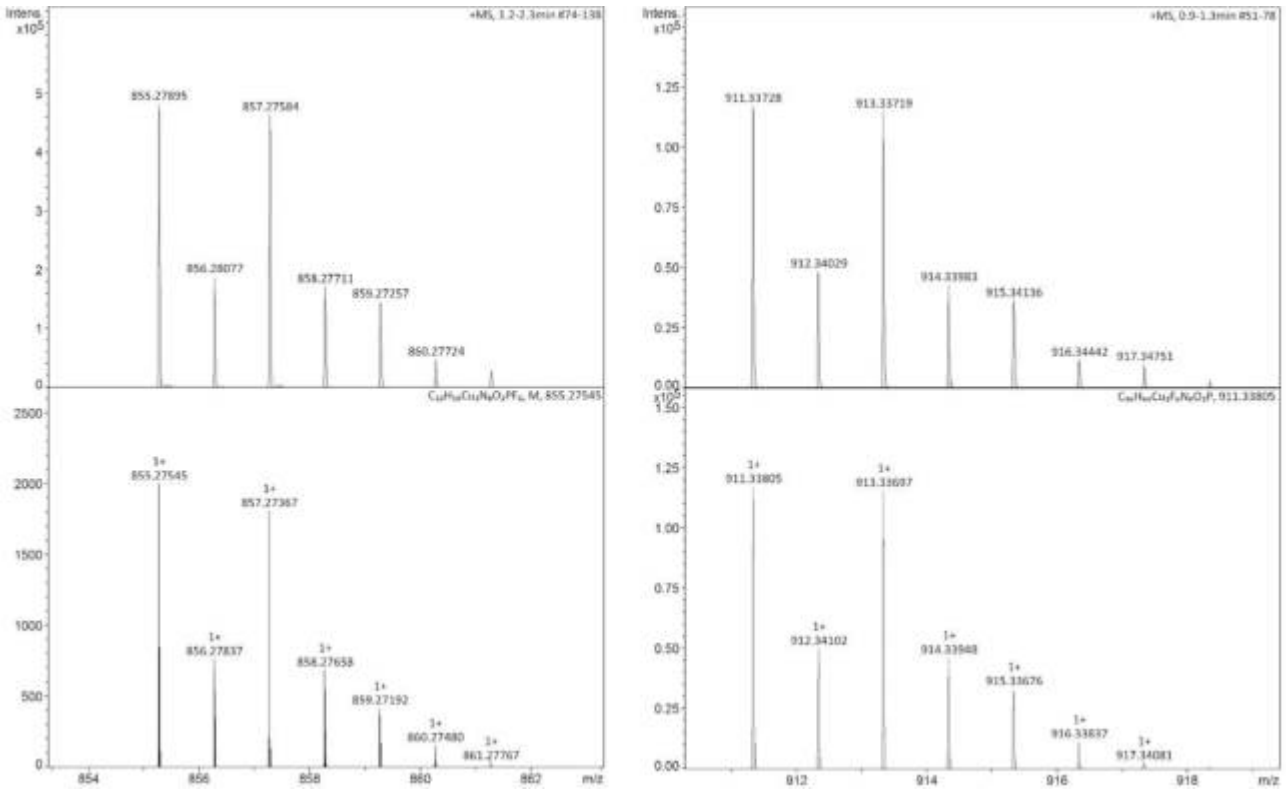

Fig. 5. Cryo-UHR-ESI mass spectrometry of [**O2**]$(PF_6)^+$ (left) and [**O3**]$(PF_6)^+$ (right) in tetrahydrofuran at −80 °C (top: experimental, bottom: calculated spectra). The isotopic pattern and corresponding m/z value revealed the mass spectrum of the monocationic species [**O2**]$(PF_6)^+$ and [**O3**]$(PF_6)^+$.

(ClO_4^-: 600 cm^{-1}), *i*PrBzTACN (ClO_4^-: 594 cm^{-1}) and *i*Pr$_3$TACN (ClO_4^-: 596 cm^{-1})), which is in accordance with our systems [13].

Cryo-UHR-ESI measurements were performed to determine the Cu—O_2 stoichiometry of the bis(μ-oxido) species [**O2**]$^{2+}$ and [**O3**]$^{2+}$ (Fig. 5, Fig. S34 – S39). The isotopic pattern and respective *m/z* value agree well with the calculated spectra of the monocationic compound [**O2**]$(PF_6)^+$ and [**O3**]$(PF_6)^+$, revealing a Cu—O_2 ratio of 2:1. Similarly, the monocationic species [**O2**]$(BF_4)^+$ and [**O2**]$(OTf)^+$ as well as [**O3**]$(BF_4)^+$ and [**O3**]$(OTf)^+$ were observed (see section 2.8.3 in the Supporting Information). It is noteworthy that the formation of bischelate complex $[Cu(L)_2]^+$ (as observed in ref. [34] for **L1**) using ligands **L2** or **L3** was observed in neither case, which resulted from a small increase of the steric demand of the ligand system.

3.3. Catalytic oxygenation reactions

The hybrid guanidine ligand TMGbenza (**L1**) has already shown its support in catalytic oxygenation reactions of a library of polycyclic aromatic alcohols [31], revealing a beneficial interplay of the strong N-donor features of the guanidine moiety, which is sterically demanding, and the space-saving weaker amine donor function with regard to the substrate accessibility of the reactive bis(μ-oxido) core. The modification of the amine donor moiety from NMe_2 to NEt_2 to N*i*Pr_2 enhances the steric demand of the ligand shielding the bis(μ-oxido) core. Therefore, the catalytic activity of bis(μ-oxido) complexes [**O2**]$(PF_6)_2$ and [**O3**]$(PF_6)_2$ was investigated towards polycyclic aromatic alcohols, evaluating the influence of the increased steric encumbrance on the substrate accessibility of the Cu_2O_2 core. The results are then compared to the related hybrid guanidine-stabilized system [**O1**]$(PF_6)_2$ [31] (Table 8). Phenolic substrates were transformed into its quinone form in a tyrosinase-like fashion and subsequently converted with 1,2-phenylenediamine in a one-pot reaction to form stable phenazines [97]. Oxygenation reactions were performed following a modified protocol established by Bulkowski [98] and refined by Tuczek and co-workers [41]. The catalyst concentration was referred to the quantitative formation of the bis(μ-oxido) complex and adapted from our study on [**O1**]$(PF_6)_2$ [31]. Two equivalents of the auxiliary base triethylamine were added to the reaction to deprotonate the substrate molecule. Molecular sieve (3 Å) was used to capture produced water molecules in order to prevent catalyst decomposition. Oxygenation experiments mediated by [**O2**]$(PF_6)_2$ and [**O3**]$(PF_6)_2$ were conducted by using 2-naphthol and 6-quinolinol, which both offer two quinone product possibilities to analyze the selectivity of the reaction. The position of the hydroxylation was anticipated earlier by DFT calculations, revealing a large value of the negative Fukui function and therefore predicting the formation of exclusively bent phenazines [31].

The oxygenation reactions were conducted upon different reaction temperatures for [**O2**]$(PF_6)_2$ and [**O3**]$(PF_6)_2$, which results from the stability of the catalysts. Therefore, the respective reaction time needed to achieve full conversion was adapted. Whereas 2-naphthol was converted by [**O2**]$(PF_6)_2$ within two hours at −100 °C at 82% (entry 2), a small loss in conversion to 78% was observed by using [**O3**]$(PF_6)_2$ (entry 3), which relates to the higher steric demand of the isopropyl groups compared to the ethyl groups, seemingly decreasing the reaction rate of substrate conversion. This is in line with the isolated yield of benzo[*a*]phenazine (**P1**). In comparison, catalyst [**O1**]$(PF_6)_2$ achieved a slightly

Table 8
Catalytic oxygenation of polycyclic aromatic alcohols mediated by a bis(μ-oxido) species and subsequent condensation of the quinone by using 1,2-phenylenediamine to generate phenazines.

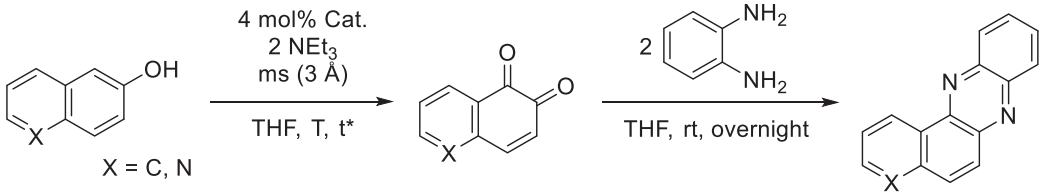

Entry	Cat.	Substrate	T [°C]	t* [h]	Conv.[a] [%]	Product P	Yield[b] [%]
1	[**O1**]$(PF_6)_2$	2-naphthol	-90	1	89	(**P1**)	31 [31]
2	[**O2**]$(PF_6)_2$	2-naphthol	-100	2	82	(**P1**)	28
3	[**O3**]$(PF_6)_2$	2-naphthol	-100	2	78	(**P1**)	23
4	[**O1**]$(PF_6)_2$	6-quinolinol	-90	1	> 99	(**P2**)	30 [31]
5	[**O2**]$(PF_6)_2$	6-quinolinol	-100	3	95	(**P2**)	31
6	[**O3**]$(PF_6)_2$	6-quinolinol	-100	3	> 99	(**P2**)	28

[a] Determined conversion of the substrate by ^{1}H NMR spectroscopy. [b] Isolated yield of the phenazine after column chromatography.

higher substrate conversion in only one hour at −90 °C (entry 1), leading to a greater amount of **P1** [31]. 6-quinolinol was transformed quantitatively by both catalysts [**O2**](PF$_6$)$_2$ and [**O3**](PF$_6$)$_2$ (entries 5–6), which is similar to the reaction with [**O1**](PF$_6$)$_2$ (entry 4). Pyrido[3,2-*a*] phenazine (**P2**) was isolated in 28–31% yield. All three catalysts depicted a high selectivity during the hydroxylation reactions of 2-naphthol and 6-quinolinol, forming exclusively the bent phenazines as predicted previously by theoretical investigations using the Fukui function [31]. Therefore, the steric influence of the modified amine donor moiety of the bis(μ-oxido) complex on the selectivity of the reaction can be neglected. The reactive Cu_2O_2 core was sufficiently accessible to the substrates despite the higher steric encumbrance of the stabilizing ligand system.

4. Conclusion

In summary, we designed new aromatic hybrid guanidine ligands with varied amine donor moiety, which exclusively formed monochelate copper(I) complexes due to the increased steric demand of the ligand system, thus eliminating a predominant equilibrium between monochelate and bischelate copper(I) complex. Oxygenation of the copper(I) complexes allowed the formation of the corresponding bis(μ-oxido) complexes in the presence of different weakly-coordinating anions, which were characterized by UV/Vis and resonance Raman spectroscopy, cryo-UHR-ESI mass spectrometry and DFT calculations. The smaller donor strength of the amine donor moiety and the enlarged steric demand of the alkyl substituents from NMe_2 to NEt_2 to $NiPr_2$ lead to a higher twist between the Cu_2O_2 core and the CuN_2 plane and a stretching of the Cu_2O_2 rhomb. All these effects result in a poorer orbital overlap, causing a redshift of the LMCT features of the bis(μ-oxido) species.

Although the bis(μ-oxido) complexes required a lower formation temperature of −100 °C, they showed high activity in oxygenation catalysis towards challenging substrates including 2-naphthol and 6-quinolinol, proposing again the bis(μ-oxido) core as catalytically active species. The higher steric demand of the alkyl groups of the supporting ligand system revealed a marginal influence on the substrate conversion. Nevertheless, increasing the shielding of the reactive Cu_2O_2 core had no measurable impact on the selectivity of the hydroxylation reaction. Thus, such small structural modifications help to move a step closer to ultimately understand the mechanisms behind structure design and catalytic reactivity.

Authors statement

Melanie Paul: Conceptualization, Synthetic and UV/Vis spectroscopic and MS spectrometric investigations, Writing, Data curation.

Melissa Teubner: Raman investigation, Writing.

Benjamin Grimm-Lebsanft: Raman investigation, Writing.

Sören Buchenau: Raman investigation.

Alexander Hoffmann: Conceptualization, DFT investigation, formal analysis, Writing, Data curation'

Michael Rübhausen: Supervision, formal analysis.

Sonja Herres-Pawlis: Conceptualization, Writing, Supervision.

Declaration of Competing Interest

The authors declare that they have no known competing financial interests or personal relationships that could have appeared to influence the work reported in this paper.

Electronic supplementary material The online version of this article (doi:https://doi.org/10.1016/j.jinorgbio.2021.XXX) contains supplementary material, which is available to authorized users.

Acknowledgements

The authors gratefully acknowledge financial support provided by the German Research Foundation (DFG), in framework of the Priority Program "Reactive Bubbly Flows" SPP 1740 (HE 5480/10-2, http://www.dfg-spp1740.de/), and further projects (RU 773/8-1). This work was also funded by the Bundesministerium für Bildung und Forschung (BMBF, project 05K19GU5). We furthermore thank the Regional Computing Center of the University of Cologne (RRZK) for providing computing time on the DFG-funded High-Performance Computing (HPC) system CHEOPS as well as support and the Paderborn Center for Parallel Computing, PC^2, for providing computing time on the High-Performance Computing (HPC) system OCuLUS as well as support.

Appendix A. Supplementary data

Supplementary data to this article can be found online at https://doi.org/10.1016/j.jinorgbio.2021.111541.

References

[1] A.N. Campbell, S.S. Stahl, Acc. Chem. Res. 45 (2012) 851–863.
[2] S.D. McCann, S.S. Stahl, Acc. Chem. Res. 48 (2015) 1756–1766.
[3] T. Dalton, T. Faber, F. Glorius, ACS Cent. Sci. 7 (2021) 245–261.
[4] E.I. Solomon, D.E. Heppner, E.M. Johnston, J.W. Ginsbach, J. Cirera, M. Qayyum, M.T. Kieber-Emmons, C.H. Kjaergaard, R.G. Hadt, L. Tian, Chem. Rev. 114 (2014) 3659–3853.
[5] C.E. Elwell, N.L. Gagnon, B.D. Neisen, D. Dhar, A.D. Spaeth, G.M. Yee, W. B. Tolman, Chem. Rev. 117 (2017) 2059–2107.
[6] Y. Matoba, T. Kumagai, A. Yamamoto, H. Yoshitsu, M. Sugiyama, J. Biol. Chem. 281 (2006) 8981–8990.
[7] A. Bijelic, M. Pretzler, C. Molitor, F. Zekiri, A. Rompel, Angew. Chem. Int. Ed. 54 (2015) 14677–14680.
[8] V. Kahn, N. Ben-Shalom, Pigment Cell Res. 11 (1998) 24–33.
[9] M. Garcia-Molina, J.L. Muñoz-Muñoz, F. Garcia-Molina, P.A. García-Ruiz, F. Garcia-Canovas, J. Agric. Food Chem. 60 (2012) 6447–6453.
[10] T.A.G. Large, V. Mahadevan, W. Keown, T.D.P. Stack, Inorg. Chim. Acta 486 (2019) 782–792.
[11] L. Chiang, E.C. Wasinger, Y. Shimazaki, V. Young, T. Storr, T.D.P. Stack, Inorg. Chim. Acta 481 (2018) 151–158.
[12] D.A. Quist, D.E. Diaz, J.J. Liu, K.D. Karlin, J. Biol. Inorg. Chem. 22 (2017) 253–288.
[13] L.M. Mirica, X. Ottenwaelder, T.D.P. Stack, Chem. Rev. 104 (2004) 1013–1046.
[14] E.A. Lewis, W.B. Tolman, Chem. Rev. 104 (2004) 1047–1076.
[15] J.N. Hamann, B. Herzigkeit, R. Jurgeleit, F. Tuczek, Coord. Chem. Rev. 334 (2017) 54–66.
[16] P. Liebhäuser, A. Hoffmann, S. Herres-Pawlis, Ref. Modul. Chem. Mol. Sci, Chem. Eng. (2019) 1–22.
[17] M. Rolff, J. Schottenheim, H. Decker, F. Tuczek, Chem. Soc. Rev. 40 (2011) 4077–4098.
[18] C.J. Cramer, B.A. Smith, W.B. Tolman, J. Am. Chem. Soc. 118 (1996) 11283–11287.
[19] V. Mahadevan, Z. Hou, A.P. Cole, D.E. Root, T.K. Lal, E.I. Solomon, T.D.P. Stack, J. Am. Chem. Soc. 119 (1997) 11996–11997.
[20] S. Mahapatra, J.A. Halfen, W.B. Tolman, J. Am. Chem. Soc. 118 (1996) 11575–11586.
[21] M.J. Henson, P. Mukherjee, D.E. Root, T.D.P. Stack, E.I. Solomon, J. Am. Chem. Soc. 121 (1999) 10332–10345.
[22] A.P. Cole, V. Mahadevan, L.M. Mirica, X. Ottenwaelder, T.D.P. Stack, Inorg. Chem. 44 (2005) 7345–7364.
[23] P. Kang, E. Bobyr, J. Dustman, K.O. Hodgson, B. Hedman, E.I. Solomon, T.D. P. Stack, Inorg. Chem. 49 (2010) 11030–11038.
[24] C. Citek, B.-L. Lin, T.E. Phelps, E.C. Wasinger, T.D.P. Stack, J. Am. Chem. Soc. 136 (2014) 14405–14408.
[25] C. Citek, J.B. Gary, E.C. Wasinger, T.D.P. Stack, J. Am. Chem. Soc. 137 (2015) 6991–6994.
[26] C. Citek, S. Herres-Pawlis, T.D.P. Stack, Acc. Chem. Res. 48 (2015) 2424–2433.
[27] W. Keown, T.A.G. Large, L. Chiang, E.C. Wasinger, T.D.P. Stack, Chem. Commun. 55 (2019) 7390–7393.
[28] S. Herres-Pawlis, P. Verma, R. Haase, P. Kang, C.T. Lyons, E.C. Wasinger, U. Flörke, G. Henkel, T.D.P. Stack, J. Am. Chem. Soc. 131 (2009) 1154–1169.
[29] S. Herres-Pawlis, R. Haase, P. Verma, A. Hoffmann, P. Kang, T.D.P. Stack, Eur. J. Inorg. Chem. (2015) 5426–5436.
[30] F. Strassl, B. Grimm-Lebsanft, D. Rukser, F. Biebl, M. Biednov, C. Brett, R. Timmermann, F. Metz, A. Hoffmann, M. Rübhausen, S. Herres-Pawlis, Eur. J, Inorg. Chem. (2017) 3350–3359.
[31] M. Paul, M. Teubner, B. Grimm-Lebsanft, C. Golchert, Y. Meiners, L. Senft, K. Keisers, P. Liebhäuser, T. Rösener, F. Biebl, S. Buchenau, M. Naumova, V. Murzin, R. Krug, A. Hoffmann, J. Pietruszka, I. Ivanović-Burmazović, M. Rübhausen, S. Herres-Pawlis, Chem. Eur. J. 26 (2020) 7556–7562.

[32] S. Herres-Pawlis, U. Flörke, G. Henkel, Eur. J. Inorg. Chem. (2005) 3815–3824.
[33] R. Trammell, K. Rajabimoghadam, I. Garcia-Bosch, Chem. Rev. 119 (2019) 2954–3031.
[34] M. Paul, A. Hoffmann, S. Herres-Pawlis, J. Biol. Inorg. Chem. 26 (2021) 249–263.
[35] F. Strassl, A. Hoffmann, B. Grimm-Lebsanft, D. Rukser, F. Biebl, M. Tran, F. Metz, M. Rübhausen, S. Herres-Pawlis, Inorganics 6 (2018) 114–136.
[36] M. Réglier, C. Jorand, B. Waegell, J. Chem. Soc. Chem. Commun. (1990) 1752–1755.
[37] L. Casella, M. Gullotti, R. Radaelli, P. Di Gennaro, J. Chem. Soc.,Chem. Commun. (1991) 1611–1612.
[38] K.V.N. Esguerra, Y. Fall, J.P. Lumb, Angew. Chem. Int. Ed. 53 (2014) 5877–5881.
[39] M.S. Askari, L.A. Rodríguez-Solano, A. Proppe, B. McAllister, J.-P. Lumb, X. Ottenwaelder, Dalton Trans. 44 (2015) 12094–12097.
[40] Z. Huang, O. Kwon, H. Huang, A. Fadli, X. Marat, M. Moreau, J.P. Lumb, Angew. Chem. Int. Ed. 57 (2018) 11963–11967.
[41] M. Rolff, J. Schottenheim, G. Peters, F. Tuczek, Angew. Chem. Int. Ed. 49 (2010) 6438–6442.
[42] J.N. Hamann, F. Tuczek, Chem. Commun. 50 (2014) 2298–2300.
[43] J. Schottenheim, C. Gernert, B. Herzigkeit, J. Krahmer, F. Tuczek, Eur. J. Inorg. Chem. (2015) 3501–3511.
[44] B. Herzigkeit, B.M. Flöser, N.E. Meißner, T.A. Engesser, F. Tuczek, ChemCatChem 10 (2018) 5402–5405.
[45] B. Herzigkeit, B.M. Flöser, T.A. Engesser, C. Näther, F. Tuczek, Eur. J. Inorg. Chem. (2018) 3058–3069.
[46] B. Herzigkeit, R. Jurgeleit, B.M. Flöser, N.E. Meißner, T.A. Engesser, C. Näther, F. Tuczek, Eur. J. Inorg. Chem. (2019) 2258–2266.
[47] A. Hoffmann, C. Citek, S. Binder, A. Goos, M. Rübhausen, O. Troeppner, I. Ivanović-Burmazović, E.C. Wasinger, T.D.P. Stack, S. Herres-Pawlis, Angew. Chem. Int. Ed. 52 (2013) 5398–5401.
[48] C. Wilfer, P. Liebhäuser, A. Hoffmann, H. Erdmann, O. Grossmann, L. Runtsch, E. Paffenholz, R. Schepper, R. Dick, M. Bauer, M. Dürr, I. Ivanovic-Burmazovic, S. Herres-Pawlis, Chem. Eur. J. 21 (2015) 17639–17649.
[49] C. Wilfer, P. Liebhäuser, H. Erdmann, A. Hoffmann, S. Herres-Pawlis, Eur. J. Inorg. Chem. (2015) 494–502.
[50] P. Liebhäuser, K. Keisers, A. Hoffmann, T. Schnappinger, I. Sommer, A. Thoma, C. Wilfer, R. Schoch, K. Stührenberg, M. Bauer, M. Dürr, I. Ivanović-Burmazović, S. Herres-Pawlis, Chem. Eur. J. 23 (2017) 12171–12183.
[51] S. Herres, A.J. Heuwing, U. Flörke, J. Schneider, G. Henkel, Inorg. Chim. Acta 358 (2005) 1089–1095.
[52] M. Wern, J. Ortmeyer, P. Josephs, T. Schneider, A. Neuba, G. Henkel, S. Schindler, Inorg. Chim. Acta 481 (2018) 171–175.
[53] C. Würtele, E. Gaoutchenova, K. Harms, M.C. Holthausen, J. Sundermeyer, S. Schindler, Angew. Chem. Int. Ed. 45 (2006) 3867–3869.
[54] S. Herres-Pawlis, S. Binder, A. Eich, R. Haase, B. Schulz, G. Wellenreuther, G. Henkel, M. Rübhausen, W. Meyer-Klaucke, Chem. Eur. J. 15 (2009) 8678–8682.
[55] A. Hoffmann, M. Wern, T. Hoppe, M. Witte, R. Haase, P. Liebhäuser, J. Glatthaar, S. Herres-Pawlis, S. Schindler, Eur. J. Inorg. Chem. (2016) 4744–4751.
[56] M. Schatz, V. Raab, S.P. Foxon, G. Brehm, S. Schneider, M. Reiher, M. C. Holthausen, J. Sundermeyer, S. Schindler, Angew. Chem. Int. Ed. 43 (2004) 4360–4363.
[57] D. Maiti, D.-H. Lee, K. Gaoutchenova, C. Würtele, M.C. Holthausen, A.A. Narducci Sarjeant, J. Sundermeyer, S. Schindler, K.D. Karlin, Angew. Chem. Int. Ed. 47 (2008) 82–85.
[58] M. Paul, F. Strassl, A. Hoffmann, M. Hoffmann, M. Schlüter, S. Herres-Pawlis, Eur. J, Inorg. Chem. (2018) 2101–2124.
[59] B. Cross, C.L. Dunn, D.H. Payne, J.D. Tipton, J. Sci. Food Agric. 20 (1969) 340–344.
[60] N. Guttenberger, W. Blankenfeldt, R. Breinbauer, Bioorg. Med. Chem. 25 (2017) 6149–6166.
[61] V.F. de Andrade-Neto, M.O.F. Goulart, J.F. da Silva Filho, M.J. da Silva, M. do Carmo, F.R. Pinto, A.V. Pinto, M.G. Zalis, L.H. Carvalho, A.U. Krettli, Bioorg. Med. Chem. Lett. 14 (2004) 1145–1149.
[62] F.B. Mortzfeld, J. Pietruszka, I.R. Baxendale, Eur. J. Org. Chem. (2019) 5424–5433.
[63] A. Chaudhary, J.M. Khurana, Res. Chem. Intermed. 44 (2018) 1045–1083.
[64] Y. Xiao, W. Hu, S. Sun, J.-T. Yu, J. Cheng Synlett 30 (2019) 2113–2122.
[65] M. Bilal, S. Guo, H.M.N. Iqbal, H. Hu, W. Wang, X. Zhang, World J. Microbiol. Biotechnol. 33 (2017) 191.
[66] A. Cimmino, A. Evidente, V. Mathieu, A. Andolfi, F. Lefranc, A. Kornienko, R. Kiss, Nat. Prod. Rep. 29 (2012) 487–501.
[67] G.J. Kubas, B. Monzyk, A.L. Crumbliss, Inorg. Synth. 19 (1979) 90–92.
[68] V. Raab, J. Kipke, R.M. Gschwind, J. Sundermeyer, Chem. Eur. J. 8 (2002) 1682–1693.
[69] W. Kantlehner, E. Haug, W.W. Mergen, P. Speh, T. Maier, J.J. Kapassakalidis, H.-J. Bräuner, H. Hagen, Liebigs Ann. Chem. (1984) 108–126.
[70] S. Herres-Pawlis, A. Neuba, O. Seewald, T. Seshadri, H. Egold, U. Flörke, G. Henkel, Eur. J. Org. Chem. (2005) 4879–4890.
[71] B. Schulz, J. Bäckström, D. Budelmann, R. Maeser, M. Rübhausen, M.V. Klein, E. Schoeffel, A. Mihill, S. Yoon, Rev. Sci. Instrum. 76 (2005), 073107–1–073107–12.
[72] B. Grimm-Lebsanft, C. Brett, F. Strassl, D. Rukser, M. Biednov, F. Biebl, M. Naumova, A. Hoffmann, L. Akinsinde, D. Brückner, S. Herres-Pawlis, M. Rübhausen, Inorg. Chim. Acta 481 (2018) 176–180.
[73] M.J. Frisch, G.W. Trucks, H.B. Schlegel, G.E. Scuseria, M.A. Robb, J.R. Cheeseman, G. Scalmani, V. Barone, G.A. Petersson, H. Nakatsuji, X. Li, M. Caricato, A. V. Marenich, J. Bloino, B.G. Janesko, R. Gomperts, B. Mennucci, H.P. Hratchian, J. V. Ortiz, A.F. Izmaylov, J.L. Sonnenberg, D. Williams-Young, F. Ding, F. Lipparini, F. Egidi, J. Goings, B. Peng, A. Petrone, T. Henderson, D. Ranasinghe, V. G. Zakrzewski, J. Gao, N. Rega, G. Zheng, W. Liang, M. Hada, M. Ehara, K. Toyota, R. Fukuda, J. Hasegawa, M. Ishida, T. Nakajima, Y. Honda, O. Kitao, H. Nakai, T. Vreven, K. Throssell, J.A. Montgomery Jr., J.E. Peralta, F. Ogliaro, M. J. Bearpark, J.J. Heyd, E.N. Brothers, K.N. Kudin, V.N. Staroverov, T.A. Keith, R. Kobayashi, J. Normand, K. Raghavachari, A.P. Rendell, J.C. Burant, S.S. Iyengar, J. Tomasi, M. Cossi, J.M. Millam, M. Klene, C. Adamo, R. Cammi, J.W. Ochterski, R.L. Martin, K. Morokuma, O. Farkas, J.B. Foresman, D.J. Fox, Gaussian Inc., Gaussian 16, Revision B.01, 2016. Wallingford, CT.
[74] J. Tao, J.P. Perdew, V.N. Staroverov, G.E. Scuseria, Phys. Rev. Lett. 91 (2003), 146401–1–146401–4.
[75] V.N. Staroverov, G.E. Scuseria, J. Tao, J.P. Perdew, J. Chem. Phys. 119 (2003) 12129–12137.
[76] V.N. Staroverov, G.E. Scuseria, J. Tao, J.P. Perdew, J. Chem. Phys. 121 (2004) 11507.
[77] F. Weigend, R. Ahlrichs, Phys. Chem. Chem. Phys. 7 (2005) 3297–3305.
[78] A. Schäfer, C. Huber, R. Ahlrichs, J. Chem. Phys. 100 (1994) 5829–5835.
[79] K. Eichkorn, F. Weigend, O. Treutler, R. Ahlrichs, Theor. Chem. Accounts Theory, Comput. Model 97 (1997) 119–124.
[80] F. Weigend, M. Häser, H. Patzelt, R. Ahlrichs, Chem. Phys. Lett. 294 (1998) 143–152.
[81] S. Grimme, S. Ehrlich, L. Goerigk, J. Comput. Chem. 32 (2011) 1456–1465.
[82] L. Goerigk, S. Grimme, Phys. Chem. Chem. Phys. 13 (2011) 6670–6688.
[83] For TPSSh, the values of the original paper have been substituted by the corrected values kindly provided by S. Grimme as private communication and published in [84].
[84] A. Hoffmann, R. Grunzke, S. Herres-Pawlis, J. Comput. Chem. 35 (2014) 1943–1950.
[85] E.D. Glendening, C.R. Landis, F. Weinhold, J. Comput. Chem. 40 (2019) 2234–2241.
[86] F. Weinhold, C. Landis, Valency and bonding – a natural bond orbital donor–acceptor perspective, Cambridge university press, 2005. N. Y.
[87] E. D. Glendening, J. K. Badenhoop, A. E. Reed, J. E. Carpenter, J. A. Bohmann, C. M. Morales, P. Karafiloglou, C. R. Landis, F. Weinhold, Theoretical Chemistry Institute, NBO 7.0., University of Wisconsin (2018), Madison, WI.
[88] M.V. Barybin, P.L. Diaconescu, C.C. Cummins, Inorg. Chem. 40 (2001) 2892–2897.
[89] J. Huang, Y. Xu, X. Qian, Dalton Trans. (2009) 1761–1766.
[90] A. Metz, R. Plothe, B. Glowacki, A. Koszalkowski, M. Scheckenbach, A. Beringer, T. Rösener, J. Michaelis de Vasconcellos, R. Haase, U. Flörke, A. Hoffmann, S. Herres-Pawlis, Eur. J. Inorg. Chem. (2016) 4974–4987.
[91] M. Rohrmüller, S. Herres-Pawlis, M. Witte, W.G. Schmidt, J. Comput. Chem. 34 (2013) 1035–1045.
[92] M. Rohrmüller, A. Hoffmann, C. Thierfelder, S. Herres-Pawlis, W.G. Schmidt, J. Comput. Chem. 36 (2015) 1672–1685.
[93] A. Hoffmann, S. Herres-Pawlis, Phys. Chem. Chem. Phys. 18 (2016) 6430–6440.
[94] A. Hoffmann, J. Stanek, B. Dicke, L. Peters, B. Grimm-Lebsanft, A. Wetzel, A. Jesser, M. Bauer, M. Gnida, W. Meyer-Klaucke, M. Rübhausen, S. Herres-Pawlis, Eur. J. Inorg. Chem. (2016) 4731–4743.
[95] R.L. Martin, J. Chem. Phys. 118 (2003) 4775–4777.
[96] B. Grimm-Lebsanft, M. Teubner, M. Paul, S. Buchenau, A. Hoffmann, S. Herres-Pawlis, M.A. Rübhausen, (2021) manuscript in preparation.
[97] J.N. Hamann, M. Rolff, F. Tuczek, Dalton Trans. 44 (2015) 3251–3258.
[98] J. E. Bulkowski, Binucleating Ligand-Metal Complexes as Oxidation Catalysts (1985), US Patent 4,545,937.

4.5 Manipulating the Electron Transfer - The Influence of Substituents on Novel Copper Guanidine Quinoline Complexes

The author has contributed to the XAS measurements and the respective data analysis.

The similarity of the Cu^{I} and Cu^{II} state in copper guanidine quinoline complexes renders these model complexes as suitable candidates for the investigation of the entatic state. In [4.5], differently modified quinoline ligands were used to test the effect they have on the entatic state in the complex. The modification addresses either the electronic or steric interaction. The study was conducted with theoretical DFT calculations, Marcus theory, XRD and XAS experiments and revealed that the substitution at the 2-position of the quinoline unit leads to better entatic state model complexes. The XANES analysis of the XAS data allowed for a identification of the correct oxidation state, whereas the EXAFS analysis gave the empirical values of the bond lengths and angles, which is necessary to investigate the structure-function relationship of the entatic state model complexes.

The first concepts of the entatic state referred to the protein matrix as a rigid framework [45] as proposed by B. L. Vallee and R. Williams. It was softened up by adding some flexibility by B. G. Malmström et al. in 1989 [121] in the induced-rack theory. To the mostly geometric understanding of the entatic state, D. Rorabacher added in 2007 [46] electronic influences and now a modern interpretation of the entatic state is the *entasis as the energetization of the reactants and products due to the adverse interaction between the protein or ligands and the metal ion* as given e.g. by P. Comba [122]. Although the microscopic theory is constantly evolving, the basic principle of the entatic state is, that the energetization lowers the activation barrier for reaction and by that increases its speed. The electron-transfer rate k_{11} can be used as a proxy for the scale of the speed of the electron-transfer. D. M. Stanbury [123] reported on slow electron self-exchange rates of 0.02-0.5 $M^{-1}s^{-1}$, the copper guanidine quinoline complexes by S. Herres-Pawlis have an electron self-exchange rate of 100-1 000 $M^{-1}s^{-1}$ [53–55, 124] and D. Rorabacher [46] and N. K. Szymczak [125] report values of 100 000 and 240 000 $M^{-1}s^{-1}$, respectively. The copper complexes in [4.5] are distorted by their ligands to strongly deviate from the preferred geometry. Cu^{I} prefers an ideal tetrahedral and Cu^{II} an ideal square-planar geometry. Based on DFT and XAS derived data on the bond lengths and angles, a structure factor τ_4 can be calculated. It is defined so that a value of zero corresponds to ideal square-planar and a value of one to ideal tetrahedral. [48] All ligands **L2-L6** are modified versions of **L1** with substitutions in the 2- or 4-position, as shown in [4.5]-Scheme 1, to investigate the influence of the electron-transfer in respect to the entatic state. **L2-L4** are substituted to influence the steric demand, **L5** is substituted to influence the steric demand and the donor properties of the ligand and **L6** is substituted to influence the donor properties. Except for **L3**, combining the ligands with the Cu^{I} and Cu^{II} salts leads to the formation of the respective copper complexes, where **L2**→**C3/4**, **L4**→**C5/6**, **L5**→**C7/8** and **L6**→**C9/10**. The aliphatic substitutions for **C3/4**-**C5/6** at the 2-position did show structurally more similar $Cu^{I/II}$ complex pairs as compared to the non-substituted **C1/2**. The best results for the investigation of this steric effect yielded a difference in structure parameter by $\Delta\tau_4 = 0.06$ by **C5/6**. Electron-transfer studies did reveal a higher electron self-exchange rate for the pairs **C3/4** and **C5/6** as compared to non-substituted **C1/2**. However, the **C5/6** pair had a smaller value as compared to the **C3/4** pair. This is explained with the fact that $\Delta\tau_4$ is small for both

pairs, but the average structure factor $\varnothing\tau_4$ is closer to the central value of 0.5 in between tetrahedral and square-planar for the **C3/4** pair. Further DFT calculations also showed that **C5/6** has a lower reorganization energy than **C3/4**, which underlines again that not only the similarity plays a role for the electron self-exchange rate, but rather that the average structure should not favor on or the other oxidation state.

Cu-O binding motifs, bond lengths and angles are measured by XAS. The XANES analysis of the XAS data yields the oxidation state of the complexes, whereas the EXAFS analysis yields the bond lengths and angles shown in the tables, which are the foundation of the structure parameter calculations and the analysis of the effect of the geometry on the entasis.

X-ray absorption spectroscopy (XAS) data were collected in the absorption mode using two ionization chambers at the beamline P65 (DESY, PETRA III, Hamburg, Germany).[101] The complexes were prepared in a glovebox under inert conditions (oxygen and water free) with a concentration of 15 mM and transferred to a custom-made PEEK cuvette with septum and Kapton (polyimide foil, *DuPont*) windows, which were sealed by a teflon O-ring. The cuvette was cooled to -30 °C to prevent sample damage and improve the data quality. The measurements were conducted in a continuous flow helium cryostat Optistat CF (Oxford Instruments, UK). The measurement time for a complete scan from 8828 eV to 9978 eV was 300 s. In total, the samples were measured up to 60 min. Copper foil was measured simultaneously and the first inflection point energy was set to 8979.0 eV and all measurements were calibrated to this shift afterwards. Data processing and analysis were done with Athena and Artemis.[103] The XANES data are shown in the top column in [4.5]-Fig. 4. The Cu^{I} complexes show the characteristic 1s→4p transition[126] as a strong peak at 8982 eV and 8985 eV and the Cu^{II} complexes show the characteristic 1s→3d transition as a smaller feature between 8977 eV and 8978 eV.[127] The EXAFS data are shown exemplary in the bottom column in [4.5]-Fig. 4 and in the supporting information in Fig. S1-S8 and Tab. S2-S9.

Manipulating the Electron Transfer - The Influence of Substituents on Novel Copper Guanidine Quinoline Complexes

Chemical Science

ROYAL SOCIETY OF CHEMISTRY

EDGE ARTICLE

View Article Online
View Journal

Cite this: DOI: 10.1039/d2sc02910c

All publication charges for this article have been paid for by the Royal Society of Chemistry

Manipulating electron transfer – the influence of substituents on novel copper guanidine quinolinyl complexes†‡

Joshua Heck, [a] Fabian Metz,[a] Sören Buchenau, [b] Melissa Teubner,[ab] Benjamin Grimm-Lebsanft, [b] Thomas P. Spaniol, [a] Alexander Hoffmann, [a] Michael A. Rübhausen[b] and Sonja Herres-Pawlis *[a]

Copper guanidine quinolinyl complexes act as good entatic state models due to their distorted structures leading to a high similarity between Cu(I) and Cu(II) complexes. For a better understanding of the entatic state principle regarding electron transfer a series of guanidine quinolinyl ligands with different substituents in the 2- and 4-position were synthesized to examine the influence on the electron transfer properties of the corresponding copper complexes. Substituents with different steric or electronic influences were chosen. The effects on the properties of the copper complexes were studied applying different experimental and theoretical methods. The molecular structures of the bis(chelate) copper complexes were examined in the solid state by single-crystal X-ray diffraction and in solution by X-ray absorption spectroscopy and density functional theory (DFT) calculations revealing a significant impact of the substituents on the complex structures. For a better insight natural bond orbital (NBO) calculations of the ligands and copper complexes were performed. The electron transfer was analysed by the determination of the electron self-exchange rates following Marcus theory. The obtained results were correlated with the results of the structural analysis of the complexes and of the NBO calculations. Nelsen's four-point method calculations give a deeper understanding of the thermodynamic properties of the electron transfer. These studies reveal a significant impact of the substituents on the properties of the copper complexes.

Received 24th May 2022
Accepted 11th June 2022

DOI: 10.1039/d2sc02910c

rsc.li/chemical-science

Introduction

Copper proteins play an essential role in biological processes of all living organisms since they are responsible for a fast and reversible electron transfer.[1] One group is the type 1 or blue copper proteins that have a mononuclear copper center, *e.g.* plastocyanin. The copper is coordinated by two nitrogen donors of histidine and two sulfur donors of methionine and cysteine.[2] Copper proteins exhibit very high electron self-exchange rates k_{11} which are a scale for the speed of the electron transfer. For these proteins the electron self-exchange rates range from 10^3 to 10^8 M^{-1} s^{-1}.[3–6] This is explained by the entatic state concept which is adaptable for different transition metal enzymes.[7–11] The exact effectiveness of the entatic state has been discussed intensively in the past and different explanations have been proposed.[9,12] In 1968, the term "entatic state" was introduced by Vallee and Williams. In their theory the protein possesses a rigid framework that does not fit the preferred geometry of the bound metal ions or the cofactor. This leads to an energization of the protein's units but not of the rigid framework.[11,13] Another explanation for the entatic state was suggested by Malmström with the induced-rack theory.[5,6,14] In contrast to the theory of Vallee and Williams the protein framework exhibits some flexibility leading in the ideal case to two different structures. One structure is energetically favored by the protein framework, but the coordination geometry of the metal ion is strained by the protein framework, which is energetically unfavored by the metal ion. In the second structure the coordination geometry is less strained which is energetically favored by the metal ion but energetically unfavored by the protein framework. Rorabacher *et al.* proposed that the entatic state of type 1 copper proteins is not just based on geometrical constraints but also on electronic effects so that they introduced the term "electronic entatic state".[15] Comba defined entasis as the energization of a complex by an adverse interaction between the metal ion and the

[a]*Institute of Inorganic Chemistry, RWTH Aachen University, Landoltweg 1a, 52074 Aachen, Germany. E-mail: sonja.herres-pawlis@ac.rwth-aachen.de*

[b]*Institute of Nanostructure and Solid State Physics, University of Hamburg, Luruper Chaussee 149, 22761 Hamburg, Germany*

† Dedicated to Professor Jun Okuda on the occasion of his 65th birthday.

‡ Electronic supplementary information (ESI) available: Experimental data of the methods and details of the synthesis with characterization (IR, NMR, and MS), crystallographic information, XAS data, UV/Vis-, CV- and stopped-flow-spectra, DFT details, pictures of all NMR spectra and additional plots and further discussions. CCDC 2132917–2132931. For ESI and crystallographic data in CIF or other electronic format see https://doi.org/10.1039/d2sc02910c

ligands.[9] In general, the entatic state describes the energization of the reactants and products due to the adverse interaction between the protein or ligands and the metal ion. This results in a lower activation barrier and a faster reaction.[10,12] In case of type 1 copper proteins the coordination geometry of the copper center is highly distorted compared to the ideal tetrahedral geometry favored by Cu(I) and the ideal square-planar geometry favored by Cu(II) leading to an easier transition between Cu(I) and Cu(II) and a promoted electron transfer.[10,16]

There are different approaches to apply the concept of the entatic state to transition metal complexes as models for metal proteins and catalysis.[7,17] One example is models for electron transfer proteins, especially for type 1 copper proteins. To quantify the electron transfer ability of a model complex redox couple the electron self-exchange rate k_{11} is necessary. The determined electron self-exchange rates of several copper complex redox couples in the literature span over a wide range. Stanbury *et al.* analyzed the $[Cu(bib)_2]^{+/2+}$ redox couple with only N donors and the $[Cu(bite)]^{+/2+}$ redox couple with N and S donors (Fig. 1). For both systems relatively slow electron self-exchange rates compared to type 1 copper proteins were detected. The electron self-exchange rates range from (0.024 ± 0.004) to (0.49 ± 0.06) M^{-1} s^{-1} for the $[Cu(bib)_2]^{+/2+}$ redox couple and $(1.22 \pm 0.29) \times 10^{-3}$ to $(6.90 \pm 1.23) \times 10^{-2}$ M^{-1} s^{-1} for the $[Cu(bite)]^{+/2+}$ redox couple in MeCN at 25 °C depending on the used counter complex (for an explanation of the term counter complex see chapter "Electron transfer studies").[18] The Cu bispidine system reported by Comba *et al.* features a rigid ligand (Fig. 1).[4,9] Due to the rigidity the ligand is preorganized and offers only one possible coordinating conformation, so the ligand is inflexible. However, the coordination sphere is slightly elastic since the metal ion is not completely fixed in the center of the ligand cavity.[9] This allows a low-energy rearrangement of the coordination sphere characterized by a low inner-sphere reorganization energy. Nevertheless, this system exhibits a quite low electron self-exchange rate of 15 ± 11 M^{-1} s^{-1} in water at 25 °C. The reason for this is that the elastic coordination geometry enables large structural changes which influence the solvation shell significantly resulting in a relatively high outer-sphere reorganization energy. This emphasizes that a low inner-sphere reorganization energy does not lead automatically to a high electron self-exchange rate.[4] In contrast, Rorabacher *et al.* achieved high electron self-exchange rates of $\sim 10^5$ M^{-1} s^{-1} for the $[Cu([15]aneS_3bpy)]^{+/2+}$ redox couple in MeCN at 25 °C (Fig. 1).[15] These values are within the range of the electron self-exchange rates of the type 1 copper proteins. Besides the determination *via* the Marcus cross relation, Rorabacher *et al.* used the NMR line-broadening method. This method was also applied by Szymczak *et al.* who measured an electron self-exchange rate of 2.4×10^5 M^{-1} s^{-1} in THF at room temperature for the $[Cu(H_2Tpy^{NMes})Cl]^{0/+}$ redox couple.[19] In the past, our group has reported the properties of copper guanidine quinolinyl complexes as entatic state models by structural analysis and determination of the electron self-exchange rates *via* Marcus theory (10^2–10^3 M^{-1} s^{-1}).[20–23] The influence of different solvents and substituents was analyzed.[22,23] The redox couple $[Cu(TMGqu)_2]^{+/2+}$ exhibits the highest electron self-exchange rate for pure N donor systems in organic solvents.[22] In copper guanidine quinolinyl complexes the structures of the Cu(I) and Cu(II) complexes are highly distorted compared to the ideal tetrahedral geometry favored by Cu(I) and the ideal square-planar geometry favored by Cu(II).[16,20] This distortion leads to a very high structural similarity between the Cu(I) and Cu(II) complexes.[20] In a previous report, substitutions in the 2-, 4- and 6-positions of the quinolinyl backbone were highlighted to have the strongest influence on the donor properties of the ligand. Substituents in the 2- and 4-position mostly affect the quinolinyl donor whereas substituents in the 6-position mostly affect the guanidine donor.[24] In another study, substituents with electronic influences were introduced in the 6-position but this did not lead to an enhancement of the entatic state.[23] Therefore, substitutions in the 2- and 4-position affecting the quinolinyl donor are of great interest where substituents in the 2-position also have a steric influence on the coordination geometry.

Herein, we examined the influence of substituents in the 2- and 4-position of the guanidine quinolinyl ligand on the properties of the corresponding Cu(I) and Cu(II) complexes. The molecular structures of the complexes were characterized by single-crystal X-ray diffraction (XRD), X-ray absorption spectroscopy (XAS) and density functional theory (DFT) calculations. Moreover, the electron transfer was investigated *via* Marcus theory and further DFT calculations.

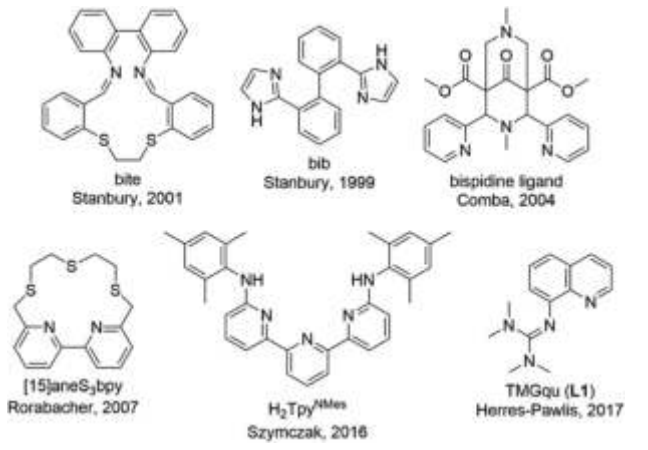

Fig. 1 Ligands used in copper complexes that were examined as entatic state models for electron transfer.[4,9,15,18–23]

Results and discussion

Strategies to manipulate the electron transfer

In order to manipulate the electron transfer performance of guanidine quinolinyl copper complexes, different substituents were introduced in the quinolinyl backbone of the ligands (Scheme 1). Thus, the steric demand and the donor properties of the ligands were modified compared to the unsubstituted ligand TMGqu (**L1**). The guanidine donor was not changed for comparability so only ligands with a TMG moiety were synthesized.

First, ligands with alkyl groups in the 2-position with different steric demand (TMG2Mequ (**L2**), TMG2^{t}Buqu (**L3**), and TMG2^{c}Hexqu (**L4**)) were synthesized. These substituents only slightly change the electronic properties due to their weak electron density donating feature while the steric requirements in the 2-position should influence the coordination properties.[24] Due to the higher steric demand of the ligands, the distortion of the resulting Cu(I) and Cu(II) complexes should be higher compared to that of the Cu(I) and Cu(II) complexes with the unsubstituted ligand (**L1**). Therefore, this should lead to an improvement of the electron transfer properties. The different alkyl groups should allow the influence of the steric demand to be determined.

Second, a ligand with a methyl ester group in the 2-position (TMG2Meequ (**L5**)) was synthesized. As the alkyl group in **L2**–**L4** the methyl ester group has an influence on the steric demand. Moreover, the negative mesomeric effect caused by the electron density withdrawing feature increases the delocalization of the π system. This should influence the electron transfer ability of the Cu complexes.

Third, a ligand with a dimethylamine group in the 4-position (TMG4NMe$_2$qu (**L6**)) was synthesized. Due to its position in the ligand, the dimethylamine group does not influence the coordination by steric demand. However, due to its positive mesomeric effect caused by the electron density donating feature an increase of the delocalization of the π system occurs. Like in **L5** but with a more electron-rich aromatic system the influence on the electron transfer properties of the Cu complexes is examined.

Synthetic strategy for the ligands

The nitro precursors for the alkyl substituted ligands **L3** and **L4** were obtained from 8-nitroquinoline by introducing the alkyl group in a silver catalyzed radical substitution reaction following a modified procedure of Minisci *et al.*[25] According to this, 2-*tert*-butyl-8-nitroquinoline and 2-cyclohexyl-8-nitroquinoline were synthesized (Scheme 1, first reaction path). The nitro precursor for **L2**, 2-methyl-8-nitroquinoline, was commercially available. For the precursor synthesis of **L5** (Scheme 1, middle reaction path), the first two steps were performed according to a slightly modified procedure of Gadomsky *et al.*[26] In the first step a bromination of the methyl group of 2-methyl-8-nitroquinoline was performed giving 2-tribromomethyl-8-nitro-quinoline. The second step was the hydrolysis to 8-nitroquinoline-2-carboxylic acid. The third step was the esterification of the carboxylic acid with MeOH giving methyl 8-nitroquinoline-2-carboxylate (Scheme 1, middle reaction path). The synthesis of **L6** (Scheme 1, lower reaction path) started with the nitration of 4-chloroquinoline in the 8-position yielding 4-chloro-8-nitroquinoline following the procedure of Mosher *et al.* modified by Yoo *et al.*[27] The next step was the substitution of the chloride by dimethylamine giving 4-dimethylamino-8-nitroquinoline. This reaction was inspired by the procedures of Pozharskii *et al.* and Matyjaszewski *et al.* (Scheme 1, lower reaction path).[28] The two final steps are the same for all ligands. The nitro precursors were reduced by hydrogen using Pd/C as catalyst yielding the amine precursors.[24] The last step is the guanidine synthesis using the Vilsmeier salt *N*,*N*,*N*′,*N*′tetramethylchloroformamidinium chloride (TMG-VS) performed according to the general procedure of Herres-Pawlis *et al.* inspired by the procedure of Kantlehner *et al.* (Scheme 1).[29] The molecular structures in the solid state of ligands **L2**, **L3** and **L6** have been determined and are depicted in Fig. S36‡ (crystallographic data are shown in Table S11 in the ESI‡).

Influence of the substituents on the electronic and donor properties of the ligands

For **L1–L6** DFT calculations with the functional TPSSh and the basis set def2-TZVP with the solvent model (PCM) and empirical dispersion correction with Becke–Johnson damping were performed in accordance to previous studies.[21–23,30–35] The structural optimizations were followed by natural bond orbital (NBO) calculations to quantify the influence of the different substituents on the guanidine N donor N_{gua} and quinolinyl N donor N_{qu} of all ligands and the acyl and alcohol O donors of the methyl ester groups O_{acyl} and O_{alc} of **L5** (Fig. 2). The charge of the N_{gua} donor shows no significant deviation after the substitution whereas the charge of the N_{qu} donor changes. In all ligands, the N_{gua} donor possesses a more negative NBO charge than the N_{qu}

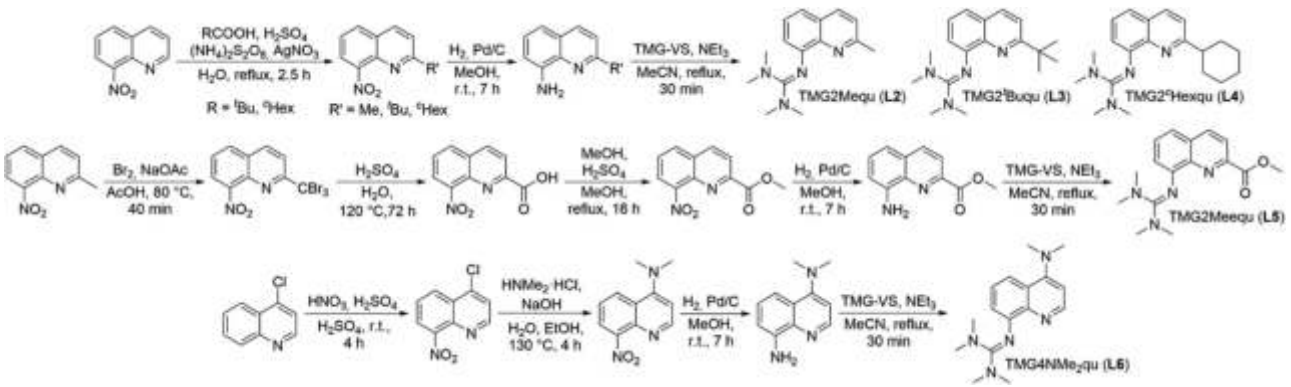

Scheme 1 Synthetic routes to a series of substituted guanidine quinolinyl ligands.[24–29] * The nitro precursor for **L2**, 2-methyl-8-nitroquinoline, was commercially available.

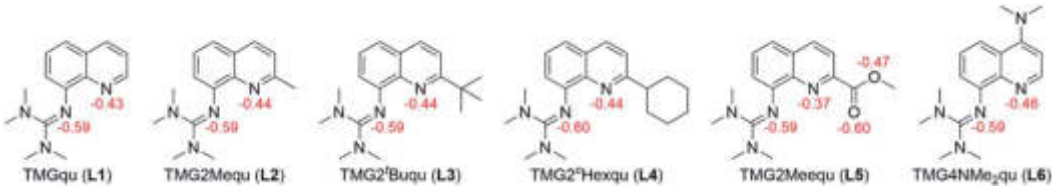

Fig. 2 Calculated NBO charges [e units] (red) for selected atoms of the ligands **L1–L6** (NBO6.0, TPSSh/def2-TZVP and PCM solvent model for MeCN and empirical dispersion correction with Becke–Johnson damping).

donor corresponding to a higher basicity of the N_{gua} donor.[21,35,36] Further work pointed out that the higher basicity of the N_{gua} donor does not implicate a higher donor strength compared to the N_{qu} donor whereas a higher basicity comparing the same type of donor leads to a higher donor strength in the Cu complexes.[21,24,31,35,36] As expected, the alkyl groups have a very weak influence on the charge of the N_{qu} donor of **L2** and **L3** so that the basicity and the donor properties are not influenced significantly compared to the unsubstituted ligand **L1**. The methyl ester group of **L5** has the strongest influence on the N_{qu} donor. Due to its electron density withdrawing effect the charge of the N_{qu} donor increases significantly whereby the N_{qu} donor is less basic compared to **L1–L4** leading to weaker donor properties. The dimethylamine group of **L6** induces a decrease of the charge of the N_{qu} donor compared to **L1** because of its electron density donating effect. Therefore, the basicity and the donor properties of the N_{qu} donor are increased compared to those of the unsubstituted ligand.

Copper complex synthesis and structural characterization

The reaction of the synthesized ligands **L2–L6** with various Cu(I) and Cu(II) salts with weakly coordinating anions leads for all ligands except **L3** to a bis(chelate) complexation of the corresponding Cu(I) and Cu(II) centers. For **L3** only a mono(chelate) complexation of the Cu(I) species is observed in solution due to the high steric encumbrance of the *tert*-butyl group (further information in ESI Section 4.3‡). Due to the different coordination behavior in the Cu(I) and Cu(II) species, **L3** is of no further interest for this study. The targeted bis(chelate) Cu(I) complexes were synthesized by dissolving the ligands **L2** and **L4–L6** and a Cu(I) salt, $[Cu(MeCN)_4]PF_6$, $[Cu(MeCN)_4]BF_4$ or $[Cu(MeCN)_4]OTf$, in DCM. By vapor diffusion or layering with pentane the complexes could be crystallized (Scheme 2, left, top). The bis(chelate) Cu(II) complexes were synthesized analogously by dissolving the ligands **L2** and **L4–L6** and a Cu(II) salt, $[Cu(MeCN)_4](BF_4)_2$ or $[Cu(MeCN)_4](OTf)_2$, in MeOH, MeCN or a mixture of MeCN and DCM. By vapor diffusion or layering with Et_2O or pentane the complexes could be crystallized (Scheme 2, left, bottom). The molecular structures of the complex cations $[Cu(TMG2Mequ)_2]^+$ (**C3**), $[Cu(TMG2Mequ)_2]^{2+}$ (**C4**), $[Cu(TMG2^cHexqu)_2]^+$ (**C5**), $[Cu(TMG2^cHexqu)_2]^{2+}$ (**C6**), $[Cu(TMG2Meequ)_2]^+$ (**C7**), $[Cu(TMG2Meequ)_2]^{2+}$ (**C8**), $[Cu(TMG4NMe_2qu)_2]^+$ (**C9**) and $[Cu(TMG4NMe_2qu)_2]^{2+}$ (**C10**) could be structurally characterized by XRD measurements (Fig. 3) of the crystallized compounds **C3**−**X** to **C10**−**X** (Scheme 2, right; key structural data in Table 1; molecular structures in the solid state and crystallographic data are shown in Fig. S37–S47 and Tables S12–S15 in the ESI‡). For the complex cations **C3**, **C4** and **C8** crystals with different anions could be characterized. Due to insignificant differences in the structures of the cationic complexes the results of **C3–OTf**, **C4–OTf** and **C8–OTf** are not discussed in the manuscript (results are shown in Table S1 in the ESI‡).

The Cu–N_{gua} bond lengths in the Cu(I) complex cations are significantly longer (approx. 0.1 Å) than in the corresponding

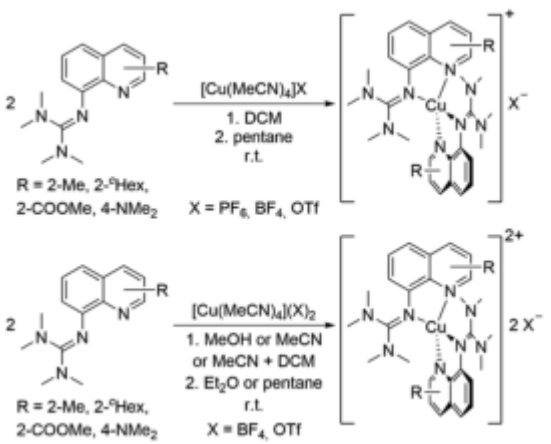

	Complex cation (Label)	Crystallized compound (Label)
L2	$[Cu(TMG2Mequ)_2]^+$ (**C3**)	$[Cu(TMG2Mequ)_2]PF_6$ (**C3–PF$_6$**)
		$[Cu(TMG2Mequ)_2]BF_4$ (**C3–BF$_4$**)
	$[Cu(TMG2Mequ)_2]^{2+}$ (**C4**)	$[Cu(TMG2Mequ)_2](BF_4)_2$ (**C4–BF$_4$**)
		$[Cu(TMG2Mequ)_2](OTf)_2$ (**C4–OTf**)
L4	$[Cu(TMG2^cHexqu)_2]^+$ (**C5**)	$[Cu(TMG2^cHexqu)_2]PF_6$·DCM (**C5–PF$_6$**)
	$[Cu(TMG2^cHexqu)_2]^{2+}$ (**C6**)	$[Cu(TMG2^cHexqu)_2](OTf)_2$ (**C6–OTf**)
L5	$[Cu(TMG2Meequ)_2]^+$ (**C7**)	$[Cu(TMG2Meequ)_2]PF_6$ (**C7–PF$_6$**)
	$[Cu(TMG2Meequ)_2]^{2+}$ (**C8**)	$[Cu(TMG2Meequ)_2](BF_4)_2$·2 MeCN (**C8–BF$_4$**)
		$[Cu(TMG2Meequ)_2](OTf)_2$·2 MeCN (**C8–OTf**)
L6	$[Cu(TMG4NMe_2qu)_2]^+$ (**C9**)	$[Cu(TMG4NMe_2qu)_2]BF_4$ (**C9–BF$_4$**)
	$[Cu(TMG4NMe_2qu)_2]^{2+}$ (**C10**)	$[Cu(TMG4NMe_2qu)_2](OTf)_2$·$Et_2O$ (**C10–OTf**)

Scheme 2 Synthesis of the bis(chelate) Cu(I) (left, top) and Cu(II) (left, bottom) complexes **C3**−**X** to **C10**−**X** and overview of all complex cations and crystallized compounds ordered by ligand (right).

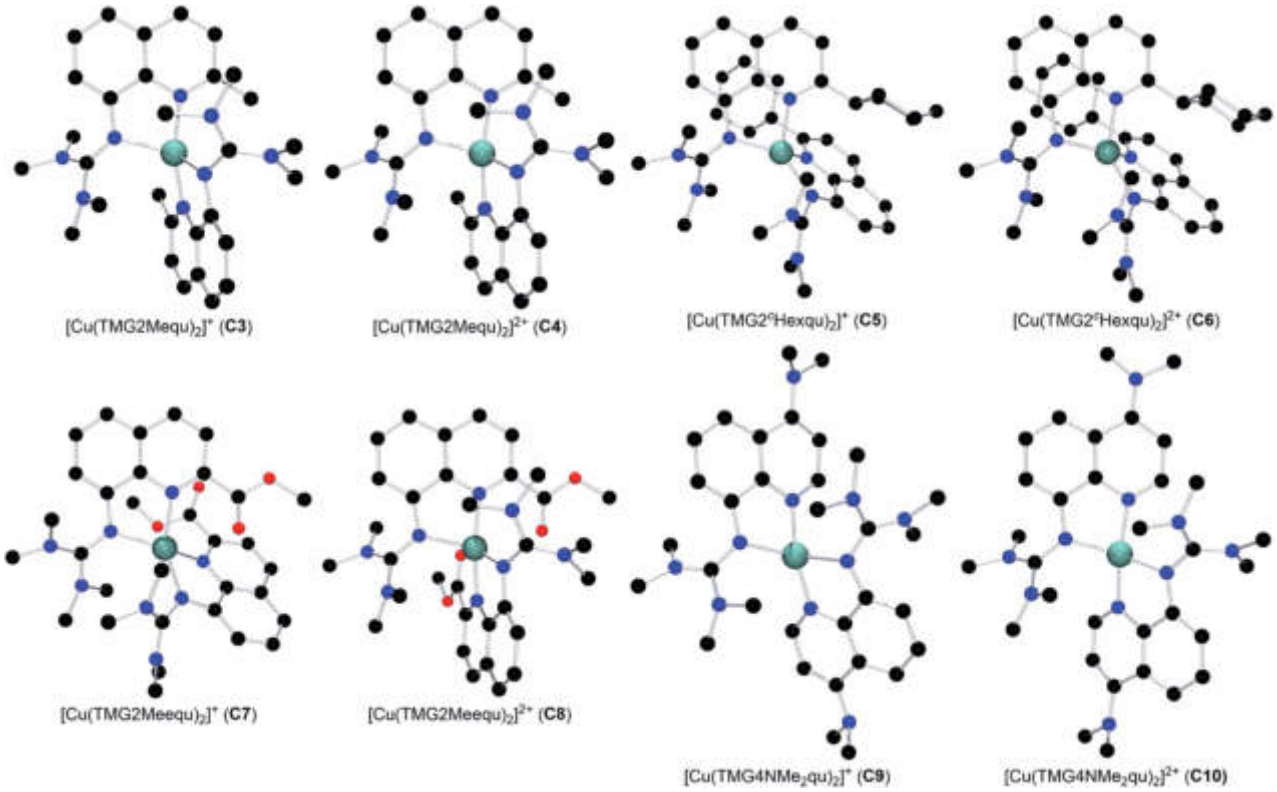

Fig. 3 Molecular structures of the Cu(I) and Cu(II) complex cations **C3–C10** in crystals of **C3–X** to **C10–X**. H atoms, non-coordinating anions and solvent molecules are omitted for clarity.

Cu(II) complex cations expect for **C7** and **C8**. This is related to the stronger coordination of the guanidine moiety to the Cu(II) center compared to the Cu(I) center due to the higher charge. Moreover, in the Cu(I) complex cations the Cu–N_{gua} bond lengths are significantly longer than the Cu–N_{qu} bond lengths expect for **C5** and **C7**. To compare the coordination geometry, the structure parameter τ_4 (ref. 37) and the plane angle $\measuredangle$ between the planes stretched by the two N donors of each ligand and the copper center are calculated. The τ_4 value describes whether the coordination is ideal square-planar ($\tau_4 = 0$) or ideal tetrahedral ($\tau_4 = 1$). The results show that for all complexes highly distorted coordination geometries were obtained. In all Cu(I) complex cations the observed τ_4 value is higher compared to that of the corresponding Cu(II) complex cations since Cu(I) prefers a tetrahedral and Cu(II) a square-planar coordination geometry.[16]

In **C3–C6** the alkyl substituents of the ligands have due to their position a steric influence on the complex cations but no significant electronic influence due to their weak electron density donation properties (see the discussion of the NBO results of the ligands (Fig. 2) and complex cations (Fig. 4)). The steric demand influences the coordination geometry significantly compared to $[Cu(TMGqu)_2]^+$ (**C1**) and $[Cu(TMGqu)_2]^{2+}$ (**C2**). An elongation of the Cu–N_{qu} bond length in the Cu(I) complexes is observed. Furthermore, a stronger steric demand of the substituent (H < Me < ^{c}Hex) leads to a higher τ_4 value for the Cu(I) and Cu(II) complex cations and therefore to a higher average $\varnothing\tau_4$ value of both complex cations. This causes a stabilization of the Cu(I) complex cation and a destabilization of the Cu(II) complex cation since Cu(I) complex cations prefer higher τ_4 values.[16] As already mentioned the influence on the Cu(II) complex cations is stronger resulting in a smaller difference between the τ_4 value of the corresponding Cu(I) and Cu(II) complex cations represented by the $\Delta\tau_4$ value. This means that the corresponding Cu(I) and Cu(II) complex cations become structurally more similar. This suggests that the introduction of alkyl substituents in the 2-position leads to better entatic state models where **C5** and **C6** are the best entatic state model couples of all investigated complexes.

In **C7** and **C8** the methyl ester substituent influences the coordination geometry in several ways. According to the alkyl substituents in **C3–C6** it has a steric demand but furthermore the substituent has an electronic influence due to its electron density withdrawing effect. This weakens the donor properties of the N_{qu} donor and therefore the Cu–N_{qu} bond length in the Cu(I) complex cation is comparatively long (see the discussion of the NBO results of the ligands (Fig. 2) and complexes (Fig. 4)). In addition, the methyl ester group itself has donor abilities leading to different effects in both oxidation states. In the Cu(II) complex cation **C8** a weak coordination of the O_{acyl} donor occurs leading to a 4 + 2 coordination motif. This results in an extended Cu–N_{gua} bond length compared to complex **C2** due to the pulling effect of the O_{acyl} donor on the Cu(II) center. In the Cu(I) complex cation **C7** two different coordination behaviors of

Table 1 Key bond lengths, bond angles and structure parameters of the Cu(I) and Cu(II) complex cations **C1–C10**

	$[Cu(TMGqu)_2]^{+/2+}$ (ref. 20)		$[Cu(TMG2Mequ)_2]^{+/2+}$		$[Cu(TMG2^cHexqu)_2]^{+/2+}$		$[Cu(TMG2Meequ)_2]^{+/2+}$		$[Cu(TMG4NMe_2qu)_2]^{+/2+}$	
	C1 (Cu(I))	**C2** (Cu(II))	**C3** (Cu(I))	**C4** (Cu(II))	**C5** (Cu(I))	**C6** (Cu(II))	**C7** (Cu(I))	**C8** (Cu(II))	**C9** (Cu(I))	**C10** (Cu(II))
Bond lengths [Å]										
$Cu–N_{gua,1/2}$	2.068(3), 2.095(3)	1.959(2), 1.964(2)	2.091(3), 2.097(3)	1.979(4), 1.978(4)	2.018(3), 2.024(3)	1.973(2), 1.973(2)	2.047(4), 2.029(4)	2.039(2), 2.043(2)	2.065(4), 2.146(4)	1.964(2), 1.968(2)
$Cu–N_{qu,1/2}$	1.966(4), 1.999(3)	1.976(2), 1.975(2)	1.994(3), 1.994(3)	1.987(4), 1.972(4)	2.084(3), 2.081(3)	1.988(2), 1.988(2)	2.053(3), 2.083(4)	1.960(2), 1.959(2)	1.983(4), 1.947(4)	1.957(2), 1.952(2)
$Cu–O_{acyl,1/2}$							2.962(4), 4.312(4)	2.616(2), 2.595(2)		
$Cu–O_{alc,1/2}$							4.511(4), 3.235(4)	4.428(2), 4.441(2)		
Bond angles [°]										
$N_{gua,1/2}–Cu–N_{qu,1/2}$	82.6(2), 82.1(2)	83.5(1), 83.7(1)	81.7(2), 81.6(2)	83.2(2), 83.6(2)	81.2(2), 81.3(2)	82.9(1), 82.9(1)	81.3(2), 81.3(2)	82.2(1), 82.2(1)	82.2(2), 82.4(2)	82.9(1), 82.9(1)
$N_{gua,1}–Cu–N_{gua,2}$	129.1(2)	149.4(1)	126.0(2)	135.9(2)	135.0(2)	124.7(2)	124.4(2)	120.2(1)	119.6(2)	150.7(1)
$N_{gua,1/2}–Cu–N_{qu,2/1}$	108.2(2), 114.1(2)	102.6(1), 103.5(1)	111.7(2), 113.2(2)	105.4(2), 107.2(2)	128.7(2), 127.9(2)	135.8(1), 135.8(1)	133.0(2), 137.8(2)	105.3(1), 106.9(1)	123.0(2), 107.1(2)	102.9(1), 104.2(1)
$N_{qu,1}–Cu–N_{qu,2}$	149.0(2)	154.9(1)	149.9(2)	154.6(2)	104.9(2)	100.7(2)	105.9(2)	163.7(1)	145.1(2)	154.9(1)
Structure parameters										
τ_4 [ ][a]	0.58	0.40	0.60	0.49	0.68	0.63	0.63	0.54[b]	0.65	0.39
$\Delta\tau_4$ [ ]	0.18		0.10		0.06		0.09[c]		0.27	
$\varnothing\tau_4$ [ ]	0.49		0.54		0.65		0.59[c]		0.52	
$\sphericalangle(CuN_2, CuN_2')$ [°]	65.1	42.5	68.2	54.7	78.1	65.5	69.0	65.6	75.6	41.8
$\Delta\sphericalangle$ [°]	22.6		13.5		12.6		3.5		33.8	
ρ [ ][d]	0.97, 0.96	1.00, 0.99	0.97, 0.98	1.00, 1.00	0.99, 0.99	1.01, 1.01	0.99, 1.00	1.01, 1.00	0.97, 0.95	1.01, 1.01

[a] $\tau_4 = \frac{360° - (\alpha + \beta)}{141°}$.[37] [b] The τ_4 value of the Cu(II) complex may be biased due to the 4 + 2 coordination motif. [c] The value may be biased due to the 4 + 2 coordination motif in the Cu(II) complex. [d] $\rho = \frac{2a}{b+c}$ with $a = d(C_{gua} - N_{gua})$, $b = d(C_{gua} - N_{amine,1})$ and $c = d(C_{gua} - N_{amine,2})$.[38]

both the ligands are taking place. One ligand shows a weak interaction between its O_{acyl} donor and the Cu(I) center and the other ligand between its O_{alc} donor and the Cu(I) center. **C7** is the only complex cation in which both ligands exhibit different coordination behaviors. Due to the different effects of the methyl ester group, the comparison of the τ_4 values of the Cu(I) and Cu(II) complex cations is not possible like for **C1–C6**.

The dimethylamine substituent in **C9** and **C10** has due to its position no steric demand, hence only its electron density donating effect influences the donor properties of the N_{qu} donor (see the discussion of the NBO results of the ligands (Fig. 2) and complexes (Fig. 4)). Moreover, the structure parameter ρ was calculated. It describes the degree of delocalization of the electrons in the guanidine moiety.[38] For Cu(II) complex cations higher values were found than for the Cu(I) complex cations. This is caused by the stronger coordination of the guanidine moiety to the Cu(II) center compared to the Cu(I) center which is also indicated by the shorter $Cu–N_{gua}$ bond lengths in the Cu(II) complex cations compared to the Cu(I) complex cations. The stronger coordination comes with a shift of electron density from the $C_{gua}–N_{gua}$ bond to the $Cu–N_{gua}$ bond leading to an elongation of the $C_{gua}–N_{gua}$ bond length. Parallelly, a shift of electron density from the amine groups to the $C_{gua}–N_{amine}$ bonds takes place to compensate for the missing electron density. This induces a shortening of the $C_{gua}–N_{amine}$ bond lengths. The results reveal that a larger difference in the $Cu–N_{gua}$ bond length between the corresponding Cu(I) and the Cu(II) complex cations leads to a larger difference in the ρ value between these two complex cations.

XAS and structural DFT calculations of the copper complexes

XAS in solution with MeCN as solvent was performed (see the ESI‡ for details) to characterize the oxidation state and structure of the novel complexes **C3–C10** in solution. This was performed to confirm that the structural information found in the solid state accords with the structures present in solution. X-ray absorption near-edge structure (XANES) spectroscopy provides information about the oxidation state of the complexes (spectra are shown in Fig. S1 in the ESI‡). The edge position and the resulting chemical shifts between two associated Cu(I) and Cu(II) complexes identify **C3**, **C5**, **C7** and **C9** as Cu(I) complexes and **C4**, **C6**, **C8** and **C10** as Cu(II) complexes. This is further supported by the pre-edge shapes of the spectra. The Cu(I) complexes show a strong characteristic peak between 8980 and 8985 eV with a normalized absorption of 0.7 to 0.9 that belongs to the 1s → 4p transition.[39] In contrast, the Cu(II)

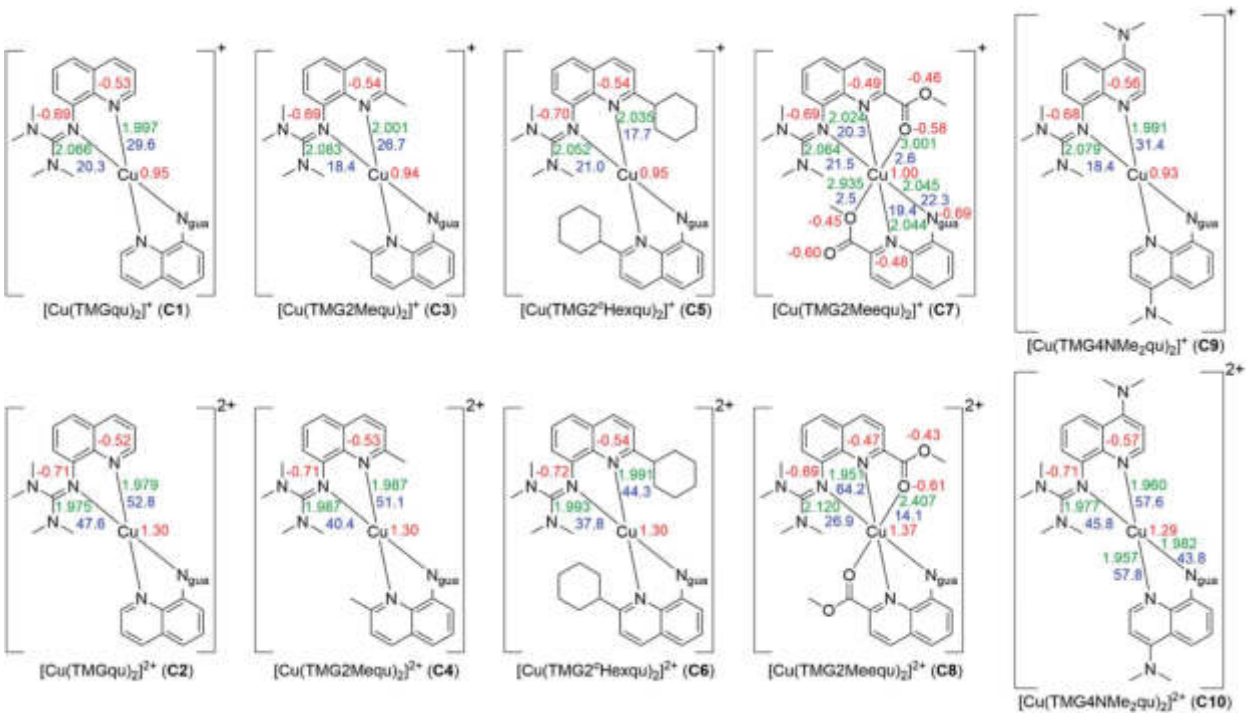

Fig. 4 Calculated NBO charges [e units] (red), charge-transfer energies E_{CT} [kcal mol^{-1}] (blue) and selected bond length [Å] (green) for the Cu(I) (top) and Cu(II) (bottom) complex cations **C1–C10** (NBO6.0, TPSSh/def2-TZVP and PCM solvent model for MeCN and empirical dispersion correction with Becke–Johnson damping). If neither of the ligands of one complex exhibits significant differences only one value is shown (all values are shown in Table S18 in the ESI‡).

complexes show in this area only a weak shoulder but moreover they show a weak peak between 8976 and 8978 eV with a normalized absorption of 40 to 60 $\times$ 10^{-3} belonging to a 1s $\rightarrow$ 3d transition.[40] The results confirm that all complexes are present in the expected oxidation states in solution. Furthermore, the extended X-ray absorption fine structure (EXAFS) spectroscopy provides information about the structure in solution (spectra and determined bond lengths are shown in Fig. S2–S9 and Tables S2–S9 in the ESI‡). The results indicate an accordance of the solid state structures of all complexes with the structures in solution (Tables S21–S24 in the ESI‡). Hence, the anion does not influence the coordination geometry of the complexes and is not responsible for the distortion of the complexes. This is in accordance with previous studies.[20]

DFT calculations were performed for all complexes **C1–C10** with the functional TPSSh and the basis set def2-TZVP with the solvent model (PCM) and empirical dispersion correction with Becke–Johnson damping.[21–23,30–35] In the first step structure optimization calculations were executed (results are shown in Table S16 in the ESI‡). All complexes exhibit a high agreement between the molecular structure in the solid state, the structure in solution and the calculated structure by DFT (Tables S20–S24 in the ESI‡).

Based on the optimized structures NBO calculations were performed for all complexes to examine the influence of the substituents on the NBO charges of the copper and the N donors and on the charge-transfer energies (E_{CT}) (Fig. 4, see the ESI‡ for details). In general, in all complexes independent of the substituent or the oxidation state of the copper the N_{gua} donor exhibits a more negative charge compared to the N_{qu} donor. For this reason, the N_{gua} donor is a stronger base than the N_{qu} donor. In all complexes except **C5** and **C7** the N_{qu} donor exhibits a higher charge-transfer energy than the N_{gua} donor. Especially in **C2**, **C4** and **C6** the charge-transfer energy of the N_{qu} donor is significantly higher compared to that of the N_{gua} donor for similar bond lengths between the Cu(II) center and the N donors. Due to this the N_{qu} donor is a stronger donor than the N_{gua} donor. Moreover, the charge-transfer energies from the N_{gua} and the N_{qu} donors to the Cu center and the charge of the Cu center are significantly higher in the Cu(II) complexes compared to the corresponding Cu(I) complex. This is in accordance with the results of previous NBO calculations of copper guanidine quinolinyl complexes.[21,31]

In the Cu(I) complexes the substituents do not influence the charge of the N_{gua} donor significantly whereas only a weak influence on the charge of the N_{qu} donor is visible except for **C7**. In contrast, the influence on the charge-transfer energy and bond length between the N_{qu} donor and the Cu(I) center in **C3**, **C5** and **C7** is evident compared to that in the unsubstituted complex **C1**. For **C3** and **C5** the weak electron density donating effect of the alkyl substituents in the 2-position becomes visible. This results in a slightly lower charge of the N_{qu} donor compared to **C1** which suggests better donor properties. Instead, a lower charge-transfer energy and a longer bond length between the N_{qu} donor and the Cu(I) center compared to **C1** occur. This is caused by the steric demand of the alkyl

Table 2 Overview of the complex cations and the corresponding complex redox couples

	Complex cation (label)	Complex redox couple (label)
L1	$[Cu(TMGqu)_2]^+$ (**C1**) $[Cu(TMGqu)_2]^{2+}$ (**C2**)	$[Cu(TMGqu)_2]^{+/2+}$ (**R1**)
L2	$[Cu(TMG2Mequ)_2]^+$ (**C3**) $[Cu(TMG2Mequ)_2]^{2+}$ (**C4**)	$[Cu(TMG2Mequ)_2]^{+/2+}$ (**R2**)
L4	$[Cu(TMG2^cHexqu)_2]^+$ (**C5**) $[Cu(TMG2^cHexqu)_2]^{2+}$ (**P6**)	$[Cu(TMG2^cHexqu)_2]^{+/2+}$ (**R3**)
L5	$[Cu(TMG2Meequ)_2]^+$ (**C7**) $[Cu(TMG2Meequ)_2]^{2+}$ (**C8**)	$[Cu(TMG2Meequ)_2]^{+/2+}$ (**R4**)
L6	$[Cu(TMG4NMe_2qu)_2]^+$ (**C9**) $[Cu(TMG4NMe_2qu)_2]^{2+}$ (**C10**)	$[Cu(TMG4NMe_2qu)_2]^{+/2+}$ (**R5**)

substituents which prevents the shortened bond length between the N_{qu} donor and the Cu(I) center. The bond length becomes elongated and therefore the charge-transfer energy decreases with the increasing steric demand of the substituent in the 2-position (H < Me < ^{c}Hex). In **C7** the same effect is active but beyond that the electron density withdrawing effect of the methyl ester group leads to an increase of the charge of the N_{qu} donor. Thus, the charge-transfer energy is lower and the bond length is longer between the N_{qu} donor and the Cu(I) center compared to **C1**. The electron density donating effect of the dimethylamine group in **C9** induces a small decrease of the charge of the N_{qu} donor provoking a slightly higher charge-transfer energy and a slightly shorter bond length between the N_{qu} donor and the Cu(I) center.

In contrast, the influence of the substituents is stronger in the Cu(II) complexes. The charges of the N_{gua} donor are similar for **C2**, **C4**, **C6** and **C10** but for **C8** the charge is significantly higher. In the complexes **C2** and **C4** to **C6** an elongation of the Cu–N_{gua} bond length occurs due to the steric influence of the alkyl substituents resulting in lower values for the charge-transfer energy. In **C8** a 4 + 2 coordination is present and the charge-transfer energy is drastically lower and the bond length much longer compared to those in the other Cu(II) complexes. This is caused by the donor ability of the O_{acyl} donor of the methyl ester group exhibited by the charge-transfer energy and bond length between the O_{acyl} donor and the Cu(II) center. Compared to the corresponding Cu(I) complex **C7** the charge-transfer energy is significantly higher and the bond length significantly shorter. This is caused by the orientation of the O_{acyl} donor to the Cu(II) center which does not occur in the Cu(I) complex. The weak coordination between the O_{acyl} donor and the Cu(II) center in turn weakens the coordination between the N_{gua} donor and the Cu(II) center by elongation. The influence of the substituents on the N_{qu} donor in the Cu(II) complexes **C2**, **C4**, **C6** and **C10** is comparable with that in the corresponding Cu(I) complexes **C1**, **C3**, **C5** and **C9**, but especially for **C10** the influence of the dimethylamine group is stronger than for **C9**. The higher steric demand of the substituent in the 2-position produces an elongation of the N_{qu}–Cu bond length and therefore a lower value of the charge-transfer energy. The Cu(II) complex **C8** exhibits the opposite effect compared to the corresponding Cu(I) complex **C7**. In this case the methyl ester substituent leads to an increase of the charge-transfer energy and a shorter bond length between the N_{qu} donor and the Cu(II) center although the methyl ester substituent still increases the charge of the N_{qu} donor due to its electron density withdrawing effect. The reason is again as for the N_{gua} donor the weak coordination between the O_{acyl} donor and the Cu(II) center. By this, the bond length between the N_{qu} donor and the Cu(II) center becomes shortened.

Electron transfer studies

The associated Cu(I) and Cu(II) complexes of one ligand form a copper complex redox couple leading to the redox couples $[Cu(TMGqu)_2]^{+/2+}$ (**R1**), $[Cu(TMG2Mequ)_2]^{+/2+}$ (**R2**), $[Cu(TMG2^cHexqu)_2]^{+/2+}$ (**R3**), $[Cu(TMG2Meequ)_2]^{+/2+}$ (**R4**) and $[Cu(TMG4NMe_2qu)_2]^{+/2+}$ (**R5**) (Table 2). To analyze the electron transfer properties of the redox couples the electron self-exchange rates k_{11} were determined by following the Marcus cross relation (eqn (1)–(4), further information in ESI Section 7‡). The Marcus cross relation emerges from Marcus theory which describes the outer-sphere electron transfer between metal complexes.[41] The electron self-exchange rate k_{11} is the reaction rate of the redox reaction of the reduced form with the oxidized form of the same redox couple. An electron is transferred from the reduced form to the oxidized form. The net result is the same oxidation states of the redox couple as before (Scheme 3, top). The electron self-exchange rate of a redox couple depends on the temperature, the solvent and the activity coefficients of the reactants. Therefore, the direct comparison of redox couples is only reasonable if the electron self-exchange rates are determined under identical conditions. For the Marcus cross relation, a cross reaction with a counter complex with a known electron self-exchange rate has to be analyzed. The function of the counter complex is to oxidize or reduce one oxidation state of the investigated redox couple during the cross reaction (further information in ESI Section 7‡). In theory it makes no difference for the determination of the electron self-exchange rate which counter complex is used and in which direction the cross reaction takes place. However, to enable

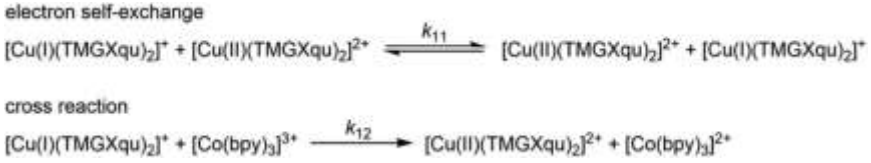

Scheme 3 Illustration of the electron self-exchange of the Cu redox couples and of the cross reaction of the Cu(I) complexes with the counter complex $[Co(bpy)_3]^{3+}$ (TMGXqu represents the guanidine quinolinyl ligands).

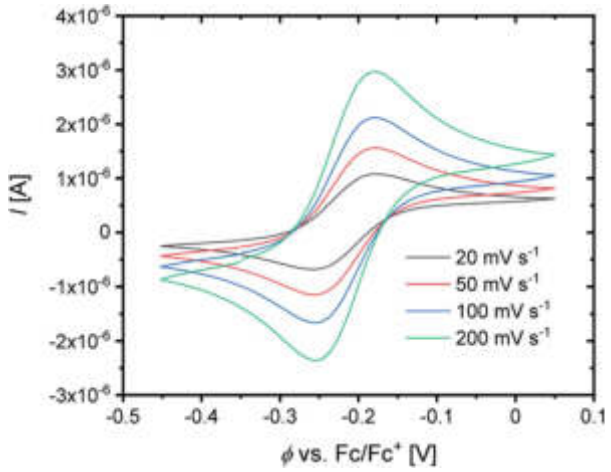

Fig. 5 Cyclic voltammogram of **R2** starting from **C3** ($c = 10^{-3}$ M) in MeCN with $[NBu_4][PF_6]$ ($c = 0.1$ M).

a direct comparison of the electron self-exchange rates of the investigated redox couples the same counter complex should be used for all cross reactions. The reason is that only small unavoidable inaccuracies in the electron self-exchange rates of different counter complexes can cause an incomparableness of the determined electron self-exchange rates. In this case the complex $[Co(bpy)_3]^{3+}$ of the redox couple $[Co(bpy)_3]^{2+/3+}$ was used as the counter complex for all cross reactions due to its properties (Scheme 3, bottom). The redox potential of the redox couple $[Co(bpy)_3]^{2+/3+}$ enables the oxidation of all Cu(I) complexes without any side reactions, it is soluble in MeCN and it has no significant absorption in the monitored spectral region.[22,23]

$$k_{11} = \frac{{k_{12}}^2}{k_{22}K_{12}f_{12}{W_{12}}^2} \quad (1)$$

$$K_{12} = \exp\left(\frac{\Delta E_{1/2}nF}{RT}\right) \quad (2)$$

$$f_{12} = \exp\left(\frac{\left(\ln K_{12} + \frac{w_{12} - w_{21}}{RT}\right)^2}{4\left(\ln\left(\frac{k_{22}k_{22}}{Z^2}\right) + \frac{w_{11} + w_{22}}{RT}\right)}\right) \quad (3)$$

$$W_{12} = \exp\left(\frac{w_{11} + w_{22} - w_{12} - w_{21}}{2RT}\right) \quad (4)$$

For the calculation of k_{11} the experimentally determined reaction rate k_{12} and equilibrium constant K_{12} (eqn (2)), the correction term f_{12} (eqn (3)), the work term W_{12} (eqn (4)) and the electron self-exchange rate k_{22} of the counter complex redox couple are necessary (eqn (1)). The equilibrium constant K_{12} depends on the difference between the redox potentials of the counter complex redox couple and the investigated copper complex redox couple $\Delta E_{1/2}$ (eqn (2)). The electron self-exchange rate k_{22} of the counter complex redox couple $[Co(bpy)_3]^{2+/3+}$ in MeCN at 298 K is used as reported in the literature.[42]

For the determination of the equilibrium constant K_{12} the redox potentials $E_{1/2}$ of the copper complex redox couples and of the counter complex redox couple are required. The redox potentials were determined by cyclic voltammetry in MeCN starting from the Cu(I) complexes (example shown for **R2** in Fig. 5, for **R1–R5** see Fig. S24–S28 in the ESI‡). The measurements indicate that the redox process of all redox couples is reversible which is caused by the small structural changes between the Cu(I) and Cu(II) complexes and by the absence of any side reactions during the cyclic voltammetry measurement. The results show that the substituents have a significant influence on the redox potentials $E_{1/2}$ of the redox couples and therefore on the equilibrium constants K_{12} (Table 3). The redox potentials span a range of 0.5 V from −0.640 V to −0.134 V *vs.* the Fc/Fc^+ potential. For **R1–R3** the introduction of an alkyl substituent in the 2-position leads to higher redox potentials. In previous work the introduction of alkyl substituents in the 6-position led to lower redox potentials due to the stronger donor properties of the ligand induced by the weak electron density donating feature of the alkyl substituent.[24] This emphasizes the effect of the steric demand of the substituent in the 2-position. The redox potentials increase with the steric demand of the substituent (H < Me < ^{c}Hex). As mentioned before, a higher steric demand of the alkyl substituents results in Cu(I) and Cu(II) structures with higher τ_4 values and therefore in a higher average $\varnothing\tau_4$ value of both. High τ_4 values are favored by Cu(I) complexes, so that the distortion caused by the substituents leads to a stabilization of the Cu(I) complexes and hence higher redox potentials. The plot of the redox potential against the

Table 3 Redox potentials $E_{1/2}$, differences between the redox potentials of the copper redox couple and the counter complex $\Delta E_{1/2}$, equilibrium constants K_{12}, reaction rates k_{12}, electron self-exchange rates k_{11}, calculated average structural parameters $\varnothing\tau_4$ of the corresponding Cu(I) and Cu(II) complexes and differences between the calculated structural parameters $\Delta\tau_4$ of the corresponding Cu(I) and Cu(II) complexes

	$E_{1/2}$ [V] *vs.* Fc/Fc^+	$\Delta E_{1/2}$ [V]	K_{12} [ ]	k_{12} [M^{-1} s^{-1}]	k_{11} [M^{-1} s^{-1}]	$\varnothing\tau_4$ (DFT)	$\Delta\tau_4$ (DFT)
$[Cu(TMGqu)_2]^{+/2+}$ (**R1**)	−0.441	0.385	3.19×10^6	$(2.31 \pm 0.07) \times 10^4$	$(2.81 \pm 0.18) \times 10^2$	0.53	0.20
$[Cu(TMG2Mequ)_2]^{+/2+}$ (**R2**)	−0.224	0.168	6.81×10^2	$(1.63 \pm 0.16) \times 10^3$	$(2.19 \pm 0.44) \times 10^3$	0.59	0.13
$[Cu(TMG2^cHexqu)_2]^{+/2+}$ (**R3**)	−0.134	0.078	2.04×10^1	$(2.25 \pm 0.14) \times 10^2$	$(1.15 \pm 0.15) \times 10^3$	0.68	0.07
$[Cu(TMG2Meequ)_2]^{+/2+}$ (**R4**)	−0.302	0.246	1.46×10^4	$(6.67 \pm 0.30) \times 10^3$	$(2.33 \pm 0.22) \times 10^3$	0.61[a]	0.00[a]
$[Cu(TMG4NMe_2qu)_2]^{+/2+}$ (**R5**)	−0.640	0.584	7.45×10^9	$(4.74 \pm 0.27) \times 10^5$	$(3.38 \pm 0.44) \times 10^2$	0.54	0.20

[a] The value may be influenced by the 4 + 2 coordination motif in the Cu(II) complex.

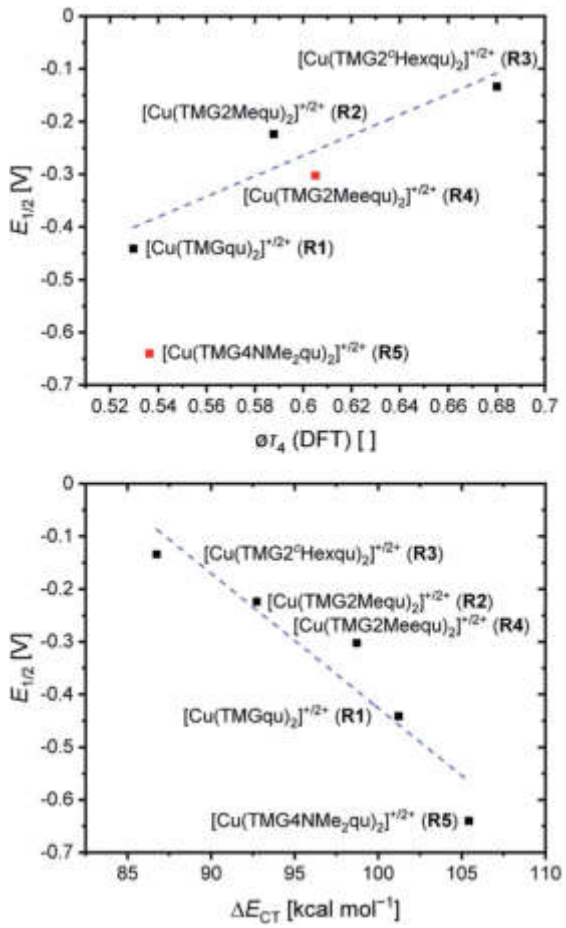

Fig. 6 Correlation between the redox potentials and the calculated $\varnothing\tau_4$ (DFT) values of the redox couples (top, R4 and R5 are marked in red due to the misfit with the correlation caused by the electronic influence by the substituents) and correlation between the redox potentials and the differences in the calculated charge-transfer energies ΔE_{CT} from all N donors to the Cu center of the corresponding Cu(II) and Cu(I) complexes (bottom).

calculated $\varnothing\tau_4$ values emphasizes this trend for **R1–R3** (Fig. 6, top; for correlation with experimental $\varnothing\tau_4$ values see Fig. S29 in the ESI‡). For **R4** this trend is also visible but due to the other influences of the methyl ester group the redox potential is not just influenced by the steric demand of the methyl ester group. Therefore, a direct comparison with **R1–R3** is not possible. The average $\varnothing\tau_4$ of **R5** is similar to the one of **R1**, but the redox potential is considerably lower. This underlines that not only is the distortion of the complexes responsible for the redox potentials but also the electronic influence of the substituents of the ligands on the coordination to the Cu center. As mentioned before, the charge-transfer energies from all donors to the Cu center are significantly higher in the Cu(II) complexes compared to the corresponding Cu(I) complexes but the differences vary depending on the substituent. The difference in the calculated charge-transfer energies ΔE_{CT} from all N donors to the Cu center of the corresponding Cu(II) and Cu(I) complexes indicates a correlation between the redox potentials and the donor properties of the ligands for all redox couples (Fig. 6, bottom). The redox potential decreases with an increasing difference in the charge-transfer energy because a higher difference induces a stronger stabilization of the electron-poor Cu(II) complex. For **R1–R3** the difference in the charge-transfer energies decreases with an increasing steric demand of the substituent in the 2-position because the steric demand causes a longer bond length between the N_{gua} and N_{qu} donors and the Cu center and therefore a weaker donation. **R4** also fits this correlation if the O donors are not considered. This indicates that only the donor properties of the N donors influence the redox potential. The methyl ester group weakens the stabilization of the Cu(II) complex compared to **R1**. This results in a higher redox potential. If the O donors are considered the stabilization would be much stronger and a lower redox potential would be expected (for comparison see Fig. S30 in the ESI‡). In the correlation the redox couple **R5** exhibits the highest difference in the charge-transfer energies and therefore the lowest redox potential. This is in accordance with previous work that investigated the influence of the dimethylamine group in the 6-position.[43] However, the effect of the dimethylamine group in the 4-position is much stronger which is also indicated in previous work. This showed that the influence of substituents in the 4-position is stronger compared to substituents in the 6-position.[24] The charge-transfer energies indicate that the electron density donating effect of the dimethylamine group on the donation of the N_{qu} donor is stronger in the Cu(II) complex than in the Cu(I) complex compared with **R1** (Fig. 4). This leads to a better stabilization of the electron-poor Cu(II) complex.

The cross reactions of the Cu(I) complexes **C1**, **C3**, **C5**, **C7** and **C9** with the counter complex $[Co(bpy)_3]^{3+}$ were monitored by stopped-flow UV/Vis spectroscopy at 298 K in MeCN. An excess of the counter complex was used so that the cross reaction is pseudo-first order and the concentration of the counter complex stays nearly constant throughout the reaction. The influence of the ionic strength on the activity coefficients of the reactants is not considered (further information in ESI Section 6.1‡). During the cross reaction the time-dependent changes in the UV/Vis spectra were examined. The absorption of the characteristic bands of the Cu(I) complexes decreases whereas the absorption of the characteristic bands of the Cu(II) complexes increases because the Cu(I) complex is oxidized to the Cu(II) complex. As an example, this is shown for the reaction of $[Cu(TMG2Meequ)_2]^+$ (**C7**) with $[Co(bpy)_3]^{3+}$ (Fig. 7, left). The reaction rate k_{obs} of the cross reaction was determined by a first-order fit of the decrease of the Cu(I) absorption against the reaction time (Fig. 7, middle). The cross reaction was performed with various concentrations of the counter complex so that the reaction rate k_{12} was determined by a linear fit of the reaction rate k_{obs} against the concentration of the counter complex (Fig. 7, right; Table 3).

The electron self-exchange rate k_{11} is calculated with the determined equilibrium constant K_{12} and the reaction rate k_{12} following the Marcus cross relation (eqn (1) and Table 3). The results implicate that all substituents have a high impact on the equilibrium constant K_{12} and the reaction rate k_{12} of the cross reaction. The differences between the equilibrium constants K_{12}

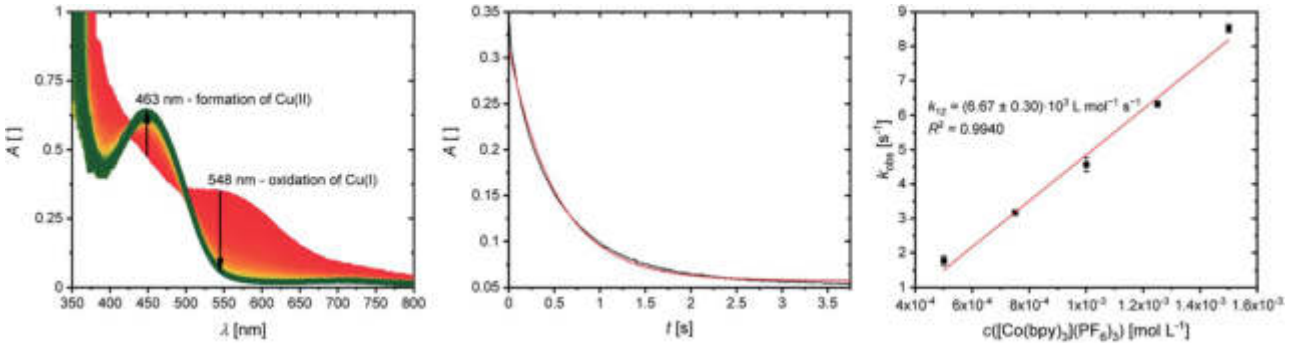

Fig. 7 Results of the cross reaction of $[Cu(TMG2Meequ)_2]^+$ (**C7**) with $[Co(bpy)_3]^{3+}$, left and middle: time-dependent change of the UV/Vis spectra and time-trace of the Cu(I) MLCT adsorption at 548 nm during the cross reaction with an excess of $[Co(bpy)_3]^{3+}$ (1 : 5) in MeCN at 298 K (black: measurement; red: fit); right: plot of the reaction rate k_{obs} against the concentration of $[Co(bpy)_3]^{3+}$.

are a result of the different redox potentials $E_{1/2}$ of the copper complex redox couples. Due to the influence of the equilibrium constant K_{12} on the reaction rate k_{12} of the cross reaction the electron self-exchange rate k_{11} is needed to compare the electron transfer properties of the copper complex redox couples. For **R2** and **R3** higher electron self-exchange rates k_{11} were obtained compared to unsubstituted redox couple **R1** which means that the alkyl substituents in the 2-position of the ligands lead to a faster electron transfer. This is caused by the steric demand of the alkyl substituents that leads to more similar structures of the corresponding Cu(I) and Cu(II) complexes and therefore to better entatic state models compared to **R1**. For this reason, the highest electron self-exchange rate would be expected for **R3** because it shows the highest structural accordance, represented by the $\Delta\tau_4$ (DFT) value, between the Cu(I) and Cu(II) complexes. However, the highest electron self-exchange rate is obtained for **R2**. This implicates that not only the structural accordance is important. Moreover, the "average" of the Cu(I) and the Cu(II) complex, represented by the $\varnothing\tau_4$ (DFT) value, is relevant. It describes whether the redox couple is in average more like a Cu(I) or a Cu(II) species. For a good entatic state model it is mandatory that the redox couple does not structurally favor one oxidation state. For **R2** a higher $\Delta\tau_4$ value is obtained compared to **R3** but the $\varnothing\tau_4$ value shows that the mean structure does not favor one oxidation state like in **R3** whose mean structure prefers the Cu(I) oxidation state. For **R4** a similar electron self-exchange rate k_{11} compared to **R2** is determined although this is not expected due to the large differences between the structures of the Cu(I) and Cu(II) complexes. Therefore, this redox couple should be a worse entatic state model. The reason for the high electron self-exchange rate could be that the donor ability of the methyl ester influences the entatic state of **R4**. In the Cu(I) complex weak interactions between the methyl ester group and the Cu center are observable although Cu(I) prefers to be coordinated tetrahedrally by four donor moieties. In the Cu(II) complex the interactions are much stronger leading to a 4 + 2 coordination motif. If Cu(II) is four-coordinate, it prefers to be coordinated in a square-planar geometry and if it is six-coordinate, it prefers to be coordinated octahedrally. The interaction between the Cu center and the methyl ester group could induce a different type of entatic state compared to the other complex redox couples that do not exhibit any further interactions between the ligand and the Cu besides the coordination of the guanidine and quinolinyl moieties. **R5** exhibits a similar electron self-exchange rate k_{11} compared to **R1**. Both redox couples have similar $\varnothing\tau_4$ and $\Delta\tau_4$ values. This suggests that no oxidation state is structurally favored by the introduction of the dimethylamine group. Characteristic of this redox couple is the extremely low redox potential which stabilizes the Cu(II) complex but this does not have a significant influence on the electron self-exchange rate. Therefore, the dimethylamine group only has a thermodynamic effect but not a kinetic effect on the electronic properties of the redox couple. Hence, the electronic influence of the dimethylamine group on the ligand does not affect the entatic state of the redox couple. For a deeper understanding between the electron transfer and the structural change during the electron transfer, the calculation of the reorganization energy is necessary.

Calculation of the reorganization energy

During the electron self-exchange reaction (characterized kinetically by k_{11}), the ligand spheres of the complexes and the solvent spheres around the complexes have to reorganize. The necessary energy for the reorganization of the ligand sphere is described by the internal reorganization energy $\lambda_{11,I}$ and the energy for the reorganization of the solvent sphere by the solvent reorganization energy $\lambda_{11,S}$. Together they result in the total reorganization energy $\lambda_{11,T}$ which describes the whole process. The reorganization energies were determined *via* DFT calculations using Nelsen's four-point method (Table 4, further information in ESI Section 9.4‡).[22,23,44]

For **R2** and **R3** with ligands with alkyl substituents in the 2-position significantly lower internal reorganization energies $\lambda_{11,I}$ were calculated compared to **R1** with the unsubstituted ligand **L1**. In contrast, for **R4** and **R5** with ligands with substituents that have an electronic influence, significantly higher internal reorganization energies were calculated. The results indicate that for **R1–R3** the internal reorganization energy shrinks with the increasing steric demand of the

Table 4 Calculated internal, solvent and total reorganization energies $\lambda_{11,I}$, $\lambda_{11,S}$, and $\lambda_{11,T}$, differences between the structural parameters $\Delta\tau_4$ and $\Delta\measuredangle$ and root-mean-square deviations (RMSD) of the calculated structures of the corresponding Cu(I) and Cu(II) complexes

	$\lambda_{11,I}$ [kJ mol^{-1}]	$\lambda_{11,S}$ [kJ mol^{-1}]	$\lambda_{11,T}$ [kJ mol^{-1}]	$\Delta\tau_4$ (DFT) [ ]	$\Delta\measuredangle$ (DFT) [°]	RMSD (DFT) [Å]
$[Cu(TMGqu)_2]^{+/2+}$ (**R1**)	66.6	135.2	201.8	0.20	23.8	0.283
$[Cu(TMG2Mequ)_2]^{+/2+}$ (**R2**)	55.2	128.6	183.8	0.13	17.06	0.191
$[Cu(TMG2^cHexqu)_2]^{+/2+}$ (**R3**)	52.7	110.7	163.3	0.07	13.3	0.147
$[Cu(TMG2Meequ)_2]^{+/2+}$ (**R4**)	81.6	123.5	205.1	0.00[a]	−7.5	2.289
$[Cu(TMG4NMe_2qu)_2]^{+/2+}$ (**R5**)	77.4	128.2	205.6	0.20	24.5	0.446

[a] The value may be influenced by the 4 + 2 coordination motif in the Cu(II) complex.

substituent (H < Me < ^{c}Hex). This is in accordance with the expectations because the higher steric demand leads to more similar structures of the Cu(I) and Cu(II) complexes and therefore to small $\Delta\tau_4$ or $\Delta\measuredangle$ values between the complexes. Similar structures reduce the internal reorganization energy necessary for the electron self-exchange. The results for **R4** and **R5** do not correlate with the $\Delta\tau_4$ or $\Delta\measuredangle$ values like for **R1–R3**. The reason is that the τ_4 value and the plane angle $\measuredangle$ do not represent all structural features of a complex because they only depend on the Cu center and the four N donors. The other atoms are not considered and therefore changes in the bond lengths and angles between the Cu(I) and Cu(II) complexes are not recognized. Hence, the root-mean-square deviation (RMSD) values of the atomic positions between the corresponding Cu(I) and Cu(II) complexes were calculated. The internal reorganization energies and the RMSD values correlate much better (Fig. 8). A lower RMSD value indicates a higher structural accordance which leads to a lower internal reorganization energy. For **R1–R3** and **R5** a linear correlation was found. The unusual coordination behavior of the ligand in **R4** could be the reason why this complex does not follow this linear correlation.

The solvent reorganization energy $\lambda_{11,S}$ decreases for **R2–R5** by the introduction of a substituent compared to the unsubstituted **R1**. For **R1–R3** the solvent reorganization energy decreases with the steric demand of the substituent (H < Me < ^{c}Hex). Due to the greater resemblance between the structures of the Cu(I) and Cu(II) complexes of **R2** and **R3** the solvent sphere is not as affected by the structural change of the complex during the electron transfer as for **R1**. Moreover, a substituent in the 2-position insulates the solvent sphere from the copper center. Hence, the influence of the change of the oxidation state during the electron transfer does not affect the solvent sphere of **R2** and **R3** as much as of **R1**. This effect is stronger in **R3** than in **R2** because the substituent is larger and therefore the shielding of the copper center stronger. A similar effect occurs in **R4** but the methyl ester group in the 2-position not only insulates the solvent sphere from the copper center structurally but also electronically and by its weak coordination ability especially in the Cu(II) species. This leads to the second lowest solvent reorganization energy of the analyzed redox couples. However, also the isolated electronic influence of the dimethylamine group in **R5** leads to a decrease of the solvent reorganization energy compared to **R1**. Due to the stronger donor properties of the N_{qu} donor caused by the electron density donating feature of the dimethylamine group the positive charge of the copper center is better stabilized especially in the Cu(II) species. This results in a weaker electronic influence on the solvent sphere and therefore a lower solvent reorganization energy.

In sum, the total reorganization energy $\lambda_{11,T}$ decreases significantly for **R2** and **R3** with the introduction of alkyl substituents in the 2-position compared to **R1** whereas for **R4** and **R5** a small increase occurs.

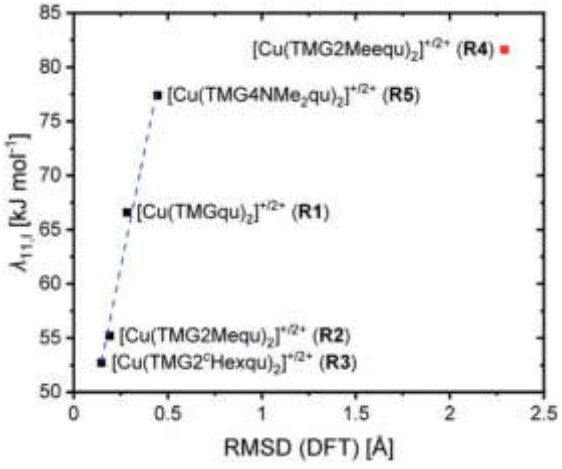

Fig. 8 Correlation between the internal reorganization energy $\lambda_{11,I}$ and the RMSD.

Discussion and correlation of the results

All complexes exhibit a strongly distorted geometry between the ideal tetrahedral and the ideal square-planar geometry. The alkyl substituents in the 2-position of **R2** and **R3** have a steric influence on the coordination where an increasing steric demand of the ligand leads to a greater similarity between the structures of the Cu(I) and Cu(II) complexes compared to the unsubstituted **R1** (Fig. 9). Further, the geometries of the Cu(I) and Cu(II) complexes approach the tetrahedral geometry with the steric demand of the substituents (H < Me < ^{c}Hex). In contrast, the methyl ester substituent in the 2-position of **R4** has in addition to the steric demand an electronic influence and weak coordination ability especially in the Cu(II) complex. This weak coordination ability leads to the least similar Cu(I) and Cu(II) complex structures. The influence of the dimethylamine group in the 4-position of **R5** is limited to an electron density

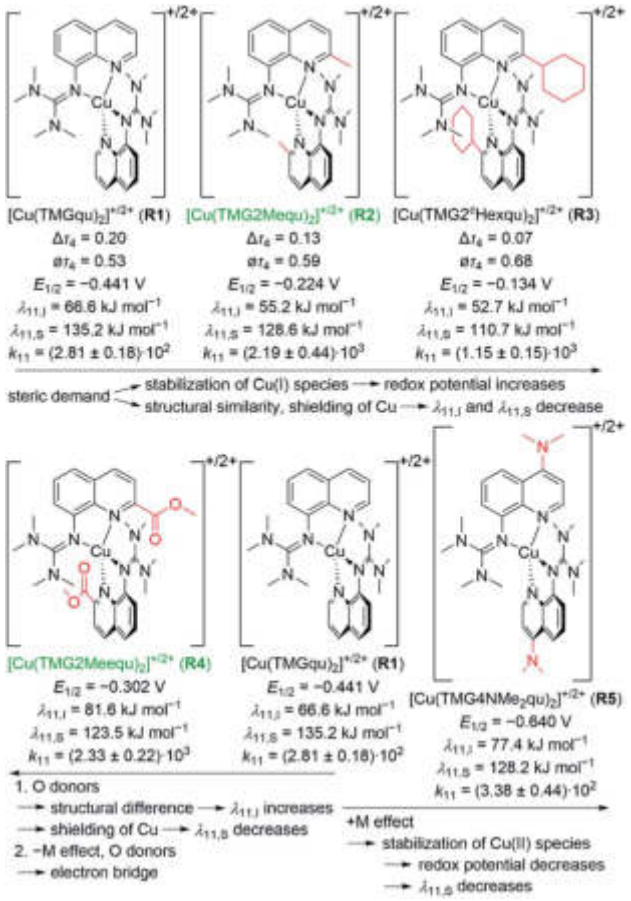

Fig. 9 Summary of the influences of the substituents on the properties of the copper complex redox couples (substituents are marked in red, the two best entatic state models are marked in green, $E_{1/2}$ *vs.* Fc/Fc^+, k_{11} in M^{-1} s^{-1}).

donating effect which does not induce a significant change in the coordination geometry. From the structural point of view **R3** should be the best entatic state model.

The redox couples' potentials possess a strong dependency on the structural and electronic properties of the complexes. In case of **R1**, **R2** and **R3** the redox potential increases with a tendency towards a tetrahedral geometry leading to a stabilization of the Cu(I) species (Fig. 9). Moreover, the redox potential decreases with an increasing difference between the charge-transfer energies of the corresponding Cu(II) and Cu(I) complexes because the Cu(II) complex becomes better stabilized. Especially in **R5**, the electron density donating feature of the dimethylamine leads to a strong stabilization of the Cu(II) complex. Furthermore, the substituents have a significant impact on the electron self-exchange rates. The introduction of an alkyl substituent leads to higher electron self-exchange rates of **R2** and **R3** compared to **R1**. This correlates with the smaller internal and solvent reorganization energies of **R2** and **R3** compared to **R1**. However, **R3** exhibits the lowest reorganization energy but not the highest electron self-exchange rate. This result emphasizes that besides a structural similarity between the Cu(I) and Cu(II) complexes a mean structure that does not favor one oxidation state of the redox couple is important for a fast electron transfer. Therefore, **R2** is a better functional entatic state model than **R3**. **R4** possesses the highest internal and the second lowest solvent reorganization energy, in sum the second highest total reorganization energy. Nevertheless, it exhibits the highest electron self-exchange rate. A correlation between the electron self-exchange rate and the reorganization energy is not possible. This underlines that a high electron self-exchange rate cannot only be achieved by a high structural accordance between the Cu(I) and Cu(II) complexes and a low total reorganization energy. A possible explanation for the high electron self-exchange rate of **R4** is that the ester group has a significant influence on the process of the outer-sphere electron transfer itself. Due to its negative mesomeric effect (−M effect) it is part of the aromatic system of the ligand in which the electrons can move freely. Moreover, the donor properties of the ester group may lead to a reinforcement of the interactions between two individual complexes. Especially in the Cu(I) species the ester groups do not exhibit any strong interactions with the Cu(I) center and could therefore interact with a different complex. In sum, the ester group could act as a bridge for the outer-sphere electron transfer and by this reduce the length of the jump of the electron through space between the two complexes. This effect is not considered in the calculated reorganization energies. An analogous but less intense effect could occur in **R5** and explain the similar electron self-exchange rate compared to **R1** although the total reorganization energy is higher. Overall, **R2** and **R4** are the best functional entatic state models but for different reasons, namely the interplay between steric and mesomeric effects. Therefore, different approaches to reach higher electron self-exchange rates and to enhance the entatic state model with the same ligand framework are possible. The steric manipulation facilitates the transition between the two oxidation states whereas the electronic manipulation by a mesomeric effect facilitates the transfer of the electron from one complex to another complex.

Conclusions

In this study, novel guanidine quinolinyl copper complexes were synthesized and their electron transfer properties analyzed to gain a deeper understanding of the entatic state for electron transfer. Ligands with substituents in the 2- or 4-position of the quinolinyl backbone that exert steric and electronic influences on the donor properties of the ligands were synthesized to design complexes with specific features. The complexes were characterized by XRD, XAS, and DFT revealing significant impacts of the substituents on the structural and electronic properties of the complexes. To examine the influence on the electron transfer, the electron self-exchange rates were determined and the reorganization energies calculated. In **R2** and **R3** the steric demand of the alkyl substituents in the 2-position leads to lower total reorganization energies and higher electron-self exchange rates compared to **R1**. Therefore, the entatic state of the electron transfer is manipulated sterically in **R2** and **R3**. The methyl ester group in the 2-position of **R4** leads to a higher

steric demand and enhanced donor properties; furthermore, it has an electron density withdrawing effect. Although **R4** exhibits a high total reorganization energy, it possesses the highest electron self-exchange rate. The ester group possibly enables a different type of manipulation of the entatic state by serving as an electron bridge in the electron transfer. The pure electron density donating feature of the dimethylamine group in the 4-position of **R5** exhibits the smallest influence on the electron transfer.

In general, the ability of the copper complex redox couples to act as functional entatic state models could be tuned and significantly improved which is due to the varied substituents in the aromatic system. This opens up new avenues in the design of entatic state complexes and, in general, electron transfer systems where the thermodynamics and kinetics can be tuned.

Data availability

All synthetic details are described in the ESI.‡ Additional information on the synthesis of the target compounds and original analysis data files are available in the Chemotion repository (for corresponding links see the ESI‡). The optimized calculated structures were deposited in the repository RADAR4Chem by FIZ Karlsruhe – Leibniz-Institut für Informationsinfrastruktur and are published under an Open Access model (CC BY-NC-SA 4.0 Attribution-NonCommercial-ShareAlike; **https://doi.org/10.22000/613**).

Author contributions

J. H. synthesized the ligands, complexes and the XAS samples. J. H. performed and evaluated the CV, NMR, IR, UV/Vis and stopped-flow spectroscopic measurements, evaluated additionally the MS data, determined the equilibrium constants and the electron self-exchange rates and performed Nelsen's four-point method calculations. Furthermore, J. H. executed the DFT and NBO calculations and the analysis under supervision of A. H. F. M. synthesized two ligands and helped to characterize the complexes with these ligands with CV and stopped-flow spectroscopy. A. H. and T. P. S. checked and finalized the crystallographic data. S. B., M. T. and B. G.-L. measured and analyzed the XAS data. J. H., A. H., M. R. and S. H.-P. wrote the manuscript. M. R. and S. H.-P. supervised the project.

Conflicts of interest

There are no conflicts to declare.

Acknowledgements

S. H.-P. and M. R. acknowledge financial support by the Deutsche Forschungsgemeinschaft (DFG, 413524714). Further, M. R. acknowledges funding by the Deutsche Forschungsgemeinschaft (DFG) *via* RU 773/8-1 and the Bundesministerium für Bildung und Forschung (BMBF) *via* 05K19GU5. We thank the Paderborn Center for Parallel Computing, PC^2, for providing computing time on the High-Performance Computing (HPC) system OCuLUS as well as support. Moreover, we thank the Regional Computing Center of the University of Cologne (RRZK) for providing computing time on the DFG-funded High Performance Computing (HPC) system CHEOPS as well as support. We thank NFDI4Chem for support and funding of the repository RADAR4Chem. Finally, we thank Edmund Welter and Wolfgang Caliebe for their support at PETRA III.

Notes and references

1 (*a*) J. Liu, S. Chakraborty, P. Hosseinzadeh, Y. Yu, S. Tian, I. Petrik, A. Bhagi and Y. Lu, *Chem. Rev.*, 2014, **114**, 4366; (*b*) E. I. Solomon and R. G. Hadt, *Coord. Chem. Rev.*, 2011, **255**, 774; (*c*) E. I. Solomon, D. E. Heppner, E. M. Johnston, J. W. Ginsbach, J. Cirera, M. Qayyum, M. T. Kieber-Emmons, C. H. Kjaergaard, R. G. Hadt and L. Tian, *Chem. Rev.*, 2014, **114**, 3659.

2 (*a*) J. Mitchell Guss and H. C. Freeman, *J. Mol. Biol.*, 1983, **169**, 521; (*b*) P. M. Colman, H. C. Freeman, J. M. Guss, M. Murata, V. A. Norris, J. A. M. Ramshaw and M. P. Venkatappa, *Nature*, 1978, **272**, 319.

3 (*a*) S. Dahlin, B. Reinhammar and M. T. Wilson, *Biochem. J.*, 1984, **218**, 609; (*b*) C. Buning, G. W. Canters, P. Comba, C. Dennison, L. Jeuken, M. Melter and J. Sanders-Loehr, *J. Am. Chem. Soc.*, 2000, **122**, 204; (*c*) F. A. Armstrong, P. C. Driscoll, H. Allen and O. Hill, *FEBS Lett.*, 1985, **190**, 242; (*d*) K. Kataoka, A. Kondo, K. Yamaguchi and S. Suzuki, *J. Inorg. Biochem.*, 2000, **82**, 79; (*e*) K. Kataoka, K. Yamaguchi, M. Kobayashi, T. Mori, N. Bokui and S. Suzuki, *J. Biol. Chem.*, 2004, **279**, 53374; (*f*) K. Kataoka, K. Yamaguchi, S. Sakai, K. Takagi and S. Suzuki, *Biochem. Biophys. Res. Commun.*, 2003, **303**, 519; (*g*) T. Kohzuma, S. Takase, S. Shidara and S. Suzuki, *Chem. Lett.*, 1993, **22**, 149; (*h*) A. Lommen and G. W. Canters, *J. Biol. Chem.*, 1990, **265**, 2768; (*i*) K. Sato, P. B. Crowley and C. Dennison, *J. Biol. Chem.*, 2005, **280**, 19281; (*j*) K. Sato, T. Kohzuma and C. Dennison, *J. Am. Chem. Soc.*, 2003, **125**, 2101; (*k*) S. Suzuki, K. Kataoka, K. Yamaguchi, T. Inoue and Y. Kai, *Coord. Chem. Rev.*, 1999, **190–192**, 245.

4 P. Comba, M. Kerscher and A. Roodt, *Eur. J. Inorg. Chem.*, 2004, **2004**, 4640.

5 B. G. Karlsson, R. Aasa, B. G. Malmström and L. G. Lundberg, *FEBS Lett.*, 1989, **253**, 99.

6 B. G. Malmström, *Eur. J. Biochem.*, 1994, **223**, 711.

7 J. Stanek, A. Hoffmann and S. Herres-Pawlis, *Coord. Chem. Rev.*, 2018, **365**, 103.

8 (*a*) D. B. Rorabacher, *Chem. Rev.*, 2004, **104**, 651; (*b*) R. J. P. Williams, *Inorg. Chim. Acta, Rev.*, 1971, **5**, 137; (*c*) W. R. Hagen, *Metallomics*, 2019, **11**, 1768.

9 P. Comba and W. Schiek, *Coord. Chem. Rev.*, 2003, **238–239**, 21.

10 P. Comba, *Coord. Chem. Rev.*, 2000, **200–202**, 217.

11 B. L. Vallee and R. J. Williams, *Proc. Natl. Acad. Sci. U. S. A.*, 1968, **59**, 498.

12 P. Comba, *Coord. Chem. Rev.*, 1999, **182**, 343.

13 R. J. Williams, *Eur. J. Biochem.*, 1995, **234**, 363.

14 B. G. Malmström, *Biol. Met.*, 1990, **3**, 64.
15 G. Chaka, J. L. Sonnenberg, H. B. Schlegel, M. J. Heeg, G. Jaeger, T. J. Nelson, L. A. Ochrymowycz and D. B. Rorabacher, *J. Am. Chem. Soc.*, 2007, **129**, 5217.
16 P. R. Raithby, G. P. Shields, F. H. Allen and W. D. S. Motherwell, *Acta Crystallogr., Sect. B: Struct. Sci.*, 2000, **56**, 444.
17 (*a*) P. Comba, S. Fukuzumi, C. Koke, B. Martin, A.-M. Löhr and J. Straub, *Angew. Chem., Int. Ed.*, 2016, **55**, 11129; *Angew. Chem.*, 2016, **128**, 11295; (*b*) Y. Ren, J. Forté, K. Cheaib, N. Vanthuyne, L. Fensterbank, H. Vezin, M. Orio, S. Blanchard and M. Desage-El Murr, *iScience*, 2020, **23**, 100955; (*c*) B. Dicke, A. Hoffmann, J. Stanek, M. S. Rampp, B. Grimm-Lebsanft, F. Biebl, D. Rukser, B. Maerz, D. Göries, M. Naumova, M. Biednov, G. Neuber, A. Wetzel, S. M. Hofmann, P. Roedig, A. Meents, J. Bielecki, J. Andreasson, K. R. Beyerlein, H. N. Chapman, C. Bressler, W. Zinth, M. Rübhausen and S. Herres-Pawlis, *Nat. Chem.*, 2018, **10**, 355; (*d*) G. D. Stroscio, R. D. Ribson and R. G. Hadt, *Inorg. Chem.*, 2019, **58**, 16800; (*e*) L. Garcia, F. Cisnetti, N. Gillet, R. Guillot, M. Aumont-Nicaise, J.-P. Piquemal, M. Desmadril, F. Lambert and C. Policar, *J. Am. Chem. Soc.*, 2015, **137**, 1141; (*f*) D. F. Schrempp, S. Leingang, M. Schnurr, E. Kaifer, H. Wadepohl and H.-J. Himmel, *Chem.–Eur. J.*, 2017, **23**, 13607; (*g*) D. F. Schrempp, E. Kaifer and H.-J. Himmel, *Eur. J. Inorg. Chem.*, 2018, **2018**, 3660.
18 (*a*) B. Xie, L. J. Wilson and D. M. Stanbury, *Inorg. Chem.*, 2001, **40**, 3606; (*b*) B. Xie, T. Elder, L. J. Wilson and D. M. Stanbury, *Inorg. Chem.*, 1999, **38**, 12.
19 E. W. Dahl and N. K. Szymczak, *Angew. Chem., Int. Ed.*, 2016, **55**, 3101.
20 A. Hoffmann, S. Binder, A. Jesser, R. Haase, U. Flörke, M. Gnida, M. Salomone Stagni, W. Meyer-Klaucke, B. Lebsanft, L. E. Grünig, S. Schneider, M. Hashemi, A. Goos, A. Wetzel, M. Rübhausen and S. Herres-Pawlis, *Angew. Chem., Int. Ed.*, 2014, **53**, 299; *Angew. Chem.*, 2014, **126**, 305–310.
21 A. Hoffmann, J. Stanek, B. Dicke, L. Peters, B. Grimm-Lebsanft, A. Wetzel, A. Jesser, M. Bauer, M. Gnida, W. Meyer-Klaucke, M. Rübhausen and S. Herres-Pawlis, *Eur. J. Inorg. Chem.*, 2016, **2016**, 4731.
22 J. Stanek, N. Sackers, F. Fink, M. Paul, L. Peters, R. Grunzke, A. Hoffmann and S. Herres-Pawlis, *Chem.–Eur. J.*, 2017, **23**, 15738.
23 J. Stanek, M. Konrad, J. Mannsperger, A. Hoffmann and S. Herres-Pawlis, *Eur. J. Inorg. Chem.*, 2018, **2018**, 4997.
24 T. Rösener, A. Hoffmann and S. Herres-Pawlis, *Eur. J. Inorg. Chem.*, 2018, **2018**, 3164.
25 F. Fontana, F. Minisci, M. C. Nogueira Barbosa and E. Vismara, *Tetrahedron*, 1990, **46**, 2525.
26 S. Y. Gadomsky and I. K. Yakuschenko, *Russ. Chem. Bull.*, 2016, **65**, 816.
27 (*a*) H. J. Cho, M. I. El-Gamal, C.-H. Oh, S. H. Lee, T. Sim, G. Kim, H. S. Choi, J. H. Choi and K. H. Yoo, *Chem. Pharm. Bull.*, 2013, **61**, 747; (*b*) R. W. Gouley, G. W. Moersch and H. S. Mosher, *J. Am. Chem. Soc.*, 1947, **69**, 303.
28 (*a*) O. V. Dyablo, E. A. Shmoilova, A. F. Pozharskii, V. A. Ozeryanskii, O. N. Burov and Z. A. Starikova, *Org. Lett.*, 2012, **14**, 4134; (*b*) T. G. Ribelli, M. Fantin, J.-C. Daran, K. F. Augustine, R. Poli and K. Matyjaszewski, *J. Am. Chem. Soc.*, 2018, **140**, 1525.
29 (*a*) W. Kantlehner, E. Haug, W. W. Mergen, P. Speh, T. Maier, J. J. Kapassakalidis, H.-J. Bräuner and H. Hagen, *Liebigs Ann. Chem.*, 1984, **1984**, 108; (*b*) S. Herres-Pawlis, A. Neuba, O. Seewald, T. Seshadri, H. Egold, U. Flörke and G. Henkel, *Eur. J. Org. Chem.*, 2005, **2005**, 4879.
30 A. Hoffmann, R. Grunzke and S. Herres-Pawlis, *J. Comput. Chem.*, 2014, **35**, 1943.
31 A. Hoffmann, M. Rohrmüller, A. Jesser, I. dos Santos Vieira, W. G. Schmidt and S. Herres-Pawlis, *J. Comput. Chem.*, 2014, **35**, 2146.
32 A. Jesser, M. Rohrmüller, W. G. Schmidt and S. Herres-Pawlis, *J. Comput. Chem.*, 2014, **35**, 1.
33 M. Rohrmüller, S. Herres-Pawlis, M. Witte and W. G. Schmidt, *J. Comput. Chem.*, 2013, **34**, 1035.
34 M. Rohrmüller, A. Hoffmann, C. Thierfelder, S. Herres-Pawlis and W. G. Schmidt, *J. Comput. Chem.*, 2015, **36**, 1672.
35 T. Rösener, O. Bienemann, K. Sigl, N. Schopp, F. Schnitter, U. Flörke, A. Hoffmann, A. Döring, D. Kuckling and S. Herres-Pawlis, *Chem.–Eur. J.*, 2016, **22**, 13550.
36 P. Liebhäuser, K. Keisers, A. Hoffmann, T. Schnappinger, I. Sommer, A. Thoma, C. Wilfer, R. Schoch, K. Stührenberg, M. Bauer, M. Dürr, I. Ivanović-Burmazović and S. Herres-Pawlis, *Chem.–Eur. J.*, 2017, **23**, 12171.
37 L. Yang, D. R. Powell and R. P. Houser, *Dalton Trans.*, 2007, 955.
38 V. Raab, K. Harms, J. Sundermeyer, B. Kovacević and Z. B. Maksić, *J. Org. Chem.*, 2003, **68**, 8790.
39 L. S. Kau, D. J. Spira-Solomon, J. E. Penner-Hahn, K. O. Hodgson and E. I. Solomon, *J. Am. Chem. Soc.*, 1987, **109**, 6433.
40 J. E. Hahn, R. A. Scott, K. O. Hodgson, S. Doniach, S. R. Desjardins and E. I. Solomon, *Chem. Phys. Lett.*, 1982, **88**, 595.
41 (*a*) R. A. Marcus, *Pure Appl. Chem.*, 1997, **69**, 13; (*b*) R. A. Marcus, *Angew. Chem., Int. Ed.*, 1993, **32**, 1111; *Angew. Chem.*, 1993, **105**, 1161–1172; (*c*) R. A. Marcus and N. Sutin, *Biochim. Biophys. Acta, Rev. Bioenerg.*, 1985, **811**, 265.
42 B. C. Dunn, L. A. Ochrymowycz and D. B. Rorabacher, *Inorg. Chem.*, 1995, **34**, 1954.
43 K. W. Kröckert, J. S. Mannsperger, T. Rösener, A. Hoffmann and S. Herres-Pawlis, *Z. Anorg. Allg. Chem.*, 2021, **647**, 832.
44 (*a*) S. F. Nelsen, S. C. Blackstock and Y. Kim, *J. Am. Chem. Soc.*, 1987, **109**, 677; (*b*) S. F. Nelsen and M. J. R. Yunta, *J. Phys. Org. Chem.*, 1994, **7**, 55.

4.6 Catecholate Formation after Phenolate Attack on a Tyrosinase Model Complex - Low Temperature UV/Vis Operando Raman Studies

The author has contributed to the Raman measurements and the respective data analysis.

In [4.6], operando Raman measurements were performed to investigate the hydroxylation mechanism of different phenolic substrates with a bis(μ-oxo) dicopper(III) complex. The study uses low-temperature UV and visible time-dependent Raman spectroscopy, cryospray-ionization mass spectrometry and DFT calculations to reveal the kinetics of the catalytic conversion reaction mechanism. Tracking the temporal behavior of the individual Raman modes shows that both, the bis(μ-oxo) and the peroxo motifs, are formed during the intermediate steps. The reaction is tracked by analyzing the exchange in intensity from the Cu_2O_2 breathing mode to the corresponding mode of the catecholate complex.

The ligand TMGdmap is combined with a copper salt to form the precursor **C1**, which is oxygenated to form the complex **O1**. Oxygenation and isotope shift reaction measurements are taken at 532 nm and shown in [4.6]-Fig. 1 (b). The isotope shift measurements showed the expected redshift, indicating the formation of the bis(μ-oxo) characteristic breathing mode at 617 cm^{-1} and 585 cm^{-1} for $^{16}O_2$ and $^{18}O_2$, respectively. The inset shows operando Raman measurements during the oxygenation of the precursor. The intensity of the aforementioned Raman mode is fitted and plotted against the time axis to reveal a complete oxygenation after 1 min. Running Raman scans continuously is the central technique in this research item and it is used to track the behavior of the catalytic conversion after addition of the phenolate substrate NaOPh in [4.6]-Fig. 2 to clearly demonstrate the formation of the catecholato complex *via* a phenolate intermediate. The data are taken at 532 nm and the figure displays the energy range of 550-800 cm^{-1}, because we find the modes containing heavier Cu atoms at lower energies. For information on the substrates and conversion products, wee see the same type of operando experiments conducted while the energy range covers 800-2200 cm^{-1} in [4.6]-Fig. 3 and 4. In [4.6]-Fig. 3 the substrate NaOPh is used at different concentrations from 1-5 equivalents of the complex. The data are taken at 240 nm and show a faster conversion for higher relative concentrations of the substrate. [4.6]-Fig. 4 shows the operando measurements for the different substrates NaOPh, Me−PhONa and MeO−PhONa taken also at 240 nm.

The Raman measurements were conducted with the Tsunami laser system using the second and third harmonic generation unit. Different wavelengths have to be tested to find good wavelengths that yield significant intensities but no parasitic fluorescence. Since operando measurements have to be conducted on 20-120 sec timescales, a strong intensity enhancement is not just a welcomed feature but necessary for the project. The achromatic entrance optics and the tunable Tangerine laser is perfectly suited for such a task. The wavelengths of 240 nm at 3ω and 532 from the Millennia diode laser are used for the main Raman measurements, while 220 nm, 230 nm, 260 nm, 280 nm, 360 nm, 414 nm and 450 nm have additionally been tested. Note that a high intensity also leads to shorter integration times, which allows for a higher precision, since every spectrum is an average over each second it took to integrate it. The precursor solution with a concentration of 10 mM was filled in a glass cuvette and closed with a lid containing a septum in the glovebox, to ensure no unwanted exposure to water or oxygen. The cuvette was cooled to -90 °C. The precursor was oxygenated *via* a cannula through the septum at 0.02 bar overpressure for a time of a few minutes. A micrometer screw was used to adjust the focal

depth to the maximum signal. The power for the continuous-wave 532 nm laser was 42 nm and for the pulsed 240 nm laser in the range from 2-3 mW. The substrates were added with a gas-tight Hamilton glass syringe.

Catecholate Formation after Phenolate Attack on a Tyrosinase Model Complex - Low Temperature UV/Vis Operando Raman Studies

Catecholate Formation after Phenolate Attack on a Tyrosinase Model Complex—Low Temperature UV/Vis Operando Raman Studies

Benjamin Grimm-Lebsanft,[a,‡] Melissa Teubner,[a,b,‡] Sören Buchenau,[a] Philipp Paetzold,[a] Melanie Paul,[b] Alexander Hoffmann,[b] Sonja Herres-Pawlis,[b] Michael A. Rübhausen[a]

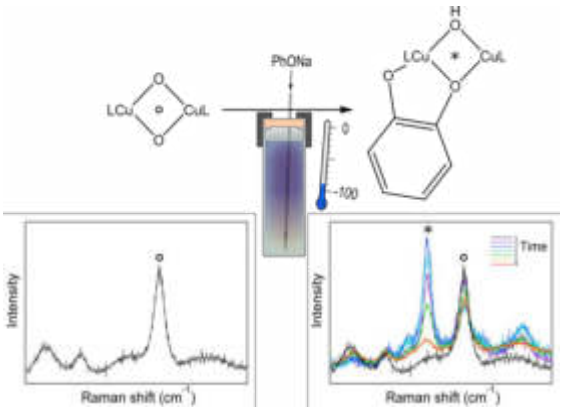

Platzhalter für TOC

Abstract

The active site of the enzyme tyrosinase, responsible for hydroxylating phenols, includes a side-on peroxo dicopper(II) center. We investigate the hydroxylation of phenolatic substrates with an isomeric bis(μ-oxo) dicopper(III) complex. We apply low-temperature operando Raman measurements in the UV as well as in the visible range to study $[Cu_2(\mu\text{-}O)_2\mathbf{L}_2](OTf)_2$ which is stabilized by 2-(3-(dimethylamino)propyl)-

[a] Dr. B. Grimm-Lebsanft, M. Teubner, S. Buchenau, P. Paetzold, Prof. Dr. M. A. Rübhausen
Department of Physics, University of Hamburg
Luruper Chaussee 149, 22761 Hamburg (Germany)
[b] Dr. M. Paul, M. Teubner, Dr. A. Hoffmann, Prof. Dr. S. Herres-Pawlis
Department of Inorganic Chemistry
RWTH Aachen University, Landoltweg 1, 52074 Aachen (Germany)
‡ Shared first authorship.

1,1,3,3-tetramethylguanidine (**L**). We observe the formation of a catecholato complex by a distinct Raman mode—visible when excited with a wavelength of 532 nm—at 586 cm^{-1} during the hydroxylation of sodium phenolate via a phenolato intermediate. The interplay between the bis(μ-oxo) complex and the formation of the intermediates can be tracked by an exchange of intensity between the characteristic Cu_2O_2 breathing mode of the bis(μ-oxo) complex and the corresponding mode of the catecholato complex. The change in intensity of higher energy modes from the phenolato and catecholato complex are best observed when excited in the UV, here at 240 nm, complementing the measurements in the visible range. Our study paves a new pathway for the investigation and corresponding development of catalytically active model complexes mimicking the tyrosinase cycle.

Introduction

Copper enzymes play essential roles in biochemical processes such as electron transfer and dioxygen transport.[1–6] Tyrosinase for example, a coupled binuclear copper enzyme that is present in all aerobic lifeforms,[7,8] can reversibly bind and thereby activate dioxygen. It can catalyze the *ortho*-hydroxylation of L-tyrosine to L-DOPA and is also able to perform the two-electron oxidation of this *ortho*-catechol to L-dopaquinone in the melanin biosynthesis.[1–3,9,10] Raman spectroscopy and X-ray crystal structures revealed that the activated dioxygen molecule is bound in a bridging side-on μ-η²:η²-peroxo dicopper(II) ([**P**]) core in the *oxy* form of tyrosinase (cf. **Scheme 1**).[7,9,11] Although it is consensus that the hydroxylation mechanism is consistent with an electrophilic aromatic substitution,[1,12,13] the intermediates of this reaction are not yet experimentally observed.[1,8] The monophenolase cycle of

tyrosinase is shown in **Scheme 1**, however, alternative pathways and structures for the intermediates are discussed.[7,8,14–18] To better understand the mechanism of tyrosinase and also to use the capability of hydroxylating the *ortho*-C–H bond in a phenol, many groups synthesized model complexes that mimic the [**P**] core of the *oxy* form of tyrosinase.[19–23] Interestingly, on account of a low isomerization barrier, there are also [**P**] complexes that are in equilibrium with their isomeric bis(μ-oxo) ([**O**]) form.[1,14,19,24,25] As it is still under debate whether the [**O**] species plays a role in biological reactions, there is also already a variety of model complexes with an [**O**] core.[19–22,26,27]

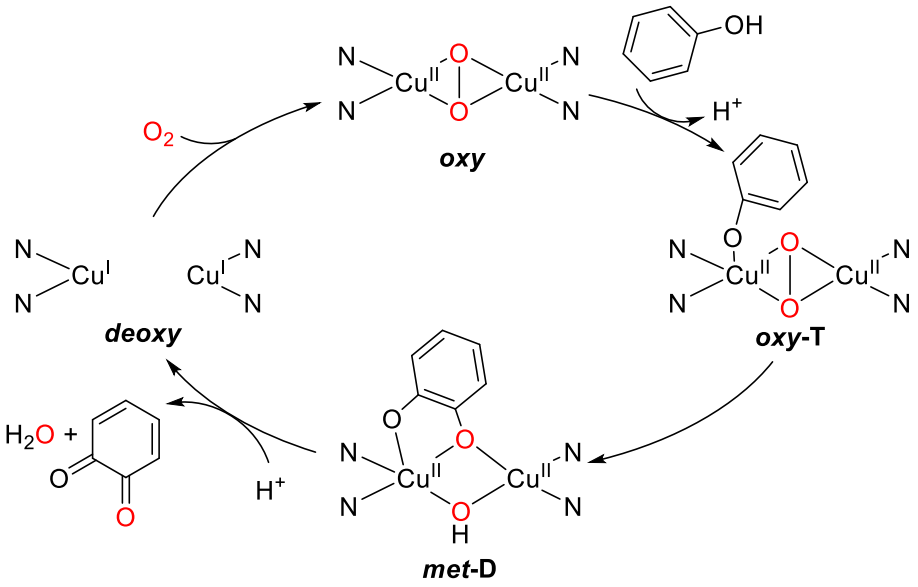

Scheme 1: Monophenolase cycle of tyrosinase. N represents His ligation from the protein. The third histidine from every Cu center is omitted for clarity. T = tyrosine bound and D = DOPA bound forms. Adapted from [1].

UV/VIS spectroscopy and Raman spectroscopy are two of the established methods to differentiate between the copper-oxygen species.[5,20,28–32] UV/Vis spectroscopy was also used to follow the reaction of tyrosinase model complexes with a phenolic substrate. The main focus being the observation of a decreasing characteristic band

of the [**P**] complex or an increase of a feature for the product, like catechol or quinone.[12,15,33–37] An intermediate catecholato complex was observed in some cases.[37,38] The decay of a phenolato complex which shows a (pseudo) first-order behavior was also monitored.[15,39] Raman spectroscopy was implemented as well to track an intermediate. It was formed after adding a phenolate to a tyrosinase model complex. New Raman modes were attributed to phenolate vibrations from an intermediate analogous to the *oxy*-T in the tyrosinase cycle (see **Scheme 1**).[14,15,17,39] The interested reader is referred to excellent reviews and a reference module with detailed descriptions of possible mechanisms of the tyrosinase reaction and different model complexes.[1,2,19–22,40]

To contribute to these findings and elucidate the steps in the hydroxylation reaction, we use a hybrid guanidine-stabilized bis(μ-oxo) dicopper(III) complex that is capable of hydroxylating various phenols[41] in this study. The complex is only stable at low temperatures, just like most tyrosinase model complexes.[14,42–44] To ensure the stability of the complex, we use an improved version of a self-designed two-stage cryostat[42] allowing for in situ oxygenation of the precursor. Furthermore, substrates can be added to study the hydroxylation operando. We accomplish this by combining a liquid ethanol chiller with a Peltier element to reach temperatures below −90 °C in a cuvette to ensure stable temperatures and measurements over a long time scale. With this method, we provide evidence for the proposed reaction steps for the complex $[Cu_2(\mu\text{-}O)_2\mathbf{L}_2](OTf)_2$ (**L** = 2-(3-(dimethylamino)propyl)-1,1,3,3-tetramethyl-guanidine, TMGdmap) with phenolatic substrates by means of low temperature operando Raman studies, using an excitation wavelength λ_{ex} in the UV as well as in the visible range. Three different substrates were used: sodium phenolate (NaOPh), sodium 4-Me-phenolate (Me-PhONa), and sodium 4-MeO-phenolate (MeO-PhONa).

We support our findings by density functional theory (DFT) calculations and cryogenic ultra-high resolution electrospray-ionization mass spectrometry (cryo-UHR ESI-MS). Most importantly, we identify the attack of the phenolate on the Cu_2O_2 core forming a catecholate intermediate that is comparable to the *met*-D form in tyrosinase via a short-lived phenolate intermediate, comparable to *oxy*-T (cf. **Scheme 1**). By using excitation wavelengths in different energy ranges, we obtain information about modes originating from the copper-oxygen core as well as from modes of the phenolic structure. We believe that our study will improve the understanding of the biological tyrosinase cycle and foster future development of catalytically active tyrosinase model complexes.

Results and Discussion

Figure 1a shows the oxygenation of the air- and moisture-sensitive Cu^I complex [**C1**]OTf in THF at –90 °C to the bis(μ-oxo) dicopper(III) complex $[Cu_2(\mu\text{-}O)_2\mathbf{L}_2](OTf)_2$ ([**O1**](OTf)$_2$). The precursor [**C1**]OTf was synthesized by mixing equimolar amounts of **L** (2-(3-(dimethylamino)propyl)-1,1,3,3-tetramethylguanidine) and $Cu(MeCN)_4OTf$ in acetonitrile at room temperature. Raman spectra (**Figure 1b**) show the oxygen isotope sensitive breathing mode of the Cu_2O_2 core that is characteristic for [**O**] complexes[29,30,45,46] at 617 cm^{-1} (**Figure 1b**, red) and 586 cm^{-1} (**Figure 1b**, blue) with $^{16}O_2$ and $^{18}O_2$, respectively. The isotopic shift of 32 cm^{-1} is in good agreement with theoretical calculations (Table 1 in SI). The intensity of the Cu_2O_2 breathing mode serves as an indicator of the formation of the complex and was plotted against time (**Figure 1b**, inset). It reveals that 70 % of the complex is formed in less than 30 seconds and a complete formation of the complex can be achieved in less than a minute. The dioxygen incorporation occurs in one observable step.

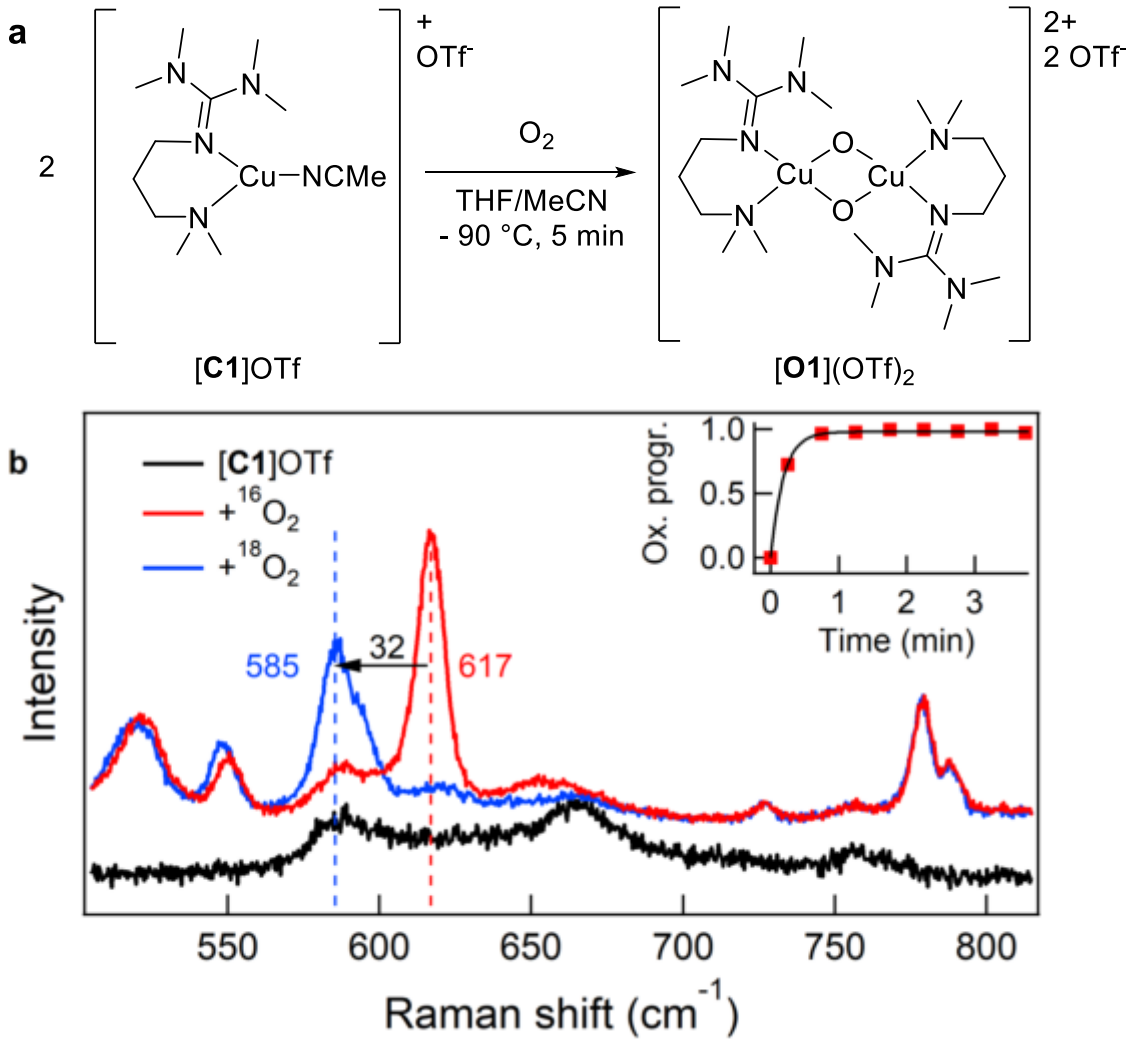

Figure 1: Oxygenation of [C1]OTf to the bis(μ-oxo) dicopper(III) complex [O1](OTf)$_2$. a Reaction scheme, **b** Raman spectra of [**C1**]OTf before (black) and after oxygenation with $^{16}O_2$ (red) and $^{18}O_2$ (blue). Inset: Oxygenation progress (Ox. progr.) tracked by the intensities of the core breathing mode at 617 cm^{-1} from [^{16}**O1**](OTf)$_2$ of the Raman spectra as a function of oxygenation time (red dots with error bars and guide to the eye in black).

Figure 2a highlights the proposed essential steps of the hydroxylation of sodium phenolate by [**O1**](OTf)$_2$ via a phenolato and a catecholato intermediate. We observe this reaction by means of low temperature operando Raman spectroscopy, combining the findings of the measurements at different excitation wavelengths. We tested various wavelengths to find a suitable energy (see SI **Figure 1**) and

determined that 532 nm and 240 nm are appropriate excitation wavelengths for the operando study of this complex with phenolate. They complement each other well. The visible wavelength shows the breathing mode of the copper-oxygen core (cf. **Figure 1b**) and other core-related modes in the low frequency range (see **Figure 2b-d**), while the wavelength in the UV enhances modes in the high frequency range from the phenolic moiety of the intermediates.

Dramatic changes in the Raman modes occurred in the first minute (compare red with orange spectrum in **Figure 2b**), showing the hydroxylating activity of the complex. The mode at 617 cm^{-1}, marked with a purple dashed line and the number **2**, can be attributed to the breathing mode of the Cu_2O_2 core of the complex. Correspondingly we attribute the new, resonance-enhanced mode at 586 cm^{-1}, marked with a red dashed line and the number **1**, to the core of a catecholato intermediate, with the vibrating catecholate still being attached to the copper complex (cf. **Figure 2a**). We make this assignment due to the expected shift to smaller wavenumbers when the effective reduced mass of the molecule is increased and support this idea with theoretical calculations (Table 1, SI). This mode is also oxygen isotope sensitive. Raman measurements revealed an isotopic shift of 10 cm^{-1} (**Figure 2c**), which is in good agreement with the theoretical shift of 5 cm^{-1} (Table 1, SI). Furthermore we can prove that the complex reacts as an [**O**] complex during the hydroxylation without changing to its isomeric form. As can be seen in **Figure 2a**, no characteristic [**P**] features, expected to be around 750 cm^{-1} for the vibration of the O-O bond,[47] arise during the reaction. All spectra were fitted with Lorentzian functions. The intensities of the before mentioned modes are plotted against time. The catecholato mode at 586 cm^{-1} (**Figure 2d**) increases fast in the first half of a minute after substrate addition and decreases exponentially. The breathing mode of the

copper-oxygen core shows complementary to the fast increase of the catecholato mode a fast decrease (see **Figure 2e**).

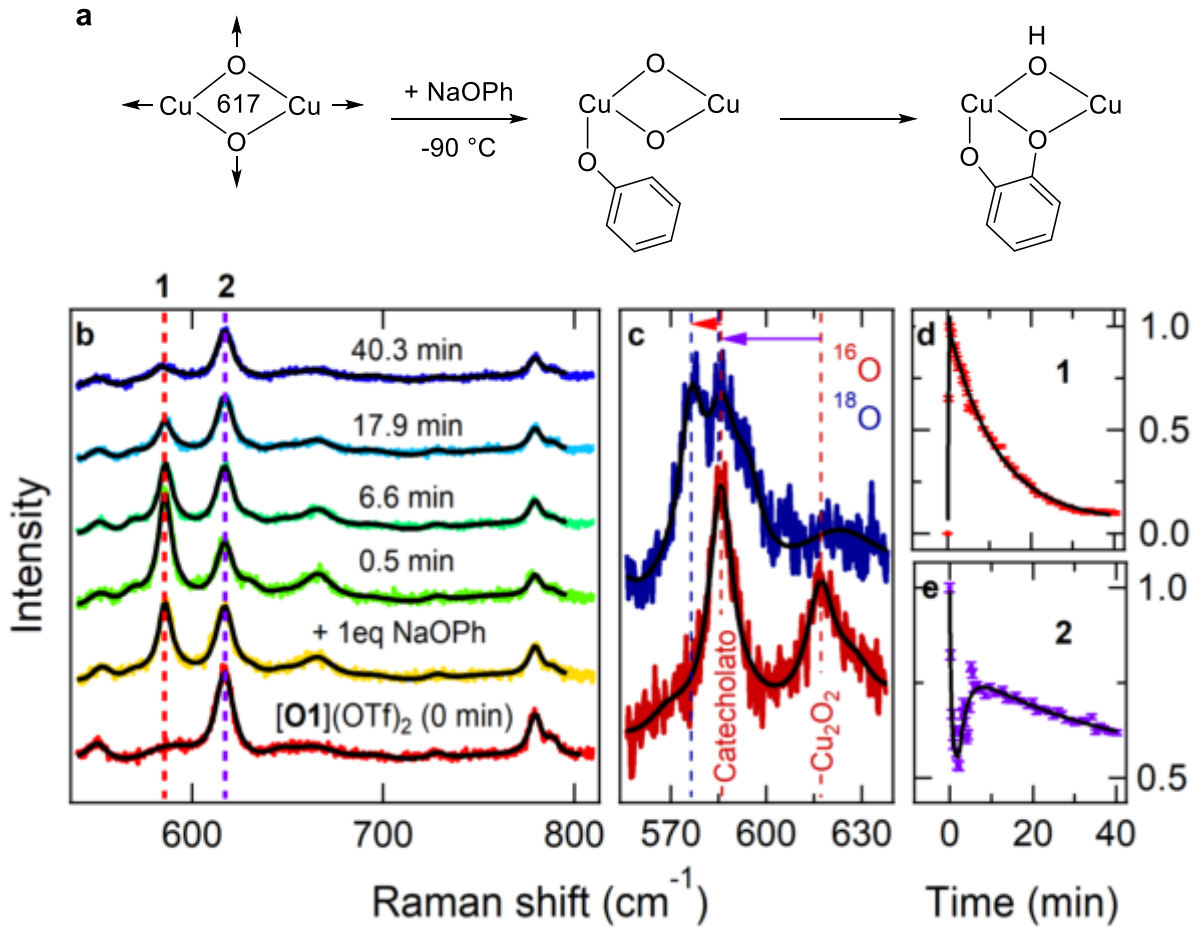

Figure *2:* Formation of the catecholato complex via a phenolato intermediate upon adding sodium phenolate to [O1](OTf)$_2$. a Reaction scheme (counter ions, charges, and ligands are omitted), arrows symbolize the breathing mode of the Cu_2O_2 core of the bis(μ-oxo) complex. **b**-**d** Operando Raman measurements of [**O1**](OTf)$_2$ with 1 eq of NaOPh in low frequency range excited at 532 nm. **b** Time-dependent representative Raman spectra with corresponding fits in black in the energy range of 540 cm^{-1} to 810 cm^{-1}. Marked modes at 586 cm^{-1} (**1**, red) and 617 cm^{-1} (**2**, purple). **c** The oxygen isotope sensitive mode of the catecholato species at 586 cm^{-1} (^{16}O, dark red) shifts to 576 cm^{-1} (^{18}O, dark blue), indicated by a red arrow. A purple arrow indicates the shift of the Cu_2O_2 breathing mode. These spectra are taken 0.8 minutes after substrate addition. All spectra are off-setted. **d**-**e**

Normalized intensity time profiles with guides to the eye of the modes at **d** 586 cm^{-1} (red) and **e** 617 cm^{-1} (purple).

It is apparent that the breathing mode and hence [**O1**](OTf)$_2$ is still present at the end of the measurement, therefore not everything was converted. However, when using more than one equivalent of NaOPh, the intensity of the breathing mode decreases rapidly within the first minute (see SI **Figure 2** and SI **Figure 3**). To ensure that the complex itself is stable over time during the measurement while being irradiated, [**O1**](OTf)$_2$ was measured for 90 minutes. The intensity of the breathing mode was again used as an indicator and plotted against time. As no significant changes can be observed during this period (see SI **Figure 4**), changes in the operando Raman spectra can be associated to the addition of substrate and the reaction. To get more information about the hydroxylation reaction and mechanism, operando Raman measurements in the deep UV at 240 nm were conducted. 1, 2, or 5 equivalents of the same substrate, NaOPh, were added to the bis(μ-oxo) complex [**O1**](OTf)$_2$ (**Figure 3**). The breathing mode is not enhanced at this wavelength (cf. SI **Figure 1**) and no mode is affected by an isotope exchange (see SI **Figure 5** and SI **Figure 6**). The mode at 1159 cm^{-1} (marked with dashed line in red and **1**) is also present in the free substrate (cf. SI **Figure 7**). This mode can be used to track the accessibility of the substrate in the excited volume. The intensity time profiles (**Figure 3d-f**) of this mode show that the reaction is faster with more equivalents. This is also reflected in the other modes. Especially interesting is the range around 1600 cm^{-1} and the mode at 2103 cm^{-1}. The dynamic changes depending on the number of equivalents and is faster with more equivalents. The modes at 1601 cm^{-1} (green, **3**) and 1630 cm^{-1} (blue, **4**) follow a sigmoidal curve. These modes might be attributed to the catecholato complex (Vergleich mit DFT). The mode at 2107 cm^{-1} first decreases and

shifts to a slightly lower frequency (2103 cm^{-1}, purple, **5**). The intensity increases until it reaches its maximum and decreases again. The maximum is reached faster with more equivalents.

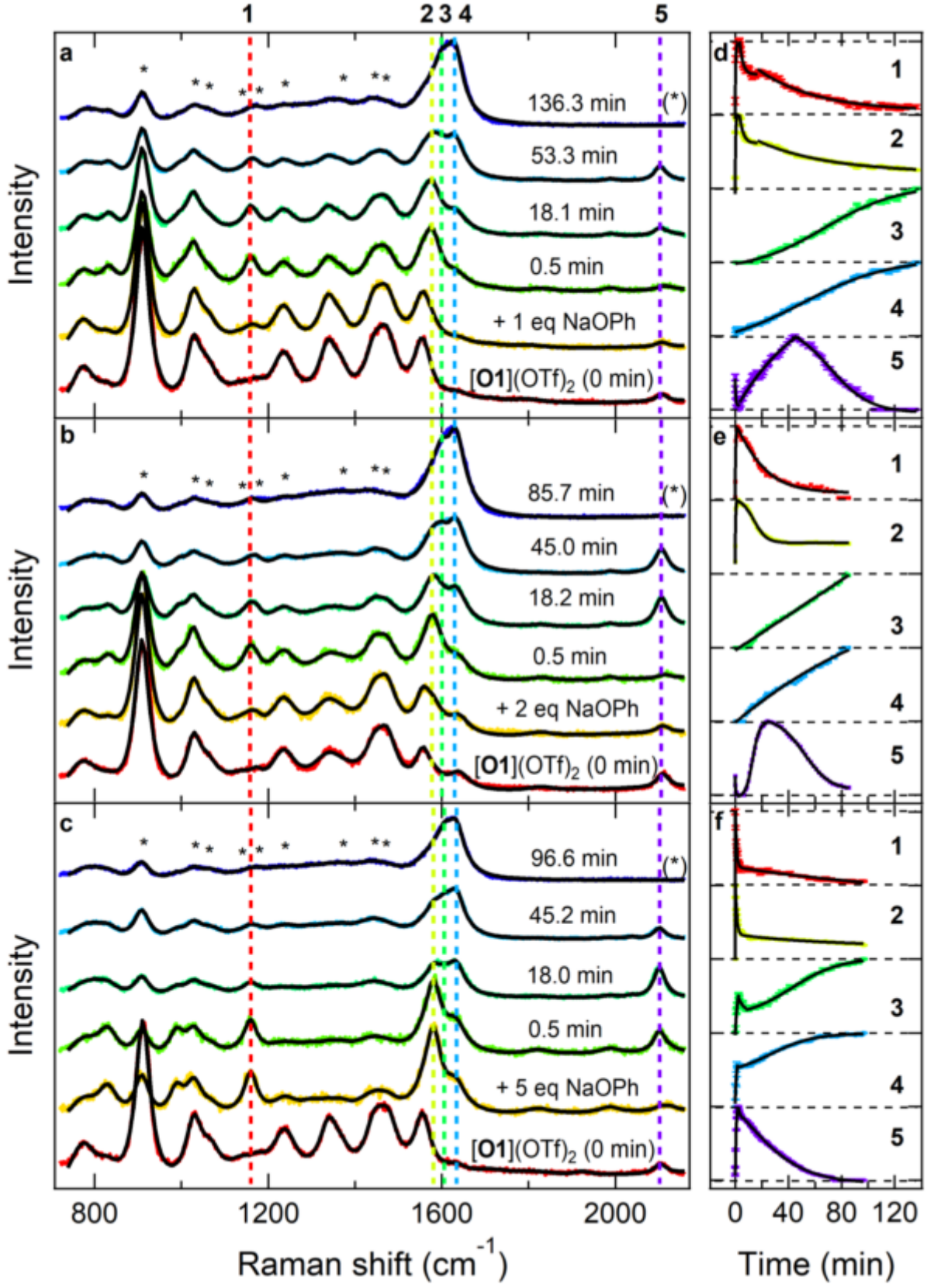

Figure 3: Operando Raman measurements in high frequency range of [O1](OTf)$_2$ excited at 240 nm with different amounts of equivalents of NaOPh. a-c Time-dependent representative Raman spectra during the reaction of [**O1**](OTf)$_2$ with NaOPh (**a**: 1 eq, **b**: 2 eq,

c: 5 eq) with corresponding fits in black in the energy range of 720 cm^{-1} to 2160 cm^{-1}. Marked modes at 1159 cm^{-1} (**1**, red), 1578 cm^{-1} (**2**, lime), 1601 cm^{-1} (**3** green), 1630 cm^{-1} (**4**, blue), 2103 cm^{-1} (**5**, purple). **d**-**f** Corresponding normalized intensity time profiles with guides to the eye of the marked Raman modes in the spectra on their respective left side. Horizontal dashed lines indicate values 0 and 1. Asterisks mark solvent signals.

A similar dynamic and peaks can be seen when using 1 eq of the substrates Me-PhONa or MeO-PhONa, as shown in **Figure 4**. It should also be noted that the mode at 1339 cm^{-1} from the complex has a similar intensity profile as the breathing mode from the Vis measurements (cf. SI **Figure 3b** with SI **Figure 8a**). Although Vis operando Raman measurements were also carried out with these two substrates (see SI **Figure 9**), the acquired data was not as promising as with NaOPh. Especially MeO-PhONa was challenging because of the superimposing fluorescence.

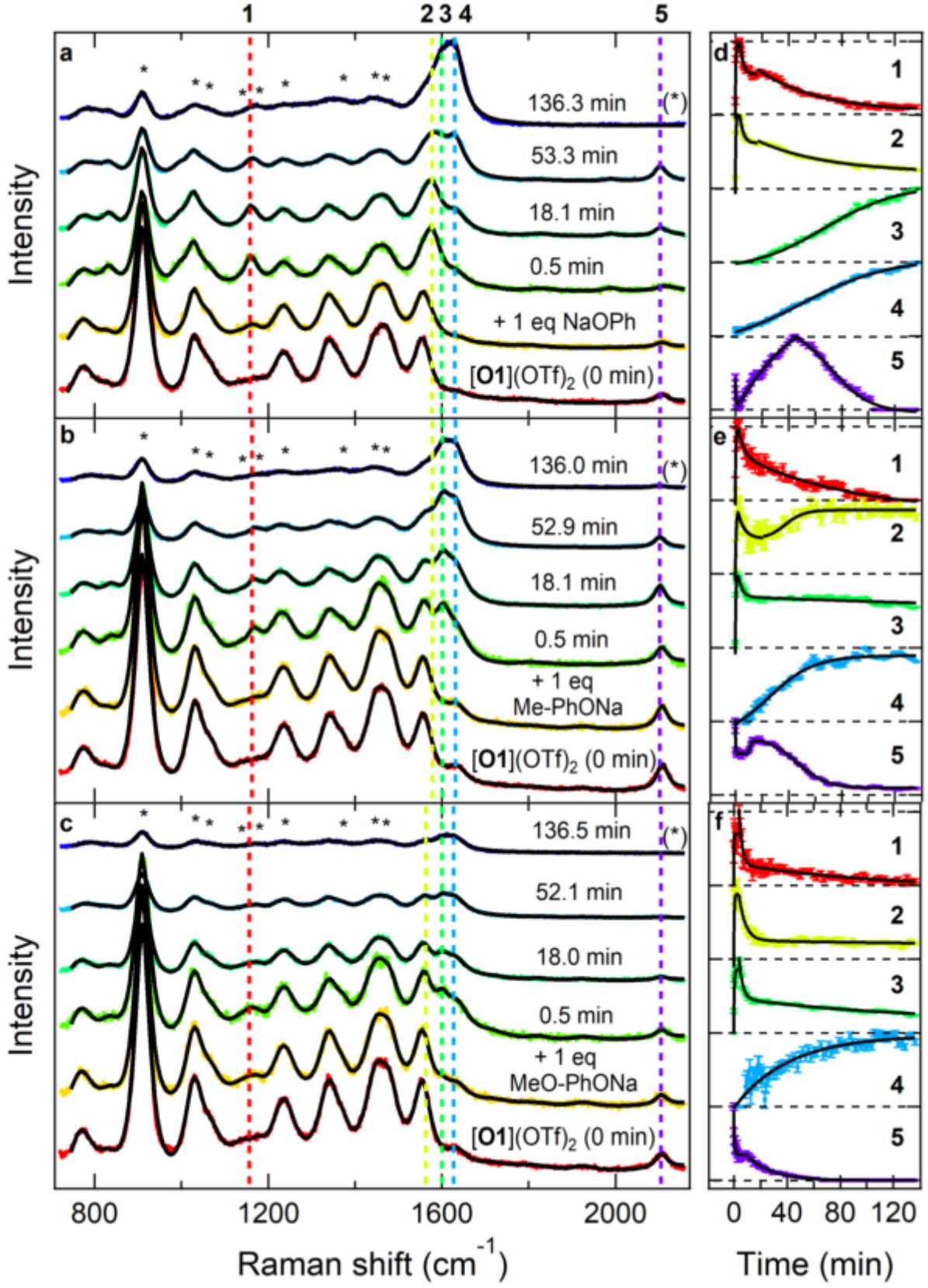

Figure 4: Operando Raman measurements in high frequency range excited at 240 nm with different kind of phenolatic substrates. a-c Time-dependent representative Raman spectra during the reaction of [**O1**](OTf)$_2$ with substrate (**a**: NaOPh, **b**: Me-PhONa, **c**: MeO-

PhONa) with corresponding fits in black in the energy range of 720 cm^{-1} to 2160 cm^{-1}. Marked modes around 1160 cm^{-1} (**1**, red), 1578 cm^{-1} (**2**, lime), 1601 cm^{-1} (**3** green), 1630 cm^{-1} (**4**, blue), 2103 cm^{-1} (**5**, purple). **d**-**f** Corresponding normalized intensity time profiles with guides to the eye of the marked Raman modes in the spectra on their respective left side. Horizontal dashed lines indicate values 0 and 1. Modes marked with **1** to **5** in **a** and **d:** 1160 cm^{-1}, 1578 cm^{-1}, 1601 cm^{-1}, 1630 cm^{-1}, and 2103 cm^{-1}, respectively. Modes in **b** and **e**: 1163 cm^{-1}, 1579 cm^{-1}, 1602 cm^{-1}, 1632 cm^{-1}, and 2102 cm^{-1}, respectively. Modes in **c** and **f:** 1158 cm^{-1}, 1564 cm^{-1}, 1601 cm^{-1}, 1628 cm^{-1}, and 2105 cm^{-1}, respectively. Asterisks mark solvent signals.

Cryospray-ionization mass spectrometry measurements were performed to further characterize the reactive intermediates of the stoichiometric hydroxylation reaction of sodium 4-methyl phenolate mediated by the bis(μ-oxo) dicopper(III) complex [**O1**](OTf)$_2$ in THF. **Figure 10** in the SI reveals the isotopic pattern and corresponding *m*/*z* values of a monocationic dinuclear copper complex, which can represent both the phenolato and the catecholato complex due to their identical chemical composition (see **Figure 11** in SI). The measured isotopic pattern and the *m*/*z* values agree well with the simulated mass spectrum.

[Theorie-Abbildung + Text]

Conclusion

In conclusion we have studied the hydroxylating activity of a biomimetic tyrosinase model complex. We especially tracked the interplay between the Cu_2O_2 core of a bis(μ-oxo) copper(III) complex—stabilized by a hybrid guanidine ligand—and the attack of a phenolate forming a phenolato and a catecholato complex as an intermediate. These are essential steps of the catalytic tyrosinase cycle.

After the addition of phenolatic substrates to our [**O1**](OTf)$_2$ complex, we find modes characteristic for the catecholato complex, as well as for the phenolato intermediate. This shows that both intermediates are formed during the reaction. Through monitoring the reaction, we could also show that this [**O**] complex, an active species that can hydroxylate phenolates, does not change to its isomeric [**P**] form. The subsequent decrease of the Cu_2O_2 core breathing mode with increase of phenolato and catecholato complex modes shows the attack of the phenolate on the Cu_2O_2 core. DFT calculations help identify the modes. Cryo-UHR-ESI MS measurements confirm the presence of a reactive intermediate. With this manuscript, we show that operando Raman measurements, especially when using different excitation wavelengths, provide a detailed view on the mechanism involved in the catalytic cycle and thus show a pathway for optimization of the catalytic activity in biomimetic complexes.

Materials and Methods

Chemicals

The copper salt $[Cu(MeCN)_4]OTf$ was synthesized by the reaction of Cu_2O (99.99%, Sigma Aldrich) and acid TfOH (Sigma Aldrich) in acetonitrile and recrystallized at least twice from acetonitrile/diethyl ether at -30 °C.[48] The guanidine-amine hybrid ligand 2-(3-(dimethylamino)propyl)-1,1,3,3-tetramethylguanidine (TMGdmap, **L**) was prepared according to a literature procedure,[28,41] distilled under vacuum (100°C, $5 \cdot 10^{-2}$ mbar) and stored in an MBraun glovebox under nitrogen atmosphere. Sodium 4-X-phenolates (X = H, Me, OMe) were synthesized according to a literature procedure.[39] The used solvents acetonitrile and tetrahydrofuran (HPLC grade, Fisher Scientific) were purified under nitrogen atmosphere via distillation from CaH_2 and sodium/benzophenone ketyl radical, respectively.

Instrumentation:

Raman Spectroscopy

Raman measurements were performed with a UT-3 triple monochromator Raman spectrometer[49], combined with a continuous wave diode laser (Millennia, Spectra Physics Lasers Inc.). This laser was used to obtain an excitation wavelength of 532 nm as well as to pump a titanium-sapphire (Ti:Sa) laser (Tsunami, Spectra Physics Lasers Inc.). The tuneable fundamental laser line from the Ti:Sa laser was frequency doubled or tripled with a flexible harmonic generator (GWU2 23-PS, Spectra Physics Lasers Inc.) or quadrupled with fourth harmonic generation (GWU-4-PL, Spectra

Physics Lasers Inc.). They generated the other excitation wavelengths (220 nm, 230 nm, 240 nm, 260 nm, 280 nm, 360 nm, 414 nm, 450 nm) that were applied in this study.

The cryostat (see SI **Figure 12**) was a slightly modified version of a setup described previously[42] with a 1.4 mL or 3.5 mL screw cap Suprasil® cuvette with septum (117104F-10-40 or 117100F-10-40, respectively, Hellma), equipped with a Peltier element (QC-127-1.4-6.0MS, QuickCool). The hot backside of the Peltier element is cooled down with ethanol from a closed-cycle chiller (Proline RP890, Lauda) and the other side cools a copper block. This copper block encloses three sides of the cuvette. The laser beam was widened with a spatial filter and then focused on the cuvette inside the cryostat. The focus spot size was around 20 µm in diameter. With a micrometer screw, the focal depth was adjusted to maximum signal. Raman scattered light was captured with the entrance optics of the UT-3 spectrometer.

The precursor [Cu(**L**)(MeCN)]OTf ([**C1**]OTf) and substrates sodium 4-X-phenolates (X = H, Me, OMe) were prepared in an MBraun glovebox ([O_2] and [H_2O] < 0.5 ppm). Anhydrous solvents were purchased from commercial suppliers and additionally dried over 3 Å molecular sieves. The precursor with a concentration of 10 mmol L^{-1} in tetrahydrofuran/acetonitrile (8:2) was transferred to a cuvette with septum and cooled in the cuvette cryostat to below –90 °C.

Dioxygen was added via a cannula through the septum (0.02 bar overpressure for 5 min) to synthesize [Cu_2(µ-O)$_2$**L**$_2$](OTf)$_2$, ([**O1**](OTf)$_2$). The used laser power in front of the entrance optics was 42 mW for the low frequency measurements excited at 532 nm and between 2.0 mW and 3.5 mW for the high frequency measurements at 240 nm. After the synthesis of [**O1**](OTf)$_2$, 1, 2, or 5 eq of substrate in THF was added quickly in one portion through the septum with a gas tight Hamilton glass syringe (Hamilton Company). The Raman measurement was started as soon as the

syringe was emptied. The integration time was 20 seconds. After a few minutes, we increased the integration time to 60 seconds per measurement to improve the signal to noise ratio. For the measurements in the UV, we additionally increased the integration time to 120 s. The complex, measured without any substrate, defines the time “0 min”. Please note that every spectrum from an assigned time is in fact a mean value over the integration time. To incorporate this, the allotted time for the measurements with substrate is the starting time of the measurement plus half of the integration time. All spectra were normalized to 1 s integration time and 1 mW laser power and the background was subtracted. The measurements were conducted in a clean room with constant temperature (20.0 °C ± 0.5 °C) and humidity (45 % ± 3 %).

Cryo-ESI Mass Spectrometry

Instrument

Cryospray-ionization mass spectrometry measurements were performed on a UHR-TOF Bruker Daltonik maXis II, an ESI-quadrupole time-of-flight (qToF) mass spectrometer capable of a resolution of at least 80.000 FWHM, which was coupled to a Bruker Daltonik Cryospray unit. Detection was either in the positive or in the negative ion mode; the source voltage was 3.5 kV. The flow rate was 3.0 µL min^{-1}. The drying gas (N_2), to achieve solvent removal, and the spray gas were both held at -80 °C. The mass spectrometer was calibrated prior to every experiment via direct infusion of Agilent ESI-TOF low concentration tuning mixture, which provided an m/z range of singly charged peaks up to 3000 Da in both ion modes.

Procedure

The precursor copper(I) complex [**C1**]OTf was prepared in a tenfold stock solution under inert conditions by dissolving equimolar amounts of **L** (20.0 mg, 0.10 mmol) and $[Cu(MeCN)_4]OTf$ (37.8 mg, 0.10 mmol) in acetonitrile (5 mL). One-tenth of the stock solution of the precursor copper(I) complex [**C1**]OTf (0.5 mL, 0.01 mmol, 2 eq) was positioned in a Hamilton syringe and added rapidly to dioxygen-saturated THF (9.5 mL) at -100 °C to generate the bis(μ-oxido) dicopper(III) complex [**O1**]$(OTf)_2$ (0.005 mmol, 1 eq).

Substrate solutions were prepared in a twentyfold stock solution under inert conditions by dissolving the respective sodium phenolate (0.2 mmol) in dried acetonitrile (4.0 mL). One-twentieth of the stock solution of the substrate (0.2 mL, 0.01 mmol, 2 eq) was positioned in a Hamilton syringe.

The substrate solution was injected into the bis(μ-oxo) dicopper(III) complex solution, and a first mass spectrum was measured immediately by sampling the reaction solution with a precooled Hamilton syringe and injecting it into the cryospray unit. After several scavenging processes with dried tetrahydrofuran, a second mass spectrum was monitored after approximately five minutes. Please note that the reaction was conducted at -100 °C to capture reactive reaction intermediates as cryo-UHR-ESI MS is no in-situ method.

Computational Details (Alexander)

Acknowledgments

The authors gratefully acknowledge financial support provided by the Federal Ministry of Education and Research (BMBF) under project 05K19GU5, as well as by

the German Research Foundation (DFG) in framework of the Priority Program SPP 1740 “Reactive Bubbly Flows” (HE 5480/10-2, http://www.dfg-spp1740.de/), and further projects (RU 773/8-1).

References

[1] E. I. Solomon, D. E. Heppner, E. M. Johnston, J. W. Ginsbach, J. Cirera, M. Qayyum, M. T. Kieber-Emmons, C. H. Kjaergaard, R. G. Hadt, L. Tian, *Chem. Rev.* **2014**, *114*, 3659–3853.

[2] A. De, S. Mandal, R. Mukherjee, *J. Inorg. Biochem.* **2008**, *102*, 1170–1189.

[3] W. Kaim, J. Rall, *Angew. Chem. Int. Ed. Engl.* **1996**, *35*, 43–60.

[4] A. Decker, E. I. Solomon, *Curr. Opin. Chem. Biol.* **2005**, *9*, 152–163.

[5] E. I. Solomon, P. Chen, M. Metz, S. K. Lee, A. E. Palmer, *Angew. Chemie - Int. Ed.* **2001**, *40*, 4570–4590.

[6] E. I. Solomon, M. J. Baldwin, M. D. Lowery, *Chem. Rev.* **1992**, *92*, 521–542.

[7] E. I. Solomon, U. M. Sundaram, T. E. Machonkin, *Chem. Rev.* **1996**, *96*, 2563–2605.

[8] W. Keown, J. B. Gary, T. D. P. Stack, *J. Biol. Inorg. Chem.* **2017**, *22*, 289–305.

[9] Y. Matoba, T. Kumagai, A. Yamamoto, H. Yoshitsu, M. Sugiyama, *J. Biol. Chem.* **2006**, *281*, 8981–8990.

[10] S. Itoh, S. Fukuzumi, *Acc. Chem. Res.* **2007**, *40*, 592–600.

[11] N. C. Eickman, E. I. Solomon, J. A. Larrabee, T. G. Spiro, K. Lerch, *J. Am. Chem. Soc.* **1978**, *100*, 6529–6531.

[12] S. Itoh, H. Kumei, M. Taki, S. Nagatomo, T. Kitagawa, S. Fukuzumi, *J. Am. Chem. Soc.* **2001**, *123*, 6708–6709.

[13] D. E. Wilcox, A. G. Porras, Y. T. Hwang, M. E. Winkler, E. I. Solomon, K. Lerch, *J. Am. Chem. Soc.* **1985**, *107*, 4015–4027.

[14] L. M. Mirica, M. Vance, D. J. Rudd, B. Hedman, K. O. Hodgson, E. I. Solomon, T. D. P. Stack, *Science* **2005**, *308*, 1890–1892.

[15] I. Garcia-Bosch, R. E. Cowley, D. E. Díaz, R. L. Peterson, E. I. Solomon, K. D.

Karlin, *J. Am. Chem. Soc.* **2017**, *139*, 3186–3195.

[16] M. E. Winkler, K. Lerch, E. I. Solomon, *J. Am. Chem. Soc.* **1981**, *103*, 7001–7003.

[17] B. T. Op't Holt, M. A. Vance, L. M. Mirica, D. E. Heppner, T. D. P. Stack, E. I. Solomon, *J. Am. Chem. Soc.* **2009**, *131*, 6421–6438.

[18] T. Inoue, Y. Shiota, K. Yoshizawa, *J. Am. Chem. Soc.* **2008**, *130*, 16890–16897.

[19] C. E. Elwell, N. L. Gagnon, B. D. Neisen, D. Dhar, A. D. Spaeth, G. M. Yee, W. B. Tolman, *Chem. Rev.* **2017**, *117*, 2059–2107.

[20] L. M. Mirica, X. Ottenwaelder, T. D. P. Stack, *Chem. Rev.* **2004**, *104*, 1013–1045.

[21] P. Liebhäuser, A. Hoffmann, S. Herres-Pawlis, *Reference Module in Chemistry, Molecular Science and Chemical Engineering* **2019**, 1–22.

[22] E. A. Lewis, W. B. Tolman, *Chem. Rev.* **2004**, *104*, 1047–1076.

[23] N. Kitajima, K. Fujisawa, Y. Moro-oka, K. Toriumi, *J. Am. Chem. Soc.* **1989**, *111*, 8975–8976.

[24] J. A. Halfen, S. Mahapatra, E. C. Wilkinson, S. Kaderli, V. G. Young, L. Que, A. D. Zuberbühler, W. B. Tolman, *Science* **1996**, *271*, 1397–1400.

[25] C. J. Cramer, B. A. Smith, W. B. Tolman, *J. Am. Chem. Soc.* **1996**, *118*, 11283–11287.

[26] V. Mahadevan, Z. Hou, A. P. Cole, D. E. Root, T. K. Lal, E. I. Solomon, T. D. P. Stack, *J. Am. Chem. Soc.* **1997**, *119*, 11996–11997.

[27] A. Spada, S. Palavicini, E. Monzani, L. Bubacco, L. Casella, *Dalt. Trans.* **2009**, *33*, 6468–6471.

[28] S. Herres-Pawlis, R. Haase, P. Verma, A. Hoffmann, P. Kang, T. D. P. Stack, *Eur. J. Inorg. Chem.* **2015**, *2015*, 5426–5436.

[29] B. F. Gherman, C. J. Cramer, *Coord. Chem. Rev.* **2009**, *253*, 723–753.

[30] M. Paul, M. Teubner, B. Grimm-Lebsanft, C. Golchert, Y. Meiners, L. Senft, K. Keisers, P. Liebhäuser, T. Rösener, F. Biebl, S. Buchenau, M. Naumova, V. Murzin, R. Krug, A. Hoffmann, J. Pietruszka, I. Ivanović-Burmazović, M. Rübhausen, S. Herres-Pawlis, *Chem. - A Eur. J.* **2020**, *26*, 7556–7562.

[31] M. Rolff, J. Schottenheim, H. Decker, F. Tuczek, *Chem. Soc. Rev.* **2011**, *40*, 4077–4098.

[32] P. E. M. Siegbahn, M. Wirstam, *J. Am. Chem. Soc.* **2001**, *123*, 11819–11820.

[33] J. Schottenheim, C. Gernert, B. Herzigkeit, J. Krahmer, F. Tuczek, *Eur. J. Inorg. Chem.* **2015**, *2015*, 3501–3511.

[34] S. Palavicini, A. Granata, E. Monzani, L. Casella, *J. Am. Chem. Soc.* **2005**, *127*, 18031–18036.

[35] M. Réglier, C. Jorand, B. Waegell, *J. Chem. Soc. Chem. Commun.* **1990**, 1752–1755.

[36] J. Schottenheim, N. Fateeva, W. Thimm, J. Krahmer, F. Tuczek, *Z. Anorg. Allg. Chem.* **2013**, *639*, 1491–1497.

[37] M. Rolff, J. Schottenheim, G. Peters, F. Tuczek, *Angew. Chemie - Int. Ed.* **2010**, *49*, 6438–6442.

[38] G. Battaini, M. De Carolis, E. Monzani, F. Tuczek, L. Casella, *Chem. Commun.* **2003**, *3*, 726–727.

[39] A. Company, S. Palavicini, I. Garcia-Bosch, R. Mas-Ballesté, L. Que, E. V. Rybak-Akimova, L. Casella, X. Ribas, M. Costas, *Chem. - A Eur. J.* **2008**, *14*, 3535–3538.

[40] M. Rolff, J. Schottenheim, F. Tuczek, *J. Coord. Chem.* **2010**, *63*, 2382–2399.

[41] S. Herres-Pawlis, P. Verma, R. Haase, P. Kang, C. T. Lyons, E. C. Wasinger, U. Florke, G. Henkel, T. D. P. Stack, *J. Am. Chem. Soc.* **2009**, *131*, 1154–

1169.

[42] B. Grimm-Lebsanft, C. Brett, F. Strassl, D. Rukser, M. Biednov, F. Biebl, M. Naumova, A. Hoffmann, L. Akinsinde, D. Brückner, S. Herres-Pawlis, M. Rübhausen, *Inorg. Chim. Acta* **2018**, *481*, 176–180.

[43] M. Lerch, M. Weitzer, T. D. J. Stumpf, L. Laurini, A. Hoffmann, J. Becker, A. Miska, R. Göttlich, S. Herres-Pawlis, S. Schindler, *Eur. J. Inorg. Chem.* **2020**, *2020*, 3143–3150.

[44] C. Citek, S. Herres-Pawlis, T. D. P. Stack, *Acc. Chem. Res.* **2015**, *48*, 2424–2433.

[45] A. Hoffmann, C. Citek, S. Binder, A. Goos, M. Rübhausen, O. Troeppner, I. Ivanović-Burmazović, E. C. Wasinger, T. D. P. Stack, S. Herres-Pawlis, *Angew. Chemie - Int. Ed.* **2013**, *52*, 5398–5401.

[46] L. Que, W. B. Tolman, *Angew. Chem. Int. Ed.* **2002**, *41*, 1114–1137.

[47] D. A. Quist, D. E. Diaz, J. J. Liu, K. D. Karlin, *J. Biol. Inorg. Chem.* **2017**, *22*, 253–288.

[48] G. J. Kubas, B. Monzyk, A. L. Crumbliss, *Inorg. Synth.* **1979**, *19*, 90–92.

[49] B. Schulz, J. Bäckström, D. Budelmann, R. Maeser, M. Rübhausen, M. V. Klein, E. Schoeffel, A. Mihill, S. Yoon, *Rev. Sci. Instrum.* **2005**, *76*, DOI 10.1063/1.1946985.

5 Experiments with Femtosecond Mid-Infrared Laser Light

5.1 Photoinduced Metastable dd-Exciton-Driven Metal-Insulator Transitions in Quasi-One-Dimensional Transition Metal Oxides

The author has contributed to the Raman and reflectivity measurements and the respective data analysis.

In [5.1] the quasi-1D metal $SrNbO_{3.4}$ was investigated by various optical technique and results showed a metastable metal-to-insulator transitions (MIT) and an insulator-to-metal transitions (IMT). Notably, UV Raman measurements, NIR-pump and MIR-probe reflectivity measurements and NIR-pump and UV-probe Raman experiments were conducted. $Sr_{1-y}NbO_x$ compounds allow for a variety of different phases with different properties,[129] however this research item analyzes the quasi-1D phase. The crystal is a layered perovskite consisting of NbO_6 octahedra, which are periodically grouped into n=5-octahedra thick slabs as shown in [5.1]-Fig. 1 (a) and (b). Although two samples with different oxygen-deficiencies were used, the n=5 $Sr_{0.95}NbO_{3.37}$ and the n=4.5 $SrNbO_{3.45}$, [5.1] focuses mostly on the n=5 sample. Along the metallic a-axis, the Nb-O-Nb bonds are chain-like and along the insulating b- and c-axis they are zig-zag-like. Mueller-matrix ellipsometry data are shown in [5.1]-Fig. 1 and 2. A Drude tail along the metallic a-axis is found together with signatures of the d-d excitonic transition at low energies of around 1 eV together with the O-2p→Nb-4d charge-transfer band at high energies of > 4.2 eV.

UV-Raman Scattering
UV Raman scattering was realized with the Tsunami laser system with the fundamental laser wavelength tuned to 720 nm, to be able to produce 240 nm light in the 3ω regime by using two different nonlinear BBO crystals. Measuring both samples with 240 nm and at a power of 5.8 mW in the charge-transfer band over a broad range of energies, the exciton is found at an energy difference of $\approx$ 1 eV, similar to the d-d excitations. The UV-data and d-d excitons are shown in [5.1]-Fig. 2 (a), (b) and inset.

NIR-Pump and MIR-Probe Reflectivity
The NIR-pump and MIR-probe reflectivity setup uses the Tangerine laser system to produce 1030 nm beam for the NIR-pump and also supplies 1030 nm to the DFG unit to produce MIR light at 7 µm for the probe beam. The DFG unit is explained in section 3.1.4 and it was slightly modified for this experiment, as shown in [5.1]-Fig. 4 (a). In the third stage, the residual 1030 nm beam is not dumped but used as the pump laser. An on-axis parabolic mirror with a hole in the center is positioned so that the sample is in the focus of the mirror. The MIR-probe beam is focused onto

the sample by the mirror, then back to the mirror and into a thermopile sensor. The NIR-pump is focused onto the sample *via* a lens and through the hole in the mirror.

The background reflectance of the metallic a-axis in the MIR-probe-only configuration is attenuated from 100 % to 10 % when measuring in pump-probe configuration. The systems response while turning the pump on and off for the decrease and subsequent increase in reflectivity is surprisingly in the order of seconds. This implies further interactions beyond the expected very fast electronic degrees of freedom. Changing the polarization of the probe beam, it was observed that while the metallic a-axis becomes less reflective, the insulating b-axis becomes more reflective, as shown in [5.1]-Fig. 4 (c). These two effects are both linear in opposite direction while increasing the pump power density, implying charge conservation. The data are shown in [5.1]-Fig. 4 (d).

NIR-Pump and UV-Probe Raman Scattering

For the NIR-pump beam, the Tangerine laser system is used to produce the 1030 nm light at varying powers and the UV-probe beam is generated with the Tsunami laser system at 2.8 mW as previously explained in the *UV-Raman Scattering* paragraph, with the alteration that a fundamental wavelength of 780 nm was chosen to produce 260 nm light. Note that temporal overlap could be ignored, since the repetition rates of the Tsunami (80 MHz) and the Tangerine (500 kHz) are to fast for the effect described previously. The Raman scattered light was collected in the range between 150 cm^{-1} and 1000 cm^{-1}, relative to the probe energy of 4.7 eV (260 nm). The polarization of the pump is altered with a polarizer-$\lambda/2$ plate combination to be either parallel to the metallic a-axis or the insulating b-axis. The data are shown in [5.1]-Fig. 5.

The results show Raman modes with the 260 nm-probe beam polarized parallel to the b-axis at energies of 440 cm^{-1}, 560 cm^{-1}, 680 cm^{-1} and 830 cm^{-1}, coinciding with oxygen-bond modes reported in cuprate superconductors.[130–132] The 830 cm^{-1} mode is also seen with the polarization parallel to the metallic a-axis. Note again, that we find zig-zag-like Nb-O-Nb bonds along the insulating b-axis and chain-like Nb-O-Nb bonds along the metallic a-axis. When probing at 260 nm and additionally pumping at 1030 nm, the data show a strong decrease in all oxygen-related modes for both polarization configurations. At high pump powers above 5 $kWcm^{-2}$ all modes, except the 830 cm^{-1} mode, are completely bleached along the b-axis direction. At those energies, the data along the a- and b-axis look identical. The aforementioned additional degrees of freedom beyond the fast electronic interactions, that limit the slow relaxation time of the systems response during the *NIR-pump and MIR-probe Reflectivity* measurements can now be discussed. (i) As can be seen in [5.1]-Fig. 5 (b), the NIR-pump causes significant changes in the oxygen-related modes and it can be assumed that the excitonic d-d pumping converts the ordering of the insulating zig-zag-like Nb-O-Nb modes towards the chain-like structure. This causes the transient insulator-to-metal transition of the insulating b-axis. Structural degrees of freedom encompassing lattice changes operate on slower timescales generally. (ii) It is hypothesized that along the metallic a-axis, the free electrons are excited to form excitons by the NIR-pump, depleting the Nb-4d band and decreasing the conductivity along the metallic a-axis. The speed of recovery of this photoinduced effect might be decreased because of the formation of room temperature Bose-Einstein-like Condensation (BEC). Excitons, being bosonic particles, can form states of coherent superpositions with longer coherence lengths. Prediction of such observations were reported for Ta_2NiSe_5 [133] and 1T-$TiSe_2$.[134]

Photoinduced Metastable dd-Exciton-Driven Metal-Insulator Transitions in Quasi-One-Dimensional Transition Metal Oxides

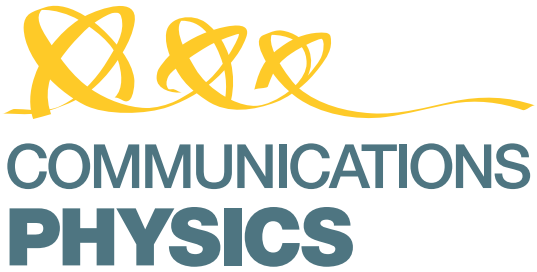

ARTICLE

https://doi.org/10.1038/s42005-020-00451-w OPEN

Photoinduced metastable *dd*-exciton-driven metal-insulator transitions in quasi-one-dimensional transition metal oxides

Teguh Citra Asmara[1,2,3,12✉], Frank Lichtenberg[4,12], Florian Biebl[5,6,12], Tao Zhu[7], Pranab Kumar Das[1], Muhammad Avicenna Naradipa[1,7], Angga Dito Fauzi[1,7], Caozheng Diao[1], Ping Yang[1,8], Philipp Lenzen[5,6], Sören Buchenau[5,6], Benjamin Grimm-Lebsanft[5,6], Dongyang Wan[2], Paolo E. Trevisanutto[7,9], Mark B. H. Breese[1,7], T. Venkatesan[2,7,8,10,11], Michael Rübhausen[5,6✉] & Andrivo Rusydi[1,2,7,9,10✉]

Photoinduced phase transitions in matters have gained tremendous attention over the past few years. However, their ultrashort lifetime makes their study and possible control very challenging. Here, we report on highly anisotropic *d*-*d* excitonic excitations yielding photo-induced metal-insulator transitions (MITs) in quasi-one-dimensional metals $Sr_{1-y}NbO_x$ using Mueller-Matrix spectroscopic ellipsometry, transient ultraviolet Raman spectroscopy, transient mid-infrared reflectivity and angular-resolved photoemission spectroscopy supported with density functional theory. Interestingly, the MITs are driven by photo-pumping of *d*-*d* excitons, causing the metallic *a*-axis to become insulating while the insulating *b*- and *c*-axis concomitantly become a correlated metal. We assign these effects to an interplay between the melting of charge and lattice orderings along the different anisotropic optical axes and Bose-Einstein-like condensation of the photoinduced excitons. The long lifetime in the order of several seconds of the metastable MITs gives greater flexibility to study and manipulate the transient excitonic state for potential applications in exciton-based optoelectronic devices.

[1] Singapore Synchrotron Light Source, National University of Singapore, Singapore 117603, Singapore. [2] NUS Nanoscience and Nanotechnology Initiative, National University of Singapore, Singapore 117411, Singapore. [3] Photon Science Division, Paul Scherrer Institute, CH-5232 Villigen PSI, Switzerland. [4] Department of Materials, ETH Zurich, CH-8093 Zurich, Switzerland. [5] Institute of Nanostructure and Solid State Physics, University of Hamburg, 22761 Hamburg, Germany. [6] Center for Free-Electron Laser Science (CFEL), Luruper Chaussee 149, 22761 Hamburg, Germany. [7] Department of Physics, National University of Singapore, Singapore 117551, Singapore. [8] Department of Materials Science and Engineering, National University of Singapore, Singapore 117575, Singapore. [9] Centre for Advanced 2D Materials, National University of Singapore, Singapore 117546, Singapore. [10] National University of Singapore Graduate School for Integrative Sciences and Engineering, Singapore 117456, Singapore. [11] Department of Electrical and Computer Engineering, National University of Singapore, Singapore 117583, Singapore. [12] These authors contributed equally: Teguh Citra Asmara, Frank Lichtenberg, Florian Biebl. ✉email: teguh.asmara@psi.ch; mruebhau@physnet.uni-hamburg.de; andrivo.rusydi@nus.edu.sg

Using light to manipulate fundamental physical properties of matter has gained tremendous attention in optical and condensed matter physics research. It has been shown that photoexcitation can induce transient exotic phases of matter that are not found in their equilibrium ground states. Examples, among others, include transient changes in crystal structures[1,2], ferroelectricity[1], metal–insulator transitions[2–4] (MITs), melting of spin and charge orders[5–7], and even superconductivity[8,9]. The most fundamental way in which light can interact with matter is by exciting electrons from occupied to unoccupied states, creating electron-hole pairs that can bind to form excitons. Thus, excitons are expected to play important roles in the dynamics of these transient phases of matter. Since excitons are bosons, high-density excitons created by high-intensity photoexcitation can potentially condense into transient Bose–Einstein condensates[10–12] (BECs), similar to what has been demonstrated by photoinduced magnon BEC transition driven by high-intensity microwave pumping[13]. However, the main difficulty with excitons (and other transient states of matter in general) is their ultrashort lifetime, which is often in the pico- to femtosecond range. This short timescale renders it challenging to probe and control these transient states.

Here, using a combination of Mueller-matrix spectroscopic ellipsometry, steady-state and transient ultraviolet Raman spectroscopies, transient mid-infrared reflectance, and angular-resolved photoemission spectroscopy (ARPES) supported by theoretical calculations, we probe both the steady-state and dynamic dielectric responses of strongly anisotropic quasi-one-dimensional (quasi-1D) correlated metals $Sr_{1-y}NbO_x$ of the type $A_nB_nO_{3n+2}$ as a model system. We reveal that the photoinduced pumping of low-energy d–d excitons in $Sr_{1-y}NbO_x$ dramatically changes their electronic, lattice, and optical properties. The d–d exciton pumping is found to drive complementary MITs along different optical axes, where the metallic axis switches to become insulating while the insulating axis concomitantly becomes more metallic by rearranging their charge and lattice orderings. The excited state is metastable with an extremely long lifetime of several seconds, caused by the slow recovery of the changes in lattice orderings and possible emergence of BEC-like excitonic phase. This long lifetime gives greater flexibility in manipulating the pumped state for both fundamental research and practical applications.

Results

Anisotropic properties of $Sr_{1-y}NbO_x$. $Sr_{1-y}NbO_x$ is known to exhibit a rich phase diagram that strongly depends on the oxygen content[14], ranging from isotropic metal $SrNbO_3$ (ref. [15]), to a quasi-1D metal $SrNbO_{3.4}$ (refs. [16–20]), and to ferroelectric insulator $SrNbO_{3.5}$ (ref. [21]). Especially, the quasi-1D metal-like phases of $Sr_{1-y}NbO_x$ are ideal to study low-dimensional and MIT physics, as shown by their transition into an insulating charge density wave state at low temperatures[17–19]. The crystal structures of $Sr_{1-y}NbO_x$ are of the type $Sr_nNb_nO_{3n+2} = SrNbO_x$, which represents a homologous layered perovskite-related series where the structure type, n, depends on the oxygen content, x. Along the c-axis, networks of NbO_6 octahedra are periodically grouped into n-octahedra thick slabs, while along the a- and b-axis the Nb–O–Nb bonds are chain-like and zig-zag-like, respectively[14]. For example, along the c-axis the slabs are 5-octahedra thick in $n = 5$ type $SrNbO_{3.4}$ (Fig. 1a, b), alternatingly 4- and 5-octahedra thick in $n = 4.5$ type $SrNbO_{3.45}$, and unlimited in isotropic perovskite $n = \infty$ type $SrNbO_3$. The chain-like bonds facilitate the metallicity along the a-axis, while the zig-zag-like bonds and slab structures hinder the charge hoppings between Nb ions along the b- and c-axis, respectively, making them more insulating. This arrangement makes $Sr_{1-y}NbO_x$ highly biaxially anisotropic, yielding an anisotropic dielectric tensor with different components of the complex dielectric function ε along different orthogonal optical axes. Thus, before probing their transient dynamical response, their steady-state diagonalized anisotropic dielectric tensors need to be determined using Mueller-matrix spectroscopic ellipsometry[22–24].

Mueller-matrix spectroscopic ellipsometry. Representative samples of $Sr_{0.95}NbO_{3.37}$ (an under-stoichiometric Sr- and O-deficient variant of $n = 5$ type $SrNbO_{3.4}$) and $n = 4.5$ type $SrNbO_{3.45}$ single crystals[14] are measured using Mueller-matrix spectroscopic ellipsometry within the photon energy range of 0.38–6.10 eV at room temperature. The resulting real parts of principal ε of the samples, Re[ε], are shown in Fig. 1c–e. Along the a-axis, the Re[ε_a] spectra of both $Sr_{0.95}NbO_{3.37}$ and $SrNbO_{3.45}$ cross zero and become negative below 1.06 and 0.76 eV, respectively. In contrast, the Re[ε] of both samples along the b- and c-axes remain positive at all measured photon energies. This means both samples are metallic along the a-axis, but non-metallic along the b- and c-axes, indicating an intrinsic room-temperature quasi-1D metallic behavior consistent with previous electrical transport, ARPES, and infrared reflectivity results[17–19].

Figure 2a–c shows the imaginary parts of principal ε, Im[ε], of the samples, which are proportional to absorption spectra. These spectra also denote the quasi-1D metallicity of the samples, as shown by the presence of metallic Drude tail along the a-axis but not along the b- and c-axes. The Drude response contribution and the Re[ε_a] zero-crossing energy of $Sr_{0.95}NbO_{3.37}$ are higher than those of $SrNbO_{3.45}$, indicating a larger carrier density in $Sr_{0.95}NbO_{3.37}$ than in $SrNbO_{3.45}$ consistent with their nominal electronic structures[14] (Nb-4$d^{0.16}$ for $Sr_{0.95}NbO_{3.37}$ and Nb-4$d^{0.10}$ for $SrNbO_{3.45}$).

In the Im[ε_b] and Im[ε_c] spectra (Fig. 2b, c) at low energies, three strong peaks are observed at ~0.7 and ~1.2 eV along the b-axis as well as at ~1.1 eV along the c-axis (Table 1). Interestingly, the intensities of these peaks are higher in $Sr_{0.95}NbO_{3.37}$ than in $SrNbO_{3.45}$, similar to the trends of the a-axis Drude response caused by the difference in the carrier density between the two samples. This reveals that the three peaks originate from the excitations of electrons, which are anisotropically-localized along the b- and c-axes but mobile along the a-axis. As discussed below (Fig. 3a), this is indeed the case; more precisely, the three peaks originate from d–d transitions between split Nb-4d bands across the Fermi level along the b- and c-axes. Thus, we name these three peaks as the d–d excitations.

At higher energies, a distinct absorption edge is seen in the Im[ε] spectra along the a- and b-axes at ~4.4 eV for $Sr_{0.95}NbO_{3.37}$ and ~4.2 eV for $SrNbO_{3.45}$ due to the O-2p→Nb-4d charge-transfer inter-band transitions (see "Discussion" below). Meanwhile, in the intervening energy range of 2–4 eV the Im[ε_a] and Im[ε_b] of both samples are very close to zero, signifying the visible-range transparency of both samples along the a- and b-axes. In contrast, the Im[ε_c] spectra of both samples are quite absorbing above the d–d excitations, characterized by the presence of several wide "humps" at varying energy positions (Table 1). Between the two samples, the overall intensities of these humps remain relatively the same (unlike the d–d excitations), indicating that these humps do not originate from carrier excitations. Instead, based on the crystal structure in Fig. 1a, b, these humps could be caused by the presence of extra O layers every few unit cells along the c-axis that create new occupied and unoccupied states that contribute to the optical absorption and modulate the shapes of ε_c.

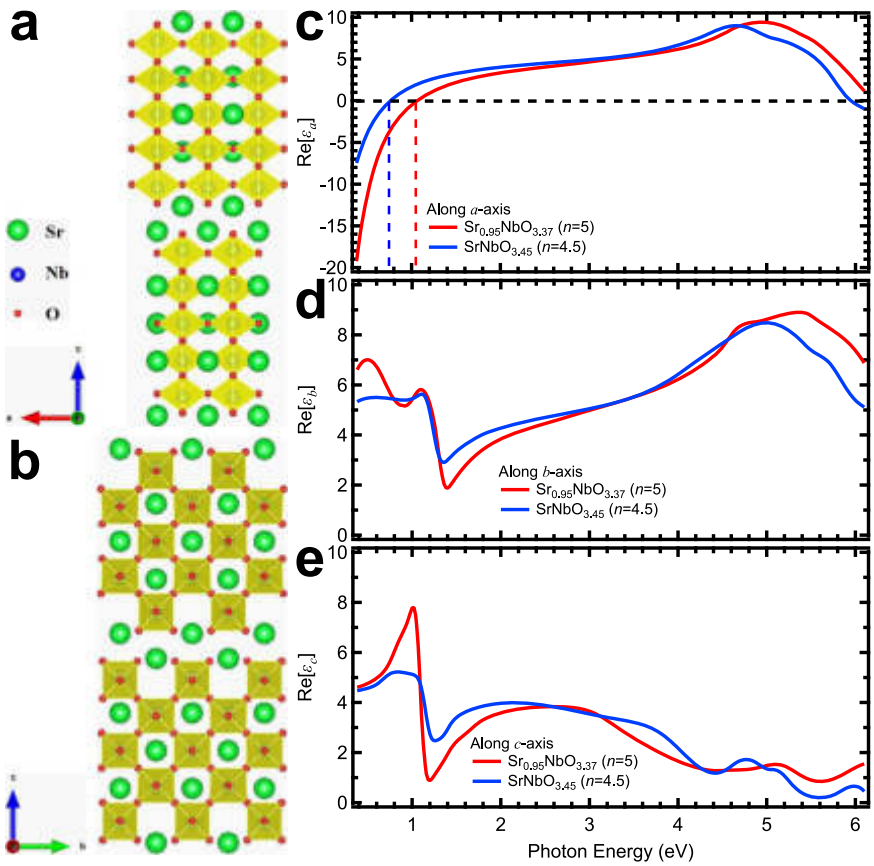

Fig. 1 Crystal structure and real part of complex dielectric functions of $Sr_{1-y}NbO_x$. **a** Crystal structure of $n = 5$ type $SrNbO_{3.4}$ as a representative case projected on the orthorhombic *ac* plane (Sr = green, Nb = blue, O = red, NbO_6 octahedra = yellow). **b** Crystal structure of $SrNbO_{3.4}$ projected on the orthorhombic *bc* plane. **c** Real part of complex dielectric function, Re[ε], spectra of $n = 5$ type $Sr_{0.95}NbO_{3.37}$ and $n = 4.5$ type $SrNbO_{3.45}$ single crystal samples along the *a*-axis. Red and blue dashed lines denote the Re[ε] zero-crossing of $Sr_{0.95}NbO_{3.37}$ and $Sr_0NbO_{3.45}$, respectively. **d** The Re[ε] spectra of the samples along the *b*-axis. **e** The Re[ε] spectra of the samples along the *c*-axis.

Excitonic ultraviolet Raman spectroscopy. To further probe these *d*–*d* excitations, we perform excitonic ultraviolet Raman spectroscopy (Fig. 2b inset) on the $n = 5$ type $Sr_{0.95}NbO_{3.37}$ sample with an incoming beam of 240 nm (5.17 eV), i.e., on the onset of the O-2*p*→Nb-4*d* charge-transfer inter-band transitions. Along the *b*-axis, we find an excitonic peak centered at 0.89 eV Raman shift consistent with the lower *d*–*d* excitation, indicating the excitonic nature of these *d*–*d* excitations. Interestingly, a similar excitonic peak is also found at 0.86 eV along the *a*-axis, which means that the lower *d*–*d* exciton also occurs along the metallic axis. In conventional metals, excitons are usually absent. Despite this, excitons are present in $Sr_{1-y}NbO_x$ because they are not conventional metals but rather correlated quasi-1D metals. In the Im[ε_a] obtained from Mueller-matrix ellipsometry, the *a*-axis *d*–*d* exciton is overshadowed by the Drude response of the correlated electrons in the metallic direction (see Fig. 2a), and the use of Raman spectroscopy allows us to resolve the exciton since Drude excitations are usually invisible in optical Raman.

Electronic band structure. To determine the origins of the peaks in Im[ε] spectra, we calculate the electronic band structure of $n = 5$ type $SrNbO_{3.4}$ (which is closely related to $n = 5$ type $Sr_{0.95}NbO_{3.37}$ and $n = 4.5$ type $SrNbO_{3.45}$) using density functional theory in Fig. 3a. The results are consistent with both experimental ARPES and ultraviolet photoemission (UPS) results and previous theoretical calculations[17,19,20]. The band structure is plotted along the high symmetry lines of Γ–X (along the *a*-axis), Γ–Y (*b*-axis), and Γ–Z (*c*-axis) to determine the possible valence and conduction band pairings that contribute to the Im[ε] spectra along each axis. The results show that the valence bands have mainly O-2*p* character while the conduction bands have mainly Nb-4*d* character, and together they contribute to the O-2*p*→Nb-4*d* charge-transfer inter-band transition edges.

Although the Nb-4*d* bands are mostly unoccupied and lie above the Fermi level, a small group of Nb-4*d* bands (red bands in Fig. 3a) cross the Fermi level, E_F, along Γ–X and lie occupied below it at Γ, along Γ–Y, and along Γ–Z. The strong dispersion and E_F crossing along Γ–X are consistent with the samples' metallic behavior along the *a*-axis and responsible for the Drude response excitation. Meanwhile, at Γ, along Γ–Y, and along Γ–Z, these bands lie below the E_F with no significant dispersion, consistent with the samples' non-metallic behavior along the *b*- and *c*-axes. The low-energy excitonic peaks in Im[ε] spectra can then be assigned to the transitions (green arrows in Fig. 3a) from these shallow occupied bands to the low-lying unoccupied bands at Γ, along Γ–Y, and along Γ–Z (blue bands in Fig. 3a). As both occupied and unoccupied bands have Nb-4*d* character, these low-energy peaks are *d*–*d* excitations. Although *d*–*d* transitions are dipole forbidden in centrosymmetric compounds, they are distinctly observed here due to the symmetry breaking caused by the layered perovskite structure. Thus, the Drude response and the *d*–*d* excitons originate from the same group of Nb-4*d* bands, but along different directions in the reciprocal Brillouin zone and thus the real space.

Furthermore, we also perform room-temperature ARPES on the $Sr_{0.95}NbO_{3.37}$ sample to verify the band structure calculations.

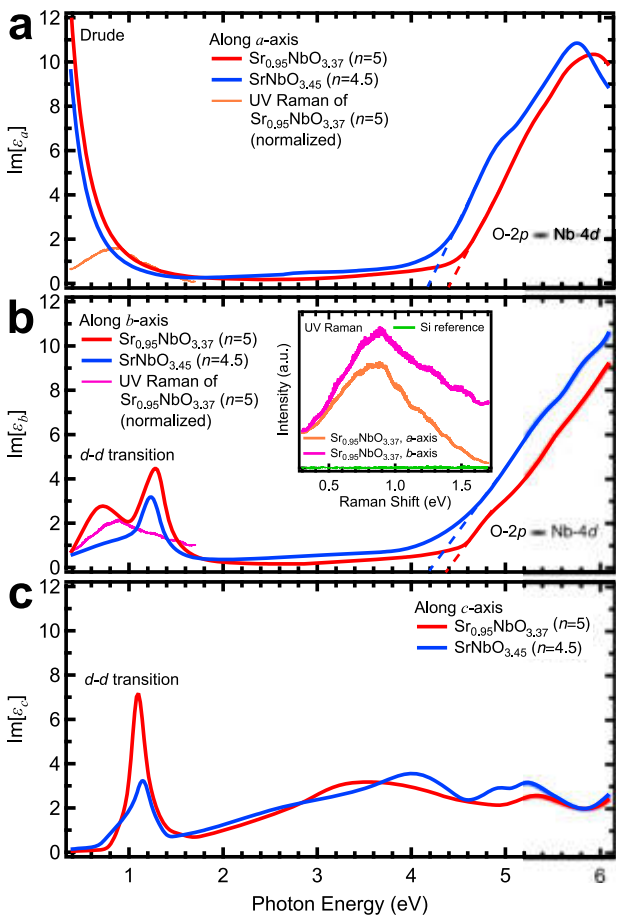

Fig. 2 Imaginary part of complex dielectric functions and ultraviolet Raman spectra of $Sr_{1-y}NbO_x$. **a** Imaginary part of complex dielectric function, Im[ε], spectra of $n = 5$ type $Sr_{0.95}NbO_{3.37}$ and $n = 4.5$ type $SrNbO_{3.45}$ single crystal samples along the *a*-axis. **b** The Im[ε] spectra of the samples along the *b*-axis. **c** The Im[ε] spectra of the samples along the *c*-axis. Red and blue dashed lines denote the linearly extrapolated O-2*p*→Nb-4*d* charge-transfer inter-band transition edges of $Sr_{0.95}NbO_{3.37}$ and $SrNbO_{3.45}$, respectively. Inset is excitonic ultraviolet (UV) Raman spectra of the samples along the *a*- and *b*-axes. These spectra, normalized with respect to the *d*–*d* transition peaks along the *b*-axis, are also superimposed on the main panels to directly compare them with the Im[ε] spectra. For reference, the UV Raman spectrum of Si is also shown.

Figure 3b shows the band dispersion of the low-lying occupied Nb-4*d* bands along the *X*–*Γ*–*X* direction. We see two dispersing bands along *Γ*–*X* direction crossing the Fermi level indicative of its metallic behavior. We observe two arms of the parabolic band (as obtained from the first-principles calculations, see Fig. 3a), while the ARPES intensity at the *Γ* point is not visible. This discrepancy could be due to the photoelectric matrix element for the chosen photon energy; however, it does not affect our main discussion. The iso-energy Fermi surface is shown in Fig. 3c. The Fermi surface is highly anisotropic; it is elongated along the *Y*–*Γ*–*Y* direction while restricted along the *X*–*Γ*–*X* direction. We see two parallel linear features, which are characteristic for their unidirectional electronic structure.

Modulation of transient reflectance by *d*–*d* excitation. As the *d*–*d* excitons originate from the same bands of electrons (red bands in Fig. 3a) as the metallic Drude response, their excitations by polarized light can modulate the free electrons along the *a*-axis. To demonstrate this, we build a laser-based mid-infrared

Table 1 Optical excitation peaks along the three optical axes of $Sr_{1-y}NbO_x$.

Peak name	Energy (eV)	
	$Sr_{0.95}NbO_{3.37}$ ($n = 5$)	$SrNbO_{3.45}$ ($n = 4.5$)
Along a-axis		
Drude	0	0
O-2*p*→Nb-4*d*	4.4	4.2
Along b-axis		
d–*d* transition	0.72	-
d–*d* transition	1.28	1.24
O-2*p*→Nb-4*d*	4.4	4.2
Along c-axis		
d–*d* transition	1.10	1.14
Hump	3.5	4.0
Hump	5.3	4.96, 5.24

The energy position of each peak is determined from their respective apparent maxima, except for O-2*p*→Nb-4*d* peaks where it is determined from their respective linearly extrapolated edge instead.

(MIR) pump-probe reflectance setup (Fig. 4a) and perform room-temperature transient pump-probe reflectivity experiments with fully controlled anisotropic polarizations on the $Sr_{0.95}NbO_{3.37}$ sample. The sample is pumped with polarization parallel to the *b*-axis ($\mathbf{E}_{pump}$ // *b*-axis) at 1030 nm wavelength (~1.20 eV) and 600 Wcm^{-2} power density to excite the *d*–*d* excitons along the *b*-axis, and then probed with polarization parallel to the *a*-axis ($\mathbf{E}_{probe}$ // *a*-axis) at 7 μm wavelength (~0.18 eV) to observe the effects of the *d*–*d* excitations on the transient reflectance along the metallic *a*-axis, $R_{trans}(a)$. The result in Fig. 4b shows that upon turning on the pump beam, $R_{trans}(a)$ drastically decreases all the way down to the steady-state reflectance of the non-metallic *b*-axis, R_b, indicating a near-100% switching from metal to insulator. When the pump beam is turned off, $R_{trans}(a)$ recovers back to the steady-state metallic level, R_a, indicating a relaxation toward the initial state. The relaxation times of the pump-on and pump-off conditions are found to be in the order of several seconds; in this particular orientation, they are fitted to be 5.8 ± 0.2 s and 4.6 ± 0.2 s, respectively.

As the optical response of the *a*-axis within the MIR range is dominated by the metallic Drude response[18,19], a decrease in its MIR transient reflectance indicates a decrease of the Drude peak, which directly translates to a decrease in the carrier density[23]. Thus, the drastic, nearly 100% decrease of $R_{trans}(a)$ toward the steady-state insulating level in Fig. 4b is strongly suggesting an exciton-driven transient metal–insulator transition (MIT), indicating a photoinduced switching capability of $Sr_{1-y}NbO_x$.

To prevent excessive heat damage, in Fig. 4c $n = 5$ type $Sr_{0.95}NbO_{3.37}$ is pumped with a lower power density of 260 Wcm^{-2}, which results in lower decrease of $R_{trans}(a)$ but excellent repeatability of the switching. Intriguingly, when $\mathbf{E}_{probe}$ is parallel to the *b*-axis, the 1.2 eV *d*–*d* exciton pumping causes an increase of the transient reflectance (and thus the metallicity) along the *b*-axis, $R_{trans}(b)$. This means that while the exciton pumping is switching the metallic *a*-axis to be more insulating, it also concomitantly switches the insulating *b*-axis to be more metallic (i.e., insulator-metal transition or IMT), making the strongly anisotropic $Sr_{0.95}NbO_{3.37}$ effectively more isotropic. More evidence can be seen in the power density, P_{pump}, dependence of the switching in Fig. 4d, which shows that while $R_{trans}(a)$ decreases linearly with increasing P_{pump}, $R_{trans}(b)$ increases concomitantly instead, outlining charge conservation. The switching effect can also be observed when $\mathbf{E}_{pump}$ // *a*-axis due to the presence of the ~0.9 eV *d*–*d* exciton along the *a*-axis as

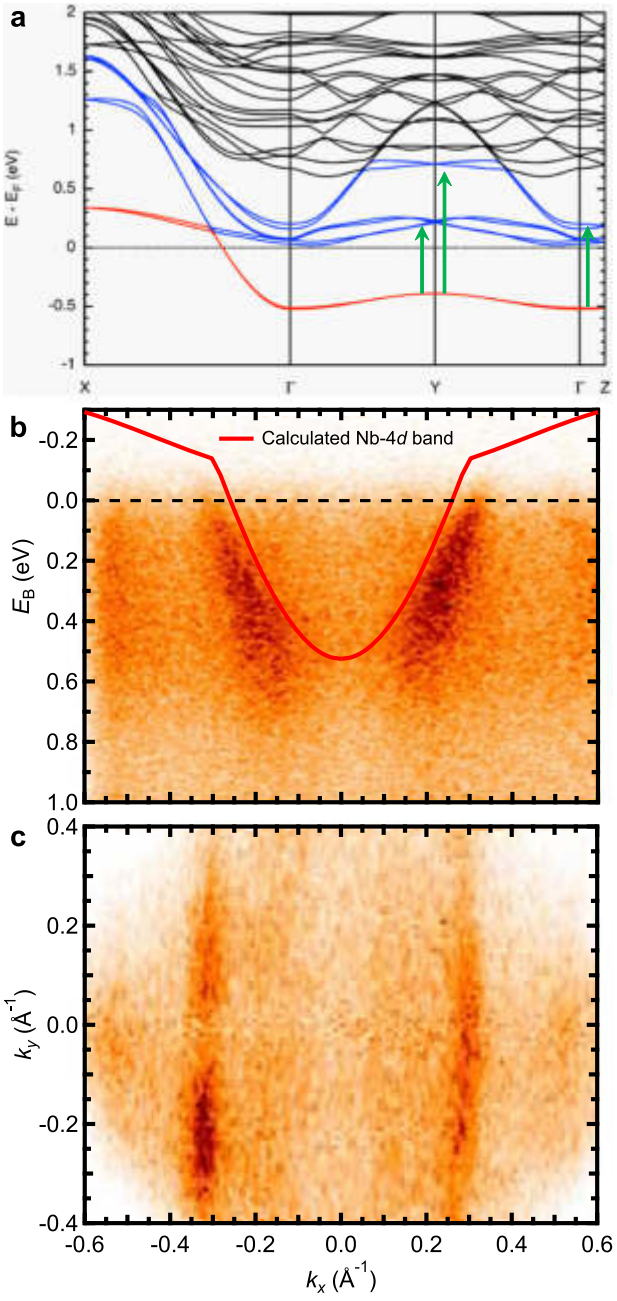

Fig. 3 Electronic band structure of $n = 5$ type $Sr_{1-y}NbO_{3.4}$. **a** Theoretically calculated band structure of $n = 5$ type $SrNbO_{3.4}$. Red and blue bands denote the occupied and unoccupied Nb-4*d* bands responsible for the *d*–*d* transition peaks (green arrows), respectively. Black dotted line denotes the Fermi level energy, E_F. The red bands strongly disperse and cross E_F along the *a*-axis (Γ–X) but stay below it with little dispersion at Γ, along the *b*-axis (Γ–Y), and *c*-axis (Γ–Z). **b** Angular-resolved photoemission spectroscopy (ARPES) result of $n = 5$ type $Sr_{0.95}NbO_{3.37}$ sample along the *a*-axis (Γ–X). The theoretically calculated red Nb-4*d* band is superimposed for comparison. **c** Iso-energy Fermi surface map of $n = 5$ type $Sr_{0.95}NbO_{3.37}$ sample.

revealed by ultraviolet Raman spectroscopy (Fig. 2d), showing further evidence of the exciton-driven nature of the switching.

Transient pump-probe phononic ultraviolet Raman spectroscopy. Furthermore, to study the effect of the exciton pumping on the transient lattice and charge orderings, we perform transient

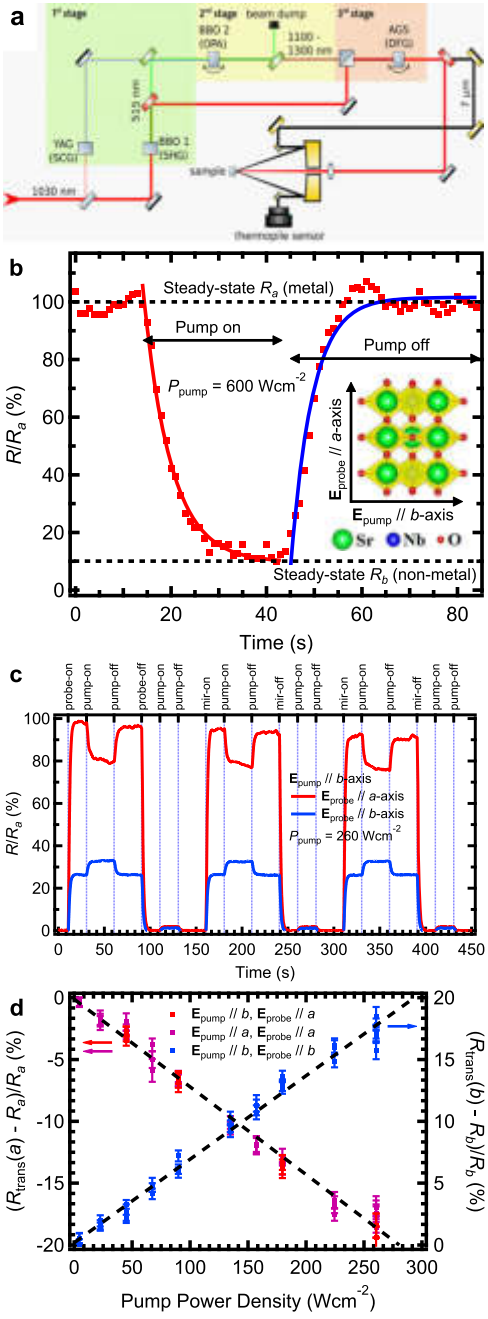

Fig. 4 Photoinduced metastable excitonic insulating state in $n = 5$ type $Sr_{0.95}NbO_{3.37}$. **a** Experimental setup of the mid-infrared transient pump-probe experiment with anisotropic pump-probe polarizations. The wavelength of the pump and probe beam is 1030 nm (~1.20 eV for the *d*–*d* excitons) and 7 μm (~0.18 eV), respectively. **b** Near-100% switching of transient reflectance along the *a*-axis of $n = 5$ type $Sr_{0.95}NbO_{3.37}$, $R_{trans}(a)$, due to the *d*–*d* exciton pumping from steady-state metallic level, R_a, all the way down to steady-state insulating level, R_b, indicating a transient photoinduced metal–insulator transition (MIT). The pump polarization, $\mathbf{E}_{pump}$, is parallel to the *b*-axis, while the probe polarization, $\mathbf{E}_{probe}$, is parallel to the *a*-axis. The pump power density, P_{pump}, is ~600 Wcm^{-2}. **c** Transient reflectance along the *a*- and *b*-axes ($R_{trans}(a)$ and $R_{trans}(b)$, respectively) of the $n = 5$ type $Sr_{0.95}NbO_{3.37}$ sample with various combinations of $\mathbf{E}_{pump}$ and $\mathbf{E}_{probe}$ polarizations as well as lower P_{pump} values to ensure repeatability of the switching. **d** The P_{pump} dependence of $R_{trans}(a)$ and $R_{trans}(b)$ switching, showing the opposite trends of $R_{trans}(a)$ and $R_{trans}(b)$ changes as P_{pump} increases. The ranges of ±standard deviation of the relative changes of $R_{trans}(a)$ and $R_{trans}(b)$ are shown by the error bars.

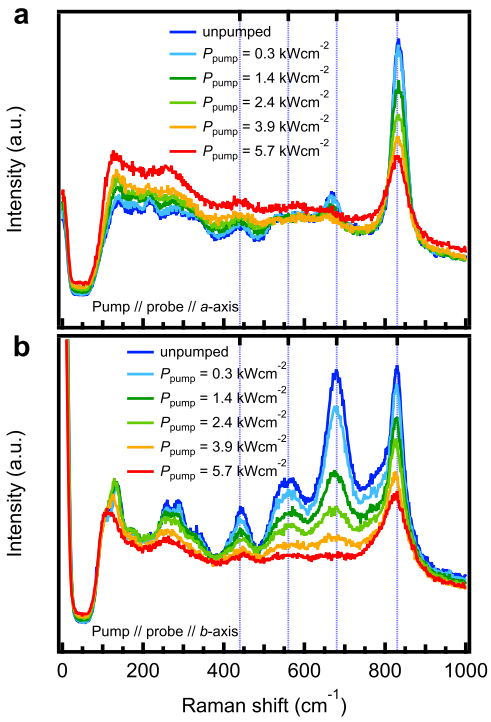

Fig. 5 Transient pump-probe Raman spectroscopy of $n = 5$ type $Sr_{0.95}NbO_{3.37}$. **a** Pump-probe transient Raman spectroscopy of the $n = 5$ type $Sr_{0.95}NbO_{3.37}$ sample with varied pump power density, P_{pump}, and pump-probe polarizations parallel to the *a*-axis. **b** Pump-probe transient Raman spectroscopy of the sample with varied P_{pump} and pump-probe polarizations parallel to the *b*-axis. The wavelength of the pump, reflectance probe, and Raman probe beam is 1030 nm (~1.20 eV for the *d*–*d* excitations), 7 μm (~0.18 eV), and 260 nm (~4.77 eV), respectively. Vertical blue dotted lines indicate the Raman modes related to oxygen chains at 830, 560, 680, and 440 cm^{-1}.

pump-probe ultraviolet Raman spectroscopy of phonons in $Sr_{0.95}NbO_{3.37}$. The pump beam is 1030 nm (1.20 eV) to match the *d*–*d* excitons and the incoming probe wavelength is 260 nm (4.77 eV) matching the O-2*p*→Nb-4*d* charge-transfer inter-band transition edge (see Fig. 2) to address the effects of oxygen and charge orderings. The resulting Raman spectrum with Raman pump and probe polarizations along the *b*-axis (Fig. 5a) without pumping shows dominant phonon modes located at 440, 560, 680, and 830 cm^{-1}. These modes are consistent with oxygen-bond-related modes observed in many different cuprate superconductors such as single-chain $YBa_2Cu_3O_{6.7}$ (ref. [25]), double-chain $YBa_2Cu_4O_8$ (ref. [26]), and spin-ladder compounds[27]. Meanwhile, along the *a*-axis (Fig. 5b), only the 830 cm^{-1} mode can be distinctly observed, while the rest are suppressed. According to Fig. 1a, b, the Nb–O–Nb bonds along the metallic *a*-axis are chain-like, while along the insulating *b*-axis they are zig-zag-like. Thus, as the 440, 560, and 680 cm^{-1} modes are observed only along the *b*-axis but not along the *a*-axis, these modes are signatures of the zig-zag-like bonds but not the chain-like bonds.

When the exciton pumping is turned on, all these zig-zag-like-related phonon modes decrease dramatically with increasing P_{pump}, indicating that the pumping changes the lattice orderings of the Nb–O–Nb bonds particularly along the *b*-axis. These decreases can already be observed even at the lowest P_{pump} of 300 Wcm^{-2}. At the highest P_{pump} of 5.7 kWcm^{-2}, the zig-zag-like-related modes become either severely diminished or completely bleached, and the shape of the Raman spectrum along the *b*-axis approaches that of along the *a*-axis. This indicates that the zig-zag-like Nb–O–Nb bonds along the *b*-axis are transformed by the *d*–*d* exciton pumping into more chain-like bonds, which facilitates easier hoppings between Nb ions and increases the conductivity of the normally insulating *b*-axis, making the *a*- and *b*-axes more isotropic consistent with pump-probe MIR-reflectance results. Note that other effects, such as screening of phonon modes by the excited photoelectrons and thermal heating by the laser pump, are unlikely to play significant roles in the evolution of the transient Raman spectra, as discussed in more detail in "Methods" and Supplementary Discussion.

Discussion

As mentioned, transient states caused by electronic and/or excitonic excitations typically have ultrashort lifetime in the pico- to femtoseconds range. Thus, the seconds-long ultraslow recovery time of the transient MITs in Fig. 4 indicates that the typically ultrafast excitonic excitations couple to additional mechanisms that have very slow recovery time. We believe that there are mainly two mechanisms that are responsible for this ultraslow recovery time.

First, as discussed above, the *d*–*d* exciton pumping causes the zig-zag-like Nb–O–Nb ordering along the *b*-axis to transform into more chain-like bonds. As this transient IMT involves changes in the lattice structure, this is an important reason for the slow recovery time along the *b*-axis, as recovery of lattice structure changes is typically orders of magnitude slower than recovery of electronic transitions.

For the long-lasting transient MIT along the *a*-axis, we are proposing a mechanism, in which the *d*–*d* exciton photo-pumping causes the conversion of most of the free electrons into excitons, depleting the red Nb-4*d* band in Fig. 3a, causing the decrease of the *a*-axis metallicity, and creating a large density of excitons. Due to the much lower effective mass of excitons (compared to atomic mass), this large density of excitons can undergo Bose–Einstein-like condensation (BEC) even at room temperature[10–12,28,29], similar to what has been observed in the case of photo-pumped magnons in yttrium–iron–garnet films[13]. The coherence of the BEC phase can lead to a very long lifetime of the transient insulating state. For example, in photo-pumped magnons[13], non-BEC phase decays quickly within 100–200 ns while the BEC phase stays coherent even after 1200 ns.

Note that these two mechanisms (changes in the lattice orderings and BEC-like phase transition) may very well be coupled, as together they resemble the signatures of excitonic insulators, a manifestation of exciton BEC in which the insulating ground state is dominated by BEC of excitons accompanied by changes in the lattice orderings[28,29]. Similar behaviors have been predicted and suspected to be observed in the two likely candidates for intrinsic excitonic insulators: semiconducting Ta_2NiSe_5 (ref. [30]) and semimetal 1*T*-$TiSe_2$ (ref. [31]).

Furthermore, with high enough pump power density of 600 Wcm^{-2}, the switching can be made to be nearly 100%, promising potential applications in future photoinduced switching devices such as exciton-based transistors and other optoelectronic devices in general. This is especially important because so far, many other photoinduced systems have only been able to be optically switched by <35% (refs. [32–35]), and/or need high switching power density requirements of >10^5–10^{10} Wcm^{-2} (refs. [32–37]). Thus, the near-100% optical switching of $Sr_{1-y}NbO_x$, which only needs a very low pump power density of 600 Wcm^{-2} to induce the switching, represents a very big leap compared to other photo-induced systems, conceptually demonstrating that it is possible to optically switch a system to near-100% switching contrast with very low pump power density.

Methods

Sample preparation. Melt-grown crystalline $n = 4.5$ type $SrNbO_{3.45}$ and Sr- and O-deficient $n = 5$ type $Sr_{0.95}NbO_{3.37}$ samples are prepared by melting, reducing, and solidifying the corresponding fully oxidized Nb^{5+} compositions of $SrNbO_{3.50}$ and $Sr_{0.95}NbO_{3.45}$ under a flow of 98% Ar + 2% H_2 gas[14]. The process is done in a GERO mirror furnace where two polycrystalline sintered rods with fully oxidized Nb^{5+} compositions of $SrNbO_{3.50}$ and $Sr_{0.95}NbO_{3.45}$, respectively, are processed by floating zone melting. The two polycrystalline sintered rods themselves are prepared by mingling an appropriate molar ratio of $SrCO_3$ and Nb_2O_5, which is then pre-reacted at an elevated temperature in air. After the pre-reaction, the mixture is ground into powder, once again mingled, pressed into the shape of two rectangular rods, and sintered at an elevated temperature in air. The experimental approaches, types, and design of used equipment, devices, and constructions are similar to those which are presented comprehensively in ref. [38]. The GERO mirror furnace is presented in Appendix 1 of ref. [38]. Photo images of melt-grown crystalline pieces of $n = 4.5$ type $SrNbO_{3.45}$ and non-stoichiometric $n = 5$ type $Sr_{0.95}NbO_{3.37}$ are shown in Supplementary Fig. 1. Pieces of the crystalline samples are then cleaved into flat plate shapes so that their surfaces are parallel to the *c*-axis (verified with X-ray diffraction, see below). A transmission electron microscopy (TEM) image of $n = 4.5$ type $SrNbO_{3.45}$ is shown in ref. [14].

X-ray diffraction. The cleaved plate-shaped $n = 5$ type $Sr_{0.95}NbO_{3.37}$ and $n = 4.5$ type $SrNbO_{3.45}$ samples are measured using high-resolution X-ray diffraction to characterize their lattice structures and verify the orientation of their cleaved surfaces. The measurements are done using a Huber 4-circle diffractometer system 90000-0216/0 at Singapore Synchrotron Light Source with a selected X-ray wavelength equal to that of Cu $K\alpha_1$ radiation ($\lambda = 1.5406$ Å). The resulting $2\theta/\theta$ XRD patterns of both samples are shown in Supplementary Fig. 2. Each major peak in both patterns is a higher-order mode of the (001) Bragg peak, which means that the surface normal of both samples are parallel to the *c*-axis. Further analysis results in a *c*-axis lattice constant of 32.404 and 59.300 Å for $Sr_{0.95}NbO_{3.37}$ and $SrNbO_{3.45}$, respectively, consistent with previous results[14,16].

Mueller-matrix spectroscopic ellipsometry. As the $Sr_{1-y}NbO_x$ samples are highly anisotropic quasi-1D metals, an advanced form of ellipsometry called Mueller-matrix spectroscopic ellipsometry is needed to unambiguously probe their principal dielectric functions along all optical axes[22–24]. Mueller matrix is a 4×4 matrix unique to each material that describes the changes in light polarizations due to the complex dielectric response of said material[23]. Conventional optical absorption spectroscopy techniques typically only measure a few elements of this matrix, making them suitable only for probing isotropic materials. In contrast, Mueller-matrix spectroscopic ellipsometry measures the majority of these elements (in some cases all), enabling us to precisely probe the principal dielectric tensors of highly anisotropic materials along all orthogonal directions. More information and a basic introduction about Mueller-matrix spectroscopic ellipsometry are given in Supplementary Methods.

In this study, the Mueller-matrix spectroscopic ellipsometry measurements are done from 0.38 to 6.10 eV using a Woollam V-VASE ellipsometer with a compensator and rotating analyzer. The cleaved samples are mounted on a precision rotation stage (Newport RS40) to perform azimuth-dependent measurements, where the in-plane rotation angle, φ, is varied from 0° to 315° in steps of 45°. At each in-plane orientation, the measurements of each Mueller-matrix element, m_{ij}, are done at three incident angles, θ, of 50°, 60, and 70° from the sample surface normal. Such an angle-resolved measurement scheme is necessary to ensure a complete characterization of arbitrary optically anisotropic samples[22–24]. This setup is capable of measuring 12 out of the 16 Mueller-matrix elements (from m_{11} to m_{34}), which is sufficient to obtain the principal ε of highly anisotropic samples.

The resulting incident-angle-, azimuth-dependent Mueller-matrix element spectra are analyzed using the Woollam WVASE software. The fitting parameters are the principal ε of the samples along the major optical axes and the Euler angles of α, β, and γ. The principal dielectric functions, ε_a, ε_b, and ε_c along the *a*-, *b*-, and *c*-axis, respectively, are modeled using the Kramers–Kronig transformable Drude[23] and Herzinger–Johs PSemi-Tri[39] oscillator functions. Meanwhile, real-valued and wavelength-independent Euler angles describe the rotation between the Cartesian laboratory frame of (x, y, z) and the samples' Cartesian optical axis frame of (a, b, c): α represents a rotation around the z-axis to rotate from (x, y, z) to (x', y', z), β represents a rotation around the x'-axis to rotate from (x', y', z) to (x', y'', z'), and γ represents a rotation around the z'-axis to rotate from (x', y'', z') to (a, b, c). The samples' surface roughnesses (~8 nm for $n = 5$ type $Sr_{0.95}NbO_{3.37}$ and ~5 nm for $n = 4.5$ type $SrNbO_{3.45}$) are modeled by a Bruggeman-mode effective medium approximation[23] with 50% material and 50% void ($\varepsilon_{void} = 1 + i0$).

The analysis is done using non-linear regression methods, where measured and calculated Mueller-matrix elements are matched until the mean-squared error (MSE) between the fit and the data is minimized. Each sample is analyzed in a multi-sample configuration analysis scheme[24], where data from all in-plane orientations and incident angles are included in the regression analysis and only the azimuthal Euler angle of α is set according to the in-plane rotation measurement configuration ($\varphi_{n+1} = \varphi_n + 45°$, thus α is also set such that $\alpha_{n+1} = \alpha_n + 45°$). The Mueller-matrix spectroscopic ellipsometry spectra are measured in an extended energy setup: the extended infrared part from 0.38 to 1.00 eV and the infrared-visible-ultraviolet part from 0.60 to 6.10 eV, both in steps of 0.02 eV. In the regression analysis, these two parts are fit simultaneously to obtain the complete principal ε from 0.38 to 6.10 eV. As representative examples, the comparisons between measured and fitted Mueller-matrix elements after the final fit for $\varphi = 0°$, 45°, 90°, and 135°; $\theta = 70°$; and energy range of 0.6–6.1 eV are shown in Supplementary Fig. 3 (for $Sr_{0.95}NbO_{3.37}$) and Supplementary Fig. 4 (for $SrNbO_{3.45}$).

The resulting principal ε of $Sr_{0.95}NbO_{3.37}$ and $SrNbO_{3.45}$ are shown in Figs. 1 and 2. The analysis also reveals that the Euler angle of β of both samples is very small (<0.1° for $Sr_{0.95}NbO_{3.37}$ and 0.6° for $SrNbO_{3.45}$), indicating that the optical *c*-axis of the samples coincides with their respective surface normal and thus, per XRD results (Supplementary Fig. 2), with their respective crystallographic *c*-axis. These minute β also mean that the Euler angles of α and γ are practically equivalent (since the z-axis is almost unchanged by the rotation of β), and the combined angle of $\alpha + \gamma$ can be used to determine the orientation of the *a*- and *b*-axis with respect to the plane of incident (POI) at a given φ. For $Sr_{0.95}NbO_{3.37}$ at $\varphi = 0°$, the *a*-axis (*b*-axis) is oriented at −11.8° (78.2°) from the intersection line between the POI and the sample surface. Meanwhile, for $SrNbO_{3.45}$ at $\varphi = 0°$, the *a*-axis (*b*-axis) is oriented at −8.4° (81.6°) from the intersection line between the POI and the sample surface.

Excitonic ultraviolet Raman spectroscopy. Ultraviolet Raman spectroscopy measurements of excitons are performed with the UT-3 Raman spectrometer[40] with 1800 s integration time. The 240 nm probe beam is obtained by frequency tripling of a Tsunami Ti:Sapphire laser (model 3950-X1BB, Spectra Physics Lasers Inc., repetition rate: 80 MHz) with a spot size of 15 μm and a power of 5.8 mW. The spectral response of the spectrometer is calibrated using a certified white light calibration lamp from Gigahertz Optik (DKD).

Density functional theory calculations. Density functional theory (DFT) calculations are done using the Perdew–Burke–Ernzerhof[41] (PBE96) exchange-correlation potential and the projector-augment wave (PAW) method[42] as implemented in the Vienna ab initio simulation package[43] (VASP). In these calculations, Sr-4*s*4*p*5*s*, Nb-4*p*5*s*4*d*, and O-2*s*2*p* orbitals are treated as valence states, employing the PAW potentials labeled as "Sr_sv", "Nb_sv", and "O" in the VASP PBE library. The cutoff energy for the plane-wave basis set is set to 500 eV and the partial occupancies for each orbital use the Gaussian smearing with a width of 0.2 eV. The atomic structure of $n = 5$ type $SrNbO_{3.4}$ is taken from experimentally determined atomic positions in ref. [16] which is modeled by supercells containing 54 atoms with a space group of *Pnnm*. The band structure is calculated with $23 \times 17 \times 3$ Γ-centered Monkhorst–Pack *k*-point meshes. The Fermi level is adjusted so that it is consistent with previous electrical transport, ARPES, and infrared reflectivity results[17–19]. The calculated band structure of $SrNbO_{3.4}$ near the Fermi level is presented in Fig. 3a, while the extended version down to $E–E_F = −7.5$ eV is shown in Supplementary Fig. 5a. Note that in the extended version, the deep-lying O-2*p* band is located below $E–E_F = −3$ eV, rather than −4 eV, according to the UPS results[17], due to the well-known Kohn–Sham bandgap underestimation problem in DFT. Similar DFT calculation results of $SrNbO_{3.4}$ that showed the O-2*p* bands have also been reported previously in ref. [17].

Angular-resolved photoemission spectroscopy (ARPES). The ARPES measurements were performed at the SUV beamline[44] of Singapore Synchrotron Light Source (SSLS) using a Scienta-Omicron DA30L electron analyzer. The single crystalline sample of $Sr_{0.95}NbO_{3.37}$ is cleaved inside the load lock chamber under pressure 5×10^{-8} mbar using the standard top-post method. The sample is then immediately transferred to the analysis chamber with base pressure 1×10^{-10} mbar. The measurements were performed at room temperature using helium lamp source (photon energy = 21.21 eV). An ARPES cut of the $n = 5$ type $Sr_{0.95}NbO_{3.37}$ sample along the *a*- (Γ–X) and *b*-axis (Γ–Y) is presented in Fig. 3b and Supplementary Fig. 5b, respectively. The ARPES cut along the *a*-axis (*b*-axis) is taken at $k_y = 0$ ($k_x = 0$) to ensure that there is no momentum contribution along the *b*-axis (*a*-axis). The ARPES cut along the Γ–Y direction shows a weak and non-dispersive band between $E_B = −(E–E_F) = 0.2$ eV and 0.6 eV, consistent with the DFT calculation in Fig. 3a that also shows non-dispersive bands at around $E–E_F = −0.5$ eV along the Γ–Y direction. Meanwhile, the Fermi surface map (Fig. 3c) is obtained using the electrostatic deflection lensing functionality of a DA30L analyzer without rotating the sample.

Mid-infrared transient pump-probe reflectivity. Since Mueller-matrix spectroscopic ellipsometry shows an onset of the Drude response for energies of the order of ~1 eV in the metallic direction, the reflectance of a laser-based mid-infrared (MIR) beam with a wavelength of 7 μm (~0.18 eV) probes predominantly the free electronic carriers associated to the Drude response. The main source laser for the MIR-reflectance setup (c.f., Fig. 4a) is a fiber amplified laser (Tangerine HP, 35 W) supplying typically 300 femtosecond pulses with 70 μJ at a 50 kHz repetition rate into the difference frequency generation setup as described by the following stages. The 1st stage is a supercontinuum generation in a YAG-crystal and second harmonic generation in a beta barium borate (BBO) type 1 crystal with 1030 nm

pump. The 2nd stage is an optical parametric amplification of 515 nm pump and supercontinuum seed in BBO type 2 crystal to generate a near-infrared beam of 1100–1300 nm. The 3rd stage is a differential frequency generation of 1030 nm pump and near-infrared seed in an AGS-crystal to generate a MIR beam of 6–12 μm. The MIR beam is focused on the sample using an on-axis parabolic mirror. The pump beam is focused on the sample through a hole in the same parabolic mirror. The reflected intensity is recorded using a thermopile power sensor (Coherent PS10). Spot diameter sizes of ~0.3 mm are determined by knife-edge experiments of pump and probe beams. The wavelength of the probe is measured with an integrated FTIR-spectrometer utilizing a pyroelectric sensor. Pump-on and pump-off are switched by an optical shutter. Data shown in Fig. 4b, c are real-time measurements of the observed reflected intensity.

The pump-on relaxation time constant, τ_{on}, is fitted from the red solid curve in Fig. 4b using

$$R_{trans}(t) = y_0 + Ae^{\left(-\frac{t-t_0}{\tau_{on}}\right)} \quad (1)$$

where t_0 is the turn-on time point, y_0 is the background level to which R_{trans} approaches as time, t, goes to infinity if the pump is perpetually turned on, and A is the amplitude of the R_{trans} change. Meanwhile, the pump-off relaxation time constant, τ_{off}, is fitted from the blue solid curve in Fig. 4b using

$$R_{trans}(t) = y_0 + A\left[1 - e^{\left(-\frac{t-t_0}{\tau_{off}}\right)}\right] \quad (2)$$

For both fittings, y_0 and A are identical within the error bars. From this analysis, τ_{on} and τ_{off} is estimated to be 5.8 ± 0.2 s and 4.6 ± 0.2 s, respectively.

Transient pump-probe Raman spectroscopy. Raman spectroscopy measurements are performed using the UT-3 Raman Spectrometer[40] with 300 s integration time. The 260 nm probe beam is obtained by frequency tripling of a Tsunami Ti:Sapphire laser (model 3950-X1BB, Spectra Physics Lasers Inc., repetition rate: 80 MHz) with a spot size of 15 μm and a power of 2.8 mW. The 1030 nm pump beam is provided by a Tangerine fiber laser (Amplitude Systemes, repetition rate: 500 kHz) with a spot size of 50 μm. The power of the pump beam is varied between 10 and 70 mW with a polarizer $\lambda/2$-waveplate combination, also controlling the polarization of the pump beam. The polarization of the probe beam is fixed, and the relative polarization with respect to the sample axes is varied by rotating the sample. Spatial overlap is ensured by imaging the laser focus on the sample. Since transient reflectivity measurements show timescales longer than the repetition rate of the laser systems, there is no need for temporal overlap of the laser pulses.

The effects of thermal heating from the pump laser are estimated by studying the changes in width and frequency of the phonon modes as a function of pump power density. This is because according to the anharmonic decay model[45], the linewidth of phonons is dependent on the temperature and thereby a good indicator for heating effects (Supplementary Fig. 6). From this we derive that the heating effect for pump power densities of up to 300 Wcm^{-2} is equivalent to an increase in temperature of <50 K, since there is no significant change in the linewidth for this power density. Heating only becomes significant (in terms of increasing the sample temperature) for pump power densities above 1 $kWcm^{-2}$, which are used only for pump-probe Raman but not for pump-probe MIR reflectance.

Data availability

The data that support the findings of this study are available from the corresponding authors upon reasonable request.

Code availability

The theoretical band structure is calculated using the openly-available VASP program and the implementation codes are available from the corresponding authors upon reasonable request.

Received: 5 July 2020; Accepted: 16 September 2020;
Published online: 10 November 2020

References

1. Collet, E. et al. Laser-induced ferroelectric structural order in an organic charge-transfer crystal. *Science* **300**, 612–615 (2003).
2. Ichikawa, H. et al. Transient photoinduced 'hidden' phase in a manganite. *Nat. Mater.* **10**, 101–105 (2011).
3. Rini, M. et al. Control of the electronic phase of a manganite by mode-selective vibrational excitation. *Nature* **449**, 72–74 (2007).
4. Hilton, D. J. et al. Enhanced photosusceptibility near T_c for the light-induced insulator-to-metal phase transition in vanadium dioxide. *Phys. Rev. Lett.* **99**, 226401 (2007).
5. Ehrke, H. et al. Photoinduced melting of antiferromagnetic order in $La_{0.5}Sr_{1.5}MnO_4$ measured using ultrafast resonant soft X-ray diffraction. *Phys. Rev. Lett.* **106**, 217401 (2011).
6. Först, M. et al. Spatially resolved ultrafast magnetic dynamics initiated at a complex oxide heterointerface. *Nat. Mater.* **14**, 883–888 (2015).
7. Zong, A. et al. Evidence for topological defects in a photoinduced phase transition. *Nat. Phys.* **15**, 27–31 (2019).
8. Fausti, D. et al. Light-induced superconductivity in a stripe-ordered cuprate. *Science* **331**, 189–191 (2011).
9. Mitrano, M. et al. Possible light-induced superconductivity in K_3C_{60} at high temperature. *Nature* **530**, 461–464 (2016).
10. Einstein, A. Quantentheorie des einatomigen idealen Gases. Zweite Abhandlung. *Sitz. ber. Preuss. Akad. Wiss.* **1**, 3–14 (1925).
11. Blatt, J. M., Böer, K. W. & Brandt, W. Bose-Einstein condensation of excitons. *Phys. Rev.* **126**, 1691–1692 (1962).
12. Moskalenko, S. A. & Snoke, D. W. *Bose-Einstein Condensation of Excitons and Biexcitons and Coherent Nonlinear Optics with Excitons* (Cambridge University Press, 2000).
13. Demokritov, S. O. et al. Bose-Einstein condensation of quasi-equilibrium magnons at room temperature under pumping. *Nature* **443**, 430–433 (2006).
14. Lichtenberg, F., Herrnberger, A., Wiedenmann, K. & Mannhart, J. Synthesis of perovskite-related layered $A_nB_nO_{3n+2} = ABO_x$ type niobates and titanates and study of their structural, electric and magnetic properties. *Prog. Solid State Chem.* **29**, 1–70 (2001).
15. Isawa, K., Sugiyama, J., Matsuura, K., Nozaki, A. & Yamauchi, H. Synthesis and transport properties of Sr_xNbO_3 ($0.75 \le x \le 0.90$). *Phys. Rev. B* **47**, 2849–2853 (1993).
16. Abrahams, S. C. et al. Centrosymmetric or noncentrosymmetric? Case study, generalization and structural redetermination of $Sr_5Nb_5O_{17}$. *Acta Cryst. B* **54**, 399–416 (1998).
17. Kuntscher, C. A. et al. Electronic structure of layered perovskite-related $Sr_{1-y}La_yNbO_{3.5-x}$. *Phys. Rev. B* **61**, 1876–1883 (2000).
18. Kuntscher, C. A. et al. Extremely small energy gap in the quasi-one-dimensional conducting chain compound $SrNbO_{3.41}$. *Phys. Rev. Lett.* **89**, 236403 (2002).
19. Kuntscher, C. A. et al. Electronic and vibrational properties of the low-dimensional perovskites $Sr_{1-y}La_yNbO_{3.5-x}$. *Phys. Rev. B* **70**, 245123 (2004).
20. Chen, C. et al. Atomic-scale origin of the quasi-one-dimensional metallic conductivity in strontium niobates with perovskite-related layered structures. *ACS Nano* **11**, 12519–12525 (2017).
21. Akishige, Y., Kobayashi, M., Ohi, K. & Sawaguchi, E. Dielectric and ferroelectric properties in the low temperature phase of strontium niobate. *J. Phys. Soc. Jpn.* **55**, 2270–2277 (1986).
22. Schubert, M. Polarization-dependent optical parameters of arbitrarily anisotropic homogeneous layered systems. *Phys. Rev. B* **53**, 4265–4274 (1996).
23. Fujiwara, H. *Spectroscopic Ellipsometry: Principles and Applications* (Wiley, 2007).
24. Schmidt, D., You, L., Chi, X., Wang, J. & Rusydi, A. Anisotropic optical properties of rhombohedral and tetragonal thin film $BiFeO_3$ phases. *Phys. Rev. B* **92**, 075310 (2015).
25. Bahrs, S. et al. Anisotropic ultraviolet Raman resonance in underdoped $YBa_2Cu_3O_{6.7}$. *Phys. Rev. B* **74**, 024519 (2006).
26. Bäckström, J. et al. Raman scattering in $YBa_2Cu_4O_8$ and $PrBa_2Cu_4O_8$: indications of pseudogap effects in nonsuperconducting $PrBa_2Cu_4O_8$. *Phys. Rev. B* **61**, 7049–7054 (2000).
27. Rusydi, A. et al. Experimental observation of the crystallization of a paired holon state. *Phys. Rev. Lett.* **105**, 026402 (2010).
28. Jérome, D., Rice, T. M. & Kohn, W. Excitonic insulator. *Phys. Rev.* **158**, 462–475 (1967).
29. Kohn, W. & Sherrington, D. Two kinds of bosons and Bose condensates. *Rev. Mod. Phys.* **42**, 1–11 (1970).
30. Lu, Y. F. et al. Zero-gap semiconductor to excitonic insulator transition in Ta_2NiSe_5. *Nat. Commun.* **8**, 14408 (2017).
31. Kogar, A. et al. Signatures of exciton condensation in a transition metal dichalcogenide. *Science* **358**, 1314–1317 (2017).
32. MacDonald, K. F., Sámson, Z. L., Stockman, M. I. & Zheludev, N. I. *Ultrafast Act. Plasmon. Nat. Photon.* **3**, 55–58 (2009).
33. Sámson, Z. L., MacDonald, K. F. & Zheludev, N. I. Femtosecond active plasmonics: ultrafast control of surface plasmon propagation. *J. Opt. A: Pure Appl. Opt.* **11**, 114031 (2009).
34. Abb, M., Albella, P., Aizpurua, J. & Muskens, O. L. All-optical control of a single plasmonic nanoantenna-ITO hybrid. *Nano Lett.* **11**, 2457–2463 (2011).
35. Vasa, P. et al. Real-time observation of ultrafast Rabi oscillations between excitons and plasmons in metal nanostructures with J-aggregates. *Nat. Photon.* **7**, 128–132 (2013).
36. Wurtz, G. A. et al. Designed ultrafast optical nonlinearity in a plasmonic nanorod metamaterial enhanced by nonlocality. *Nat. Nanotech.* **6**, 107–111 (2011).
37. Wu, H.-Y. et al. Ultrasmall all-optical plasmonic switch and its application to superresolution imaging. *Sci. Rep.* **6**, 24293 (2016).

38. Lichtenberg, F. *Presentation of a Laboratory for the Synthesis and Study of Special Oxides and Melt-grown Crystalline Materials*. https://doi.org/10.3929/ethz-a-010817148 (ETH Zurich, 2017).
39. Johs, B., Herzinger, C. M., Dinan, J. H., Cornfeld, A. & Benson, J. D. Development of a parametric optical constant model for $Hg_{1-x}Cd_xTe$ for control of composition by spectroscopic ellipsometry during MBE growth. *Thin Solid Films* **313–314**, 137–142 (1998).
40. Schulz, B., Bäckströmb, J., Budelmann, D., Maeser, R. & Rübhausen, M. Fully reflective deep ultraviolet to near infrared spectrometer and entrance optics for resonance Raman spectroscopy. *Rev. Sci. Instrum.* **76**, 073107 (2005).
41. Perdew, J. P., Burke, K. & Ernzerhof, M. Generalized gradient approximation made simple. *Phys. Rev. Lett.* **77**, 3865–3868 (1996).
42. Kresse, G. & Joubert, D. From ultrasoft pseudopotentials to the projector augmented-wave method. *Phys. Rev. B* **59**, 1758–1775 (1999).
43. Kresse, G. & Furthmüller, J. Efficient iterative schemes for ab initio total-energy calculations using a plane-wave basis set. *Phys. Rev. B* **54**, 11169–11186 (1996).
44. Yu, X. J., Diao, C. Z., Venkatesan, T., Breese, M. B. H. & Rusydi, A. A soft x-ray-ultraviolet (SUV) beamline and diffractometer for resonant elastic scattering and ultraviolet-vacuum ultraviolet reflectance at the Singapore synchrotron light source. *Rev. Sci. Instrum.* **89**, 113113 (2018).
45. Klemens, P. G. Anharmonic decay of optical phonons. *Phys. Rev.* **148**, 845–848 (1966).

Acknowledgements

The authors thank Nicola Spaldin, Joël Mesot, and Peter Abbamonte for useful discussions and various support as well as Jason Chee Wai Lim for technical support. The crystalline niobate samples were prepared at the University of Augsburg and F.L. thanks German Hammerl, Alexander Herrnberger, Thilo Kopp, Jochen Mannhart, and Klaus Wiedenmann for their support. The authors also thank the Singapore Synchrotron Light Source (SSLS) for providing the facility necessary for conducting the research. SSLS is a National Research Infrastructure under the Singapore National Research Foundation. This work was supported by the Singapore National Research Foundation under its Competitive Research Funding (No. NRF-CRP 8-2011-06 and No. R-398-000-087-281), MOE-AcRF Tier-2 (MOE2015-T2-1-099, MOE2015-T2-2-065, and MOE2015-T2-2-147), NUS YIA, MOE-AcRF Tier-1 (R-144-000-423-114, R-144-000-398-114, R-144-000-388-114 and R-144-000-439-114), and NUS Core Support (C-380-003-003-001). The work at Hamburg by M.R, F.B., B.G.L., and S.B. was supported by BMBF via VUVFAST (05K14GUB) and DFG via RU773/8-1.

Author contributions

T.C.A., M.A.N., and A.R. performed Mueller-matrix spectroscopic ellipsometry measurements and analysis. F.L. prepared the crystalline niobate samples. F.B., P.L., S.B., B.G.L., A.R., and M.R. set up and performed pump-probe mid-infrared reflectance and ultraviolet Raman spectroscopy measurements. T.Z., P.E.T., and A.R. performed theoretical band structure calculations. P.K.D., T.C.A., and A.R. performed ARPES measurements. P.Y. and T.C.A. performed X-ray diffraction measurements. A.D.F., C.D., and A.R. performed X-ray absorption spectroscopy experiment for checking the samples surface quality and orientation. T.C.A. and A.R. predicted and proposed the metal–insulator transitions induced by excitonic excitations. A.R. and T.C.A. analyzed the data comprehensively and wrote the paper with inputs from all co-authors including D.W., M.B.H.B., and T.V. A.R. and T.C.A initiated, planned, and coordinated the project. A.R. led the project.

Competing interests

The authors declare no competing interests.

Additional information

Supplementary information is available for this paper at https://doi.org/10.1038/s42005-020-00451-w.

Correspondence and requests for materials should be addressed to T.C.A., M.R. or A.R.

Reprints and permission information is available at http://www.nature.com/reprints

Publisher's note Springer Nature remains neutral with regard to jurisdictional claims in published maps and institutional affiliations.

5.2 Excitonic Quenching of the Oxygen-Chain Phonon in the Photo-induced Metal to Insulator Transition of $Sr_{0.95}NbO_{3.37}$ Studied by Transient UV-Resonance Raman Scattering

The author has contributed to the Raman and reflectance measurements and the respective data analysis.

In [5.2] the quenching of the oxygen-related Raman modes, that are correlated with the metal-to-insulator transition of the a-axis, shown in [5.1], are investigated in detail and a microscopic theory of the interactions of the electronic and phononic degrees of freedom is developed. For further information on the $Sr_{0.95}NbO_{3.37}$ compound, please see 5.1. The multitude of experiments contain angle-dependent transient MIR reflectance, angle-dependent UV Raman scattering, transient NIR-pump and UV-probe Raman scattering and a detailed resonance Raman UV study of 17 different wavelengths over the range of 318 nm to 217 nm. A temperature-dependent study with 260 nm from 6 K to 350 K was conducted to rule out heating effects, which is shown in the supporting information. The experimental data are complemented with theoretical calculations of the phonon dispersion and electronic band structure.

Angle-Dependent transient MIR Reflectance
The NIR-pump and MIR-probe reflectivity setup uses the Tangerine laser system to produce 1030 nm beam for the NIR-pump and also to supply 1030 nm to the DFG unit to produce MIR light at 7 µm for the probe beam. The DFG unit is explained in section 3.1.4 and it was slightly modified for this experiment, as shown in [5.1]-Fig. 4 (a). In the third stage, the residual 1030 nm beam is not dumped but used as the pump laser. An on-axis parabolic mirror with a hole in the center is positioned so that the sample is in the focus of the mirror. The MIR-probe beam is focused onto the sample by the mirror, then back to the mirror and into a thermopile sensor. The NIR-pump is focused onto the sample *via* a lens and through the hole in the mirror. The sample is mounted on a rod that can be manually rotated for the angle-dependence. The angle-dependent transient reflectance data, as shown in [5.2]-Fig. 2 (a) and (b), show a sinusoidal behavior with a changing angle between the polarization and the metallic a-axis. If the angle is zero, the reflectance decreases and for orthogonal polarization the reflectance increases.

Angle-Dependent UV Raman Scattering
The angle-dependent UV Raman scattering is conducted with the Tsunami laser system using nonlinear BBO crystal to produce third harmonic light from a 780 nm fundamental. The angle-dependent UV Raman scattering data are shown in [5.2]-Fig. 2 (c) and (d). The data show only a weak modulation of the intensity of the 840 cm^{-1} mode and a strong modulation of the 680 cm^{-1} mode, but both follow a clear sinusoidal pattern. The comparison of both angle-dependencies suggests a common underlying origin of both these effects. Subsequent phonon simulations, shown in [5.2]-Fig. 3, revealed that the 680 cm^{-1} mode stems from the central NbO_6 octahedra, while the 840 cm^{-1} mode stems from the outer NbO_6 octahedra within the 5-octahedra-thick layers.

UV Resonance Raman Scattering
For the UV resonance Raman scattering, the Tsunami laser system was used with

nonlinear BBO crystals to produce third and fourth harmonic light. For the third harmonic light, the fundamental frequency is doubled to the second harmonic and combined with the residual first harmonic in a second nonlinear BBO crystal. For the fourth harmonic generation, second harmonic light is produced in one BBO crystal and the created beam is sent into another BBO crystal to nonlinearly mix with itself and generate fourth harmonic light. In both of these processes, the underlying interaction is sum-frequency mixing. Third harmonic generation is defined by $1\omega + 2\omega = 3\omega$ and fourth harmonic generation by $2\omega + 2\omega = 4\omega$. Seventeen wavelengths have been used to carefully study the electronic resonance behavior of both relevant Raman modes. The data are shown in [5.2]-Fig. 4 (a) and (b). The study revealed a single and distinct peak at the onset of the charge-transfer transition. This implies that the intensity change in the 680 cm^{-1} mode can be assigned to the oxygen chains and is resonantly enhanced at 4.6 eV (260 nm).

NIR-Pump and UV-Probe Raman Scattering

For details on the NIR-pump and UV-Probe Raman Scattering, see 5.1. The data are shown in [5.2]-Fig. 4 (e) and (f). By comparison of the data sets, it is found that the mechanism of the reduction of charge carriers along the metallic a-axis and the quenching of the central oxygen chain mode is of electronic nature, in that the charge-transfer transition is bleached by the NIR-pump.

Excitonic Quenching of the Oxygen-Chain Phonon in the Photo-induced Metal to Insulator Transition of $Sr_{0.95}NbO_{3.37}$ Studied by Transient UV-Resonance Raman Scattering

Currently under submission at Physical Review B.

Excitonic quenching of the oxygen-chain phonon in the photo-induced metal to insulator transition of $Sr_{0.95}NbO_{3.37}$ studied by transient UV-resonance Raman scattering

Sören Buchenau,* Florian Biebl, Benjamin Grimm-Lebsanft, and Philipp Lenzen
Institute of Nanostructure and Solid State Physics,
University of Hamburg, Hamburg, 22607, Hamburg, Germany

Teguh C. Asmara† and Andrivo Rusydi
Nanoscience and Nanotechnology Initiative, National University of Singapore,
Lower Kent Ridge, Singapore, 119077, Singapore

Frank Lichtenberg
Department of Materials, ETH Zurich, Zürich, 8093, Zürich, Switzerland

Michael Rübhausen‡
Institute of Nanostructure and Solid State Physics,
University of Hamburg, Hamburg, 22607, Hamburg, Germany
(Dated: October 12, 2022)

The quasi-1D metal $Sr_{0.95}NbO_{3.37}$ shows a metal to insulator transition upon laser induced pumping of the d-d exciton at 1.1 eV. The oxygen-chain related phonon modes are highly susceptible to this metal to insulator transition due to their sensitivity to structural and electronic changes. We employ angle-dependent and transient UV-resonance Raman spectroscopy to probe the oxygen-chain related phonon dynamics and the concomitant changes in the angle-dependent transient mid-infrared reflectance. The latter shows the expected reduction of charge carrier density upon pumping, whereas the central chain mode at 680 cm^{-1} can be selectively quenched upon pumping the d-d excitons. We find that the underlying quenching mechanism for this phonon is electronically driven and related to the photo-induced bleaching of the charge-transfer transition. First principle calculations show the connection between phonon dispersion and electronic band structure leading to the selective quenching of the oxygen-chain mode. Our results contribute to a deeper understanding of the interplay between lattice and charge degrees of freedom for exciton-based transient optoelectronics.

I. INTRODUCTION

Transition metal compounds exhibit many exciting properties ranging from high-temperature superconductivity [1–3], colossal magnetic resistance [4], multiferroic properties [5], to metal to insulator transitions (MIT) [6]. The complex phase diagram of many transition metal compounds is the consequence of competing interactions that couple charge, spin, and lattice degrees of freedom [7]. These materials exhibit a strong structural anisotropy, furthermore these materials are susceptible to photo-induced effects, opening the pathway for novel applications such as in optically switchable optoelectronics [8, 9]. They are visible, e.g. in the oxygen-chain related modes of the cuprate superconductor single chain $YBa_2Cu_3O_{6.7}$ [10] and the double chain $YBa_2Cu_4O_8$ [11] as well as in spin ladder compounds [12]. For the case of non-stoichiometric $YBa_2Cu_3O_{6.7}$ a strong enhancement of the chain related modes, especially the oxygen related modes around 600 cm^{-1}, in resonance with the ultraviolet charge-transfer band is visible. Upon illumination with light, changes can be observed in the Raman spectra and the corresponding reflection anisotropy data [13].

Perovskite-related, layered, and quasi-1D metallic oxides of the type $A_nB_nO_{3n+2} = ABO_x$ [14, 15], so-called Carpy-Caly phases [16], are promising transition metal materials for optoelectronic devices. A topical review of optoelectronics of quasi-1D layered transition metal trichalcogenides was published in 2017 by J. O. Island et al.[17] An anisotropic MIT, induced by optically pumping the d-d exciton, was recently reported in the Sr- and O-deficient n=5 type quasi-1D metal $Sr_{0.95}NbO_{3.37}$ [18]. In this article we report on the interplay between structural and charge degrees of freedom, induced by optically pumping the d-d exciton. We employ transient UV resonance Raman scattering in resonance with the charge transfer transition in combination with transient mid-infrared (MIR) reflectance measurements. We show that the oxygen related Raman mode at 680 cm^{-1} can be selectively quenched upon excitonic pumping, while the MIR-reflectance shows the MIT leading to an excitonic switching mechanism. First principle calculations show the connection between phonon dispersion and electronic band structure leading to the selective quenching of the oxygen-chain mode, revealing the selective interplay between electronic and structural degrees of freedom.

* sbuchena@physnet.uni-hamburg.de
† Photon Science Division, Paul Scherrer Institut, Villigen, 5232, Aargau, Switzerland
‡ mruebhau@physnet.uni-hamburg.de

II. EXPERIMENTAL PART

The Sr- and O-deficient n=5 type $Sr_{0.95}NbO_{3.37}$ samples were prepared by melting, reducing, and solidifying the corresponding fully oxidized Nb^{5+} composition of $Sr_{0.95}NbO_{3.45}$ under 98 % Ar + 2 % H_2 [18]. Raman spectroscopy measurements were performed in a custom made setup using the UT-3 Raman Spectrometer [19]. All measurements, if not otherwise stated, were carried out at room temperature. No structural phase transitions were observed in the Raman spectra in the temperature range between 4 Kelvin to 350 Kelvin as shown in the SI. This rules out that the observed effects shown in the following are related to temperature induced structural phase transitions. This setup previously has been used for transient Raman spectroscopy in superconductors [20]. The probe beam was obtained by second, third, and fourth harmonic generation of a Tsunami Ti:Sapphire laser (Spectra Physics Lasers Inc., repetition rate: 80 MHz). Transient Raman spectroscopy was performed with a probe beam of 260 nm. The 1030 nm pump beam was provided by a Tangerine fiber laser (Amplitude Systemes, repetition rate: 500 kHz). This is also the pump laser for the MIR-reflectance setup. The MIR beam is focused on the sample using an on-axis parabolic mirror. The pump beam is focused on the sample through a hole in this mirror. The wavelength of the probe is measured with a FTIR-spectrometer using a pyroelectric sensor (MPY-01, WiredSense, Germany). Band structure calculations were performed using Quantum Espresso [21]. Phonon simulations were done using the Phonopy package [22]. More details can be found in the supporting information.

III. RESULTS AND DISCUSSION

The crystal structure of $Sr_{0.95}NbO_{3.37}$ together with its refractive index and extinction coefficient along the metallic a- and insulating b-axis is shown in Fig. 1 (a,b). The complex refractive index is given as the sum of the real part of the refractive index n, which describes the phase velocity, and the imaginary part k, which describes the attenuation of waves propagating through the material. Since the extinction coefficient of $Sr_{0.95}NbO_{3.37}$ shows an onset of the Drude response for energies below 1 eV in the metallic direction, the reflectance in the mid-infrared probes predominantly the free electronic carriers associated to the Drude response. The reflectance shows a strong response upon illumination with a pump beam of 1030 nm, corresponding to the energy of the d-d excitation at 1.1 eV, which can be seen in the b-axis refractive index and extinction coefficient in Fig. 1 (b). In Fig. 2 the MIR transients during the switching process are shown. Without the pump beam, the expected anisotropy can be seen: The reflected power changes by a factor of more than 5 when turning the sample by 90°. This angular change corresponds to a rotation from the metallic (high reflectance) to the insulating (low reflectance) direction

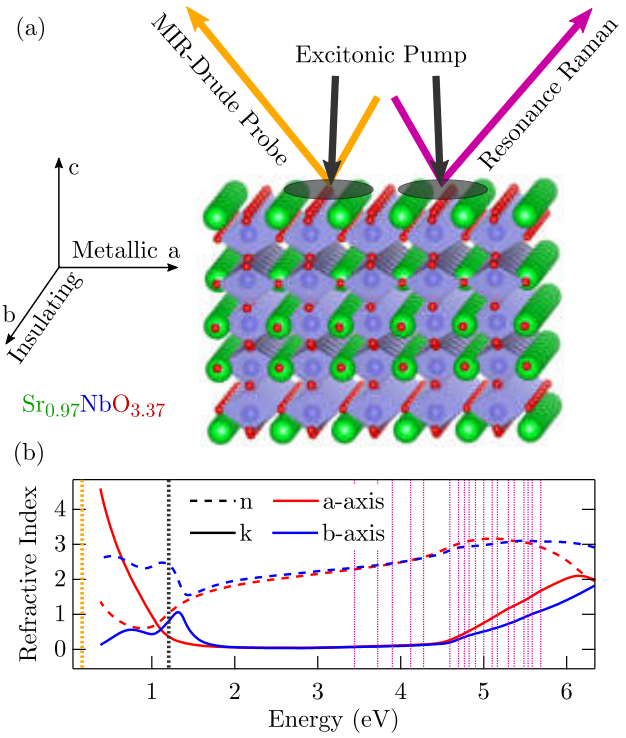

FIG. 1. (a) Crystal structure of n=5 type $Sr_{0.95}NbO_{3.37}$. Along the c-axis, networks of NbO_6 octahedra are periodically grouped into 5-octahedra-thick slabs, while along the a- and b-axis the Nb–O–Nb linkages are chain-like and zig-zag-like, respectively. (b) Refractive index n and extinction coefficient k of $Sr_{0.95}NbO_{3.37}$ [18]. The extinction coefficient k shows a strong Drude response at low energies for the a-axis, showing its metallic character. The energies of the MIR-Drude probe, excitonic pump and Raman probe beams are marked with yellow, grey and pink lines, respectively.

of the in-plane crystallographic axis. Under illumination with the pump beam, the reflectance signal changes within several seconds. At 0° the steady state reflectance is strongly suppressed. When the probe is rotated from 0°, where the crystallographic a-axis and the E-field of the pump beam are parallel, to an angle of 90°, where they are orthogonal, the difference in reflectance changes from a negative effect at 0°, to an enhancement of the reflectance at 90°. The antisymmetric behavior of the steady state reflectance and the transient change of the reflectance with the angle of the probe beam with respect to the crystal axis are summarized in Fig. 2 (b). When the beam polarization changes from the metallic a-axis to the insulating b-axis, the steady state reflectance decreases by a factor of 5 and the transient of the reflectance changes its sign. The transient reflectance changes sign upon rotation of the sample relative to the pump beam, due to optical transition depending on the orientation of the electric field. The time scales associated with the switching of the MIR reflectance suggests a structural involvement of the oxygen chains responsible for the metal-

lic state.

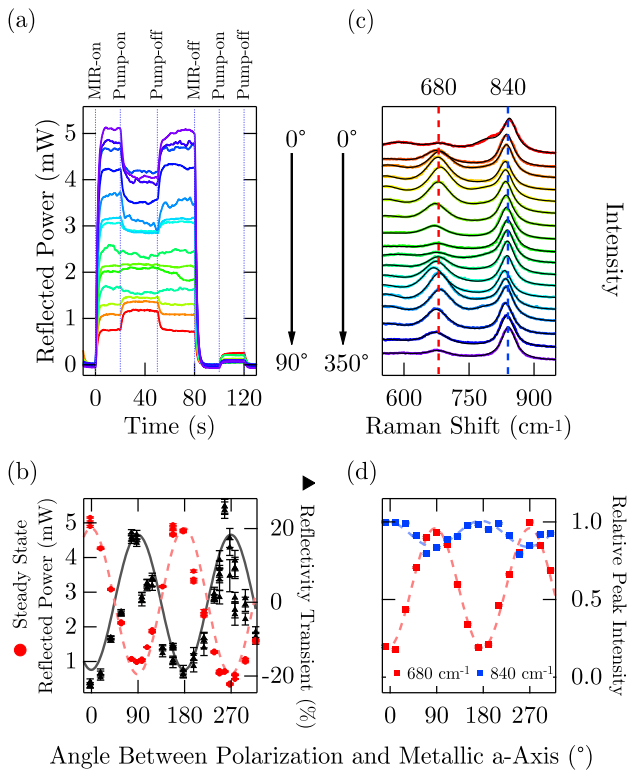

FIG. 2. Transient MIR-reflectance measurements and angle dependence of the UV resonance Raman spectra taken at room temperature. (a) Absolute power during a pump-probe cycle for different polarization angles relative to the metallic a-axis of the crystal. The residual power when the pump is on is a stray light effect caused by the pump beam. (b) Reflectance of the unpumped system and the reflectance change upon pumping as a function of the angle between the MIR-polarization and metallic a-axis fitted with a sinusoidal function. (c) Raman spectra of $Sr_{0.95}NbO_{3.37}$ at 260 nm with different angles between the metallic a-axis and the beam polarization. Note that the frequency analysis is shown in the SI. (d) Relative peak intensity changes as a function of the polarization of the incident beam and the metallic a-axis for the 640 cm^{-1} and 840 cm^{-1} modes, respectively.

To investigate the possible involvement of the oxygen chains, we used transient UV-resonance Raman scattering with a probe beam at 260 nm (4.8 eV), which is the onset wavelength of the charge-transfer band in $Sr_{0.95}NbO_{3.37}$, as visible in Fig. 1 (b) being highly sensitive to the oxygen chain related phonon modes. Fig. 2 (c) shows the angular dependence of the steady state Raman spectra. The dominant modes are located at 840 cm^{-1} and 680 cm^{-1}. Fig. 2 (c) shows the phonon at 680 cm^{-1} vanishing for light polarization along the metallic a-axis and peaking in intensity for light polarization along the insulating b-direction. This sinusoidal behavior of the phonon mode intensity is summarized in Fig. 2 (d) and it corresponds well with the modulation of the steady state MIR reflectance. It is worthwhile to remark that the phonon mode intensity at 840 cm^{-1} only weakly modulates as a function of angle with a phase shift of 90°. In order to understand the angular dependence of the Raman data, we calculated the phonon dispersion in the stoichiometric variant $SrNbO_{3.4}$ (=$Sr_5Nb_5O_{17}$) [23], which is shown in Fig. 3 (a). Visualizations of the identified relevant phonon modes are shown in Fig. 3 (b-d). The phonon at 680 cm^{-1} can be assigned to the chains of NbO_6-octahedra in the center of the 5 NbO_6 octahedra thick layers, whereas the phonon at 840 cm^{-1} is associated to vibrations in the outer region of the layers. The Nb ions in the center of the layers are also mainly responsible for the conductivity along the metallic a-axis [24]. Thus, we have established a link between the switching effect and the oxygen-chain phonon modes in the Raman spectra by comparing the respective angle-dependencies. The phonon analysis shows that the common denominator for both these effects are the oxygen-related chain modes allowing us to investigate the structural changes of oxygen-chains upon d-d excitonic pumping by transient UV resonance Raman spectroscopy.

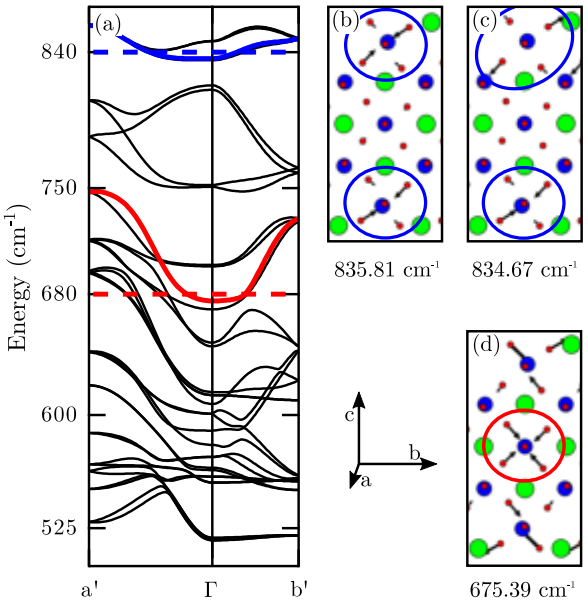

FIG. 3. Simulation of the phonon dispersion in $SrNbO_{3.4}$ (a) Phonon dispersion for the investigated Raman active modes at 680 cm^{-1} and 840 cm^{-1} highlighted in red and blue, respectively. (b-d) Visualization of the relevant oxygen related vibrations.

However, both, electronic and structural and degrees of freedom are highly anisotropic and therefore, a possible Raman matrix element effect, explaining the observed angular dependencies in the main Raman modes has to be addressed. In order to reveal the relevant electronic transitions, involved in the Raman matrix element, we performed a detailed resonance Raman study

in the energy range covering the charge-transfer transition. The resonance study is shown in Fig. 4 (a-b). The phonon mode intensities are evaluated in Fig. 4 (c,d) together with the changes in the imaginary part of the refractive index for the metallic a- and insulating b-direction. It is clearly visible, that the peak at 680 cm^{-1} is strongly resonantly enhanced by a single electronic transition at 4.6 eV along the b-direction, whereas the peak at 840 cm^{-1} shows multiple resonances along both, the a- and b-axis. The resonance energy of the phonon at 680 cm^{-1} coincides with the sharp onset of the charge-transfer transition visible in Fig. 1 (b) and Fig. 4 (d). The many-fold of different transition-metal to oxygen transitions in $Sr_{0.95}NbO_{3.37}$ would naturally lead to multiple resonances in the charge transfer enhanced Raman matrix element. The observation of a single distinct angle dependent resonance at 4.6 eV of the 680 cm^{-1} phonon mode intensity further supports its exclusive assignment to the oxygen chains.

To study the influence of the excitonic switching mechanisms on the phonons in $Sr_{0.95}NbO_{3.37}$, we have performed transient UV resonance Raman measurements. The modification of the Raman spectra upon excitation of the sample with the 1030 nm pump beam can be seen in Fig. 4 (e) for the insulating direction. In fact, there is an immanent change of the intensity of the mode at 680 cm^{-1}, whereas the mode at 840 cm^{-1} stays unaffected. Upon pumping with 93 mW the spectra start to resemble the transient spectra along the metallic direction, indicating, similar to the reflectance, that the system becomes more isotropic in the pumped state. For an increase in pump power, the 680 cm^{-1} phonon vanishes and is completely quenched. Thus, these results, together with the transient MIR-reflectance data, indicate that upon pumping, the electronic configuration is strongly modified. It should be noted that the effect of other excitations, such as polarons, is ruled out, because a change of the charges associated with a polaronic excitation would lead to a substantial change in the Raman signal [25], that we do not observe. The charge anisotropy induced by the chains in $Sr_{0.95}NbO_{3.37}$ activates the strongly polarized Raman response along the chains and perpendicular to them. This effect gets diminished upon pumping as evidenced by the reduction of the Raman mode at 680 cm^{-1} related to the central chains of NbO_6 octahedra.

In order to reveal the detailed mechanism behind this combined effect, covering the changes in the MIR Drude response and the charge-transfer associated Raman modes, we performed a band structure calculation of the stoichiometric variant $SrNbO_{3.4}$. We have studied in detail the density of states associated with O_{2p} and Nb_{4d} orbitals in the different chains. Based on the fact, that the transient Raman spectrum shows the largest difference in the central chain 680 cm^{-1} Raman mode, we analyzed the density of states of the involved atoms. We identify that the oxygen atoms at the tip of the NbO_6 octahedra have a peak in the density of states along

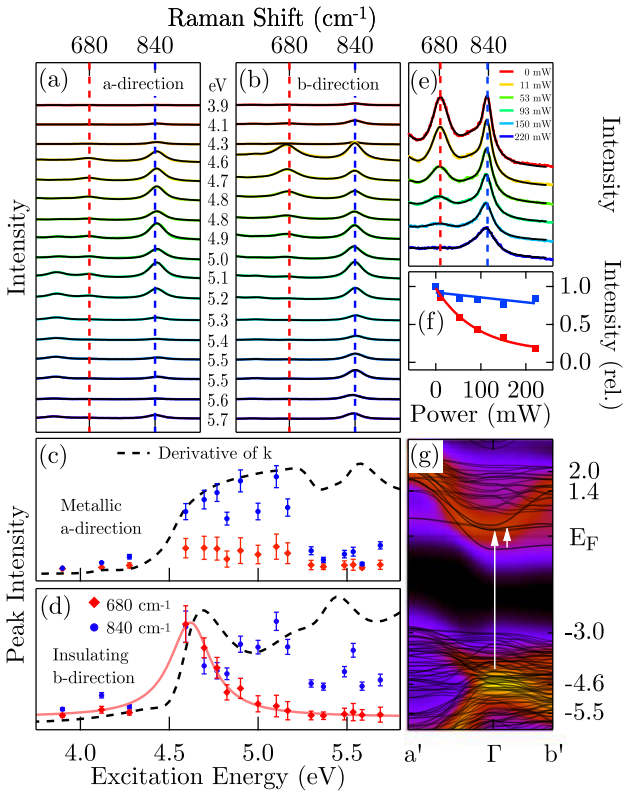

FIG. 4. Resonant and transient Raman spectroscopy taken at room temperature and band structure calculation. Raman spectrum of $Sr_{0.95}NbO_{3.37}$ at different incident photon energies with polarization along the (a) metallic and (b) insulating axis. (c,d) Fit of the relevant peak intensities as a function of the incident photon energy. Dashed lines show the derivative of k for the (c) metallic and (d) insulating direction. For k itself, see Fig. 1 (b). (e) Transient Raman spectroscopy data (reprinted from Ref. [18]) with the pump beam parallel to the b-axis (90°) and (f) fit of the corresponding peak intensities. (g) Band structure calculation of the electronic levels for resonance Raman scattering of $SrNbO_{3.4}$ with the color-coded density of states of O_{2p} and Nb_{4d}-orbitals in the central oxygen chain. White arrows indicate the electronic transitions for the Raman resonance and the excitonic pump.

the insulating b-direction. The joined density of state of O_{2p} and Nb_{4d} together with the band structure is shown in Fig. 4 (g). The white arrows indicate the pump and the probe energies. Pumping the d-d excitons at 1.1 eV (short white arrow) populates states directly above the Fermi energy and simultaneously quenches the Raman matrix element associated to the charge transfer transition in the oxygen chains. The lowest Nb_{4d} band, which crosses the Fermi energy, being responsible for the unpumped conductivity along the a-direction, is depopulated. Simultaneously, the band directly above the Fermi energy is populated. However, this level is required for the strong resonance enhancement of the charge-transfer related central oxygen chain mode at 680 cm^{-1}. This

leads to the conclusion, that the pumping of the d-d exciton, results in both, the induced MIT and the selective quenching of the central Raman chain mode.

IV. CONCLUSION

In conclusion we have investigated the influence of the interplay of the lattice and electronic degrees of freedom related to the excitonic switching mechanism in $Sr_{0.95}NbO_{3.37}$. The reduction of charge carrier density upon pumping occurs concomitantly with the quenching of the central chain related mode at $680\,cm^{-1}$, which is completely suppressed upon excitonic pumping. We show by a combination of MIR-pump reflectance- and Raman-probe as well as by DFT calculations that the underlying quenching mechanism is electronically driven and related to the photo-induced bleaching of the charge-transfer transition. We reveal that transient UV-resonance Raman spectroscopy is a highly selective tool to study the functional elements of complex transition metal oxides such as the metallic chains in e.g. $Sr_{0.95}NbO_{3.37}$.

ACKNOWLEDGMENTS

We thank the German Research Foundation and the Federal Ministry of Education and Research (Germany) for funding via DFG-RU 773/8-1 and BMBF-05K19GU5, respectively. F. L. thanks Nicola Spaldin for her support. The melt-grown crystalline $Sr_{0.95}NbO_{3.37}$ samples were prepared at the University of Augsburg and F. L. thanks German Hammerl, Alexander Herrnberger, Thilo Kopp, Jochen Mannhart, and Klaus Wiedenmann for their support. The authors thank Prof. Dr. Christine Kuntscher for access to raw data from the previous Phys. Rev. Lett. paper by Kuntscher et al.[26] on $SrNbO_{3.41}$ for comparison to theoretical data.

[1] K. Isawa, J. Sugiyama, K. Matsuura, A. Nozaki, and H. Yamauchi, Physical Review B **47**, 2849 (1993).
[2] D. J. Scalapino, Physics Reports **250**, 329 (1995).
[3] D. Fausti, R. Tobey, N. Dean, S. Kaiser, A. Dienst, M. C. Hoffmann, S. Pyon, T. Takayama, H. Takagi, and A. Cavalleri, Science **331**, 189 (2011).
[4] A. Ramirez, Journal of Physics: Condensed Matter **9**, 8171 (1997).
[5] E. Collet, M.-H. Lemée-Cailleau, M. Buron-Le Cointe, H. Cailleau, M. Wulff, T. Luty, S.-Y. Koshihara, M. Meyer, L. Toupet, P. Rabiller, *et al.*, Science **300**, 612 (2003).
[6] A. Rusydi, R. Rauer, G. Neuber, M. Bastjan, I. Mahns, S. Müller, P. Saichu, B. Schulz, S. Singer, A. Lichtenstein, *et al.*, Physical Review B **78**, 125110 (2008).
[7] R. H. McKenzie, Science **278**, 820 (1997).
[8] M. Rini, N. Dean, J. Itatani, Y. Tomioka, Y. Tokura, R. W. Schoenlein, A. Cavalleri, *et al.*, Nature **449**, 72 (2007).
[9] M. Först, A. Caviglia, R. Scherwitzl, R. Mankowsky, P. Zubko, V. Khanna, H. Bromberger, S. Wilkins, Y.-D. Chuang, W. Lee, *et al.*, Nature materials **14**, 883 (2015).
[10] S. Bahrs, S. Müller, M. Rübhausen, B. Schulz, A. Goni, G. Nieva, and C. Thomsen, Physical Review B **74**, 024519 (2006).
[11] D. Budelmann, J. Holmlund, J. Andreasson, H. Rodríguez, J. Bäckström, L. Börjesson, H. Adrian, U. Merkt, and M. Rübhausen, Physical Review B **67**, 140507 (2003).
[12] A. Rusydi, W. Ku, B. Schulz, R. Rauer, I. Mahns, D. Qi, X. Gao, A. Wee, P. Abbamonte, H. Eisaki, *et al.*, Physical review letters **105**, 026402 (2010).
[13] D. Mihailovic, K. McCarty, and D. Ginley, Physical Review B **47**, 8910 (1993).
[14] F. Lichtenberg, A. Herrnberger, K. Wiedenmann, and J. Mannhart, Progress in Solid State Chemistry **29**, 1 (2001).
[15] F. Lichtenberg, A. Herrnberger, and K. Wiedenmann, Progress in Solid State Chemistry **36**, 253 (2008).
[16] F. Lichtenberg, ETH Research Collection 10.3929/ethz-b-000424221 (2020).
[17] J. O. Island, A. J. Molina-Mendoza, M. Barawi, R. Biele, E. Flores, J. M. Clamagirand, J. R. Ares, C. Sánchez, H. S. Van Der Zant, R. D'Agosta, *et al.*, 2D Materials **4**, 022003 (2017).
[18] T. C. Asmara, F. Lichtenberg, F. Biebl, T. Zhu, P. K. Das, M. A. Naradipa, A. D. Fauzi, C. Diao, P. Yang, P. Lenzen, *et al.*, Communications Physics **3**, 1 (2020).
[19] B. Schulz, J. Bäckström, D. Budelmann, R. Maeser, M. Rübhausen, M. Klein, E. Schoeffel, A. Mihill, and S. Yoon, Review of scientific instruments **76**, 097203 (2005).
[20] R. Saichu, I. Mahns, A. Goos, S. Binder, P. May, S. Singer, B. Schulz, A. Rusydi, J. Unterhinninghofen, D. Manske, *et al.*, Physical review letters **102**, 177004 (2009).
[21] P. Giannozzi, O. Baseggio, P. Bonfà, D. Brunato, R. Car, I. Carnimeo, C. Cavazzoni, S. De Gironcoli, P. Delugas, F. Ferrari Ruffino, *et al.*, The Journal of chemical physics **152**, 154105 (2020).
[22] A. Togo and I. Tanaka, Scripta Materialia **108**, 1 (2015).
[23] S. Abrahams, H. Schmalle, T. Williams, A. Reller, F. Lichtenberg, D. Widmer, J. Bednorz, R. Spreiter, C. Bosshard, and P. Günter, Acta Crystallographica Section B: Structural Science **54**, 399 (1998).
[24] C. A. Kuntscher, S. Schuppler, P. Haas, B. Gorshunov, M. Dressel, M. Grioni, and F. Lichtenberg, Physical Review B **70**, 245123 (2004).
[25] P. Björnsson, M. Rübhausen, J. Bäckström, M. Käll, S. Eriksson, J. Eriksen, and L. Börjesson, Physical Review B **61**, 1193 (2000).
[26] C. A. Kuntscher, S. Schuppler, P. Haas, B. Gorshunov, M. Dressel, M. Grioni, F. Lichtenberg, A. Herrnberger, F. Mayr, and J. Mannhart, Physical review letters **89**, 236403 (2002).

5.3 Optically Induced Avoided Crossing in Graphene

The author has contributed to the Raman measurements and the respective data analysis.

Introduction

In [5.3], the femtosecond MIR-pump and Raman-probe setup was used as introduced and explained in section 3.1.4. The DFG was tuned to produce MIR light as a pump in the range of 6-6.5 µm with a pulsewidth of 500 fs, while 515 nm light was used with a pulsewidth of 5 ps as an optical probe. With this experimental setup, graphene samples with different layers were investigated by changing the MIR frequency, the delay between pump and probe pulse and the MIR fluence. Monolayer graphene exhibits the prominent G-phonon at 1580 cm^{-1} (196 meV). It is a non-polar Raman-active E_{2g} vibration. In order to fully describe the crystal, the unit cell in bi- and multilayer systems has to be extended from two to four atoms, which is refered to as Davydov splitting.[136–138] Therefore, when going from one to two layers, the AB-stacking of bi- and multilayer graphene causes a second polar IR-active vibration of E_{1u} symmetry to exist. The two basic vibrations are depicted as insets in [5.3]-Fig. 2 (a). Since graphene systems only contain carbon atoms with one distinct atom-atom distance in-plane, these two vibrational modes are degenerate at the same energy.[139, 140] As depicted in [5.3]-Fig. 1 (a), IR- and Raman-active modes are not expected to mix due to their orthogonality, even when they oscillate at the same frequency. As shown in [5.3]-Fig. 1 (b), a strongly driven IR-active mode can lead to a lifting of the degeneracy Δ and by that to two unique composite vibrational states $\beta^+ + \beta^-$ and $\beta^+ - \beta^-$ that each consist of the optically coupled harmonic oscillators β^+ and β^-. Note that the resonance condition of the MIR pump pulse at 196 meV leads to a substantial excitation of the E_{1u} mode. The magnitude of the lifting is proportional to the applied field E, i.e. the fluence of the MIR laser. The IR and Raman modes of the novel vibronic state oscillate at the previously degenerate eigenfrequency ω_0, which is modulated by a field-dependent subharmonic frequency $\omega_\pm = \omega_0^2 \pm \Delta$. Additionally, the oscillations are damped by a modified damping $\gamma_\pm = \gamma_0 \pm \delta/\omega$.

Results

The experiment is outlined in [5.3]-Fig. 2 (a). The MIR pulse excites the graphene sample which is probed by the 515 nm Raman pulse. The unpumped and pumped configurations show a strong transient signal, as depicted in [5.3]-Fig. 2 (b) for the bi- and multilayer sample. The panel shows data with the MIR in resonance with the E_{1u} mode and at zero delay. All other signals are shown as transient signals by subtracting the unpumped from the pumped signal. Monolayer graphene shows no transient signal since its symmetry representation does not allow for the polar E_{1u} mode. [5.3]-Fig. 2 (c) and (d) show the transient signals for the resonance tuning at constant delay and the delay measurements at constant pump frequency, respectively. Most notably in [5.3]-Fig. 2 (c), the sharp resonance bandwith comprises of only a few meV, which underlines that the resonance is of phononic nature and not related to electronics. The lifetime of the excited state in [5.3]-Fig. 2 (d) is very long with a duration of several picoseconds.

We have developed a model for the data that uses the modified propagators $\beta^+ = X_{IR} + X_R$ and $\beta^- = X_{IR} - X_R$ to link the IR- and Raman-active phonons. In the limit of weak coupling with the coupling constant α, the equation of motions for the the IR-active phonon X_{IR} and the Raman-active phonon X_R are given in [5.3]-Eq. (1a,b). Adding und subtracting each equation links the two coordinates together

and allows one to express the modified propagators $\beta^{\pm}$ as given in [5.3]-Eq. (2a,b). As explained in section 2.1, the intensity can be calculated with the inverse Fourier transform of the respective propagator and leads to [5.3]-Eq. (3a,b) for the scattering intensity of the Raman probe. Note that the difference between the two propagators $\beta^{\pm}$ scales with the anharmonic coupling constant α and the electric field of the driving laser pulse. For the case of no interaction $\alpha \rightarrow 0$, we find $\omega_+ = \omega_- = \omega_0$, i.e. $\Delta \rightarrow 0$ and $\gamma_+ = \gamma_- = \gamma_0$, i.e. $\delta \rightarrow 0$. This would lead to a remaining unpumed and equilibrium Raman susceptibility, but no *transient* Raman susceptibilty as we find under MIR pumping conditions.

The results and the comparison of the resonance study are depicted in [5.3]-Fig. 3, showing that the simulation reproduces the data well. The data show the transient signal peaking at the IR mode resonance in [5.3]-Fig. 3 (c), the shifting frequency in [5.3]-Fig. 3 (d) and the decreasing width in [5.3]-Fig. 3 (e). The results and the comparison of the delay study are depicted in [5.3]-Fig. 4, showing that the simulation also reproduces the delay data well in [5.3]-Fig. 4 (c) and (d). For the simulation of the delay data, a dephasing between the IR- and Raman-active data was assumed, which itself leads to an increase of the ration of Δ and δ. Deviations, such as the anti-resonances at the flanks in the simulation in [5.3]-Fig. 3 (b) and [5.3]-Fig. 4 (b) and the different scale of magnitude of the change in width in [5.3]-Fig. 3 (e) and [5.3]-Fig. 4 (d) are attributed to neglected higher-order terms and electron-phonon interactions,[141] respectively. The fluence study is shown in [5.3]-Fig. 5. The model correctly predicts the relative increase and abscence of frequency shifts, as can be seen in [5.3]-Fig. 5 (a) and (b). The magnitude of lifting of the degeneracy Δ and the subharmonic frequency scales with the driving MIR field intensity, as shown in [5.3]-Fig. 5 (c). Exemplary calculations based on the DFT results for β^+ and β^- at 60 meV cm^{-2} are shown in [5.3]-Fig. 5 (d). Combining the energetic contribution from each $\beta^{\pm}$-mode is shown exemplary for 24 and 60 meV cm^{-2} in [5.3]-Fig. 5 (e) at the upper and lower panel, respectively. In this excited non-equilibrium state, the state of zero energy occurs periodically with a frequency defined by the fluence of driving MIR laser field.

Optically Induced Avoided Crossing in Graphene

Currently under submission at Nature Physics.

Springer Nature 2021 LaTeX template

Optically Induced Avoided Crossing in Graphene

Sören Buchenau[1*], Janika Reichstetter[2], Benjamin Grimm-Lebsanft[1], Florian Biebl[1], Michael Fechner[4], Sonja Herres-Pawlis[3], Dirk Manske[2], Andrea Cavalleri[4] and Michael Rübhausen[1*]

[1*]Institute of Nanostructure and Solid State Physics, University Hamburg, Notkestraße 85, Hamburg, 22607, Hamburg, Germany.
[2]Quantum Many-Body Theory, Max Max Planck Institute for Solid State Research, Heisenbergstraße 1, Stuttgart, 70569, Baden-Württemberg, Germany.
[3]Bioinorganic Chemistry, RWTH Aachen University, Landoltweg 1a, Aachen, 52074, Nordrhein-Westfalen, Germany.
[4]Condensed Matter Department, Max Planck Institute for the Structure and Dynamics of Matter, Luruper Chaussee 149, Hamburg, 22761, Hamburg, Germany.

*Corresponding author(s). E-mail(s): sbuchena@physnet.uni-hamburg.de; mruebhau@physnet.uni-hamburg.de;

Abstract

In recent years, the quasi-relativistic electronic properties of graphene materials made them model compounds for novel states of matter. With more than one layer these 2D materials also display peculiar phononic properties through degenerate IR- and Raman-active phonon modes. We show that driving the IR mode by applying intense mid-IR pulses creates two unique non-degenerate coupled vibronic states, observable by transient spontaneous Raman measurements. The non-equilibrium response shows two hybridized states of Raman and IR phonons representing an optically induced avoided crossing. Most notably, we find strongly enhanced lifetimes of the optically controlled states compared to the equilibrium, revealing an increased robustness. The population of the two hybridized and orthogonal states shows subharmonic oscillations with a frequency proportional to the optically induced degeneracy breaking. We discuss the nature of this new state of matter exhibiting a discrete time translational symmetry.

Keywords: Pump-Probe, Raman, Simulation

1 Introduction

Graphene is well known for its unconventional electronic properties such as the quasi-relativistic linear dispersion and unconventional superconductivity in magic-angle superlattices.[1–4] It has attracted an unprecedented attention as a Dirac material and is a key candidate for carbon based electronics.[5, 6] However, hardly any work has been done to exploit the peculiar properties of graphene with respect to its coupled *intrinsic* degenerate vibronic states.

Monolayer graphene exhibits the prominent G-phonon that is Raman-active and has been studied intensively.[7] On the other hand, from two to multilayer graphene, the material exhibits nearly fully

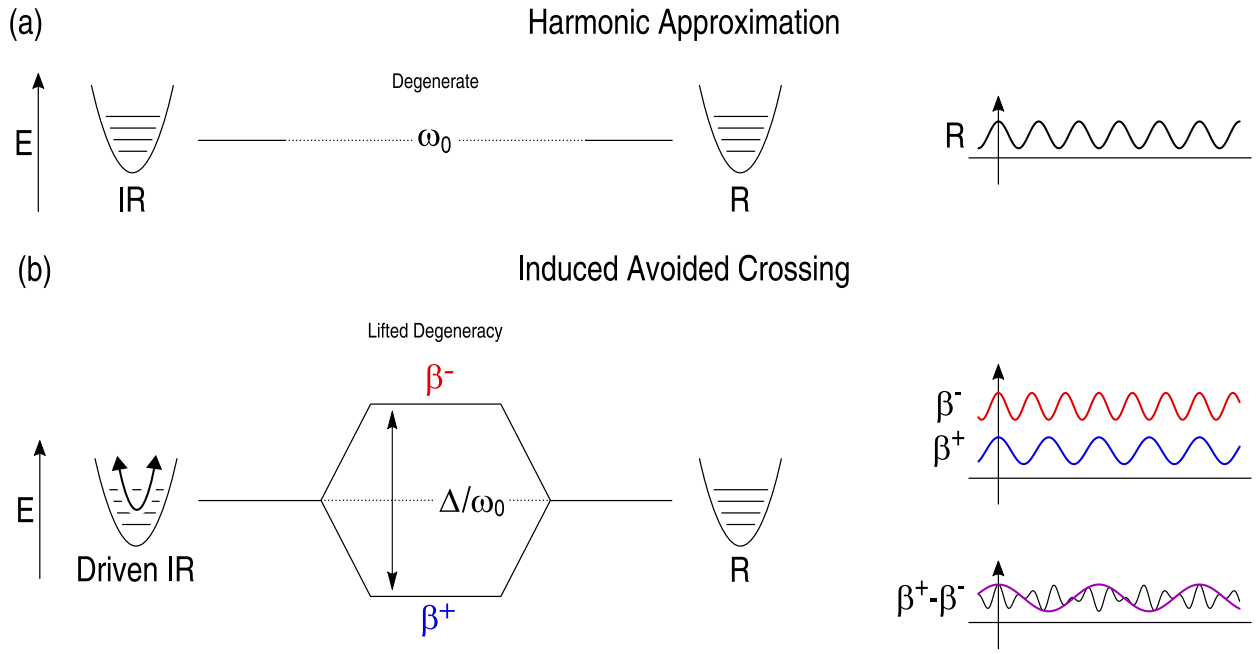

Fig. 1 Lifting of the degeneracy and resulting subharmonic frequencies. (a) In equilibrium the two degenerate, but orthogonal modes do not mix and oscillate at their common frequency ω_0. (b) For a strong driving of the IR mode, the two modes couple anharmonically and the vibrational modes mix with the common coordinates β^+ and β^-. They are shifted in frequency by $\pm\Delta/2\omega_0$ each, representing the lifted degeneracy in the optically driven state. The transient Raman active vibration $\beta^+ - \beta^-$ is only present in the symmetry broken state and exhibits a subharmonic frequency tunable by the magnitude of the electric field dependent splitting Δ.

degenerate IR- and Raman-active phonons with orthogonal E_{1u} and E_{2g} symmetry.[8, 9] These modes are ideal candidates for strong anharmonic coupling due to their strongly related eigenvectors and degenerate energies. Fig. 1 illustrates the unique properties of degenerate versus non-degenerate *orthogonal* vibrational states in optically controlled multilayer graphene. Fig. 1(a) shows the conventional situation of non or weakly coupled harmonic IR- and Raman-active oscillators at the same eigenfrequencies. Since both vibrations are in orthogonal states they do not couple in equilibrium. In the optically driven state with strong anharmonic coupling,[10] as shown in Fig. 1(b), it is possible to lift the degeneracy of the vibrational states by driving the IR-active mode with a laser field. This optically induced lifting of the degeneracy generates two new vibrational states of matter that can be expressed by a superposition of the energy-shifted states β^+ and β^-, representing the optically coupled harmonic oscillators. From those, the IR- and Raman-active modes can be obtained by $\beta^+ + \beta^-$ and $\beta^+ - \beta^-$, respectively. Hence the transient Raman signal vanishes in the degenerate state, i.e. $\beta^+ = \beta^-$.

If one considers a relative shift of the respective eigenvalues in the limit of small Rabi frequencies, the energy-shifted values β^- and β^+ can be expressed by $\omega_\pm \approx \omega_0(1 \pm \Delta/2\omega_0^2)$, with ω_0 as the degenerate frequency of the phonons in the equilibrium state and Δ lifting of the degeneracy. Thus, the orthogonal harmonic motions of the IR- and Raman-active vibrations are $\sim e^{i\omega_0 t}\sin(\Delta \cdot t/2\omega_0)$ and $\sim e^{i\omega_0 t}\cos(\Delta \cdot t/2\omega_0)$, respectively. Accordingly, the IR and Raman coordinates vibrate with the original degenerate eigenfrequency ω_0, modulated by a subharmonic frequency and are phase-shifted by $\pi/2$. In conventional, static quantum systems the emergence of lowered eigenvalues are a consequence of the avoided crossing,[11, 12] leading to enhanced stability of e.g. a molecular system in the bonded state. In a optically driven non-equilibrium system, the strength of the lifting of the degeneracy Δ depends on the strength of the electric field. Consequently, the populations of the lower and higher energy state show an oscillation in time and by this breaking the continuous translation in time. The ideal observation of these states is transient spontaneous Raman scattering of a Raman-active

phonon that is driven by an IR-active degenerate phonon, yielding only a finite response in the limit of the optically driven avoided crossing, i.e. for $\beta^+ \neq \beta^-$.

2 Results

The general outline of the experiment is shown in Fig. 2(a). A tunable mid-IR pulse drives the E_{1u} IR phonon mode in resonance at 196 meV. At a given time delay, the Raman-active E_{2g} mode is probed by transient spontaneous Raman scattering. In multilayer graphene, the AB-stacking order causes the atoms to experience different fields and the unit cell of the system has to be extended from two to four atoms. This Davydov splitting [13] leads to the existence of the additional polar IR mode with E_{1u} symmetry.[8, 9] Both vibrations move in-plane and because the material is monoatomic, the respective frequencies of each of the modes are degenerate.

With the presence of the polar IR-active phonon, bi- and multilayer systems show a strong transient response in the excited state, as shown in Fig. 2(b). The corresponding transients are then calculated by subtracting the unpumped signal from the pumped signal, yielding the sole response of the IR driven Raman mode. Note, that monolayer graphene exhibits only a non-polar vibrational mode[7] and accordingly no transient response is visible. In multilayer graphene, the spontaneous Raman signal in the pumped state is enhanced on the Stokes and Anti-Stokes side. In the following we show the transient spontaneous Raman data on the Anti-Strokes side with the expected stronger transient. The transient Anti-Stokes Raman response as function of the energy of the mid-IR pump is shown in Fig. 2(c). The first apparent observation is the ultra-sharp resonance with a width of less than 5 meV peaking at 196 meV. This, together with the absence of a transient Raman response in monolayer graphene, highlights the direct coupling of the transient Raman E_{2g} phonon to the IR-active E_{1u} phonon. We also note the changes in shape of the transient Anti-Stokes Raman response as the energy of the mid-IR pump is changed and detuned from the energy of the E_{1u} phonon. Fig. 2(d) displays the change of the transient Raman response driven at the resonance energy of 196 meV as a function of delay between pump and probe pulses. The transient is visible for several picoseconds. This is remarkable, since in the static limit the widths of the phonons correspond to a lifetime of about 200 fs. The observation of the transient Raman response on the time scale of several picoseconds implies an increased robustness of the non-equilibrium coupled driven state compared to the equilibrium. This is further supported by the fact that the transient Raman response is substantially sharper as compared to its static spontaneous Raman response.

The incident mid-IR pump photon drives the E_{1u} phonon, which alters the response of the Raman signal of the E_{2g} phonon. The degeneracy of the two phonons leads to strong anharmonic coupling.[10, 14] Without the pump interaction, the Raman response is given by the Raman susceptibility, yielding a typical lorentzian lineshape. The anharmonic coupling α between a Raman- and IR-active phonon requires a quadratic coupling to the Raman-active phonon. This leads to a set of equation of motions describing the electric field driven IR-active phonon $X_{\mathrm{IR}}(t)$ and Raman-active phonon $X_{\mathrm{R}}(t)$

$$\widetilde{D}(\omega_0,\gamma_0)X_{\mathrm{IR}}(t) = \alpha X_{\mathrm{R}}(t)X_{\mathrm{IR}}(t) + F_{\mathrm{L}}(t) \quad (1a)$$

$$\widetilde{D}(\omega_0,\gamma_0)X_{\mathrm{R}}(t) = \alpha X_{\mathrm{IR}}^2(t). \quad (1b)$$

Here, $\widetilde{D}(\omega_0,\gamma_0) = \partial_t^2 + \gamma_0\partial_t + \omega_0^2$ is the operator describing a damped harmonic oscillator and $F_{\mathrm{L}}(t)$ represents the gaussian laser beam with frequency ω_{L} and width σ. Assuming that IR- and Raman-active phonons are degenerate, the above set of coupled nonlinear differential equations can be solved analytically in the weak coupling limit. For this procedure one adds and subtracts both equations from each other and introduces common coordinates, linking the coordinates of the IR- and Raman-active phonons by $\beta^+ = X_{\mathrm{IR}} + X_{\mathrm{R}}$ and $\beta^- = X_{\mathrm{IR}} - X_{\mathrm{R}}$. The inverse Fourier transformation of $\beta^\pm$ then yields the expressions for these effective phonon propagators, after applying the convolution theorem for the quadratic parts of the equation

$$\beta^+(\omega) = \frac{\alpha\left[(\beta^- * \beta^+)(\omega)\right] + 2F_{\mathrm{L}}(\omega)}{2(\omega_-^2 - \omega^2 + i\gamma_-\omega)} \quad (2a)$$

$$\beta^-(\omega) = \frac{-\alpha\left[(\beta^+ * \beta^-)(\omega)\right] + 2F_{\mathrm{L}}(\omega)}{2(\omega_+^2 - \omega^2 + i\gamma_+\omega)}, \quad (2b)$$

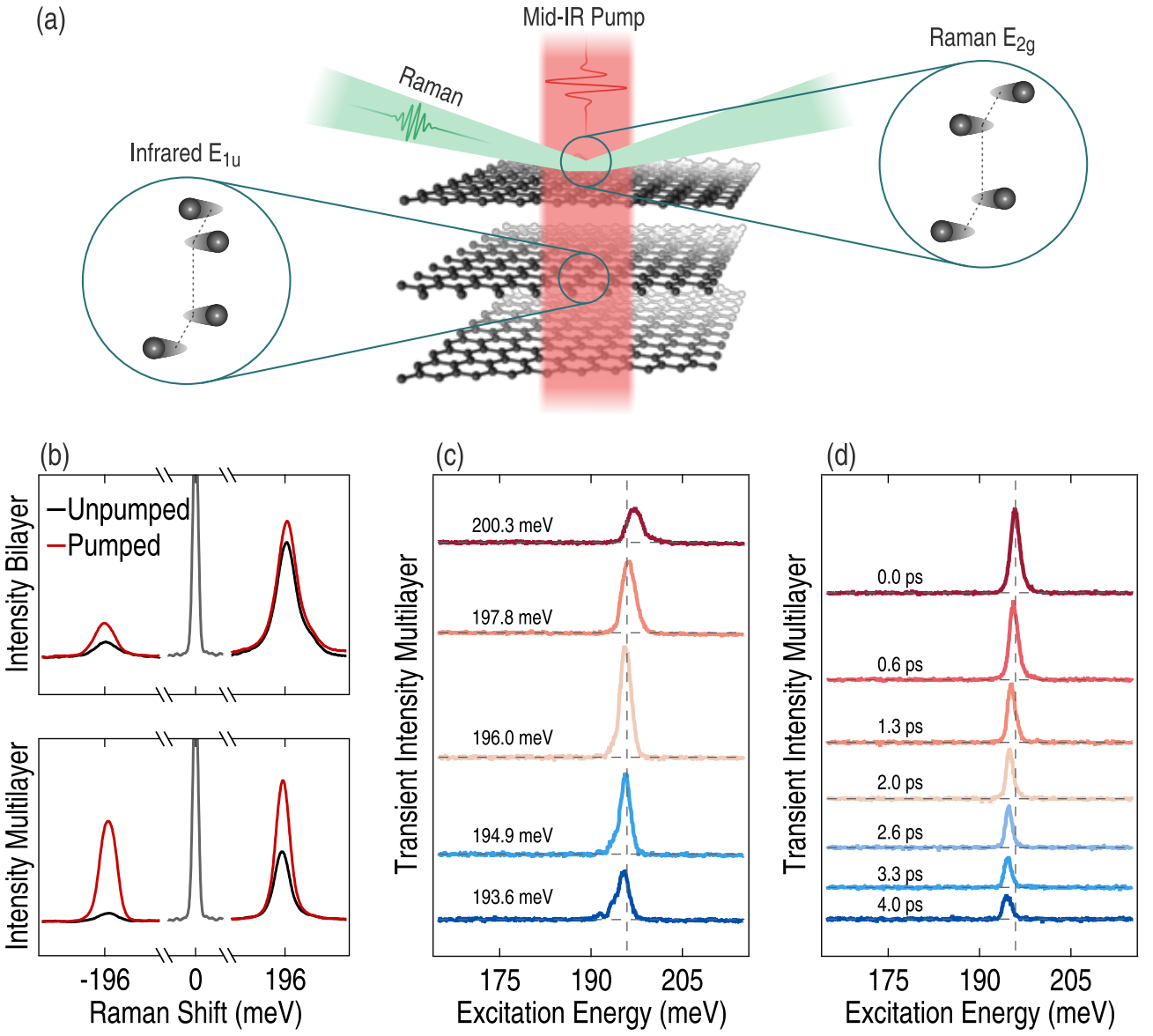

Fig. 2 Outline of the transient spontaneous Anti-Stokes and Stokes Raman scattering experiment. (a) A mid-IR pump pulse excites the IR vibration in the sample, which is probed by a Raman pulse. The delay, pump energy, and fluence are controlled. (b) Resonant mid-IR pumping causes a strong enhancement of the signal in bi- and multilayer graphene. (c) Selective driving of the E_{1u} vibration by tuning the pump energy through the sharp resonance. (d) Lifetime of the vibronic state as observed by changing the delay between the driving mid-IR pump and the Raman probe beam. Horizontal grey dashed lines indicate the zero line for each spectrum and vertical ones the energy of the unpumped IR phonon.

with the shifted eigenfrequencies $\omega_\pm^2 = \omega_0^2 \pm \Delta$ and modified damping constants $\gamma_\pm = \gamma_0 \pm \delta/\omega$. These changes scale with the anharmonic coupling constant α and the square of the electric field E_0^2. The contribution from the non-mixed convolution integrals $(\beta^+ * \beta^+)(\omega)$ and $(\beta^- * \beta^-)(\omega)$ vanishes and they are omitted in equation (2a) and (2b). The mixed terms $(\beta^- * \beta^+)(\omega)$ have to be evaluated self-consistently. The leading order contribution results in the modified propagators with the driving pump laser in the numerators, shown in equation (2a) and (2b). The Green's function of the Raman-active vibration can now be calculated by $X_\mathrm{R}(\omega) = \frac{1}{2}(\beta^+ - \beta^-)$ and the Raman scattering intensity is given by $-\mathrm{Im}[X_\mathrm{R}(\omega)]$

$$I(\omega) = \frac{F_\mathrm{L}(\omega)\Delta\omega(\gamma_+(\omega_-^2-\omega^2)+\gamma_-(\omega_+^2-\omega^2))}{\mathcal{D}} + \frac{F_\mathrm{L}(\omega)\delta\omega(\gamma_-\gamma_+\omega^2-(\omega_-^2-\omega^2)(\omega_+^2-\omega^2))}{\mathcal{D}} \quad (3a)$$

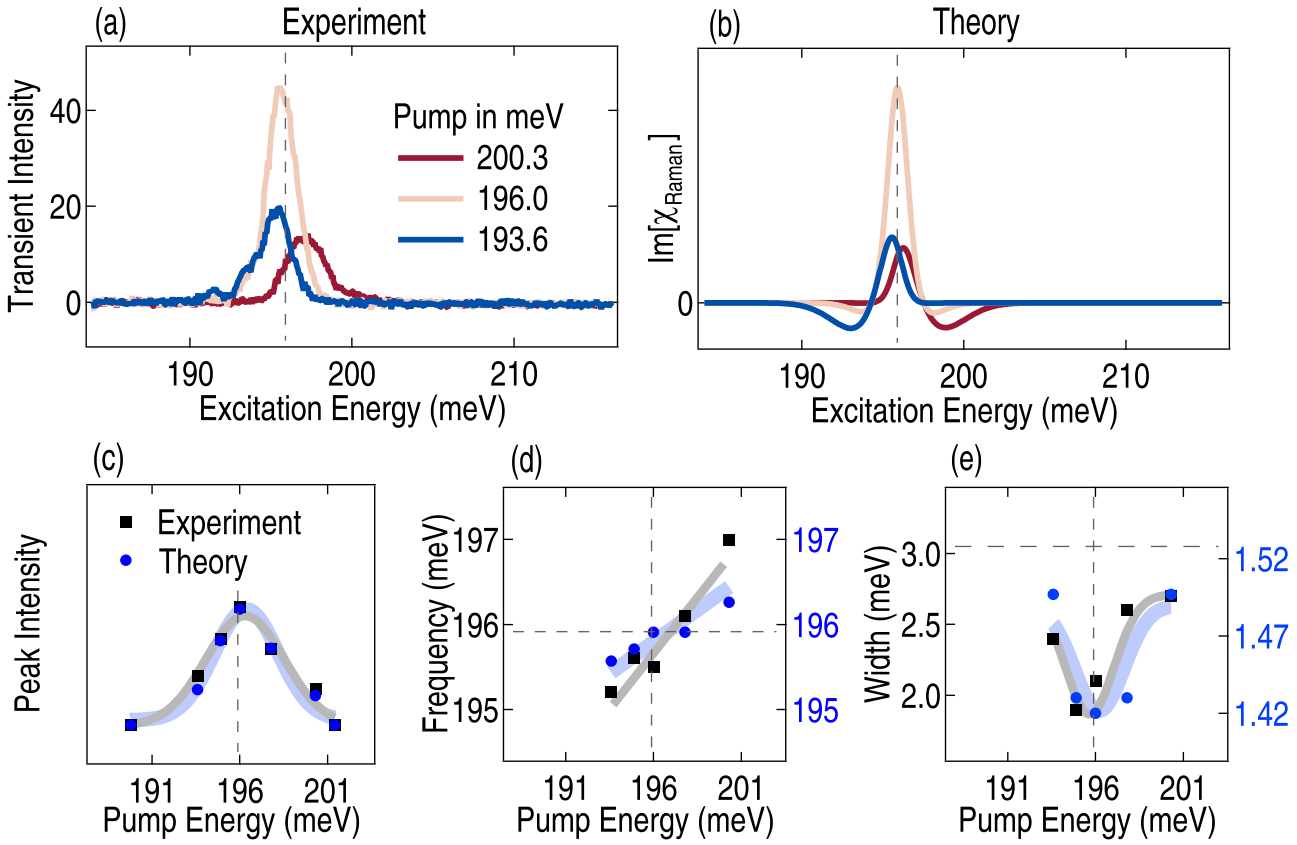

Fig. 3 Experimental and calculated transients for mid-IR resonant driving. (a) Exemplary transient spectra around the resonance energy of the E_{1u} mode for multilayer graphene. (b) Simulation results obtained by equation (3a) for the values of $\Delta = 4\,\mathrm{meV}^2$ and $\delta = 0.12\,\mathrm{meV}^2$. (c) Intensity scaling of the transient as a function of pump energy. (d) Frequency tuning of the transient as a function of pump energy. (e) Change of the width as a function of pump energy. In (c) to (e) black squares represent experimental results and blue circles the calculation. Horizontal grey dashed lines indicate the frequency and width of the unpumped Raman phonon and vertical ones the energy of the IR phonon. Solid grey and blue lines are guides to eye for each parameter.

$$\mathcal{D} = ((\omega_+^2 - \omega^2)(\omega_-^2 - \omega^2) - \gamma_-\gamma_+\omega^2)^2 + \omega^2(\gamma_+(\omega_-^2 - \omega^2) + \gamma_-(\omega_+^2 - \omega^2))^2 \tag{3b}$$

$$F_\mathrm{L}(\omega) = \frac{f_\mathrm{L}}{\sqrt{2\pi}}(e^{-\frac{1}{2}\sigma^2(\omega-\omega_\mathrm{L})^2} + e^{-\frac{1}{2}\sigma^2(\omega+\omega_\mathrm{L})^2}). \tag{3c}$$

As expected the transient Raman response vanishes for $\omega_+ = \omega_- = \omega_0$, i.e. $\Delta \to 0$ and $\gamma_+ = \gamma_- = \gamma_0$, i.e. $\delta \to 0$, representing the case of two non-interacting oscillators at identical frequencies and $\alpha = 0$. The response resulting from the expression above exhibits a classical anti-resonance contribution in the first term and a sharpened Lorentzian contribution from the second term. It is, therefore, the unusual case of a Fano-like response resulting from the interaction of two discrete states, which is quite different from the typical case of a Fano lineshape where a discrete excitation interacts with a continuum of states as in electron-phonon coupled systems.[15–18] It is also remarkable that the strength of the change in frequency and width, i.e. the changes in real and imaginary parts of the phonon susceptibility, directly influences the lineshape and the strength of the response. Both are proportional to the square of the electric field, which drives the IR phonon. Stronger changes in the frequency lead to a more asymmetric Fano-like lineshape and larger changes in the width lead to a more symmetric Lorentzian response. We can now model the observed resonance interaction between IR- and Raman-active phonons as shown in Fig. 3. The frequencies and widths ω_0, γ_0, ω_L, and σ are known. The only two model parameters are the modifications to the frequency Δ and the width δ. For the sake of clarity we have kept them constant and set to $\Delta = 4\,\mathrm{meV}^2$ and $\delta = 0.12\,\mathrm{meV}^2$. The lineshape obtained as such is only dependent

on the ratio of the parameters Δ and δ, so that these values are subject to an unknown scaling parameter that is given by the enhancement of the response. The results of our simulation are shown in Fig. 3(a) and (b) for the experimental and calculated transients. The data are reproduced very well. The signal enhancement, the shifting of mode frequencies and the sharpening of the transient response is recovered by the simulation where the ratio of Δ/δ was kept constant. The two anti-resonances in the transient in Fig. 3(b) are not observed in the experiment. We attribute these differences to higher-order coupling terms that we have neglected in our calculation. The shape of the resonance tuning of the intensity and the absolute frequency shifts are well recovered as can be seen in Fig. 3(c) and (d). Even the effect of the sharpening as such is present in our calculation in Fig. 3(e). However, the details of the broadening when tuning out of the resonance are not captured. The FWHM of the Raman mode measured in the probe spectra is 3 meV, the width of the observed transient in resonance is 2 meV and the width of the calculated transient is 1.4 meV. The linewidth variation with the pump energy is well reproduced, but takes place on a smaller scale when compared to the experiment.

Fig. 4 compares the model and the experimental data of the temporal change of the transient shapes, by assuming a dephasing between IR- and Raman-active phonons. This leads to an increase of the ratio between Δ and δ, i.e. real and imaginary parts of the coupled susceptibilities. After the pump excitation, IR- and Raman-active modes will dephase and accordingly the ratio between Δ and δ will increase. We have used this behavior to model the delay measurements shown in Fig. 4 (a), which are well recovered in Fig. 4 (b). Indeed, we can also reproduce the observed frequency shift and change in width as shown in Fig. 4 (c) and (d) as a function of delay, respectively.

Increasing the fluence at constant mid-IR pump frequency and delay, leads to a linearly increasing transient signal, as shown in Fig. 5(a), which is well recovered by the simulation in Fig. 5(b). The symmetry breaking of the degenerate energy levels is directly proportional to the fluence of the mid-IR pulse and so is the transient Raman signal. Since the ratio between Δ and δ is unchanged, there are only weak dependencies

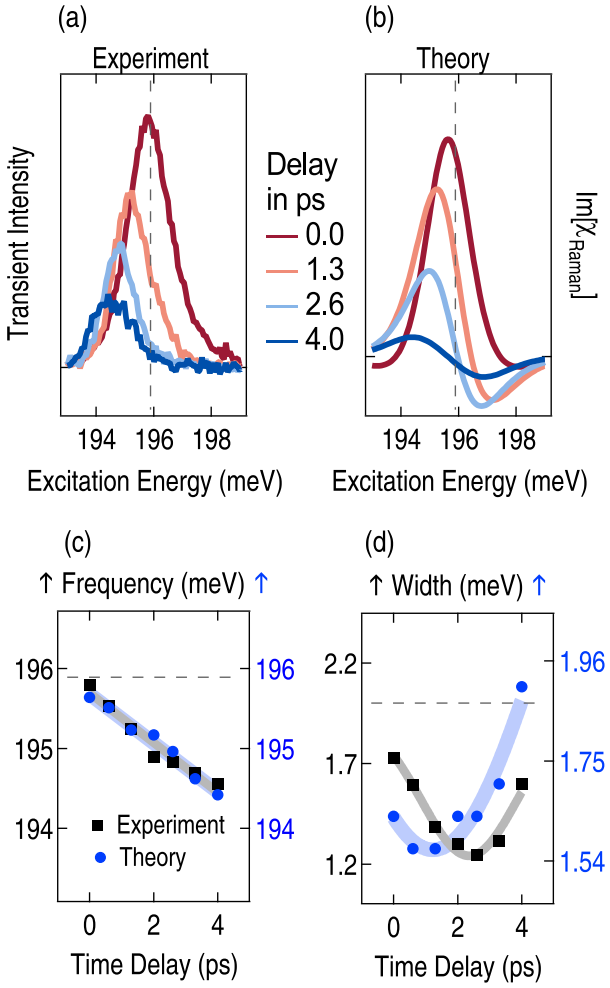

Fig. 4 Dephasing in experimental and calculated transients. (a) Exemplary time-resolved transient signals. (b) Exemplary calculated transient signals obtained by equation (3a). The temporal evolution of the ratio of Δ to δ is shown in the SI. (c) Frequency tuning of the transient as a function of delay. (d) Change of width as a function of delay. Black squares represent experimental results and blue circles the calculation. Horizontal grey dashed lines indicate the frequency and width of the unpumped Raman phonon and vertical ones the energy of the unpumped IR phonon. Solid grey and blue lines are guides to eye for each parameter.

of the lineshape on the fluence. Fig. 5(c) shows a DFT calculation of the magnitude of the energy splitting of the common coordinates β^+ and β^- as a function of the field strength of the driving mid-IR field. The DFT calculation allows now to determine real values of Δ and accordingly δ and to calculate the effective vibrational patterns as shown in Fig. 5(d), clearly resembling a novel non-equilibrium system of two coupled quantum states.

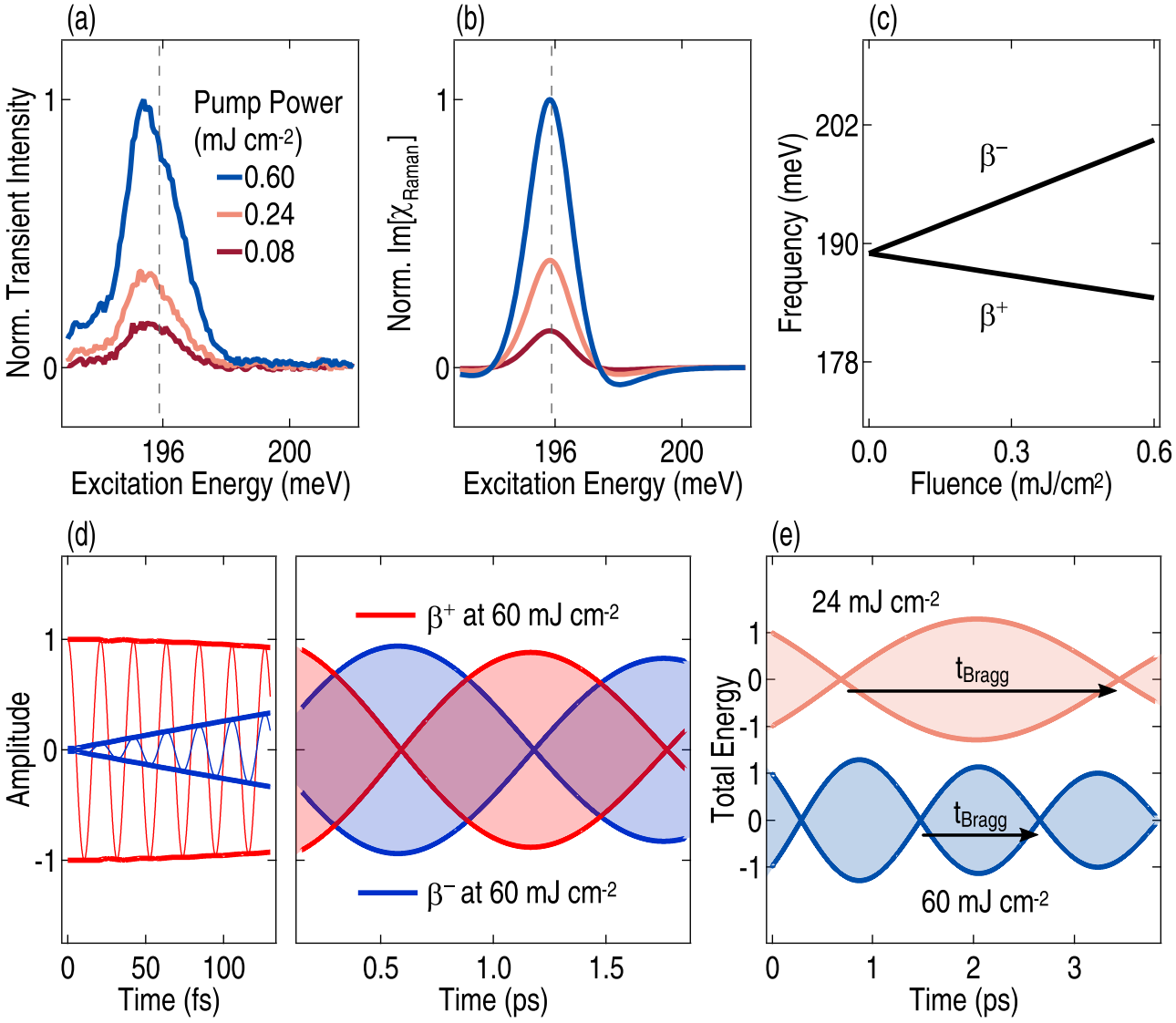

Fig. 5 Fluence-dependence of the lifting of the degeneracy. (a) Fluence-dependent transient signals. (b) Calculated transient signals obtained by equation (3a). (c) DFT calculation of the splitting of the frequencies as a function of the fluence of the driving IR field. (d) Amplitude of the β^+ and β^- oscillations at 60 mJ cm^{-2}. The data are derived from the simulation and by comparison to the DFT calculated fluence-dependent splitting of the frequencies. (e) Total energy from the mixed vibrational state for 24 and 60 mJ cm^{-2}. The magnitude of the vector t_{Bragg} scales with the lifting of the degeneracy Δ.

The unique features of this coupled photon-driven quantum state are the exchange of population with the subharmonic Rabi frequency Δ, an enhanced robustness as compared to the equilibrium states, and the breaking of time-translation symmetry. We also show that the mid-IR pump spontaneous Raman probe experiment is excellently suited to discover the symmetry breaking triggered by the optically induced avoided crossing. We believe that graphene related materials in combination with targeted photonic control in the mid-IR are adding another exciting aspect of novel quantum states in matter.

3 Methods

Raman spectroscopy measurements were performed with the UT-3 Raman Spectrometer[19]. The 515 nm second harmonic of a Tangerine fiber laser (France, Amplitude Systemes) was used as the probe beam. The probe beam was widened with a spatial filter and focused on the sample, using the on-axis parabola mirror of the entrance objective, that also collects the scattered light. Energy-dependent measurements shown were taken at 170 kHz, 7 mW probe power and ≈ 14 mW pump power. The focus spot sizes of

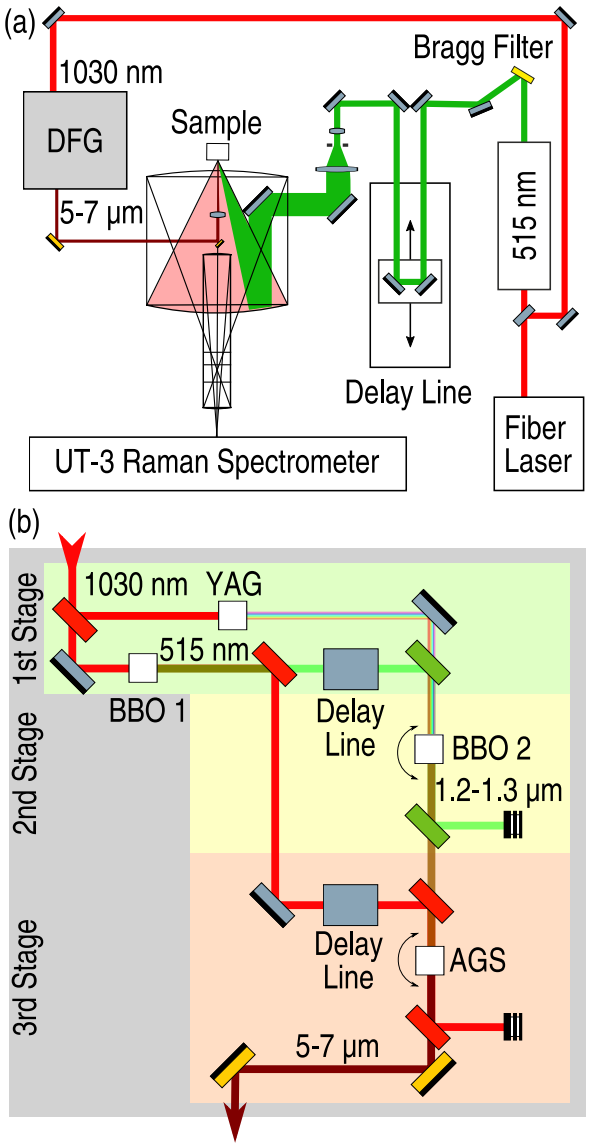

Fig. 6 Schematic of the pump-probe laser setup and the DFG setup. (a) Overview of the laser system including the Tangerine fiber laser, DFG system, entrance optics and the spectrometer. (b) Detailed depiction of the DFG system.

probe and pump beams on the sample were 25 µm and 100 µm, respectively. This leads for the probe (pump) beam to a pulse energy of 41 (82) nJ and a peak power density of 3.3 (4.2) GW/cm^2. Time-dependent measurements were taken at 350 kHz, 2 mW probe power and ≈ 11 mW pump power. This leads for the probe (pump) beam to a pulse energy of 6 (31) nJ and a peak power density of 0.5 (1.6) GW/cm^2. The wavelength of the probe-beam is 515 nm and probe-pulses have a FWHM of approximately 4 ps. The wavelength of the pump beam is varied between 6.0 to 6.5 µm and pump-pulses have a FWHM of approximately 0.5 ps.

The mid-IR pump beam was obtained using a difference frequency generation (DFG) setup as described by the following stages. 1st stage: Super continuum generation in a YAG-crystal and second harmonic generation in a BBO-type-1 crystal with 1030 nm pump. 2nd stage: Optical parametric amplification of the 515 nm pump and super continuum seed in a BBO-type-2 crystal to generate the near-infrared (NIR) beam of 1200-1300 nm. 3rd stage: DFG of 1030 nm pump and NIR seed in an AGS-crystal to generate the mid-IR beam (3-10 µm). The mid-IR beam was focused on the sample using a 40 mm ZnSe-lens.

To obtain spatial overlap, a 100 µm pinhole was positioned in the focal point of the entrance objective of the spectrometer. The beam path of the mid-IR beam was optimized for maximum transmission through the pinhole. To ensure temporal overlap, the 515 nm beam was used to induce carriers in a silicon wafer[20] and the transmission of the mid-IR beam was measured as a function of the time delay. The inflection point of the transmission curve was used as zero position.

The monolayer and bilayer samples were bought from Matexcel (New York, USA). Both are CVD grown on a 0.5 mm silicon quartz chip with the in-plane dimensions of 1x1 cm^2. The in-plane dimensions are 1x1 cm^2. The multilayer graphene sample was CVD grown on a silicon chip following Ref. [21–23], with the multilayer graphene on a silicon substrate.

To estimate the frequency splitting of the IR-active and Raman-active phonon mode, we perform computations in the first-principle framework of density functional theory (DFT). We performed our computations with the Vienna ab-initio simulation package VASP.6.2.[24] Moreover, for the phonon calculation, we used the Phonopy software package.[25] Our computations utilize pseudopotentials generated within the Projected Augmented Wave (PAW) [26] method. Specifically, we take the following configurated default potential: C 2s^{2}2p^2. We applied the PBEsol [27] approximation for the exchange-correlation potential. As a numerical setting, we used a 27x27x11 or 27x27x1 Monkhorst [28] generated k-point-mesh sampling of the Brillouin zone of graphite or bilayer graphene, respectively. Further we apply

a plane-wave energy cutoff of 750 eV. The self-consistent calculations were reiterated until the change in total energy becomes less than 10^{-9} eV.

References

[1] P. Kim, in *Dirac Matter* (Springer, 2017), pp. 1–23

[2] Y. Cao, V. Fatemi, S. Fang, K. Watanabe, T. Taniguchi, E. Kaxiras, P. Jarillo-Herrero, Unconventional superconductivity in magic-angle graphene superlattices. Nature **556**(7699), 43–50 (2018)

[3] H. Isobe, N.F. Yuan, L. Fu, Unconventional superconductivity and density waves in twisted bilayer graphene. Physical Review X **8**(4), 041,041 (2018)

[4] M.L. Kiesel, C. Platt, W. Hanke, D.A. Abanin, R. Thomale, Competing many-body instabilities and unconventional superconductivity in graphene. Physical Review B **86**(2), 020,507 (2012)

[5] T.O. Wehling, A.M. Black-Schaffer, A.V. Balatsky, Dirac materials. Advances in Physics **63**(1), 1–76 (2014)

[6] K.S. Novoselov, A.K. Geim, S.V. Morozov, D. Jiang, M.I. Katsnelson, I. Grigorieva, S. Dubonos, a. Firsov, Two-dimensional gas of massless dirac fermions in graphene. nature **438**(7065), 197–200 (2005)

[7] L. Malard, M.A. Pimenta, G. Dresselhaus, M. Dresselhaus, Raman spectroscopy in graphene. Physics reports **473**(5-6), 51–87 (2009)

[8] A.C. Ferrari, D.M. Basko, Raman spectroscopy as a versatile tool for studying the properties of graphene. Nature nanotechnology **8**(4), 235–246 (2013)

[9] R. Nemanich, G. Lucovsky, S. Solin, Infrared active optical vibrations of graphite. Solid State Communications **23**(2), 117–120 (1977)

[10] M. Först, C. Manzoni, S. Kaiser, Y. Tomioka, Y.n. Tokura, R. Merlin, A. Cavalleri, Nonlinear phononics as an ultrafast route to lattice control. Nature Physics **7**(11), 854–856 (2011)

[11] L.D. Landau, A theory of energy transfer ii. Phys. Z. Sowjetunion **2**(46), 19 (1932)

[12] C. Zener, Non-adiabatic crossing of energy levels. Proceedings of the Royal Society of London. Series A, Containing Papers of a Mathematical and Physical Character **137**(833), 696–702 (1932)

[13] A.S. Davydov, The theory of molecular excitons. Soviet Physics Uspekhi **7**(2), 145 (1964)

[14] D. Nicoletti, A. Cavalleri, Nonlinear light–matter interaction at terahertz frequencies. Advances in Optics and Photonics **8**(3), 401–464 (2016)

[15] U. Fano, Effects of configuration interaction on intensities and phase shifts. Physical Review **124**(6), 1866 (1961)

[16] E.H. Hasdeo, A.R. Nugraha, M.S. Dresselhaus, R. Saito, Breit-wigner-fano line shapes in raman spectra of graphene. Physical Review B **90**(24), 245,140 (2014)

[17] W.L. Zhang, H. Li, D. Xia, H. Liu, Y.G. Shi, J. Luo, J. Hu, P. Richard, H. Ding, Observation of a raman-active phonon with fano line shape in the quasi-one-dimensional superconductor k 2 cr 3 as 3. Physical Review B **92**(6), 060,502 (2015)

[18] A. Bock, S. Ostertun, R.D. Sharma, M. Rübhausen, K.O. Subke, C. Rieck, Anomalous self-energy effects of the b 1 g phonon in y 1- x (pr, ca) x ba 2 cu 3 o 7 films. Physical Review B **60**(5), 3532 (1999)

[19] B. Schulz, J. Bäckström, D. Budelmann, R. Maeser, M. Rübhausen, M. Klein, E. Schoeffel, A. Mihill, S. Yoon, Fully reflective deep ultraviolet to near infrared spectrometer and entrance optics for resonance raman spectroscopy. Review of scientific instruments **76**(7), 097,203 (2005)

[20] H. Lo, A. Compaan, Raman measurement of lattice temperature during pulsed laser heating of silicon. Physical Review Letters **44**(24), 1604 (1980)

[21] H. Baek, H. Kwak, M.S. Song, G.E. Ha, J. Park, Y. Tchoe, J.K. Hyun, H.Y. Park, E. Cheong, G.C. Yi, Zno nanotube waveguide arrays on graphene films for local optical excitation on biological cells. APL Materials **5**(4), 046,106 (2017)

[22] Y.J. Kim, J.H. Lee, G.C. Yi, Vertically aligned zno nanostructures grown on graphene layers. Applied Physics Letters **95**(21), 213,101 (2009)

[23] Y.J. Hong, H.S. Jung, J. Yoo, Y.J. Kim, C.H. Lee, M. Kim, G.C. Yi, Shape-controlled nanoarchitectures using nanowalls. Advanced Materials **21**(2), 222–226 (2009)

[24] G. Kresse, J. Furthmüller, Efficient iterative schemes for ab initio total-energy calculations using a plane-wave basis set. Physical review B **54**(16), 11,169 (1996)

[25] A. Togo, I. Tanaka, First principles phonon calculations in materials science. Scripta Materialia **108**, 1–5 (2015)

[26] G. Kresse, D. Joubert, From ultrasoft pseudopotentials to the projector augmented-wave method. Physical review b **59**(3), 1758 (1999)

[27] G.I. Csonka, J.P. Perdew, A. Ruzsinszky, P.H. Philipsen, S. Lebègue, J. Paier, O.A. Vydrov, J.G. Ángyán, Assessing the performance of recent density functionals for bulk solids. Physical Review B **79**(15), 155,107 (2009)

[28] H.J. Monkhorst, J.D. Pack, Special points for brillouin-zone integrations. Physical review B **13**(12), 5188 (1976)

6 Summary and Outlook

Summary
In this work a multitude of inelastic light scattering experiments were designed, conducted and analyzed to shine light on the structure-function relationship and charge-transfer processes of different biomimetic inorganic copper-complexes and low-dimensional condensed matter systems. The Raman experiments contain continuous, pulsed, pump-probe, liquid-ethanol-chiller and helium-cryogenic setups at wavelengths ranging from the deep-UV to the MIR. Many intricate nonlinear processes are readily used for UV and deep-UV laser generation with the Tsunami laser system, but the installation and optimization of the difference frequency generation unit to be able to use femtosecond MIR light with all its successive and parallel nonlinear interactions proved to be a difficult task. Machine problems with practically all parts of the Tangerine source laser and the corona pandemic further complicated this endeavor. However, it was possible to finish the task and use the MIR light for reflection measurements and for an entire MIR-pump and Raman-probe study on graphene. In several beam times, additional X-ray absorption spectroscopy experiments were conducted at the synchrotron source Petra III at DESY in Hamburg, Germany and analyzed to further characterize the model complexes. This involved on-site oxygenation of sensitive molecular species, cryostate usage for liquid samples and the beamline operation.

A model complex for the enzyme peptidylglycine α-hydroxylating monooxygenase was investigated in [4.1]. Raman spectroscopy was used to characterize the complex, which was studied to reveal information on the cooperative effect of the two copper centers during hydroxylation. In another study, Raman and X-ray absorption were used to fully characterize the formation and intermediate structures of a methane-monooxygenase model complex in [4.3]. The ability to set the temperature in each of the experiments and the ability to oxygenate as desired and with different oxygen-atom transfer reagents allowed for full experimental control. It was possible to find a mixed-valent tetranuclear Cu_4O_2 intermediate, which after homolytic O-O bond cleavage forms two Cu_2O complexes. The cleavage is induced by heating up the solution and is irreversible, as the Raman data show. The EXAFS analysis of the interatomic distances leave no doubt about the molecular structure of the intermediate forming a tetranuclear motif.

In [4.6] low-temperature Raman experiments were conducted on the tyrosinase enzyme model complex stabilized by the hybrid TMGdmap ligand consisting of a propylene-bridged guanidine and amine unit. While oxygenation, substrate attack and subsequent conversion, Raman data were taken live to monitor the reaction of substrates with the model complex. With the fully achromatic entrance optics and the tunable Tsunami laser systems, it was possible to find wavelengths with Raman cross-sections high enough to yield sufficient signals for the fast chemical reactions. The catecholato formation after the phenolate attack was clearly visible and it was shown that Raman scattering can be used as a tool to study not only the ligands, oxygenated complexes and substrate conversion products *ex-situ*, but also the reaction dynamics *in-operando* in one coherent experiment.

A further tyrosinase model complex stabilized by the hybrid TMGbenza ligand consisting of an aromatic-backbone-bridged guanidine and amine unit was investigated with Raman and X-ray absorption experiments for [4.2]. The complex showed a surprising variety of phenolic substrates it converted at predictable molecular positions and therefore allows for new opportunities to design phenazines. In the following publication in [4.4] Raman spectroscopy was used to characterize the aforementioned complex and two modified amine donor functions and it was found that small changes in the ligand sphere affect the characteristic ligand-to-metal charge transfer transition, as evidenced by a redshift with weaker N-donor function.

Modified versions of an entatic state model complex stabilized by the hybrid TMGqu ligand consisting of one guanidine and quinolinyl unit were investigated with X-ray absorption in [4.5]. Different chemical modifications at different positions were used to investigate the effect of the nature of the ligand on the entasis, which was measured with the different $Cu^{I/II}$ pairs. It was found that a low difference in structure factor $\Delta\tau_4$ is vital and that furthermore the average difference $\varnothing\tau_4$ has to be neutral, i.e. not favor one or the other geometry.

The MIR laser light was used for the quasi-1D metal $Sr_{0.95}NbO_{3.37}$ in [5.1] and [5.2] to measure the reflectance as a probe of the metallicity of the different crystallographic axis. A multitude of different types of angle-dependencies, Raman resonance studies and pump-probe Raman scattering studies ranging from the deep-UV to the MIR were conducted and a photoinduced metal-insulator transition and its physical origin was found and investigated in detail. The MIR laser was also used as a pump pulse for graphene-related condensed matter systems, which are subsequently probed with a 515 nm laser to collect the Raman signal. The delay-setup allowed to investigate the picosecond dynamics of the systems response to the pump beam. The pump beam itself was continously tuned through the resonance of an IR-active vibrational mode. The pump energy-dependent study revealed strong phonon renormalization effects, not only of the prominent G-mode frequency, but also on the linewidth and the peak intensity. The effect stems from anharmonic nonlinear interaction of the pumped E_{1u} infrared mode which is coupled to the E_{2g} Raman mode, showing the capability to control condensed matter systems deliberately with the lattice degrees of freedom.

Outlook

The X-ray experiments are well optimized and further change in the setup is related to the decision making of the corresponding beamline scientists and the upcoming Petra IV upgrade. However, the difference frequency setup allows for further modification and optimization. The silver thiogallate crystal is especially a weak spot since the DFG process, without any amplification process, works with two watt-level input laser beams. Motorized movement to prevent overheating might be a potential solution. The high pulsed peak energy density in the crystal is potentially exciting charges, which themselves are changing the absorption unfavorably so that grounding the mirror to allow charge neutrality can be tried. To allow for a broader range of possible experiments, the helium-cryostat can be installed for MIR-pump and Raman-probe experiments. Overcoming problems for this mostly includes finding suitable windows for the cryostat that are transparent in both regions, the UV-Vis and the MIR. However, all the previous work has now clearly paved the way for future measurements with MIR pumping the vibrational modes of the ligand sphere and to use an optical probe to investigate how the modified structure relates to the different properties of the entatic state model complexes.

Although modifying and optimizing the model complexes is itself a task more suited for the chemists, one could experiment with adding substances such as dissolved metal nanoparticles to solutions or on dry powder samples to potentially increase the intensity without significantly changing the frequencies in the Raman investigations. Other than smaller quality-of-life features such as that, designing and developing new ligands is outside the scope of the optical lab. The technique that holds promises for future development is undoubtedly the operando setup with its far-ranging capabilities to introduce more alterations to the sample environment while taken spectra. More substances can be added, such as acid or bases or the temperature can be varied. The feasibility for such experiments has been established, which paves the way for further investigations. Most notably, the operation principle does not only produce useful information for inorganic model complexes but can also be used for other chemical reactions in molecules or even phase transition, adsorption reactions or ligand-exchange reactions in dissolved nanoparticles.

Irrespective of the nature of the aforementioned sample or the sample environment, the MIR laser light opens up the pathway to a variety of interesting spectroscopic molecular and solid-state experiments. The advantage of this MIR-pump system lies in its flexible production of laser wavelengths in a broad range of single micrometers to manipulate the sample with a high degree of *specificity*. The energy range of such wavelengths is not easy to produce with lasers as it stands, but the excitations can be controlled easily to generate a clear interpretation of the interactions of the sample systems. For example, high-energy excitations of > 1 eV or even > 4 eV for UV light couple to different electronic transitions, which leads to a cascade of different intertwined follow-up reactions and decay channels. Also, heating up a sample is technically a very dispersive manipulation since many different possible vibrations of different symmetries at different energies change their population number. Exciting one vibration by setting an MIR pump laser in the respective resonance allows for clear interpretation of the data after probing the manipulated system. One can e.g. excite with high efficiency the vibrational modes of the ligands of inorganic metal complexes and probe the direct influence that each of them have on the entire molecule. To illustrate a simple example, the vibrations of different chemical groups within different moieties of one ligand can each be excited and their individual influence investigated. Note that MIR-pump and X-ray probe measurements at the DESY might be complemented too yield a more concise understanding of the pump-effect on the sample. When considering condensed matter systems, the phonon-pumping can still be used when the materials consist of sufficiently lightweight atoms such as graphene-related materials for basic research or e.g. silicon-carbide for the modern semiconductor industry. Additionally, quasiparticles, many-body interactions and phase-transitions can be investigated and the pump-probe setup with femtosecond pulses allows for detailed study on the dynamics of the respective matter excitation.

A Additional Publications

A.1 Temperature and Magnetic Field Dependent Raman Study of Electron-Phonon Interactions in Thin Films of Bi_2Se_3 and Bi_2Te_3 Nanoflakes

Copyright by the American Physical Society. Reproduced with permission from Ref. [144]. The author has conducted the Raman measurements and contributed to the theoretical analysis.

PHYSICAL REVIEW B **101**, 245431 (2020)

Temperature and magnetic field dependent Raman study of electron-phonon interactions in thin films of Bi_2Se_3 and Bi_2Te_3 nanoflakes

Sören Buchenau,[1,*] Sarah Scheitz,[1] Astha Sethi,[2] John E. Slimak,[2] Tomke Eva Glier,[1] Pranab Kumar Das,[3] Torben Dankwort,[4] Lewis Akinsinde,[1] Lorenz Kienle,[4] Andrivo Rusydi,[3] Clemens Ulrich,[5] S. Lance Cooper,[2] and Michael Rübhausen[1]

[1]*CFEL, University Hamburg, Luruper Chaussee 175, 22761 Hamburg, Germany*
[2]*Department of Physics and Materials Research Laboratory, University of Illinois, Urbana, Illinois 61801, USA*
[3]*Singapore Synchrotron Light Source, National University of Singapore, Singapore 117603, Singapore*
[4]*Institute for Materials Science, Kiel University, Kaiserstrasse 2, 24143 Kiel, Germany*
[5]*School of Physics, The University of New South Wales, New South Wales 2052, Sydney, Australia*

(Received 8 October 2019; accepted 26 May 2020; published 22 June 2020)

We have investigated two-dimensional nanostructures of the topological insulators Bi_2Se_3 and Bi_2Te_3 by means of temperature and magnetic field dependent Raman spectroscopy. The surface contribution of our samples was increased by using thin films of dropcasted nanoflakes with the aim of enhancing their topological properties. Raman spectroscopy provides a contact-free method to investigate the behavior of topological properties with temperature and magnetic fields at lower dimensions. The temperature dependent Raman study reveals anharmonic phonon behavior for Bi_2Te_3 indicative of a two-phonon relaxation mechanism in this material. Contrary to this, Bi_2Se_3 shows clear deviations from a two-phonon anharmonic decay model at temperatures below 120 K exhibiting a hardening and broadening, especially of the A_{1g}^2 mode. Similarly, the magnetic field dependent self-energy effects are only observed for the A_{1g}^2 mode of Bi_2Se_3, showing a broadening and hardening with increasing field. We interpret our results in terms of corrections to the phonon self-energy for Bi_2Se_3 at temperatures below 120 K and magnetic fields above 4 T due to electron-hole pair excitations associated with the conducting surface states. The phonon renormalization with increasing magnetic field is explained by a gap opening in the Dirac cone that enables phonon coupling to the changing electric susceptibility.

DOI: 10.1103/PhysRevB.101.245431

I. INTRODUCTION

Topological insulators (TIs) are a new class of materials, which are insulating in the bulk and host conducting surface states (CSSs) at the interface between the TI and conventional insulators [1]. The idea of topological states was strongly promoted during the aftermath of the discovery of the quantum Hall effect by von Klitzing [2], who identified specific quantized changes in the Hall conductance, which turn out to be topological quantum numbers. After several incremental steps, modern three-dimensional (3D) TIs were predicted in 2007 by Fu *et al.* [3]. The strong spin-orbit coupling leads, in specific materials, to a band inversion of two p bands [4], which is essential for the CSSs. In addition, the electron transport is characterized by spin-momentum locking and a linear dispersion relation, known as a Dirac cone, superimposed on the bulk bands [5]. Bi_2X_3 (X=Se, Te) belongs to the most frequently studied 3D TI with a single Dirac cone at the Γ point of the Brillouin zone [6,7] and bulk band gaps of 0.3 eV [8] and 0.1 eV [9] for Bi_2Se_3 and Bi_2Te_3, respectively.

To explicitly study the CSSs and reduce contributions from the bulk, we have examined dropcasted nanoflakes with high aspect ratios that lead to an increased surface contribution.

In order to evaluate the fundamental limit of the conductivity of electrons in the CSSs at lower dimensions, it is important to study the electron-phonon interactions of these 2D materials [10,11].

A unique technique to study phononic and electronic properties of solids simultaneously is Raman scattering, which has been widely applied to investigate bulk samples and conventional 2D films of Bi_2Se_3 [12–15] and Bi_2Te_3 [14,16,17]. Bi_2Se_3 and Bi_2Te_3 are layered materials with a rhombohedral crystal structure that grow in multiples of so-called quintuple layers (QLs) consisting of alternating Bi and Se or Te layers, as depicted in Fig. 1(a) [18]. The primitive unit cell consists of five atoms, which results in 15 lattice dynamical modes that are classified in three acoustic and 12 optical modes. The optical modes are further grouped into four Raman-active modes with two modes each of A_{1g} and E_g symmetry and four infrared(IR)-active modes with two modes each of A_{1u} and E_u symmetry according to group theory [18]. Due to the inversion symmetry of the crystal structure, these phonon modes are exclusively either Raman or IR active [18]. Of the Raman-active phonons, the A_{1g} modes are out-of-plane vibrations, whereas the E_g modes vibrate in-plane.

Systematic temperature dependent Raman studies have been conducted before on Bi_2Se_3 single crystals [19,20] and nanoplates [21], and on Bi_2Te_3 thin films [22]. In this work, we report on a temperature and magnetic field dependent high-energy-resolution Raman study of thin films of individual Bi_2Se_3 and Bi_2Te_3 nanoflakes with average heights in the range of 8 and 14 QLs, respectively.

*Corresponding author: sbuchena@physnet.uni-hamburg.de

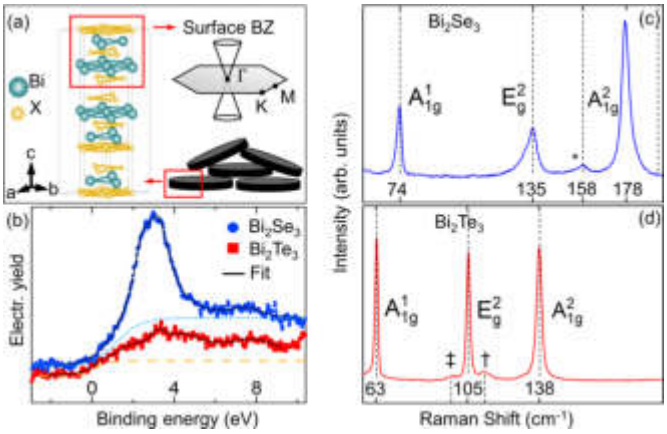

FIG. 1. (a) Schematic illustration of a thin film of Bi_2X_3 (X=Se, Te) nanoflakes. This configuration greatly enhances the amount of surface, which hosts massless Dirac electrons due to the linear Dirac cone at the Γ point [29], as shown in the surface Brillouin zone in the upper right corner. The figure further shows the crystal structure with blue spheres representing Bi atoms and yellow spheres representing either Se or Te atoms. (b) Valence-band emission spectra extracted from XPS spectra of both materials. The Fermi edge modeled by a step function shows a highly increased electron density for Bi_2Se_3 (light-blue, dotted graph) compared to Bi_2Te_3 (orange, dashed graph). (c),(d) Raman spectra at 3 K in $z(xx)\bar{z}$ geometry showing three labeled bulk modes for Bi_2Se_3 and Bi_2Te_3, respectively. The asterisk, dagger, and double dagger mark Raman-forbidden infrared modes.

Magnetic field dependent Raman measurements are of utmost importance as they allow for investigations of the destruction of the CSSs by gapping of the Dirac cone induced by the presence of a magnetic field [1]. It was theoretically predicted that the CSSs are sensitive to the application of a magnetic field [23] and an opening of the Dirac cone has indeed been observed in magnetically doped TIs [24,25] or by exchange coupling TIs to magnetic insulators [26–28]. The tuning of the CSSs with an applied magnetic field is expected to display a spectroscopic signature, which is amplified due to the highly increased surface contributions of our nanoflakes. We therefore interpret our results by means of self-energy corrections of the phonons due to electron-phonon interactions.

II. EXPERIMENTAL PART

Figure 1(a) shows an illustration of strongly anisotropic nanoflakes. The Bi_2Se_3 nanoflakes were grown with the chemical polyol method following our earlier work [30]. The Bi_2Te_3 nanoflakes were synthesized using a slightly modified route according to Zhang *et al.* [31]. Details on the synthesis are presented in Ref. [30] and in the Supplemental Material [32]. The clean flakes were dropcasted on a Si substrate and the solvent evaporated. It should be noted that the structures are not damaged by these preparatory steps, as can be seen in Fig. S-2 of the Supplemental Material [32]. The required stoichiometry, single crystallinity, and morphology of both samples were confirmed using energy dispersive x-ray spectroscopy (EDX), x-ray photoelectron spectroscopy (XPS), transmission electron microscopy (TEM), selected area electron diffraction (SAED), and atomic force microscopy (AFM). A detailed characterization of the nanoflakes can be found in the Supplemental Material [32].

The topological insulator Bi_2X_3 (X=Se, Te) features Dirac states at the interface with conventional insulators, but not at the interface of every QL [28]. It has furthermore been shown for Bi_2Se_3, that the CSS wave functions hybridize below a critical flake thickness of 6 QLs, which results in a gap opening in the Dirac cone [33]. To investigate the intact CSSs, it is hence necessary to grow flakes of certain thicknesses and maintain enough space between dropcasted flakes to prevent hybridization of the CSSs from neighboring flake surfaces. With average heights of 8 and 14 QLs for our Bi_2Se_3 and Bi_2Te_3 flakes, respectively, we expect our samples to host unperturbed CSSs. In addition, our flakes were grown covered with the ligand polyvinylpyrrolidone (PVP) to facilitate a 2D growth. The PVP layers act as conventional insulators and thus provide sufficient spacing between neighboring flakes. It is known that the CSSs are robust against different kinds of adsorbates and are maintained even under ambient environmental conditions [24,34]. However, adsorbates are known to induce a band bending of the bulk bands near the surface due to charge accumulation [6,35]. This leads to the creation of additional surface quantum well states originating from the bulk bands coexisting next to the CSSs. Nonetheless, the CSSs stay intact, but are pushed deeper into the bulk separating them from the surface defects [36]. Thus, for volume scattering techniques, the CSSs stay detectable as Raman scattering is able to probe the whole volume including the deeper-lying CSSs, in contrast to surface sensitive techniques such as angle-resolved photoemission spectroscopy (ARPES). In fact, Raman scattering probes the complete thickness of a flake of about 10 nm. Therefore, probing a thin film of dropcasted nanoflakes is expected to contain a manifold of topologically nontrivial contributions, as illustrated in Fig. 1(a), making it easier to observe phenomena that have their origin in those exotic states.

We conducted Raman measurements on films of dropcasted nanoflakes using the 647.1 nm excitation line of a continuous-wave Kr^+ gas laser. The incident laser power was limited to 6.2 mW and focused on a 50-μm-diameter spot size to prevent laser induced heating or damage of the sample, which is shown in detail in the Supplemental Material [32]. The sample was mounted so that the incident light impinged on the flakes perpendicular to their surfaces. The scattered light from the sample was collected in a backscattering configuration, dispersed through a triple-stage spectrometer, and then detected with a liquid-nitrogen-cooled charged-coupled-device detector. The horizontal polarization of the incident light with regard to the setup was selected with a polarization rotator and the scattered light was analyzed by the triple-stage gratings of the spectrometer that is primarily sensitive to horizontally polarized light [37]. Our scattering configuration denoted in Porto notation is hence $z(xx)\bar{z}$ [38]. The samples were inserted into a continuous He-flow cryostat, which itself was horizontally mounted in the open bore of a superconducting magnet. This setup allowed for simultaneous temperature (3–295 K) and magnetic field (0–7 T) dependent measurements. Magnetic field dependent measurements were performed in Faraday geometry with the wave vector of the incident light $\vec{q}$ parallel to the applied field $\vec{H}$.

III. RESULTS AND DISCUSSION

Figure 1(b) shows the valence-band spectra extracted from XPS measurements of the Bi_2Se_3 and Bi_2Te_3 films. The indicated Fermi edges modeled by step functions reveal, for Bi_2Se_3, a highly increased electron density near the Fermi edge compared to Bi_2Te_3. Differences in the two samples are also reflected in their phononic properties measured by Raman spectroscopy. The implication of the enhanced surface contribution of our flakes is already observable in the representative Raman spectra shown in Figs. 1(c) and 1(d). Next to the three identified bulk phonon modes that are in good agreement with previous experiments [18,39,40], additional IR-active modes at 158 cm^{-1} in Bi_2Se_3 and at 98 cm^{-1} and 113 cm^{-1} in Bi_2Te_3 are detected [14,15,41]. The IR-active modes become Raman active because of the breaking of the crystal's inversion symmetry at the surface of the nanoflakes [15]. This aspect is a direct manifestation of the enhanced surface-to-volume ratio of the dropcasted nanoflakes compared to the bulk material. The bulk material crystallizes in the D_{3d} space group with inversion symmetry, whereas the symmetry at the surface is reduced to C_{3v} [15]. Gnezdilov *et al.* [15] reported that the A_{2u}^2 mode at 158 cm^{-1} in the case of Bi_2Se_3 is only observable at temperatures below 10 K for their bulk crystalline sample. In contrast, for our nanoflake samples, we were able to observe this mode even at elevated temperatures up to ∼160 K (see Fig. S-9 in the Supplemental Material [32]), indicating enhanced surface contributions with respect to the scattering volume at lower temperatures. Likewise, the IR modes in the Bi_2Te_3 films are detected for temperatures up to 100 K (see Fig. S-9 in the Supplemental Material [32]). Furthermore, the high single crystalline quality of our flakes is indicated by the nearly resolution-limited linewidths of the Bi_2Te_3 phonons. In Sec. 5 in the Supplemental Material [32], we discuss in detail that the narrow linewidths and high quality of the Bi_2Se_3 spectra suggest nearly stoichiometric samples with only a few Se vacancies. Furthermore, a sensitivity of the phonons to band-bending effects due to adsorbates at the surface and consequent localized electronic surface states cannot be seen. Since Raman is a volume scattering technique, we do not expect to observe any contributions from possible highly localized electronic states at the sample surface. This leads us to conclude that the phonons track the CSSs and electronic states associated to the Fermi level of our sample. Furthermore, we conclude from the low number of Se vacancies that the Fermi level in our sample lies indeed between the bulk valence and conduction band.

We conducted a detailed temperature dependent Raman study by acquiring 30 spectra for each material system in a temperature range from 3 to 295 K. To investigate the phonon dynamics, we extracted the values of the frequency ω and the linewidth Γ [full width at half maximum (FWHM)] from the respective Voigt fits to the phonon modes. The Voigt profile is represented by a Lorentz profile broadened by a Gaussian that accounts for the spectral resolution of the spectrometer, and is given as

$$V(\omega) = y_0 + A\frac{2\ln 2}{\pi^{3/2}}\frac{\Gamma_L}{\Gamma_G^2} \times \int_{-\infty}^{\infty} \frac{e^{-t^2}}{\left(\sqrt{\ln 2}\frac{\Gamma_L}{\Gamma_G}\right)^2 + \left(\sqrt{4\ln 2}\frac{\omega-\omega_0}{\Gamma_G} - t\right)^2} dt. \quad (1)$$

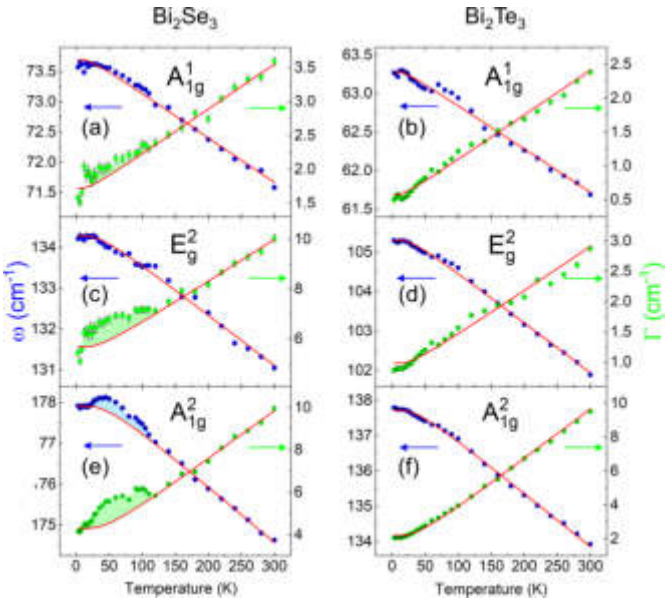

FIG. 2. Self-energy effects from Voigt fits of the temperature dependent Raman response for Bi_2Se_3 (left column) and Bi_2Te_3 (right column). (a),(b) The A_{1g}^1 phonons, (c),(d) the E_g^2 phonons, and (e),(f) the A_{1g}^2 phonons. The red lines are fits using the model of an anharmonic decay with a symmetric decay channel into two acoustic phonons. The data show the general trend of an anharmonic decay consisting of broadening and softening with increasing temperature. Clear deviations from the model are present for the high-energy modes in Bi_2Se_3 [(c) and (e)], which are mirrored in energy and linewidth. Below ∼120 K, the phonons exhibit higher energies and linewidths than expected from the usual anharmonic phonon decay, as an indication for additional phonon interactions with the electronic system.

Hereby, $\Gamma_{G,L}$ denotes the linewidth of both convoluted peaks, with a spectral resolution of the setup of Γ_G=1.4 cm^{-1}, ω_0 is the peak center, A is the integrated area of the Lorentzian peak, and y_0 is the offset.

We have analyzed the three higher-energy modes of the commonly known [14,39] four bulk modes in Bi_2X_3 (X=Se, Te) because the lowest-energy E_g^1 mode was covered by the strong Rayleigh background due to the enhanced elastic scattering from the nanoflakes. Figure 2 shows the behavior of the frequency ω_0 and linewidth Γ_L of the A_{1g}^1, E_g^2, and A_{1g}^2 modes for Bi_2Se_3 (left column) and Bi_2Te_3 (right column). The frequencies and linewidths show a general trend of phonon softening and broadening with increasing temperature by several wave numbers. This phonon behavior can be described by the model of an anharmonic decay (AD) assuming a symmetric decay of the optical phonon into two acoustic phonons [42]. Within this model, the temperature dependences of the phonon frequency and linewidth are given by

$$\omega_{anh}(T) = \omega_0 - \frac{a}{e^{\frac{\hbar\omega_0}{2\cdot k_B T}} - 1}, \quad (2)$$

$$\Gamma_{anh}(T) = \Gamma_0 + \frac{a}{e^{\frac{\hbar\omega_0}{2\cdot k_B T}} - 1}, \quad (3)$$

with T as the temperature, ω_{anh} and Γ_{anh} as the modulated frequency and linewidth, respectively, and ω_0 and Γ_0 as the bare phonon frequency and linewidth of a particular phonon, respectively. a contains the transition matrix element and the two-phonon density of states of the anharmonic decay. Fits of the data according to the AD model are shown as red lines in Fig. 2. For Bi_2Te_3, the anharmonic fits show very good agreement with the data, especially for the highest-energy A_{1g}^2 mode in Fig. 2(f). This indicates a more bulklike behavior typical for semiconductors and insulators with phonon-phonon interactions as the dominant scattering mechanism in the Bi_2Te_3 sample. Compared to Bi_2Te_3, the linewidths for all Raman modes in Bi_2Se_3 show clear deviations from the AD model at temperatures below 120 K; see Figs. 2(a), 2(c) and 2(e). The linewidth of the A_{1g}^1 mode exhibits only weak deviations from the AD model, whereas the higher-energy modes deviate more strongly. For the A_{1g}^2 mode, the deviation in linewidth is mirrored in frequency, illustrated in Fig. 2(e), as expected by the Kramers-Kronig relation. In previous temperature dependent Raman investigations on Bi_2Se_3 crystals [19,20], no phonon anomalies were observed. This hints to an origin of these deviations stemming from the increased electronic surface contributions of the investigated flakes at lower temperatures. This aspect is supported by the enhanced electron density near the Fermi edge in Bi_2Se_3, shown in Fig. 1(b).

Since the AD model is not sufficient to describe the low-temperature behavior of phonons, additional scattering mechanisms need to be taken into consideration. As Bi_2Se_3 is nonmagnetic, additional scattering channels could stem from electron-phonon interactions since the only available states at these energies and low temperatures must be of an electronic nature. The coupling of phonons to available electronic susceptibilities would result in a decay of the phonons by creating electron-hole pairs [43,44]. The possibility of this interaction is plausible since our XPS data show a higher electron density near the Fermi edge for Bi_2Se_3. The coupling of phonons to an electric susceptibility $\chi^{\mathrm{el}}(\omega)$ leads to a correction in the phonon self-energy, which manifests itself in a modified Raman response. This response $I^{\mathrm{ph}}(\omega)$ of a phonon coupled to an electric susceptibility $\chi^{\mathrm{el}}(\omega)$,

$$\chi^{\mathrm{el}}(\omega) = R(\omega) + i\rho(\omega), \tag{4}$$

with its real $R(\omega)$ and imaginary part $\rho(\omega)$, is expressed by [45,46]

$$I^{\mathrm{ph}}(\omega) \propto \frac{[g^2\rho(\omega) + \Gamma_{\mathrm{anh}}]\omega_{\mathrm{anh}}}{\left\{\omega^2 - \underbrace{\omega_{\mathrm{anh}}^2\left[1 - g^2\frac{R(\omega)}{\omega_{\mathrm{anh}}}\right]}_{\omega_{\mathrm{exp}}^2}\right\}^2 + \omega_{\mathrm{anh}}^2\underbrace{[\Gamma_{\mathrm{anh}} + g^2\rho(\omega)]^2}_{\Gamma_{\mathrm{exp}}^2}}. \tag{5}$$

Here, ω_{anh} and Γ_{anh} correspond to the frequency and linewidth expected from the AD model, and g is a coupling constant determining the coupling strength between the phonon and the electric susceptibility. Equation (5) describes a Lorentz profile with a phonon frequency ω_{anh} that is modified by coupling to the real part $R(\omega)$ of the electric susceptibility and a linewidth Γ_{anh} modified by coupling to the imaginary part $\rho(\omega)$. As a result, the values for the frequency ω_{exp} and linewidth Γ_{exp} extracted from Voigt fits of the phonons differ from the values expected for an anharmonic decay due to corrections from the electric susceptibility. We hence interpret the deviations in linewidth and frequency expected from the AD model as arising from additional contributions caused by the decay of phonons coupling to an available electronic transition. When the electron-phonon coupling g is strong enough, the extracted phonon linewidths and frequencies are therefore given as follows:

$$\omega_{\mathrm{exp}} = \sqrt{\omega_{\mathrm{anh}}(T)^2 - \omega_{\mathrm{anh}}(T)\cdot g^2 R(\omega)}, \tag{6}$$

$$\Gamma_{\mathrm{exp}} = \Gamma_{\mathrm{anh}}(T) + g^2\rho(\omega). \tag{7}$$

The deviations from the AD model could be caused by an interaction of the phonons with an electric susceptibility with an energy in the meV range. The lack of any electronic renormalization in Bi_2Te_3 is thus indicating that there are no available electronic states in this energy range. This is further verified by the strongly diminished electronic density near the Fermi edge in Bi_2Te_3 compared to Bi_2Se_3 seen by XPS, as shown in Fig. 1(b).

Since the A_{1g}^2- and E_g^2-symmetry phonons show deviations from the AD model, it can be argued that both phonons couple to a close-lying electronic transition. The different energies of the two phonons lead to different corrections from the real and imaginary parts of the electric susceptibility according to Eqs. (6) and (7).

The strong electronic renormalization in Bi_2Se_3 for the E_g^2 mode in linewidth but none in frequency, shown in Fig. 2(c), leads to the assumption that the E_g^2 phonon couples to an electric susceptibility with an energy identical to the E_g^2 energy, as visualized in Fig. 3(a). In that way, the E_g^2 phonon would get a strong correction from the imaginary part $\rho(\omega)$ since it is located at the maximum, resulting in an increased linewidth Γ_{exp} according to Eq. (7). On the other hand, there would not be any corrections in frequency because at ω_{ph} the real part $R(\omega)$ is zero and thus ω_{exp} corresponds to ω_{anh} according to Eq. (6). The temperature dependence of the E_g^2 frequency is then sufficiently well described by the AD model, as evident in Fig. 2(c). Following this hypothesis, the A_{1g}^2 phonon with an energy of 22 meV would couple to $\rho(\omega)$ and a negative $R(\omega)$ of the same electric susceptibility, as illustrated in Fig. 3(b). This would again result in increased linewidths and additionally in increased frequencies according to Eqs. (6) and (7). Our hypothesis agrees well with the observed deviations in frequency and linewidth at lower temperatures for the A_{1g}^2 phonon shown in Fig. 2(e). In this picture, we expect to observe these effects at lower temperatures where phonons are frozen out and the scattering mechanism is dominated by the electron-phonon coupling. This is again in good agreement with our data, where we observe deviations from the AD model setting in at temperatures below 120 K. Heid *et al.* have calculated the coupling strengths of the Bi_2Se_3 CSSs to optical modes as a function of phonon energy [47]. They show that enhanced coupling occurs to phonons within an energy range of 17 to 22 meV with a reduced coupling for modes below 10 meV [47]. Even though Heid *et al.* state that the dominant coupling occurs via polar-type optical modes, significant coupling to Raman-active modes of the electron-

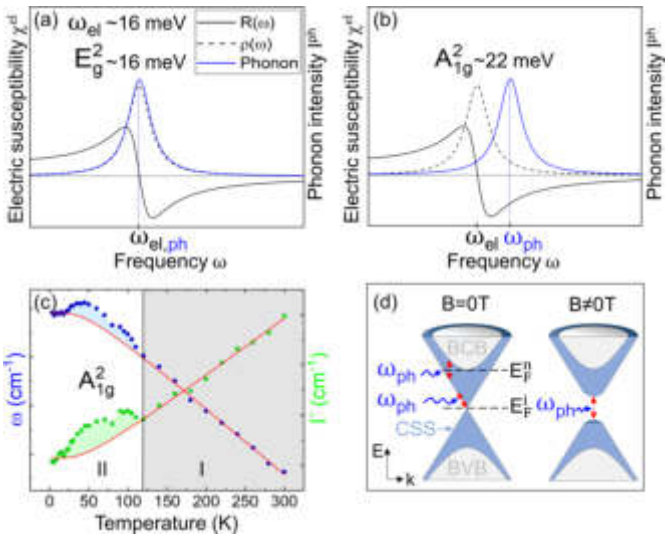

FIG. 3. (a),(b) The real $R(\omega)$ and imaginary $\rho(\omega)$ parts of the electric susceptibility are plotted together with the discrete state of a phonon modeled by a simple Lorentzian with a phonon frequency ω_{ph}. An overlap of both states is shown for the E_g^2 mode in (a) and the A_{1g}^2 mode in (b). (c) Temperature dependence of frequency and linewidth of the Bi_2Se_3 A_{1g}^2 phonon. Two areas are indicated that account for different decay mechanisms of the phonon. (d) Schematic band structure of Bi_2Se_3 with two possible locations of the Fermi level in an intrinsic (E_F^i) and n-doped (E_F^n) Bi_2Se_3 nanoflake. The bulk conduction band (BCB) and bulk valence band (BVB) are labeled. Red arrows illustrate creations of electron-hole pairs by a Raman phonon ω_{ph}. The gapped Dirac cone is shown when a magnetic field $B \neq 0$ T is applied.

phonon interaction is still present, as suggested in several studies [11,48]. Thus, our observations are in good agreement with the calculated coupling strengths, which support our findings for only very weak renormalizations in the A_{1g}^1 mode at 9 meV and strong renormalizations in the E_g^2 (16.7 meV) and A_{1g}^2 (21.9 meV) modes. The preceding analysis leads to the identification of two temperature regions with different dominant scattering mechanisms that are shown in Fig. 3(c). In region I, at higher temperatures, phonon-phonon coupling dominates the phonon decay by the anharmonic interaction and additional contributions from electron-phonon coupling are no longer evident. Therefore, we observe good agreement with the classic AD model in region I, where the bulk properties mask all surface-related effects. In region II, electron-phonon coupling is significant and phonon renormalization can be observed when the surface contribution is high enough.

So far, we discussed the electron-phonon coupling from an energetic point of view. The A_{1g}^1 phonon with an energy of around 9 meV should interfere with the electric susceptibility around 16 meV by coupling to the positive imaginary and real part. However, we do not observe electronic renormalizations for this mode. Hence, an additional aspect has to be considered that affects the coupling strength g between the phonons and the electric susceptibility. The eigenvectors of the phonons show significantly different displacement vectors for the A_{1g}^1 phonon compared to the E_g^2 and A_{1g}^2 phonons. The atomic displacements for the E_g^2 and A_{1g}^2 modes modulate the electric susceptibility related to the CSSs in the following way: For both modes, the partially negatively charged chalcogene (Se, Te) atoms terminating each QL vibrate opposite to the positively charged Bi atoms [18,49], whereas they vibrate in phase for the A_{1g}^1 mode. The electronic polarizability is, therefore, affected more strongly by the E_g^2 and A_{1g}^2 phonons, resulting in a stronger electron-phonon coupling and enhanced self-energy effects.

In a perfect single-crystalline Bi_2Se_3 sample the Fermi level is expected to be located at the Dirac point [7], as indicated in Fig. 3(d). In this case, intracone electronic transitions in the upper Dirac cone are available. The electron-phonon coupling strength increases linearly with the energy distance from the Dirac point due to the linear increase of the density of states expected for the 2D Dirac dispersion [47]. It is also possible that the Fermi level lies closer to the bulk conduction band due to inherent n doping that is often reported for naturally grown Bi_2Se_3 [33] and is also shown in Fig. 3(d). In that case, transitions of the Dirac fermions into the bulk conduction band become possible and add to the intracone contributions. The coupling strength is expected to be enhanced when additional interband transitions are available [47], which explains our observed strong phonon renormalizations. We, therefore, expect the Fermi level in our Bi_2Se_3 samples to lie within the bulk gap but closer to the bulk conduction bands.

The assumption of χ^{el} being related to the CSSs is justified by two aspects. First, we were able to show the enhanced surface contributions of our flakes by the detection of IR modes up to high temperatures. Second, the electric susceptibility in the meV range can be associated with transitions involving Dirac cone states. Additional insight can be gained by manipulating the Dirac cone and the associated electric susceptibility by means of a magnetic field. Since the Dirac cone determines the low-energy electric susceptibility, its modification is also indicative of the presence of the CSSs. The changes in frequency and linewidth of the phonons as a function of magnetic field for Bi_2Se_3 and Bi_2Te_3 are shown in Figs. 4(a) to 4(f).

In agreement with our temperature dependent study and XPS results, we observe a magnetic field dependent renormalization of phonon energies and linewidths in Bi_2Se_3, but not in Bi_2Te_3. The absence of any phonon renormalization in Bi_2Te_3 is again consistent with the reduced electronic density near the Fermi edge compared to the Bi_2Se_3 sample. For Bi_2Se_3, however, magnetic field dependent self-energy corrections are observed in frequency and linewidth for the A_{1g}^2 mode at 177 cm^{-1}. At fields above 3 T, we find a simultaneous hardening and broadening of about 0.6 cm^{-1} and 1.5 cm^{-1}, respectively. Since it is known that in topological insulators a gap opening in the Dirac cone occurs in the presence of a magnetic field [23], our results point to a change in the electric susceptibility of the Dirac cone by the magnetic field. The change in the electric susceptibility would lead to a renormalization in the A_{1g}^2 mode in Bi_2Se_3. A gap opening would shift and redistribute the electric susceptibility. The hardening and broadening of the A_{1g}^2 mode with increasing field strengths indicate the coupling to an electric

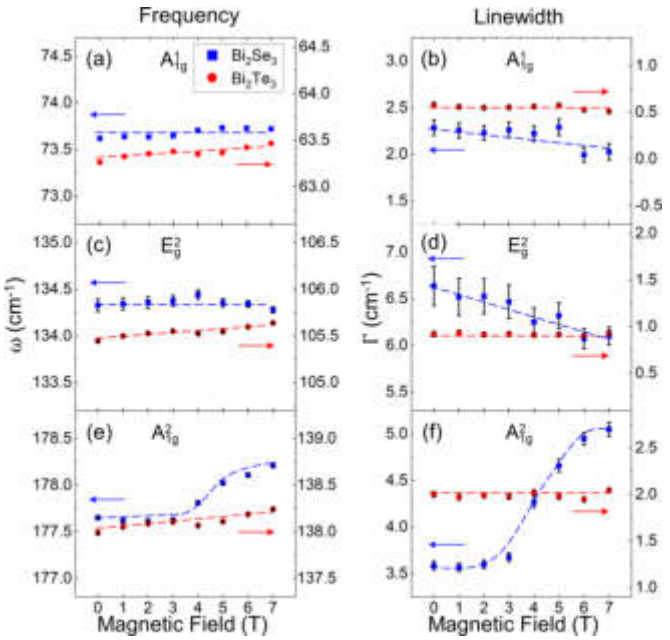

FIG. 4. Magnetic field dependent self-energy effects for Bi_2Se_3 and Bi_2Te_3 nanoflakes at 3 K in (X-)scattering geometry and Faraday configuration. The dependency of the three Raman modes in energy (left column) and linewidth (right column) with magnetic field is shown. All y axes are set to intervals of 2.0 cm^{-1} for easier comparability. Bi_2Te_3 phonons (red curves) show no significant change in energy and linewidth over the applied magnetic field range. For the Bi_2Se_3 phonons (blue curves), clear changes in energy and linewidth can be observed for magnetic fields above 3 T. The dashed lines represent guides to the eye.

susceptibility with a lower energy than the phonon according to Eqs. (6) and (7). The decreasing linewidth of the E_g^2 mode, on the other hand, shows a reduced coupling to the electric susceptibility. We can therefore estimate the energy of a gap opening in the Dirac cone to be in the range of 16 to 22 meV, which would explain the phonon renormalizations. This finding is in agreement with results of Gooth *et al.* [50], who report a gap opening in the order of tens of meV by magnetic interactions in TI. According to our model, the phonons decay by coupling to interband transitions from the lower gapped Dirac cone to the upper one, as visualized in Fig. 3(d). The strong phonon self-energy corrections due to the electron-phonon interactions provide direct evidence for the changes in the electric susceptibility in the CSSs at magnetic field strengths above 3 T.

IV. CONCLUSION

In conclusion, we have investigated thin films of drop-casted Bi_2Se_3 and Bi_2Te_3 nanoflakes by means of temperature and magnetic field dependent Raman spectroscopy. The temperature dependence of the phonon dynamics in our Bi_2Te_3 sample is readily described by the anharmonic phonon-phonon interaction, indicating a dominant bulk behavior. For Bi_2Se_3, we observe deviations from the AD model, which can be linked to additional contributions from the electron-phonon interaction originating from the increased surface contribution. Our study suggests that the Dirac fermions contribute significantly to the electron-phonon interactions, which manifest in the strong phonon renormalizations in Bi_2Se_3 at temperatures below 120 K. Additional magnetic field dependent Raman spectroscopy reveals strong phonon self-energy corrections in Bi_2Se_3, indicating the renormalization of the phonons by the continuum free carriers and a significant magnetoelectric coupling. The self-energy changes in the Bi_2Se_3 phonons provide direct evidence for the manipulation of the CSSs by an applied magnetic field, which can be associated with a gap opening in the Dirac cone.

ACKNOWLEDGMENTS

This work was funded by the Deutsche Forschungsgemeinschaft (DFG; German Research Foundation), DFG RU 773/8-1. Work at the University of Illinois was supported by the National Science Foundation under Grant No. NSF DMR 1800982. S.B., C.U., and M.R. would like to acknowledge the support from the Australian Research Council (ARC) through Grant No. DP170100415. The work at National University of Singapore is supported by the Ministry of Educations of Singapore AcRF Tier-2 (Grants No. MOE2017-T2-1-135, No. 323 MOE2018-T2-2-117, and No. MOE2018-T2-2-117), and Ministry of Education AcRF-1 (Grant No. R-144-000-423-114) and is acknowledged by the support of the Singapore Synchrotron Light Source (SSLS), which is a National Research Infrastructure under the National Research Foundation Singapore via NUS Core Support Grant No. C-380-003-003-001. We thank Robert Frömter and Dorota Koziej for the use of their scanning electron microscopes. We are further thankful for Robert Zierold and Stephan Martens for helpful discussions and magnetization measurements of our samples.

[1] M. Z. Hasan and C. L. Kane, *Colloquium:* Topological insulators, Rev. Mod. Phys. **82**, 3045 (2010).

[2] K. Von Klitzing, The quantized Hall effect, Rev. Mod. Phys. **58**, 519 (1986).

[3] L. Fu, C. L. Kane, and E. J. Mele, Topological Insulators in Three Dimensions, Phys. Rev. Lett. **98**, 106803 (2007).

[4] J. Betancourt, S. Li, X. Dang, J. Burton, E. Tsymbal, and J. Velev, Complex band structure of topological insulator Bi_2Se_3, J. Phys.: Condens. Matter **28**, 395501 (2016).

[5] Y. Ando, Topological insulator materials, J. Phys. Soc. Jpn. **82**, 102001 (2013).

[6] J. G. Analytis, J.-H. Chu, Y. Chen, F. Corredor, R. D. McDonald, Z. X. Shen, and I. R. Fisher, Bulk Fermi surface coexistence with Dirac surface state in Bi_2Se_3: A comparison of photoemission and Shubnikov–de Haas measurements, Phys. Rev. B **81**, 205407 (2010).

[7] H. Zhang, C.-X. Liu, X.-L. Qi, X. Dai, Z. Fang, and S.-C. Zhang, Topological insulators in Bi_2Se_3, Bi_2Te_3 and Sb_2Te_3

with a single Dirac cone on the surface, Nat. Phys. **5**, 438 (2009).

[8] Y. Xia, D. Qian, D. Hsieh, L. Wray, A. Pal, H. Lin, A. Bansil, D. Grauer, Y. S. Hor, R. J. Cava, and M. Z. Hasan, Observation of a large-gap topological-insulator class with a single Dirac cone on the surface, Nat. Phys. **5**, 398 (2009).

[9] Y. L. Chen, J. G. Analytis, J.-H. Chu, Z. K. Liu, S.-K. Mo, X. L. Qi, H. J. Zhang, D. H. Lu, X. Dai, Z. Fang, S. C. Zhang, I. R. Fisher, Z. Hussain, and Z.-X. Shen, Experimental realization of a three-dimensional topological insulator, Bi_2Te_3, Science **325**, 178 (2009).

[10] D. Kim, Q. Li, P. Syers, N. P. Butch, J. Paglione, S. D. Sarma, and M. S. Fuhrer, Intrinsic Electron-Phonon Resistivity of Bi_2Se_3 in the Topological Regime, Phys. Rev. Lett. **109**, 166801 (2012).

[11] C. Chen, Z. Xie, Y. Feng, H. Yi, A. Liang, S. He, D. Mou, J. He, Y. Peng, X. Liu *et al.*, Tunable Dirac fermion dynamics in topological insulators, Sci. Rep. **3**, 2411 (2013).

[12] M. Eddrief, P. Atkinson, V. Etgens, and B. Jusserand, Low-temperature Raman fingerprints for few-quintuple layer topological insulator Bi_2Se_3 films epitaxied on GaAs, Nanotechnology **25**, 245701 (2014).

[13] S. Zhao, C. Beekman, L. Sandilands, J. Bashucky, D. Kwok, N. Lee, A. LaForge, S.-W. Cheong, and K. Burch, Fabrication and characterization of topological insulator Bi_2Se_3 nanocrystals, Appl. Phys. Lett. **98**, 141911 (2011).

[14] K. Shahil, M. Hossain, V. Goyal, and A. Balandin, Micro-Raman spectroscopy of mechanically exfoliated few-quintuple layers of Bi_2Te_3, Bi_2Se_3, and Sb_2Te_3 materials, J. Appl. Phys. **111**, 054305 (2012).

[15] V. Gnezdilov, Y. G. Pashkevich, H. Berger, E. Pomjakushina, K. Conder, and P. Lemmens, Helical fluctuations in the Raman response of the topological insulator Bi_2Se_3, Phys. Rev. B **84**, 195118 (2011).

[16] D. Teweldebrhan, V. Goyal, and A. A. Balandin, Exfoliation and characterization of bismuth telluride atomic quintuples and quasi-two-dimensional crystals, Nano Lett. **10**, 1209 (2010).

[17] K. M. F. Shahil, M. Hossain, D. Teweldebrhan, and A. Balandin, Crystal symmetry breaking in few-quintuple Bi_2Te_3 films: Applications in nanometrology of topological insulators, Appl. Phys. Lett. **96**, 153103 (2010).

[18] W. Richter, C. R. Becker, and H. Köhler, A Raman and far-infrared investigation of phonons in the rhombohedral V_2-VI_3 compounds, Phys. Status Solidi (b) **84**, 619 (1977).

[19] B. Irfan, S. Sahoo, A. P. S. Gaur, M. Ahmadi, M. J.-F. Guinel, R. S. Katiyar, and R. Chatterjee, Temperature dependent Raman scattering studies of three dimensional topological insulators Bi_2Se_3, J. Appl. Phys. **115**, 173506 (2014).

[20] Y. Kim, X. Chen, Z. Wang, J. Shi, I. Miotkowski, Y. P. Chen, P. A. Sharma, A. L. Lima Sharma, M. A. Hekmaty, Z. Jiang, and D. Smirnov, Temperature dependence of Raman-active optical phonons in Bi_2Se_3 and Sb_2Te_3, Appl. Phys. Lett. **100**, 071907 (2012).

[21] F. Zhou, Y. Zhao, W. Zhou, and D. Tang, Temperature-dependent Raman scattering of large size hexagonal Bi_2Se_3 single-crystal nanoplates, Appl. Sci. **8**, 1794 (2018).

[22] D. Li, L. Li, D.-W. Liu, and J.-F. Li, Temperature dependence of the Raman spectra of Bi_2Te_3 and $Bi_{0.5}Sb_{1.5}Te_3$ thermoelectric films, Phys. Status Solidi RRL **6**, 268 (2012).

[23] X.-L. Qi, T. L. Hughes, and S.-C. Zhang, Topological field theory of time-reversal invariant insulators, Phys. Rev. B **78**, 195424 (2008).

[24] Y. Chen, J.-H. Chu, J. Analytis, Z. Liu, K. Igarashi, H.-H. Kuo, X. Qi, S.-K. Mo, R. Moore, D. Lu *et al.*, Massive Dirac fermion on the surface of a magnetically doped topological insulator, Science **329**, 659 (2010).

[25] P. Sessi, R. R. Biswas, T. Bathon, O. Storz, S. Wilfert, A. Barla, K. A. Kokh, O. E. Tereshchenko, K. Fauth, M. Bode *et al.*, Dual nature of magnetic dopants and competing trends in topological insulators, Nat. Commun. **7**, 12027 (2016).

[26] W. Luo and X.-L. Qi, Massive Dirac surface states in topological insulator/magnetic insulator heterostructures, Phys. Rev. B **87**, 085431 (2013).

[27] P. Wei, F. Katmis, B. A. Assaf, H. Steinberg, P. Jarillo-Herrero, D. Heiman, and J. S. Moodera, Exchange-Coupling-Induced Symmetry Breaking in Topological Insulators, Phys. Rev. Lett. **110**, 186807 (2013).

[28] S. Buchenau, P. Sergelius, C. Wiegand, R. Zierold, H. S. Shin, M. Rübhausen, J. Gooth, K. Nielsch *et al.*, Symmetry breaking of the surface mediated quantum Hall effect in Bi_2Se_3 nanoplates using Fe_3O_4 substrates, 2D Mater. **4**, 015044 (2017).

[29] D. Biswas, S. Thakur, K. Ali, G. Balakrishnan, and K. Maiti, Anomalies of a topologically ordered surface, Sci. Rep. **5**, 10260 (2015).

[30] S. Buchenau, L. O. Akinsinde, M. Zocher, D. Rukser, U. Schürmann, L. Kienle, B. Grimm-Lebsanft, and M. Rübhausen, Scalable polyol synthesis for few quintuple layer thin and ultra high aspect ratio Bi_2Se_3 structures, Solid State Commun. **281**, 49 (2018).

[31] Y. Zhang, L. P. Hu, T. J. Zhu, J. Xie, and X. B. Zhao, High yield Bi_2Te_3 single crystal nanosheets with uniform morphology via a solvothermal synthesis, Crystal Growth Des. **13**, 645 (2013).

[32] See Supplemental Material at http://link.aps.org/supplemental/10.1103/PhysRevB.101.245431 for details of the nanoflake synthesis and characterization, additional Raman measurements, and *n*-doping study of the Bi_2Se_3 nanoflakes.

[33] Y. Zhang, K. He, C.-Z. Chang, C.-L. Song, L.-L. Wang, X. Chen, J.-F. Jia, Z. Fang, X. Dai, W.-Y. Shan, S.-Q. Shen, Q. Niu, X.-L. Qi, S.-C. Zhang, X.-C. Ma, and Q.-K. Xue, Crossover of the three-dimensional topological insulator Bi_2Se_3 to the two-dimensional limit, Nat. Phys. **6**, 584 (2010).

[34] H. M. Benia, C. Lin, K. Kern, and C. R. Ast, Reactive Chemical Doping of the Bi_2Se_3 Topological Insulator, Phys. Rev. Lett. **107**, 177602 (2011).

[35] D. Kong, J. J. Cha, K. Lai, H. Peng, J. G. Analytis, S. Meister, Y. Chen, H.-J. Zhang, I. R. Fisher, Z.-X. Shen *et al.*, Rapid surface oxidation as a source of surface degradation factor for Bi_2Se_3, ACS Nano **5**, 4698 (2011).

[36] B. Yan, D. Zhang, and C. Felser, Topological surface states of Bi_2Se_3 coexisting with Se vacancies, Phys. Status Solidi RRL **7**, 148 (2013).

[37] B. Schulz, J. Bäckström, D. Budelmann, R. Maeser, M. Rübhausen, M. V. Klein, E. Schoeffel, A. Mihill, and S. Yoon, Fully reflective deep ultraviolet to near infrared spectrometer and entrance optics for resonance Raman spectroscopy, Rev. Sci. Instrum. **76**, 073107 (2005).

[38] C. Arguello, D. L. Rousseau, and S. P. d. S. Porto, First-order Raman effect in wurtzite-type crystals, Phys. Rev. **181**, 1351 (1969).

[39] J. Zhang, Z. Peng, A. Soni, Y. Zhao, Y. Xiong, B. Peng, J. Wang, M. S. Dresselhaus, and Q. Xiong, Raman spectroscopy of few-quintuple layer topological insulator Bi_2Se_3 nanoplatelets, Nano Lett. **11**, 2407 (2011).

[40] Y. Liang, W. Wang, B. Zeng, G. Zhang, J. Huang, J. Li, T. Li, Y. Song, and X. Zhang, Raman scattering investigation of Bi_2Te_3 hexagonal nanoplates prepared by a solvothermal process in the absence of naoh, J. Alloys Compd. **509**, 5147 (2011).

[41] R. He, Z. Wang, R. L. J. Qiu, C. Delaney, B. Beck, T. E. Kidd, C. C. Chancey, and X. P. A. Gao, Observation of infrared-active modes in Raman scattering from topological insulator nanoplates, Nanotechnology **23**, 455703 (2012).

[42] P. G. Klemens, Anharmonic decay of optical phonons, Phys. Rev. **148**, 845 (1966).

[43] N. Bonini, M. Lazzeri, N. Marzari, and F. Mauri, Phonon Anharmonicities in Graphite and Graphene, Phys. Rev. Lett. **99**, 176802 (2007).

[44] E. H. Hasdeo, A. R. T. Nugraha, M. S. Dresselhaus, and R. Saito, Breit-Wigner-Fano line shapes in Raman spectra of graphene, Phys. Rev. B **90**, 245140 (2014).

[45] M. A. Rübhausen, Electronic correlations in cuprate superconductors - An inelastic light scattering study, Ph.D. thesis, Universität Hamburg, 1998.

[46] M. Cardona, *Light Scattering in Solids I - Introductory Concepts*, edited by M. Cardona (Springer-Verlag, Berlin, 1983).

[47] R. Heid, I. Yu. Sklyadneva, and E. V. Chulkov, Electron-phonon coupling in topological surface states: The role of polar optical modes, Sci. Rep. **7**, 1095 (2017).

[48] T. Kondo, Y. Nakashima, Y. Ota, Y. Ishida, W. Malaeb, K. Okazaki, S. Shin, M. Kriener, S. Sasaki, K. Segawa *et al.*, Anomalous Dressing of Dirac Fermions in the Topological Surface State of Bi_2Se_3, Bi_2Te_3, and Cu-Doped Bi_2Se_3, Phys. Rev. Lett. **110**, 217601 (2013).

[49] S. Mishra, S. Satpathy, and O. Jepsen, Electronic structure and thermoelectric properties of bismuth telluride and bismuth selenide, J. Phys.: Condens. Matter **9**, 461 (1997).

[50] J. Gooth, R. Zierold, P. Sergelius, B. Hamdou, J. Garcia, C. Damm, B. Rellinghaus, H. J. Pettersson, A. Pertsova, C. Canali *et al.*, Local magnetic suppression of topological surface states in Bi_2Te_3 nanowires, ACS Nano **10**, 7180 (2016).

A.2 Quantum Confinement Induced Excitonic Mechanism in Zinc-Oxide-Nanowalled Microrod Arrays for UV-Vis Surface-Enhanced Raman Scattering

The author has contributed to the Raman measurements and the respective data analysis.

THE JOURNAL OF PHYSICAL CHEMISTRY C

Article

Cite This: *J. Phys. Chem. C* 2019, 123, 24957−24962

pubs.acs.org/JPCC

Quantum Confinement Induced Excitonic Mechanism in Zinc-Oxide-Nanowalled Microrod Arrays for UV−Vis Surface-Enhanced Raman Scattering

Jayeong Kim,*[,†,∥] Tomke E. Glier,*[,‡,∥] Benjamin Grimm-Lebsanft,[‡] Sören Buchenau,[‡] Melissa Teubner,[‡] Florian Biebl,[‡] Nam-Jung Kim,[§] Heehun Kim,[§] Gyu-Chul Yi,[§] Michael Rübhausen,*[,‡] and Seokhyun Yoon*[,†]

[†]Department of Physics, Ewha Womans University, 52 Ewhayeodae-gil, Seodaemun-gu, Seoul 03760, Korea

[‡]Institut für Nanostrukturforschung, Center for Free Electron Laser Science (CFEL), Universität Hamburg, Luruper Chaussee 149, Hamburg 22761, Germany

[§]Department of Physics and Astronomy, Institute of Applied Physics, and Research Institute of Advanced Materials (RIAM), Seoul National University, 1 Gwanak-ro, Gwanak-gu, Seoul 08826, Korea

Supporting Information

ABSTRACT: We studied surface-enhanced Raman spectroscopy (SERS) in 4-mercaptopyridine (4-Mpy) deposited on zinc oxide (ZnO) nanostructures, by using resonance Raman scattering covering a range of incident photon energies from 1.7 to 5.7 eV. We investigated all primary routes of the energy-specific resonances that are associated with the electronic transitions between the ZnO valence band (VB) to the lowest unoccupied molecular orbital (LUMO) and the highest occupied molecular orbital (HOMO) to the ZnO conduction band (CB), respectively. Two resonances at 5.55 and 5.15 eV in the ultraviolet (UV) spectral range can be associated with transitions into the CB and most importantly into an excitonic-related state below the ZnO CB, respectively. The energy difference between the UV resonances is 0.4 eV corresponding to the excitonic binding energy as a result of excitonic quantum confinement in the 10−20 nm thick ZnO nanowalls. The observed excitonic SERS resonance enhancement of the ring-breathing mode of 4-Mpy is about 15 times stronger than for the VB resonance observed at 2.43 eV and free of luminescence background. Hence, we outline new pathways of improving the detectability of molecules by chemical SERS due to tuning of the quantum confinement in the excitonic resonance enhancement.

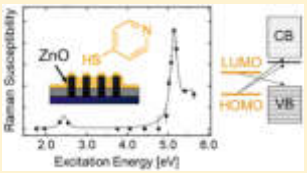

INTRODUCTION

Since its first observation, surface-enhanced Raman scattering (SERS) has been widely used to enhance the often relatively weak Raman cross section.[1−12] SERS has been a subject of intense research in various disciplines such as nanoscale physics, analytical chemistry, and biological physics.[13−15] Very importantly, its extremely high sensitivity makes it possible to realize Raman fingerprinting of a single molecule.[16] This makes SERS a very attractive technique, which can be applied to diverse areas including pharmacy, biological sciences, and forensics.[17,18] However, SERS involves light−matter interaction on a small scale, where quantum mechanical confinement effects could be important.[19] It is generally accepted that there are two main pathways to apply SERS.

Plasmonic SERS involves surface plasmon resonances yielding an electric field enhancement in metallic nanostructures of, e.g., silver and gold, leading to typical enhancement factors (EF) of 10^6.[7−9,20] The near-field enhancement is strongly associated with the shape of the nanoparticles[9] and their geometric arrangement, leading to the strongest enhancement when the gap between the nanostructure reaches molecular dimensions.[21] It is reported that the EF can reach giant values as high as 10^{12} in some cases.[13]

The other pathway is associated with a resonance enhancement mechanism. In general, this effect is the result of charge-transfer resonances between a molecule and a semiconductor or insulator. Since these resonances have to occur between occupied and unoccupied states, they are chemically highly selective, coining the term chemical SERS.[22,23] This effect has no specific constraints regarding the arrangement of the used nanostructures. Here, the nanostructuring is known to enhance the SERS active area.[22−25] Moreover, since substrates for chemical SERS are not metals, there is no intense heating of the nanostructure due to light absorption during the Raman measurements.[26,27]

There are two charge-transfer processes between a molecule and a semiconductor that can lead to resonance Raman enhancement. The first process is associated with transitions between the valence band (VB) of the semiconductor and the

Received: August 1, 2019
Revised: September 13, 2019
Published: September 16, 2019

lowest unoccupied molecular orbital (LUMO). The second process occurs between the highest occupied molecular orbital (HOMO) and the conduction band (CB) of the semiconductor. Moreover, it is known that particularly sharp in-gap excitonic states show strong resonance Raman enhancements,[28] making them prime candidates for enhancing the chemical SERS effect. Excitonic states are also subject to many interesting design options to change their properties that relate, e.g., to doping, to the size of the nanostructure, especially quantum confinement, and to external parameters such as temperature.[29]

Within this Article we report on the nature of the expected charge-transfer resonances between a molecule and a nanostructured semiconductor substrate in chemical SERS. For the case of 4-mercaptopyridine (4-Mpy) on zinc oxide (ZnO) one would expect the VB to LUMO resonance in the visible, which is commonly used in many studies[25] and the HOMO to CB resonance in the deep ultraviolet spectral range, which has not been utilized before. Most importantly, we identify a novel contribution to the UV resonance that can be tracked down to excitonic states. These states can be tuned by the thickness of the ZnO. Due to quantum confinement in the 10−20 nm thick ZnO nanowalls the expected exciton binding energy is shifted from 50 meV in the bulk to 400 meV below the band gap, as also seen in photoluminescence spectra.[30] In order to study all resonance pathways, we utilize a unique resonance Raman setup that is equipped with a fully reflective parabolic entrance objective and a broad range of 15 different laser energies covering the visible to UV spectral range.[31−33]

EXPERIMENTAL METHODS

For the nanostructured ZnO SERS substrates, position-controlled ZnO microrod structures with nanowalls inside were grown on chemical vapor deposition (CVD) graphene films through the catalyst-free CVD process. We obtained ZnO nanowall growth selectivity by depositing an SiO_2 growth mask on the graphene films. The SiO_2 growth masks were prepared by plasma-enhanced CVD (PECVD). Dimensional parameters including the height and diameter of the obtained microrods can be controlled by modifying the lithographic pattern mask or varying the growth parameters of the catalyst-free CVD process. In this work, highly oriented and ordered ZnO mircrorods with an outer diameter of 4 μm and a height of 5 μm were typically employed. The detailed process for growing ZnO nanostructures is described in previous reports.[23,34,35]

For molecule deposition, we immersed the substrates in a 4-Mpy molecular solution ($c = 10^{-4}$ M in methanol) for 2 h and subsequently washed the samples with deionized water.

Raman measurements in the UV and visible spectral range were obtained by the UT-3 Raman spectrometer,[31] which is equipped with a fully reflective custom-made entrance objective allowing an all achromatic focusing of light in the studied spectral range. A Tsunami Ti:sapphire laser system, model 3950-X1BB (Spectra Physics Lasers Inc., California), which was pumped with a green Millennia Pro Xs 10sJS diode laser (Spectra Physics Lasers Inc., California) was used as primary laser source. The fundamental laser line was frequency doubled, tripled, or quadrupled with second harmonic generation, third harmonic generation or fourth harmonic generation (Spectra Physics Lasers Inc., California), respectively. The pulse width of the laser was monitored with an auto correlator (APE GmbH, Berlin) and around 1.7 ps. A gray filter unit enables power reduction of the laser. The laser beam was widened with a spatial filter and then focused on the sample by the main parabola of the objective also collecting the backscattered Raman signal. Measurements at 532 nm were carried out by using a green CW Millennia laser.

For Raman measurement in the visible, we used two additional setups. Measurements at 488 nm (diode laser) and 532 nm (diode-pumped solid state (DPSS) laser) were carried out by using a McPherson 207 spectrometer equipped with a nitrogen-cooled charge-coupled-device (CCD) array detector. A LabRam HREvo 800 spectrometer and a helium−neon laser were used for the 632.8 nm measurement. The excitation power was less than 0.2 mW to avoid laser heating.

The raw Raman spectra were corrected for the spectral response of the Raman spectrometer and normalized to the used laser power and integration time,[31] yielding the Raman susceptibility. The measured intensity of 4-Mpy deposited on ZnO-rods directly represents the Raman susceptibility since a monolayer of molecules was measured.

RESULTS AND DISCUSSION

Figure 1 shows measured corrected Raman intensities (see Experimental Methods for details) of a monolayer of 4-Mpy

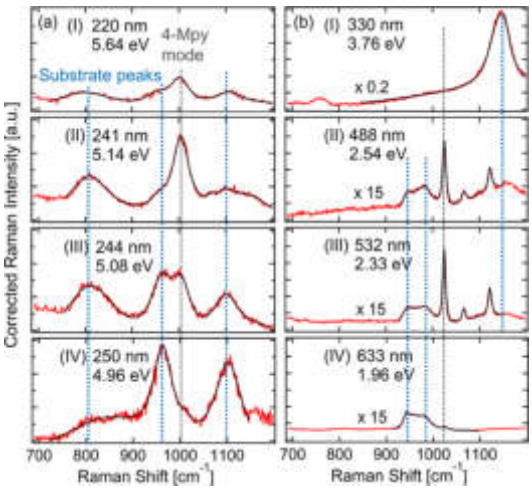

Figure 1. (a) Raman spectra of a monolayer of 4-Mpy deposited on nanostructured ZnO rods for four exemplarily laser energies in the deep UV range between 5.64 eV (220 nm) and 4.96 eV (250 nm). Around 1000 cm^{-1}, the breathing mode of the pyridine ring can be observed. The maximum measured Raman response of this mode was reached at 5.14 eV (241 nm). Other modes only get weakly enhanced, outlining the mode selective enhancement of the chemical SERS effect. (b) Raman spectra of a monolayer of 4-Mpy deposited on ZnO rods for excitation energies covering the mid UV to visible spectral range, i.e., of 3.76 eV (I), 2.54 eV (II), 2.44 eV (III), and 1.96 eV (IV). At 3.76 eV, no 4-Mpy mode can be observed, but at 2.54, 2.33, and 1.96 eV, it can be observed.

adsorbed on nanostructured ZnO-rods for eight exemplarily selected excitation energies out of 15 from 1.96 to 5.64 eV. These excitation energies cover both expected resonances from the molecular HOMO level to the semiconductor CB (deep ultraviolet (UV) spectral range) and the semiconductor VB to the molecular LUMO (visible). In Figure 1a we can observe that the 4-Mpy ring-breathing mode at around 1000 cm^{-1} [23,36,37] is strongly enhanced when tuning the incident photon energy from 4.96 to 5.14 eV, showing an extremely sharp resonance directly below the CB minimum. At

DOI: 10.1021/acs.jpcc.9b07329
J. Phys. Chem. C 2019, 123, 24957−24962

even higher incident photon energies up to 5.64 eV, we still find a substantial resonance enhancement of this mode due to transitions into the continuous CB states. In Figure 1b resonance of the ring-breathing mode in the visible can be observed. At 3.76 eV (330 nm), i.e., in the mid UV, no 4-Mpy mode can be detected, while the ZnO mode is resonant according to the expected VB-CB transition close to 3.4 eV (see also Figure 3).[30] However, concomitantly with the proximity to this interband transition, we observe enhanced fluorescence making Raman measurements between 330 and 488 nm very difficult or even impossible. At 488 nm we can already observe the 4-Mpy modes, which get slightly further enhanced toward 532 nm and then again strongly suppressed at 633 and 704 nm (not shown). Therefore, the maximum Raman response of the ring-breathing mode in the visible can be estimated to be around 2.4 eV. Note that the visible and the UV resonance have different mode-selective couplings since for the UV the coupling to the molecular vibration occurs through the molecular HOMO, whereas the visible resonance occurs through the molecular LUMO. When comparing Figure 1a,b one can also observe a significant line width broadening in the UV, which is attributed to the difference in coupling between HOMO and LUMO states, respectively. It is also noteworthy to mention that the measurements in the UV are highly reproducible due to the lack of any fluorescence backgrounds. In order to discuss the resonance Raman effect that is responsible for the chemical SERS effect, we utilize a simplified Feynman diagram approach of Kawabata.[38]

The Feynman diagram in Figure 2 illustrates the resonant Raman scattering process due to molecular vibrations. For the UV resonance shown in Figure 2a, the light couples to electrons via the $\hat{p}\cdot\vec{A}$ matrix element of a photon with energy $\hbar\omega_{inc}$ and momentum $\hbar k_{inc}$, exciting an electron from the 4-Mpy HOMO to levels near the ZnO CB. The holes of the HOMO in turn couple mode selectively to molecular vibrations. After recombination of the electrons with the holes in the HOMO, photons with ω_{sc} and k_{sc} are emitted. Equivalently, Figure 2b shows the transition of electrons from the VB to the LUMO, which also couple mode selectively to the molecular vibrations of 4-Mpy. The resonance energies are determined by the transitions between HOMO and CB and between VB and LUMO, respectively (see Figure 3b).

The measured intensity of the scattered light $I(\omega)$ is proportional to the imaginary part of the Raman response function $\tilde{R}(\omega)$. For resonance Raman scattering the response function depends on the incidence photon energy $\hbar\omega_{inc}$. After correction for the scattering volume and for a constant temperature, we can calculate the scattering intensity as[31]

$$I(\omega,\omega_{inc}) = -\mathrm{Im}(\tilde{R}(\omega,\omega_{inc})) \tag{1}$$

We can express eq 1 in terms of the Feynman diagram representing the four-photon Green's function, as shown in Figure 2a,b as a resonant Raman response function.[38] In order to derive a simple expression for the modeling of our results, the Feynman diagram can be approximated with the following simplifying assumptions:

- The vibrational excitation itself is independent of the electronic susceptibility requiring that the energy scales of electronic degrees of freedom (a few eV) are decoupled from the molecular vibrational degrees of freedom (smaller than 0.1 eV).

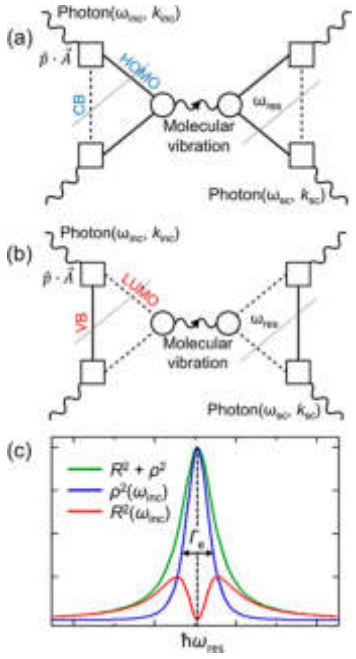

Figure 2. Feynman diagram illustrating the four-photon Green's function of the resonant Raman scattering process coupling electronic states to vibrations. (a) shows the UV resonance occurring between the molecular HOMO level and the semiconductor CB, whereas (b) shows the visible resonance occurring between the semiconductor VB and the molecular LUMO. Both resonances are denoted as dotted lines. Squares depict the photon−electron interaction, where $\hat{p}\cdot\vec{A}$ denotes the matrix element that is linear in the vector potential $\vec{A}$. Photons are represented by wavy lines. The electronic transitions occur between occupied states (solid lines, HOMO, VB) and unoccupied states (dashed lines, CB, LUMO). Circles represent the coupling between electrons and the molecular vibration, which is shown in the middle of the diagram as a wavy line with a rightward arrow. (c) Representation of the squared real part $R^2(\omega)$ (red) and the squared imaginary part $\rho^2(\omega)$ (blue) of the polarization as expressed in eqs 4, 7a, and 7b. The sum of both parts shown in green represents the resonance enhancement of the Raman susceptibility. We have set $\Gamma_e/\hbar\omega_{res}$ equal to 0.02.

- Couplings are constant, real, and independent of the momentum.

Then, we can simplify the Feynman diagram to the following expression

$$\tilde{R}(\omega,\omega_{inc}) = T_e{}^4 g_{ep}{}^2 \left(\quad\right)^2 D_0\,, \tag{2}$$

where T_e is the photon−electron interaction, g_{ep} denotes the electron−phonon coupling constant, D_0 is the vibrational excitation, and denotes the electronic polarizability. Since g_{ep} represents the coupling between an electronic state and molecular vibration, mode selective enhancement can be induced by this factor. The vibrational excitation D_0 with an eigenfrequency of ω_0 and a damping Γ_{vib}, consisting of an imaginary part D_0^{Im} and a real part D_0^{Re} is given by eq 3. The electronic polarizability consists of imaginary and real parts as shown in eq 4, where ω_{inc} is the frequency of the incident photons.

$$D_0 = \frac{1}{\omega^2 - \omega_0{}^2 + 2i\Gamma_{vib}\omega} = D_0^{Re} + iD_0^{Im} \tag{3}$$

DOI: 10.1021/acs.jpcc.9b07329
J. Phys. Chem. C 2019, 123, 24957−24962

$$\left(\vec{\ }\right)^2 = [R(\omega_{inc}) + i\rho(\omega_{inc})]^2 = R^2(\omega_{inc}) + \rho^2(\omega_{inc}) \quad (4)$$

After substitution eqs 4 and 3 into eq 2 and calculating the imaginary part to obtain the scattering intensity according to eq 1, we find the following expression:

$$I(\omega,\omega_{inc}) = T_e^4 g_{ep}^2 \cdot [R^2(\omega_{inc}) + \rho^2(\omega_{inc})] \cdot \frac{2\Gamma_{vib}\omega}{(\omega^2 - \omega_0^2)^2 + (2\Gamma_{vib}\omega)^2} \quad (5)$$

In order to find an expression for the polarization, we have to understand it as a collective excitation between the HOMO and CB, or VB and LUMO, respectively. In discrete molecular states, the polarization is given by a constant C_{max}. The general form of the propagator in the CB or VB is given in eq 6, where ε_k is the respective dispersion relation of electrons and holes in the semiconductor, ω_{elec} is the electronic energy, and δ_k represents the electronic damping.

$$G_0(\vec{k},\omega_{elec}) = \frac{1}{\omega_{elec} - \varepsilon_k + i\delta_k} \quad (6)$$

The real part $R(\omega_{inc})$ and imaginary part $\rho(\omega_{inc})$ of the polarization (see eq 4) can now be written as shown in eqs 7a and 7b. From eq 6 we can derive that the maximum contribution to the transition within the semiconductor occurs at the top of the VB and the bottom of the CB. Note that with the experimentally observed lifetime of the electronic states and the small energy difference between ingoing and outgoing resonances, as shown in Figure 2 as dotted lines cannot be resolved. Hence, we set the resonance energy as simply $E_{HOMO} - E_{CB,min} = \hbar\omega_{res}$ (see also Figure 3b).[39] The inverse lifetime of this electronic excitation is denoted as Γ_e. Figure 2c shows the square of the real and imaginary parts of the electronic susceptibility, $R^2(\omega_{inc})$ and $\rho^2(\omega_{inc})$, to which the phonon couples, respectively. The sum of both parts yields the resonance enhancement factor, $R^2(\omega_{inc}) + \rho^2(\omega_{inc})$. We use this for fitting the resonance profile, as shown in Figure 3a. It is interesting to observe that the enhancement gets significantly widened by considering the real part of the electronic susceptibility and that this is also generating the dominant "off-resonance" contribution.

$$C_{max}^2 \cdot R^2(\omega_{inc}) = C_{max}^2 \cdot \left(\frac{(\omega_{res} - \omega_{inc})}{(\omega_{inc} - \omega_{res})^2 + \Gamma_e^2}\right)^2 \quad (7a)$$

$$C_{max}^2 \cdot \rho^2(\omega_{inc}) = C_{max}^2 \cdot \left(\frac{\Gamma_e}{(\omega_{inc} - \omega_{res})^2 + \Gamma_e^2}\right)^2 \quad (7b)$$

In the case of several resonance levels, a simple superposition of the Feynman diagram in Figure 2 leads after a similar calculation to eq 8, where $\tilde{\alpha}_i = T_{e,i}^4 g_{ep,i}^2 C_{max,i}^2$.

$$I(\omega,\omega_{inc}) = \sum_i \tilde{\alpha}_i \cdot [R_i^2(\omega_{inc}) + \rho_i^2(\omega_{inc})] \cdot \frac{2\Gamma_{vib}\omega}{(\omega^2 - \omega_0^2)^2 + (2\Gamma_{vib}\omega)^2} \quad (8)$$

Our model is in agreement with the approach by others representing the effective resonance process as product of electronic and vibrational wave functions.[39,40]

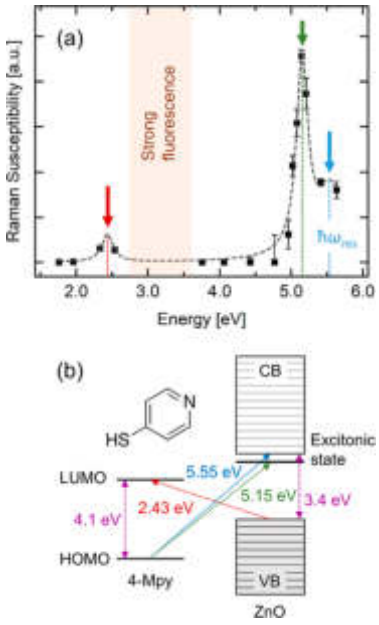

Figure 3. (a) SERS Raman susceptibility (intensity of the Raman response of a 4-Mpy monolayer on ZnO rods) of the mode at 1000 cm^{-1} plotted against the excitation energy. We found a resonance at 2.43 eV and two further resonance levels in the ultraviolet spectral range at 5.15 and 5.55 eV. The resonance profile was fitted by eq 8 (detailed information in the text). (b) Pictorial energy model of the investigated system, outlining the observed resonances in (a) due to the indicated optical transitions. The intrinsic resonance transition of 4-Mpy from HOMO to LUMO (4.1 eV) and the band gap of ZnO (3.4 eV) are shown in violet.

Figure 3a shows the results of our fit to the vibrational intensities, i.e., the resonance Raman profile of the 4-Mpy ring-breathing mode according to the resonance enhancement factors in eq 8. As expected we observe two main resonances, which we can attribute to transitions from the molecular HOMO to the CB in the UV and from the semiconductor VB to the molecular LUMO in the visible. Surprisingly, the UV resonance consists of two contributions. The initial resonance at 5.15 eV is very sharp and responsible for the strong resonance enhancement observed at 5.14 eV in Figure 1a. Above 5.25 eV we observe a shoulder with substantial scattering intensity, as evidenced by the 5.64 eV measurement in Figure 1a. The fit of these resonance levels shows that they are split by about 400 meV. This corresponds in good agreement to the energy difference between the CB and the quantum confined excitonic state in 10−20 nm thick ZnO.[30] As shown in Table 1, the excitonic state exhibits a long lifetime resulting in a damping of only 0.0967 eV, leading to a surprisingly sharp resonance. It is shifted from 50 meV to about 400 meV below the band gap due to confinement effects in thin films. In our case the internal structure of the nanowalled microrods is about 10−20 nm, leading to an enhanced binding energy and stabilization of the exciton.[29,30] Since ZnO has a polar termination surface, one would expect that the direct interface of ZnO is passivated by environmental gases such as H_2O and CO_2 adsorbed directly after the manufacturing process, which prevents the formation of hybrid states with the adsorbed molecule.[30]

Thus, the sharp resonance enhancement in the deep UV is dominated by the presence of an excitonic state induced by the

DOI: 10.1021/acs.jpcc.9b07329
J. Phys. Chem. C 2019, 123, 24957−24962

Table 1. Fit Parameters Corresponding to Figure 2a and Eqs 7a, 7b, and 8 for the Two Observed Resonance in the UV and the Visible[a]

resonance	$\hbar\omega_{res}$ [eV]	σ_E [eV]	$\hbar\Gamma_e$ [eV]	σ_Γ [eV]	$\tilde{\alpha}$	σ_α
UV 1	5.152	6.76×10^{-3}	0.09667	1.15×10^{-2}	4.433×10^{-3}	0.487×10^{-3}
UV 2	5.551	53.1×10^{-3}	0.2500		7.046×10^{-3}	0.565×10^{-3}
Vis	2.435		0.09282	1.16	1.636×10^{-3}	8.92×10^{-3}

[a] σ_E, σ_Γ, and σ_α denote the standard deviations of $\hbar\omega_{res}$, $\hbar\Gamma_e$, and $\tilde{\alpha}$, respectively.

quantum confinement of the 10−20 nm thick ZnO. In the visible the resonance is by a factor of 15 weaker and occurs due to the transition between the semiconductor VB and molecular LUMO without the involvement of any excitonic states. The competing resonance phenomena are summarized in Figure 3b. The red arrow shows the transition at 2.43 eV between the VB and the LUMO, whereas the green and blue arrows denote the deep UV transitions from the HOMO to the excitonic states and the CB. However, it is also clear that the deep UV excitation energies are above the intrinsic "bulk" resonance energies in 4-Mpy, specifically the HOMO to LUMO transition. In Figure 3b the energy splitting of both the molecular HOMO−LUMO levels that is expected to be around 4.1 eV and the ZnO CB to VB splitting that is expected to be around 3.4 eV are shown in violet.[30] The mid UV resonance enhancement of the ZnO modes can be exemplarily seen in Figure 1b for the measurement at 3.76 eV. The presence of intramolecular resonances and charge-transfer resonances between molecule and semiconductor will modify the nominal SERS enhancement factor. Details on the SERS enhancement can be found in the Supporting Information.

CONCLUSION

We studied the SERS effect of 4-mercaptopyridine adsorbed on an array of nanostructured zinc-oxide microrods by resonance Raman spectroscopy in the ultraviolet and visible spectral range. We described the observed resonances by using a phenomenological model based on a four-photon Green's function calculation of the Raman intensity. Two resonances in the UV at 5.15 and 5.55 eV as well as one resonance in the visible at around 2.43 eV were observed. The strongest resonance is found in the UV at 5.15 eV and results from transitions into an excitonic-related state below the ZnO CB. This excitonic resonance is the result of quantum confinement effects in the 10−20 nm thick ZnO nanowalls and the signal enhancement exceeds the visible resonance by a factor of 15. Our results lead to a better detectability and new opportunities to optimize the chemical SERS effect of molecules adsorbed on semiconductor nanostructured rods.

ASSOCIATED CONTENT

Supporting Information

The Supporting Information is available free of charge on the ACS Publications website at DOI: 10.1021/acs.jpcc.9b07329.

Details on the experimental section (SERS substrate preparation and Resonance Raman setup) and the phonon fitting, as well as an estimate on the UV SERS factor (PDF)

AUTHOR INFORMATION

Corresponding Authors

*jayeongkim93@gmail.com.
*tglier@physnet.uni-hamburg.de.
*ruebhausen@physnet.uni-hamburg.de.
*syoon@ewha.ac.kr.

ORCID

Jayeong Kim: 0000-0003-3975-0856
Tomke E. Glier: 0000-0001-8943-1509
Seokhyun Yoon: 0000-0002-4533-646X

Author Contributions

J.K., T.E.G., B.G.L., S.B., M.T., F.B., M.R., and S.Y. conducted the UV−vis Raman measurements. T.E.G., M.R., J.K., and S.Y. analyzed the data and wrote the manuscript. N.J.K., H.K., G.C.Y., and J.K. produced the samples. All authors reviewed the manuscript and did approve submission.

Author Contributions

‖These authors contributed equally.

Notes

The authors declare no competing financial interest.

ACKNOWLEDGMENTS

This work is supported by Basic Science Research Program (NRF-2016R1D1A1B01009032, NRF-2018R1A6A1A03025340) through the National Research Foundation of Korea (NRF) and the Global Research Laboratory Program through the National Research Foundation of Korea (NRF) funded by the Ministry of Science, ICT, and Future Planning (NRF-2015K1A1A2033332 and NRF-2015R1A5A1037627). T.E.G. is partially funded by the Helmholtz Society through DESY, DFG (Deutsche Forschungs Gesellschaft) RU773/8-1.

ABBREVIATIONS

4-Mpy, 4-mercaptopyridine; CB, conduction band; CCD, charge-coupled device; CVD, chemical vapor deposition; EF, SERS enhancement factor; HOMO, highest occupied molecular orbital; LUMO, lowest unoccupied molecular orbital; SERS, surface-enhanced Raman spectroscopy; SiO_2, silicon dioxide; UV, ultraviolet; VB, valence band; vis, visible; ZnO, zinc oxide

REFERENCES

(1) Fleischmann, M.; Hendra, P. J.; McQuillan, A. J. Raman Spectra of Pyridine Adsorbed at a Silver Electrode. *Chem. Phys. Lett.* **1974**, *26*, 163−166.
(2) Moskovits, M. Surface-Enhanced Spectroscopy. *Rev. Mod. Phys.* **1985**, *57*, 783−826.
(3) Jeanmaire, D. L.; Van Duyne, R. P. Surface Raman Spectroelectrochemistry. *J. Electroanal. Chem. Interfacial Electrochem.* **1977**, *84*, 1−20.
(4) Smith, E.; Dent, G. *Modern Raman Spectroscopy - A Practical Approach*; John Wiley & Sons, Ltd.: Chichester, U.K., 2005.
(5) Otto, A. Surface-Enhanced Raman Scattering of Adsorbates. *J. Raman Spectrosc.* **1991**, *22*, 743−752.
(6) Moskovits, M. Surface-Enhanced Raman Spectroscopy: A Brief Retrospective. *J. Raman Spectrosc.* **2005**, *36*, 485−496.

DOI: 10.1021/acs.jpcc.9b07329
J. Phys. Chem. C 2019, 123, 24957−24962

(7) Stiles, P. L.; Dieringer, J. A.; Shah, N. C.; Van Duyne, R. P. Surface-Enhanced Raman Spectroscopy. *Annu. Rev. Anal. Chem.* **2008**, *1*, 601−626.
(8) Xu, H.; Bjerneld, E. J.; Käll, M.; Börjesson, L. Spectroscopy of Single Hemoglobin Molecules by Surface Enhanced Raman Scattering. *Phys. Rev. Lett.* **1999**, *83*, 4357−4360.
(9) Nie, S.; Emory, S. R. Probing Single Molecules and Single Nanoparticles by Surface-Enhanced Raman Scattering. *Science* **1997**, *275*, 1102−1106.
(10) Li, J. F.; Huang, Y. F.; Ding, Y.; Yang, Z. L.; Li, S. B.; Zhou, X. S.; Fan, F. R.; Zhang, W.; Zhou, Z. Y.; Wu, D. Y.; et al. Shell-Isolated Nanoparticle-Enhanced Raman Spectroscopy. *Nature* **2010**, *464*, 392−395.
(11) Tao, A.; Kim, F.; Hess, C.; Goldberger, J.; He, R.; Sun, Y.; Xia, Y.; Yang, P. Langmuir−Blodgett Silver Nanowire Monolayers for Molecular Sensing Using Surface-Enhanced Raman Spectroscopy. *Nano Lett.* **2003**, *3*, 1229−1233.
(12) Santoro, G.; Yu, S.; Schwartzkopf, M.; Zhang, P.; Koyiloth Vayalil, S.; Risch, J. F. H.; Rübhausen, M. A.; Hernández, M.; Domingo, C.; Roth, S. V. Silver Substrates for Surface Enhanced Raman Scattering: Correlation between Nanostructure and Raman Scattering Enhancement. *Appl. Phys. Lett.* **2014**, *104*, 243107.
(13) David, C.; Guillot, N.; Shen, H.; Toury, T.; Chapelle, M. L. de la SERS Detection of Biomolecules Using Lithographed Nanoparticles towards a Reproducible SERS Biosensor. *Nanotechnology* **2010**, *21*, 475501.
(14) Fan, M.; Andrade, G. F. S.; Brolo, A. G. A Review on the Fabrication of Substrates for Surface Enhanced Raman Spectroscopy and Their Applications in Analytical Chemistry. *Anal. Chim. Acta* **2011**, *693*, 7−25.
(15) Kneipp, K.; Kneipp, H.; Itzkan, I.; Dasari, R. R.; Feld, M. S. Surface-Enhanced Raman Scattering and Biophysics. *J. Phys.: Condens. Matter* **2002**, *14*, R597−R624.
(16) Kneipp, K.; Wang, Y.; Kneipp, H.; Perelman, L. T.; Itzkan, I.; Dasari, R. R.; Feld, M. S. Single Molecule Detection Using Surface-Enhanced Raman Scattering (SERS). *Phys. Rev. Lett.* **1997**, *78*, 1667−1670.
(17) Fini, G. Applications of Raman Spectroscopy to Pharmacy. *J. Raman Spectrosc.* **2004**, *35*, 335−337.
(18) Izake, E. L. Forensic and Homeland Security Applications of Modern Portable Raman Spectroscopy. *Forensic Sci. Int.* **2010**, *202*, 1−8.
(19) Xue, X.; Ji, W.; Mao, Z.; Mao, H.; Wang, Y.; Wang, X.; Ruan, W.; Zhao, B.; Lombardi, J. R. Raman Investigation of Nanosized TiO_2: Effect of Crystallite Size and Quantum Confinement. *J. Phys. Chem. C* **2012**, *116*, 8792−8797.
(20) Stockman, M. I. Electromagnetic Theory of SERS. In *Surface-Enhanced Raman Scattering*; Kneipp, K., Moskovits, M., Kneipp, H., Eds.; Springer: Berlin, Heidelberg, 2006; pp 47−65.
(21) Santoro, G.; Yu, S.; Schwartzkopf, M.; Zhang, P.; Koyiloth Vayalil, S.; Risch, J. F. H.; Rübhausen, M. A.; Hernández, M.; Domingo, C.; Roth, S. V. Silver Substrates for Surface Enhanced Raman Scattering: Correlation between Nanostructure and Raman Scattering Enhancement. *Appl. Phys. Lett.* **2014**, *104*, 243107.
(22) Alessandri, I.; Lombardi, J. R. Enhanced Raman Scattering with Dielectrics. *Chem. Rev.* **2016**, *116*, 14921−14981.
(23) Kim, N.-J.; Kim, J.; Park, J.-B.; Kim, H.; Yi, G.-C.; Yoon, S. Direct Observation of Quantum Tunnelling Charge Transfers between Molecules and Semiconductors for SERS. *Nanoscale* **2019**, *11*, 45−49.
(24) Wang, X.; Shi, W.; She, G.; Mu, L. Surface-Enhanced Raman Scattering (SERS) on Transition Metal and Semiconductor Nanostructures. *Phys. Chem. Chem. Phys.* **2012**, *14*, 5891−5901.
(25) Shin, H.-Y.; Shim, E.-L.; Choi, Y.-J.; Park, J.-H.; Yoon, S. Giant Enhancement of the Raman Response Due to One-Dimensional ZnO Nanostructures. *Nanoscale* **2014**, *6*, 14622−14626.
(26) Ding, S.-Y.; You, E.-M.; Tian, Z.-Q.; Moskovits, M. Electromagnetic Theories of Surface-Enhanced Raman Spectroscopy. *Chem. Soc. Rev.* **2017**, *46*, 4042−4076.
(27) Caldarola, M.; Albella, P.; Cortés, E.; Rahmani, M.; Roschuk, T.; Grinblat, G.; Oulton, R. F.; Bragas, A. V.; Maier, S. A. Non-Plasmonic Nanoantennas for Surface Enhanced Spectroscopies with Ultra-Low Heat Conversion. *Nat. Commun.* **2015**, *6*, 7915.
(28) Yu, P. Y.; Cardona, M. *Fundamentals of Semiconductors*, 4th ed.; Springer: Heidelberg, Dordrecht, London, New York, 1996.
(29) Ramsay, A. J. A. Review of the Coherent Optical Control of the Exciton and Spin States of Semiconductor Quantum Dots. *Semicond. Sci. Technol.* **2010**, *25*, 103001.
(30) Mosquera, A. A.; Horwat, D.; Rashkovskiy, A.; Kovalev, A.; Miska, P.; Wainstein, D.; Albella, J. M.; Endrino, J. L. Exciton and Core-Level Electron Confinement Effects in Transparent ZnO Thin Films. *Sci. Rep.* **2013**, *3*, 1714.
(31) Schulz, B.; Bäckström, J.; Budelmann, D.; Maeser, R.; Rübhausen, M.; Klein, M. V.; Schoeffel, E.; Mihill, A.; Yoon, S. Fully Reflective Deep Ultraviolet to near Infrared Spectrometer and Entrance Optics for Resonance Raman Spectroscopy. *Rev. Sci. Instrum.* **2005**, *76*, 073107.
(32) Krüger, R.; Schulz, B.; Naler, S.; Rauer, R.; Budelmann, D.; Bäckström, J.; Kim, K. H.; Cheong, S.-W.; Perebeinos, V.; Rübhausen, M. Orbital Ordering in $LaMnO_3$ Investigated by Resonance Raman Spectroscopy. *Phys. Rev. Lett.* **2004**, *92*, 097203.
(33) Hoffmann, A.; Binder, S.; Jesser, A.; Haase, R.; Flörke, U.; Gnida, M.; Salomone Stagni, M.; Meyer-Klaucke, W.; Lebsanft, B.; Grünig, L. E.; et al. Catching an Entatic State-A Pair of Copper Complexes. *Angew. Chem., Int. Ed.* **2014**, *53*, 299−304.
(34) Park, S. I.; Tchoe, Y.; Baek, H.; Heo, J.; Hyun, J. K.; Jo, J.; Kim, M.; Kim, N.-J.; Yi, G.-C. Growth and Optical Characteristics of High-Quality ZnO Thin Films on Graphene Layers. *APL Mater.* **2015**, *3*, 016103.
(35) Kim, Y.-J.; Yoo, H.; Lee, C.-H.; Park, J. B.; Baek, H.; Kim, M.; Yi, G.-C. Position- and Morphology-Controlled ZnO Nanostructures Grown on Graphene Layers. *Adv. Mater.* **2012**, *24*, 5565−5569.
(36) Zhang, L.; Bai, Y.; Shang, Z.; Zhang, Y.; Mo, Y. Experimental and Theoretical Studies of Raman Spectroscopy on 4-Mercaptopyridine Aqueous Solution and 4-Mercaptopyridine/Ag Complex System. *J. Raman Spectrosc.* **2007**, *38*, 1106−1111.
(37) Hu, H.; Song, W.; Ruan, W.; Wang, Y.; Wang, X.; Xu, W.; Zhao, B.; Ozaki, Y. Fabrication of One-Dimensional ZnO/4-Mpy/Ag Assemblies and Their Spectroscopic Studies. *J. Colloid Interface Sci.* **2010**, *344*, 251−255.
(38) Kawabata, A. Green Function Theory of Raman Scattering. *J. Phys. Soc. Jpn.* **1971**, *30*, 68−85.
(39) Galperin, M.; Ratner, M. A.; Nitzan, A. Raman Scattering in Current-Carrying Molecular Junctions. *J. Chem. Phys.* **2009**, *130*, 144109.
(40) Lombardi, J. R.; Birke, R. L. Theory of Surface-Enhanced Raman Scattering in Semiconductors. *J. Phys. Chem. C* **2014**, *118*, 11120−11130.

DOI: 10.1021/acs.jpcc.9b07329
J. Phys. Chem. C 2019, 123, 24957−24962

A.3 Quantum Confinement of the Spin Berry Phase on 1D Topological Surfaces of Single Bi_2Se_3 Nanowires

The author has contributed to the design of the study, transport measurements, device fabrication and the analysis.

Quantum Confinement of the Spin Berry Phase on 1D Topological Surfaces of Single Bi_2Se_3 Nanowires

Christian Nweze[*‡1], *Tomke E. Glier*[*‡1], *Sarah Scheitz*[1], *Lea Westphal*[1], *Florian Biebl*[1], *Sören Buchenau*[1], *Lewis O. Akinsinde*[1,2], *Niklas Kohlmann*[2], *Lorenz Kienle*[2], *Isabel González Díaz-Placio*[3], *Robert Frömter*[3], *Robert Zierold*[3], *Robert Blick*[3], *Nils Huse*[3], *and Michael Rübhausen*[*‡1]

[1] Institut für Nanostruktur- und Festkörperphysik, Center for Free Electron Laser Science (CFEL), Universität Hamburg, Luruper Chaussee 149, 22761, Hamburg, Germany

[2] Institute for Materials Science, Faculty of Engineering, Kiel University, Kaiserstrasse 2, 24143 Kiel, Germany

[3] Institut für Nanostruktur- und Festkörperphysik, Center for Hybrid Nanostructures (CHyN), Universität Hamburg, Luruper Chaussee 149, 22761, Hamburg, Germany

KEYWORDS: Topological Insulator, Surface Enhanced Raman Scattering, Spin-Berry Phase; Magnetic Field, One-Dimensional, Micro-Raman Spectroscopy

Topological insulators (TIs) exhibit unconventional quantum phases that can be tuned by external quantum confinements. The geometrical crossover from 2D to 1D in a TI results in a novel state with a Spin Berry Phase (SBP). We use Raman scattering on single crystalline Bi_2Se_3-TI nanowires to track the geometrical crossover from quasi 2D to quasi 1D. It is marked by the sudden appearance of plasmonic surface-enhanced Raman scattering (SERS) in nanowires below 100 nm diameter. A magnetic field applied along the wire axis results in a quenched SERS, providing clear evidence that spin-polarized plasmonic excitations of the SBP dominate the electronic excitation spectrum.

Topological insulators (TIs) exhibit Dirac cones, segments of nearly linear dispersion, where both dispersion branches have opposite spin orientation.[1–3] The spin-polarized bands make TIs interesting candidates for many applications such as room-temperature spintronics, quantum computing, and thermoelectric generators.[4] Experimental studies report on the investigation of electrical transport properties from nano-ribbons.[5–11] TIs offer an exciting avenue to study physical anomalies and unconventional states in matter.[6] In particular, geometric quantum confinement leads to exciting effects. For instance, morphing a 3D TI such a Bi_2Se_3 into a 1D cylinder leads to a splitting of the 2D conical Dirac band structure of the SS into 1D discrete subbands.[12,13] As a consequence, 1D plasmonic bands are formed with gaps in the electronic excitation spectrum due to self-interference of the electronic wave functions around the cylinder perimeter. These gaps are inversely proportional to the wire diameter.[12,14] Electronic bands of the TI are spin-polarized and consequently a Spin Berry Phase (SBP) is formed. The application of a magnetic field along the wire axis adds an additional phase shift to the electronic wave function

yielding a high sensitivity to small magnetic fluxes and as a consequence the restoration of the Dirac cone for magnetic fields of the order of a single flux quantum.[12,14,15]

In 3D TIs with planar geometry, such as 2D-flakes and thin films, optical studies of plasmons have provided a deep insight into their electronic structure.[16–22] Raman scattering on TIs has revealed the thickness-dependent quantum confinement of phonons in Bi_2Se_3 flakes and thin films.[20–23] Plasmonic excitations at surfaces can enhance the Raman scattering cross-section by surface-enhanced Raman scattering (SERS).[24,25] Thus, Raman scattering is a powerful tool to study the low-energy excitation spectrum, which is determined by novel plasmonic states, and to understand the coupling between spin, charge, and lattice degrees of freedom in TIs.

Low-energy 1D plasmonic excitations of TIs have an energy scale of the order of 10 meV.[12,13] Direct absorption measurements of the plasmonic excitations will fail, as these low energies correspond to electromagnetic wavelengths of more than 100 µm exceeding the nanowire diameter by far. In this letter, we report on the study of single nanowires in a diameter range suitable to study the geometrical crossover from 2D to 1D TI SS and provide evidence for the presence of a SBP in nanowires with a diameter below 100 nm. We have designed a micro-Raman setup[26] that uses a circular diffraction limited spot with a diameter of (544 ± 13) nm within a magnetic field provided by two permanent magnets (Fig. 1(a) and (b), see SI 4). The heating of the wire even for powers of 140 µW from a 532 nm diode laser, was mitigated by scanning along the nanowire axis (see Fig. 1(a)). We have synthesized circular Bi_2Se_3 nanowires with lengths from 5 µm to 35 µm (see Fig. 1(d)-(f)) and diameters ranging from 22 nm to 800 nm (see SI 2). Bi_2Se_3 nanowires with diameters down to 42 nm together with the laser focus were observed in the custom-made optical microscope, enabling a precise control of the scanning procedure (see Fig. 1(d)). The cylindrical shape of the nanowires is demonstrated by scanning

electron microscopy (SEM) and atomic force microscopy (AFM) images (Fig. 1(e) and (f), see SI 2). High-resolution transmission electron microscopy (HRTEM) confirms the single crystallinity of the wires and a 1D wire growth perpendicular to c-axis direction along the [11-20] axis (Fig. 1(c)) in agreement with previous growth mechanisms.[8,27] The wires exhibit an amorphous oxide shell as can be seen in Fig. 1(c), which is also evident in energy filtered TEM maps of the Oxygen-K edge (see lower inset and SI 2). Energy-dispersive X-ray spectroscopy (EDX) studies shown in the SI (SI 2) support the 2:3 (Bi:Se) stoichiometry. The wire, its quintuple layers, and orientation during the experiment are shown in Fig. 1(b) with the c-axis being perpendicular to the wire axis. We expect a Raman spectrum of phonons that is essentially comparable to that of a conventional 2D-flake of Bi_2Se_3.[23,28] Magneto-transport measurements on devices as shown in Fig. 1(g) obtained from a 260 nm diameter wire reveal the presence of metallic SS. Weak anti-localization effects prove the strong spin-orbit coupling, which is prerequisite for the band inversion and the formation of Dirac-like SS. The measurements show a magnetic field-dependent crossover between 2D- and 1D-electrical transport in agreement with previous observations.[29–31] From the transport measurements the Fermi vectors can be estimated to be $k_F = (1.24 \pm 0.42) \cdot 10^{-2}$ Å^{-1} leading to an effective carrier concentration $n = (k_F)^2/2\pi = 4.9 \cdot 10^{11}$ cm^{-2} in good agreement with the 2:3 stoichiometry. More details are given in SI 8.

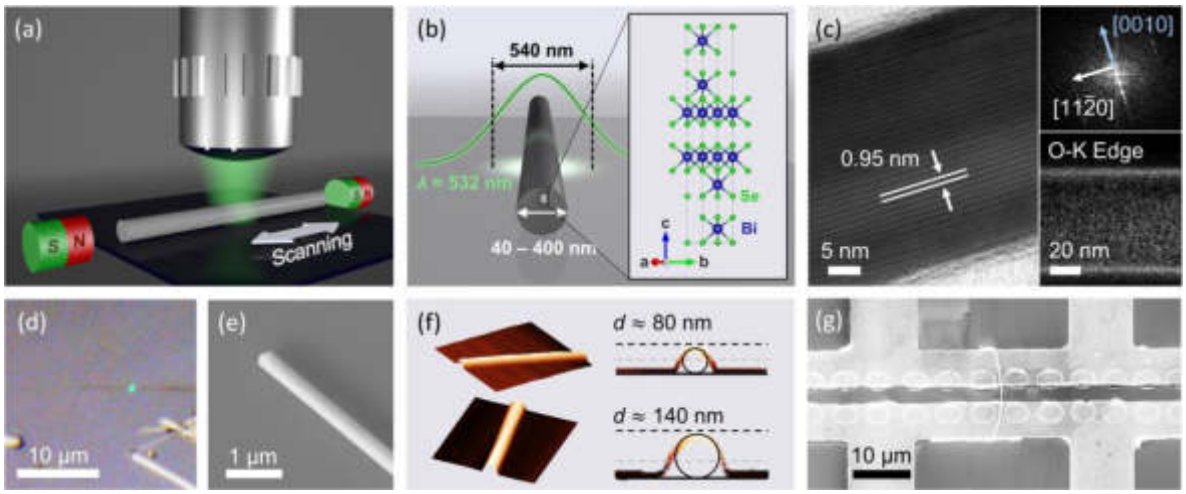

Figure 1. Experimental setup and sample characterization: (a) Sketch of the experimental Raman setup. A 532 nm diode laser beam is focused on a single Bi_2Se_3 nanowire. The scan direction along the wire axis is shown (white arrow). A magnetic field can be applied along the wire axis. (b) Schematic illustration of the quintuple layers and the wire growth in relation to the Raman experiments. (c) HRTEM micrograph of a wire (42 nm diameter). The wire is viewed along [2-1-10] showing the quintuple layer stacking. The FFT shown in the upper inset reveals a growth direction of [11-20] orthogonal to the c-axis. The lower inset presents an exemplary EFTEM elemental map of the O-K edge at 530 eV. (d) Microscopy image of a wire with 73 nm diameter and the laser spot (green). (e) SEM image of a 316 nm wire. (f) Cross-sections as determined by AFM on wires with 80 nm and 140 nm diameter, respectively. The shapes are approximated by circles. (g) Device for transport measurements. The SEM image shows the 260 nm wire connected to the Cr contacts.

The results of the Raman measurements as a function of nanowire diameter are shown in Fig. 2. In Fig. 2(a) we observe the E^2_g- and A^2_{1g}-modes of the Bi_2Se_3 phonons characteristic for the structure building quintuple layers.[32] The measurements of the 2D flake and the 411 nm

nanowire show nearly identical phonon modes, which is in agreement with the stacking of the quintuple layers perpendicular to the wire elongation. The observed Raman intensity decreases proportional to the square of the wire diameter reflecting the decreased scattering volume. Finally, at around 200 nm, the signal strength of the nanowires is lost. Four nanowires with diameters between 180 nm and 225 nm were measured confirming this result. Surprisingly, the intensity of the Raman signal from wires smaller than 100 nm starts to increase again, peaking around 60 nm. This observation marks a clear crossover from a 2D to a 1D behaviour. In order to model the contributing phonons, the line shape can be described by Lorentz- or Fano-profiles.[33–36] The details of the line shape analysis are given in SI 6. For the sake of clarity, we fit Lorentz-profiles to the phonons. In Fig. 2(b) we plot the energy difference between the E^2_g- and A^2_{1g}-modes, which is reduced by about 0.3 meV as the wire diameter is decreased. The simultaneous changes in intensity and relative phonon position point clearly towards the interaction of the phonon with an electronic mode that is characteristic for a 1D confined TI (see SI 7). The intensities of the E^2_g- and A^2_{1g}-modes divided by the square of the wire diameter and normalized to the susceptibility of the 411 nm wire are plotted in Fig. 2(c) and (d). While the E^2_g-mode intensity peaks at a wire diameter of 55 nm the A^2_{1g}-modes intensity continues to rise indicating that the highest intensity of the A^2_{1g}-mode occurs below 40 nm. These results suggest a coupling of these phonons to an electronic low-energy excitation with an excitation energy depending on the diameter of the wire.

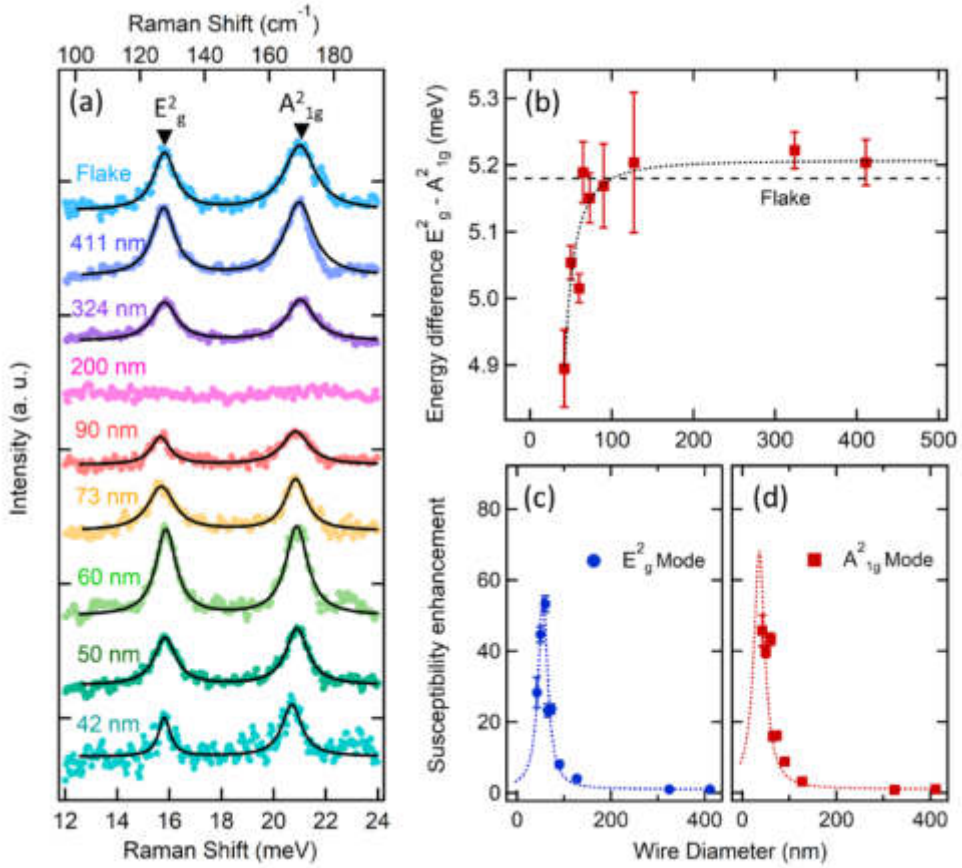

Figure 2. Experimental Raman data: (a) Raman spectra of Bi_2Se_3 nanowires with diameters from 411 nm to 42 nm, as well as from a Bi_2Se_3 flake with a thickness of 10 nm. (b) Energy difference between the E^2_g- and the A^2_{1g}-modes as function of wire diameter. The dashed line guides the eye. (c) Raman susceptibility of the E^2_g-mode and (d) Raman susceptibility of the A^2_{1g}-mode as function of wire diameter. Curves were normalized to their respective susceptibilities at 411 nm. A Lorentzian with a maximum at a wire diameter of 55 nm models the E^2_g-mode susceptibility. (d) A Lorentzian with a maximum at 36 nm was added as guide to the eye.

For circular 3D TIs, surface charges build up with decreasing wire diameter.[12] The resulting electric field can couple to the photon field in Raman scattering. Surface enhanced Raman scattering (SERS) shows Raman enhancements between 10^2 and 10^9 in resonance with surface plasmons of metallic nanoparticles.[24,25] Since the frequency of the optical photons and the frequency of the plasmons in TIs are expected to be different by two orders of magnitude, we adopt a non-resonant picture of the Raman process. This assumption is supported by the fact that the spectra in the 1D regime reveal the same contributing phonons that are present in the 2D limit, suggesting that a local field enhancement effect amplifies the conventional response. This mechanism is pictorially shown in Fig. 3(a). For 3D TI SS that are confined in 1D a photon excites plasmons and the phonons coupling to them get enhanced. In this context, the phonons act as low-energy probe of the electronic excitation spectrum. The energies of the E^2_g-mode and the A^2_{1g}-mode are 15.6 meV and 20.86 meV matching the expected energy scale of the plasmon in the 1D confined SS.[12] The largest effect is expected when the energy of the plasmon matches the phonon energy. Note, the same plasmon that is responsible for the enhancement of the Raman process also interacts with the phonon so that we would expect changes in the phonon frequencies as observed in Fig. 2(b). As shown in SI 6, the E_g^2-mode exhibits a distinctive enhancement of the Fano-parameter at smaller NW diameter concomitantly with an enhanced width (broadening) and shift in mode frequency (hardening) clearly indicating the presence of a novel low-energy mode.[33–35]

A novel quasi-particle excitation in an unconventional quantum state reveals itself by its dispersion relation. Experimentally, one would vary the momentum to probe the dispersion relation. However, the plasmonic dispersion relation depends strongly on the wire diameter. Therefore, our study on single nanowires as a function of wire diameter is suitable to track the

dispersion of electronic excitations in the SBP. The dispersion relation of electronic states of a 1D cylinder in a magnetic field is given by[12,37],

$$\varepsilon_{k,m,r}(R_0) = \pm C_2\sqrt{k^2 + (1 + 2m - 2r)^2\,\tilde{\Delta}^2(R_0)} \quad , \tag{1}$$

with a gap opening in the electronic excitation spectrum that is inversely proportional to the wire diameter

$$\tilde{\Delta}(R_0) = \frac{C_1}{C_2}\frac{1}{2R_0} = \frac{\alpha}{d} \quad . \tag{2}$$

C_1 and C_2 are the inter-spin and inter-orbital coupling constants. R_0 and d are the radius and diameter of the wire, respectively. k is the momentum, m is the sub-band quantum number, and r is the magnetic flux ratio along the wire axis in units of an elementary flux quantum. We take the following values. $m = 0$ assuming that only one sub-band is occupied. This is motivated by the 2:3 stoichiometry (see EDX analysis in SI 2) and transport studies (see SI 8). $k = 0.0005$ Å^{-1} is compatible with the averaged photon momentum transferred to the electrons along the wire axis. From Ref. [12] one obtains $C_2 = C_1 = 3.33$ eV Å. However, we have obtained $\alpha = 0.866$ leading to $C_1 = 2.88$ eV Å. With these parameters, we plot the electronic energies of the first sub-band as a function of wire diameter in Fig. 3(b). The energies of the E^2_g- and A^2_{1g}-phonons are marked by straight lines. Two essential conclusions can be made: Firstly, the impact of the cylindrical quantum confinement becomes relevant for wire diameters below 100 nm and, secondly, the energies of E^2_g-mode and the A^2_{1g}-mode match the excitation energies of the 1D plasmon at slightly different wire diameters of 55 nm and 36 nm, respectively. Both observations are well in line with the key findings in our experiment (Fig. 2(c) and (d)), strongly suggesting that the phonons couple to the photons by means of the electronic SS of the cylindrical TI. Note, with

increasing magnetic flux parallel to the NW axis, it is possible to quench these plasmonic excitations, which vanish for a fractional magnetic flux quantum of $r = 0.5$.[12] Since the topological properties are dominated by the centre of the Brillouin Zone and as we apply a $q \approx 0$ Raman probe, we will evaluate the Feynman diagram in the $k = q \approx 0$ limit. From the Feynman diagram shown in Fig. 3(a)[38] we obtain:

$$I(\omega, R_0) = -\mathrm{Im}\left[M_0^2\, \chi_{\mathrm{Plas}}^2(R_0)\, \chi_{\mathrm{Phon}}\right] \ , \tag{3}$$

where $M_0^2 = \left|\frac{A_{\mathrm{local}}^2}{A^2}\right|^2 g^2$, with A^2 being the first order non-resonant term of the light-matter interaction to a free electronic particle and g being the electron-phonon coupling constant. A_{local}^2 is representing the local field enhancement, which we estimate to be of the order of 10 A^2. The plasmonic susceptibility depends now critically on R_0 due to the dispersion relation (equation (1)). The real and imaginary parts of the plasmonic susceptibility can be modelled by[39]

$$\chi_{\mathrm{Plas}}(R_0) = \frac{1}{\omega^2 - \left(2\varepsilon_{k,m,r}(R_0)\right)^2 + 2i\frac{\varepsilon_{k,m,r}(R_0)}{\tau_k}} \ , \tag{4}$$

with τ_k being the plasmon lifetime. The phonon susceptibility is given by

$$\chi_{\mathrm{Phon}}(\omega_0, \Gamma) = \frac{1}{\omega^2 - \omega_0^2 + 2i\Gamma} \ . \tag{5}$$

The observed Raman intensity depends on the radius of a nanowire *via* the dispersion relation (equation (1)) in the susceptibility of the 1D-plasmon. The required input parameters were fixed in the following way. The bare phonon frequencies ω_0 and damping constants Γ for both phonons were taken from the 2D limit, i.e. fits to the phonon spectrum of the flake. The dispersion in equation (4) was identical to the one shown in Fig. 3(b). The only unknown

parameter is the plasmon lifetime. It determines the width of the resonance as a function of wire diameter. For the calculations shown in Fig. 3(c) we have assumed an interaction of both phonons with one and the same plasmonic excitation and an estimated plasmon lifetime of 500 ps. When comparing Fig. 2(c) and (d) with Fig. 3(d), it is evident that our simplified calculation can reproduce the experimentally derived different resonance behaviours of the E^2_g- and A^2_{1g}-modes by considering a single plasmonic mode that obeys the dispersion relation of equation (1) with $m = 0$ and $r = 0$ (for more details see SI 7).

If these plasmons originate from the proposed SBP they should be very sensitive to the application of even small magnetic fields, as indicated by the sensitivity of the dispersion (equation (1)) to an applied magnetic field (see Fig. 3(b)). The critical value is half a flux quantum.[12] For wires of 90 nm and 62 nm diameter this corresponds to magnetic fields of about 165 mT and 350 mT, respectively. We have applied a field in axial geometry as outlined in Fig. 1(a). The results are shown for a 62 nm wire in Fig. 3(e) with a field of 80 mT corresponding to $r = 0.13$ in equation (1). The effect was reproduced for a wire with a diameter of 90 nm (see SI 4). The SERS is completely quenched with an applied magnetic field and recovers to the original results without field. This behaviour is even more dramatic than anticipated by our model. The calculation in Fig. 3(f), performed with the same parameters as the calculations in Fig. 3(c), would indicate a strongly suppressed E^2_g-mode but only a 40 % suppression on the high energy A^2_{1g}-mode. Yet, we could not find any sign of the A^2_{1g}-mode in magnetic field measurements on wires with diameters of 62 nm and 90 nm. The extraordinarily strong magnetic field suppression clearly supports the presence of the SBP in 1D quantum confined TIs. Furthermore, the strong dependence suggest that magnetic fields applied along the

wire axis influence parameters such as the ratio α indicating changed inter-spin or inter-orbital coupling constants.

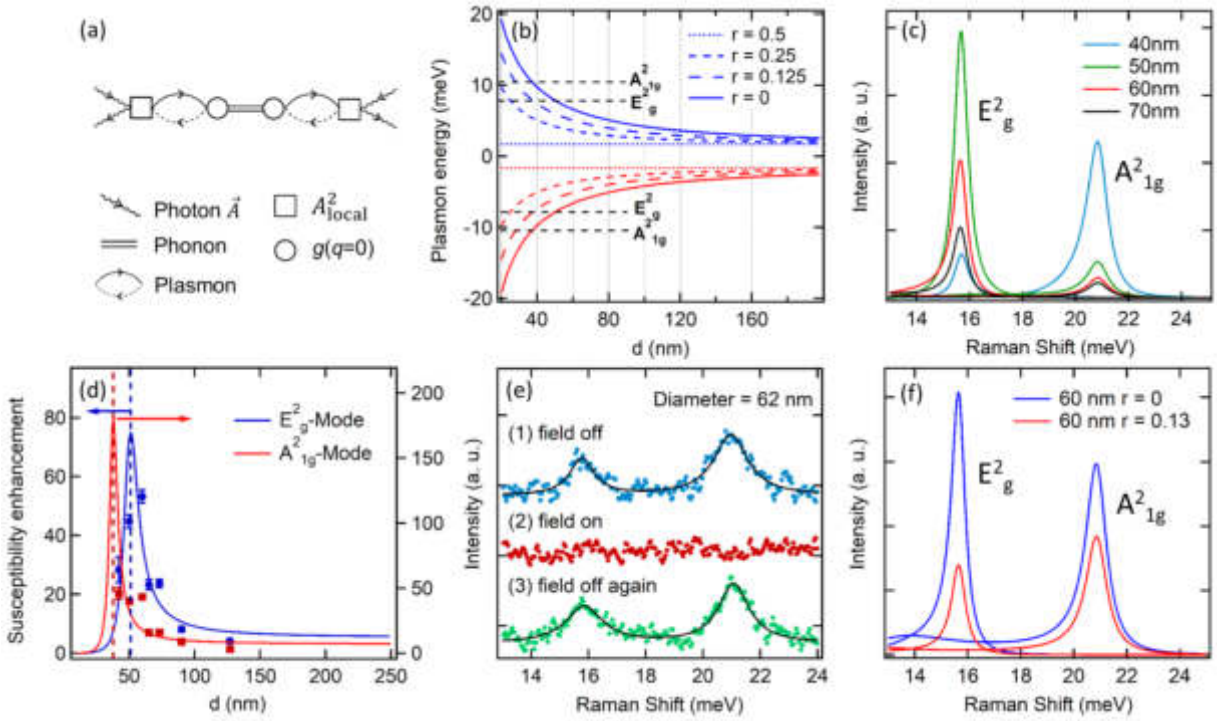

Figure 3. Simulation of the Raman data: (a) Feynman diagram showing the Raman process for phonons. (b) Dispersion $\varepsilon_{k,m,r}(R_0)$ for $m = 0$ (first sub band) of a cylindrical nanowire for finite momentum $k = 0.0005$ Å^{-1} as a function of wire diameter with $\alpha = 0.866$ and ratios r of the magnetic flux quantum ($r = 0$ to r = 0.5). Dashed straight lines mark the phonon energies. As the gap opens, the surface plasmons interact with the phonons and enhance the observed Raman phonon intensities. (c) Calculated non-resonant SERS of the 1D TI nanowires for different wire diameters. The E^2_g-mode at 15.6 meV goes into resonance for larger wire diameters as compared to the A^2_{1g}-mode at 20.86 meV. (d) Calculated (solid line) and experimentally observed (markers) susceptibility enhancement of the E^2_g- and A^2_{1g}-mode. The Raman susceptibilities were normalized to the susceptibilities at 411 nm. (e) Experimental Raman spectra of a 62 nm

wire without, with, and again without magnetic field of 80 mT (see SI 4). (f) Simulated Raman spectra as a function of magnetic field.

In conclusion, we have shown the geometrical crossover from a 2D to 1D confined topologically protected SS below a critical nanowire diameter of about 100 nm. The 1D TI SS exhibits SERS that is strongly dependent on the diameter of the nanowires. We attribute these effects to novel spin-polarized plasmonic excitations within the SBP. We support this assignment by the observed SERS signal and the signal quenching induced by very small magnetic fluxes along the wire axis. The basic features of our experiments could be understood by modelling the coupling between spin-polarized 1D plasmons of the TI with the phonons. The 1D plasmons obey the expected dispersion relation and the only free parameters used in our model are α and τ representing the ratio between inter-spin to inter-orbital coupling strengths and the plasmon lifetime, respectively. Thus, we have provided clear evidence that spin-polarized plasmonic excitations of the SBP dominate the electronic excitation spectrum and we have established a new route to study low-energy excitation spectrum of 1D TI nanowires by means of Raman scattering.

ASSOCIATED CONTENT

Supporting Information. PDF is available divided into the following sections: Bi_2Se_3 nanowire synthesis (SI 1); Sample characterization (SI 2); Raman measurements (SI 3); Magnetic field dependent Raman measurements (SI 4); Data analysis (SI 5); Line shape analysis (SI 6); Calculation (SI 7); Nanowires and magnetic-transport measurements (SI 8).

AUTHOR INFORMATION

Corresponding Author

* C.N.: cnweze@physnet.uni-hamburg.de, T.E.G.: tglier@physnet.uni-hamburg.de, M.R.: ruebhausen@physnet.uni-hamburg.de

Author Contributions

Design of the study: M.R., C.N., T.E.G.; Oven CVD: C.N. L.A. S.B.; Sample synthesis and fabrication: C.N.; Raman setup: M.R., T.E.G., L.W., F.B.; Raman measurements: T.E.G., L.W., S.S., C.N., M.R.; SEM/EDX: R.F., C.N., N.H., S.S.; TEM/EDX: N.K., C.N., L.K., L.A.; AFM: S.S., F.B., C.N.; Transport measurements, device fabrication, and analysis: R.Z., R.B., I.G.D.-P., C.N., S.B.; Theory and simulation: M.R. and T.E.G.; Writing of the manuscript: M.R., T.E.G., C.N., N.H., with input from all co-authors. ‡These authors contributed equally.

Funding Sources

We acknowledge financial support via HGF/DESY and DFG 773/8-1 (M.R.) and KI 1263/17-1 (L.K.). C.N. is Funded by Tertiary Education Trust Fund (TETFund) Abuja, Nigeria, through Nnamdi Azikiwe University, Awka, Nigeria under Academic Staff Training and Development Programme.

ACKNOWLEDGMENT

The authors thank Dirk Manske (MPI Stuttgart), Andrivo Rusydi (NUS), and Lance Cooper (UIUC) for productive discussions. We acknowledge the Siemens PLM Software for using Solid Edge 2020.

ABBREVIATIONS

AFM, atomic force microscopy; EFTEM, energy filtered TEM; FFT, fast Fourier transformation; SBP, Spin Berry Phase; SEM, scanning electron microscopy; SERS, surface enhanced Raman scattering; SS, surface states; TEM, transmission electron microscopy; HRTEM, high resolution TEM; TI, topological insulator.

REFERENCES

(1) Fu, L.; Kane, C. L.; Mele, E. J. Topological Insulators in Three Dimensions. *Phys. Rev. Lett.* **2007**, *98* (10), 106803. https://doi.org/10.1103/PhysRevLett.98.106803.

(2) Fu, L.; Kane, C. L. Topological Insulators with Inversion Symmetry. *Phys. Rev. B* **2007**, *76* (4), 045302. https://doi.org/10.1103/PhysRevB.76.045302.

(3) Qi, X.-L.; Zhang, S.-C. Topological Insulators and Superconductors. *Rev. Mod. Phys.* **2011**, *83* (4), 1057–1110. https://doi.org/10.1103/RevModPhys.83.1057.

(4) Eibl, O.; Nielsch, K.; Peranio, N.; Völklein, F. *Thermoelectric Bi2Te3 Nanomaterials*; Eibl, O., Nielsch, K., Peranio, N., Völklein, F., Eds.; Wiley-VCH Verlag GmbH & Co. KGaA: Weinheim, Germany, 2015. https://doi.org/10.1002/9783527672608.

(5) Dufouleur, J.; Veyrat, L.; Teichgraeber, A.; Neuhaus, S.; Nowka, C.; Hampel, S.; Cayssol, J.; Schumann, J.; Eichler, B.; Schmidt, O.; et al. Quasi-Ballistic Transport of Dirac Fermions in a Bi2Se3 Nanowire. *Phys. Rev. Lett.* **2012**, *110* (18), 186806. https://doi.org/10.1103/PhysRevLett.110.186806.

(6) Gooth, J.; Niemann, A. C.; Meng, T.; Grushin, A. G.; Landsteiner, K.; Gotsmann, B.; Menges, F.; Schmidt, M.; Shekhar, C.; Süß, V.; et al. Experimental Signatures of the Mixed

Axial–Gravitational Anomaly in the Weyl Semimetal NbP. *Nature* **2017**, *547* (7663), 324–327. https://doi.org/10.1038/nature23005.

(7) Peng, H.; Lai, K.; Kong, D.; Meister, S.; Chen, Y.; Qi, X.-L.; Zhang, S.-C.; Shen, Z.-X.; Cui, Y. Aharonov–Bohm Interference in Topological Insulator Nanoribbons. *Nat. Mater.* **2010**, *9* (3), 225–229. https://doi.org/10.1038/nmat2609.

(8) Kong, D.; Randel, J. C.; Peng, H.; Cha, J. J.; Meister, S.; Lai, K.; Chen, Y.; Shen, Z.-X.; Manoharan, H. C.; Cui, Y. Topological Insulator Nanowires and Nanoribbons. *Nano Lett.* **2010**, *10* (1), 329–333. https://doi.org/10.1021/nl903663a.

(9) Hong, S. S.; Zhang, Y.; Cha, J. J.; Qi, X.-L.; Cui, Y. One-Dimensional Helical Transport in Topological Insulator Nanowire Interferometers. *Nano Lett.* **2014**, *14* (5), 2815–2821. https://doi.org/10.1021/nl500822g.

(10) Zhang, K.; Pan, H.; Wei, Z.; Zhang, M.; Song, F.; Wang, X.; Zhang, R. Synthesis and Magnetotransport Properties of Bi2Te3 Nanowires. *Chinese Phys. B* **2017**, *26* (9), 096101. https://doi.org/10.1088/1674-1056/26/9/096101.

(11) Bardarson, J. H.; Brouwer, P. W.; Moore, J. E. Aharonov-Bohm Oscillations in Disordered Topological Insulator Nanowires. *Phys. Rev. Lett.* **2010**. https://doi.org/10.1103/PhysRevLett.105.156803.

(12) Iorio, P.; Perroni, C. A.; Cataudella, V. Plasmons in Topological Insulator Cylindrical Nanowires. *Phys. Rev. B* **2017**, *95* (23), 235420. https://doi.org/10.1103/PhysRevB.95.235420.

(13) Imura, K.-I.; Takane, Y.; Tanaka, A. Spin Berry Phase in Anisotropic Topological Insulators. *Phys. Rev. B* **2011**, *84* (19), 195406. https://doi.org/10.1103/PhysRevB.84.195406.

(14) Iorio, P.; Perroni, C. A.; Cataudella, V. Quantum Interference Effects in Bi2Se3 Topological Insulator Nanowires with Variable Cross-Section Lengths. *Eur. Phys. J. B* **2016**, *89* (4), 97. https://doi.org/10.1140/epjb/e2016-70041-7.

(15) Shi, L.-K.; Lou, W.-K. Surface States of Bi2Se3 Nanowires in the Presence of Perpendicular Magnetic Fields. *Chinese Phys. Lett.* **2014**, *31* (6), 067304. https://doi.org/10.1088/0256-307X/31/6/067304.

(16) Zhang, H.; Liu, C.-X.; Qi, X.-L.; Dai, X.; Fang, Z.; Zhang, S.-C. Topological Insulators in Bi2Se3, Bi2Te3 and Sb2Te3 with a Single Dirac Cone on the Surface. *Nat. Phys.* **2009**, *5* (6), 438–442. https://doi.org/10.1038/nphys1270.

(17) Fei, Z.; Andreev, G. O.; Bao, W.; Zhang, L. M.; McLeod, A. S.; Wang, C.; Stewart, M. K.; Zhao, Z.; Dominguez, G.; Thiemens, M.; et al. Infrared Nanoscopy of Dirac Plasmons at the Graphene–SiO2 Interface. *Nano Lett.* **2011**, *11* (11), 4701–4705. https://doi.org/10.1021/nl202362d.

(18) Lai, Y.-P.; Lin, I.-T.; Wu, K.-H.; Liu, J.-M. Plasmonics in Topological Insulators. *Nanomater. Nanotechnol.* **2014**, *4* (1), 13. https://doi.org/10.5772/58558.

(19) Autore, M.; Engelkamp, H.; D'Apuzzo, F.; Gaspare, A. Di; Pietro, P. Di; Vecchio, I. Lo; Brahlek, M.; Koirala, N.; Oh, S.; Lupi, S. Observation of Magnetoplasmons in Bi2Se3 Topological Insulator. *ACS Photonics* **2015**, *2* (9), 1231–1235.

https://doi.org/10.1021/acsphotonics.5b00036.

(20) Glinka, Y. D.; Babakiray, S.; Lederman, D. Plasmon-Enhanced Electron-Phonon Coupling in Dirac Surface States of the Thin-Film Topological Insulator Bi2Se3. *J. Appl. Phys.* **2015**, *118* (13), 135713. https://doi.org/10.1063/1.4932667.

(21) Shahil, K. M. F.; Hossain, M. Z.; Goyal, V.; Balandin, A. A. Micro-Raman Spectroscopy of Mechanically Exfoliated Few-Quintuple Layers of Bi2Te3, Bi2Se3, and Sb2Te3 Materials. *J. Appl. Phys.* **2012**, *111* (5), 054305. https://doi.org/10.1063/1.3690913.

(22) Eddrief, M.; Atkinson, P.; Etgens, V.; Jusserand, B. Low-Temperature Raman Fingerprints for Few-Quintuple Layer Topological Insulator Bi2Se3 Films Epitaxied on GaAs. *Nanotechnology* **2014**, *25* (24), 245701. https://doi.org/10.1088/0957-4484/25/24/245701.

(23) Zhang, J.; Peng, Z.; Soni, A.; Zhao, Y.; Xiong, Y.; Peng, B.; Wang, J.; Dresselhaus, M. S.; Xiong, Q. Raman Spectroscopy of Few-Quintuple Layer Topological Insulator Bi2Se3 Nanoplatelets. *Nano Lett.* **2011**, *11* (6), 2407–2414. https://doi.org/10.1021/nl200773n.

(24) Lee, S. J.; Guan, Z.; Xu, H.; Moskovits, M. Surface-Enhanced Raman Spectroscopy and Nanogeometry: The Plasmonic Origin of SERS. *J. Phys. Chem. C* **2007**, *111* (49), 17985–17988. https://doi.org/10.1021/jp077422g.

(25) Santoro, G.; Yu, S.; Schwartzkopf, M.; Zhang, P.; Koyiloth Vayalil, S.; Risch, J. F. H.; Rübhausen, M. A.; Hernández, M.; Domingo, C.; Roth, S. V. Silver Substrates for Surface Enhanced Raman Scattering: Correlation between Nanostructure and Raman Scattering Enhancement. *Appl. Phys. Lett.* **2014**, *104* (24), 243107. https://doi.org/10.1063/1.4884423.

(26) Schulz, B.; Bäckström, J.; Budelmann, D.; Maeser, R.; Rübhausen, M.; Klein, M. V.; Schoeffel, E.; Mihill, A.; Yoon, S. Fully Reflective Deep Ultraviolet to near Infrared Spectrometer and Entrance Optics for Resonance Raman Spectroscopy. *Rev. Sci. Instrum.* **2005**, *76* (7), 073107. https://doi.org/10.1063/1.1946985.

(27) Yan, Y.; Liao, Z.-M.; Zhou, Y.-B.; Wu, H.-C.; Bie, Y.-Q.; Chen, J.-J.; Meng, J.; Wu, X.-S.; Yu, D.-P. Synthesis and Quantum Transport Properties of Bi2Se3 Topological Insulator Nanostructures. *Sci. Rep.* **2013**, *3* (1), 1264. https://doi.org/10.1038/srep01264.

(28) Buchenau, S.; Akinsinde, L. O.; Zocher, M.; Rukser, D.; Schürmann, U.; Kienle, L.; Grimm-Lebsanft, B.; Rübhausen, M. Scalable Polyol Synthesis for Few Quintuple Layer Thin and Ultra High Aspect Ratio Bi2Se3 Structures. *Solid State Commun.* **2018**, *281*, 49–52. https://doi.org/10.1016/j.ssc.2018.07.003.

(29) Buchenau, S.; Sergelius, P.; Wiegand, C.; Bäßler, S.; Zierold, R.; Shin, H. S.; Rübhausen, M.; Gooth, J.; Nielsch, K. Symmetry Breaking of the Surface Mediated Quantum Hall Effect in Bi2Se3 Nanoplates Using Fe3O4 Substrates. *2D Mater.* **2017**, *4* (1), 015044. https://doi.org/10.1088/2053-1583/aa525e.

(30) Bäßler, S.; Hamdou, B.; Sergelius, P.; Michel, A.-K.; Zierold, R.; Reith, H.; Gooth, J.; Nielsch, K. One-Dimensional Edge Transport on the Surface of Cylindrical Bi x Te 3−y Se y Nanowires in Transverse Magnetic Fields. *Appl. Phys. Lett.* **2015**, *107* (18), 181602. https://doi.org/10.1063/1.4935244.

(31) Hamdou, B.; Gooth, J.; Dorn, A.; Pippel, E.; Nielsch, K. Aharonov-Bohm Oscillations and Weak Antilocalization in Topological Insulator Sb 2 Te 3 Nanowires. *Appl. Phys. Lett.*

2013, *102* (22), 223110. https://doi.org/10.1063/1.4809826.

(32) Richter, W.; Becker, C. R. A Raman and Far-Infrared Investigation of Phonons in the Rhombohedral V2–VI3 Compounds Bi2Te3, Bi2Se3, Sb2Te3 and Bi2(Te1−xSex)3 (0 <x < 1), (Bi1−ySby)2Te3 (0 <y < 1). *Phys. Status Solidi* **1977**, *84* (2), 619–628. https://doi.org/10.1002/pssb.2220840226.

(33) Bock, A.; Ostertun, S.; Das Sharma, R.; Rübhausen, M.; Subke, K.-O.; Rieck, C. T. Anomalous Self-Energy Effects of the B1g Phonon in Y1-x(Pr,Ca)XBa2Cu3O7 Films. *Phys. Rev. B* **1999**, *60* (5), 3532–3537. https://doi.org/10.1103/PhysRevB.60.3532.

(34) Chen, X. K.; Altendorf, E.; Irwin, J. C.; Liang, R.; Hardy, W. N. Oxygen-Concentration Dependence of the Raman Continua in YBa2Cu3Oy Single Crystals. *Phys. Rev. B* **1993**, *48* (14), 10530–10536. https://doi.org/10.1103/PhysRevB.48.10530.

(35) Friedl, B.; Thomsen, C.; Cardona, M. Determination of the Superconducting Gap in RBa2Cu3O7−δ. *Phys. Rev. Lett.* **1990**, *65* (7), 915–918. https://doi.org/10.1103/PhysRevLett.65.915.

(36) Cooper, S. L.; Klein, M. V. Light Scattering Studies of the Low Frequency Excitation Spectra of High Temperature Superconductors. *Comments Cond. Mat. Phys* **1990**, *15* (2), 99–124. https://doi.org/10.1007/978-3-662-04221-2_6.

(37) Bechstedt, F. *Many-Body Approach to Electronic Excitations - Concepts and Applications*; 2015. https://doi.org/10.1007/978-3-662-44593-8_19.

(38) Kawabata, A. Green Function Theory of Raman Scattering. *J. Phys. Soc. Japan* **1971**, *30*

(1), 68–85. https://doi.org/10.1143/JPSJ.30.68.

(39) Mattuck, R. D. *A Guide to Feynman Diagrams in the Many-Body Problem*; 1967.

Table of Contents:

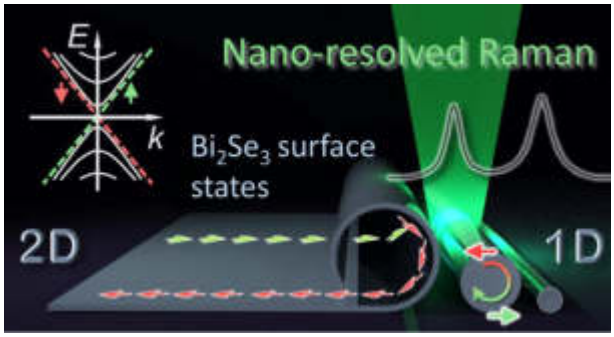

B List of Publications

Sören Buchenau

June 2022 *Manipulating Electron Transfer – The Influence of Substituents on Novel Copper Guanidine Quinolinyl Complexes*
Chemical Science, Vol. 13, P. 8274-8288
Heck, Joshua and Metz, Fabian and **Buchenau, Sören** and Teubner, Melissa and Grimm-Lebsanft, Benjamin and Spaniol, Thomas P and Hoffmann, Alexander and Rübhausen, Michael A and Herres-Pawlis, Sonja

November 2021 *Influence of the Amine Donor on Hybrid Guanidine-Stabilized bis-(μ-oxido) Dicopper (III) Complexes and their Tyrosinase-Like Oxygenation Activity Towards Polycyclic Aromatic Alcohols*
Journal of Inorganic Biochemistry, Vol. 224, P. 111541
Paul, Melanie and Teubner, Melissa and Grimm-Lebsanft, Benjamin and **Buchenau, Sören** and Hoffmann, Alexander and Rübhausen, Michael and Herres-Pawlis, Sonja

June 2021 *Catalytic Oxygenation of Hydrocarbons by Mono-μ-oxo Dicopper (II) Species Resulting from O–O Cleavage of Tetranuclear CuI/CuII Peroxo Complexes*
Angewandte Chemie International Edition, Vol. 60, 25, P. 14154–14162
Jurgeleit, Ramona and Grimm-Lebsanft, Benjamin and Flöser, Benedikt Maria and Teubner, Melissa and **Buchenau, Sören** and Senft, Laura and Hoffmann, Jonas and Naumova, Maria and Näther, Christian and Ivanović-Burmazović, Ivana and others

November 2020 *Photoinduced Metastable dd-Exciton-Driven Metal-Insulator Transitions in Quasi-One-Dimensional Transition Metal Oxides*
Communications Physics, Vol. 3, 1, P. 1–9
Asmara, Teguh Citra and Lichtenberg, Frank and Biebl, Florian and Zhu, Tao and Das, Pranab Kumar and Naradipa, Muhammad Avicenna and Fauzi, Angga Dito and Diao, Caozheng and Yang, Ping and Lenzen, Philipp and **Buchenau, Sören** and others

June 2020 *Temperature and Magnetic Field Dependent Raman Study of Electron-Phonon Interactions in Thin Films of Bi_2Se_3 and Bi_2Te_3 Nanoflakes*
Physical Review B, Vol. 101, 24, P. 245431
Buchenau, Sören and Scheitz, Sarah and Sethi, Astha and Slimak, John E and Glier, Tomke Eva and Das, Pranab Kumar and Dankwort, Torben and Akinsinde, Lewis and Kienle, Lorenz and Rusydi, Andrivo and others

June 2020 *Exceptional Substrate Diversity in Oxygenation Reactions Catalyzed by a Bis(μ-oxo) Copper Complex*
Chemistry–A European Journal, Vol. 26, 34, P. 7556–7562
Paul, Melanie and Teubner, Melissa and Grimm-Lebsanft, Benjamin and Golchert, Christiane and Meiners, Yannick and Senft, Laura and Keisers, Kristina and Liebhäuser, Patricia and Rösener, Thomas and Biebl, Florian and **Buchenau, Sören** and others

September 2019 *Quantum Confinement Induced Excitonic Mechanism in Zinc-Oxide-Nanowalled Microrod Arrays for UV–Vis Surface-Enhanced Raman Scattering*
The Journal of Physical Chemistry C, Vol. 123, 40, P. 24957–24962

Kim, Jayeong and Glier, Tomke E and Grimm-Lebsanft, Benjamin and **Buchenau, Sören** and Teubner, Melissa and Biebl, Florian and Kim, Nam-Jung and Kim, Heehun and Yi, Gyu-Chul and Rübhausen, Michael and others

August 2018 *On the Metal Cooperativity in a Dinuclear Copper–Guanidine Complex for Aliphatic C-H Bond Cleavage by Dioxygen*
Chemistry–A European Journal, Vol. 25, 48, P. 11257–11268
Schön, Florian and Biebl, Florian and Greb, Lutz and Leingang, Simone and Grimm-Lebsanft, Benjamin and Teubner, Melissa and **Buchenau, Sören** and Kaifer, Elisabeth and Rübhausen, Michael A and Himmel, Hans-Jörg

July 2018 *Scalable Polyol Synthesis for Few Quintuple Layer Thin and Ultra High Aspect Ratio Bi_2Se_3 Structures*
Solid State Communications, Vol. 281, P. 49–52
Buchenau, Sören and Akinsinde, Lewis Olaniyi and Zocher, Michael and Rukser, Dieter and Schürmann, Ulrich and Kienle, Lorenz and Grimm-Lebsanft, Benjamin and Rübhausen, Michael

January 2017 *Symmetry Breaking of the Surface Mediated Quantum Hall Effect in Bi_2Se_3 Nanoplates using Fe_3O_4 substrates*
2D Materials, Vol. 4, 1, P. 15044
Buchenau, Sören and Sergelius, Philip and Wiegand, Christoph and Zierold, Robert and Shin, Ho Sun and Rübhausen, Michael and Gooth, Johannes and Nielsch, Kornelius and others

Bibliography

[1] Edward I Solomon et al. "Electronic structures of metal sites in proteins and models: contributions to function in blue copper proteins". In: *Chemical reviews* 104.2 (2004), pp. 419–458.

[2] Margarita Kanteev, Mor Goldfeder, and Ayelet Fishman. "Structure–function correlations in tyrosinases". In: *Protein Science* 24.9 (2015), pp. 1360–1369.

[3] Wei Cao et al. "Unraveling the structure and function of melanin through synthesis". In: *Journal of the American Chemical Society* 143.7 (2021), pp. 2622–2637.

[4] Henry Stanley Raper. "The tyrosinase-tyrosine reaction: production from tyrosine of 5: 6-dihydroxyindole and 5: 6-dihydroxyindole-2-carboxylic acid - the precursors of melanin". In: *Biochemical Journal* 21.1 (1927), p. 89.

[5] Qing Zhe Ni et al. "Chemoenzymatic elaboration of the Raper–Mason pathway unravels the structural diversity within eumelanin pigments". In: *Chemical science* 11.30 (2020), pp. 7836–7841.

[6] Greta Faccio et al. "Bacterial tyrosinases and their applications". In: *Process Biochemistry* 47.12 (2012), pp. 1749–1760.

[7] Peter MH Kroneck and Martha E Sosa Torres. *Sustaining life on planet earth: Metalloenzymes mastering dioxygen and other chewy gases*. Springer, 2015.

[8] Raquel L Lieberman and Amy C Rosenzweig. "Biological methane oxidation: regulation, biochemistry, and active site structure of particulate methane monooxygenase". In: *Critical reviews in biochemistry and molecular biology* 39.3 (2004), pp. 147–164.

[9] Rahul Banerjee, Jason C Jones, and John D Lipscomb. "Soluble methane monooxygenase". In: *Annual review of biochemistry* 88 (2019), pp. 409–431.

[10] Manoj Ravi, Marco Ranocchiari, and Jeroen A van Bokhoven. "The direct catalytic oxidation of methane to methanol—A critical assessment". In: *Angewandte Chemie International Edition* 56.52 (2017), pp. 16464–16483.

[11] Anders Holmen. "Direct conversion of methane to fuels and chemicals". In: *Catalysis Today* 142.1-2 (2009), pp. 2–8.

[12] Kenneth D Karlin et al. "Copper-mediated hydroxylation of an arene: model system for the action of copper monooxygenases. Structures of a binuclear copper (I) complex and its oxygenated product". In: *Journal of the American Chemical Society* 106.7 (1984), pp. 2121–2128.

[13] Laura Santagostini et al. "Reversible dioxygen binding and phenol oxygenation in a tyrosinase model system." In: *Chemistry (Weinheim an der Bergstrasse, Germany)* 6.3 (2000), pp. 519–522.

[14] Shinobu Itoh et al. "Oxygenation of phenols to catechols by a (μ-η2: η2-peroxo) dicopper (II) complex: mechanistic insight into the phenolase activity of tyrosinase". In: *Journal of the American Chemical Society* 123.27 (2001), pp. 6708–6709.

[15] Giuseppe Battaini et al. "Tyrosinase-catalyzed oxidation of fluorophenols". In: *Journal of Biological Chemistry* 277.47 (2002), pp. 44606–44612.

[16] Malte Rolff et al. "The first catalytic tyrosinase model system based on a mononuclear copper (I) complex: kinetics and mechanism". In: *Angewandte Chemie International Edition* 49.36 (2010), pp. 6438–6442.

[17] Cooper Citek et al. "Self-assembly of the oxy-tyrosinase core and the fundamental components of phenolic hydroxylation". In: *Nature Chemistry* 4.4 (2012), pp. 317–322.

[18] Alexander Hoffmann et al. "Catalytic phenol hydroxylation with dioxygen: extension of the tyrosinase mechanism beyond the protein matrix". In: *Angewandte Chemie International Edition* 52.20 (2013), pp. 5398–5401.

[19] Claudia Wilfer et al. "Efficient biomimetic hydroxylation catalysis with a bis (pyrazolyl) imidazolylmethane copper peroxide complex". In: *Chemistry–A European Journal* 21.49 (2015), pp. 17639–17649.

[20] Liviu M Mirica et al. "Tyrosinase reactivity in a model complex: an alternative hydroxylation mechanism". In: *Science* 308.5730 (2005), pp. 1890–1892.

[21] Liviu M Mirica et al. "μ-η2: η2-Peroxodicopper (II) complex with a secondary diamine ligand: a functional model of tyrosinase". In: *Journal of the American Chemical Society* 128.8 (2006), pp. 2654–2665.

[22] Adam P Cole et al. "Bis (μ-oxo) dicopper (III) complexes of a homologous series of simple peralkylated 1, 2-diamines: Steric modulation of structure, stability, and reactivity". In: *Inorganic chemistry* 44.21 (2005), pp. 7345–7364.

[23] Sonja Herres-Pawlis et al. "Phenolate hydroxylation in a bis (μ-oxo) dicopper (III) complex: lessons from the guanidine/amine series". In: *Journal of the American Chemical Society* 131.3 (2009), pp. 1154–1169.

[24] Sonja Herres-Pawlis et al. "Formation of Hybrid Guanidine-Stabilized Bis (μ-oxo) dicopper Cores in Solution: Electronic and Steric Perturbations". In: *European journal of inorganic chemistry* 2015.32 (2015), pp. 5426–5436.

[25] Marijke H Groothaert et al. "Selective oxidation of methane by the bis (μ-oxo) dicopper core stabilized on ZSM-5 and mordenite zeolites". In: *Journal of the American Chemical Society* 127.5 (2005), pp. 1394–1395.

[26] Pieter Vanelderen et al. "Coordination chemistry and reactivity of copper in zeolites". In: *Coordination Chemistry Reviews* 257.2 (2013), pp. 483–494.

[27] Pieter Vanelderen et al. "Cu-ZSM-5: A biomimetic inorganic model for methane oxidation". In: *Journal of catalysis* 284.2 (2011), pp. 157–164.

[28] Edward I Solomon et al. "Copper dioxygen (bio) inorganic chemistry". In: *Faraday discussions* 148 (2011), pp. 11–39.

[29] Christopher W Koo and Amy C Rosenzweig. "Biochemistry of aerobic biological methane oxidation". In: *Chemical Society Reviews* 50.5 (2021), pp. 3424–3436.

[30] Matthew O Ross et al. "Particulate methane monooxygenase contains only mononuclear copper centers". In: *Science* 364.6440 (2019), pp. 566–570.

[31] Hyun Jin Kim et al. "Biological conversion of methane to methanol through genetic reassembly of native catalytic domains". In: *Nature Catalysis* 2.4 (2019), pp. 342–353.

[32] Jung Yoon Lee and Kenneth D Karlin. "Elaboration of copper–oxygen mediated C–H activation chemistry in consideration of future fuel and feedstock generation". In: *Current opinion in chemical biology* 25 (2015), pp. 184–193.

[33] Richa Sharma et al. "Approaches for selective oxidation of methane to methanol". In: *Catalysts* 10.2 (2020), p. 194.

[34] Soo Y Ro et al. "Native top-down mass spectrometry provides insights into the copper centers of membrane-bound methane monooxygenase". In: *Nature communications* 10.1 (2019), pp. 1–12.

[35] Lili Cao et al. "Quantum refinement does not support dinuclear copper sites in crystal structures of particulate methane monooxygenase". In: *Angewandte Chemie International Edition* 57.1 (2018), pp. 162–166.

[36] Benjamin ER Snyder et al. "Iron and copper active sites in zeolites and their correlation to metalloenzymes". In: *Chemical reviews* 118.5 (2017), pp. 2718–2768.

[37] Peter Haack and Christian Limberg. "Molecular CuII-O-CuII Complexes: Still Waters Run Deep". In: *Angewandte Chemie International Edition* 53.17 (2014), pp. 4282–4293.

[38] Mayuko Miyanishi et al. "Role of amino acid residues for dioxygen activation in the second coordination sphere of the dicopper site of pMMO". In: *Inorganic chemistry* 58.18 (2019), pp. 12280–12288.

[39] Vincent C-C Wang et al. "Alkane oxidation: methane monooxygenases, related enzymes, and their biomimetics". In: *Chemical reviews* 117.13 (2017), pp. 8574–8621.

[40] Sunney I Chan et al. "Efficient oxidation of methane to methanol by dioxygen mediated by tricopper clusters". In: *Angewandte Chemie International Edition* 52.13 (2013), pp. 3731–3735.

[41] Steven G Bratsch. "Standard electrode potentials and temperature coefficients in water at 298.15 K". In: *Journal of Physical and Chemical Reference Data* 18.1 (1989), pp. 1–21.

[42] David B Rorabacher. "Electron transfer by copper centers". In: *Chemical Reviews* 104.2 (2004), pp. 651–698.

[43] Harry B Gray, Bo G Malmström, and RJP Williams. "Copper coordination in blue proteins". In: *JBIC Journal of Biological Inorganic Chemistry* 5.5 (2000), pp. 551–559.

[44] Peter Comba. "Coordination compounds in the entatic state". In: *Coordination Chemistry Reviews* 200 (2000), pp. 217–245.

[45] Bert L Vallee and RtJ Williams. "Metalloenzymes: the entatic nature of their active sites." In: *Proceedings of the National Academy of Sciences of the United States of America* 59.2 (1968), p. 498.

[46] Gezahegn Chaka et al. "A definitive example of a geometric "entatic state" effect: Electron-transfer kinetics for a Copper (II/I) complex involving a quinquedentate macrocyclic trithiaether- bipyridine ligand". In: *Journal of the American Chemical Society* 129.16 (2007), pp. 5217–5227.

[47] Julia Stanek, Alexander Hoffmann, and Sonja Herres-Pawlis. "Renaissance of the entatic state principle". In: *Coordination Chemistry Reviews* 365 (2018), pp. 103–121.

[48] Lei Yang, Douglas R Powell, and Robert P Houser. "Structural variation in copper (I) complexes with pyridylmethylamide ligands: structural analysis with a new four-coordinate geometry index, τ 4". In: *Dalton Transactions* 9 (2007), pp. 955–964.

[49] VA Serebryakov et al. "Medical applications of mid-IR lasers. Problems and prospects". In: *Journal of Optical Technology* 77.1 (2010), pp. 6–17.

[50] HHP Th Bekman et al. "Development of a mid-infrared laser for study of infrared countermeasures techniques". In: *Technologies for optical countermeasures*. Vol. 5615. International Society for Optics and Photonics. 2004, pp. 27–38.

[51] A Fried et al. "Laboratory, ground-based, and airborne tunable diode laser systems: performance characteristics and applications in atmospheric studies". In: *Applied Physics B* 67.3 (1998), pp. 317–330.

[52] C Bauer et al. "Potentials and limits of mid-infrared laser spectroscopy for the detection of explosives". In: *Applied Physics B* 92.3 (2008), pp. 327–333.

[53] Alexander Hoffmann et al. "Implications of Guanidine Substitution on Copper Complexes as Entatic-State Models". In: *European Journal of Inorganic Chemistry* 2016.29 (2016), pp. 4731–4743.

[54] Julia Stanek et al. "Copper Guanidinoquinoline Complexes as Entatic State Models of Electron-Transfer Proteins". In: *Chemistry–A European Journal* 23.62 (2017), pp. 15738–15745.

[55] Alexander Hoffmann et al. "Catching an entatic state—a pair of copper complexes". In: *Angewandte Chemie International Edition* 53.1 (2014), pp. 299–304.

[56] B Dicke et al. "Transferring the entatic-state principle to copper photochemistry". In: *Nature chemistry* 10.3 (2018), pp. 355–362.

[57] Tobia F Nova et al. "Controlling coherent energy flow between collective THz excitations in condensed matter". In: *International Conference on Ultrafast Phenomena*. Optical Society of America. 2014, 07–Mon.

[58] Tobias Kampfrath, Koichiro Tanaka, and Keith A Nelson. "Resonant and nonresonant control over matter and light by intense terahertz transients". In: *Nature Photonics* 7.9 (2013), pp. 680–690.

[59] H Okamoto et al. "Photoinduced metallic state mediated by spin-charge separation in a one-dimensional organic Mott insulator". In: *Physical review letters* 98.3 (2007), p. 037401.

[60] H Ehrke et al. "Photoinduced melting of antiferromagnetic order in La 0.5 Sr 1.5 MnO 4 measured using ultrafast resonant soft X-ray diffraction". In: *Physical review letters* 106.21 (2011), p. 217401.

[61] Alexander von Hoegen et al. "Probing the interatomic potential of solids with strong-field nonlinear phononics". In: *Nature* 555.7694 (2018), pp. 79–82.

[62] Jeff Hecht. "A short history of laser development". In: *Applied optics* 49.25 (2010), F99–F122.

[63] Arthur L Robinson. "History of synchrotron radiation". In: *Synchrotron Radiation News* 28.4 (2015), pp. 4–9.

[64] Adolf Smekal. "Zur quantentheorie der dispersion". In: *Naturwissenschaften* 11.43 (1923), pp. 873–875.

[65] Chandrasekhara Venkata Raman. "A new radiation". In: *Indian Journal of physics* 2 (1928), pp. 387–398.

[66] D Gerald. *Mahan, Many-Particle Physics*. 2000.

[67] B Schulz et al. "Fully reflective deep ultraviolet to near infrared spectrometer and entrance optics for resonance Raman spectroscopy". In: *Review of scientific instruments* 76.7 (2005), p. 097203.

[68] Arisato Kawabata. "Green Function Theory of Raman Scattering". In: *Journal of the Physical Society of Japan* 30.1 (1971), pp. 68–85.

[69] Richard D Mattuck. *A guide to Feynman diagrams in the many-body problem*. Courier Corporation, 1992.

[70] Cristian Manzoni and Giulio Cerullo. "Design criteria for ultrafast optical parametric amplifiers". In: *Journal of Optics* 18.10 (2016), p. 103501.

[71] Paul N Butcher and David Cotter. *The elements of nonlinear optics*. 9. Cambridge university press, 1990.

[72] Robert W Boyd. *Nonlinear optics*. Academic press, 2020.

[73] David S Hum and Martin M Fejer. "Quasi-phasematching". In: *Comptes Rendus Physique* 8.2 (2007), pp. 180–198.

[74] Irina T Sorokina and Konstantin L Vodopyanov. *Solid-state mid-infrared laser sources*. Vol. 89. Springer Science & Business Media, 2003.

[75] G Boyd, H Kasper, and J McFee. "Linear and nonlinear optical properties of AgGaS 2, CuGaS 2, and CuInS 2, and theory of the wedge technique for the measurement of nonlinear coefficients". In: *IEEE Journal of Quantum Electronics* 7.12 (1971), pp. 563–573.

[76] Gopal C Bhar. "Refractive index interpolation in phase-matching". In: *Applied optics* 15.2 (1976), 305_1–307.

[77] Grant Bunker. *Introduction to XAFS: a practical guide to X-ray absorption fine structure spectroscopy*. Cambridge University Press, 2010.

[78] Susan E Shadle et al. "X-ray absorption spectroscopic studies of the blue copper site: metal and ligand K-edge studies to probe the origin of the EPR hyperfine splitting in plastocyanin". In: *Journal of the American Chemical Society* 115.2 (1993), pp. 767–776.

[79] Edward I Solomon and Ryan G Hadt. "Recent advances in understanding blue copper proteins". In: *Coordination Chemistry Reviews* 255.7-8 (2011), 774–789.

[80] Jennifer L DuBois et al. "A systematic K-edge X-ray absorption spectroscopic study of Cu (III) sites". In: *Journal of the American Chemical Society* 122.24 (2000), pp. 5775–5787.

[81] Jeroen A Van Bokhoven and Carlo Lamberti. *X-ray absorption and X-ray emission spectroscopy: theory and applications*. Vol. 1. John Wiley & Sons, 2016.

[82] John J Rehr and Robert C Albers. "Theoretical approaches to x-ray absorption fine structure". In: *Reviews of modern physics* 72.3 (2000), p. 621.

[83] Scott Calvin. *XAFS for Everyone*. CRC press, 2013.

[84] Martin Rohrmüller et al. "Bis-μ-Oxo and μ-η2: η2-peroxo dicopper complexes studied within (time-dependent) density-functional and many-body perturbation theory". In: *Journal of Computational Chemistry* 34.12 (2013), pp. 1035–1045.

[85] Karl F Renk. "Laser principle". In: *Basics of Laser Physics*. Springer, 2012, 17–41.

[86] AW Tucker et al. "Stimulated-emission cross section at 1064 and 1342 nm in Nd: YVO4". In: *Journal of Applied Physics* 48.12 (1977), pp. 4907–4911.

[87] JT Lin, JL Montgomery, and K Kato. "Temperature-tuned noncritically phase-matched frequency conversion in LiB3O5 crystal". In: *Optics Communications* 80.2 (1990), pp. 159–165.

[88] HW Lo and A Compaan. "Raman measurement of lattice temperature during pulsed laser heating of silicon". In: *Physical Review Letters* 44.24 (1980), p. 1604.

[89] Chuangtian Chen et al. "A New-Type Ultraviolet SHG Crystal——β-BaB 2 O 4". In: *Science in China Series B-Chemistry, Biological, Agricultural, Medical & Earth Sciences* 28.3 (1985), pp. 235–243.

[90] DN Nikogosyan. "Beta barium borate (BBO)". In: *Applied Physics A* 52.6 (1991), pp. 359–368.

[91] RR Alfano and SL Shapiro. "Emission in the region 4000 to 7000 Å via four-photon coupling in glass". In: *Physical Review Letters* 24.11 (1970), p. 584.

[92] Alexander L Gaeta. "Catastrophic collapse of ultrashort pulses". In: *Physical Review Letters* 84.16 (2000), p. 3582.

[93] Anne-Laure Calendron et al. "White-light generation with sub-ps pulses". In: *Optics express* 23.11 (2015), pp. 13866–13879.

[94] L Bergé et al. "Ultrashort filaments of light in weakly ionized, optically transparent media". In: *Reports on progress in physics* 70.10 (2007), p. 1633.

[95] Xiaowei Chen et al. "Pulse self-compression in normally dispersive bulk media". In: *Optics communications* 259.1 (2006), pp. 331–335.

[96] Maximilian Bradler, Peter Baum, and Eberhard Riedle. "Femtosecond continuum generation in bulk laser host materials with sub-μJ pump pulses". In: *Applied Physics B* 97.3 (2009), pp. 561–574.

[97] AS Pine. "Doppler-limited molecular spectroscopy by difference-frequency mixing". In: *JOSA* 64.12 (1974), pp. 1683–1690.

[98] DS Chemla et al. "Silver thiogallate, a new material with potential for infrared devices". In: *Optics Communications* 3.1 (1971), pp. 29–31.

[99] EC Cheung, Karl Koch, and Gerald T Moore. "Silver thiogallate, singly resonant optical parametric oscillator pumped by a continuous-wave mode-locked Nd: YAG laser". In: *Optics letters* 19.9 (1994), pp. 631–633.

[100] Wolfgang A Caliebe et al. "High-flux XAFS-beamline P64 at PETRA III". In: *AIP Conference Proceedings*. Vol. 2054. 1. AIP Publishing LLC. 2019, p. 060031.

[101] Edmund Welter et al. "A beamline for bulk sample x-ray absorption spectroscopy at the high brilliance storage ring PETRA III". In: *AIP Conference Proceedings*. Vol. 2054. 1. AIP Publishing LLC. 2019, p. 040002.

[102] Gopal Shenoy. "Basic characteristics of synchrotron radiation". In: *Structural Chemistry* 14.1 (2003), pp. 3–14.

[103] Bruce Ravel and MATHENA Newville. "ATHENA, ARTEMIS, HEPHAESTUS: data analysis for X-ray absorption spectroscopy using IFEFFIT". In: *Journal of synchrotron radiation* 12.4 (2005), pp. 537–541.

[104] B Grimm-Lebsanft et al. "A cryostat for low temperature resonance Raman measurements on operando oxygenated bioinorganic model complexes". In: *Inorganica Chimica Acta* 481 (2018), pp. 176–180.

[105] Markus Schatz et al. "Combined Spectroscopic and Theoretical Evidence for a Persistent End-On Copper Superoxo Complex". In: *Angewandte Chemie International Edition* 43.33 (2004), pp. 4360–4363.

[106] Christian Würtele et al. "Kristallographische Charakterisierung eines synthetischen 1: 1-End-on-Kupferdisauerstoff-Adduktkomplexes". In: *Angewandte Chemie* 118.23 (2006), pp. 3951–3954.

[107] Florian Schön et al. "On the Metal Cooperativity in a Dinuclear Copper–Guanidine Complex for Aliphatic C-H Bond Cleavage by Dioxygen". In: *Chemistry–A European Journal* 25.48 (2019), pp. 11257–11268.

[108] Marius Réglier, Catherine Jorand, and Bernard Waegell. "Binuclear copper complex model of tyrosinase". In: *Journal of the Chemical Society, Chemical Communications* 24 (1990), pp. 1752–1755.

[109] Luigi Casella et al. "A tyrosinase model system. Phenol ortho-hydroxylation by a binuclear three-coordinate copper (I) complex and dioxygen". In: *Journal of the Chemical Society, Chemical Communications* 22 (1991), pp. 1611–1612.

[110] Kenneth Virgel N Esguerra, Yacoub Fall, and Jean-Philip Lumb. "A biomimetic catalytic aerobic functionalization of phenols". In: *Angewandte Chemie* 126.23 (2014), pp. 5987–5991.

[111] Melanie Paul et al. "Exceptional Substrate Diversity in Oxygenation Reactions Catalyzed by a Bis (μ-oxo) Copper Complex". In: *Chemistry (Weinheim an der Bergstrasse, Germany)* 26.34 (2020), p. 7556.

[112] Jorge Manzur et al. "Synthesis and magnetostructural characterization of dinuclear copper (II) complexes with the diazine ligand, 3, 6-bis (di-2-pyridylmethyl) pyridazine". In: *Journal of the Chemical Society, Dalton Transactions* 6 (1993), pp. 905–911.

[113] Amy M Barrios and Stephen J Lippard. "Amide hydrolysis effected by a hydroxo-bridged dinickel (II) complex: insights into the mechanism of urease". In: *Journal of the American Chemical Society* 121.50 (1999), pp. 11751–11757.

[114] Geoffrey Davies, Mohamed A El-Sayed, and Maher Henary. "Stoichiometry and kinetics of low-temperature oxidation of di-. mu.-chlorobis (N, N, N′, N′-tetraethylethylenediamine) dicopper by dioxygen in methylene chloride and properties of the peroxocopper products". In: *Inorganic Chemistry* 26.20 (1987), pp. 3266–3273.

[115] Julia S Woertink et al. "A [Cu2O] 2+ core in Cu-ZSM-5, the active site in the oxidation of methane to methanol". In: *Proceedings of the National Academy of Sciences* 106.45 (2009), pp. 18908–18913.

[116] Peter Haack et al. "Access to a CuII–O–CuII motif: spectroscopic properties, solution structure, and reactivity". In: *Journal of the American Chemical Society* 135.43 (2013), pp. 16148–16160.

[117] Melvyn Rowen Churchill et al. "Crystal and molecular structure of bis (. mu.-bromo) bis (N, N, N′, N′-tetraethylethylenediamine) dicopper (I) and the kinetics of its oxidation by dioxygen in nitrobenzene". In: *Inorganic Chemistry* 23.6 (1984), pp. 783–787.

[118] Mohamed A El-Sayed, Ahmed El-Toukhy, and Geoffrey Davies. "Stoichiometry and kinetics of oxidation of dimeric bis (. mu.-halo)-bis-((diamine) copper (I)) complexes L2Cu2X2 by dioxygen in aprotic solvents". In: *Inorganic Chemistry* 24.21 (1985), pp. 3387–3390.

[119] Ramona Jurgeleit et al. "Catalytic Oxygenation of Hydrocarbons by Mono-μ-oxo Dicopper (II) Species Resulting from O- O Cleavage of Tetranuclear CuI/CuII Peroxo Complexes". In: *Angewandte Chemie International Edition* (2021).

[120] Melanie Paul et al. "Influence of the amine donor on hybrid guanidine-stabilized bis (μ-oxido) dicopper (III) complexes and their tyrosinase-like oxygenation activity towards polycyclic aromatic alcohols". In: *Journal of Inorganic Biochemistry* 224 (2021), p. 111541.

[121] B Göran Karlsson et al. "Rack-induced bonding in blue copper proteins: Spectroscopic properties and reduction potential of the azurin mutant Met-121→ Leu". In: *FEBS letters* 253.1-2 (1989), pp. 99–102.

[122] Peter Comba and Wolfgang Schiek. "Fit and misfit between ligands and metal ions". In: *Coordination chemistry reviews* 238 (2003), pp. 21–29.

[123] Boping Xie, Lon J Wilson, and David M Stanbury. "Cross-electron-transfer reactions of the [CuII/I (bite)] 2+/+ redox couple". In: *Inorganic Chemistry* 40.14 (2001), pp. 3606–3614.

[124] Julia Stanek et al. "Influence of Functionalized Substituents on the Electron-Transfer Abilities of Copper Guanidinoquinoline Complexes". In: *European Journal of Inorganic Chemistry* 2018.46 (2018), pp. 4997–5006.

[125] Eric W Dahl and Nathaniel K Szymczak. "Hydrogen Bonds Dictate the Coordination Geometry of Copper: Characterization of a Square-Planar Copper (I) Complex". In: *Angewandte Chemie* 128.9 (2016), pp. 3153–3157.

[126] Lung Shan Kau et al. "X-ray absorption edge determination of the oxidation state and coordination number of copper. Application to the type 3 site in Rhus vernicifera laccase and its reaction with oxygen". In: *Journal of the American Chemical Society* 109.21 (1987), pp. 6433–6442.

[127] James E Hahn et al. "Observation of an electric quadrupole transition in the X-ray absorption spectrum of a Cu (II) complex". In: *Chemical Physics Letters* 88.6 (1982), pp. 595–598.

[128] Joshua Heck et al. "Manipulating electron transfer–the influence of substituents on novel copper guanidine quinolinyl complexes". In: *Chemical Science* (2022).

[129] Frank Lichtenberg. "Carpy-Galy phases $A_nB_nO_{3n+2}$=ABO_x: General overview, properties, special and hypothetical systems, and melt-grown synthesis of A- and O-deficient n=5 types such as $Sr_{19}Nb_{19}WO_{66}$ and $Sr_{17}Ca_2Nb_{19}WO_{64}$ and n=6 type $Ln_6Ti_4Fe_2O_{20}$ and $Ca_6Nb_5FeO_{20}$". In: *ETH Research Collection* (2020). DOI: 10.3929/ethz-b-000424221.

[130] S Bahrs et al. "Anisotropic ultraviolet Raman resonance in underdoped Y Ba 2 Cu 3 O 6.7". In: *Physical Review B* 74.2 (2006), p. 024519.

[131] Joakim Bäckström et al. "Raman scattering in YBa 2 Cu 4 O 8 and PrBa 2 Cu 4 O 8: Indications of pseudogap effects in nonsuperconducting PrBa 2 Cu 4 O 8". In: *Physical Review B* 61.10 (2000), p. 7049.

[132] Andrivo Rusydi et al. "Experimental observation of the crystallization of a paired holon state". In: *Physical review letters* 105.2 (2010), p. 026402.

[133] YF Lu et al. "Zero-gap semiconductor to excitonic insulator transition in Ta2NiSe5". In: *Nature communications* 8.1 (2017), pp. 1–7.

[134] Anshul Kogar et al. "Signatures of exciton condensation in a transition metal dichalcogenide". In: *Science* 358.6368 (2017), pp. 1314–1317.

[135] Teguh Citra Asmara et al. "Photoinduced metastable dd-exciton-driven metal-insulator transitions in quasi-one-dimensional transition metal oxides". In: *Communications Physics* 3.1 (2020), pp. 1–9.

[136] Aleksandr Sergeevich Davydov. "The theory of molecular excitons". In: *Soviet Physics Uspekhi* 7.2 (1964), p. 145.

[137] RJ Nemanich, G Lucovsky, and SA Solin. "Infrared active optical vibrations of graphite". In: *Solid State Communications* 23.2 (1977), pp. 117–120.

[138] Andrea C Ferrari and Denis M Basko. "Raman spectroscopy as a versatile tool for studying the properties of graphene". In: *Nature nanotechnology* 8.4 (2013), pp. 235–246.

[139] LM Malard et al. "Raman spectroscopy in graphene". In: *Physics reports* 473.5-6 (2009), pp. 51–87.

[140] Stephanie Reich and Christian Thomsen. "Raman spectroscopy of graphite". In: *Philosophical Transactions of the Royal Society of London. Series A: Mathematical, Physical and Engineering Sciences* 362.1824 (2004), pp. 2271–2288.

[141] Isabella Gierz et al. "Phonon-pump extreme-ultraviolet-photoemission probe in graphene: Anomalous heating of Dirac carriers by lattice deformation". In: *Physical Review Letters* 114.12 (2015), p. 125503.

[142] Sören Buchenau et al. "Symmetry breaking of the surface mediated quantum Hall Effect in Bi2Se3 nanoplates using Fe3O4 substrates". In: *2D Materials* 4.1 (2017), p. 015044.

[143] Sören Buchenau et al. "Scalable polyol synthesis for few quintuple layer thin and ultra high aspect ratio Bi2Se3 structures". In: *Solid State Communications* 281 (2018), pp. 49–52.

[144] Sören Buchenau et al. "Temperature and magnetic field dependent Raman study of electron-phonon interactions in thin films of Bi 2 Se 3 and Bi 2 Te 3 nanoflakes". In: *Physical Review B* 101.24 (2020), p. 245431.

[145] Jayeong Kim et al. "Quantum Confinement Induced Excitonic Mechanism in Zinc-Oxide-Nanowalled Microrod Arrays for UV–Vis Surface-Enhanced Raman Scattering". In: *The Journal of Physical Chemistry C* 123.40 (2019), pp. 24957–24962.